

ADVANCES IN POLYMER SCIENCE

239

Volume Editor G. Heinrich

# Advanced Rubber Composites

 Springer

**Editorial Board:**

**A. Abe · A.-C. Albertsson · K. Dušek · J. Genzer  
W.H. de Jeu · H.-H. Kausch · S. Kobayashi · K.-S. Lee  
L. Leibler · T.E. Long · I. Manners · M. Möller  
E.M. Terentjev · M. Vicent · B. Voit · G. Wegner  
U. Wiesner**

# Advances in Polymer Science

Recently Published and Forthcoming Volumes

## **Advanced Rubber Composites**

Volume Editor: Heinrich, G.

Vol. 239, 2011

## **Polymer Thermodynamics**

Volume Editors: Enders, S., Wolf, B.A.

Vol. 238, 2011

## **Enzymatic Polymerisation**

Volume Editors: Palmans, A.R.A., Heise, A.

Vol. 237, 2010

## **High Solid Dispersion**

Volume Editor: Cloitre, M.

Vol. 236, 2010

## **Silicon Polymers**

Volume Editor: Muzafarov, A.

Vol. 235, 2011

## **Chemical Design of Responsive Microgels**

Volume Editors: Pich, A., Richtering, W.

Vol. 234, 2010

## **Hybrid Latex Particles – Preparation with Emulsion**

Volume Editors: van Herk, A.M.,

Landfester, K.

Vol. 233, 2010

## **Biopolymers**

Volume Editors: Abe, A., Dušek, K.,

Kobayashi, S.

Vol. 232, 2010

## **Polymer Materials**

Volume Editors: Lee, K.-S., Kobayashi, S.

Vol. 231, 2010

## **Polymer Characterization**

Volume Editors: Dušek, K., Joanny, J.-F.

Vol. 230, 2010

## **Modern Techniques for Nano- and Microreactors/-reactions**

Volume Editor: Caruso, F.

Vol. 229, 2010

## **Complex Macromolecular Systems II**

Volume Editors: Müller, A.H.E.,

Schmidt, H.-W.

Vol. 228, 2010

## **Complex Macromolecular Systems I**

Volume Editors: Müller, A.H.E.,

Schmidt, H.-W.

Vol. 227, 2010

## **Shape-Memory Polymers**

Volume Editor: Lendlein, A.

Vol. 226, 2010

## **Polymer Libraries**

Volume Editors: Meier, M.A.R., Webster, D.C.

Vol. 225, 2010

## **Polymer Membranes/Biomembranes**

Volume Editors: Meier, W.P., Knoll, W.

Vol. 224, 2010

## **Organic Electronics**

Volume Editors: Meller, G., Grasser, T.

Vol. 223, 2010

## **Inclusion Polymers**

Volume Editor: Wenz, G.

Vol. 222, 2009

## **Advanced Computer Simulation**

## **Approaches for Soft Matter Sciences III**

Volume Editors: Holm, C., Kremer, K.

Vol. 221, 2009

## **Self-Assembled Nanomaterials II**

Nanotubes

Volume Editor: Shimizu, T.

Vol. 220, 2008

## **Self-Assembled Nanomaterials I**

Nanofibers

Volume Editor: Shimizu, T.

Vol. 219, 2008

## **Interfacial Processes and Molecular Aggregation of Surfactants**

Volume Editor: Narayanan, R.

Vol. 218, 2008

## **New Frontiers in Polymer Synthesis**

Volume Editor: Kobayashi, S.

Vol. 217, 2008

## **Polymers for Fuel Cells II**

Volume Editor: Scherer, G.G.

Vol. 216, 2008

# Advanced Rubber Composites

Volume Editor: Gert Heinrich

With contributions by

G.C. Basak · M. Bhattacharya · A.K. Bhowmick · A.  
Choudhury · A. Das · R.N. Datta · W.K. Dierkes · K. Dinesh  
Kumar · J. Fritzsche · J.J. George · R. Guo · G. Heinrich ·  
R. Jurk · M.S. Khan · M. Klüppel · P.K. Maji · T. Mathew ·  
S. Mitra · K. Naskar · J.W.M. Noordermeer · W. van Ooij ·  
R. Rajesh Babu · K.W. Stöckelhuber · A.G. Talma ·  
M. Tiwari · D.-Y. Wang

 Springer

*Editor*

Prof. Gert Heinrich  
Leibniz-Institut für Polymerforschung Dresden e.V.  
Hohe Strasse 6  
01069 Dresden  
Germany  
gheinrich@ipfdd.de

ISSN 0065-3195                      e-ISSN 1436-5030  
ISBN 978-3-642-19503-7            e-ISBN 978-3-642-19504-4  
DOI 10.1007/978-3-642-19504-4  
Springer Heidelberg Dordrecht London New York

Library Control Congress Number: 2011923530

© Springer-Verlag Berlin Heidelberg 2011

This work is subject to copyright. All rights are reserved, whether the whole or part of the material is concerned, specifically the rights of translation, reprinting, reuse of illustrations, recitation, broadcasting, reproduction on microfilm or in any other way, and storage in data banks. Duplication of this publication or parts thereof is permitted only under the provisions of the German Copyright Law of September 9, 1965, in its current version, and permission for use must always be obtained from Springer. Violations are liable to prosecution under the German Copyright Law.

The use of general descriptive names, registered names, trademarks, etc. in this publication does not imply, even in the absence of a specific statement, that such names are exempt from the relevant protective laws and regulations and therefore free for general use.

*Cover design:* WMXDesign GmbH, Heidelberg

Printed on acid-free paper

Springer is part of Springer Science+Business Media ([www.springer.com](http://www.springer.com))

---

## Volume Editor

Prof. Gert Heinrich  
Leibniz-Institut für Polymerforschung  
Dresden e.V.  
Hohe Strasse 6  
01069 Dresden  
Germany  
*gheinrich@ipfdd.de*

## Editorial Board

Prof. Akihiro Abe  
Professor Emeritus  
Tokyo Institute of Technology  
6-27-12 Hiyoshi-Honcho, Kohoku-ku  
Yokohama 223-0062, Japan  
*aabe34@xc4.so-net.ne.jp*

Prof. A.-C. Albertsson  
Department of Polymer Technology  
The Royal Institute of Technology  
10044 Stockholm, Sweden  
*aila@polymer.kth.se*

Prof. Karel Dušek  
Institute of Macromolecular Chemistry  
Czech Academy of Sciences  
of the Czech Republic  
Heyrovský Sq. 2  
16206 Prague 6, Czech Republic  
*dusek@imc.cas.cz*

Prof. Jan Genzer  
Department of Chemical &  
Biomolecular Engineering  
North Carolina State University  
911 Partners Way  
27695-7905 Raleigh, North Carolina,  
USA

Prof. Dr. Wim H. de Jeu  
Polymer Science and Engineering  
University of Massachusetts  
120 Governors Drive  
Amherst MA 01003, USA  
*dejeu@mail.pse.umass.edu*

Prof. Hans-Henning Kausch  
Ecole Polytechnique Fédérale de Lausanne  
Science de Base  
Station 6  
1015 Lausanne, Switzerland  
*kausch.cully@bluewin.ch*

Prof. Shiro Kobayashi  
R & D Center for Bio-based Materials  
Kyoto Institute of Technology  
Matsugasaki, Sakyo-ku  
Kyoto 606-8585, Japan  
*kobayash@kit.ac.jp*

Prof. Kwang-Sup Lee  
Department of Advanced Materials  
Hannam University  
561-6 Jeonmin-Dong  
Yuseong-Gu 305-811  
Daejeon, South Korea  
*kslee@hnu.kr*

Prof. L. Leibler

Matière Molle et Chimie  
Ecole Supérieure de Physique  
et Chimie Industrielles (ESPCI)  
10 rue Vauquelin  
75231 Paris Cedex 05, France  
*ludwik.leibler@espci.fr*

Prof. Timothy E. Long

Department of Chemistry  
and Research Institute  
Virginia Tech  
2110 Hahn Hall (0344)  
Blacksburg, VA 24061, USA  
*telong@vt.edu*

Prof. Ian Manners

School of Chemistry  
University of Bristol  
Cantock's Close  
BS8 1TS Bristol, UK  
*ian.manners@bristol.ac.uk*

Prof. Martin Möller

Deutsches Wollforschungsinstitut  
an der RWTH Aachen e.V.  
Pauwelsstraße 8  
52056 Aachen, Germany  
*moeller@dwi.rwth-aachen.de*

Prof. E.M. Terentjev

Cavendish Laboratory  
Madingley Road  
Cambridge CB 3 0HE, UK  
*emt1000@cam.ac.uk*

Prof. Dr. Maria Jesus Vicent

Centro de Investigacion Principe Felipe  
Medicinal Chemistry Unit  
Polymer Therapeutics Laboratory  
Av. Autopista del Saler, 16  
46012 Valencia, Spain  
*mjvicent@cipf.es*

Prof. Brigitte Voit

Leibniz-Institut für Polymerforschung Dresden  
Hohe Straße 6  
01069 Dresden, Germany  
*voit@ipfdd.de*

Prof. Gerhard Wegner

Max-Planck-Institut  
für Polymerforschung  
Ackermannweg 10  
55128 Mainz, Germany  
*wegner@mpip-mainz.mpg.de*

Prof. Ulrich Wiesner

Materials Science & Engineering  
Cornell University  
329 Bard Hall  
Ithaca, NY 14853, USA  
*ubw1@cornell.edu*

---

## **Advances in Polymer Sciences Also Available Electronically**

*Advances in Polymer Sciences* is included in Springer's eBook package *Chemistry and Materials Science*. If a library does not opt for the whole package the book series may be bought on a subscription basis. Also, all back volumes are available electronically.

For all customers who have a standing order to the print version of *Advances in Polymer Sciences*, we offer free access to the electronic volumes of the Series published in the current year via SpringerLink.

If you do not have access, you can still view the table of contents of each volume and the abstract of each article by going to the SpringerLink homepage, clicking on "Browse by Online Libraries", then "Chemical Sciences", and finally choose *Advances in Polymer Science*.

You will find information about the

- Editorial Board
- Aims and Scope
- Instructions for Authors
- Sample Contribution

at [springer.com](http://springer.com) using the search function by typing in *Advances in Polymer Sciences*.

*Color figures* are published in full color in the electronic version on SpringerLink.



## Aims and Scope

The series *Advances in Polymer Science* presents critical reviews of the present and future trends in polymer and biopolymer science including chemistry, physical chemistry, physics and material science. It is addressed to all scientists at universities and in industry who wish to keep abreast of advances in the topics covered.

Review articles for the topical volumes are invited by the volume editors. As a rule, single contributions are also specially commissioned. The editors and publishers will, however, always be pleased to receive suggestions and supplementary information. Papers are accepted for *Advances in Polymer Science* in English.

In references *Advances in Polymer Sciences* is abbreviated as *Adv Polym Sci* and is cited as a journal.

Special volumes are edited by well known guest editors who invite reputed authors for the review articles in their volumes.

Impact Factor in 2009: 4.600; Section "Polymer Science": Rank 4 of 73

# Preface

It is known that at least 3,000 years before the first Europeans saw natural rubber, and the Mesoamerican communities had developed ways of collecting it and forming it into a variety of objects such as toys, domestic products, and items related to ritual sacrifice to tribute payments [1]. However, rubber became an indispensable factor of industry and of daily life after one of the effective discoveries and developments of mankind, namely the vulcanization technology in years 1839–1844 by Charles Goodyear and Thomas Hancock, i.e., the transformation of a material, which is sticky when warm and brittle when cold, to a high-deformable chemically cross-linked elastic solid. Since that time the rubber industry was established and has shown a markedly progressive development over the last period of more than 100 years. Developments in the field of synthetic elastomers have progressed so rapidly that the whole concept of rubber technology has changed several times and became adapted to changing demands from society. Currently, a larger number of activities are directed to ways to improve fuel economy, having in mind that world population is growing and the demand for transportation vehicles is increasing rapidly, especially in developing countries. One example to improve fuel economy – with respect to rubber materials – is by reducing the rolling resistance of tires. For every rotation of a tire, it consumes energy as it deforms going through the footprint area in contact with the road surface. Under the condition that other tire properties such as wear, abrasion, and wet skid properties will not fail, this goal can be reached to a large extent by the development of new tire tread rubbers.

In order to produce high-performance elastomeric materials, the incorporations of different types of nanoparticles such as layered silicates, layered double hydroxides, carbon nanotubes, and nanosilica into the elastomer matrix are now growing areas of rubber research. However, the reflection of the “nano effect” on the properties and performance can be realized only through a uniform and homogeneous good dispersion of filler particles in the rubber matrix.

Furthermore, another advantage of nanofillers is not only to reinforce the rubber matrix but also to impart a number of other properties such as barrier properties, flammability resistance, electrical/electronic and membrane properties, and polymer blend compatibility. In spite of tremendous research activities in the field of polymer nanocomposites during the last two decades, elastomeric nanocomposites

are still in a stage of infancy as far as their application is concerned. The major challenge in this regard is the replacement of carbon black and silica which are mostly used in bulk amount in rubber compositions by a small amount of nanofillers to achieve desirable combination of properties. Corresponding recent research activities are described in the contributions of Bhowmick et al. and Das et al. within the prevailing volume about Advanced Rubber Composites. In both contributions, the reader finds also useful information about how the emergence of advanced characterizing techniques has facilitated the present surge in the field of rubber nanotechnology. Insightful research has combined the advances in diverse disciplines to elucidate the structure–property bonhomie in polymer nanocomposites. Developments in synthesis and processing have enabled formation and monitoring of engineered nanoassemblies, while giant steps in analytical techniques such as microscopy and diffraction studies have enabled the precise determination of structural evolution across various length scales in the rubber material.

The contribution of Noordermeer et al. reports about progress how plasma polymerization of acetylene, thiophene, and pyrrole is used to modify the polar nature of silica and carbon black powders as reinforcing fillers for rubber. Silica turns out to be very easy to modify with plasma polymerization because of its reactive surface containing a large amount of siloxane and silanol species. These research activities are straightforward directed to “green tires” because the potential advantages of silane-coupled silicas for reducing rolling resistance in high-performance passenger car tire treads were demonstrated in tire results since approximately 15 years.

The contribution of Babu and Naskar gives a comprehensive overview on the recent developments of the thermoplastic vulcanizates (TPVs) with special reference to the technological advancement. TPVs combine high volume molding capability of thermoplastic with elastomeric properties of thermoset rubber. Therefore, they land themselves to broad area of applications in various fields.

The last contribution in the prevailing volume deals with the application of a relatively new class of materials based on the addition of (electron-beam) activated polytetrafluoroethylene (PTFE) powder in rubber matrixes for preparing PTFE-based elastomeric composites. Besides other properties, the remarkably lower friction coefficient of PTFE enables its utilization for tribological applications. However, PTFE in rubbers has not been fully explored mainly due to its inherent chemical inertness and incompatibility. The present work signifies the electron modification of PTFE powder to improve its compatibility with rubber matrixes, the state of the art regarding its application in rubbers, and the preparation of PTFE-based elastomeric composites for several tribological applications.

Dresden  
April 2010

Gert Heinrich

## Reference

1. Loadman J (2005) Tears of the tree. The story of rubber – a modern marvel. Oxford University Press, Oxford

# Contents

<b>Morphology–Property Relationship in Rubber-Based Nanocomposites: Some Recent Developments</b> .....	1
A.K. Bhowmick, M. Bhattacharya, S. Mitra, K. Dinesh Kumar, P.K. Maji, A. Choudhury, J.J. George, and G.C. Basak	
<b>Rubber–Clay Nanocomposites: Some Recent Results</b> .....	85
Amit Das, De-Yi Wang, Klaus Werner Stöckelhuber, René Jurk, Juliane Fritzsche, Manfred Klüppel, and Gert Heinrich	
<b>Surface Modification of Fillers and Curatives by Plasma Polymerization for Enhanced Performance of Single Rubbers and Dissimilar Rubber/Rubber Blends</b> .....	167
J.W.M. Noordermeer, R.N. Datta, W.K. Dierkes, R. Guo, T. Mathew, A.G. Talma, M. Tiwari, and W. van Ooij	
<b>Recent Developments on Thermoplastic Elastomers by Dynamic Vulcanization</b> .....	219
R. Rajesh Babu and Kinsuk Naskar	
<b>PTFE-Based Rubber Composites for Tribological Applications</b> .....	249
M. S. Khan and G. Heinrich	
<b>Index</b> .....	311



# Morphology–Property Relationship in Rubber-Based Nanocomposites: Some Recent Developments

A.K. Bhowmick, M. Bhattacharya, S. Mitra, K. Dinesh Kumar, P.K. Maji,  
A. Choudhury, J.J. George, and G.C. Basak

**Abstract** Recently, rubber nanocomposites reinforced with a low volume fraction of nanofillers have attracted great interest due to their fascinating properties. Incorporation of nanofillers such as layered and fibrillated silicate clays, carbon nanotubes and nanofibers, calcium carbonate, metal oxides, or silica nanoparticles into elastomers can significantly improve their mechanical, thermal, dynamic mechanical, electrical, aging, barrier, adhesion, and flame retardancy properties. These also significantly alter the rheological behavior of polymers, even at low filler loading. The properties of nanocomposites depend greatly on the structure of the polymer matrices, the nature of nanofillers, and the method by which they are prepared. It has been established that uniform dispersion of nanofillers in rubber matrices is a general prerequisite for achieving desired mechanical, rheological, and physical characteristics. This review paper addresses some recent developments on the morphology–property relationship of rubber-based nanocomposites reinforced with various nanoparticles. New insights into understanding the properties of these nanocomposites and morphology development will be discussed.

**Keywords** Clay · Elastomer · Mechanical properties · Morphology · Nanocomposite · Nanofiller · Rubber

---

A.K. Bhowmick (✉)

Rubber Technology Centre, Indian Institute of Technology, Kharagpur 721302, India  
Indian Institute of Technology, Patna 800013, India  
e-mail: anilkb@rtc.iitkgp.ernet.in, director@iitp.ac.in

M. Bhattacharya, S. Mitra, K. Dinesh Kumar, P.K. Maji, A. Choudhury, J.J. George, and  
G.C. Basak

Rubber Technology Centre, Indian Institute of Technology, Kharagpur 721302, India

## Contents

1	Introduction .....	4
2	Morphology Development During Preparation of Nanocomposites .....	7
2.1	Understanding Morphology and Its Characterization in Polymer Nanocomposites .....	7
2.2	Influence of Mean-Field-Lattice-Based Theory on the Morphology Development of Polymer-Based Nanocomposites .....	8
2.3	Important Characterization Techniques for Study of Morphology .....	10
2.4	Development of Characteristic Morphologies During Preparation .....	15
3	Influence of Morphology on Properties .....	20
3.1	Rheological and Processing Behavior .....	20
3.2	Mechanical Properties .....	25
3.3	Dynamic Mechanical Analysis .....	38
3.4	Thermal Properties .....	44
3.5	Electrical Properties and EMI Shielding .....	51
3.6	Barrier Properties .....	53
3.7	Adhesion .....	57
4	New Insights into Understanding Morphology–Property Relationships .....	62
4.1	Quantification of Nanoassembly Exfoliation .....	62
4.2	New Interface Area Function to Investigate Swelling Behavior and Young’s Modulus in Nanocomposites .....	64
4.3	Role of Polymer–Solvent and Clay–Solvent Interaction Parameters on the Morphology Development of Polymer-Based Nanocomposite .....	72
4.4	Multiscale Modeling and Simulation of Polymer Nanocomposites .....	75
5	Conclusions .....	77
	References .....	77

## Symbols and Abbreviations

$\chi_{AB}$	Rubber–solvent interaction parameter
$\chi_{CD}$	Clay–solvent interaction parameter
10A	Cloisite 10A
15A	Cloisite 15A
20A	Cloisite 20A
30B	Cloisite 30B
ACM	Acrylic rubber
AFM	Atomic force microscopy
BIMS	Brominated poly(isobutylene-co-para-methylstyrene)
BR	Polybutadiene rubber
Ch	Chloroform
CNF	Carbon nanofiber
CNT	Carbon nanotube
CPE	Chlorinated polyethylene
CR	Chloroprene rubber
DMA	Dynamic mechanical analysis

DS-LDH	Laboratory-synthesized organophilic dodecyl sulfate-intercalated layered double hydroxide
EB	Electron beam
EELS	Electron energy loss spectroscopy
EG	Expanded graphite
EMI	Electromagnetic interference
ENR	Epoxidized natural rubber
EPDM	Ethylene propylene diene methylene rubber
EPR	Electron paramagnetic resonance
EVA	Ethylene vinyl acetate
FEM	Finite element method
FKM	Fluorocarbon elastomer
$F_{\max}$	Maximum force value
FTIR/IR	Fourier transform infrared spectroscopy
HNBR	Hydrogenated acrylonitrile-butadiene rubber
HPU	Hyperbranched polyurethane
HRTEM	High resolution transmission electron microscopy
IAF	Interface area function
iPP	Isotactic polypropylene
$k$	Consistency index
$K^+$	MMT Potassium montmorillonite clay
LDH	Layered double hydroxide
MD	Molecular dynamics
MEK	Methyl ethyl ketone
MWCNT	Multiwall carbon nanotubes
$n$	Flow behavior index
NA	Unmodified sodium montmorillonite clay, Cloisite Na <sup>+</sup>
NBR	Acrylonitrile-butadiene rubber
NR	Natural rubber
o-MMT	Organically modified sodium montmorillonite clay
PEB	Polyethylene butylene
phr	Parts per hundred parts rubber
PNC	Polymer nanocomposite
PP	Polypropylene
PPU	Polyester polyurethane
PS	Polystyrene
PU	Polyurethane
PVA	Polyvinyl alcohol
RF	Reinforcement factor
SAF	Surface area factor
SALS	Small angle light scattering
SANS	Small angle neutron scattering
SAXS	Small angle X-ray scattering
SBR	Styrene butadiene rubber
SEBS	Poly(styrene–ethylene- <i>co</i> -butylene–styrene) triblock copolymer



SEM	Scanning electron microscopy
Si-69	Bis(3-triethoxy silylpropyl) tetra sulfide
SP	Sepiolite clay
SPM	Scanning probe microscopy
SSEBS	Sulfonated poly(styrene–ethylene- <i>co</i> -butylene–styrene) triblock copolymer
SSNMR	Solid state nuclear magnetic resonance
STEM	Scanning tunneling electron microscopy
TEM	Transmission electron microscopy
TEOS	Tetraethoxysilane
$T_g$	Glass transition temperature
THF	Tetrahydrofuran
TPU	Thermoplastic polyurethane
WAXD	Wide angle X-ray diffraction
XRD	X-ray diffraction

## 1 Introduction

In the last two decades, the omnipresence of nanomaterials in polymeric systems has ushered in a new era of nanostructured polymeric materials. Proliferating in the realm of interdisciplinary sciences, the prodigious growth of these advanced materials has obliterated the boundaries of the conventional academic disciplines of chemistry, biology, materials science, and engineering. The exemplary interfacial interaction between the matrix and the nanofiller particles via small-scale design enables these organic–inorganic hybrid materials to play important roles as structural composites [1].

Interfacial structure is known to be different from bulk structure, and in polymers filled with nanofillers possessing extremely high specific surface areas, most of the polymers is present near the interface, in spite of the small weight fraction of filler. This is one of the reasons why the nature of the reinforcement is different in nanocomposites and is manifested even at very low filler loadings (<10 wt%). Crucial parameters in determining the effect of fillers on the properties of composites are filler size, shape, aspect ratio, and filler–matrix interactions [2–5]. In the case of nanocomposites, the properties of the material are more tied to the interface. Thus, the control and manipulation of microstructural evolution is essential for the growth of a strong polymer–filler interface in such nanocomposites.

The emergence of advanced characterizing techniques like high resolution transmission electron microscopy (HRTEM) [6], scanning probe microscopy (SPM) [7], small angle X-ray and neutron scattering [8], Raman spectra [9] etc. has facilitated the present surge in the field of nanotechnology. Insightful research has combined the advances in such diverse disciplines to elucidate the structure–property relationship in polymer nanocomposites (PNCs). Developments in synthesis and processing have enabled the formation and monitoring of engineered

nanoassemblies, while giant steps in analytical techniques such as microscopy and diffraction studies have enabled the precise determination of structural evolution across various length scales. Finally, polymer physics and computer simulation have not only successfully performed structure–property correlations by integrating the observed properties with the concomitant structure, but have also been extended to describe and prognosticate the micromechanics of these PNCs [10, 11].

The PNC properties depend not only on the properties of the individual components, but also on the entwined morphology and interfacial characteristics of the constituting phases. Hence, research has focused on the ability to generate and control nanoscale structures through innovative synthetic approaches. Analogous to polymer blends, any physical mixture of a polymer and nanoparticle does not necessarily form a nanocomposite, and particle agglomeration tends to reduce the strength and produce weaker materials. Lamellar nanocomposites provide opportunities to enhance the interface interactions between the two phases by rendering the intralamellar space potentially accessible to a polymer and other foreign species. The complete dispersion of nanolayers in a polymer optimizes the number of available elements for carrying an applied load, deflecting cracks, conducting electrons (through graphitic layers), and hindering solvent/fluid transport across the matrix etc. However, it is not easy to achieve complete exfoliation of clays and, with few exceptions, the majority of the PNCs reported in the literature were found to have intercalated or mixed intercalated exfoliated nanostructures [12, 13]. Thus, the importance of establishing the best-suited morphological structure to elicit the desired performance property can never be overemphasized.

The structure–property correlation of one rubber-based nanocomposites has been studied by various authors in different forms by using different techniques. For instance, brominated poly(isobutylene-*co-para*-methylstyrene) BIMS/clay nanocomposites have been investigated with different nanoclays modified by organoamines (octadecyl amine, a primary amine, and hexadecyltrimethylammonium bromide, a tertiary amine) by Maiti et al. [14], while those of polyester-based polyurethane nanocomposites have been investigated by Maji et al. [15]. They confirmed from X-ray diffraction and transmission electron micrographs that dispersion of the modified nanoclay in polymer with 3% loading exhibited an excellent improvement in tensile strength (by  $\sim 100\%$ ), thermal stability ( $20^\circ\text{C}$  higher), storage modulus at  $25^\circ\text{C}$  (by  $\sim 135\%$ ), and adhesive properties (by  $\sim 300\%$ ) over the pristine polyurethane (PU) [15].

Mohammadpour and Katbab observed that the melt rheological behavior and broadening of the retardation time spectra in ethylene propylene diene methylene rubber (EPDM) rubber having high molecular weight but low branching suggests a high degree of exfoliation, demonstrating the matrix microstructure dependence of nanofiller dispersion [16]. The three-dimensional (3D) state of silica or carbon black dispersion in nanocomposites has been visualized using 3D-TEM by Kohjiya et al. [17], and the authors found a kind of network structure being formed in the rubber. Conjoining the resistivity results with a structural parameter, i.e., the nearest neighbor distance from 3D-TEM images, between carbon black aggregates revealed that enhanced electron conductivity in such carbon black composites

was because of electrons hopping over the rubber phase (which is an insulator) into the black aggregates.

The morphology and mechanical behavior of styrene-based block copolymer/silicate nanocomposites tailored through selective incorporation of silicate via domain-targeted in situ sol-gel reactions were studied by Kwee and Mauritz using transmission electron microscope (TEM) and mechanical testing and were found to exhibit frustrated morphologies [18]. Vaia et al. observed deconvolution of in situ X-ray scattering during deformation, indicating that carbon nanotubes (CNTs) not only brings about mechanical enhancements, but also impacts the soft-segment crystallization in TPU nanocomposites [19]. This is attributed to the change in yield and strain hardening characteristics of the nanocomposites with deformation-induced morphological changes. Similar insights have been provided by Krishnamoorti and coworkers with regard to the rheological [20] and viscoelastic properties of nanocomposites based on polymer blends [21].

In rubber-plastic blends, clay reportedly disrupted the ordered crystallization of isotactic polypropylene (iPP) and had a key role in shaping the distribution of iPP and ethylene propylene rubber (EPR) phases: larger filler contents brought about smaller, less coalesced and more homogeneous rubber domains [22]. Clays, by virtue of their selective residence in the continuous phase and not in the rubber domains, exhibited a significant effect on mechanical properties by controlling the size of rubber domains in the heterophasic matrix. This resulted in nanocomposites with increased stiffness, impact strength, and thermal stability.

Microstructure-property correlations in dynamically vulcanized thermoplastic elastomers based on polypropylene (PP)/EPDM have shown that clay was nearly exfoliated and randomly distributed into the continuous polypropylene phase [23]. SEM photomicrographs revealed that the size of rubber particles increased with clay incorporation. Also, the clay layers act as nucleating agents, resulting in higher crystallization temperature and reduced degree of crystallinity.

Multiscale modeling and simulation strategies have been devised to obtain fundamental understanding of the hierarchical structures and behaviors necessary for development of polymeric nanocomposites. Till date, some theoretical efforts have addressed the structural changes in polymer chains due to the addition of spherical nanoparticles. The variables like particle size, particle loading, chain length, and particle-polymer interaction strength have been studied. Sharaf and coworkers [10, 24] found that the volume fraction and/or the size of nanoparticles as well as their spatial arrangement in a polymer matrix significantly affect the end-to-end chain distance. Buxton and Balazs [11] used a lattice spring model to investigate the effects of filler geometry and intercalation and/or exfoliation of clay platelets. They attributed the reinforcement efficiency to the volume of polymer matrix constrained in the proximity of the particles.

In order to understand the effects of filler loading and filler-filler interaction strength on the viscoelastic behavior, Chabert et al. [25] proposed two micromechanical models (a self-consistent scheme and a discrete model) to account for the short-range interactions between fillers, which led to a good agreement with the experimental results. The effect of the filler-filler interactions on the viscoelasticity

of filled crosslinked rubber was studied by Raos et al. [26] via dissipative particle dynamics simulation, and filler–filler interactions were found to have a clear effect on the dynamic shear modulus.

The effect of polymer–filler interaction on solvent swelling and dynamic mechanical properties of the sol–gel-derived acrylic rubber (ACM)/silica, epoxidized natural rubber (ENR)/silica, and polyvinyl alcohol (PVA)/silica hybrid nanocomposites was described by Bandyopadhyay et al. [27]. Theoretical delineation of the reinforcing mechanism of polymer-layered silicate nanocomposites has been attempted by some authors while studying the micromechanics of the intercalated or exfoliated PNCs [28–31]. Wu et al. [32] verified the modulus reinforcement of rubber/clay nanocomposites using composite theories based on Guth, Halpin–Tsai, and the modified Halpin–Tsai equations. On introduction of a modulus reduction factor (MRF) for the platelet-like fillers, the predicted moduli were found to be closer to the experimental measurements.

New strategies for multiscale modeling and simulation may be essential for accurate prediction of the physicochemical properties and material behavior, which link the methods from microscale to mesoscale and macroscale levels [33]. In this chapter, we have highlighted the current research on rubber nanocomposites using a broad gamut of nanofillers, with particular reference to enhancement of typical properties. In addition, we have tried to provide newer insights into understanding morphology–property correlations.

## 2 Morphology Development During Preparation of Nanocomposites

### 2.1 *Understanding Morphology and Its Characterization in Polymer Nanocomposites*

A thorough knowledge of the morphological traits encountered in PNCs is the first prerequisite for any attempt at comprehension and analysis of their performance and properties. Depending on the strength of interfacial interactions, the intralamellar composition, and the length scales of lamellar separation, lamellar nanocomposites can be divided into two distinct classes: intercalated and exfoliated. In the former, the polymer chains alternate with the inorganic layers in a fixed compositional ratio and have a well-defined number of polymer layers in the intralamellar space. The result is a well-ordered multilayer structure of alternating polymeric and inorganic layers, with a repeat distance between them. Intercalation causes typically less than 2–3 nm separation between the platelets [34].

In exfoliated nanocomposites, delaminated structures are obtained if a large number of polymer chains are present between the layers and the layers stand >10 nm apart. Thus, the interlayer expansion is comparable to the radius of gyration of the polymer rather than that of an extended chain, as in the case of intercalated hybrids [35].

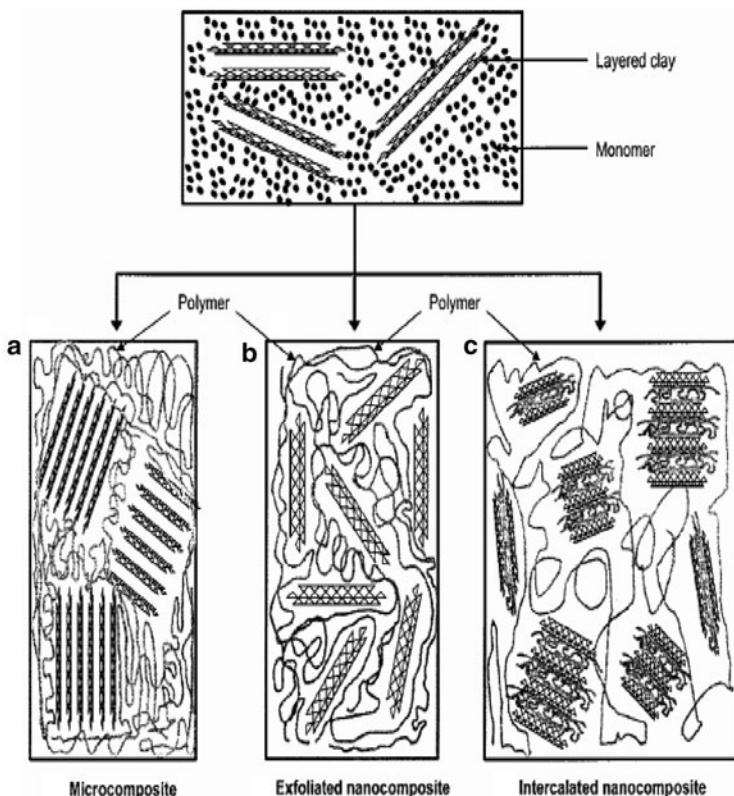


**Fig. 1** Types of lamellar polymer-nanocomposites

When the polymer is unable to intercalate between the lamella (for example, in silicate sheets) a phase-separated (aggregated) composite is obtained, whose properties are in the same range as for traditional microcomposites. The two types of lamellar PNCs are depicted in Fig. 1.

The exfoliation or delamination configuration is of particular interest because it maximizes the polymer–clay interactions, making the entire surface of layers available for a polymer, and thereby yields better properties than intercalated ones.

## 2.2 Influence of Mean-Field-Lattice-Based Theory on the Morphology Development of Polymer-Based Nanocomposites

Choudhury et al. [36] in their work on hydrogenated nitrile butadiene rubber (HNBR)-nanoclay systems showed the thermodynamic aspects of nanocomposite formation using the mean-field-lattice-based description of polymer melt intercalation, which was first proposed by Vaia and Giannelis [37]. Briefly, the free

energy change per interlayer volume,  $\Delta f_v$ , associated with polymer intercalation, is expressed as [37]:

$$\Delta f_v = \Delta e_v - T\Delta s_v, \quad (1)$$

where  $\Delta e_v$  and  $\Delta s_v$  are the internal energy and the entropy change per interlayer volume, respectively, given as:

$$\begin{aligned} \Delta s_v &= N_A K_B [\Delta s_v^{\text{chain}} + \Delta s_v^{\text{polymer}}] \\ &= N_A K_B \left[ \frac{\phi_2}{v_2} \ln(c)(\chi_s - \chi_{s0}) - \frac{\phi_1}{v_1} \left\{ \frac{\pi^2}{6} \left( \frac{a_1}{h} \right)^2 + \sqrt{3} \frac{u}{\sqrt{m_1}} \frac{a_1}{h} \right\} \right]. \end{aligned} \quad (2)$$

$$\Delta e_v = \phi_1 \phi_2 \frac{1}{Q} \left( \frac{2}{h_0} \varepsilon_{\text{sp,sa}} + \frac{2}{r_2} \varepsilon_{\text{ap}} \right). \quad (3)$$

$\Delta s_v$  is expressed as the sum of the entropy change associated with organically modified silicate  $\Delta s_v^{\text{chain}}$ , and the entropy change associated with confinement of the polymer,  $\Delta s_v^{\text{polymer}}$ .  $N_A$  is Avogadro's number and  $K_B$  is the Boltzmann constant.  $h_0$  and  $h$  are the initial and final gallery heights after polymer intercalation, respectively.  $m_i$ ,  $v_i$ ,  $\varphi_i$ ,  $r_i$ , and  $a_i$  are the number of segments per chain, the molar volume per segment, the interlayer volume fraction, the radius of the interaction surface, and the segment length of the  $i$ th interlayer species.  $u$  is a dimensionless excluded volume parameter,  $Q$  is a constant near unity, and  $\chi_s$  and  $\chi_{s0}$  are the fraction of interlayer volume near the surface at height  $h$  and  $h_0$ , respectively, which influence the potential chain conformations.  $\varepsilon_{\text{ap}}$  represents the pairwise interaction energy per area between the aliphatic chains and the polymer, and  $\varepsilon_{\text{sp,sa}} = \varepsilon_{\text{sp}} - \varepsilon_{\text{sa}}$ , is the difference between the pairwise interaction energy per area between the aliphatic chain and the surface ( $\varepsilon_{\text{sa}}$ ) and that between the polymer and the surface ( $\varepsilon_{\text{ap}}$ ).  $\chi_s(h)$  can be constructed as:

$$\chi_s(h) = \frac{a_2}{h} \cos^2 \left( \frac{\pi}{2} \frac{h}{h_\infty} \right). \quad (4)$$

The values of  $\Delta s_v$  and  $\Delta e_v$  calculated for different nanocomposites from (2) and (3) are listed in Table 1.

It is well known that mixing of two components is most favorable when the free energy change ( $\Delta G_S$  or  $\Delta f_v$ ) of the system, is negative. Table 1 shows that  $\Delta e_v$  for S1-30B-4 is negative and lowest. Hence,  $\Delta G_S$  or  $\Delta f_v$  is lowest for these two nanocomposites. In the case of S1-NA-4,  $\Delta e_v$  is  $+0.84 \text{ nm}^{-1}$ , indicating the fact that mixing of this clay in the rubber matrix is not favorable. Table 1 also shows that the entropy

**Table 1** Values of internal energy ( $\Delta e_v$ ) and entropy change ( $\Delta s_v$ ) for different nanocomposites

Sample name	$\Delta e_v$ ( $\text{nm}^{-1}$ )	$\Delta s_v$ ( $\text{JK}^{-1} \text{mol}^{-1} \text{m}^{-3}$ ) $\times 10^{-3}$
S1-30B-4	-0.20	1.58
S1-15A-4	-0.05	0.77
S1-NA-4	+0.84	-20

S1 hydrogenated nitrile butadiene rubber

change per interlayer volume for S1-30B-4 and S1-15A-4 is positive, while for S1-NA-4 it is negative. These results prove that for S1-NA-4, the interaction between polymer and clay is not favorable and, hence, it forms agglomerates when added into the rubber matrix. Qualitatively, when the polymer chains enter and become trapped in the rubber matrix in the initial stage as in S1-30B-4, then motion is restricted and as a result  $\Delta S_E$  is expected to be negative. However, in the later stage, the polymer chains break the layer structure of the clay until complete exfoliation occurs and the silicates are distributed throughout the matrix, accounting for a highly positive  $\Delta S_C$  and compensating the entropy loss in the initial stage. Hence, the overall entropy change  $\Delta S_S$  is expected to be positive, making  $\Delta G_S$  negative.  $\Delta S_E$ ,  $\Delta S_C$  and  $\Delta S_S$  are the entropy increments associated with the mixing process for the elastomer, the nanofillers and the system, respectively.

### 2.3 *Important Characterization Techniques for Study of Morphology*

For appropriate comprehension of morphology and the concomitant structure–property correlations in nanocomposites, knowledge of the state and extent of nanofiller dispersion in the matrix is of paramount importance. Numerous methods have been reported in the literature in this regard, for instance, WAXD [6, 38], SAXS [8, 39], SANS [40], SEM, TEM [6, 41], AFM [7, 42], HRTEM, STEM, EELS [43], SSNMR [44], EPRS [45], UV/vis/NIR, FTIR [46], Raman spectroscopy [9], and SALS [47].

Amongst all those listed above, the two methods often used to determine the structure of nanocomposites are WAXD and TEM. Although WAXD offers a convenient and often-practiced method to determine the interlayer spacing, it cannot be considered all-conclusive. The absence of Bragg diffraction peaks alone means that it cannot be used to determine the formation of an exfoliated structure, as it might lead to false interpretations. Several factors such as clay dilution, peak broadening, and preferred orientation make XRD characterization of PNCs susceptible to errors. To supplement the deficiencies of WAXD, TEM can be used [6, 48]. XRD data are averaged over all the regions of the specimen, whereas TEM can provide a qualitative understanding of the internal structure, spatial distribution of the various phases and, hence, the morphology of the nanocomposites.

In subsequent discussion, we will demonstrate the use and interpretation of some of these techniques. Figure 2a shows typical XRD traces of nanocomposite systems of styrene butadiene rubber (SBR) containing unmodified and modified nanoclay, describing an exfoliated and intercalated nanocomposite [5]. TEM photographs of these systems are also given in the same figure (Fig. 2b, c). In the present case, the information obtained from both the techniques is complimentary.

AFM is a state of the art technique for characterizing nanocomposites. Ganguly et al. [49] used AFM for qualitative phase morphological mapping as well as for quantitative investigation of surface forces at constituting blocks and clay regions

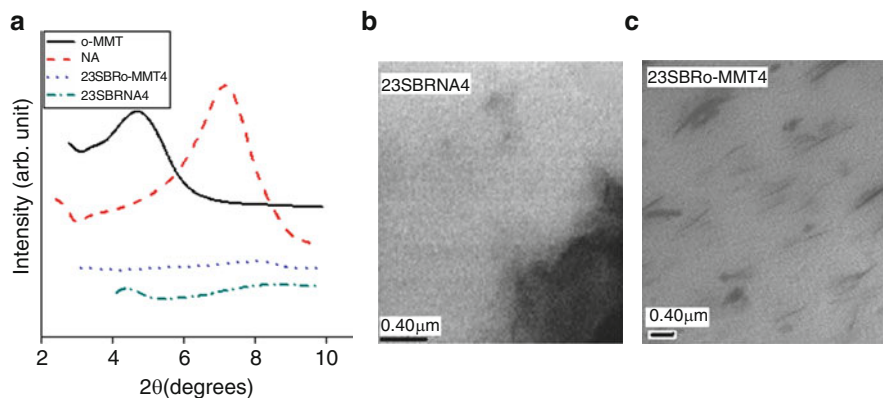


**Fig. 2** **a** XRD spectra of nanoclays and SBR-based nanocomposites. **b–c** TEM images of SBR-based nanocomposites

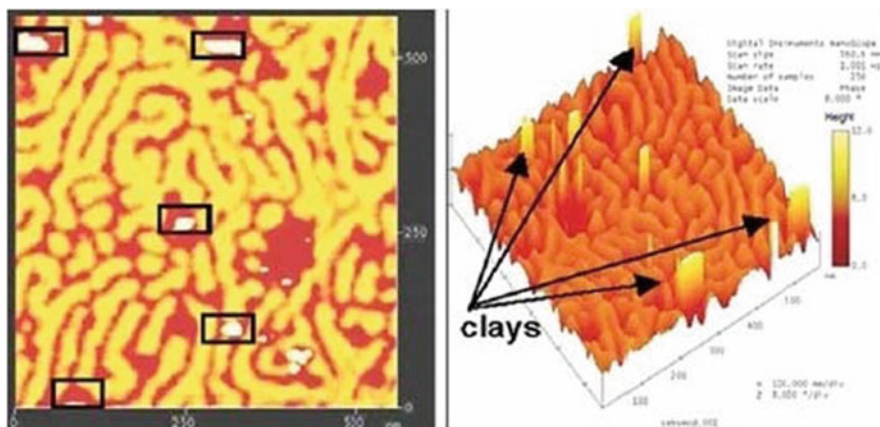


**Fig. 3** AFM tapping mode phase morphology of the SEBS/20A nanocomposites

of these thermoplastic elastomeric nanocomposites [49]. Figure 3 shows the tapping mode phase morphology of the poly(styrene–ethylene-*co*-butylene–styrene) (SEBS) nanocomposites using the AFM technique.

Mapping of the elastic modulus of the glassy and rubbery blocks and clay regions was probed by employing Hertzian and Johnson–Kendall–Roberts (JKR) models from both approaching and retracting parts of the force–distance curves. In order to determine the elastic properties of SEBS nanocomposites in its different constituting zones, the corrected force–distance curve was fitted to the Hertz model:

$$\delta = \sqrt{\frac{\pi k \Delta (1 - \nu^2)}{2E \tan \alpha}}, \quad (5)$$



where  $\partial$  is the depth of penetration on the domains, and  $E$  is the modulus from load curve (the contact portion of force curves).  $\alpha$  is the half angle of the tip geometry, and  $k\Delta$  gives the force exerted on the SEBS sample. Modulus ( $E_{\text{Sample}}$ ) can be calculated from  $\partial$ , using:

$$\partial = (z^* - d^*) = 0.825 \left[ \frac{k^2 (R_{\text{tip}} + w_{\text{sample}}) (1 - \nu_{\text{sample}}^2)^2}{E_{\text{sample}}^2 R_{\text{tip}} w_{\text{sample}}} \right]^{1/3} (d^*)^{2/3} \quad (6)$$

and assuming the AFM tip apex as sphere and the AFM cantilever as a spring attached to the sphere in series. The penetration by the tip,  $\partial$ , is measured from the difference between cantilever traversed ( $z^* - d^*$ ), where  $|z^* = z - z_0|$  is the distance traversed from just-contact point ( $z^*$ ) to present  $z$  scan position ( $z_0$ ) calculated from force plot, and the term  $|d^* = d - d_0|$  is the difference between non-contact deflection ( $d_0$ ) and present deflection ( $d$ ) at present  $z$  position.  $k$  is the spring constant ( $0.12 \text{ nm}^{-1}$ ) for contact mode AFM tip;  $R_{\text{tip}}$  is the radius of curvature of the hemispherical portion of the apex of the contact mode tip,  $\sim 10 \text{ nm}$ ; and  $w_{\text{sample}}$  is assumed to be the lamellar width or thickness of the domains or the clay regions on the surface of nanocomposite under investigation.  $\nu_{\text{sample}}$  is Poisson's ratio of the selected segments on the surface, namely soft PEB (0.5), harder PS (0.33) and clay (0.25).

Values of  $E_{\text{sample}}$  were calculated for the constituting domains of SEBS (PS and PEB) and for the nanoclay regions in the SEBS/clay nanocomposite using (6) and are provided in Table 2. The modulus of the clay platelets was found to be 100 MPa, whereas the modulus for PS and PEB blocks was determined to be 22 and 12 MPa, respectively. These modulus values tallied with the slow strain-rate macromechanical tensile data of 26 MPa for the SEBS/clay nanocomposite (Table 2). The lower calculated modulus values of nanoclays compared to the literature might be due to adhering soft rubber on the nanoclays, which reduces the overall modulus of clay regions in the composite.

Due to adhesive interaction in the retracting portion of the force–distance ( $f$ – $d$ ) curve, the JKR model registered better insight into nano-mechanical measurements

**Table 2** Modulus of SEBS/clay nanocomposites from models and the actual bulk modulus

Block and clay regions of SEBS nanocomposite	Modulus from Hertz model ( $E_{\text{Sample}}$ ), MPa	Localized sample deformation ( $\partial$ ), nm	Modulus from JKR model ( $E_{\text{Sample}}^{\text{JKR}}$ ), MPa	Bulk modulus <sup>a</sup> of SEBS/clay nanocomposite, MPa
Soft PEB block	12 ± 1	50	15 ± 1	26 ± 1
Hard PS block	22 ± 1	30	24 ± 1	
Clay regions	100 ± 5	02	105 ± 5	

<sup>a</sup>Measured with 50 mm  $\text{min}^{-1}$  strain rate in Universal Testing Machine Zwick 1445 (Zwick, Ulm, Germany)

of forces, where large deformation and adhesive energy were involved. Elastic modulus of the sample could be obtained from JKR theory by:

$$E_{\text{Sample}}^{\text{JKR}} \approx 0.95 \frac{F_{\text{adh}}(1 - \nu^2)}{\sqrt{R\delta^3}}, \quad (7)$$

where  $F_{\text{adh}}$  is the pull-off force,  $\nu$  is Poisson's ratio,  $R$  is the radius of curvature of the probe tip, and  $\delta$  is the localized sample deformation in PS, PEB, or clay regions in the SEBS/clay nanocomposite.

From the calculation in (7), the softer PEB region was shown to have maximum adhesive force in nature with the calculated modulus in the range of  $15 \pm 1$  MPa (Table 2). The harder PS domains found to have modulus in the range of  $24 \pm 1$  MPa in the SEBS/clay nanocomposite. The non attractive clay regions generally did not fit the JKR model. This was the reason for obtaining much less modulus than that of the literature values for clays in the GPa range. The discussion infers that the bulk modulus of the SEBS/clay nanocomposite ( $26 \pm 1$  MPa as shown in Table 2) was dictated by the contribution from PS domains in the matrix.

SAXS presents itself as significant tool when the layer spacings exceed 6–7 nm in intercalated nanocomposites or when the layers become relatively disordered in exfoliated nanocomposites. The effects of nanoclay on the order structure of SEBS have been studied by Ganguly et al. [50] by comparing the intensity versus scattering vector plots by SAXS (Fig. 4a) for neat SEBS and its nanocomposites. All the samples show at least two-order scattering with the peak position ratio of 1:2, indicating the layered (lamellar) structures (Fig. 4a). With nanoclay loading, the corresponding lengths calculated from scattering vector positions ( $q$ ,  $\text{nm}^{-1}$ ), for both the first and the second order peaks, are found to increase. Among these, the incorporation of 2 pbw (parts per 100 parts rubber by weight) loading of Cloisite 20A shows the maximum increase, with 4 pbw depicting an almost similar effect as shown in the *Lorentz* corrected SAXS profiles in Fig. 4a, b. In order to further confirm the effects of nanoclays on SEBS, 2D SAXS studies clearly detect a distinct pattern at 2 pbw of Cloisite 20A loading. Isotropic circular rings are observed in the 2D SAXS pattern for the as-cast sample films. These rings were ascribed to diffraction resulting from 1D alternating lamellar microdomains and the ratio of  $q$  values for the first and second diffraction rings can relatively be assigned to 1:2. After 4 pbw loading of Cloisite 20A, the patterns become more and more diffused and corroborated well with the SAXS profile (Fig. 4b).

However, caution must be exerted with regard to overreliance on scattering techniques used for delineation of nanoscale morphologies. The underlying reason is the fact that phase information is lost in scattering and, as more than one morphology could account for the observed scattering, one cannot uniquely determine the structure. Electron microscopic imaging, on the other hand, corresponds to real-space analysis and thus is in principle more powerful than small-angle scattering (reciprocal-space analysis) for a description of nanoscale morphologies [51].

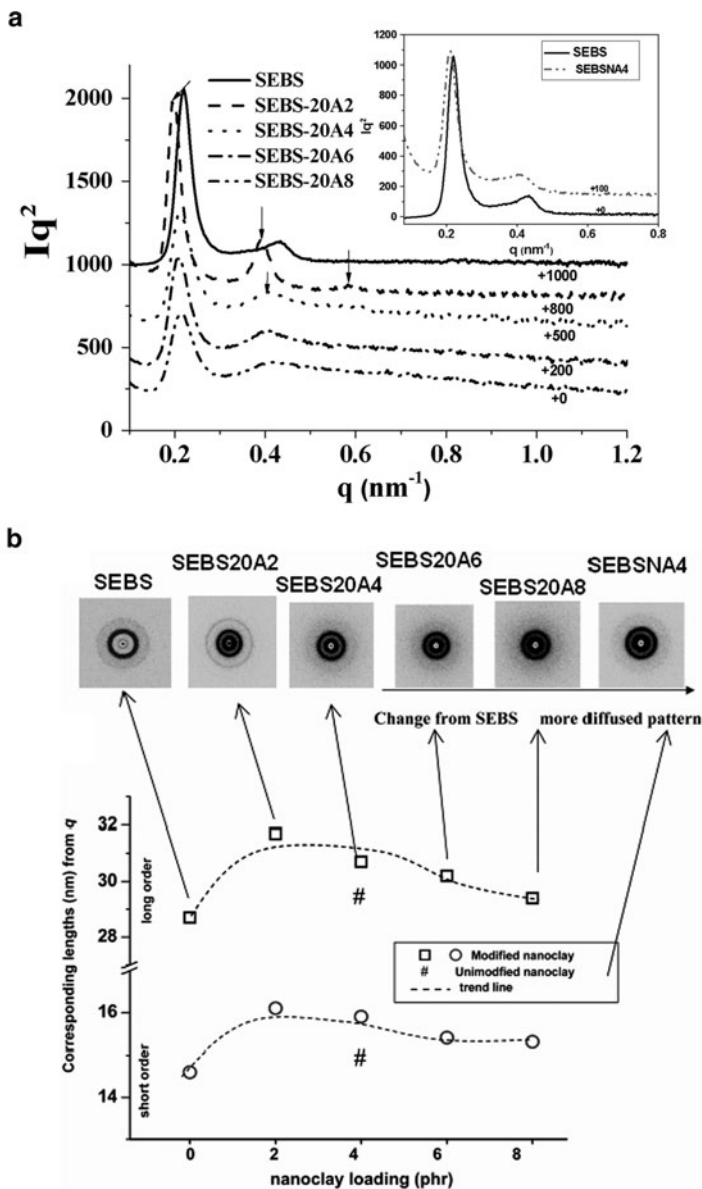


**Fig. 4** Effect of nanoclay loading on neat SEBS: **a** Lorentz -corrected SAXS profiles (vertically shifted for better clarity) showing effect of nanoclay; *arrows* indicate peak positions. **b** Lengths corresponding to first- and second- order scattering vector positions along with the 2D SAXS patterns for each sample of clay-loaded nanocomposites

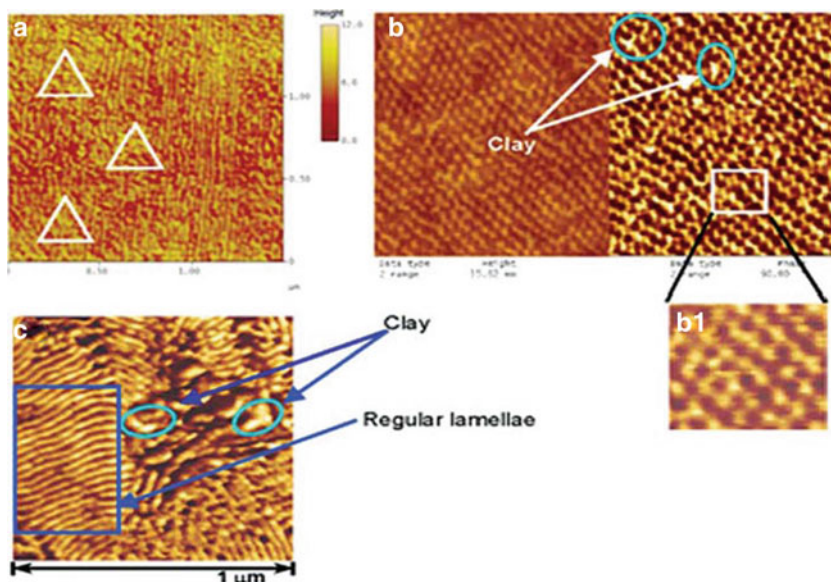
## ***2.4 Development of Characteristic Morphologies During Preparation***

The delayed development of elastomeric nanocomposites, compared to thermoplastic or thermoset nanocomposites, can be attributed to the fact that for elastomers to exhibit real-life functionality, several ingredients (e.g., curing agents, coagents, processing aids, reinforcements, and fillers) have to be incorporated into them. These additives might interact with the nanofillers and hinder the development of the requisite and desirable morphology. Hence, it was a great challenge. It is necessary to recognize and utilize the best mixing technique for dispersing nanofillers in rubber matrices. Once researchers understood this prerequisite, there was a spur in activities in this field. The ensuing development of rubber nanocomposites, from the very nascent stages, has been collated in two review papers [5, 52].

The effects of the type of nanofiller, its loading, the modifier, and the nature of the rubber used etc. all have a bearing on the eventual property manifestations. However, the preparation of these nanocomposites through their actual processing and curing conditions casts the final die with regard to mechanical [53], barrier [54], thermal [55, 56], flame retardance [57], electrical [58], and optical properties [59]. Various techniques have been explored for achieving the often illusive exfoliated morphology [5]. These include solution blending [9, 50, 60–64], latex compounding [65–69], melt intercalation [49, 70–78], and in situ polymerization [79–82]. For instance, unmodified-clay-loaded SBR [83] and natural rubber (NR) [84] nanocomposites showed agglomeration when prepared using melt mixing technique. Interestingly, a few rubbers like nitrile butadiene rubber (NBR) [83], SEBS, and fluorocarbon elastomer (FKM) [85] could even exfoliate unmodified clay, thus leading to enhanced properties of the nanocomposites. It must be noted here that the latter nanocomposites were all prepared using the solution mixing technique. Also, it is common knowledge that the nature of solvent used to prepare the nanocomposites affects the morphology and properties [86].

### **2.4.1 Solution and Melt Mixing**

Ganguly et al. [49] compared two processing techniques, namely, solution and melt blending, from the point of view of morphological differences. With state-of-the-art AFM, they showed distinctly different morphologies in nanocomposites prepared through solution and melt processing. Figure 5 shows the morphology of SEBS nanocomposites prepared by solution mixing techniques. The morphology changes as soon as different techniques for the preparation are adapted. The lamellar thickness of the soft phases of SEBS was widened in nanocomposites, where the layered clay silicates were embedded in the soft rubbery phases in the block copolymeric matrix of the nanocomposite (also shown in Fig. 3). In the new morphology, when nanoclays are embedded in the matrix, the soft phases are widened to 50–75 nm patches from their original width of 12–15 nm.



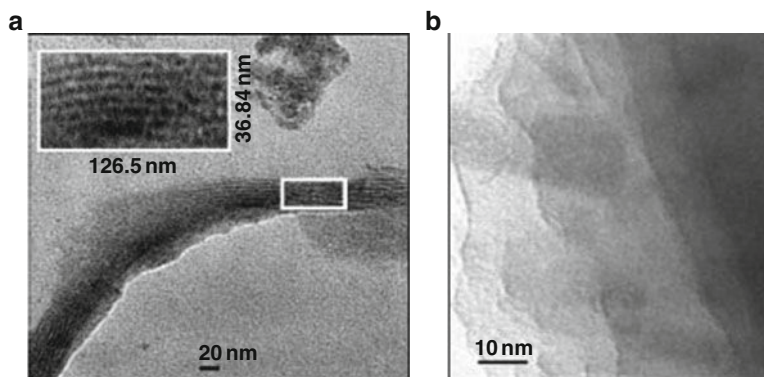
**Fig. 5** a Surface phase morphology of melt-processed neat SEBS. b Height and phase images of bulk melt intercalated SEBS/20A; the *inset* shows the hexagonal packed morphology of PS blocks. c Solution-cast bulk phase morphology of SEBS/20A showing lamellar architecture with clay positioning

Figure 5a shows the regular array along with some frustrated portions (marked with the triangular boxes within the image) due to the high pressure and temperature associated with melt processing of neat SEBS. Extrusion and subsequent molding of SEBS/20A nanocomposite also generates a regular array-like morphology for both the surface and the bulk morphologies of the nanocomposites (Fig. 5b). However, this type of morphology undergoes transformation during solution blending into a worm-like morphology (Fig. 5c).

#### 2.4.2 In Situ Preparation and Solution Mixing

Morphological structures and properties of a series of poly(ethyl acrylate)/clay nanocomposites prepared by the two distinctively different techniques of in situ ATRP and solution blending were studied by Datta et al. [79]. Tailor-made PNCs with predictable molecular weights and narrow polydispersity indices were prepared at different clay loadings. WAXD and TEM studies revealed that the in situ approach is the better option because it provided an exfoliated morphology. By contrast, conventional solution blending led only to interlayer expansion of the clay gallery.

The dispersion behavior of organoclay affected the visual appearance of the hybrid composites (Fig. 6a, b). The composites containing Si particles predominantly as a finely dispersed phase were transparent, e.g., PNC12 [nanocomposite prepared in



**Fig. 6** TEM micrographs of the PNCs: **a** PNC SL2 and **b** PNC I2

situ by atom transfer radical polymerization (ATRP) with 2 wt% of 30B nanoclay loading], whereas the composites having some localized agglomerated Si particles were optically translucent in nature, e.g., PNC SL2 (nanocomposite prepared by solution blending with 2 wt% of 30B nanoclay loading). As shown in Fig. 6a, the nanocomposites prepared by solution blending had parallel stacks of clay lamella (dark contrast), and this also supported the intercalated structure obtained from the XRD data.

The same group carried out ATRP of EA in bulk at 90°C in the presence of organically modified nanoclay as an additive. They found remarkable enhancement in the rate of polymerization as compared with the ATRP of EA without nanoclay. Interestingly, the resulting nanocomposites had exfoliated clay particles, as evident from WAXD and TEM studies [80].

The necessity of dispersion of nanofillers for enhancement of properties of nanocomposites has been well-documented. Literature describes various techniques used for preparation of the rubber-based nanocomposites [5]. These processes have their inherent pros and cons, but seldom have these issues been quantitatively documented or the processes combined together to synergize and overcome the failings of a technique.

### 2.4.3 Mixing in an Extruder

Dennis et al. [87] described morphology generation using extruders having differences in screw design and flow rates. They concluded that the degree of delamination and dispersion of nylon-6/clay nanocomposites were affected by the type of extruder and its screw design. The nonintermeshing twin screw extruder yielded the best results. A balance was found to be necessary between the residence time and an optimum shear intensity to dissociate the clay particles first and then to allow polymer to enter the clay galleries and peel the platelets further apart for successful exfoliation.

Sadhu et al. [88] reported interesting observations when they processed their nanocomposites through a capillary using the Monsanto Processability Tester. They found that different morphologies were formed and more ordering took place because of the shearing of the nanocomposites through the capillary.

#### 2.4.4 Effect of Curing Techniques and Ingredients

Maiti et al. [64] took typical fluorocarbon-based exfoliated nanocomposites and observed that they reaggregate while they are processed in a hydraulic press during the curing operation. Their XRD studies revealed that the level of exfoliation was, however, not disturbed if oven curing was performed, instead of press curing.

The morphology of rubber-based nanocomposites also seems to change in the presence of compounding ingredients [89, 90]. HNBR, when melt-compounded with organo-modified sodium montmorillonite clays (o-MMTs) prior to sulfur curing, resulted in the formation of nanocomposites with exfoliated or intercalated structures. In stark contrast, under similar conditions HNBR compounded with unmodified sodium montmorillonite clays (NA) formed microcomposites [90]. This was traced to its reactivity with the sulfur in the presence of amine-type organomodifiers.

Similar observations were made by Bhattacharya and Bhowmick [91] for the NR matrix. They found that entrapment of the curatives in close proximity to the nanoclay not only altered the cure and rheological behavior favorably, but also catalyzed the formation of a supramolecular structure by helping the formation of sulfur-amine complexes involved in sulfur curing.

Das et al. [89] observed that both sulfur and peroxide vulcanizations of NBR filled with organoclay lead to intercalated-exfoliated structures of the layered silicate. They also reported that the use of excess stearic acid could lead to exfoliation of the clay layers in NBR when cured with sulfur.

#### 2.4.5 Latex, Melt, and Latex-in-Melt Mixing

For the first time, Bhowmick et al. [92] merged and compared two different mixing and curing techniques on a single platform. They prepared nanocomposites by conventional and latex mixing, and also a combination of both in which the clay was preexfoliated using latex blending, after optimizing the swelling (stirring) time and clay concentration from an exploratory survey. Other ingredients were thereafter mixed in an open two-roll mill and then compression molded. It has been reported in the literature that conventional mixing and subsequent press curing leads to the considerable reaggregation of individual silicate layers dispersed in the nanocomposite [93]. Thus, the as-prepared latex-blended nanocomposites were also subjected to in situ curing in the latex stage itself by means of prevulcanization. Although such techniques cater to very different types and grades of the rubber, the

obvious benefits of combining the two techniques are reflected in the morphology development and concomitant enhancement of properties.

Figure 7 shows the representative bright field HRTEM images of nanocomposites of NR and unmodified montmorillonite (NR/NA) prepared by different processing and curing techniques. It is apparent that the methodology followed to prepare the nanocomposites by latex blending facilitates the formation of exfoliated clay structure, even with unmodified nanoclays. It has been reported in the literature that hydration of montmorillonite clay leads to extensive delamination and breakdown of silicate layers [94, 95]. It has also been shown that NA disperses fully into the individual layers in its dilute aqueous dispersion (clay concentration <10%) [94]. This is truly reflected in the morphology of the uncured clay preexfoliated rubber nanocomposite films ( $N_{LU}$  NA) prepared by the latex blending method (Fig. 7a). Curing the NR/NA nanocomposites in situ prevulcanization ( $N_{LP}$ NA) does not alter the arrangements of dispersed clay layers greatly, as seen from the

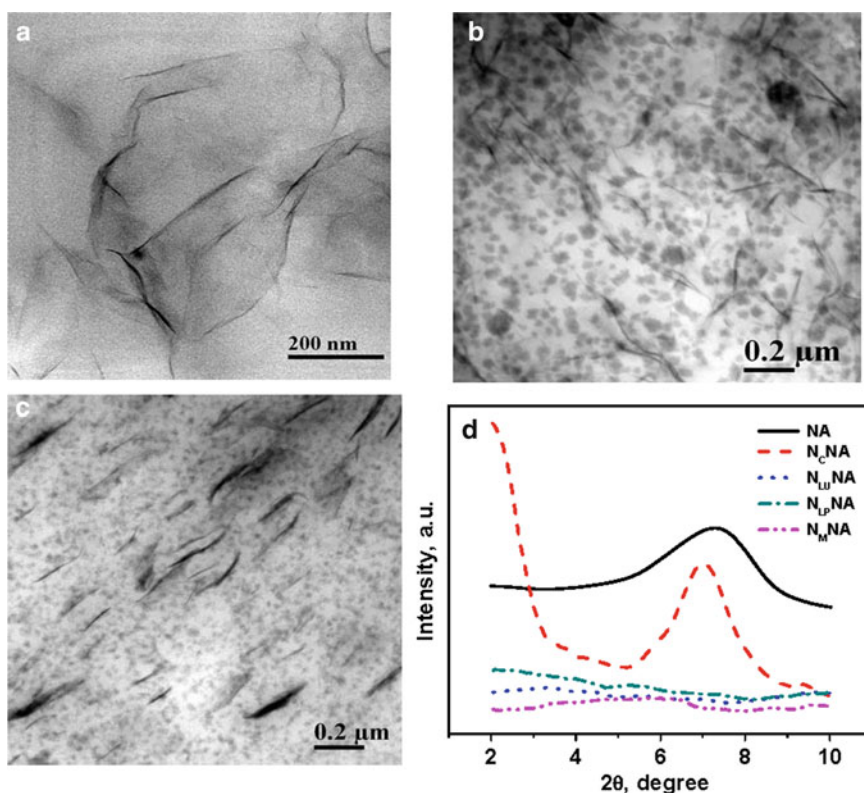


**Fig. 7** Bright field HRTEM images showing the development of morphology in 4 phr NA-filled NR nanocomposites under different processing and curing conditions: **a** latex-blended uncured NC ( $N_{LU}$ NA); **b** prevulcanized NC ( $N_{LP}$ NA); and **c** conventionally cured NC ( $N_{MNA}$ ). **d** X-ray diffractograms of NA and its nanocomposites



Fig. 7b. In both cases, near fully exfoliated morphology is observed, with almost no sign of any clay particle agglomeration. However, conventional curing of NR/NA nanocomposites ( $N_MNA$ ) generates an interesting morphology (Fig. 7c). The NA clay platelets are aligned in the molding/flow direction. In all the HRTEM images, well distributed individual NA clay platelets can be seen easily, along with a few intercalated clay layers consisting of a few clay platelets stacked together. However, it seems that conventional processing and subsequent curing increases the tendency of reagglomeration of clay platelets (Fig. 7c). It can be noted here that the advantage of using the preexfoliated clay suspension to form NR nanocomposites is partially suppressed after conventional processing, as evident from the evolved morphology.

The XRD traces of NA and its nanocomposites prepared using the different techniques corroborate the above observation (Fig. 7d). NA has a peak at  $7.3^\circ$  (Fig. 7d). The XRD peaks of melt-mixed NR-unmodified montmorillonite ( $N_cNA$ ) at 4 phr (parts per hundred parts rubber) loading hover around the same position, at  $7.0^\circ$ , suggesting slight intercalation. These peaks correspond to  $d$ -spacings of 1.18 and 1.45 nm, respectively. Of special interest is the fact that all the samples that were latex-blended ( $N_{LU}NA$ ,  $N_{LP}NA$ , and  $N_MNA$ ) exhibit high degrees of exfoliation when swollen for 72 h.

Morphology evolution is thus found to be dependent on the processing technique applied to disperse the nanoparticles. The latex-blended and pre vulcanized nanocomposites show predominant exfoliation with some intercalation, especially in uncured and pre vulcanized samples. In conventionally cured but latex-blended nanocomposites, realignment of NA particles is visible, with a greater tendency of NA platelets towards agglomeration. In solid state mixing, the dispersion is still poorer. XRD studies also corroborate the above observations.

### 3 Influence of Morphology on Properties

#### 3.1 Rheological and Processing Behavior

The evolution of nanocomposite structure and morphology as described above has direct consequences on its rheological and processing behavior. The knowledge of rheological and processing characteristics of rubber-based nanocomposites plays a vital role in determining the design and subsequent fabrication aspects of any finished product. Therefore, it is of great interest to investigate the rheological and processing behavior of rubber-based nanocomposites. Many researchers have studied the dynamic oscillatory and steady-shear rheology of rubber-based nanocomposites [96–102]. The dependence of rheological properties on the nanocomposite morphology has also been reported in the literature [96, 97]. Kim et al. reported that use of o-MMT in NBR resulted in an increase in Mooney viscosity and torque values [96]. The rheological behavior of o-MMT-filled NR/ENR blend

nanocomposite systems was investigated through Mooney viscosity measurements [97]. It has been observed that the viscosity of NR blend nanocomposites increases slightly with the incorporation of the organoclay (5 phr). The increase in viscosity was attributed to the improvement in the filler–rubber compatibility by the addition of ENR, which not only causes a better dispersion of the clay particles in the rubber matrix with an increase of interphase, but also increases the filler–rubber interactions and decreases the agglomeration of filler particles. In the presence of ENR, the blend nanocomposites showed predominately exfoliated morphology due to the better dispersion of the clays. Lim et al. reported the rheological properties of organophilic montmorillonite clay and polyepichlorohydrin rubber nanocomposites prepared by the solvent-casting method [102]. It was found that the steady shear viscosity increased with the clay loading, and the shear thinning viscosity data were fitted well with the Carreau model. The above investigations, in general, revealed enhancement in viscosity values as compared to the pristine rubber matrix and can be attributed to the formation of an intercalated or exfoliated network structure by the clay platelets.

However, in one of the seminal works on the rheology of elastomer-based nanocomposites, Sadhu and Bhowmick reported the unique rheological behavior of unmodified and modified montmorillonite clay-based NBR, SBR, and polybutadiene rubber (BR) nanocomposites studied using the Monsanto Processability Tester (capillary rheometer) [88]. Interestingly, the shear viscosity decreased with increasing shear rate and with the incorporation of the unmodified and the modified clays up to a certain loading when compared to the unfilled rubbers. The nanocomposites were prepared by solution blending using NBR having 19% acrylic rubber (ACN) content (19NBR), 34% ACN content (34NBR), and 50% ACN content (50NBR), SBR with 23% styrene content (23SBR) and BR, and nanoclays (NA and o-MMT). The effect of nanoclay loading (0, 2, 4, 8 phr) on the rheological properties of polar 34NBR is shown in Fig. 8. The viscosity decreases with increasing filler loading up to 4 phr, beyond which it increases. All the systems show well-defined pseudoplastic or shear thinning behavior and obey the power law model. Interestingly, the modified-clay-filled system 34NBRo-MMT4 generates lower shear viscosity when compared to its unmodified counterpart (34NBRNA4) at 4 phr loading. This has been explained with the help of the XRD data [62], whereby the modified clays have been shown to be well-dispersed and best-intercalated at 4 phr loading. The gallery distance is maximum at this loading among all the 34NBRo-MMTs. The orientation of the dispersed modified clays in the present systems causes a decrease in viscosity in 34NBRo-MMT4. They start forming agglomerates above this loading. This has been well supported by TEM images [62]. As reported in Table 3, in the case of SBR, the viscosity of 23SBRNA4 is lower than that of gum rubber (23SBR). However, with addition of the modified filler, the viscosity of 23SBRo-MMT4 decreases even further (Table 3). The TEM images and the XRD of 23SBR nanocomposites also confirm the orientation of the exfoliated clay particles in the matrix, which can behave as capillaries [62]. As a result, due to the better orientation and dispersion of the exfoliated clay layers, the viscosity decreases in comparison to the gum or the unmodified-clay-filled

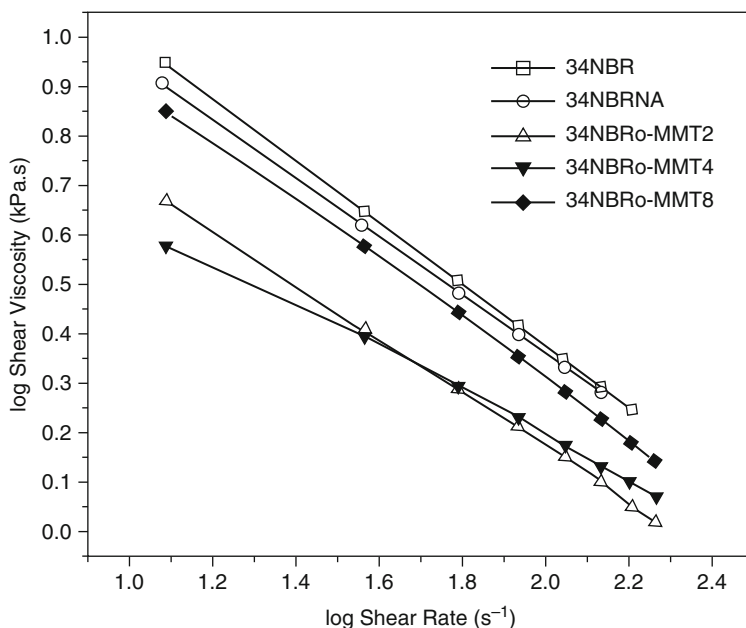


**Fig. 8** The log shear viscosity versus log shear rate plot of 34NBRo-MMT at various filler loadings

**Table 3** Shear viscosity, die swell, flow behavior index, and consistency index of various samples at a shear rate of  $61.2 \text{ s}^{-1}$

Sample designation	Shear viscosity (kPa-s)	Die swell (%)	Flow behavior index ( $n$ )	Consistency index ( $k$ ) ( $\times 10^{-4}$ kPa-s)
BR	2.88	52.9	1.00	8.87
BRNA4	2.90	46.4	1.00	8.12
BRo-MMT4	3.26	59.7	1.00	9.93
23SBR	4.60	39.1	1.00	8.06
23SBRNA4	4.13	38.4	1.00	9.35
23SBRo-MMT4	3.94	34.8	1.00	6.87
19NBR	4.53	49.7	0.99	10.63
19NBRNA4	4.52	37.7	0.37	10.05
19NBRo-MMT4	4.48	44.4	0.36	54.83
34NBR	3.23	62.2	0.36	43.36
34NBRNA4	3.03	52.0	0.39	37.00
34NBRo-MMT4	1.94	49.1	0.56	11.90
50NBR	3.65	61.2	0.35	51.28
50NBRNA4	2.68	55.5	0.43	26.24
50NBRo-MMT4	2.06	52.2	0.43	20.46

composite of 23SBR. In the case of BR, the unmodified-clay-filled system (BRNA4) shows almost the same viscosity as the gum rubber (BR). The modified clay (BRo-MMT4) at 4 phr loading, on the other hand, shows a marginal increase in viscosity (Table 3). It has been observed that the above effects become more

prominent with an increase in matrix polarity that is either changing from nonpolar to polar rubber, or with an increase in the acrylonitrile content in the case of NBR. The consistency index ( $k$ ) and the flow behavior index ( $n$ ) of the systems are also reported in Table 3. The values show that the nonpolar BR and 23SBR systems behave predominantly as Newtonian fluids, whereas the NBRs generate pseudo-plastic behavior. This is mainly due to the more polar nature of NBR.

The die swell values, which are a measure of elastic recovery, consistently decrease with the increase in clay loading irrespective of matrix or clay type. Figure 9 illustrates the plot of die swell versus shear rate for 34NBR and its nanocomposites. Addition of 4 phr of both unmodified and modified nanoclay reduces the die swell of 34NBR considerably. The trend is more prominent with polar rubber and with an increase in polarity such as for 34NBR and 50NBR (Table 3). There is a 14.7% decrease in die swell in 50NBR, just by incorporation of 4 phr of o-MMT. SBR behaves similarly. 19NBR and BR, however, register a decrease with NA, but a marginal increase again with o-MMT. In all cases, the exfoliated clay, due to better dispersion and interaction in the case of SBR or to higher extent of intercalation in the case of NBR, is responsible for the reduction of die swell. But, if the clay is agglomerated, the die swell becomes higher. However, the lower die swell of the nanoclay-filled samples is due to lower volume fraction of the rubber.

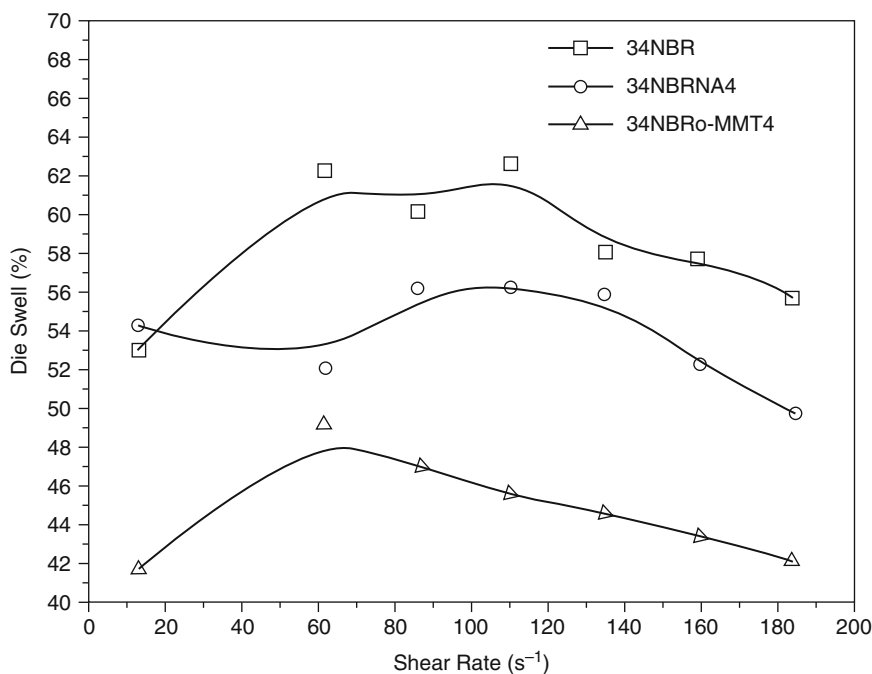


**Fig. 9** Die swell versus shear rate plot of 34NBR and its nanocomposites

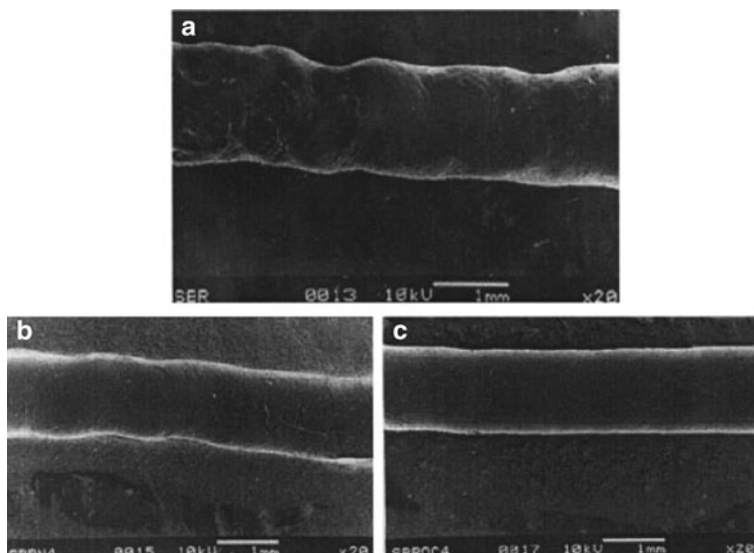


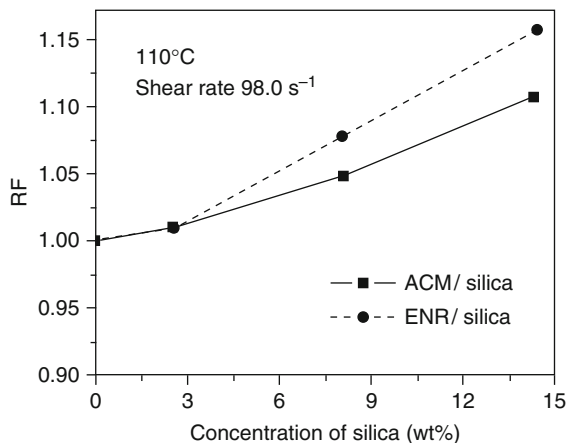
**Fig. 10** SEM micrographs of the extrudates of **a** 23SBR, **b** 23SBRNA4, and **c** 23SBRo-MMT4 at 20 $\times$  magnification. Scale bar: 1 mm

The lowering of die swell values has a direct consequence on the improvement of processability. It is apparent that the processability improves with the incorporation of the unmodified and the modified nanofillers. Figure 10a–c show the SEM micrographs of the surface of the extrudates at a particular shear rate of  $61.2 \text{ s}^{-1}$  for the unfilled and the nanoclay-filled 23SBR systems. The surface smoothness increases on addition of the unmodified filler, and further improves with the incorporation of the modified filler. This has been again attributed to the improved rubber–clay interaction in the exfoliated nanocomposites.

Similar observations were noted when FKM/o-MMT clay nanocomposites were prepared by melt blending and the as-prepared nanocomposites showed both intercalated as well as exfoliated structure [103]. The apparent shear viscosity of the FKM/o-MMT nanocomposites was lower than that of the pristine polymer at all shear rates and temperatures. The nanocomposites exhibited reduced equilibrium die swell with a smooth extrudate appearance. A comparison of the flow properties of the nanocomposites with the conventional composites revealed that the nanocomposites exhibited improved processability.

Rubber-based nanocomposites were also prepared from different nanofillers (other than nanoclays) like nanosilica etc. Bandyopadhyay et al. investigated the melt rheological behavior of ACM/silica and ENR/silica hybrid nanocomposites in a capillary rheometer [104]. TEOS was used as the precursor for silica. Both the rubbers were filled with 10, 30 and 50 wt% of tetraethoxysilane (TEOS). The shear viscosity showed marginal increment, even at higher nanosilica loading, for the rubber/silica nanocomposites. All the compositions displayed pseudoplastic behavior and obeyed the power law model within the experimental conditions. The

**Fig. 11** Plots of the reinforcement factor (RF) versus concentration of silica in ACM/silica and ENR/silica hybrid nanocomposites



reinforcement factor (RF) calculated from the ratio of the viscosities of the filled and the unfilled systems was found to increase with nanosilica content at a particular shear rate. The plot of RF versus nanosilica content at a representative shear rate of  $98 \text{ s}^{-1}$  is shown in Fig. 11. ENR/silica nanocomposites display a higher increment of RF when compared to the ACM/silica system, which has been attributed to the better polymer–filler interaction in the former (Fig. 11). The RF remained almost constant for both the systems with the variation of temperature. For both ACM and ENR nanocomposites, the hybrid nanocomposites showed lower die swell values than the gum rubber systems, which is again ascribed to the polymer–filler interactions, reduction in polymer content per unit volume of the composites, decrease in elastic nature and development of relatively higher viscosities. As a result of this, nanosilica-filled hybrid nanocomposites showed distinctly smoother extrudate profile with an enhancement in overall processability.

### 3.2 Mechanical Properties

Filler in a polymer matrix can enhance the mechanical properties of the composites. It can increase composite properties either by inhibiting propagation of cracks for failure, or by imparting additional strength and toughness through its own high mechanical strength, or by changing the structure of the polymer layer near the filler surface. It is generally well established that the enhancement is dependent on the filler properties, e.g., particle size, shape and aspect ratio, dispersion of filler in the polymer matrix and interaction with polymer. With reduction of filler size from macro- to nano-level, a significant improvement in mechanical properties of the composites has been noticed. A general reason for improvement of the elastic modulus after incorporating filler to polymers is due to reinforcement mechanisms

described by theories for composites, which have been thoroughly illustrated in the literature [28, 105]. The Halpin–Tsai and Mori–Tanaka relations are two equations that are frequently used for composite calculations; the former shows a higher level of reinforcement whereas the latter shows lower reinforcement in comparison to experimental reinforcement values [106, 107]. The theories only predict the effects of simple reinforcement mechanism instead of any “nanoeffects” and consider only the aspect ratio, volume fraction, and orientation of filler in the matrix; the absolute filler particle size does not take part in the calculations. Paul and Robeson, in their review paper, have discussed in detail the reinforcement mechanisms of nanofillers in polymers [108]. Zeng et al. [33] in their review paper have covered in great detail the contribution made by various researchers on computer modeling and simulation methods for determining mechanical properties of the PNCs. These include molecular scale (e.g., molecular dynamics, Monte Carlo), microscale (e.g., Brownian dynamics, dissipative particle dynamics, lattice Boltzmann, time-dependent Ginzburg–Landau method, dynamic density functional theory method), mesoscale and macroscale (e.g., micromechanics, equivalent-continuum and self-similar approaches, finite element method), among others. They have also summarized the recent advances in the fundamental understanding of PNCs reinforced by nanofillers (e.g., spherical nanoparticles, nanotubes, and clay platelets) and stimulated further research in this area.

Many researchers have shown that incorporation of nanoscale dimension particles (inorganic fillers, nanotubes, nanofibers etc) into a polymer matrix enhances the mechanical properties of the polymer without significantly raising its density or sacrificing its light transmission property. For instance, the Toyota research groups [2] were the first to show the influence of nanoclays on the mechanical properties of polymers. They have introduced nylon-6/clay nanocomposites by the in situ method and observed that such nanocomposites exhibit 40% improvement in tensile strength, 60% in flexural strength, 68% in tensile modulus, and 126% in flexural modulus as compared to pristine polymer [4]. Ganter et al. [109, 110] have prepared rubber nanocomposites based on SBR and BR containing o-MMT. The o-MMT vulcanizates exhibit enhanced hysteresis when compared with the silica-filled vulcanizates and the results have been explained by the orientation and sliding of the anisotropic silicate layers as evidenced from online WAXS measurements during cyclic testing. Kojima et al. have incorporated laboratory prepared organoclay in NBR and noticed that 10 phr organoclay is necessary to achieve tensile strength comparable to the 40 phr carbon-black-loaded NBR composites [111]. Similarly, Joly et al. have observed that NR nanocomposites loaded with 10 wt% o-MMT show a comparable modulus value to that achieved by NR composites containing conventional fillers at very high concentrations [112]. Similar behavior has also been observed by Arroyo et al. [76]. Wang et al. have prepared NR/NA and CR/NA clay nanocomposites by coagulating the rubber latex and the aqueous clay suspension. Compared to NR/carbon black composites, 10 phr clay-loaded NR or CR nanocomposites exhibit high hardness, modulus, and tear strength values [113]. Wang et al. [114] have also compared the mechanical properties of both NA and o-MMT-based SBR nanocomposites by solution and latex blending techniques.

They have observed that clay/SBR nanocomposites prepared by the latex-blending technique show better properties than nanocomposites prepared by the solution technique. Lopez-Monchado et al. [115] have investigated the physical and mechanical properties of nanocomposites based on NR/o-MMT by both solution and mechanical mixing procedures. Varghese and Karger-Kocsis have shown that NR-based nanocomposites with 10 wt% natural sodium bentonite and synthetic sodium fluorohectorite layered silicates display better mechanical properties than commercial clay-loaded NR composites [65]. Varghese and Karger-Kocsis have produced composites based on sulfur-cured NR containing organophilic and pristine layered silicates of natural and synthetic origin by a melt compounding procedure (two-roll mill) and have ranked the property improvement by filler loading as organophilic clays > sodium fluorohectorite > sodium bentonite > precipitated silica [78]. Schon and Gronski have investigated the contribution of filler network to SBR loaded with silica and o-MMT. The magnitude of properties is greatly enhanced by incorporation of organoclay, due to its anisotropic structure, in comparison to silica-filled samples [116]. Usuki et al. [117] have prepared EPDM/o-MMT clay hybrids by mixing with EPDM and o-MMT and vulcanizing them using five different types of accelerator: thiourea, thiazole, sulfenamide, thiuram, and dithiocarbamate. They noticed that among the various accelerators used, thiuram and dithiocarbamate show maximum improvement of properties (e.g., tensile stress of the vulcanized hybrids was 40% higher than that of gum EPDM rubber). They have explained in a mechanistic way that thiuram- and dithiocarbamate-containing EPDM/o-MMT hybrids show good properties due to the better dispersion and exfoliation of silicate layers in EPDM rubber. Similar type of work has also been done by Gatos et al. [72]. Netrabukkana and Pattamaprom have studied the effect of compatibilizing agents on the mechanical properties of natural rubber/montmorillonite clay nanocomposites and observed that surface treatment of the clays with Si-69 gives superior tensile strength to the rubber compound [118]. Jia et al. [119] have investigated the combined effect of nanoclay and nanocarbon black on the properties of NR nanocomposites and observed that there is a synergistic effect of the fillers. Kim et al. have studied the effect of nanoclays on the properties of NR/BR blends [120]. Chang et al. [121] have modified the sodium montmorillonite by using octadecyl ammonium ions and incorporated the modified nanoclay into EPDM. They have observed the tremendous improvement in tensile and tear strength. Peeterbroeck et al. have investigated the effects of the nature of the clay and organic modifiers on mechanical properties [122]. Petrovic et al. [123] have prepared PU/silica nanocomposites and observed that the nanocomposites display higher strength and elongation at break but lower modulus than the corresponding micrometer-sized silica-based nanocomposites. Several researchers have prepared the nanocomposites from polymer latex and studied the mechanical properties [124–126]. The effect of carbon nanoparticles, nanotubes, and graphite nanoparticles on the mechanical and physical properties of NR nanocomposites has also been studied [127–129]. Zhou et al. [126] have prepared CNT-filled powder SBR composites by spray drying of the suspension of CNTs in SBR latex and found that the hardness, tensile and tear strengths of the



composites filled with 60 phr CNTs are enhanced by 73.9%, 327.7%, and 191.1%, respectively, in comparison to the unfilled SBR.

Sadhu and Bhowmick have studied the preparation and properties of SBR nanocomposites based on NA, o-MMT, bentonite, and potassium montmorillonite ( $K^+$ -MMT). They have also examined the effect of variable chain lengths of organic amine modifiers [130]. They reported that the tensile strength, elongation at break, modulus, and work to break all improve with the addition of nanoclays into SBR. The tensile strength increases with increasing chain length of the amine modifiers used in the clays. Among the various clays, o-MMT exhibits better mechanical properties than bentonite and  $K^+$ -MMT and this has been explained by the X-ray data and TEM images. Compared with the SBR rubber, all the nanocomposites displayed better mechanical properties. Sadhu and Bhowmick [131] have also studied the effects of the styrene content in SBR, the solvent used for preparation of nanocomposites, the curing systems, and aging on the mechanical properties of the nanocomposites prepared from SBR rubber and o-MMT nanoclay. All the modified clay/rubber nanocomposites show improved mechanical strength. The properties enhance with increasing styrene content. Dicumyl peroxide and sulfur-cured systems display similar strength, but higher elongation and slightly lower modulus values have been obtained with the sulfur-cured system. It has been observed that the highest tensile strength is observed for toluene cast samples, whereas the highest elongation at break is observed for chloroform cast samples. This is due to decoiling of the SBR matrix in toluene because of its similar polarity and solubility parameters. Furthermore, Sadhu and Bhowmick [132] also examined the effects of styrene content on the morphology and mechanical properties of SBR-based nanocomposites. In another study, the mechanical properties of NBR, SBR and BR containing NA and o-MMT were studied by Sadhu and Bhowmick [62]. In addition, they have also shown the effect of polarity of the NBR rubber (19%, 34%, and 50% ACN group), concentration of nanoclay used (2, 4, 6 and 8 phr clay loading), nature of the rubber, and structure of the clay on the mechanical properties of these nanocomposites. A good correlation between different nanocomposites and mechanical properties has been established. In all cases, nanocomposites show improved mechanical properties. The stress–strain curves of the unfilled and filled 19NBR (19% ACN content), 34NBR (34% ACN content), 50NBR (50% ACN content), BR, and SBR are shown in Fig. 12a–e. An improvement in the mechanical properties with the degree of filler loading up to a certain level has been observed. The changes in the mechanical properties, with changes in the nature and polarity of the rubbers, have been explained with the help of XRD and TEM results.

In an interesting work, Ganguly and Bhowmick synthesized SSEBS by reaction of acetyl sulfate with SEBS [133]. SSEBS/clay nanocomposites were then prepared from NA and o-MMT at very low loading. SEBS does not show much improvement in the mechanical properties with NA-based nanocomposites. However, on sulfonation (3 and 6 wt%, S3SEBS and S6SEBS) of SEBS, NA-based nanocomposites exhibited better mechanical properties. The microstructure of these nanocomposites has been determined by XRD, AFM, and TEM. Figure 13a–f illustrates the

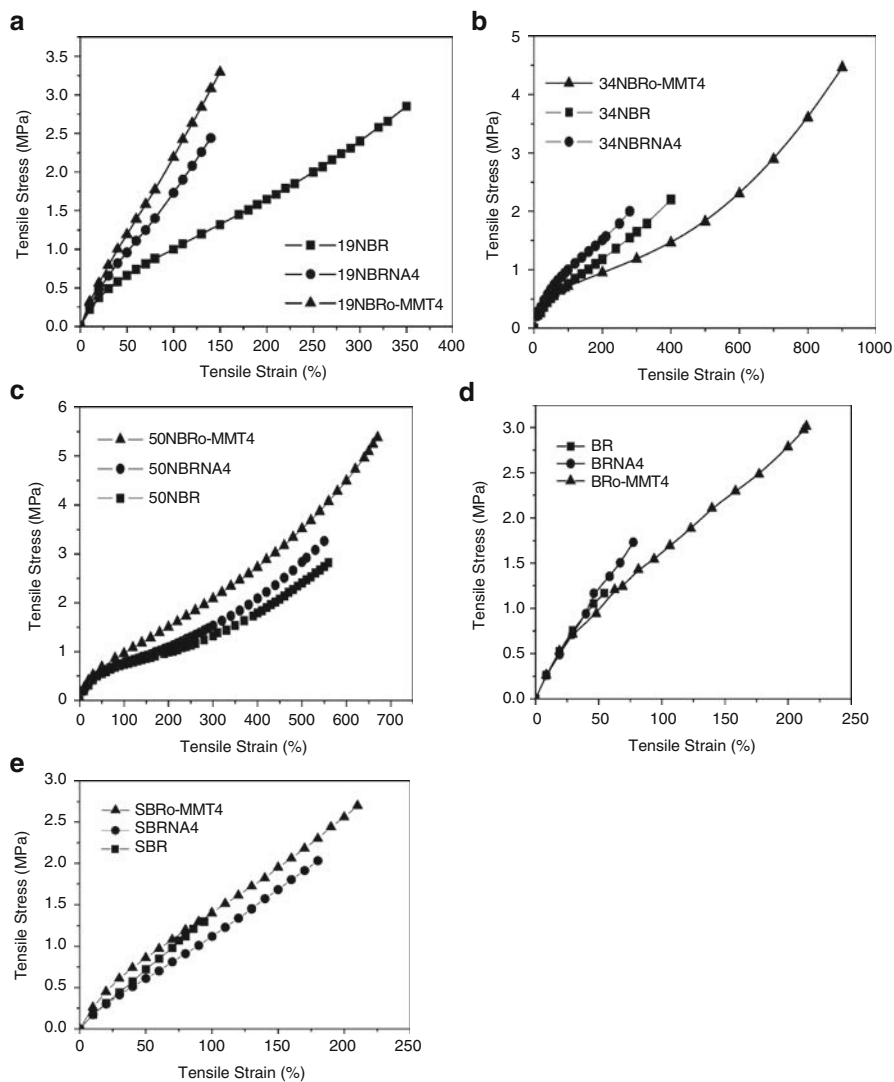


**Fig. 12** Stress–strain curves of **a** 19NBR, **b** 34NBR, **c** 50NBR, **d** BR, and **e** SBR and their nanocomposites with control unmodified (NA) and modified (o-MMT) montmorillonite clays

resulting morphology of SEBS and SSEBS-based nanocomposites. The improvement in the properties has been ascribed to the better dispersion of NA nanoclay particles and interaction of NA with the SSEBS matrix.

Maiti et al. [14] have studied the effects of different nanoclays (namely, NA, 10A, 20A, and 30B) on the properties of BIMS rubber. They have characterized the clays and the rubber nanocomposites by means of FTIR, TEM, and XRD.

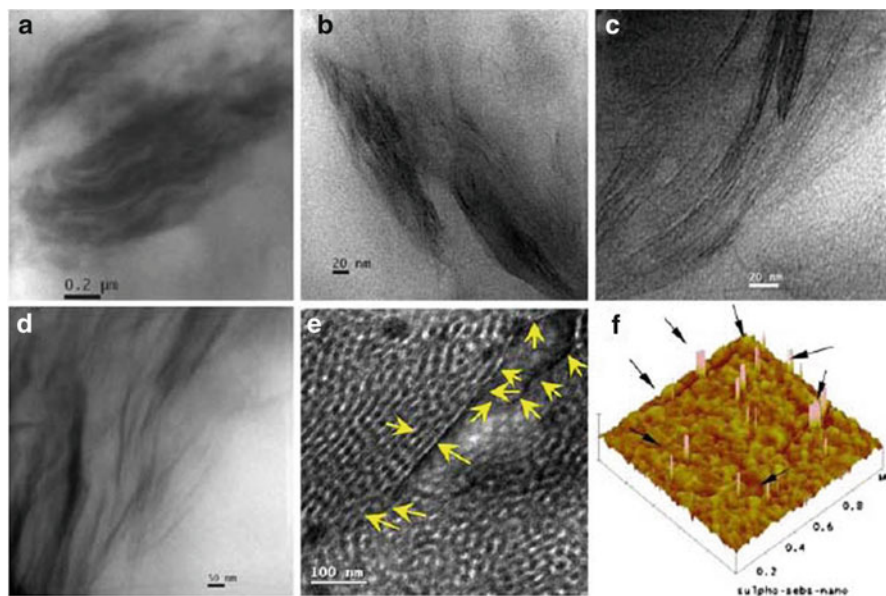


**Fig. 13** Bright field TEM morphology of **a** thick stacks of SEBS-NA4, **b** intercalated exfoliated S3SEBS-NA4, **c** exfoliated S6SEBS-NA4, **d** intercalated S6SEBS-o-MMT4, **e** regenerated distinct lamellae of sulfonated polystyrene (SPS) and PEB domains of exfoliated S6SEBS-NA4 nanocomposites as seen after selective staining (clays are indicated by *arrows*). **f** 3D AFM phase image of S6SEBS-NA4 showing fine clay layers (*arrows* indicate thickness of 2–6 nm) impregnated from SPS domains of the matrix

The X-ray diffraction peaks observed in the range of  $3^{\circ}$ – $10^{\circ}$  for the modified clays disappear in the rubber nanocomposites. TEM photographs show predominantly exfoliation of the clays in the range of  $12 \pm 4$  nm in the BIMS. Consequently, excellent improvement in mechanical properties like tensile strength, elongation at break, and modulus is observed by the incorporation of the nanoclays in the BIMS. Maiti and Bhowmick have also studied the effect of solution concentration (5, 10, 15, 20, and 25 wt%) on the properties of fluorocarbon clay nanocomposites [64]. They noticed that optimum properties are achieved at 20 wt% solution. At the optimized solution concentration, they also prepared rubber/clay nanocomposites by a solution mixing process using fluoroelastomer and different nanoclays (namely NA, 10A, 20A, and 30B) and the effect of these nanoclays on the mechanical properties of the nanocomposites has been reported, as shown in Table 4 [93].

In addition, Maiti and Bhowmick [93] also used fluoroelastomers having different microstructure and viscosity (Viton B-50, Viton B-600, Viton A-200, and VTR-8550). Viton is a terpolymer of vinylidene fluoride (VF2), hexafluoropropylene (HFP), and tetrafluoroethylene (TFE). Even with the addition of only 4 phr of clay in Viton B-50, the tensile strength and modulus improved by 30–96% and 80–134%, respectively, depending on the nature of the nanoclays. The better polymer–filler interaction in the case of NA clay and the fluoroelastomers has

**Table 4** Mechanical properties of different unvulcanized fluoroelastomer-based nanocomposites

Sample designation <sup>a</sup>	Modulus at 100% elongation (MPa)	Elongation at break (%)	Maximum stress (MPa)
F	0.35 ± 0.02	110 ± 5	0.46 ± 0.02
FNA2	0.46 ± 0.05	160 ± 5	0.60 ± 0.02
FNA4	0.88 ± 0.01	520 ± 5	0.90 ± 0.01
FNA8	1.04 ± 0.02	309 ± 3	1.20 ± 0.02
FNA16	1.06 ± 0.00	185 ± 4	1.10 ± 0.01
F10A4	0.58 ± 0.01	175 ± 3	0.63 ± 0.01
F20A4	0.64 ± 0.01	444 ± 5	0.70 ± 0.01
F30B4	0.65 ± 0.05	265 ± 3	0.70 ± 0.01

<sup>a</sup>F fluorocarbon elastomer; 2, 4, 8, and 16 correspond to the nanoclay loading in phr

been explained on the basis of thermodynamics. The authors have calculated the enthalpy change with the help of Fowkes's equation and found that NA nanoclays show negative enthalpy in comparison to other nanoclays having either zero or a small positive value. Therefore, NA is thermodynamically more feasible for the preparation of nanocomposites with the fluoroelastomers in comparison to other nanoclays. In addition to this, they have explained for the first time the better interaction between the unmodified clay and fluoroelastomer in terms of surface energy. Maiti and Bhowmick have also prepared fluoroelastomer nanocomposites in which the layered silicates (such as montmorillonite and hectorite) used have been synthesized in the laboratory. Furthermore, structure–property relationships of these nanocomposites have been established, with special reference to the characteristics of the synthesized nanoclays [134, 135]. Synthetic-clay-filled samples show better properties than the natural-clay-filled samples. For example, the synthetic-hectorite-filled sample exhibited a 75% increment in tensile strength and 24% improvement in the 100% modulus (elastic modulus at 100% elongation) compared with the natural-hectorite-based system. The results were well explained with the help of thermodynamics and morphology [135].

Choudhury et al. [86] have studied the effect of polymer–solvent and clay–solvent interaction on the mechanical properties of the HNBR/sepiolite nanocomposites. They chose nine different sets of solvent composition and found that chloroform/methyl ethyl ketone (Ch/MEK) (i.e., HNBR dissolved in Ch and sepiolite dissolved in MEK) is the best solvent combination for improvement in mechanical properties. XRD, AFM, TEM, and UV–vis spectroscopy studies show that the dispersion of clay is best in the Ch/MEK solvent combination and hence polymer–filler interaction is also the highest. TEM images shown in Fig. 14a, b clearly elucidate the aforementioned phenomena. Consequently, the tensile strength and modulus are found to be higher (5.89 MPa and 1.50 MPa, respectively) for the Ch/MEK system due to the minimum difference in interaction parameter of HNBR–solvent ( $\chi_{AB}$ ) and sepiolite–solvent ( $\chi_{CD}$ ). Choudhury et al. have also studied the effect of different nanoclays [NA, 30B, 15A, and sepiolite (SP)] and nanosilica (Aerosil 300) on the mechanical properties of HNBR [36]. The tensile

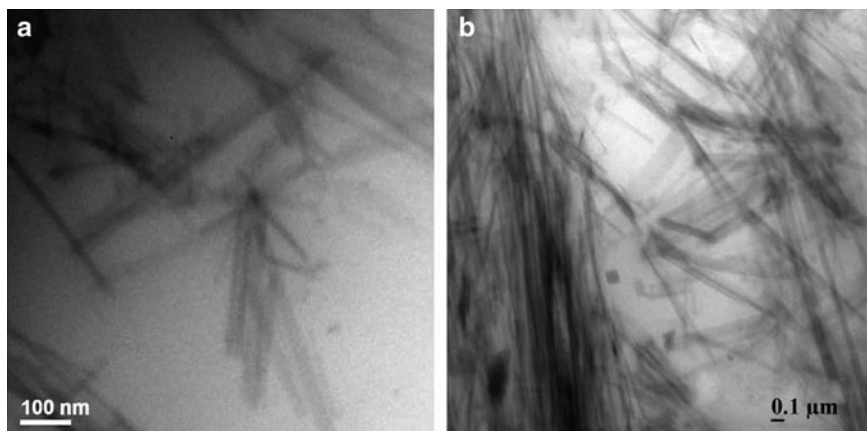


**Fig. 14** TEM photographs of HNBR/SP nanocomposites in **a** chloroform/MEK and **b** chloroform/ethanol solvent combinations

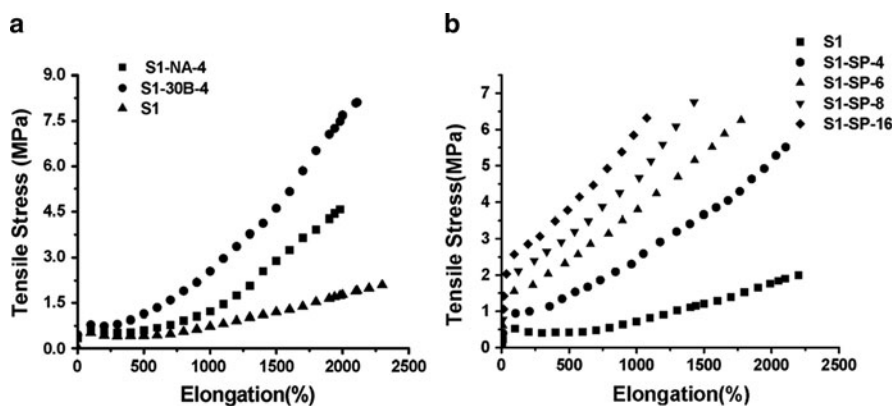


**Fig. 15** Stress–strain curves of **a** neat HNBR and its nanocomposites with different fillers at 4 phr loading, and **b** HNBR and SP-based nanocomposites at variable clay loadings

stress–strain curves are shown in Fig. 15a, b. From Fig. 15a, it is seen that 30B at 4 phr loading shows the best mechanical properties whereas, from Fig. 15b, it can be concluded that SP at 4 phr loading shows maximum modulus at 100% elongation. They have correlated the above results with the XRD and TEM results.

Maji et al. [136] have examined the effect of 30B loading on the mechanical properties of hyperbranched polyurethane (PU) nanocomposites. The extent of clay loading was varied from 2 to 16 phr. The nanocomposite containing 8 wt% 30B clay shows a  $\sim 100\%$  increase in the tensile strength as compared to unmodified-clay-filled samples. Above 8 wt% clay loading, the mechanical properties decrease. The efficiency and good dispersion of 30B in the hyperbranched PU40

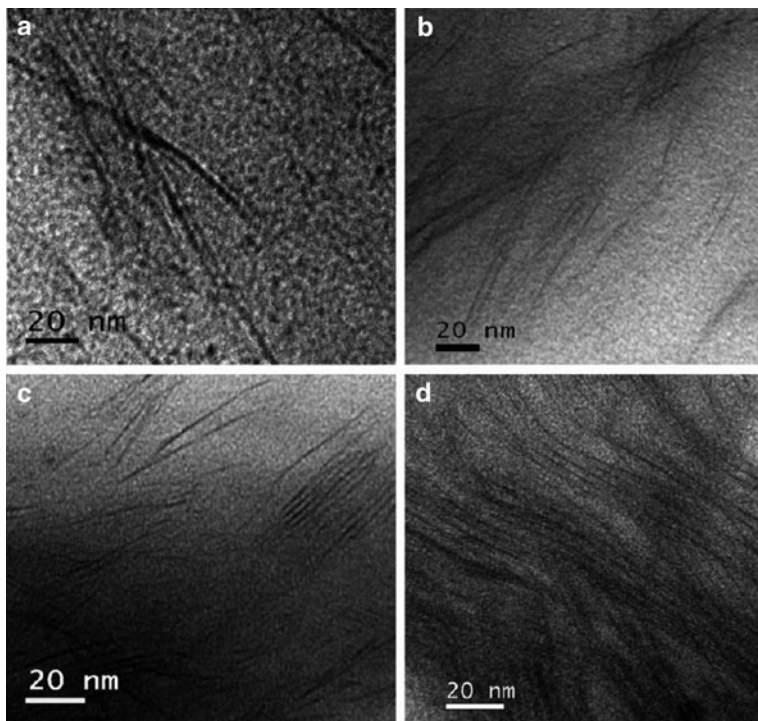


**Fig. 16** TEM photographs of different PU40- and 30B-based nanocomposites at various clay loadings: **a** 2, **b** 4, **c** 8, and **d** 16 phr

(hyperbranched PU prepared using fourth-generation hyperbranched polyester) have been explained on the basis of XRD and TEM results. The TEM images shown in Fig. 16a, b clearly demonstrate the good dispersion of 30B nanoclay in PU40 matrix. At and above 8 phr of clay loading, considerable agglomeration of nanoclays is observed (Fig. 16c, d).

The interaction between the isocyanate of hyperbranched PU and the OH group of clay, which helps dispersion of clay easily in the hyperbranched PU matrix, has been proved from FTIR analysis. The effects of NA and 30B loading on the physicomechanical properties of polyester/polyurethane nanocomposites have been also explored by Maji et al. [15]. They noticed that the modulus of the nanocomposites increases monotonically with increasing clay content. However, at higher filler loading, the 30B/PU nanocomposites display a greater increment in modulus than the NA/PU nanocomposites. There is  $\sim 54$  and 17% increase of the 100% modulus with the incorporation of 3 phr of the 30B and NA clays into the PU matrix, respectively. The greater improvement of tensile modulus for 30B/PU composites in comparison to NA/PU nanocomposites can be attributed to the better dispersion and intercalation/exfoliation of the nanoclays, as proved from high and low magnification TEM images. Beyond 3 wt% clay loading, the tensile strength

decreases, which is due to formation of agglomerated clay structures that make homogeneous dispersion difficult. The authors have established a good correlation between mechanical properties and morphology.

The incorporation of unmodified and organically modified montmorillonite nanoclays (namely 15A and 30B) in chlorinated polyethylene (CPE) by the solution intercalation method and their influence on mechanical properties of the nanocomposites have been studied by Kar et al. [137]. The o-MMT-embedded nanocomposites show enhanced tensile strength and Young's modulus in comparison to the nanocomposites containing the unmodified nanoclay. They have shown from TEM and XRD analyses that organically modified clay shows better dispersion in the CPE matrix. This has been further substantiated from FTIR analysis, which proves an interaction between the CPE matrix and the clay intercalates.

Bandyopadhyay et al. [138] have also studied the distribution of nanoclays such as NA and 30B in NR/ENR (containing 50 mol% epoxy) and NR/BR blends and their effect on the overall properties of the resultant nanocomposite blends. They calculated the preferential distribution of clays at various loadings in the blend compounds from the viscoelastic property studies from DMA. The tensile properties of the 50:50 NR/ENR and 50:50 NR/BR blend nanocomposites are shown in Table 5. It is apparent that in both the blends that the mechanical properties increase with increasing clay concentration up to a certain extent and then decrease. These results have been found to depend on matrix polarity and the viscosity of the blend compounds.

Kuila et al. [139] have studied the effect of laboratory synthesized organophilic dodecylsulfate-intercalated layered double hydroxide (DS-LDH) on the mechanical properties of EVA/EPDM blends. They observed that maximum improvement in mechanical properties is attained at 3 wt% DS-LDH loading (tensile strength and elongation at break are 35 and 12% higher than neat EVA/EPDM blends). Pramanick et al. [140] have found that ethylene vinyl acetate (EVA) containing 45% vinyl acetate content shows ~1.6 times higher tensile strength than neat rubber at 6 wt% loading of o-MMT.

In order to prepare ENR/silica nanoscale organic–inorganic hybrid composites, nanosilica has been generated by the sol–gel technique using TEOS as a precursor. Their effect on mechanical properties of the resultant nanocomposites have been

**Table 5** Increments in maximum force value ( $F_{\max}$ ) and tear strength with nanoclay loading in 50:50 NR/ENR blends and 50:50 NR/BR blends

Blend	Nanoclay	Clay loading	Increment in $F_{\max}$ (%)	Increment in tear strength (%)
NR/ENR	Cloisite 30B	2	14	13
		4	40	29
		8	55	34
NR/BR	Cloisite Na <sup>+</sup>	4	−4	−2
		Cloisite 30B	2	17
	Cloisite 30B	4	33	9
		8	29	7
NR/BR	Cloisite Na <sup>+</sup>	4	29	20

studied by Bandyopadhyay et al. [61]. The composites show superior tensile strengths and tensile moduli compared to the gum rubber samples. Further reinforcement has been noticed when the rubber phase in the nanocomposites has been cured with either benzoyl peroxide or dicumyl peroxide. The dicumyl-peroxide-cured hybrid composites display 112% improvement in tensile strength over the control crosslinked rubber sample, which is probably due to synergism of nanosilica reinforcement and crosslinking of the rubber phase in the hybrids. A similar effect has also been noticed for acrylic rubber/silica hybrid composites by Bandyopadhyay et al. [141]. In another work, PVA/silica organic inorganic hybrid composites have been prepared by Bandyopadhyay et al. using the sol–gel technique [142]. In this work also, TEOS has been used as the precursor for nanosilica generation. The reaction was carried out in an aqueous medium having a pH of 1.5, with concentrated hydrochloric acid as the catalyst. A significant improvement in the Young's modulus and the tensile strength of the samples was observed. Interaction at organic–inorganic interfaces because of hydrogen bonding has been speculated from IR analysis of the hybrid composites, and uniform dispersion of nanoparticles has been proved from TEM analysis and from results obtained from energy dispersive X-ray mapping of silicon. Bandyopadhyay et al. [143] have prepared ACM/silica hybrid nanocomposites using the sol–gel technique. The effects of a few reaction parameters, i.e., type of solvents, TEOS-to-H<sub>2</sub>O mole ratio, and temperature of gelation at constant concentration of TEOS (45 wt%) and pH of 1.5 have been investigated. Compared to other solvents used, THF generated maximum silica formation in the hybrid matrix due to its maximum miscibility with the water. Beyond 1:2 molar ratios of THF/H<sub>2</sub>O and at high temperature, aggregation of silica particles is observed. The best properties of the nanocomposites were observed when THF was used as solvent, the THF/H<sub>2</sub>O ratio was kept at 1:2, and the temperature did not go above room temperature. The nanocomposite exhibits superior mechanical properties (tensile strength and tensile modulus) compared to the microcomposites in both the cured and the uncured states. Bandyopadhyay et al. have reported a comparative study on the structure–property relationship of ACM/silica, ENR/silica and PVA/silica hybrid nanocomposites prepared by the sol–gel technique at different pH levels (pH = 1.0–13.0) [110]. TEOS-to-H<sub>2</sub>O mole ratio was maintained at 1:2 for the rubber/silica systems to accomplish the sol–gel reaction. The silica particles have been found to exist as nanoparticles (average diameter <100 nm) at low pH ( $\leq 2.0$ ), beyond which they form aggregates. It has also been observed that the amount of silica generation is independent of the various pH conditions used for all the systems. The maximum improvement of mechanical properties was observed with the PVA/silica nanocomposites due to the higher level of interaction between the –OH of PVA and the –OH–Si groups of the silica phase.

The effect of the microstructure of acrylic copolymer/terpolymer on the properties of silica-based nanocomposites prepared by the sol–gel technique using TEOS has been further studied by Patel et al. [144]. The composites demonstrate superior tensile strength and tensile modulus with increasing proportion of TEOS up to a certain level. At a particular TEOS concentration, the tensile properties improve with increasing hydrophilicity of the polymer matrix and acrylic acid modification.



The mechanism for improvement in mechanical properties of the hybrids has been explained. The effect of acrylic copolymer and terpolymer composition on the properties of in situ polymer/silica hybrid nanocomposites has been further studied by Patel et al. [145]. They have observed that terpolymer–silica hybrids demonstrate superior mechanical properties compared to the copolymer–silica hybrids.

George and Bhowmick have investigated the influence of reinforcement produced by unmodified and surface-modified (by electron beam, gamma irradiation, and chemical treatment by acid, amine, or silane) carbon nanofibers (CNFs) on the mechanical properties of EVA/CNF nanocomposites in which the percentage of vinyl acetate in the EVA matrix is 50% [146]. An improvement of tensile strength of 61 and 125% was observed after the addition of 1 and 4 wt% of untreated CNFs, respectively. Further addition of untreated CNF (8 wt%) caused a decline in tensile strength due to poor dispersion and agglomeration of filler particles, as observed in TEM photographs. The modulus shows a remarkable increment of 350 and 520% with the addition of 4 and 8 wt% of CNFs, respectively. By contrast, the elongation at break shows a steep decrease with the increased amount of untreated CNF. All the tensile properties show an increase with EB dose up to 800 kGy. On the other hand, gamma irradiation of 1 kGy provides the best tensile properties, beyond which there is no significant improvement. Among the chemical modifications, silane- and amine-treated CNFs show improvement in tensile properties, whereas acid-treated CNFs adversely affect the tensile properties due to degradation of the CNFs. In Table 6, the tensile properties of nanocomposites reinforced with CNFs treated with electron beam, gamma irradiation, and various chemicals are also compared with those of virgin EVA and untreated-CNF-reinforced nanocomposites at 1 wt% loading.

George and Bhowmick [147] have also studied the influence of the polarity of EVA (40, 50, 60, and 70% vinyl acetate content) and the nature of the nanofiller [expanded graphite (EG), multiwall carbon nanotubes (MWCNTs), and CNFs] on the mechanical properties of EVA/carbon nanofiller nanocomposites. They pointed out that the enhancement in mechanical properties with the addition of various

**Table 6** Tensile properties of various EVA-based nanocomposites

Sample designation	Tensile strength (MPa)	Elongation at break (%)	Modulus at 100% elongation (MPa)
EVA	5.05 ± 0.15	490 ± 30	0.74 ± 0.17
EVA-1F	8.14 ± 0.20	410 ± 20	1.04 ± 0.21
EVA-1FEB	8.53 ± 0.11	465 ± 20	1.25 ± 0.12
EVA-1F $\gamma$	8.60 ± 0.15	440 ± 15	1.38 ± 0.15
EVA-1AF	8.25 ± 0.12	432 ± 25	1.30 ± 0.10
EVA-1XF	6.86 ± 0.18	323 ± 30	1.02 ± 0.16
EVA-1SF	8.50 ± 0.10	436 ± 15	1.36 ± 0.14

*EVA* neat elastomer, *EVA-1F* EVA filled with 1 wt% of untreated CNF, *EVA-1FEB* EVA filled with 1 wt% CNF treated with 800 kGy electron beam, *EVA-1F $\gamma$*  EVA filled with 1 wt% CNF treated with 1 kGy gamma irradiation, *EVA-1AF* EVA filled with 1 wt% of amine-treated CNF, *EVA-1XF* EVA filled with 1 wt% of acid-treated CNF, *EVA-1SF* EVA filled with 1 wt% of silane-treated CNF

nanofillers is the highest for EVA with high vinyl acetate content. Addition of 4 wt% of EG enhances the tensile strength of EVA having 40% vinyl acetate by 11.5%, whereas MWCNTs and CNFs increase it by 7 and 32.8%, respectively. On the other hand, the increments are 58, 14, and 150%, respectively, in EVA having 70% vinyl acetate content. The high vinyl-acetate-containing polymers show more affinity toward fillers due to the large free volume available, and allow easy dispersion of nanofillers in the amorphous rubbery phase. The authors have confirmed the results with morphological studies.

In a detailed review, Maiti et al. [5] have shown the influence of various nanofillers (silicate clays, carbon nanotubes, nanofibers, calcium carbonate, metal oxides, or silica nanoparticles) on the mechanical properties of elastomers. They have shown that the uniform dispersion of nanofillers in elastomer matrices is a general prerequisite for achieving desired mechanical properties. They have clearly established that the properties of nanocomposites depend greatly on the chemistry of polymer matrices, nature of nanofillers, and the method by which they are prepared. Bhattacharya et al. [84] studied the effects of varying morphological and chemical constitution of nanofillers and various dispersion methods on NR nanocomposites prepared by conventional processing techniques. They used various nanofillers like montmorillonite, SP, hectorite, CNFs, and EG. The 4 phr needle-like SP-loaded NR nanocomposite registers an increment of 26% in the modulus, and 6 phr-loaded fluorocarbon elastomer (F) increases the tear strength by 18% over the gum. Nanofiller dispersion has been improved by various compatibilizers such as bis (3-triethoxysilylpropyl)-tetrasulfide, sodium lauryl sulfate, and triethoxyvinylsilane. Additionally, various mixing techniques such as premixing by means of the solution process and ultrasonication, changes in the process variables and conditions of mixing (time, temperature, or rpm) etc. also result in better dispersion. Incorporation of compatibilizers and surfactants results in 56 and 113% increment in the modulus of the nanocomposites over the gum rubber vulcanizate for SP and F, respectively. They have also noticed that for CNF-filled systems, the tear strength is increased up to 28% over the gum. Bhattacharya et al. have also compared the organic–inorganic nanocomposite hybrids of SBR prepared from various nanofillers such as modified and unmodified montmorillonite, SP, hectorite, CNFs, and EG on the basis of mechanical properties [13]. They noticed that an increment of 230% in the tensile strength at 8 phr loading is observed for 15A, whereas increases of the modulus and tear strength of 101 and 79%, respectively, are observed for CNFs at 6 phr loading as compared to its gum. On chemical modification, 15A registered a 146% increase in modulus and 303% in tensile strength, while CNF showed 150% increment in modulus and 113% in tensile strength of the nanocomposites over the gum.

Recently, Mitra et al. have prepared chemically crosslinked nanosized gels from different rubber lattices [148, 149]. When added in small quantity (2–16 phr), these low moduli deformable gels have been found to influence the mechanical properties of virgin elastomers like NR and SBR considerably. For example, sulfur pre vulcanized nanosized SBR latex gels were prepared and characterized using various methods [148]. The morphology of gel-filled NR and SBR systems has been studied

using X-ray dot mapping, TEM, and AFM [148]. These show that the gels are evenly distributed at low loadings, whereas they tend to form agglomerates at relatively higher loadings. Addition of chemically crosslinked nanogels considerably improves the tensile strength and modulus of the gel-filled rubbers compared to the pristine one. The tensile strength (or maximum stress) and Young's modulus of the gel-filled elastomer systems increase with the increase in nanogel loading. The reinforcement ability of the gels depends on their crosslinking densities. Guth–Gold and Kerner particulate composite reinforcement models have been used to understand the reinforcement behavior of these nanogels [149].

### 3.3 *Dynamic Mechanical Analysis*

Dynamic mechanical analysis (DMA) measures the response of a viscoelastic material to a cyclic or sinusoidal deformation as a function of the temperature. DMA results are interpreted in terms of three main parameters: (1) the storage modulus ( $E'$  or  $G'$ ), corresponding to the material's elastic response to the deformation; (2) the loss modulus ( $E''$  or  $G''$ ), corresponding to the material's plastic response to the deformation; and (3) the loss factor ( $\tan \delta$ ), i.e., the  $E''/E'$  (or  $G''/G'$ ) ratio, which indicates the occurrence of molecular mobility and segmental transitions such as the glass transition temperature ( $T_g$ ) [150]. It has already been mentioned in Sect. 3.2 that better mechanical properties of rubber-based nanocomposites originate from stronger polymer–filler interaction and a large interfacial area per unit volume of the filler particles. Addition of nanofillers considerably modifies the low strain dynamic mechanical properties of the rubber-based nanocomposites, depending on the nature of the filler used. Generally, in the case of PNCs, the storage modulus invariably increases with the addition and subsequent dispersion of a layered silicate in a polymer [151, 152]. This increase is more prominent above  $T_g$  when the matrix gets soft. As a result, the reinforcement effect of clay particles becomes more pronounced. The  $\tan \delta$  values are affected in different ways by nanocomposite formation, depending on the polymer matrix. For example, in PS based nanocomposites, a shift of  $\tan \delta$  to higher temperatures has been observed, accompanied by a broadening of this transition [153], while the opposite effect has been reported in the case of PP-based nanocomposites [154]. Some authors have observed a decrease in  $\tan \delta$  peak heights, and considered this as indicative of glass transition suppression in the presence of the clay.

#### 3.3.1 **Transitions in Rubber-Based Nanocomposites**

The DMA of rubber-based nanocomposites has been the subject of recent research. Many literature reports describe the dynamic mechanical behavior of rubber-based nanocomposites [155, 156]. Das et al. have studied the DMA of CR nanocomposites based on montmorillonite clay and LDH [157]. The montmorillonite clay is

found to enhance the crystallization tendency of CR chains, whereas LDH resists it, as observed from the DMA. The DMA results also show that the presence of a small amount of nanoclay enhances the storage modulus of CR-based vulcanizates, which becomes more pronounced in the case of organically modified clays. This type of behavior is attributed to development of the “house of cards” morphology of exfoliated montmorillonite platelets in the CR matrix due to the mechanical shear mixing. In the case of natural rubber and layered silicate nanocomposites prepared by melt blending, DMA with varying temperature shows that the peak of the loss modulus broadens with increasing clay content, though the peak temperature is scarcely affected [158]. The constraint effect of exfoliated montmorillonite layers on EPDM chains in the case of EPDM/montmorillonite nanocomposites has been established by the DMA technique [159]. This effect contributes to the increased storage modulus, and increased  $T_g$  in the nanocomposites.

In this laboratory, rubber-based nanocomposites have been prepared from SBR (with 23% styrene content, 23SBR) and NBR with varying acrylonitrile content (19%, 34%, and 50%) using NA and o-MMT clays [160]. Figure 17 illustrates the temperature dependencies of the storage modulus for SBR and its nanocomposites. With the addition of 4 phr of nanoclays, the clay-filled nanocomposites give higher storage modulus values compared to unfilled SBR in both the glassy and rubbery regions. The peak  $\tan \delta$  value (i.e.,  $T_g$  shifts from  $-57^\circ\text{C}$  in unfilled SBR to  $-50^\circ\text{C}$  in the case of modified-clay-filled sample. The magnitude of the  $\tan \delta$  peak height also reduces drastically from the control SBR (1.74) to o-MMT-filled SBR (1.10). Better polymer–filler interaction has been attributed for the lowering in  $\tan \delta$  peak height and shifting of the  $T_g$  towards higher temperature. It has been found that the dynamic mechanical properties are greatly influenced by the nature and polarity of the base rubber due to the change in degrees of intercalation and interactions. For example, the storage modulus of o-MMT-filled NBR systems increases steadily with nanofiller loading. However, NBR with 50% ACN content shows the maximum increment in storage modulus with clay loading.

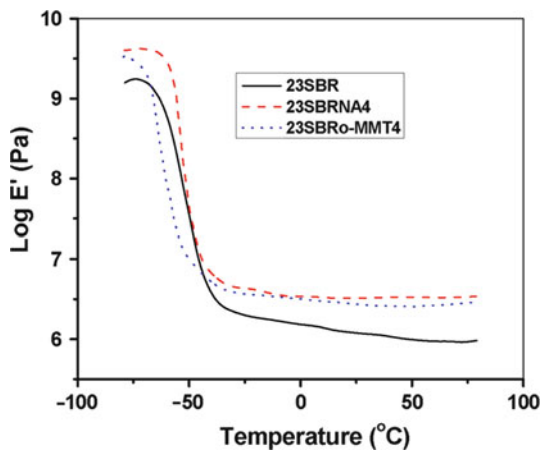
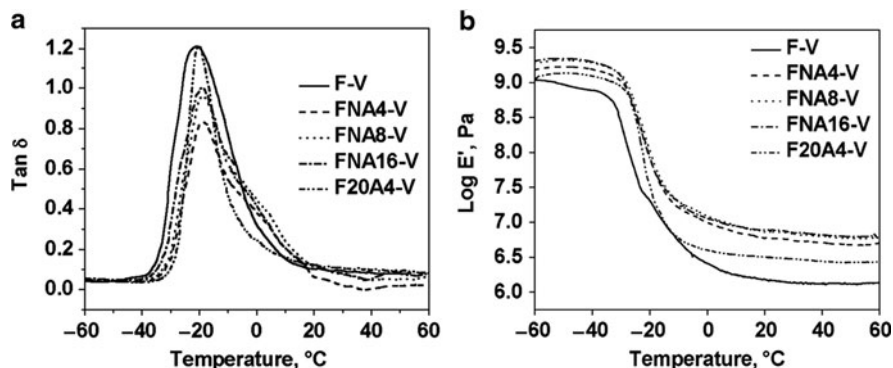


Fig. 17 Log  $E'$  versus temperature plot for SBR and its nanocomposites



**Fig. 18** Variation of **a**  $\tan \delta$  versus temperature, and **b**  $\log E'$  versus temperature for different fluorocarbon rubber nanocomposites (V refers to vulcanized samples)

Figure 18a shows the plot of loss tangent as a function of temperature of different fluorocarbon-rubber-based nanocomposites having different loadings of NA and 20A [161]. The  $T_g$  of these nanocomposites has been calculated from the peak maximum in the curve. With the addition of the unmodified clay,  $T_g$  shifts towards higher temperature by  $5^\circ\text{C}$ , whereas a  $2^\circ\text{C}$  rise is observed in the modified-clay-filled system at 4 phr loading (FNA4-V). The change in  $T_g$  is attributed to the increase in volume fraction of the rubber, arising from the increased rubber–filler interaction. This results in restricted segmental mobility of the polymer chains. Of all the filler-loaded samples, the maximum shift in  $T_g$  can be observed at 4 phr loading. The magnitude of  $\tan \delta_{\max}$  is also lowest for this nanocomposite compared to the gum vulcanizate. At still higher loading, the  $\tan \delta$  peak height starts to increase. As the rubber–filler interaction increases, the available free-chains decrease, resulting in a decrease in  $\tan \delta_{\max}$ . The lowest value of  $\tan \delta_{\max}$  in FNA4-V is due to better filler dispersion and higher interaction between the fluoroelastomer and polar unmodified clay compared to the organically modified clay. This observation has been found to be very unique for the fluoroelastomer nanocomposite system. Over a wide range of temperatures, both the unmodified- and the modified-clay-filled systems show increased storage modulus compared to the gum vulcanizate (Fig. 18b). For example, at  $25^\circ\text{C}$ , 10% improvement in  $\log E'$  can be observed with 4 phr of unmodified clay compared to the control. The improvement in storage modulus is higher in the case of the unmodified-clay-filled system than for the modified clay system. The storage modulus increases marginally on changing the filler loading from 4 to 16 phr in the transition region, while in rubbery region in general it increases slightly [161].

Figure 19a, b compares the storage modulus as well as  $\tan \delta$  for various nanocomposites prepared from EVA rubber having 50% vinyl acetate content and loaded with MWCNT, as a function of temperature [162]. Throughout the experimental temperature range of  $-35$  to  $20^\circ\text{C}$ , the storage moduli show steady increase from the virgin rubber with the increase in MWCNT level (see Fig. 19a). For example, there is

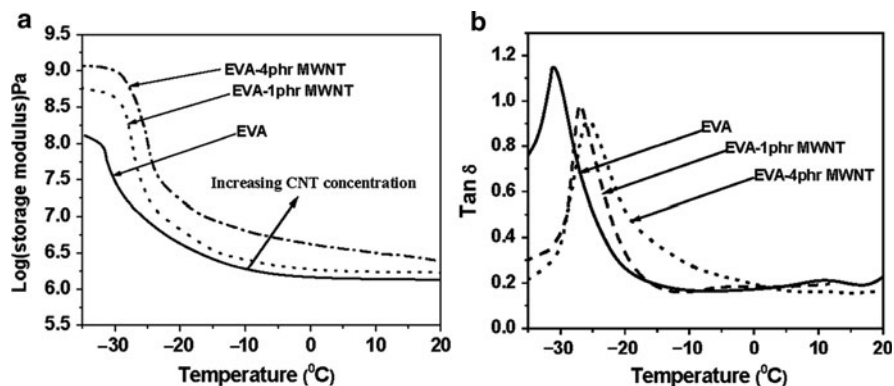


Fig. 19 DMA plots of EVA with MWCNT, showing temperature dependence of **a** storage modulus and **b** tan  $\delta$

10% increase of storage modulus with 4% MWCNT. The increase in modulus on addition of MWCNT is due to rubber–filler interactions. In the case of tan  $\delta$ , it shows significant decrease in the peak height with increasing MWCNT concentration (see Fig. 19b). A steady shift in the tan  $\delta_{\max}$  (which indicates the  $T_g$  of the system) to higher temperature regions as a result of addition of MWCNT is also noted.

Recently, PU-based nanocomposites have been prepared from toluene diisocyanate, poly (propylene glycol), hyperbranched polymers (HBPs), and layered silicate clays to investigate the effect of the layered silicate loading and the functionality of HBP on the structure and properties [136].  $T_g$  increases almost linearly with the increase in clay loading, whereas the magnitude of the tan  $\delta$  peak decreases steadily. This is mainly attributed to good adhesion between the PU and the clay particles, as a result of which the nanometer-sized particles can restrict the segmental motion near the organic–inorganic interface. With an increase in the functionality of the HBP, the  $T_g$  also increases in the resultant nanocomposites. The addition of layered silicate clays leads to an increase in the storage modulus, which is due to the reinforcing action of the nanoclays. However, the enhancement in modulus is lower at higher concentrations of clays, which has been attributed to intercalation and agglomeration of the clays [136].

On the other hand, Bhattacharya et al. have reported the plasticization effect of organically modified layered silicates on dynamic mechanical properties [13]. In this work, nanocomposites of SBR have been prepared using various nanofillers like modified and unmodified montmorillonite, SP, hectorite etc. It has been observed that the  $T_g$  shifts to lower temperature in all the nanocomposites, except for systems from hectorite and NA. This is due to the fact that clay layers form capillaries parallel to each other as they become oriented in a particular direction. Due to wall slippage of the unattached polymer through these capillaries, the  $T_g$  is lowered, which could be even more in the absence of organo-modifiers [13]. A similar type of plasticization effect is also noted in the case of the low

temperature storage modulus of the nanocomposites prepared from modified montmorillonite clay.

### 3.3.2 Effect of Frequency and Strain

Bandyopadhyay et al. have studied the effect of nanosilica concentration on the frequency dependence of the dynamic storage modulus of the nanocomposites prepared from ACM-based (ACMD) and in situ generated (prepared by the sol-gel technique using TEOS) nanosilica at 50°C [27]. The frequency sweep plot of ACM nanocomposites having 10% (ACMD10), 30% (ACMD30) and 50% (ACMD50) nanosilica respectively with control ACM is depicted in Fig. 20. The nanocomposites containing higher silica concentration show higher modulus, which increases with the increase in frequency. With the increasing frequency, in the case of the neat elastomer, maximum increase in the storage modulus is observed from the initial value, compared to their nanocomposite counterparts, up to 8 Hz frequency. The low frequency region corresponds to the behavior at higher temperature, whereas the high frequency region is equivalent to low temperature characteristics. The consistent increase in dynamic modulus with frequency in ACM/silica nanocomposites, indicates more time acquired for the relaxation of the polymer chains. It can be seen from Fig. 20 that the slopes of the modulus–frequency curves are slightly higher at higher frequency (beyond 8 Hz) in the ACM/silica nanocomposites compared with those in ACM, because of the easier detachment of the polymer chains in nanocomposites under high frequency or higher deformation conditions. Similar results are also obtained in the case of other nanocomposites systems [161].

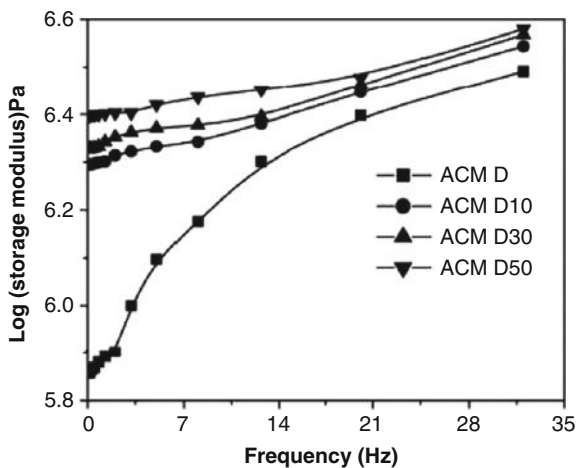
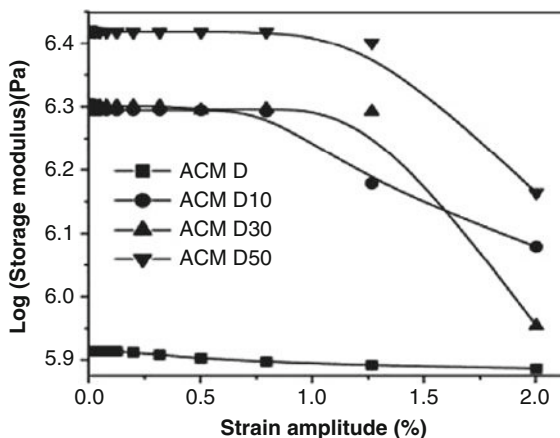


**Fig. 20** Plots of log storage modulus versus frequency at 50°C for the hybrid ACM/silica nanocomposites

**Fig. 21** Plots of log dynamic storage modulus versus strain amplitude for ACM/silica hybrid nanocomposites at different silica concentrations at 50°C



The same authors have also studied the effect of dynamic deforming strain on the storage modulus of ACM/silica nanocomposites [27]. Figure 21 illustrates the dynamic strain dependence of storage modulus for the above system at 50°C. It can be clearly seen that the storage modulus of the neat polymer (ACMD) does not change appreciably with the increase in applied strain amplitude over the experimental range. At very low strain (up to 0.2%), the modulus is independent of the applied strain and shows linear viscoelastic behavior. After that, it reduces slightly with the increasing strain, indicating the onset of a nonlinear viscoelastic regime. However, in the case of ACM/silica nanocomposites, the storage modulus decreases drastically with the increasing strain in the nonlinear viscoelastic portion. This type of behavior is commonly known as the Payne effect, which has also been observed extensively in the case of carbon-black-filled rubber composites [163].

### 3.3.3 Time–Temperature Superposition

Very recently, Kumar et al. [164] have studied the variation of storage modulus ( $E'$ ) and loss modulus ( $E''$ ) against reduced frequency for the pristine uncured BIMS rubber (B) and 8 phr of NA-filled uncured BIMS rubber (BCLNA8). Figure 22a, b shows the logarithmic plots of  $E'$  and  $E''$  master curves against frequency for samples B and BCLNA8. The storage modulus values of nanoclay-loaded sample are higher in the entire frequency range in comparison with the unfilled sample. This suggests the reinforcing action of nanoclay in the BIMS matrix. The effect of nanoclay reinforcement on the important molecular parameters of elastomers, such as relaxation times (terminal relaxation time,  $\tau_{te}$  and onset of transition zone relaxation time,  $\tau_{tr}$ ) and monomer friction coefficient ( $\zeta_0$ ), have been estimated from the different crossover frequencies (as shown in Fig. 22a, b), and the values are reported in Table 7. The terminal relaxation time  $\tau_{te}$  is the time required for a molecule to completely rearrange its configuration by snaking itself through



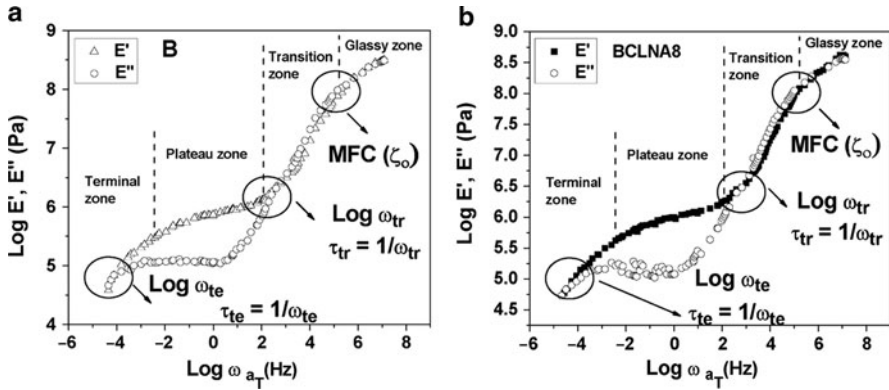


Fig. 22 a  $E'$  and  $E''$  master curves for B at 25°C. b  $E'$  and  $E''$  master curves for BCLNA8 at 25°C

**Table 7** Relaxation time ( $\tau$ ), self-diffusion coefficient ( $D$ ), and monomer friction coefficient ( $\zeta_0$ ) of unfilled (B) and nanoclay-filled (BCLNA8) BIMS rubber

Sample designation	$\tau_{tr} (\times 10^{-3} \text{ s})$	$\tau_{te} = \tau_{rep} \text{ (s)}$	$D = \frac{(R_g)^2}{2\tau_{rep}} (\times 10^{-21} \text{ m}^2 \text{ s}^{-1})$	$\text{Log } \zeta_0 \text{ (gm s}^{-1}\text{)}$
B	2	15,848	9.1	-1.39
BCLNA8	3	25,118	5.7	-0.64

$\tau_{tr}$  is transition zone relaxation time,  $\tau_{te}$  is terminal relaxation time,  $\tau_{rep}$  is reptation time

numerous entanglements [150]. The onset of terminal relaxation time  $\tau_{tr}$  is the measure of the time required for complete configurational rearrangement of a piece of macromolecule caught between two crosslinks or two entanglements [150]. The monomer friction coefficient ( $\zeta_0$ ) is the average resistance force per monomer unit encountered when a polymer chain moves through its surroundings at a unit speed [150]. From Table 7, it is seen that the addition of nanoclay increases the relaxation times and the monomer friction coefficient values of BIMS rubber. This has been attributed to the reinforcement effect of nanoclay in BIMS matrix and also to the topological constraints imposed by the nanoclay particles for the BIMS rubber molecules to move.

### 3.4 Thermal Properties

#### 3.4.1 Thermal Degradation Behavior of Rubber-Based Nanocomposites

The formation of polymer–filler nanocomposite affects the thermal behavior of the matrix because the well-dispersed nanofillers lead to modification of the degradation pathways [165–168]. This concept was first introduced by researchers from Toyota [169] who discovered the possibility to build nanocomposites from nylon-6

and organophilic clay. Recent studies on these clay nanocomposites reveal that inclusion of this nanoclay improves the barrier properties and lowers the coefficient of thermal expansion of the polyimide films. In addition to the mechanical properties, heat release rates from cone calorimetric experiments have also been reduced typically by 50% or more for both intercalated and exfoliated materials [170].

Bhowmick et al. have done extensive work to improve the thermal stability of polymers like BR, NBR, SBR, FKM, nylon-6 and HNBR by using different types of nanofillers [36, 90, 171–174]. The thermal degradation behavior of fluoroelastomer nanocomposites both in nitrogen and oxygen atmosphere and also at high and low temperatures has been studied [171]. A shift of  $T_{\max}$  (temperature corresponding to the maximum degradation) by 15 and 11°C to higher temperatures in the case of samples filled with unmodified and modified (4 phr) clay, respectively, was observed from this study, as represented in Fig. 23a, b. Also, a significant reduction in the rate of decomposition in the presence of the unmodified clay at the major degradation step was obtained from the same study. The two nonisothermal kinetics methods (Kissinger and Flynn–Wall–Ozawa) and isothermal kinetics methods have been used to study the thermal degradation of fluoroelastomer/clay nanocomposites. The activation energies increase with the addition of nanoclays. The activation energy of the unmodified-clay-filled sample ( $169 \text{ kJ mol}^{-1}$ ) is higher than those of neat fluoroelastomer ( $145 \text{ kJ mol}^{-1}$ ) and the modified-clay-filled samples ( $155 \text{ kJ mol}^{-1}$ ) as calculated from Flynn–Wall–Ozawa method. The higher thermal stability of the unmodified-clay-filled fluoroelastomer in both nitrogen and oxygen atmospheres is due to better polymer–filler interaction, which is due to polar–polar interaction between the unmodified clay and the polar fluoroelastomer. Polar hydroxyl groups of the unmodified clay attract the chains of fluoroelastomers having  $\text{C}^{\delta+}-\text{F}^{\delta-}$  bonds. In the case of the modified clays, there may be some incompatibility with the matrix due to modification by long chain aliphatic amines. The better interaction in the case of the unmodified clay is also evident from the higher gel-fraction of the corresponding nanocomposite (3.41%) than that of modified-clay-filled sample (2.19%).

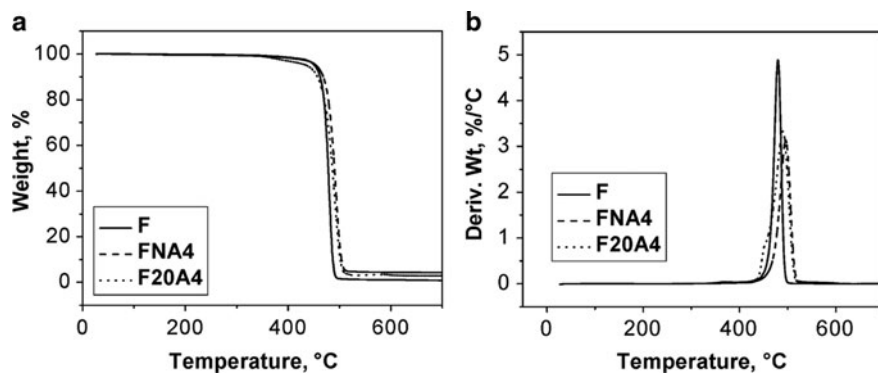


**Fig. 23** Typical **a** TG and **b** DTG traces for different nanocomposites (in  $\text{N}_2$ ). *F* fluorocarbon elastomer

The effect of the modified clay on the thermal properties of SBR, NBR, and BR was investigated by Sadhu et al. in order to understand the thermal and thermo-oxidative behavior of these nanocomposites, with special reference to the nature of matrix and clay [173]. Figure 24a represents the derivative thermogravimetry (DTG) curves of unfilled BR and unmodified- and modified-clay-filled nanocomposite (BRNA4 and BRo-MMT4). As observed from Fig. 24a, decomposition of gum BR takes place mainly in two steps. The first degradation step is due to the cyclization of the butadiene part, and the second step (where 90% of the weight loss takes place) corresponds to the decomposition of the cyclized polybutadiene structure and limited depolymerization of the first stage. Incorporation of the unmodified nanoclay to the BR does not cause a major increase in the  $T_{max}$  value corresponding to the last degradation step ( $T_{max} = 459^{\circ}\text{C}$ ). However, there is a significant improvement in thermal stability when the modified clay is present in the matrix, which is evident from the higher  $T_{max}$  value ( $T_{max} = 467^{\circ}\text{C}$ ) of the modified-clay-filled BR vulcanizate. There is a significant reduction in the rate of decomposition in the presence of the modified clay, especially in the case of the major degradation step. The rate decreases from  $45\% \text{ min}^{-1}$  for the gum to  $37\% \text{ min}^{-1}$  in the case of the modified-clay-filled sample. In the case of SBR-based vulcanizate and its nanocomposites, with 4 phr clay loading (unlike BR) the addition of modified clay causes only slight improvement in the major degradation step (from  $448$  to  $451^{\circ}\text{C}$ ). The rate of degradation at the  $T_{max}$  is again decreased significantly ( $32$ – $25\% \text{ min}^{-1}$ ) in the case of the modified-clay-filled SBR compared to that of the unmodified-clay-filled or unfilled elastomer. For NBR and its nanocomposite, filled with modified and unmodified clay (NBRo-MMT4 and NBRNA4, respectively), the DTG curves show multiple decomposition steps in nitrogen atmosphere (see Fig. 24b). The initial decomposition is characterized by a  $T_{max}$  of  $371^{\circ}\text{C}$  for the gum NBR, which disappears in the case of the vulcanizates filled with unmodified or modified clay. Presence of the modified clay shifts the  $T_{max3}$  to  $467^{\circ}\text{C}$  with a reduction in decomposition rate from  $29\% \text{ min}^{-1}$  to  $26\% \text{ min}^{-1}$ . Because BR and SBR are nonpolar in nature, they have good interaction with the organically modified filler. The major chain scission step is predominantly influenced by the presence of the clays because it directly interacts with the main chain.

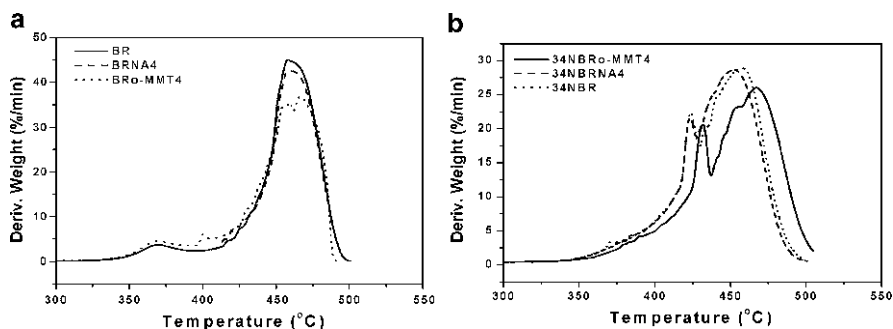


Fig. 24 The DTGs for curve a BR and b NBR and their nanocomposites

In the case of 34NBR, the polymer chains have H-bonding interactions with the clay along with van der Waals interactions. These in turn improve the thermal stability of the nanocomposite.

The effect of various nanofillers on the thermal stability and degradation kinetics of HNBR nanocomposites have been reported by Choudhury et al. [36, 174]. In this work, five different nanofillers were selected: two-dimensional montmorillonite, one-dimensional SP and zero-dimensional nanosilica (A300). Typical TG and DTG curves in air atmosphere at a heating rate of  $20^{\circ}\text{C min}^{-1}$  for unfilled HNBR and its nanocomposites are shown in Fig. 25a (where HNBR is designated as S1 and the nanocomposite with 4 phr filler loading is designated as S1-X-4, where X is the filler). For neat HNBR, there appear three degradation temperatures, whereas for the nanocomposites, the DTG curves show almost single-step degradation with well-defined initial and final degradation temperatures (as depicted in Fig. 25a), which could be a result of the scission of the main macromolecular chains. Shift in  $T_{\text{max}}$  values towards a higher temperature by 12, 6, 4, 12, and  $16^{\circ}\text{C}$  is observed for S1-30B-4, S1-15A-4, S1-NA-4, S1-SP-4, and S1-A300-4, respectively, as compared with the neat elastomer. Thus, improvement in thermal stability ( $T_{\text{max}}$ ) is highest for S1-A300-4 with 4 phr filler loading, followed by S1-30B-4 and S1-SP-4. From the TG curves of the A300, 30B, and SP (Fig. 25b), it is observed that the thermal stability of A300 is much higher than of the other two. Also, silica nanofillers contain a lot of surface hydroxyl groups which might interact with the polar groups present in the elastomer. Moreover, silica acts as a heat sink. Its specific heat capacity value is  $700 \text{ J (kg K)}^{-1}$ , which is high enough to increase the thermal stability of the corresponding nanocomposites. Thus, the thermal stability of the nanosilica-filled composite is excellent, especially for low filler loading. However, with an increase in filler loading, 30B and SP provide much higher stability to HNBR than the nanosilica-filled sample (A300). Only a marginal improvement in the thermal stability for S1-15A-4 is observed and there is no such improvement for S1-NA-4 over the neat rubber.

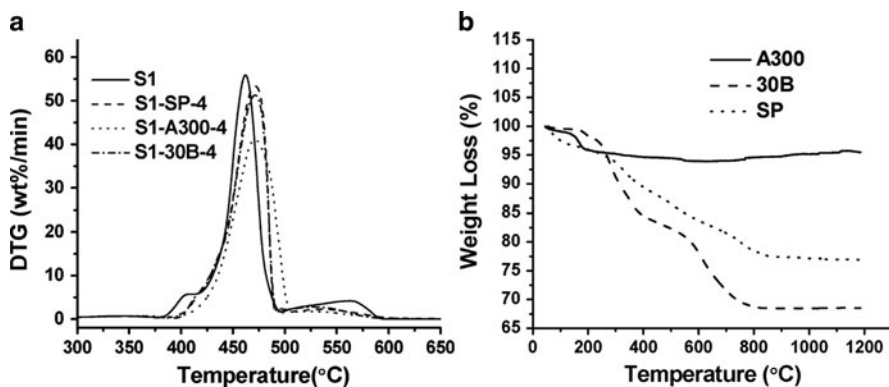


Fig. 25 a Typical DTG and TG traces for different nanocomposites in air. b Weight loss versus temperature for different nanofillers

Compatibility of NA with organic polymer is much inferior to the compatibility of 30B, 15A, and SP. Thus, S1-NA-4 has inferior thermal stability as compared to the other three clays. Moreover, the intergallery spacing of NA is very small (only 1.22 nm, obtained from XRD results, Fig. 26a). Only a few chains of HNBR (with 34% acrylonitrile content), being bulky in nature, can find their way into such a small gallery space, which results in poor polymer–filler interaction. This is confirmed by both XRD and TEM (Fig. 26a, b).

In the case of 30B, the intergallery cations are replaced by polar surfactant, and hence its gallery spacing is (1.95 nm) higher than NA. Thus, HNBR molecules can easily enter in to the gallery space to break the layer structure, resulting in fully exfoliated nanoclay within the matrix, which is confirmed by XRD, TEM, and AFM (Fig. 27a). As a consequence, it provides excellent thermal stability to the nanocomposite ( $T_{\max}$  increased by 12°C over neat elastomer). 15A is another organically modified montmorillonite and is modified by long amine chains and thus has a larger intergallery spacing (3.26 nm as obtained from the XRD studies, Fig. 27b) than 30B. It is known that a longer chain is always thermally less stable than a shorter one. Further, the XRD, TEM, and AFM results (Fig. 27b) for 15A indicate a partial intercalated morphology. It is well known that exfoliated silicate layers provide better barrier properties than an intercalated layer [171]. 30B acts as a strong barrier to gases such as oxygen and nitrogen, while the intercalated morphology of 15A makes the barrier property of the corresponding nanocomposite ( $T_{\max}$  increased by 6°C over neat elastomer) inferior to that of 30B. On the other hand, fibrous or rod-like SP particles are distributed uniformly throughout the matrix (as evident from the TEM and AFM photographs Fig. 27c), and can improve the thermal properties of HNBR (just like 30B) because of the high thermal stability of this filler.

The activation energy of degradation of unfilled HNBR and its nanocomposites has been determined by using the nonisothermal Flynn–Waal–Ozawa and Kissinger models as well as by isothermal methods [174]. The total activation energy of degradation of the nanocomposite (a sum of the activation energy of degradation of the matrix, the activation energy of degradation of the nanofillers, and the energy required to break the interaction between the filler and the matrix) has been found to

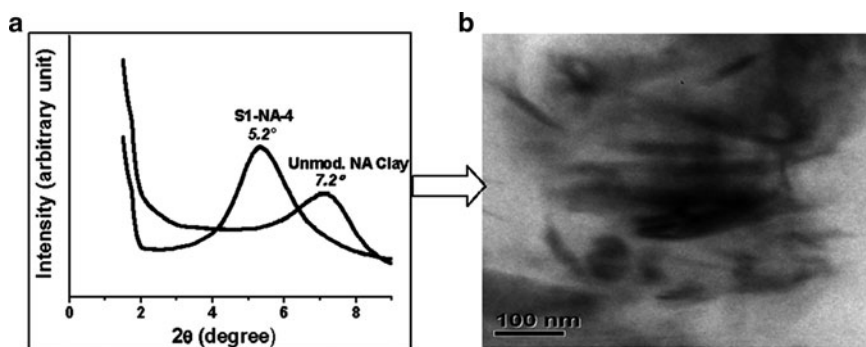
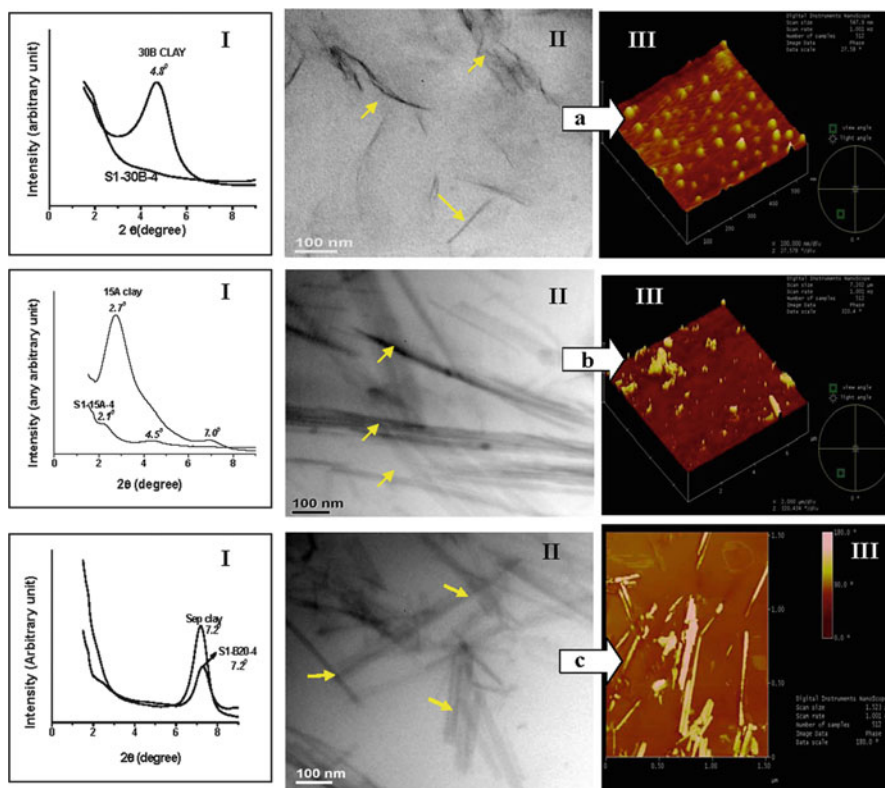


Fig. 26 a XRD traces and b TEM photographs of S1-NA-4



**Fig. 27** XRD traces (*I*), and TEM (*II*) and AFM (*III*) photographs of S1-30B-4 (*a*), S1-15A-4 (*b*), and S1-SP-4 (*c*). Arrows indicate rod-like SP particles

be much higher than that of the neat elastomer in nonisothermal and isothermal methods. Since the activation energy of the nanofiller is highest for nanosilica, and the energy required to break polymer–filler interaction is highest for S1-30B-4 and S1-SP-4, the total activation energy is observed to be much higher for S1-A300-4, S1-30B-4, and S1-SP-4. The values obtained are 169, 166 and 168  $\text{kJ mol}^{-1}$ , respectively, the by Kissinger method and 162, 163, and 161  $\text{kJ mol}^{-1}$ , respectively, by the Flynn–Waal–Ozawa method. The values for the neat elastomer have been found to be 125 and 138  $\text{kJ mol}^{-1}$  respectively, by these methods.

### 3.4.2 Mechanism of Degradation

Two mechanisms have been suggested to account for the reduction in the heat release rate: a barrier mechanism, in which the clay functions as a barrier to mass transfer of the polymer, and a radical trapping mechanism, which occurs due to the presence of iron or other paramagnetic impurities as a structural component in the

clay. The mechanism of degradation of the fluoroelastomer in terms of two competing net processes [175, 176] have been explained by Maiti et al. [171]:

1. Degradation of the main chain carbon bonds, i.e., main chain scission
2. Degradation by the splitting off of an adjacent hydrogen and fluorine as hydrogen fluoride, generating a double bond

It is explained in the report that the degradation mechanism remains the same, even after addition of nanoclays.

Choudhury et al. [174] have explained the degradation mechanism of HNBR and its nanocomposites using FT-IR spectroscopy. For the neat HNBR (S1), the peaks at 1,446–1,463  $\text{cm}^{-1}$  for  $-\text{CH}_2-$  deformation, at 990  $\text{cm}^{-1}$  for disubstituted double bonds (trans- $\text{CH}-$  wagging vibration), at 2,213  $\text{cm}^{-1}$  for acrylonitrile group, and at 970  $\text{cm}^{-1}$  for  $\text{CH}-$  wagging absorbance of the hydrogenated polymer are observed, as depicted in Fig. 28. For the aged sample, a broad absorption at 1,760–1,720  $\text{cm}^{-1}$  due to  $\text{C}=\text{O}$  functionality is observed. In order to quantify this increase for the aged sample, the absorbance at 1,730  $\text{cm}^{-1}$  is divided by absorbance at 1,460  $\text{cm}^{-1}$  due to  $\text{CH}_2$  deformation. It is assumed that the concentration of  $-\text{CH}_2$  groups remains constant throughout the low temperature aging process and that the attack takes place first on the double bonds. The K value, the ratio of absorbance at 1,730  $\text{cm}^{-1}$  to absorbance at 1,460  $\text{cm}^{-1}$  is found to be much higher for the neat elastomer than for the nanocomposites. This confirms that the level of oxidation reaction is higher in the case of neat elastomer than for the nanocomposites. A similar observation is made when the ratio of absorbance at 1,730  $\text{cm}^{-1}$  to absorbance at 2,213  $\text{cm}^{-1}$  (for the  $-\text{CN}$  group) is analyzed. An additional peak at 970  $\text{cm}^{-1}$ , in the case of S1-aged sample, may be due to the formation of some secondary cyclic alcohol. However, in the case of S1-A300-4 nanocomposite (aged) this peak is absent. Nanofillers, having a higher thermal conductivity as well as a greater heat capacity value than the elastomer, absorb the heat transmitted from the surroundings and retard the direct thermal impact to the polymer backbone [177, 178]. As a result, the temperature at which major degradation of the neat elastomer takes place is shifted to

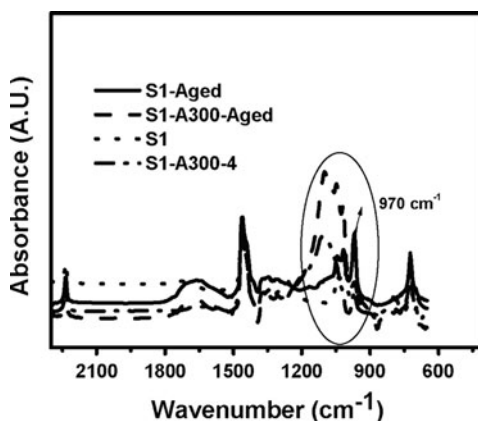


**Fig. 28** FTIR spectra of S1 and S1-A300-4 after aging at 175°C for 12 h. The circled area indicates the additional peak of S1-aged sample

higher temperature by about 16°C for the nanocomposites. This observation shows that nanofillers form shielding layers on the surface of clay, which in turn protect the rubber from the attack of oxygen to some extent and inhibit the degradation process.

### 3.5 *Electrical Properties and EMI Shielding*

Polymers are inherently low in electrical conductivity. Because of this, applications that require conducting properties cannot take advantage of these necessary materials, which are having light weight, high strength/weight ratio, easy moldability, etc. Admixing inert, conducting fillers into nonconducting polymers is an effective and economic way to produce electrically conducting polymer components with better processability, flexibility, and mechanical properties. These are generally used for shielding electromagnetic interference (EMI) [179, 180].

Carbon fillers have lower density compared to metal powders. Also, they are more inert and compatible with most of the polymers than are the metal powders [181]. Carbon materials provide electrical conduction through the pi bonding system that exists between adjacent carbon atoms in the graphite structure [182]. Electrical properties of nanocomposites based on conducting nanofillers such as EG [183–187], CNTs [188–190], and CNFs [191], dispersed in insulating polymer matrix have found widespread applications in industrial sectors.

The EG is prepared by the rapid heating of pretreated (oxidized) graphite. As a result, it expands several times along the *c*-axis, resulting in a puffed-up material with a low density [192]. EG exhibits a layered structure similar to layered silicates. An exfoliated graphite nanoparticle is composed of stacks of nanosheets with thickness that varies from 20 to 30 nm. Although similar in chemical composition to graphite, CNTs are highly isotropic, and it is this topology that distinguishes them from other carbon structures and gives them their unique properties. CNFs are mainly differentiated from CNTs by the orientation of the graphene planes: whereas the graphitic layers are parallel to the axis in nanotubes, nanofibers can show a wide range of orientations of the graphitic layers with respect to the fiber axis. CNFs consist of a highly graphitic structure that is composed of an inner filament (diameter of 10 nm) thickened by a carbon chemical vapor deposition process. The length of CNFs can vary between 50 and 100 μm and therefore high aspect ratios can be obtained [193].

The effects of carbon-based nanofillers of EG, MWCNTs, and CNFs on the AC conductivity and dielectric constant of elastomeric grade EVA (50% vinyl acetate content) at a particular frequency of 12 Hz, are shown in Fig. 29a, b [194]. EVA-EG, EVA-T, and EVA-F represent EVA-based nanocomposites reinforced with EG, MWCNT, and CNF respectively.

EVA shows a percolation threshold after the addition of 8.2 vol% CNF, whereas a higher amount of EG (10.9 vol%) is required to reach percolation. MWCNT exhibits a percolation at 10.0 vol% and shows an increase of five orders of magnitude as



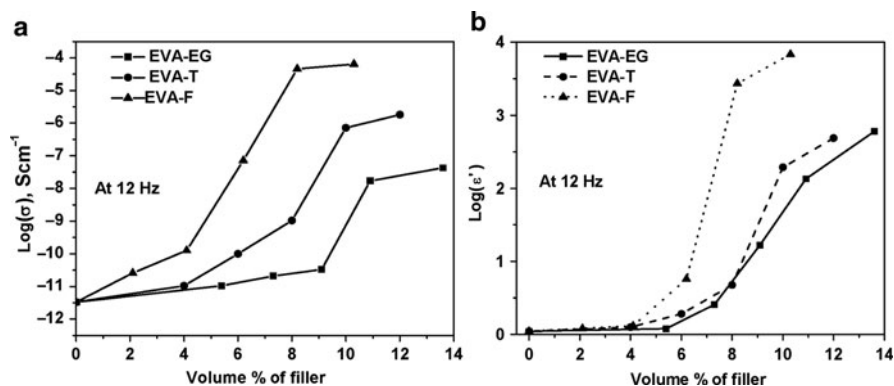


**Fig. 29** Effect of filler loading on **a** AC conductivity and **b** dielectric constant. *EVA-EG*, *EVA-T*, and *EVA-F* represent EVA-based nanocomposites reinforced with EG, MWCNTs, and CNFs, respectively

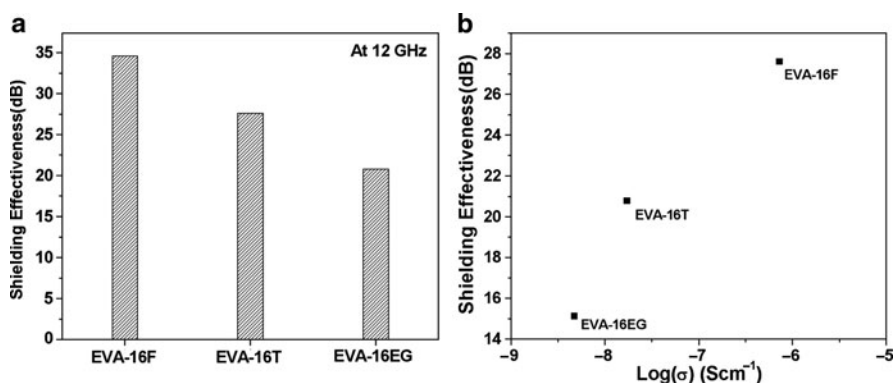


**Fig. 30** **a** Shielding effectiveness of various composite systems (at 12 GHz). **b** EMI shielding effectiveness as a function of conductivity at 16 wt% filler loading

compared to neat EVA. The CNFs show maximum increment of seven orders of magnitude with 8.2 vol% of CNF incorporation. The lower percolation threshold of CNFs is due to its high intrinsic conductivity and also high aspect ratio ( $\sim 500$ ). On the other hand, MWCNTs used here possess a lower aspect ratio of around 100. Similarly, EG also has a comparatively lower aspect ratio. Several investigations have proven that the conducting properties and structure of the graphite nanocomposites are affected by the high temperature treatment while expanding during their preparation and intensive processing [188, 189, 195] during composite development. Similarly, compared to the neat polymer, the composite films display a significant increase in the dielectric constant. The dielectric constant of the EVA-F composite film shows values several times higher than those of neat EVA.

Figure 30a depicts the comparative plots of the EMI shielding effectiveness (SE) of all the three composite systems at a particular frequency of 12 GHz [196].

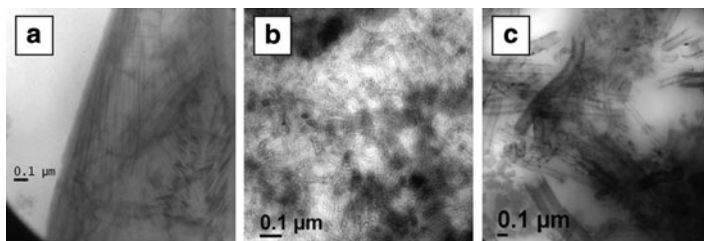


**Fig. 31** TEM photographs of **a** EVA-16EG, **b** EVA-16CNT, and **c** EVA-16CNF

The optimum filler loading of CNFs for SE (34.4 dB at 12 GHz) is 16 wt%. This result is very much comparable with the values reported by Zhang et al. [197]. The target value of the EMI SE for commercial applications is in the range of 10–20 dB [197]. Even a minimum addition of 4 wt% CNF provides sufficient SE. With a SE of 10–20 dB, a sample can block 90–99% of the incident electromagnetic signals [197, 198].

It is well established that the SE of a conductive composite is related to its conductivity. The interconnected CNF networks within the composite establish the electrical conduction pathway, leading to good electrical properties and SE. The correlation between the SE and electrical conductivity of EVA-F composites is displayed in Fig. 30b [196].

Generally, conductive network or conductive mesh formation and the nature of reinforcing fillers decide the SE of a particular composite. Finer conductive mesh can produce more effective shielding against electromagnetic waves. The distributions of various fillers (at 16 phr concentration) in the EVA matrix are shown in Fig. 31a–c [194]. These justify the results obtained from EMI SE and conductivity measurements. Percolation theory predicts that there is a critical concentration of the conducting filler (percolation threshold), at which a conductive path is formed in the composite, causing the material to convert from an insulator to a conductor. As the amount of filler is increased, the number of interfiller connections increases and many conductive paths become available. The percolation threshold is reached when a conducting path of interconnected conducting fillers is formed across the volume of the composite. Also, the percolation threshold for the electrical conductivity depends very much on the geometry of the conducting filler, such as aspect ratio. The higher the aspect ratio, the lower the percolation threshold necessary for forming a conducting network.

### 3.6 Barrier Properties

The migration of gases through materials has been a crucial factor in the ability of food packagers to increase the shelf-life of products. The migration of oxygen through auto and truck tires causes the steel belt to rust, reducing the tire's life [199].

Research on the introduction of clay and clay-like nanoparticles, both natural and synthetic, into polymers is centered on the maximization of these barrier properties. The major benefit of the nanocomposites is their improved barrier properties along with the excellent improvement of other properties. The addition of silicate layers into the above polymer matrix could affect the gas diffusion mechanism through the material because of the different permeability properties of the matrix and the inorganic particles. This phenomenon is particularly interesting when a filler of nanometer size is dispersed into the polyurethane matrix. The impermeable clays or clay-like particles force a tortuous pathway for a permeant transversing the nanocomposite. From a literature review, it seems that gas permeability through polymer films can be reduced by 50–500, times even with small loadings of nanoclays [200]. The barrier property of rubber–clay nanocomposites concerns mostly oxygen, carbon dioxide, nitrogen, helium, and water vapor barrier films.

In general, there are three reasons for enhancement of gas barrier properties for polymer/clay nanocomposites. Firstly, gas-impermeable nanoclay layers dispersed in the polymer matrix form tortuous pathways, which retard the progress of gas molecules through the composite. Secondly, exfoliated clay layers and intercalated clay layer bundles strongly restrict the motion of the polymer chains, probably reducing the coefficient of diffusion of the gas molecules. Thirdly, the smaller  $M_c$  (molecular weight between crosslinks), which increases the cross-linking density due to reaction between the reacting groups (if any) in the nanoclay and the polymer, restricts the motion of the diffusion of the gas molecules.

From a morphological point of view, there are four fundamental parameters that can be adjusted to maximize the barrier properties of clay nanocomposites.

1. Dispersion: The degree of dispersion of the nanoplatelets is determined by the degree of delamination of the clay. The fully delaminated (exfoliated) nanocomposite presents much higher values for the tortuosity factor and the aspect ratio in comparison with the partially delaminated (intercalated) nanocomposite. This means that the clay particles that grow as aggregates or “books” of sheets must be broken up or exfoliated into individual sheets that have a thickness of the order of 1 nm, with lengths and widths of the order of 500 nm.
2. Compatibility: The particles must be compatible with the polymeric substrate. Since natural clays are aluminosilicates, they must be prepared or “functionalized” so that they will be compatible with a polymer. For natural clay products, this process can be quite complex, given the wide chemical variability of different samples, even from the same mine.
3. Orientation: Once the particles are dispersed in the polymer, they must be oriented so that the flat surface of the clay is parallel to the surface of the packaging material to maximize the barrier effect. Several models have been developed in order to describe the mass transfer within the nanocomposites. Most models assume that the platelets have a regular and uniform shape (rectangular, sanidic, or circular) and form a regular array in space. They are either parallel to each other or have a distribution of orientations, with the

average orientation at an angle to the main direction of diffusion of the gas molecules.

4. Reaggregation: During processing, these particles must be kept from reaggregating or “clumping up,” thus destroying the benefits of the approach.

Recently, Maji et al. have developed novel hyperbranched polyurethane nanocomposites with high gas barrier properties [201]. It was observed that for the polyurethane matrix cured with third generation hyperbranched polyol (PU<sub>30</sub>), the permeability of helium decreases with the increase in clay (30B) concentration (Fig. 32). The composition containing 8 wt% of clay shows permeability reduction by about 76% over the pristine polyurethane; but beyond that, the decrease is not so significant (for 16 wt% loading, the reduction is 78%). The same trend of decrease of permeability of nanocomposites based on for both PU<sub>20</sub> (polyurethane cured with second generation hyperbranched polyol) and PU<sub>40</sub> (polyurethane cured with fourth generation hyperbranched polyol) is shown in Fig. 32. PU<sub>40</sub> nanocomposites exhibit lowest permeability.

Tortusity factors have been calculated based on different models adopted by different theories. The ribbon and disk-like shapes of nanoclay have been considered in this study. Maji et al. [201] and Sun et al. [202] tabulated most of theories for permeability model equations. The brief descriptions of the theories are tabulated in Table 8. Figure 32 shows the experimental value of relative

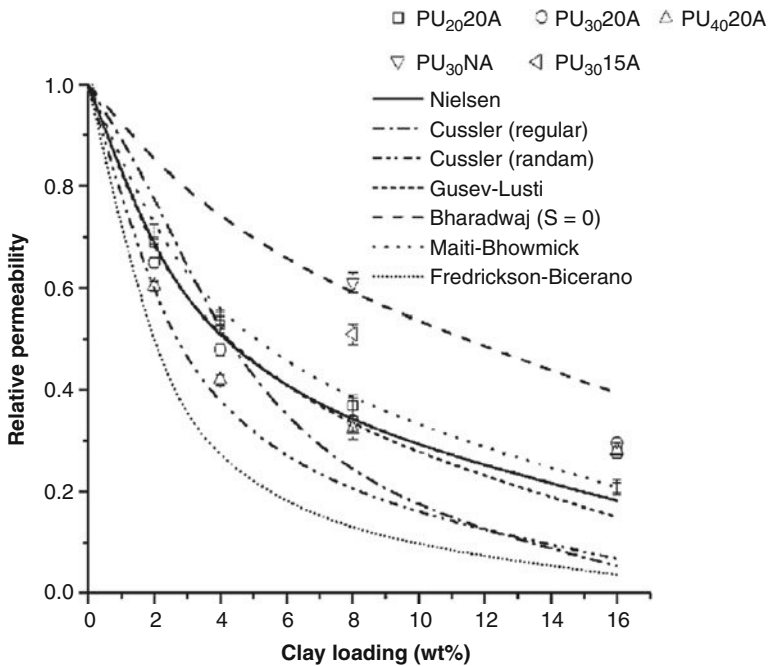
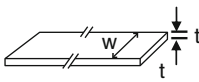
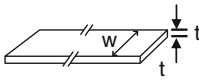
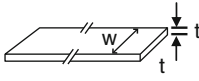
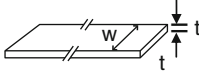
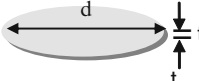
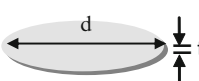
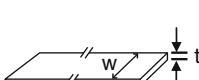


Fig. 32 Validation of different permeability models in the PU-based nanocomposite systems

**Table 8** Summary of the different models for the gas permeation

Model	Ref	Filler type	Particle geometry	Formula
Nielsen	[203]	Ribbon		$R_p = \frac{1 - \phi}{1 + \alpha\phi/2}$
Cussler-regular array	[204]	Ribbon		$R_p = \frac{1 - \phi}{1 + \alpha^2\phi^2/4}$
Maiti and Bhowmick	[205]	Ribbon		$R_p = \frac{1 - \phi}{(1 + \alpha\phi/2)^2}$
Cussler-random array	[204]	Ribbon		$R_p = \frac{1 - \phi}{(1 + \alpha\phi/3)^2}$
Gusev-Lusti	[206]	Disk		$R_p = \frac{1 - \phi}{\exp[(\alpha\phi/3.47)^{0.71}]}$
Fredrickson-Bicerano	[207]	Disk		$R_p = \frac{1 - \phi}{4[(1 + x + 0.1245x^2)/(2 + x)]^2}$ where, $x = \frac{\pi\alpha\phi}{2 \ln \alpha/2}$
Bharadwaj	[208]	Ribbon		$R_p = \frac{1 - \phi}{1 + \alpha\phi(2S + 1)/6}$ where, $S = (3\cos^2\theta - 1)/2$

$\alpha$  aspect ratio of the filler,  $\phi$  volume fraction of the filler,  $R_p$  relative permeability, ( $\theta$  angle between the direction of penetrant flow and normal of the layer

permeability of the three different nanocomposites with varying levels of clay, as compared to the theoretical prediction.

Maiti and Bhowmick [205] have established a good correlation between the aspect ratio of clay in fluoroelastomer/clay nanocomposites and the transport properties of solvent. For fluoroelastomer/clay nanocomposites, permeability decreases significantly with the addition of only 4 phr of the unmodified montmorillonite clay ( $0.14 \times 10^{-8} \text{ cm}^2 \text{ s}^{-1}$ ) compared with that of neat polymer ( $2.29 \times 10^{-8} \text{ cm}^2 \text{ s}^{-1}$ ).

Hence, the addition of inorganic impermeable nanoplatelets improves the barrier properties of polymers. This is attributed mostly to the lengthening of the diffusion path of the permeating gas molecules due to the increase of the tortuosity. Increasing the aspect ratio of the platelets and their volume fraction improves these

properties. The addition of solute scavengers enhances these properties, at least by prolonging the induction period for permeation.

### 3.7 Adhesion

The earlier sections of this chapter provide convincing evidence that the elastomer based nanocomposites have superior mechanical, dynamic mechanical, rheological, thermal, barrier, and various multifunctional properties when compared with the pristine elastomers and conventional elastomer-filler microcomposites. However, to date, very little research has been done to understand the influence of nanoclays and other hybrid nanomaterial on the adhesive behavior of elastomers. On the other hand, extensive studies have been performed to understand the effect of different nanoclays in epoxy resins, which are widely used in the adhesive industry [209–218]. Lan and Pinnavaia [209] are the first to report the effect of different nanoclays on the tensile strength of epoxy resin. Park and Jana [210] have proposed a mechanism for achieving a fully exfoliated morphology of nanoclays in epoxy matrix. Various other researchers have reported the influence of preparation methods, nature of epoxy monomer, nature of curing agents, and cure temperature in determining the level of dispersion (morphology) of nanoclays and extent of adhesion, which, in turn, dictate the entire composite properties [212–214]. Unfortunately, there are no reports in the literature that describe the role of nanofillers and their extent of dispersion on the adhesive behavior of elastomers. This section explains the efficacy of nanoclays and hybrid nanomaterial on the adhesion and tack behavior of elastomers.

#### 3.7.1 Acrylic Rubber Adhesion

Patel et al. [219] have studied the adhesive nature of rubber/silica hybrid nanocomposite adhesives and rubber/clay nanocomposite adhesives on various substrates. The rubber/silica hybrid nanocomposites have been synthesized through in situ silica formation from TEOS in strong acidic pH within acrylic copolymer (ethyl acrylate–butyl acrylate) and terpolymer (ethyl acrylate–butyl acrylate–acrylic acid) matrices. The rubber/clay nanocomposite adhesives are prepared by mixing the 10A nanoclay dispersion with the above-mentioned individual polymer solutions. Both the nanocomposite adhesives have been applied in between the aluminum (Al), wood (W), and biaxially oriented polypropylene (PP) sheets separately and have been tested for peel strength, lap shear strength, and static holding power of the adhesive joints. Both the nanocomposite adhesives show superior peel and lap shear strengths when compared to their virgin counterparts. Because of the greater polarity of the nanocomposite adhesives, the enhancement in the strength of the adhesive joints is significantly high for high energy substrates like Al, but relatively low for nonpolar, low-energy substrates like PP. The cohesive failure

pattern of the adhesives is same in polar substrates like Al and W, but very low in PP (nonpolar).

### 3.7.2 Liquid Rubber Adhesion

Pradhan et al. [220] have studied the influence of 30B nanoclay on the adhesive behavior of liquid polysulfide elastomer between aluminum foil–aluminum foil substrate. The nanocomposite adhesives have been prepared by mixing the nanoclay dispersion with the solution of liquid polysulfide elastomer and then curing the rubber and clay mixture with ammonium dichromate (curing agent) and diphenyl guanidine (accelerator) at room temperature for 24 h, followed by vacuum treatment for 24 h at 70°C. The XRD spectra and TEM micrographs of the nanocomposite adhesives indicates that the clay layers are completely exfoliated in the polysulfide matrix even at 8 phr of clay loading. The 180° peel strength of the polysulfide elastomer significantly increases with the addition of nanoclay (see Fig. 33). For example, adhesive strengths of the samples PSC0 and PSC8 are  $58 \pm 10 \text{ N m}^{-1}$  and  $323 \pm 15 \text{ N m}^{-1}$ , respectively. The force versus distance curves from the peel tests are shown in Fig. 34. Also, the adhesive strength increases with nanoclay concentration.

The addition of nanoclay slightly increases the polar component of the polysulfide elastomer. The increase in the polar component of the surface free energy for the polysulfide elastomer is due to the presence of hydroxyl functional groups on the clay surface. As a result, the polar (–OH) groups of the nanoclay establish strong interfacial interactions (hydrogen bonding) with the hydroxyl groups (Al–OH) of the aluminum substrate, and hence, result in very strong adhesion. In addition, here, the nanoclays show a good capacity to absorb the loosely bound water layer present in between the sealant and the aluminum substrate, thereby resulting in a better molecular contact between the sealant and the aluminum substrate. Further, the incorporation of nanoclay concomitantly increases the tensile strength and elongation at break of the polysulfide elastomer. This clearly explains the excellent

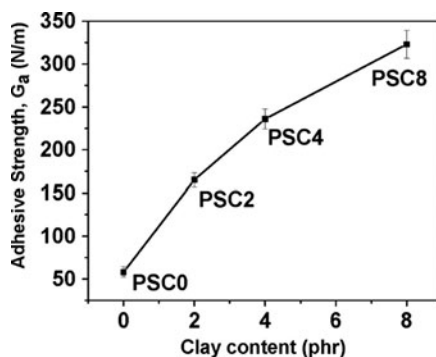


**Fig. 33** Effect of nanoclay content on adhesive strength of polysulfide elastomer/clay nanocomposites; samples containing 0, 2, 4, and 8 phr of nanoclay are designated as PSC0, PSC2, PSC4, and PSC8, respectively

**Fig. 34** Peel force versus distance curves for polysulfide/nanoclay adhesive systems

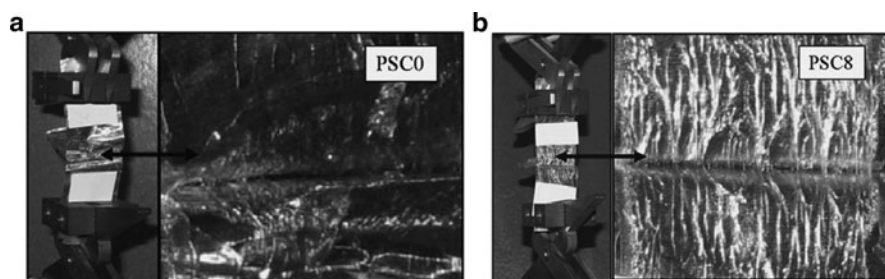
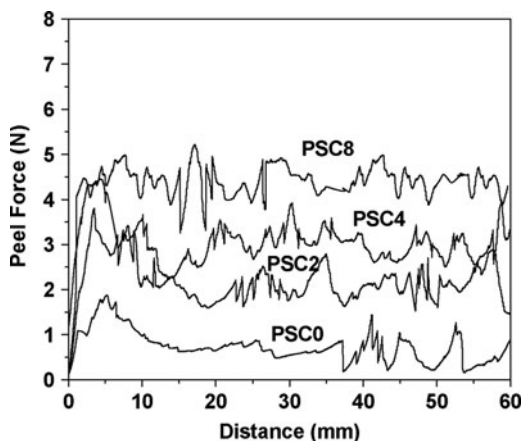


**Fig. 35** **a** Failure pattern in the neat polysulfide adhesive sample PSC0. **b** Failure pattern in clay-loaded sample PSC8

interaction between the nanoclay and the polysulfide elastomer. In addition, the  $W_b$  (area under the tensile stress–strain curve) value of unfilled polysulfide elastomer gradually increases with the loading of nanoclay. This suggests that the clay-loaded samples have the potential to dissipate a greater amount of energy during the peeling process in comparison with the unfilled polysulfide elastomer.

There is smooth failure pattern during the debonding process of the neat polysulfide adhesive (Fig. 35a). However, the clay-loaded samples clearly shows the formation and growth of fibrils during bond separation (Fig. 35b). Kaelble [221] and Zosel [222, 223] reported that the adhesive must dissipate a larger amount of energy during the debonding process of the peel test to have higher adhesive strength. In the literature, it is also shown that this energy dissipation level strongly depends on the extent of fibril formation [222–224]. Here, the formation of fibrils in the nanoclay-loaded samples clearly indicates the capacity of the clay-loaded adhesive to a dissipate greater amount of energy than their unfilled counterpart.



### 3.7.3 Autohesive Tack

In the literature, there are several reports that examine the role of conventional fillers like carbon black on the autohesive tack (uncured adhesion between a similar pair of elastomers) [225]. It has been shown that the incorporation of carbon black at very high concentration ( $>30$  phr) can increase the autohesive tack of natural and butyl rubber [225]. Very recently, for the first time, Kumar et al. [164] reported the effect of NA nanoclay (at relatively very low concentration) on the autohesive tack of BIMS rubber by a  $180^\circ$  peel test. XRD and AFM show intercalated morphology of nanoclay in the BIMS rubber matrix. However, the autohesive tack strength dramatically increases with nanoclay concentration up to 8 phr, beyond which it apparently reaches a plateau at 16 phr of nanoclay concentration (see Fig. 36). For example, the tack strength of 16 phr of nanoclay-loaded sample is nearly 158% higher than the tack strength of neat BIMS rubber. The force versus. distance curves from the peel tests for selected samples are shown in Fig. 37.

Various factors govern autohesive tack, such as relaxation times ( $\tau$ ) and monomer friction coefficient ( $\zeta_0$ ) and have been estimated from the different crossover frequencies in the DMA frequency sweep master curves (as shown in Fig. 22a, b). The self-diffusion coefficient ( $D$ ) of the samples has been calculated from the terminal relaxation time,  $\tau_{te}$ , which is also called as the reptation time,  $\tau_{rep}$ . The  $D$  value has been calculated using the following equation:

$$D = \frac{(R_g)^2}{2\tau_{rep}}, \quad (8)$$

where  $R_g$  is the radius of gyration of BIMS rubber and  $\tau_{rep}$  is the reptation time of filled and unfilled samples. The relaxation time, monomer friction coefficient, and self-diffusion coefficient values of B and BCLNA8 are included in Table 7.

The addition of nanoclay reduces the extent of molecular diffusion at the tack junction by reducing the chain mobility; however, the diffusion is still sufficient to achieve bond formation. Furthermore, the less diffused chains of the

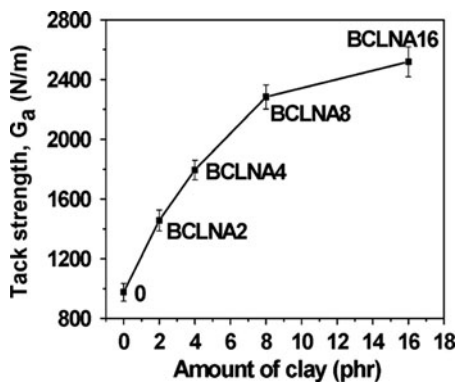
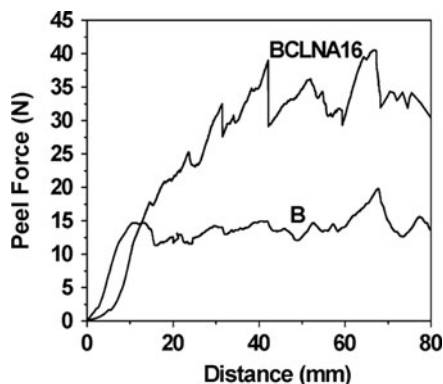


**Fig. 36** Effect of nanoclay content on tack strength; samples containing 0, 2, 4, 8 and 16 phr of nanoclay are designated as B, BCLNA2, BCLNA4, BCLNA8, and BCLNA16, respectively

**Fig. 37** Peel force versus distance curves of B and BCLNA16



nanocomposite samples show greater resistance to bond breaking due to an increase in cohesive strength, onset of transition zone relaxation time, and monomer friction coefficient of the BIMS matrix owing to the nanoclay reinforcement (see Table 7). On the other hand, the more diffused chains of the unfilled sample exhibit facile chain separation due to the poor cohesive strength of the BIMS matrix.

### 3.7.4 Polyurethane Elastomer Adhesion

Maji et al. [15] have studied the effect of the nature and content of nanoclays on the lap shear strength of polyester polyurethane (PPU) adhesive between Al–Al joints. Incorporation of 30B into the PPU matrix results in an improvement of the joint strength up to 3 wt% of nanoclay content. Addition of 3 wt% of 30B nanoclay to PPU matrix results in a 320% increase in the lap shear strength over the unfilled PPU. NA nanoclay shows little effect on the adhesive properties of PPU matrix. The lap shear strength values are 4.3 and 8.0 kN m<sup>-2</sup> for 3 wt% of NA- and 30B-filled systems, respectively. XRD and TEM suggest excellent dispersion of 30B nanoclay platelets in the PPU matrix. On the other hand, the NA clay platelets are very poorly dispersed in the PPU matrix. The superior reinforcement of the PPU matrix by 30B clay platelets increases the cohesive strength of the base polymer and thus increases the joint strength. The failure patterns in the lap joints are of cohesive type. It has been established that the OH groups (from the modifier compound of 30B clay) on the clay surface form strong interfacial hydrogen bonds with the Al–OH groups on the aluminum surface. This enhances the clay–metal adhesion. Since the clay platelets are dispersed well in the polymer matrix, it is also predicted that the nanoclay particles can act as an interphase between the aluminum adherent and the polymer, and thereby help in better adhesion. Accordingly, the lap shear strength increases with the increase in the clay concentration. Furthermore, addition of modified nanoclay to PPU matrix concomitantly increases the tensile strength and the elongation at break values of the PPU adhesive. This suggests the good ductile nature as well as the higher strain energy density of the PPU nanocomposite adhesive in

comparison with the unfilled PPU adhesive. As a result, the nanocomposite adhesive dissipates a greater amount of energy during the bond rupture process in the lap shear test, which in turn increases the joint strength. Maji et al. [136] have also studied the adhesive behavior of polyurethane nanocomposite adhesive derived from different hyperbranched polyols (HBPs) and nanoclay. It is interesting that the HBPs having a higher level of functionality impart higher lap shear strength (between Al–Al) and 180° peel strength (between aluminum plate and nylon fabric).

## 4 New Insights into Understanding Morphology–Property Relationships

### 4.1 Quantification of Nanoassembly Exfoliation

In Sect. 2, morphological studies based on high resolution TEM (HRTEM) and XRD gave ample proof of homogeneous dispersion and exfoliation in the nanocomposites prepared by the latex-blending technique, to which the much-improved properties could be ascribed. As the level of dispersion of nanofillers has a direct consequence on the nanocomposite properties, it is of significance to quantitatively correlate the extent of exfoliation with the increment observed in properties. This quantification was done through image analysis of HRTEM photomicrographs performed using ImageJ software. The necessary correlation can be achieved by following a relatively simple but accurate methodology devised by Bhowmick et al. [92], elucidated below.

The intercalation or stacking of clay platelets restricts the surface area available for interaction with the polymer chain and, thus, the effective surface area available for polymer–filler interaction can be defined as the actual surface area per clay platelet available for interaction. From extensive image analysis of HRTEM images (Fig. 38), the number of clay platelets per stack of nanoclays present inside the nanocomposites were categorized in groups of 1–3, 4–9, and  $\geq 10$  (in order of their increasing level of stacking). Their contribution or weightage in terms of effective surface area ( $A$ ) was calculated as 0.33, 0.15, and 0.10, respectively. The numbers were arrived at from the fractions: 1/3, 1/7, and 1/10; the statistical mode of the number of clays in each cluster being 3, 7 and 10, respectively.

The exact number of clay stacks having the above three categories of platelet stacking were measured by taking at least six different HRTEM images for each type of nanocomposite sample and the average distribution of the clay platelets were noted down (Fig. 38). This has been represented as the extent of exfoliation ( $B$ ) in Table 9. It is apparent that as the level of exfoliation increases, the number of clay platelets per stack decreases and their effective surface area contribution increases.

In order to quantify the level of exfoliation, a surface area factor (SAF) has been proposed, which is the sum of the numerical products of  $A$  and  $B$ , as defined above.

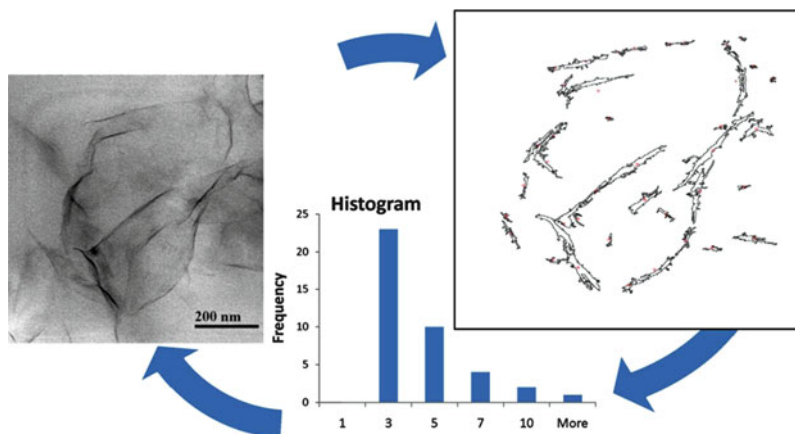


**Fig. 38** Representative protocol for analysis of HRTEM images using ImageJ software

**Table 9** Calculated values of number of platelets per stack and surface area factor as obtained from HRTEM image analysis

Number of clay platelets per stack	Effective surface area contribution of clay platelets ( <i>A</i> )	Extent of exfoliation in nanocomposite sample as obtained from image analysis ( <i>B</i> )		
		$N_{LU}$	$N_{LPNA}$	$N_{MNA}$
1–3	0.33	0.63	0.50	0.16
4–9	0.15	0.28	0.27	0.40
$\geq 10$	0.10	0.09	0.23	0.44
Surface area factor ( $\Sigma AB$ )		0.26	0.23	0.16

From Table 9, it can be noted that the level of exfoliation is highest in  $N_{LU}$  with a SAF value of 0.25, while it is lowest in  $N_{MNA}$  (0.16). Hence, it can be comprehended that the increased level of exfoliation results in an increase in the SAF function and, consequently, a higher proportion of surface area is available for polymer–filler interaction. The high value of SAF in the uncured sample,  $N_{LU}$ , is attributed to the isotropic and homogeneous distribution of nanoclays attained through latex blending. The preferential realignment of the clay layers during the stages of curing diminishes the obvious benefits of such a highly exfoliated morphology in the case of the cured samples. This is also reflected in the lowering of SAF in the cured samples  $N_{MNA}$  and  $N_{LPNA}$  (Table 9).

The increment in mechanical properties (tensile strength, 300% modulus, and Young’s modulus) as a function of SAF is plotted in Fig. 39. In general, the higher level of SAF, which in turn indicates better exfoliation, results in high level of property enhancement. However, the level of increment with the increase in SAF is different in all three cases and follows a typical exponential growth pattern. The apparent nonlinear curve fitting of the experimental values presented in Fig. 39 is a measure of the dependence of mechanical properties on the proposed SAF function.

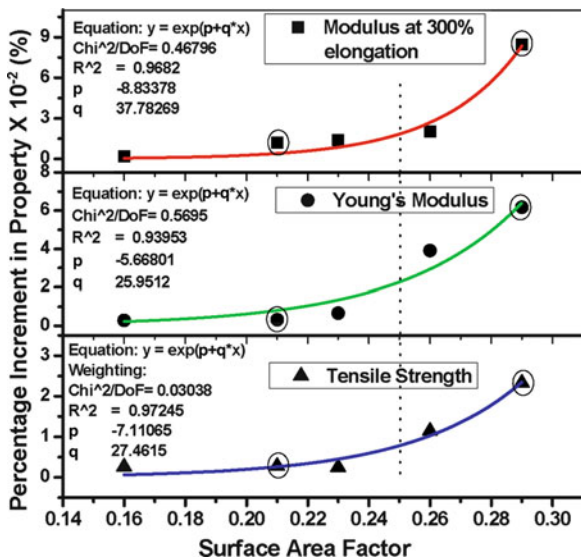


**Fig. 39** Plots showing the effect of surface area factor on the extent of property improvement. Symbols represent experimental values, and the lines are their apparent fitting. Encircled data points are taken from unpublished research work on NR latex-based NA nanocomposites. Vertical dotted line indicates the critical point

The relationship between the SAF and the percentage increment in the respective property can be mathematically represented as:

$$y = \exp(p+qx), \quad (9)$$

where,  $y$  is the percentage increment in the property,  $x$  is the SAF function,  $p$  and  $q$  are constants characteristics of the polymer–filler system. It shows that the newly proposed SAF function can be effectively used to predict and correlate the morphology with the mechanical properties. It is interesting to note that the apparent fit lines demonstrate a critical point (at about SAF value of 0.25) beyond which there is sharp decline in the extent of property enhancement. This is because of the morphological transition from a state of exfoliation to one of greater intercalation (disorder–order transition).

#### 4.2 New Interface Area Function to Investigate Swelling Behavior and Young's Modulus in Nanocomposites

The degree of crosslink density in vulcanized elastomeric gum compounds can be estimated by applying the Flory–Rehner network theory [226]. But, their

extrapolation into the domain of filled compounds presents certain theoretical and practical complications, prime among them being the restriction to deformation in proportion with the sample dimension. The observations of Lorenz and Parks [227] have led to the conclusion that the swelling of bulk rubber is essentially the same in both the filled and the unfilled compounds and that the effect of the inclusion is predominantly felt in the interfacial region only. Within this region, the restriction to swelling is maximum due to adherence of rubber to filler by means of adsorption. On moving radially outwards from the filler, which is the epicenter of the restraining forces, the effect subsides and beyond a certain imaginary sphere of influence, the rubber swells to the same extent as the bulk of the gum compound. This swelling model was effectively utilized by Kraus [228] to quantize the effect on swelling exerted by bonded spherical particles in rubber matrices.

Although the swelling in the case of PNCs agrees in principle with this, it undervalues the importance of the extended interface offered by the change in filler shape and aggregate characteristics. The nanofillers, particularly the nanoclays, are structurally different and resemble an ellipse. Thus, the model generated with spherical filler as the restraining body is inexpedient and it is imperative to consider the entrapment of nonexpansible elliptical filler (with eccentricity,  $\varepsilon$ , within the rubber matrix) (Fig. 40). With this adjustment, the Kraus plot has been integrated by Bhattacharya and Bhowmick into the domain of PNCs containing platelet-like nanofillers [31].

Analogous to the spherical filler of radius  $R$  in the Kraus model, Bhattacharya and Bhowmick [31] consider an elliptical filler represented by  $R(1 + \varepsilon \cos \theta)$ , in the polar coordinate. The swelling is completely restricted at the surface and the restriction diminishes radially outwards (Fig. 40 where,  $q_t$  and  $q_r$  are the tangential and the radial components of the linear expansion coefficient,  $q_0$ ). This restriction is experienced till the hypothetical sphere of influence of the restraining filler is existent. One can designate  $r_{app}$  [ $> R(1 + \varepsilon \cos \theta)$ ] as a certain distance away from the center of the particle where the restriction is still being felt. As the distance approaches infinity, the swelling assumes normality, as in a gum compound. This distance,  $r_{app}$ , however, is not a fixed or well-defined point in space and in fact is variable and is conceived to extend to the outer surface of the hypothetical sphere of influence.

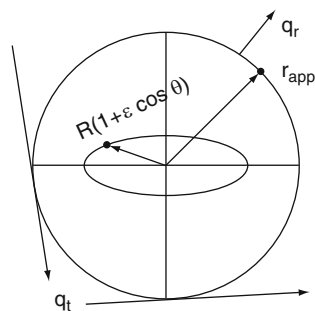


**Fig. 40** Elliptical nanofiller embedded in a rubber matrix, showing parameters used in the model of Bhattacharya and Bhowmick [31]

Now, if one is to assume that the rubber swells equally in all directions, even in the presence of the filler, the swollen volume in presence of filler is:

$$\int_0^{2\pi} \int_0^{\pi} \int_{R(1+\varepsilon \cos \theta)}^{r_{\text{app}}} q_r q_t^2 r^2 \sin \theta \, dr d\theta \, d\psi. \quad (10)$$

Thus, the swelling deficiency will be felt within a shell of rubber bound between  $R(1 + \varepsilon \cos \theta)$  and  $r_{\text{app}}$  and the swelling deficiency per particle,  $\Delta v$ , is:

$$\Delta v = \int_0^{2\pi} \int_0^{\pi} \int_{R(1+\varepsilon \cos \theta)}^{r_{\text{app}}} (q_r q_t^2 - q_0^3) r^2 \sin \theta \, dr d\theta \, d\psi. \quad (11)$$

Integrating the definite integral and rearranging gives:

$$\Delta v = \frac{4\pi q_0^3 R^3}{3} \left[ (1 - 1/q_0^3)(1 + \varepsilon^2) + \frac{r_{\text{app}}^3 \{q_t^3(r)/q_0^3 - 1\}}{R^3} \right]. \quad (12)$$

Presuming that within each unit volume of rubber the filler platelets are segregated in such a way that the filler–filler interactions are negligible, the swelling deficiency for all  $N$  particles can be designated as  $\Delta V = N \Delta v$ .

Also:

$$N = 3\phi/4\pi a^2 b(1 - \phi), \quad (13)$$

where,  $\phi$  is the filler volume fraction and  $a$  and  $b$  are the major and minor axes of the ellipse representing the filler.

Thus, combining (12) and (13):

$$\Delta V = \frac{R^3}{a^2 b} q_0^3 [(1 - 1/q_0^3)(1 + \varepsilon^2) - 3k(1 - 1/q_0)] [\phi/(1 - \phi)]. \quad (14)$$

The volume swelling ratios ( $V_r$ ) are inversely proportional to the equilibrium volume fraction of the rubber in the corresponding swollen systems (filled and gum, represented by subscripts f and 0, respectively), such that:

$$\begin{aligned} Q/Q_0 &= V_{r_0}/V_{r_f} \quad \frac{1}{q^3} = v_r \\ Q/Q_0 &= \frac{(q_0^3 + \Delta v)}{q_0^3} = 1 + [(1 - 1/q_0^3)(1 + \varepsilon^2) - 3k(1 - 1/q_0)] \frac{R^3}{a^2 b} [\phi(1 - \phi)]. \end{aligned} \quad (15)$$

Factoring out  $(1 + \varepsilon^2)$ , one arrives at the final form:

$$V_{r_0}/V_{r_f} = 1 - \left[ \frac{3k(1 - v_{r_0}^{1/3})}{(1 + \varepsilon^2)} + v_{r_0} - 1 \right] \frac{R^3}{a^2b} (1 + \varepsilon^2) [\phi/(1 - \phi)]. \quad (16)$$

Thus, it is understood that  $V_{r_0}/V_{r_f}$  varies linearly, although not with  $\tilde{\phi}(1 - \phi)$ , but with a somewhat similar function that continues to bear the nanofillers' characteristic. In order to isolate the function, (16) is rearranged to get:

$$\frac{1 - V_{r_0}/V_{r_f}}{\left[ \frac{3k}{(1 + \varepsilon^2)} - 1 - \frac{3k}{(1 + \varepsilon^2)} v_{r_0}^{1/3} + v_{r_0} \right] \frac{R^3}{a^2b} (1 + \varepsilon^2)} = \phi(1 - \phi)$$

by substituting  $m'$  for the complex function below:

$$\left[ \frac{3k}{(1 + \varepsilon^2)} - 1 - \frac{3k}{(1 + \varepsilon^2)} v_{r_0}^{1/3} + v_{r_0} \right] \frac{R^3}{a^2b} (1 + \varepsilon^2) = m' \quad (17)$$

the above equation can be reduced to the form:

$$\phi/(1 - \phi) = \frac{1 - (V_{r_0}/V_{r_f})}{m'}.$$

The original Kraus's equation can be similarly rearranged to:

$$\phi' = [1 - (V_{r_0}/V_{r_f})]/[1 - (V_{r_0}/V_{r_f}) + m].$$

Thus, if a function has to accurately map the nanofiller characteristics, the presence of such characteristics as additional terms in the expression for the slope notwithstanding, it needs to be defined as the ratio of the two terms above, such that:

$$\phi/\phi' = \psi = [1 - (V_{r_0}/V_{r_f}) + m]/[1 - (V_{r_0}/V_{r_f}) + m']. \quad (18)$$

In an ideal case, when,  $b = a = R$ , so that  $\varepsilon = 0$ , the derived equation (16) reduces to the Kraus' equation [228] and the above function,  $\psi$ , equates to 1.

Else:

$$\psi = \frac{1 - (V_{r_0}/V_{r_f}) + [3c - 1 - 3cv_{r_0}^{1/3} + v_{r_0}]}{1 - (V_{r_0} + V_{r_f}) + \left[ \frac{3k}{\left(\frac{2a-b}{a}\right)} - 1 - \frac{3k}{\left(\frac{2a-b}{a}\right)} v_{r_0}^{1/3} + v_{r_0} \right] \frac{R^3}{a^2b} \left(\frac{2a-b}{a}\right)}. \quad (19)$$

The introduction of  $\psi$  into to the original Kraus equation would thus incorporate the necessary amendment to accommodate the nanofiller characteristics. But, the



function,  $\psi$ , thus arrived at is complicated and intractable because of the presence of the terms  $a$ ,  $b$  and  $k$  (each of which is filler and system dependent). Hence, it is required to replace the above function (19) with one comprising of known and easily measurable variables by logically deducing a corrective interface area function (IAF).

Since these nanofillers often have a rectangular shape, the elliptical shape assigned introduces some errors in calculation. An ellipse having major axis  $a$  and minor axis  $b$ , which can map the platelet-like nanofiller, would have a deficit of  $(4 - \pi)$  in the interfacial area per particle. This is the difference between the rectangular area ( $4ab$ ) and that of the ellipse ( $\pi ab$ ). Thus, a correction factor corresponding to the interface area needs to be introduced. The discrepancy due to shape and the aggregation effects is addressed by introducing an interfacial area function (IAF). The shape factor can be resolved by introducing the aspect ratio. However, the aspect ratio determination for each particle in a PNC is impractical. It would require rigorous sample preparation, followed by TEM imaging and its complicated image analysis. It would also depend on the extent of exfoliation/intercalation achieved, which varies with the system and the processing conditions introduced, thereby preventing any attempt at generalizations.

Hence, it is supplanted by the filler density ( $\rho$ ) and its specific surface area ( $\zeta$ ) to address the shape factors. This can successfully represent the aspect ratio effects because changes in aspect ratio are reflected in the ratio of particle surface area to particle volume, i.e., density  $\times$  surface area/gram.

Also, the loss in available surface area due to overlapping and aggregation is quite substantial in the case of nanofiller. As illustrated in Fig. 41, the loss is directly dependent on the interparticle distance between the fillers and, hence, also on the filler loading. Introduction of these two terms into the IAF in the form of the correlation length between the nanoparticles ( $\xi$ ) and the filler volume fraction ( $\phi$ ), respectively, mitigates the problem.

The IAF is thus designed to represent the filler characteristics [ $R^3 (1 + \varepsilon^2)/a^2b$ ] that surfaced in (16). Thus, the corrective function,  $\psi$ (IAF), introduced to accommodate the shape and aggregation effects, can be defined as:

$$\psi = \rho \zeta \xi \phi. \quad (20)$$

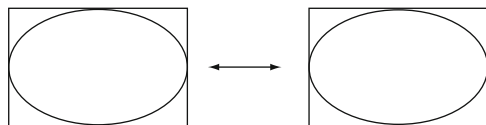
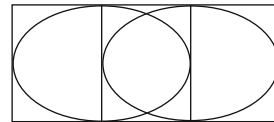


**Fig. 41** Depiction of change in available and lost surface due to differing correlation length

This customized function also circumvents the intractability problem pertinent to (19). Unlike the area function discussed previously to relate the physical properties of carbon black to the overall viscoelastic properties of the composite [229], the function introduced here is unique because it is a dimensionless quantity. Thus, it represents the property better and is devoid of any significant bias arising out of the differences in magnitudes of the constituting components.

Thus, the modified Kraus equation can be represented as:

$$V_{r0}/V_{rf} = 1 - m[\psi\phi/(1 - \psi\phi)], \quad (21)$$

where  $\psi$  is the new IAF.

Without introduction of IAF into the Kraus plot, the coefficients of determination generated for the rubber nanocomposites are found to be significantly less than unity (around 0.608). In terms of statistics, it means that although the present function relating the independent variable to the dependent variable is robust, its accuracy of mapping is hindered possibly because of neglecting certain other parameters that influence the independent variable.

Further, some discrepancy in determining the trend amongst the different nanofillers (especially in the case of natural rubber systems) was observed in the Kraus plots, which suggests that the interaction parameter would follow the order: SP > CNFs > 15A. Following the Zisman approach, the trend for polymer–nanofiller interaction is expected to be decisively in favor of carbon nanofiber by virtue of its higher surface energy (from contact angle studies) [84]. Thus, it can be inferred that the Kraus plot fails to display the right trend. Taking into account the surface energy, cleavage energy, and morphological parameters, the expected order for polymer–filler interaction is CNFs > SP > 15A for NR, and CNFs > 15A > SP for SBR.

This is also reflected in the trends in the mechanical property enhancements [13, 84].

On introduction of the IAF to the erstwhile Kraus equation, the order of the polymer–nanofiller interaction of nanocomposites, as determined from the swelling experiments (Fig. 42a, b), not only agrees with that predicted above from contact angle measurements, but also conforms to those in modulus (Fig. 43), shown later. The modified Kraus plots for the three sets of fillers are shown in Fig. 42a, b, which correspond to the swelling studies in benzene of the natural rubber (NR) and styrene-butadiene rubber (SBR) nanocomposites, respectively. The lines drawn are the best fit lines of the corresponding scatter points of the experimental data sets. Also, the coefficients of determination values of the best-fit lines of the corresponding swelling studies are satisfactory. These results have been found to hold good for various elastomer/solvent combinations [84].

The above observations highlight that the amendment of the Kraus plot by the introduction of the IAF renders the plot applicable to PNCs.

The elastic modulus of composite materials reinforced by discontinuous cylindrical fibers or lamellar shapes is expressed by the Halpin–Tsai equations [106, 230], as shown in the following equation:

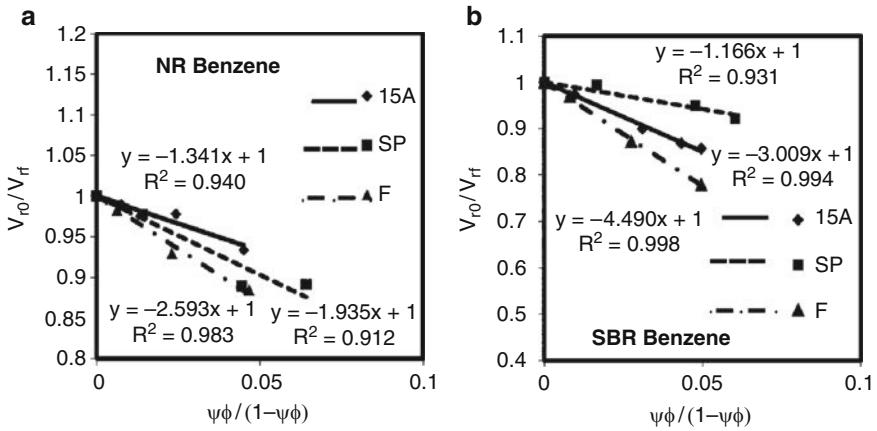


**Fig. 42** Modified Kraus plots for the three sets of filler for **a** NR and **b** SBR swelled in benzene. See text for details

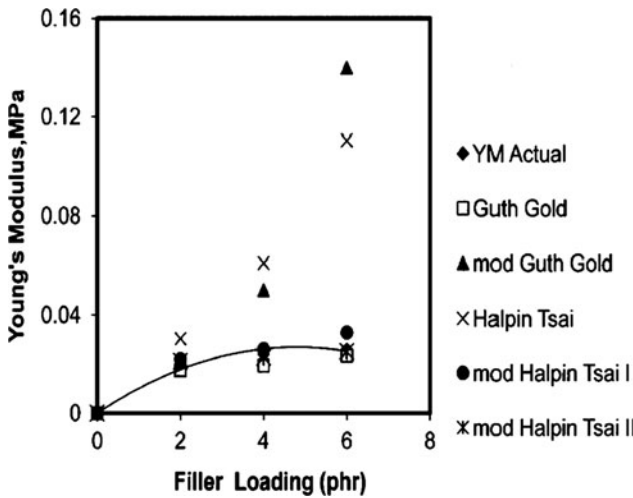


**Fig. 43** Fitting of composite models on introduction of IAF, for the sepiolite-filled NR nanocomposites; *symbols* represent predicted values and the *line* indicates the best fit of the experimental data. *YM* Young's modulus

$$E = E_m \left\{ \frac{1 + \zeta \eta \phi}{1 - \eta \phi} \right\}, \tag{22}$$

where,  $\zeta = 2\alpha$  and  $\eta = \frac{\left[ \frac{E_f}{E_m} \right] - 1}{\left[ \frac{E_f}{E_m} \right] + \zeta}$ .

For rubber/clay systems,  $E_f \gg E_m$ . Therefore,  $\left( \frac{E_f}{E_m} \right) - 1 \approx \left( \frac{E_f}{E_m} \right) + \zeta \approx E_f/E_m$ , and  $\eta \approx 1$ . This reduces the Halpin–Tsai equation (22) to:

$$E = E_m \left\{ \frac{1 + 2\alpha\phi}{1 - \phi} \right\}. \quad (23)$$

The Halpin–Tsai equation can thus be tailored into a much simpler form for PNCs comprising matrix–filler combinations having inordinately disparate sets of Young’s moduli by addressing the shape-, size-, and aggregate-related factors *a priori* in order to adequately supplant those in (22).

As seen, the Halpin–Tsai equation has a term  $\alpha$ , raised to the power of one, to accommodate the filler aspect ratio. Since IAF intends to supplant the same, the new equation is expected to have a reduced dependence on the aspect ratio. Thus, the presence of aspect ratio in the equation needs to be diluted. Two constitutive equations are suggested: the first one contains a correction term in the form of a shape reduction factor ( $\alpha^{0.5}$ ) (24), while the second (25), is devoid of any extra-shape related corrections: Modified Halpin–Tsai I:

$$E = E_m \left\{ \frac{1 + \alpha^{0.5}\psi\phi}{1 - \psi\phi} \right\} \quad (24)$$

and Modified Halpin–Tsai II:

$$E = E_m \left\{ \frac{1 + \psi\phi}{1 - \psi\phi} \right\}. \quad (25)$$

Since the polymer–filler interaction has direct consequence on the modulus, the derived function is subjected to validation by introducing the function in established models for determination of composite modulus. The IAF is introduced in the Guth–Gold, modified Guth–Gold, Halpin–Tsai and some variants of modified Halpin–Tsai equations to account for the contribution of the platelet-like filler to Young’s modulus in PNCs. These equations have been plotted after the introduction of IAF into them.

Figure 43 shows the experimental data alongside the data predicted using the above equations. The line is the best fit line of the experimental data, while the scatter points are the corresponding values predicted using the various equations as indicated by their respective legends in the graph. The Young’s modulus was calculated from the slope of the tensile curve in the linear region (upto 30% elongation). The error is within 2–4% and hence the error bars are not visible. The scatter points are, however, unique values predicted by the modified equations, and hence do not bear error bars.

Table 10 compiles the percent average deviations of the values predicted by the various constitutive equations studied after introduction of the IAF. It is observed from the deviation data (Table 10) that predictions by even the simple Guth–Gold equation derived for spherical fillers are quite accurate, whereas the complex equations (modified Guth–Gold and Halpin–Tsai) containing shape factors and other similar parameters give exceedingly large deviations (Fig. 43). The deviation

**Table 10** Percent average deviation of the various constitutive equations after introduction of the interfacial area function

Model	Filler					
	Cloisite 15A		Sepiolite clay		Carbon nanofibers	
	NR	SBR	NR	SBR	NR	SBR
Guth–Gold	16	19	14	13	9	15
Modified Guth–Gold	248	178	184	190	14	15
Halpin–Tsai	265	181	177	182	44	46
Modified Halpin–Tsai I	17	15	15	16	5	2
Modified Halpin–Tsai II	25	0	1	0	0	7

in the case of Guth–Gold equation is 9–19% whereas those for modified Guth–Gold and Halpin–Tsai equations are 248% and 265%, respectively, due to the above-mentioned factors.

Even without the introduction of the correction factor, the Guth equation per se gives error in prediction as high as 17–35% for the nanocomposites studied. The modified Guth–Gold and Halpin–Tsai equations are also found to be error prone, with 21–101% and 29–107% error in prediction. These errors increase continually with nanofiller loading. The preincorporation of shape-related factors in the IAF causes a multiplicative term to be carried through in the case of modified Guth–Gold and Halpin–Tsai equations. Since these equations already have a shape-related correction introduced (to address rod-like fillers instead of spherical fillers) the inclusion of IAF results in gross overestimation, especially at higher loading of nanofillers with high specific surface areas.

The close fit of the experimental data and the values predicted by the constitutive modified Halpin–Tsai equations I and II (24) and (25), as seen in Fig. 43 (for NR) illustrates the appropriate definition of the IAF. Table 10 also confirms that newly devised equations (24) and (25) provide astounding results because their predictions conform to the experimental data. The introduction of IAF imparts a definitive change to the predicting ability of the constitutive equations for polymer/filler nanocomposites (Fig. 43; Table 10).

These results indicate both the necessity and efficacy of the IAF in understanding the polymer–nanofiller interaction parameter. It also justifies the approach undertaken to identify the possible constituents of this function, specifically for PNCs filled with platelet-type nanofiller.

### ***4.3 Role of Polymer–Solvent and Clay–Solvent Interaction Parameters on the Morphology Development of Polymer-Based Nanocomposite***

Solvent–polymer and solvent–clay interactions are very important in determining the morphology of polymer/clay nanocomposites. There are many reports describing the preparation of PNCs by solution mixing [65, 231–235]. Ho and Glinka [38]

in their work have highlighted the effect of the solvent solubility parameter on the dispersion of clay. Lift et al. have used a solvent exchange process for the proper dispersion of nanoparticles in thermoplastic elastomers [236]. Lim et al. measured the Flory–Huggins interaction parameter to determine the extent of miscibility between the blend of Poly(Ethylene Oxide) and Poly(Methyl Methacrylate) with o-MMT [237]. Choudhury et al. have illustrated how the solvent combination and the difference in the interaction parameters of solvent–polymer (here, HNBR) and solvent–clay (here, sepiolite) affect the morphology of the nanocomposite, which in turn influence the thermal, mechanical, and optical properties of the nanocomposite [86]. In the work, nine different sets of solvent combinations have been chosen on the basis of their solubility parameter. A correlation between the morphology of different nanocomposites prepared with different solvent combinations and the difference in their interaction parameters with various solvents ( $\chi_{AB}-\chi_{CD}$ ) have been analyzed. The dispersion of clay in the rubber matrix for different solvent systems has been characterized by XRD, AFM and TEM.

The X-ray diffractograms of the sepiolite clay and HNBR/sepiolite nanocomposites in different solvent combinations are shown in Fig. 44. Both the clay as well as the nanocomposites have peak position in the range of  $7.2-7.4^\circ$  ( $2\theta$ ), corresponding to a  $d$ -spacing of 1.22–1.24 nm. This indicates that, unlike montmorillonite which is a layered silicate, sepiolite clay does not undergo exfoliation on addition to the rubber matrix [93]. Wang and Sheng [238] have made similar observations for polypropylene/attapulgite nanocomposites. A decrease in the peak intensity in the case of nanocomposites reveals that clay sheets become delaminated to a certain extent; the lower the intensity of peak, the greater is the delamination. As in the case of the combination of HNBR in chloroform and clay in MEK the peak intensity is the lowest because clay layers undergo maximum delamination in this solvent combination. The morphology obtained from the AFM and TEM photographs (Fig. 44) also confirm the above observations. Optical transmittance study

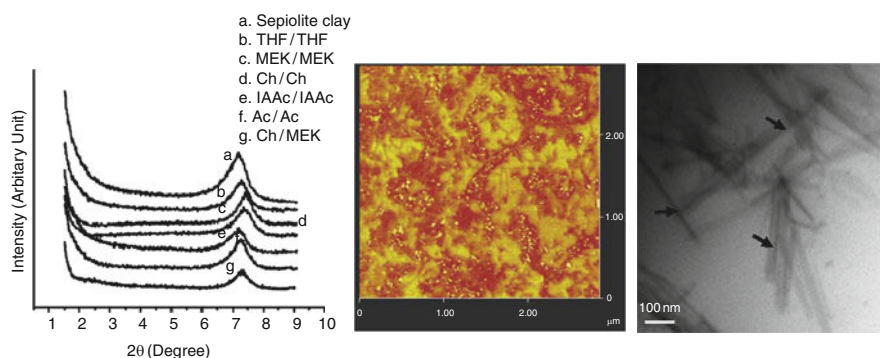


**Fig. 44** a XRD curves of sepiolite and HNBR/sepiolite nanocomposite for various solvent combinations. b AFM phase image of HNBR/sepiolite nanocomposite for chloroform/MEK solvent combination. c TEM photograph HNBR/sepiolite nanocomposite for chloroform/MEK solvent combination

(not shown here) has shown that light transparency is highest for nanocomposite made with the Ch/MEK solvent combination. The higher the transparency, the better is the dispersion of clay in the matrix.

It has been found that the HNBR/SP nanocomposite provides the best thermal and mechanical properties when HNBR is dissolved in Ch and SP is dispersed in MEK. XRD, AFM, TEM, and optical transmittance studies show that the dispersion of clay is best in the Ch/MEK solvent combination and, hence, polymer–filler interaction is also highest in this system. Thus, rather than implying that the solvent selection directly affects the physical properties of the nanocomposite, solvent acts on the properties through its influence on the developed morphology.

Ch and MEK are two different solvents, but having almost the same solubility parameter (18.76 and 18.91 MPa<sup>1/2</sup>, respectively); hence, they are thermodynamically miscible. According to Hildebrand, the enthalpy of mixing can be related to the solubility parameter as:

$$\Delta H_m = \phi_1 \phi_2 (\delta_1 - \delta_2)^2, \tag{26}$$

where  $\phi_1$  and  $\phi_2$  are the volume fractions of components 1 and 2, and  $\delta_1$  and  $\delta_2$  are the solubility parameters of components 1 and 2.

Equation (26) predicts that  $\Delta H_m = 0$  if  $\delta_1 \approx \delta_2$ ; thus Ch and MEK, having similar solubility parameters, are miscible with each other.

In order to understand the relationship between the difference in the interaction parameter of rubber–solvent ( $\chi_{AB}$ ) and clay–solvent ( $\chi_{CD}$ ) systems and the properties of HNBR/SP nanocomposites, the plots of modulus at 100% elongation and tensile strength versus  $\chi_{AB} - \chi_{CD}$  are represented in Fig. 45a, b. An exponential decay in both modulus and tensile strength is observed with the increase in difference of interaction parameter.  $T_i$  and  $T_{max}$  follow the same trend as above.

The temperature at which maximum degradation took place is denoted as  $T_{max}$  and the corresponding onset temperature of degradation (5% degradation) is

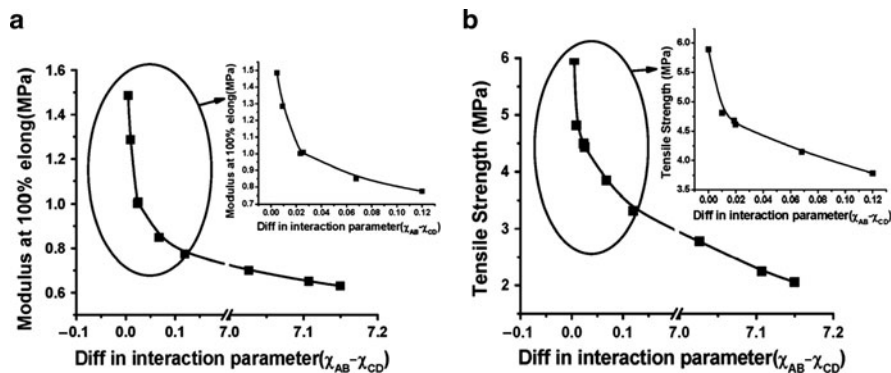


Fig. 45 Plots of **a** modulus at 100% elongation and **b** tensile strength versus difference in interaction parameters ( $\chi_{AB} - \chi_{CD}$ )

represented as  $T_i$ . Better dispersion of clay as well as good polymer–filler interaction in the case of the Ch/MEK solvent combination has also explained using the thermodynamic point of view. Choudhury et al. [86] have derived a relationship between Gibb’s free energy ( $G$ ) and interaction parameter ( $\chi$ ):

$$\Delta G_M = kTN_1\varphi_2\chi - T\Delta S_M. \quad (27)$$

Equation (27) is true for both polymer–solvent and clay–solvent systems.

It is well known that the lower the  $\Delta G_M$  value, the better is the rubber–filler interaction. As for the Ch/MEK solvent combination  $\chi$  is zero, hence the  $kTN_1\varphi_2\chi$  term of (27) is zero for such a solvent combination. In all other solvent combinations, where  $\chi \neq 0$ , the  $kTN_1\varphi_2\chi$  term of (27) is positive. Thus,  $\Delta G_M$  of the system for the Ch/MEK solvent combination is the least, and dispersion (if clay is in the rubber matrix) is also best in this solvent combination, giving rise to the highest polymer–filler interaction.

#### 4.4 *Multiscale Modeling and Simulation of Polymer Nanocomposites*

In PNCs, the details of molecular structure and dynamics in the periphery of the nanoparticles (for example, within the lamellar gallery or at the interface) is quite difficult to establish by regular experimental techniques. The inability to monitor the thermodynamics and kinetics of the molecular interactions between the different constituents that determine the structural evolution and final morphology of the materials hinders progress in this field. This is probably the domain where there is an increasing need for computer modeling and simulations.

The formation of the equilibrium morphological structures (discussed in Sect. 2) is believed to be determined by the interplay of entropic (i.e., intermolecular interactions) and enthalpic (i.e., configurational changes in the components) factors. Some theoretical and simulation efforts have been made recently to elucidate the formation of nanoparticlePNCs from the point of view of thermodynamics at a molecular level. The simulation methods used include the mean-field model [37, 239], a combined model of density functional theory (DFT) and self-consistent field theory (SCF) [240], and molecular dynamic (MD) models [241, 242]. The kinetics of nanocomposite formation through the intercalation process of clay-based PNCs was first investigated by Loring and coworkers [243, 244] by using the coarse-grained MD simulations. They found that interlayer swelling of clay requires a moderate polymer–surface affinity, beyond which the flow slows down.

Processing conditions are known to play a critical role in establishment of morphology and final properties of the materials. Balazs and coworkers [245, 246] designed a multiscale method (coarse-grained Cahn–Hilliard approach and Brownian dynamics) and found that addition of solid particles significantly



changes both the speed and the morphology of the phase separation, which itself demonstrates shear-induced anisotropic growth.

Mechanical properties of PNCs can also be estimated by using computer modeling and simulation methods at a wide range of length and time scales. Seamless movement from one scale to another, for example, from the molecular scale (e.g., MD) and microscale (e.g., Halpin–Tsai) to macroscale (e.g., finite element method, FEM), and the combination of scales (or the so-called multiscale methods) is the most important prerequisite for the efficient transfer and extrapolation of calculated parameters, properties, and numerical information across length scales.

Recently, some models (e.g., Halpin–Tsai, Mori–Tanaka, lattice spring model, and FEM) have been applied to estimate the thermo–mechanical properties [247, 248], Young’s modulus [249], and reinforcement efficiency [247] of PNCs and the dependence of the materials modulus on the individual filler parameters (e.g., aspect ratio, shape, orientation, clustering) and on the modulus ratio of filler to polymer matrix.

Gersappe [250] used an MD simulation to probe the molecular mechanisms by which nanofillers reinforce the polymer matrix. Liao and Li [251] used Molecular Modeling to quantify CNT–polymer interfacial shear stress and found it to be about one order of magnitude higher than that of microfiber-reinforced composites.

The formation of hydrogen bonding between the amine hydrogen of octadecylamine and the hydroxyl oxygen of the ethylene–vinyl alcohol copolymer was found to contribute to the improved storage modulus. This was established by Aleperstein et al. [252] by employing MD simulations on ethylene–vinyl alcohol copolymer/organoclay nanocomposites.

Chauve et al. [253] utilized the same technique to examine the reinforcing effects of cellulose whiskers in EVA copolymer nanocomposites. It was shown that larger energy is needed to separate polar EVA copolymers from cellulose than for the nonpolar ethylene homopolymer. The elastomeric properties in the presence of spherical nanoparticles were studied by Sen et al. [254] utilizing Monte Carlo simulations on polypropylene matrix. They found that the presence of the nanofillers, due to their effect on chain conformation, significantly affected the elastomeric properties of nanocomposites.

Compared to other models (e.g., Voigt–Reuss, Halpin–Tsai, modified mixture law, and Cox), the dilute suspension of clusters model promulgated by Villoria and Miravete [255] could estimate the influence of the dispersion of nanofillers in nanocomposite Young’s modulus with much improved theoretical–experimental correlation.

Wu et al. [32] introduced the MRF of 0.66 for the platelet-like fillers into established composite models to account for the lower contribution of the platelet-like filler to the Young’s modulus than the contribution of the fiber-like filler. This apparently improved the predicting ability of the models in the case of elastomeric nanocomposites.

FEM has also been used to predict the mechanical properties of PNCs. These studies reasonably reproduced the nanocomposite microstructure (i.e., particle size, amount, and spatial arrangement) and underlined the importance of including an

interphase layer around particles as a third constituent material (apart from the filler and the matrix) in the prediction of mechanical properties. In PNCs, the constituting components have equivalent size and the polymer–filler interactions are highly dependent on the local molecular structure and bonding at the interface. Fisher et al. [256] developed a model that combines FEM with a micromechanical method (i.e., Mori–Tanaka model) to determine the effective reinforcing modulus of a wavy embedded nanotube. The effective elastic properties of PNCs reinforced with silica nanoparticles were predicted by means of various FEM-based computational models [257–259]. FEM has nowadays been incorporated into some commercial software packages and open source codes (e.g., ABAQUS, ANSYS, Palmyra, and OOF) and widely used to evaluate the mechanical properties of polymer composites.

Hbaieb et al. [260] recently suggested that Mori–Tanaka and 2D FEM models do not predict accurately the elastic modulus of real clay/PNCs. The Mori–Tanaka model underestimates the stiffness at higher volume fractions (>5%) and overestimates the stiffness of exfoliated clay/PNCs.

## 5 Conclusions

In this chapter, an attempt has been made to review the state-of-the-art in rubber-based nanocomposites, especially from the morphology–property relationship point of view. As described, rubber-based nanocomposites often exhibit properties superior to conventional composites, such as processability, strength, thermal and oxidative stability, electrical and barrier properties, as well as adhesive strength. These improvements in properties are generally attained at much lower filler content in comparison with conventionally filled systems. This chapter specifically highlights the vital role played by the development of proper morphology in determining the magnitude of improvements in the properties. Numerous examples are provided that establish the morphology–property dependence in rubber-based nanocomposites.

## References

1. Calvert PD (1992) *Mater Res Soc Bull* 17:37
2. Mark JE, Erman B, Eirich FR (2005) *Science and technology of rubber*, 3rd edn. Elsevier, Amsterdam
3. Goettler LA, Cole WF (2001) Short fiber-filled rubber composites. In: Bhowmick AK, Stephens HL (eds) *Handbook of elastomers*, 2nd edn. Marcel Dekker, New York
4. Kojima Y, Usuki A, Kawasumi M, Okada A, Fukushima Y, Kurauchi T, Kamigaito O (1993) *J Mater Res* 8:1185
5. Maiti M, Bhattacharya M, Bhowmick AK (2008) *Rubber Chem Technol* 81:384
6. Morgan AB, Gilman JW (2003) *J Appl Polym Sci* 87:1329
7. Magonov SN, Whangbo MH (1996) *Surface analysis with STM and AFM*. Weinheim, VCH

8. Roe R (2000) *Methods of X-Ray and neutron scattering in polymer science*. Oxford University Press, New York, p 199
9. George JJ, Sengupta R, Bhowmick AK (2007) *J Nanosci Nanotechnol* 8:1
10. Sharaf MA, Mark JE (2004) *Polymer* 45:3943
11. Buxton GA, Balazs AC (2002) *J Chem Phys* 117:7649
12. Chin IJ, Thurn-Albrecht T, Kim HC, Russell TP, Wang J (2001) *Polymer* 42:5947
13. Bhattacharya M, Maiti M, Bhowmick AK (2009) *Polym Eng Sci* 49:81
14. Maiti M, Sadhu S, Bhowmick AK (2004) *J Polym Sci B Polym Phys* 42:4489
15. Maji PK, Guchhait PK, Bhowmick AK (2009) *J Mater Sci* 44:5861
16. Mohammadpour Y, Katbab AA (2007) *J Appl Polym Sci* 106:4209
17. Kohjiya S, Kato A, Ikeda Y (2008) *Prog Polym Sci* 33:979
18. Kwee T, Mauritz KA (2003) *Polymer Prepr* 44:1106
19. Vaia R, Mirau P, Alexander M, Koerner H, Hsiao BS, Sics I (2005) 167th Spring Technical Meeting – American Chemical Society, Rubber Division, San Antonio, TX, United States, 16–18 May 2005, 63/1–63/8
20. Krishnamoorti R, Silva AS (2000) Rheological properties of polymer layered-silicate nanocomposites. In: Pinnavaia TJ, Beall G (eds) *Polymer nanocomposites*. Wiley, New York
21. Ren J, Silva AS, Krishnamoorti R (2000) *Macromolecules* 33:3739
22. Causin V, Marega C, Marigo A, Ferrara G, Ferraro A, Selleri R (2008) *J Nanosci Nanotechnol* 8:1823
23. Naderi G, Lafleur PG, Dubois C (2007) *Polym Eng Sci* 47:207
24. Kloczkowski A, Sharaf MA, Mark JE (1994) *Chem Eng Sci* 49:2889
25. Chabert E, Dendievel R, Gauthier C, Cavaille JY (2004) *Compos Sci Technol* 64:309
26. Raos G, Moreno M, Elli S (2006) *Macromolecules* 39:6744
27. Bandyopadhyay A, De Sarkar M, Bhowmick AK (2005) *J Polym Sci B Polym Phys* 43:2399
28. Fornes TD, Paul DR (2003) *Polymer* 44:4993
29. Brune DA, Bicerano J (2002) *Polymer* 43:369
30. Shia D, Hui CY, Burnside SD, Giannelis EP (1998) *Polym Compos* 19:608
31. Bhattacharya M, Bhowmick AK (2008) *Polymer* 49:4808
32. Wu Y, Jia Q, Yu D, Zhang L (2004) *Polym Test* 23:903
33. Zeng QH, Yu AB, Lu GQ (2008) *Prog Polym Sci* 33:191
34. Alexandre M, Dubois P (2000) *Mater Sci Eng* 28:1
35. Giannelis EP (1996) *Adv Mater* 8:29
36. Choudhury A, Bhowmick AK, Ong C (2010) *J Appl Polym Sci* 116:1428
37. Vaia RA, Giannelis EP (1997) *Macromolecules* 30:7990
38. Park CI, Park OO, Lim JG, Kim HJ (2001) *Polymer* 42:7465
39. Causin V, Marega C, Mariog A, Ferrara G (2005) *Polymer* 46:9533
40. Ho DL, Glinka CJ (2003) *Chem Mater* 15:1309
41. Eckel DF, Balogh MP, Fasulo PD, Rodgers WR (2004) *J Appl Polym Sci* 93:1110
42. Maiti M, Bhowmick AK (2006) *Polymer* 47:6156
43. Wang ZL (2003) *Adv Mater* 15:1497
44. VanderHart DL, Asano A, Gilman JW (2001) *Macromolecules* 34:3819
45. Jeschke G, Panek G, Schleidt S, Jonas U (2004) *Polym Eng Sci* 44:1112
46. Loo LS, Gleason KK (2003) *Macromolecules* 36:2587
47. Bafna A, Beaucage G, Mirabella F, Skillas G, Sukumaran S (2001) *J Polym Sci B Polym Phys* 39:2923
48. Eckel DF, Balogh MP, Fasulo PD, Rodgers WR (2004) *J Appl Polym Sci* 93:1110
49. Ganguly A, De Sarkar M, Bhowmick AK (2006) *J Polym Sci B Polym Phys* 45:52
50. Ganguly A, Li Y, Bhowmick AK (2008) *Macromolecules* 41:6246
51. Schaefer DW, Justice RS (2007) *Macromolecules* 40:8501
52. Karger-Kocsis J, Wu CM (2004) *Polym Eng Sci* 44:1083
53. Yano K, Usuki A, Okada A (1991) *Polymer Prepr* 32:65

54. Yano K, Usuki A, Okada A, Kurauchi T, Kamigaito O (1993) *J Polym Sci A Polym Chem* 31:2493
55. Blumstein A (1965) *J Polym Sci A Polym Chem* 3:2665
56. Messersmith PB, Giannelis EP (1995) *J Polym Sci A Polym Chem* 33:1047
57. Gilman JW (1999) *Appl Clay Sci* 15:31
58. Vaia RA, Vasudevan S, Krawiec W, Scanlon LG, Giannelis EP (1995) *Adv Mater* 7:154
59. Alexandre M, Dubois P (2000) *Mater Sci Eng* 28:1
60. Joly S, Garnaud G, Ollitrault R, Bokobza L (2002) *Chem Mater* 14:4202
61. Bandyopadhyay A, De Sarkar M, Bhowmick AK (2004) *Rubber Chem Technol* 77:830
62. Sadhu S, Bhowmick AK (2004) *J Polym Sci B Polym Phys* 42:1573
63. Liang Y, Wang Y, Wu Y, Lu Y, Zhang H, Zhang L (2005) *Polymer Test* 24:12
64. Maiti M, Bhowmick AK (2006) *J Appl Polym Sci* 101:2407
65. Varghese S, Karger-Kocsis J (2003) *Polymer* 44:4921
66. Ma J, Xiang P, Mai YW, Zhang LQ (2004) *Macromol Rapid Commun* 25:1692
67. Jia QX, Wu YP, Wang YQ, Lu M, Yang J, Zhang LQ (2007) *J Appl Polym Sci* 103:1826
68. Wang Y, Zhang H, Wu Y, Yang J, Zhang L (2005) *J Appl Polym Sci* 96:318
69. Wu YP, Jia QX, Yu DS, Zhang LQ (2003) *J Appl Polym Sci* 89:3855
70. Wu YP, Ma Y, Wang YQ, Zhang LQ (2004) *Macromol Mater Eng* 289:890
71. Usuki A, Tukigase A, Kato M (2002) *Polymer* 43:2185
72. Gatos KG, Thomann R, Karger-Kocsis J (2004) *Polym Int* 53:1191
73. Gatos KG, Karger-Kocsis J (2005) *Polymer* 46:3069
74. Ma Y, Wu YP, Wang YQ, Zhang LQ (2006) *J Appl Polym Sci* 99:914
75. Varghese S, Karger-Kocsis J, Gatos KG (2003) *Polymer* 44:3977
76. Arroyo M, Lopez-Manchado MA, Herrero B (2003) *Polymer* 44:2447
77. Lopez-Manchado MA, Arroyo M, Herrero B, Biagiotti J (2003) *J Appl Polym Sci* 89:1
78. Varghese S, Karger-Kocsis J (2004) *J Appl Polym Sci* 91:813
79. Datta H, Singha NK, Bhowmick AK (2008) *J Appl Polym Sci* 108:2398
80. Datta H, Singha NK, Bhowmick AK (2008) *Macromolecules* 41:50
81. Xu J, Pang W, Shi W (2006) *Thin Solid Films* 514:69
82. Blanc D, Zhang W, Massard C, Mugnier J (2006) *Optical Mater* 28:331
83. Sadhu S, Bhowmick AK (2005) *J Mater Sci* 40:1633
84. Bhattacharya M, Maiti M, Bhowmick AK (2008) *Rubber Chem Technol* 81:782
85. Bhowmick AK, Ganguly A, Maiti M (2006) *Kautsch Gummi Kunstst* 59:437
86. Choudhury A, Bhowmick AK, Ong C (2009) *Polymer* 50:201
87. Dennis HR, Hunter DL, Chang D, Kim S, White JL, Cho JW, Paul DR (2001) *Polymer* 42:9513
88. Sadhu S, Bhowmick AK (2005) *J Polym Sci B Polym Phys* 43:1854
89. Das A, Jurk R, Stöckelhuber KW, Heinrich G (2007) *Express Polym Lett* 1:717
90. Gatos KG, Sawanis NS, Apostolov AA, Thomann R, Karger-Kocsis J (2004) *Macromol Mater Eng* 289:1079
91. Bhattacharya M, Bhowmick AK (in press) *Rubber Chem Technol*
92. Bhowmick AK, Bhattacharya M, Mitra S (2009) Rubber Division ACS 176th Fall Technical Meeting and Rubber Mini Expo<sup>TM</sup>, Paper No: 103, Pittsburgh, USA, Oct 2009
93. Maiti M, Bhowmick AK (2006) *J Polym Sci B Polym Phys* 44:162
94. Wu YP, Wang YQ, Zhang HF, Wang YZ, Yu DS, Zhang LQ, Yang J (2005) *Compos Sci Technol* 65:1195
95. Katti KS, Katti DR (2006) *Langmuir* 22:532
96. Kim JT, Oh TS, Lee DH (2003) *Polym Int* 52:1203
97. Arroyo M, López-Manchado MA, Valentín JL, Carretero J (2007) *Compos Sci Technol* 67:1330
98. Valsecchi R, Viganò M, Levi M, Turri S (2006) *J Appl Polym Sci* 102:4484
99. Ibarra L, Rodríguez A, Mora I (2007) *Eur Polym J* 43:753
100. Mousa A, Karger-Kocsis J (2001) *Macromol Mater Eng* 286:260

101. Tan H, Isayev AI (2008) *J Appl Polym Sci* 109:767
102. Lim SK, Kim JW, Chin IJ, Choi HJ (2002) *J Appl Polym Sci* 86:3735
103. Kader MA, Lyu MY, Nah C (2006) *Compos Sci Technol* 66:1431
104. Bandyopadhyay A, De Sarkar M, Bhowmick AK (2005) *Rubber Chem Technol* 78:806
105. Sen S, Thomin JD, Kumar SK, Keblinski P (2007) *Macromolecules* 40:4059
106. Halpin JC, Kardos JL (1976) *Polym Eng Sci* 16:344
107. Mori T, Tanaka K (1973) *Acta Metall* 21:571
108. Paul DR, Robeson LM (2008) *Polymer* 49:3187
109. Ganter M, Gronski W, Reichert P, Mulhaupt R (2001) *Rubber Chem Technol* 74:221
110. Ganter M, Gronski W, Semke H, Zilg T, Thomann C, Mulhaupt R (2001) *Kautsch Gummi Kunstst* 54:166
111. Kojima Y, Fukumori K, Usuki A, Okada A, Kurauchi T (1993) *J Mater Sci Lett* 12:889
112. Joly S, Garnaud G, Ollitrault R, Bokobza L (2002) *Chem Mater* 14:4202
113. Wang Y, Zhang H, Wu Y, Yang J, Zhang L (2005) *J Appl Polym Sci* 96:318
114. Wang Y, Zhang L, Tang C, Yu D (2000) *J Appl Polym Sci* 78:1879
115. Lopez-Manchado MA, Herrero B, Arroyo M (2004) *Polym Int* 53:1766
116. Schon F, Gronski W (2003) *Kautschuk Gummi Kunststoffe* 56:166
117. Usuki A, Tugigase A, Kato M (2002) *Polymer* 43:2185
118. Netrabukkana S, Pattamaprom C, Chiang MJ (2005) *Science* 32:391
119. Jia Q, Wu Y, Ping X, Xin Y, Wang Y, Zhang L (2005) *Polym Polym Comp* 13:709
120. Kim W, Kim SK, Kang JH, Choe Y, Chang YW (2006) *Macromol Res* 14:187
121. Chang Y, Yang Y, Nah C (2001) Abstracts of Papers, 221st ACS National Meeting, San Diego, CA, USA
122. Peeterbroeck S, Alexandre M, Jerome R, Dubois P (2005) *Polym Degrad Stab* 90:288
123. Petrovic ZS, Javni I, Waddon A, Banhegyi G (2000) *J Appl Polym Sci* 76:133
124. Jia QX, Wu YP, Xu YL, Mao HH, Zhang LQ (2006) *Macromol Mater Eng* 291:218
125. Kim W, Kang BS, Cho SG, Ha CS, Bae JW (2007) *Compos Interf* 14:409
126. Zhou X, Zhu Y, Gong Q, Liang J (2006) *Mater Lett* 60:3769
127. Wang JD, Zhu YF, Zhou XW, Sui G, Liang J (2006) *J Appl Polym Sci* 100:4697
128. M Knite, Teteris V, Kiploka A, (2003) *Mater Sci Eng C Biomim Supramol Syst* C23: 787
129. Zhang L, Wang Y, Yuan S, Yu D (2000) *J Appl Polym Sci* 78:1873
130. Sadhu S, Bhowmick AK (2003) *Rubber Chem Technol* 76:860
131. Sadhu S, Bhowmick AK (2004) *J Appl Polym Sci* 92:698
132. Sadhu S, Bhowmick AK (2004) *Adv Eng Mater* 6:738
133. Ganguly A, Bhowmick AK (2008) *Nanoscale Res Lett* 3:36
134. Maiti M, Bhowmick AK (2008) *Compos Sci Technol* 68:1
135. Maiti M, Bhowmick AK (2009) *J Appl Polym Sci* 111:1094
136. Maji PK, Guchhait PK, Bhowmick AK (2009) *ACS Appl Mater Interf* 1:289
137. Kar S, Maji PK, Bhowmick AK (2010) *J Mater Sci* 45:64
138. Bandyopadhyay A, Thakur V, Pradhan S, Bhowmick AK (2010) *J Appl Polym Sci* 115:1237
139. Kuila T, Srivastava SK, Bhowmick AK (2009) *Polym Eng Sci* 49:585
140. Pramanik M, Srivastava SK, Samantaray BK, Bhowmick AK (2003) *J Appl Polym Sci* 87:2216
141. Bandyopadhyay A, Bhowmick AK, De Sarkar M (2004) *J Appl Polym Sci* 93:2579
142. Bandyopadhyay A, De Sarkar M, Bhowmick AK (2005) *J Mater Sci* 40:5233
143. Bandyopadhyay A, De Sarkar M, Bhowmick AK (2005) *J Appl Polym Sci* 95:1418
144. Patel S, Bandyopadhyay A, Vijayabaskar V, Bhowmick AK (2005) *Polymer* 46:8079
145. Patel S, Bandyopadhyay A, Vijayabaskar V, Bhowmick AK (2006) *J Mater Sci* 41:927
146. George JJ, Bhowmick AK (2008) *Nanoscale Res Lett* 3:508
147. George JJ, Bhowmick AK (2009) *Nanoscale Res Lett* 4:655
148. Mitra S, Chattopadhyay S, Bhowmick AK (2008) *Rubber Chem Technol* 81:842
149. Mitra S, Chattopadhyay S, Bhowmick AK (2009) *Nanoscale Res Lett* 4:420
150. Ferry JD (1982) *Viscoelastic properties of polymers*. Wiley, New York

151. Liu X, Wu Q (2001) *Polymer* 42:10013
152. Messersmith PB, Giannelis EP (1994) *Chem Mater* 6:1719
153. Noh MW, Lee DC (1999) *Polym Bull* 42:619
154. Nam PH, Maiti P, Okamoto M, Kotaka T, Hasegawa N, Usuki A (2001) *Polymer* 42:9633
155. Sengupta R, Chakraborty S, Bandyopadhyay S, Dasgupta S, Mukhopadhyay R, Auddy K, Deuri AS (2007) *Polym Eng Sci* 47:1956
156. Jurkowska B, Jurkowski B, Oczkowski M, Pesetskii SS, Koval V, Olkhov YA (2007) *J Appl Polym Sci* 106:360
157. Das A, Costa FR, Wagenknecht U, Heinrich G (2008) *Eur Polym J* 44:3456
158. Ramorino G, Bignotti F, Conzatti L, Ricco T (2007) *Polym Eng Sci* 47:1650
159. Liu B, Ding Q, He Q, Cai J, Hu B, Shen J (2006) *J Appl Polym Sci* 99:2578
160. Sadhu S, Bhowmick AK (2005) *Rubber Chem Technol* 78:32
161. Maiti M, Bhowmick AK (2007) *Polym Eng Sci* 47:1777
162. George JJ, Bandyopadhyay A, Bhowmick AK (2009) *J Appl Polym Sci* 108:1603
163. Payne AR (1962) *J Polym Sci* 6:57
164. Dinesh Kumar K, Tsou AH, Bhowmick AK (2010) *J Adhes Sci Technol*. DOI: [10.1163/016942409X12598231568348](https://doi.org/10.1163/016942409X12598231568348)
165. Maity A, Sinha Ray S (2009) *J Nanosci Nanotechnol* 9:5223
166. Jang BN, Wilkie CA (2005) *Polymer* 46:9702
167. Weifu D, Liu X, Zhang Y, Gui H, Wang Q, Gao J, Song Z, Lai J, Huang F, Qiao J (2006) *Eur Polym J* 42:2515
168. Golebiewski J, Galeski A (2007) *Compos Sci Technol* 67:3442
169. Okada O, Kawasumi M, Usuki A, Kojima Y, Karauchi T, Kamigaito O (1990) *Mater Res Soc Symp Proc* 171:452
170. Jianxin D, Jin Z, Charles WA, Jianqi W (2002) *Polym Degrad Stab* 77:377
171. Maiti M, Mitra S, Bhowmick AK (2008) *Polym Degrad Stab* 93:188
172. Sengupta R, Sabharwal S, Chaki TK, Bhowmick AK (2006) *Polym Degrad Stab* 91:1311
173. Sadhu SD, Rajeev RS, Bhowmick AK (2008) *Polym Polym Compos* 16:283
174. Choudhury A, Bhowmick AK, Ong C, Soddemann M (2010) *J Nanosci Nanotechnol* 10:5056
175. Wang H, Yang J, Long S, Wang X, Yang Z, Li G (2004) *Polym Degrad Stab* 83:229
176. Wall LA (1972) *Fluoropolymers*. Wiley Interscience, New York
177. Zhong R, Hu Y, Wang S, Song L (2004) *Polym Degrad Stab* 83:423
178. Sengupta R, Bandyopadhyay A, Sabharwal S, Chaki TK, Bhowmick AK (2005) *Polymer* 46:3343
179. Chung DDL (2001) *Carbon* 39:279
180. Luo X, Chung DDL (1996) *Carbon* 34:1293
181. Saroop M, Ghosh AK, Mathur GN (2003) *Int J Plastics Technol* 7:41
182. Takai K, Oga M, Sato H, Enoki T, Ohki Y, Taomoto A, Suenaga K, Iijima S (2003) *Phys Rev B* 67:214202
183. Zheng W, Wong SC, Sue HJ (2002) *Polymer* 73:6767
184. Xiao M, Sun L, Liu J, Li Y, Gong K (2002) *Polymer* 43:2245
185. Ramanathan T, Stankovich S, Dikin DA, Liu H, Shen H, Guyen STN, Brinson LC (2007) *J Polym Sci B Polym Phys* 45:2097
186. Cerezo FT, Preston CML, Shanks RA (2007) *Compos Sci Technol* 67:79
187. Vovchenko L, Matzui L, Tzaregradska T, Stelmakh O (2003) *Compos Sci Technol* 63:807
188. Liang GD, Tjong SC (2006) *Mater Chem Phys* 100:132
189. Chang TE, Kisliuk A, Rhodes SM, Brittain WJ, Sokolov AP (2006) *Polymer* 47:7740
190. Moiala A, Li Q, Kinloch IA, Windle AH (2006) *Compos Sci Technol* 66:1285
191. Yang S, Benitez R, Fuentes A, Lozano K (2007) *Compos Sci Technol* 67:1159
192. Datta SK, Chaki TK, Khastgir D, Bhowmick AK (1996) *Polym Polym Compos* 4:419
193. Yang S, Benitez R, Fuentes A, Lozano K (2007) *Compos Sci Technol* 67:1159
194. George JJ, Bhadra S, Bhowmick AK (2010) *Polym Compos* 31:218

195. Banik I, Chaki TK, Tikku VK, Bhowmick AK (1998) *Ang Makromol Chem* 263:5
196. Roy M, George JJ, Bhowmick AK (2010) *Polym Polym Compos* 18:59
197. Zhang CS, Ni QQ, Fu SY, Kurashiki K (2007) *Compos Sci Technol* 67:2973
198. Li Y, Chen C, Zhang S, Ni Y, Huang J (2008) *Appl Surf Sci* 254:5766
199. Choudalakis G, Gotsis AD (2009) *Eur Polym J* 45:967
200. Bridges WT, Gulati ST, Baum G (1975) *J Mater Sci* 10:2044
201. Maji PK, Das NK, Bhowmick AK (2010) *Polymer* 51:1100
202. Sun L, Boo WJ, Clearfield A, Sue HJ, Pham HQ (2008) *J Membr Sci* 318:129
203. Nielsen LE (1967) *J Macromol Sci A1*:929
204. Lape NK, Nuxoll EE, Cussler EL (2004) *J Memb Sci* 236:29
205. Maiti M, Bhowmick AK (2007) *J Appl Polym Sci* 105:435
206. Gusev AA, Lusti HR (2001) *Adv Mater* 13:1641
207. Fredrickson GH, Bicerano J (1999) *J Chem Phys* 110:2181
208. Bharadwaj RK (2001) *Macromolecules* 34:9189
209. Lan T, Pinnavaia TJ (1994) *Chem Mater* 6:2216
210. Park JH, Jana SC (2003) *Macromolecules* 36:2758
211. Mai Y, Yu Z (2006) *Polymer nanocomposites*. Woodhead, Cambridge, pp 29–54
212. Dean K, Krstina J, Tian W, Varley R (2007) *Macromol Mater Eng* 292:415
213. Wang H, Hoa S, Wood-Adams P (2006) *J Appl Polym Sci* 100:4286
214. McIntyre S, Kaltzakorta I, Liggat J, Pethrick R, Rhoney I (2005) *Ind Eng Chem Res* 44:8573
215. Boukerrou A, Duchet J, Fellahi S, Kaci M, Sautereau H (2006) *J Appl Polym Sci* 103:3547
216. Sun L, Boo W, Sun D, Clearfield A, Sue H (2007) *Chem Mater* 19:1749
217. Boo W, Sun L, Warren G, Moghbelli E, Pham H, Clearfield A, Sue H (2007) *Polymer* 48:1075
218. Ngo T, Ton-That M, Hoa S, Cole K (2007) *Polym Eng Sci* 47:649
219. Patel S, Bandyopadhyay A, Ganguly A, Bhowmick AK (2006) *J Adhes Sci Technol* 20:371
220. Pradhan S, Guchhait PK, Dinesh Kumar K, Bhowmick AK (2009) *J Adhes Sci Technol* 23:2013
221. Kaelble DH (1969) *Trans Soc Rheol* 9:135
222. Zosel A (1998) *Int J Adhes Adhes* 18:265
223. Zosel A (1989) *J Adhes* 30:135
224. Urhama YJ (1989) *J Adhes* 31:47
225. Hamed GR (1981) *Rubber Chem Technol* 54:576
226. Flory PJ, Rehner J Jr (1943) *J Chem Phys* 1:521
227. Lorenz O, Parks CR (1961) *J Polym Sci* 50:299
228. Kraus G (1963) *J Appl Polym Sci* 7:861
229. Caruthers JM, Cohen RE, Medalia AI (1976) *Rubber Chem Technol* 49:1076
230. Halpin JC (1969) *J Compos Mater* 3:732
231. Shen Z, Simon GP, Cheng YB (2002) *Polymer* 43:4251
232. Strawhecker K, Manias E (2000) *Chem Mater* 12:2943
233. Plummer CJG, Garamszegi L, Leterrier Y, Rodlert M, Manson JE (2002) *Chem Mater* 14:486
234. Sur GS, Sun HL, Lyu SG, Mark JE (2001) *Polymer* 42:9783
235. Malwitz MM, Lin-gibson S, Hobbie EK, Butler PD, Schmidt G (2003) *J Polym Sci B Polym Phys* 41:3237
236. Lift SM, Kumar N, McKinley GH (2007) *Nat Mater* 6:76–83
237. Lim SK, Kim JW, Chin I, Kwon YK, Choi HJ (2002) *Chem Mater* 14:1989
238. Wang L, Sheng J (2005) *Polymer* 46:6243
239. Vaia RA, Giannelis EP (1997) *Macromolecules* 30:8000
240. Balazs AC, Singh C, Zhulina E (1998) *Macromolecules* 31:8370
241. Tanaka G, Goettler LA (2002) *Polymer* 43:541
242. Fermeglia M, Ferrone M, Pricl S (2003) *Fluid Phase Equilib* 212:315
243. Lee JY, Baljon ARC, Loring RF, Panagiotopoulos AZ (1998) *J Chem Phys* 109:10321

244. Baljon ARC, Lee JY, Loring RF (1999) *J Chem Phys* 111:9068
245. Balazs AC, Ginzburg VV, Qiu F, Peng GW, Jasnow D (2000) *J Phys Chem B*104:3411
246. Ginzburg VV, Peng G, Qiu F, Jasnow D, Balazs AC (1999) *Phys Rev E* 60:4352
247. Yoon PJ, Fornes TD, Paul DR (2002) *Polymer* 43:6727
248. Brune DA, Bicerano J (2002) *Polymer* 43:369
249. Zheng XY, Forest MG, Lipton R, Zhou RH (2007) *Continuum Mech Therm* 18:377
250. Gersappe D (2002) *Phys Rev Lett* 89:058301
251. Liao K, Li S (2001) *Appl Phys Lett* 79:4225
252. Aleperstein D, Artzi N, Siegmann A, Narkis M (2005) *J Appl Polym Sci* 97:2060
253. Chauve G, Heux L, Arouini R, Mazeau K (2005) *Biomacromolecules* 6:2025
254. Sen TZ, Sharaf MA, Mark JE, Kloczkowski A (2005) *Polymer* 46:7301
255. de Villoria RG, Miravete A (2007) *Acta Mater* 55:3025
256. Fisher FT, Bradshaw RD, Brinson LC (2003) *Compos Sci Technol* 63:1689
257. Avella M, Bondioli F, Cannillo V, Errico ME, Ferrari AM, Focher B (2004) *Mater Sci Technol* 20:1340
258. Bondioli F, Cannillo V, Fabbri E, Messori M (2005) *J Appl Polym Sci* 97:2382
259. Cannillo V, Bondioli F, Lusvardi L, Montorsi M, Avella M, Errico ME (2006) *Compos Sci Technol* 66:1030
260. Hbaieb K, Wang QX, Chia YHJ, Cotterell B (2007) *Polymer* 48:901





## Rubber–Clay Nanocomposites: Some Recent Results

Amit Das, De-Yi Wang, Klaus Werner Stöckelhuber, René Jurk,  
Juliane Fritzsche, Manfred Klüppel, and Gert Heinrich

**Abstract** In order to produce high-performance elastomeric materials, the incorporation of different types of nanoparticles such as layered silicates, layered double hydroxides (LDHs), carbon nanotubes, nanosilica, etc. into the elastomer matrix is now a growing area of rubber research. However, the reflection of the “nanoeffect” on the properties and performance can be realized only through a uniform and homogeneous dispersion of filler particles in the rubber matrix. Generally, the properties and the performance of a reinforced elastomeric composite predominantly depend on the crosslinking chemistry of the rubbers, the nature of the fillers, the physical and chemical interaction of the fillers with the rubber matrix and, especially, on the degree of filler dispersion in the rubber matrix. This article is therefore aimed exclusively at addressing the prevailing problems related to the filler dispersion, intercalation, and exfoliation of layered clays in various rubber matrices and compositions to produce advanced high-performance elastomeric nanocomposites. The effect of two chemically distinct layered nanofillers, namely montmorillonite and LDH, on the curing behavior, mechanical, thermo-mechanical, and dielectric properties, etc. are systematically discussed with respect to various elastomeric systems. Different attempts, such as melt interaction, master batch

---

A. Das (✉), K.W. Stöckelhuber, and R. Jurk

Leibniz-Institut für Polymerforschung Dresden e.V., Hohe Strasse 6, 01069 Dresden, Germany  
e-mail: das@ipfdd.de

D.-Y. Wang

Center for Degradable and Flame-Retardant Polymeric Materials (ERCEPM-MoE), College of Chemistry; State Key Laboratory of Polymer Materials Engineering, Sichuan University, 610064 Chengdu, China

J. Fritzsche and M. Klüppel

Deutsches Institut für Kautschuktechnologie e.V., Eupener Strasse 33, 30519 Hannover Germany

G. Heinrich

Leibniz-Institut für Polymerforschung Dresden e.V., Hohe Strasse 6, 01069 Dresden, Germany  
Technische Universität Dresden, Institut für Werkstoffwissenschaft, 01069 Dresden, Germany

dilution techniques, and further chemical modification of the organoclay, have been taken into consideration and a major portion of this paper will be dedicated to these works.

**Keywords** Layered double hydroxides · Layered silicates · Nanocomposites · Organic modification · Reinforcement · Rubber · Rubber curatives

## Contents

1	Introduction .....	86
2	Preparation and Properties .....	89
2.1	Carboxylated Nitrile Rubber .....	89
2.2	Acrylonitrile Butadiene Rubber .....	94
2.3	Chloroprene Rubber .....	99
2.4	Styrene Butadiene Rubber .....	104
3	Characteristics of the Nanocomposites .....	109
3.1	Dynamic Mechanical Properties .....	109
3.2	Dielectric Analysis .....	114
3.3	XRD Studies .....	117
3.4	Transmission Electron Microscopy .....	120
3.5	Infrared Spectroscopy .....	123
4	Effect of Vulcanization Ingredients .....	125
4.1	Effect of Sulfur and Peroxide Curing .....	125
4.2	Effect of Accelerator Type .....	128
4.3	Effect of Stearic Acid .....	129
5	Clay in Rubber Blends .....	135
5.1	CR/EPDM .....	137
5.2	CR/XNBR .....	143
6	Rubber–Anionic Clay Nanocomposites .....	156
6.1	Synthesis .....	157
6.2	Preparation and Characterization of Rubber–LDH Nanocomposites .....	157
7	Conclusion .....	163
	References .....	164

## 1 Introduction

Filler, in general, can be defined as finely divided particles that are often used to enhance the performance and various desirable properties of the host matrix, depending on a typical application. A great deal of research endeavors have been dedicated to the development and the use of different fillers with a dimension at the nanometer level. In rubber technology the term “nano” is not unfamiliar to a rubber specialist. Since the start of the twentieth century, carbon black and silica have been utilized as effective reinforcing agents in various rubber formulations for a variety of applications. The primary particle sizes of these fillers remain in the nanometer range. However, with these conventional fillers the dispersion toward individual

primary particles is significantly difficult to achieve. Nowadays, with the help of modern techniques and methods, particles such as layered silicates, layered double hydroxide (LDH), sol–gel silica, carbon nanotubes, polyoligo sesquioxane (POSS), graphene, etc. can be dispersed in a polymer matrix as single isolated particles. For example, organic modification of clay particles could offer totally exfoliated clay layers in some polymer matrices. The outcome of such a technique has been realized by observing a significant improvement in the physical properties of the composites containing a very small amount of nanofiller. Nevertheless, the main advantages of nanofillers are not only to reinforce the rubber matrix but also to impart a number of other properties such as barrier properties, flammability resistance, electrical/electronic and membrane properties, polymer blend compatibility, etc. In spite of tremendous research activities in the field of polymer nanocomposites during the last two decades, elastomeric nanocomposites are still at a stage of infancy as far as their application is concerned. The major challenge in this regard is the replacement of carbon black and silica, which are mostly used in bulk amounts in rubber compositions, by a small amount of nanofillers such as layered silicates in order to achieve a desirable combination of properties. In typical polymer–clay nanocomposites, the filler concentration hardly exceeds 10 wt%, whereas in common rubber composites the reinforcing fillers are often incorporated to above 30 wt%. Therefore it is of great interest to meet desired combinations of different properties in an elastomeric nanocomposite at a very small concentration of filler. The major problem associated with nanoparticles is the degree of dispersion in the rubber matrix. Due to the extraordinarily high viscosity of the rubber matrix, the dispersion of any foreign materials is an extremely challenging task. In order to achieve the desired dispersion of the nanoparticles, various methods have been taken into consideration, such as in situ polymerization, solution casting, latex coagulation, melt compounding, etc. Though rubber is an amorphous material, high temperature shear mixing could be a promising method because it is economical, more flexible in formulation, and the existing facility for compounding and extrusion can be utilized without any complication. This review will discuss rubber nanocomposites based on different rubbers and clays prepared by different compounding techniques.

Layered silicates are now being used widely for preparation of rubber-based nanocomposites. These layered silicates are a class of inorganic materials that have a naturally layered structure. The technique to convert this individually layered structure into a single silicate sheet ( $\sim 1$  nm thick) in the polymer matrix was first reported by the Toyota group [1]. Among natural clays, montmorillonite (MMT) is the most commonly used layered silicate in nanocomposite preparation due to its high cation exchange capacities, large surface area, good surface reactivity and surface adsorptive properties. Beyond MMT, other clay minerals have been used, such as hectorite, synthetic fluoro-hectorite, sepiolite and synthetic micas [2]. MMT belongs to the 2:1 family of phyllosilicate clay minerals, where each crystal layer is composed of a silica tetrahedral layer sandwiched between two octahedral sheets of aluminum and magnesium hydroxides. In MMT, the isomorphous substitution of  $\text{Al}^{3+}$  by  $\text{Mg}^{2+}$ ,  $\text{Fe}^{2+}$ , etc. in the octahedral sheets results in a net negative charge

in the sandwiched layers (Fig. 1). As a result, cations ( $\text{Na}^+$ ,  $\text{K}^+$ , etc.) and water molecules are intercalated in the interlayer region of MMT. The ideal dispersion of the layered silicate is realized if all the layers are sufficiently separated from one another in the polymer matrix. Unfortunately, the space between two successive layers is too small to allow polymer molecules into it. Organic modification is one of the techniques that can be used to overcome this problem by enhancing the gap distance between the layers. In this method, the cations (present in the gallery to counterbalance the excess charge) are replaced by some quaternary ammonium compound with a long hydrophobic tail. However, organic modification is not a sufficient step to obtain intercalated and exfoliated structures in the rubber matrix. This means that incorporating an organomodified layered silicate in an amorphous rubber medium does not always result in markedly improved mechanical properties of the rubber vulcanizates. This may be due to the inability of a substantial portion of the layered material to dissociate into individual layers. This has also been attributed, in part, to a lack of affinity between organic polymers and the inorganic layered silicates. For most purposes, complete exfoliation of the clay platelets (i.e., separation of platelets from one another and dispersed individually in the polymer matrix) is the desired goal of the formation process. However, this ideal morphology is frequently not achieved, and varying degrees of dispersion are more common. Compared with thermoplastics, the dispersion of organoclay in rubber is more difficult; high viscosity, amorphous nature, and low surface energy of the rubber polymers being the main causes. Significant attention has already been paid to preparation of rubber–clay nanocomposites, characterization of their fundamental behavior, and their use in a wide variety of applications. This review paper is a humble effort by the authors to summarize the outcome of a research project while working on a related project.

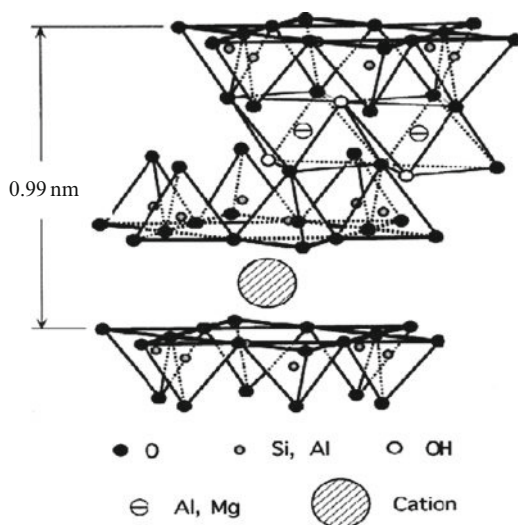


**Fig. 1** Chemical structure of MMT showing tetrahedral layer sandwiched between two octahedral sheets

## 2 Preparation and Properties

### 2.1 Carboxylated Nitrile Rubber

Carboxylated nitrile rubber (XNBR), a high-performance elastomer, is remarkable for providing vulcanizates that exhibit enhanced tensile strength, elastic modulus, hardness, and improved resistance to tear, abrasion, and the deleterious action of oil. On the other hand, XNBR, being a polar rubber, is expected to interact with layered silicate more efficiently in comparison to other diene rubbers. Only a few reports could be found in the literature concerning the utilization of layered silicate in XNBR. Very recently, it was reported that in the presence of layered silicate the tensile properties of the XNBR vulcanizates were decreased to a considerable extent [3]. The explanation given for this undesired effect is a reduction of the amount of ionic crosslinking due to the consumption of ionic clusters formed by the metal and carboxylic groups by the layered silicates. Successful preparation of layered silicate nanocomposites by a latex coagulation method was also reported [4]. However, this method and the physical properties are not very acceptable for practical applications. On the other hand, direct polymer intercalation and subsequent exfoliation from the melt using various types of polymer compounding equipment provides a straightforward commercial process, but may not be completely effective. Thus, for compounding of nanocomposites, conditions such as the rotor speed (which governs the mixing intensity and heat generation), mixing temperature, and mixing time should still be optimized. Preferred conditions would generally feature a long mixing time at low mixing temperature to avoid undesirable degradation of the materials [5]. The effect of temperature on the intercalation–exfoliation process of the layered silicate in the XNBR matrix has been studied, keeping the other parameters of the internal mixer such as rotor speed and mixing time fixed. In this study, a clay was selected that had been modified with quaternary ammonium salt, and the basal spacing of this organoclay was 2.98 nm. In order to optimize the mixing temperature for this particular compound, the mixing temperature of the internal mixer was selected at 40, 80, 120, and 160°C for four different batches [6]. The amount of organoclay was also varied between 2.5 and 10 phr (part per hundred parts rubber).

As can be seen from the rheometric data summarized in Table 1, the maximum rheometric torque ( $R_{\infty}$ ) is slightly higher for those mixes derived from the internal mixer at 160°C compared to the curing torque produced by the gum. In most cases, the maximum rheometric torque increases with increasing filler amount. The compounds mixed at 40, 80, and 120°C show lower torque compared to the gum. Additionally, the effect on the curing time of the incorporation of organoclay is negligible. The preliminary rheometric study shows that the compounds mixed at 160°C exhibit better curing activity compared to the compounds mixed at lower temperatures.

XNBR shows excellent physical properties, even in the gum form. Nevertheless, it is expected that with the addition of a reinforcing filler, the properties of XNBR

**Table 1** Formulations and curing characteristics of organoclay-filled XNBR vulcanized at 160°C

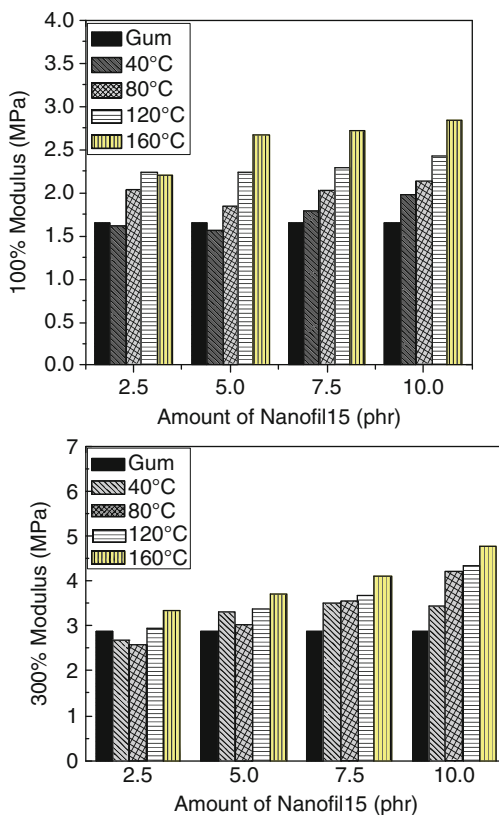
Mix number <sup>a</sup>	Mixing temperature (°C)	Organoclay loading (phr)	$R_{\infty}$ (dNm)	Scorch time $t_2$ (min)	Optimum cure time $t_{90}$ (min)
1	40	0	8.53	1.1	16.4
2	40	2.5	7.84	1.1	16.6
3	40	5	7.82	1.0	16.9
4	40	7.5	7.12	1	16.1
5	40	10	8.17	0.9	16.5
6	80	2.5	7.05	0.8	16.0
7	80	5	7.47	0.8	15.7
8	80	7.5	7.22	0.7	15.5
9	80	10	7.36	0.7	15.8
10	120	2.5	7.23	0.8	15.3
11	120	5	7.44	0.9	16.6
12	120	7.5	7.49	0.8	15.4
13	120	10	7.73	0.7	15.5
14	160	2.5	8.59	0.9	16.8
15	160	5	8.91	0.9	15.9
16	160	7.5	9.39	0.9	16.1
17	160	10	9.31	0.8	15.8

<sup>a</sup>All the mixes were vulcanized with 3 phr ZnO, 2 phr stearic acid, 1.4 phr sulfur, 1.7 phr CBS and 2 phr DPG

will be enhanced. It has been found that even a very small amount of organoclay, like 5 phr, enhances the XNBR physical properties to a remarkable extent.

In Fig. 2, the stresses at 100% elongation (the so-called 100% modulus) are plotted against loading of the clay mixed at different temperatures. It is evident from this figure that with the increase of clay loading, the values rise gradually and the effect is much more pronounced with a higher mixing temperature. A sharp increase in the 100% modulus can be found from 2.5 to 5 phr loading at 160°C mixing temperature. At 5 phr content of organoclay, the 100% modulus was increased by 72% compared to the vulcanizates mixed at 40 and 160°C. It can be said that at elevated temperatures the extent of the intercalation–exfoliation process is facilitated. At lower loading of organoclay (e.g., 2.5 and 5 phr), the addition of the filler mixed at a low temperature like 40°C does not produce any significant change in the rubber matrix in terms of the 100% elongation compared to the gum value. However, in high temperature mixes, the difference is quite remarkable. Obviously, at low loadings and low temperatures, no proper dispersion of the organoclay can take place, which explains the indifferent nature of the physical properties. Also in Fig. 2, the modulus at 300% elongation is plotted against loading of the organoclay and, as observed, a high mixing temperature has a strong effect on the physical properties. For example, at 10 phr organoclay loading, an increment of 39% in the 300% modulus was found for those vulcanizates mixed at 160°C as compared to 40°C. In addition, it can be seen from Fig. 3 that, with the same loading of organoclay, the tensile strength increases quite sharply with increasing temperature.

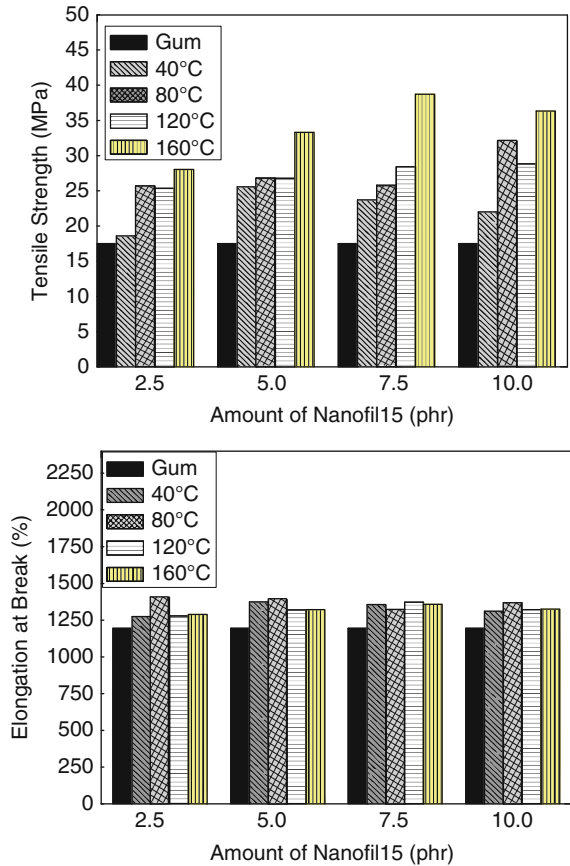
**Fig. 2** Variation of 100% (top) and 200% (bottom) modulus values of XNBR–organoclay composites mixed at different temperatures



The maximum tensile strength was found for the vulcanizates containing 7.5 phr organoclay mixed at 160°C. Here, the increment of the tensile properties is 120% compared to the gum without filler. This type of strong reinforcement is only possible with such a low concentration of inorganic filler if exfoliation and intercalation occur to a considerable extent. In this context, a mechanical scheme is shown in Fig. 4 to explain the exfoliation–intercalation process. It is assumed that at higher mixing temperature, a reaction between the silanol (–OH) groups on the edge of the clay and carboxylic (–COOH) groups of the XNBR takes place, forming an ester-type bond. This type of chemical bond between clay and rubber (first step) is formed under the conditions of high shearing force (internal mixer) and at a high temperature such as 160°C. So, it is expected that the strong shearing force can be transferred from the rubber to the layered silicate and delaminate the staged layers by overcoming the force between two adjacent silicate layers, and ultimately results in an exfoliated clay structure in the rubber matrix. However, the exfoliation and intercalation processes have no significant effect on the elongation at break values, as seen from Fig. 3. The tensile experiment can also be depicted as stress versus strain curves. The stress–strain curves obtained from different mixing temperatures



**Fig. 3** Variation of tensile strength (*top*) and elongation at break (*bottom*) values of XNBR–organoclay composites mixed at different temperatures



at a loading of clay of 5 phr are shown in Fig. 5. In the low strain region (0–300% elongation), the curves are steeper with the increase of mixing temperature at 5 phr filler loading. So, it can reasonably be said that the reinforcing efficiency of organoclay increases with the increase of mixing temperature, as well as with the shearing forces given on the silicate layers, which also supports the scheme in Fig. 4. It is also interesting to discuss the nature of the stress–strain plot at higher elongation. It is surprising to note the three crossovers of the gum over the 40, 120, and 140°C mixed vulcanizates (circled in Fig. 5). It can be assumed that at low temperature mixing (40–120°C), there may exist some clusters of organoclay in a local filler–filler network. These local networks do not exist in a continuous fashion over the whole rubber matrix but in discrete zones, which affects the homogeneity in the rubber matrix and ultimately deteriorates the reinforcement. At higher elongation, the stress cannot be transferred from one side of the clay cluster to the other side and, as a consequence, the initiation of cracks takes place. On the other hand, for the 160°C mixing temperature, such cluster or aggregate formation

**Fig. 4** Mechanism of exfoliation and intercalation of layered silicate in XNBR matrix

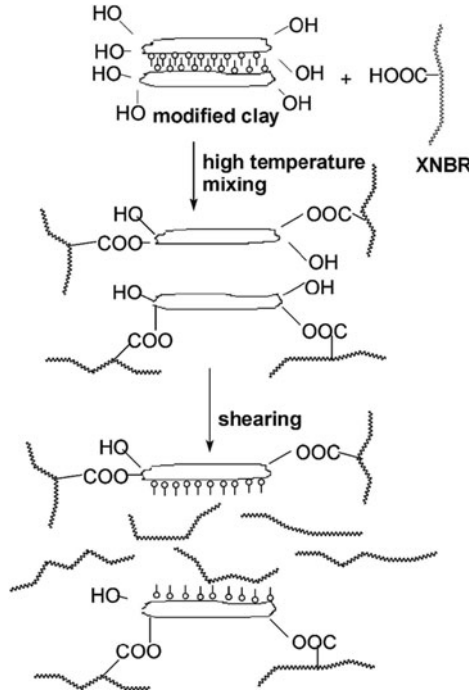
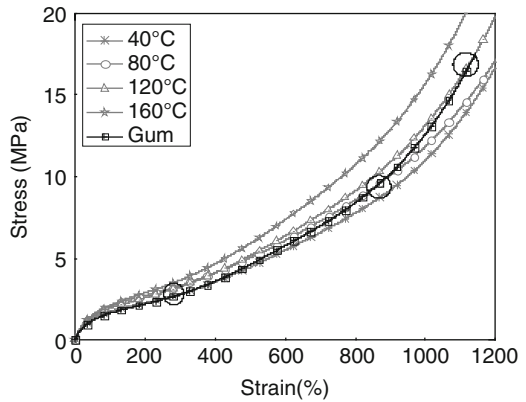


**Fig. 5** Stress–strain diagram of rubber composite mixed at different temperatures containing 5 phr organoclay in a XNBR matrix. Circles indicate crossover points



of the filler, which can deteriorate the stress at the same strain, is absent. Obviously, this is the possible reason for the strange behavior of the filled vulcanizates. This behavior also supports a better degree of dispersion (through the intercalation–exfoliation process) of the vulcanizates mixed at 160°C.

## 2.2 Acrylonitrile Butadiene Rubber

Nitrile rubber (NBR) is a copolymer of acrylonitrile and butadiene and is mainly made by emulsion polymerization. This rubber is one of the most-used commercial rubbers for manufacturing technical rubber goods. By selecting an appropriate acrylonitrile content, one can tailor the different properties in order to use NBR for different applications like roll covers, hydraulic hoses, conveyor belting, oil field packers, seals for all kinds of plumbing and appliances, and also for oil-, fuel-, and chemically resistant materials. It has also excellent temperature resistance properties with a wide short- and long-term operating temperature range (as much as  $-40^{\circ}\text{C}$  to  $+125^{\circ}\text{C}$ ). Like most unsaturated thermoset elastomers, NBR requires formulating with added ingredients, and further processing to make useful articles. Additional ingredients typically include reinforcement fillers, plasticizers, weather protectants, and vulcanization packages. Plenty of literature can be found describing where layered silicate has been used as nanofiller in NBR [7–9]. Nanocomposites of intercalated and exfoliated organosilicates in NBR have been prepared by solution-blending methods and dramatic enhancement in the mechanical and thermal properties of NBR are found by the incorporation of very small amount of organosilicates. The degradation temperature for NBR with 10 phr loading of organosilicate was found to be  $25^{\circ}\text{C}$  higher than that of pure NBR [10]. Reactive mixing intercalation was also used for the preparation of NBR–clay composites. Resorcinol and hexamethylenetetramine were used for the reactive mixing process. It was proposed that rubber and organoclay were chemically attached by the help of the resorcinol–tetramine complex. It was also noticed that the  $d$ -spacing of the layered silicate increased substantially when the resorcinol–tetramine complex was added to the rubber compounds [11]. Layered silicate was modified by  $N,N'$ -dimethylalkyl- $(p$ -vinylbenzyl)-ammonium chloride, an ammonium compound containing a vinyl group, and this organoclay was used for the preparation of NBR–clay composites [12]. The mechanical properties as well as gas barrier properties were improved considerably when the organic modifier contained vinyl groups. Measurements of the X-ray diffraction (XRD) of modified clay showed that, as the alkyl chain length was varied from 7, 11, to 17 carbon atoms, the  $d$ -spacing of the organoclay increased from 1.8, 2.3, to 2.7 nm, respectively. These enhancements probably result from strong interactions between NBR and clay, promoted by the alkyl chains and, possibly, from extra crosslinking of the vinyl groups with rubber molecules. A silane-coupling agent, 3-(mercapto propyl) trimethoxy silane, was added during the preparation of organoclay–NBR composites and it was observed that the silane-coupling agent established a chemical interaction between the silanol group of the silicate layers and the rubber chains [13]. Elastomer nanocomposites consisting of NBR latex and layered silicates were prepared by a modified latex shear blending process aided by ball milling [7]. A schematic presentation is shown in Fig. 6. A partly exfoliated and partly intercalated morphology of the layered silicate was found when the concentration of the layered silicate was less than 7.5%. The tensile and tear strength of NBR–clay increased by 200% and 60%,

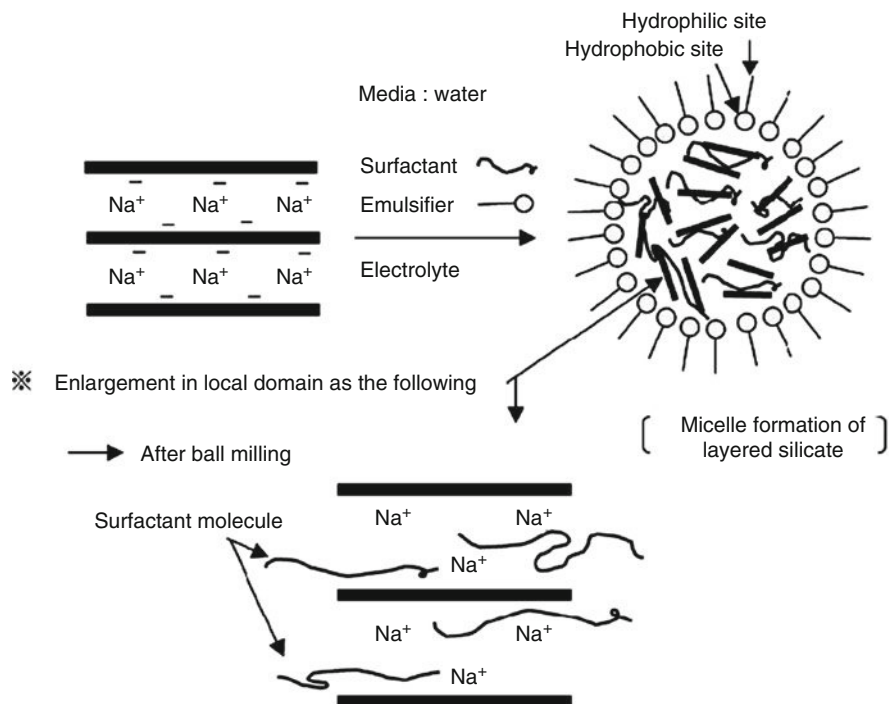


**Fig. 6** Latex blending of NBR-layered silicate composites (reprinted from [10], with the permission from Elsevier)

respectively. But there are very few reports [14–18] concerned with the interactions of different types of rubber additives with the layered silicate or with organomodified layered silicate. The understanding of these interactions is very important to exploit layered silicate as potential filler in practical rubber goods. Studies have been done with different kinds of rubber vulcanization packages in order to find the suitability of those ingredients for the reinforcement process by layered silicates. The detailed formulations and processing methods are given in Table 2.

The rheometric study was done at 160°C and the obtained data are shown in Table 3. It can be seen that the addition of 5 phr organoclay in the NBR matrix has a profound effect in raising the ultimate torque for all cases, as compared with gum and the filled systems (comparing mix 1 with mixes 2–5, and mix 6 with mixes 7, 8). This observation indicates that the NBR matrix becomes harder and stronger with the addition of only 5 phr organoclay. The increment of torque with respect to gum is remarkably higher in the case of a peroxide-cured system compared with sulfur-cured systems (Fig. 7a). Here, it can be said that the presence of organoclay in the NBR matrix facilitates the extent of cure (difference between maximum and minimum rheometric torque) of NBR. Among the sulfur-cured systems, the torque decreases with the increase of stearic acid content (Fig. 7b). This behavior is

**Table 2** Formulation of NBR filled with organoclay and carbon black

Mix	Accelerator <sup>b</sup>	Organoclay loading (phr)	DCP <sup>c</sup> (phr)	Stearic acid (phr)	ZnO (phr)
1. Gum, sulfur	ZDMC	–	–	1	5
2. Filled, sulfur	ZDMC	5	–	1	5
3. Filled, sulfur	ZDMC	5	–	2	5
4. Filled, sulfur	ZDMC	5	–	4	5
5. Filled, sulfur	ZDP	5	–	2	5
6. Gum, peroxide	–	–	2	–	–
7. Filled, peroxide	–	5	2	–	–
8. Filled, peroxide, sulfur	ZDMC	5	2	2	5
9. Filled, peroxide, ZnO	–	5	2	–	2
10. Filled, peroxide, ZDMC	ZDMC	5	2	–	–
11. Filled, carbon black <sup>a</sup> , sulfur	ZDMC	–	–	2	5

<sup>a</sup>Carbon black N330 loading was 5 phr

<sup>b</sup>ZDMC (zinc dimethyldithiocarbamate) and ZDP (zinc dithiophosphate) were used as conventional and multifunctional accelerators, respectively

<sup>c</sup>dicumyl peroxide

**Table 3** Physical properties of NBR filled with layered silicate and carbon black

Mix	Maximum rheometric torque ( $R_{\infty}$ ) (dNm)	Scorch time ( $t_2$ ) (min)	Cure time (min)	100% modulus (MPa)	Tensile strength (MPa)	Elongation at break (%)	Hardness (Shore A)
1	4.22	0.3	5.4	0.96	2.86	650	49
2	5.14	0.3	4.8	1.48	5.03	586	56
3	4.52	0.3	4.5	1.31	4.58	747	55
4	4.71	0.2	5.8	1.52	8.58	794	59
5	4.45	0.4	23.8	1.38	12.79	1,211	57
6	5.94	0.7	19.1	0.84	2.85	693	47
7	7.75	0.7	18.3	1.51	8.64	826	56
8	6.43	0.2	6.6	1.47	4.86	551	57
9	7.38	0.7	19.6	1.43	7.95	826	56
10	3.10	1.0	24.8	0.90	8.25	1,931	47
11	4.56	0.2	3.6	1.17	5.49	786	52

expected if one considers the softening effect of stearic acid. Generally, 2 phr is the optimum dose of stearic acid in diene rubbers such as natural rubber (NR), styrene butadiene rubber (SBR), polybutadiene rubber, etc. In our study, we varied the stearic acid content to see the effect of this long chain fatty acid on the intercalation–exfoliation process. It is reported that an excess amount of stearic acid in ethylene-propylene-diene monomer (EPDM)–clay nanocomposites facilitated the intercalation process of clay layers [17]. The explanation behind this observation is the chemical interaction between the acid group of stearic acid with the silanol group of silicate. These interactions help the intercalation of the polymer into the

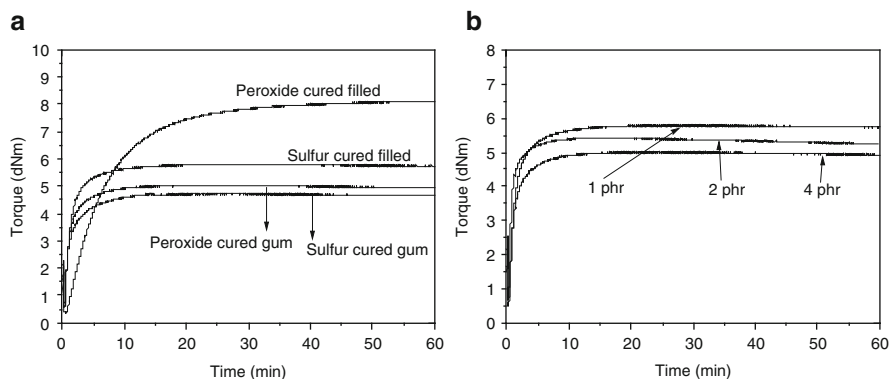


**Fig. 7** Rheographs of the layered-silicate-filled NBR cured at 160°C in the presence of sulfur and peroxide (a), and different amounts of stearic acid (b)

gallery. Here, it is important to note the adverse effect of zinc dimethyl dithiocarbamate (ZDMC) by decreasing the rheometric torque (Table 3) when this additive is added in the peroxide curing (mix 10). It has also been reported that ZDMC-type curatives can help the exfoliation–intercalation process of layered silicates by providing free radicals to the layered silicate–EPDM system [14].

Unfortunately, it was found that, in the presence of peroxide, ZDMC does not facilitate the intercalation process of the clay minerals. On the contrary, it seems that ZDMC consumes the free radicals generated from peroxide and that the rubber matrix remains in the under-cured state with a very low “maximum rheometric torque” value. As far as the scorch time is concerned, there is no such considerable difference between filled and gum compounds. However, prolonged cure time has been observed where ZDP (zinc dithiophosphate, a multifunctional rubber accelerator) has been used as an accelerator in the sulfur curing packages. The stress–strain curves of the crosslinked NBR–silicate nanocomposites are shown in Fig. 8a–c. Figure 8a shows that layered silicate particles can improve the tensile properties significantly, irrespective of their curing type (peroxide or sulfur). This means that it is immaterial to consider the effect of curing type on the reinforcement process since in both cases the nature of the stress–strain curves is identical. It is also evident from Fig. 8a that NBR filled with 5 phr organoclay gives stronger vulcanizates, even compared with NBR loaded with 5 phr carbon black. This behavior can only be explained from the nanoscale distribution phenomenon of layered silicate in the rubber matrix. In this study, a carbon black (N330) with a primary particle size of 28–36 nm was also used. However, the reinforcing efficiency of this black filler at 5 phr loading is much lower than with layered silicate. Obviously, the high aspect ratio (in our case 100–500) of layered silicate is responsible for adding such reinforcing capability to a rubber matrix. The mechanical properties of the NBR vulcanizates are shown in Table 3. In the case of peroxide-cured vulcanizates containing layered silicates, we observed a 179% increment of the 100% modulus

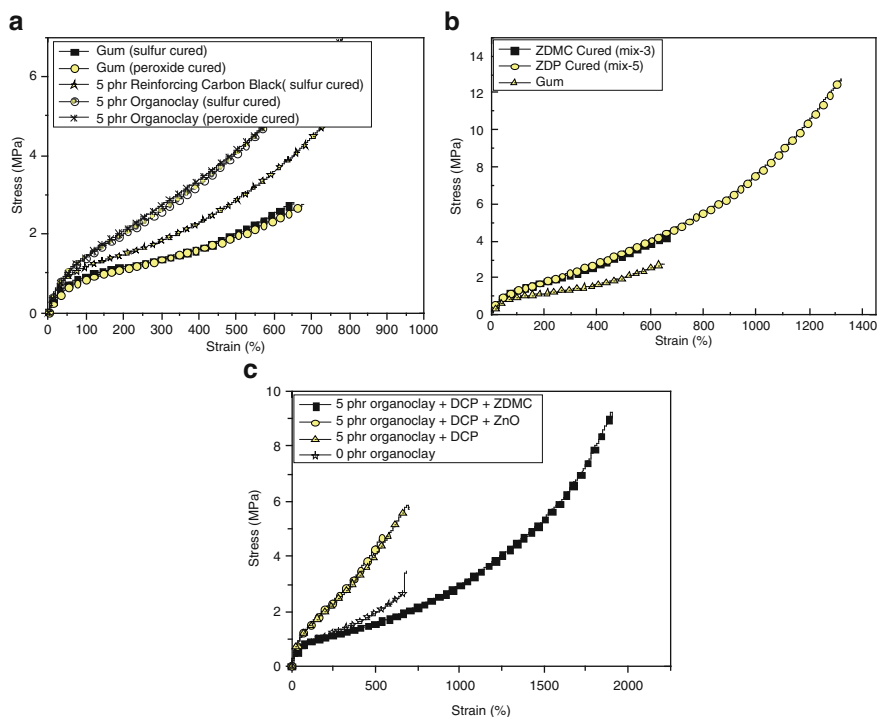
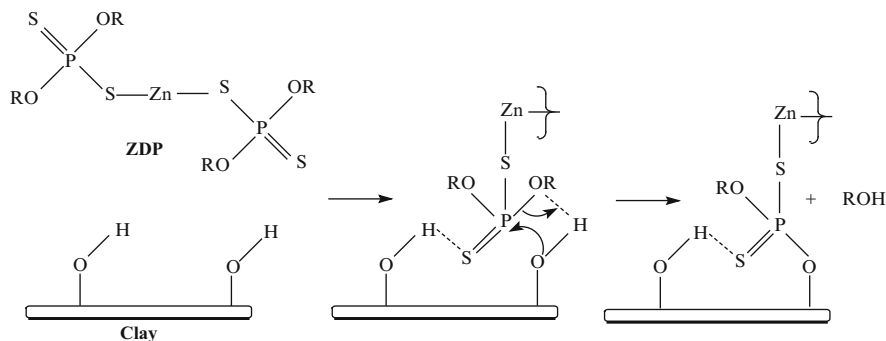


**Fig. 8** Stress–strain plots of layered-silicate-filled NBR cured by sulfur and peroxide (a), sulfur in the presence of different zinc organic salts (b), and peroxide in the presence of different vulcanizing ingredients (c)

and 216% increment of the 300% modulus with respect to gum rubber. The tensile strength is about 3–4 times higher, as compared with the corresponding gum vulcanizates, and the Shore A hardness increased by 9 points. These observations indicate that the layered particles are distributed very uniformly and dispersed in intercalated and exfoliated form. The variation of stearic acid content does not affect the modulus of the vulcanizates significantly, but the tensile strength has been increased to a considerable extent with higher elongation at break values. Therefore, it can be concluded that the physical properties in terms of tensile strength can be increased to a considerable extent by a stearic acid content up to 4 phr. This may be due to the fact that stearic acid helps to intercalate rubber chains into the space between two clay layers and thus the reinforcing capability of the given amount of layered silicate is increased and reflected in the higher tensile strength. Ma et al. [17] also found that the tensile strength increased from 4.3 MPa with 2 phr stearic acid to 20.1 MPa with 10 phr stearic acid, without effecting stress values up to 350% elongation in EPDM rubber. Very interesting observations were also noticed when the effect of ZDP was analyzed. About a fivefold increment of tensile strength was achieved with the help of 5 phr organoclay in the ZDP-cured



**Scheme 1** Probable chemical interaction between ZDP and silanol group of clay surface

vulcanizates (Fig. 8b). Based on the above observations, a reaction mechanism has been proposed (Scheme 1). The ZDP contains active alkoxy ( $-OR$ ) groups attached to a five-valent phosphorus atom (Scheme 1). This  $-OR$  group can interact with the silanol groups of silica to form a  $Si-O-P$  linkage [19, 20]. On the other hand, it is an established fact that the thiophosphoryl additive can form a pendant accelerator moiety on the NBR rubber backbone. In our study, it can be imagined that the fragment of accelerator group might interact with the silanol groups of the layered silicate and, thus, the ultimate chemical linkage between layered silicate particle and rubber could offer a higher compatibility between them. It is also evident from Fig. 8b that the ZDP-cured vulcanizates behave at low strains similarly to the ZDMC-cured vulcanizates, but that the stress increases dramatically at high strain. Therefore, it can be reasonably assumed that for NBR vulcanizates that include ZDP, a remarkable increase in stress in the high-strain region results from the effect of molecular chain orientation, together with the resultant orientation of layered silicates brought about by the rubber molecule orientation. Such characteristics of ZDP-cured layered silicate nanocomposites indicate a good possibility for ZDP application in producing rubber-layered silicate nanocomposites. A very peculiar behavior is observed in Fig. 8c: the vulcanizates including ZDMC and peroxide show a much smaller modulus at small strain, but at higher elongation the rubber matrix becomes stronger. The tensile strength and elongation at break values are surprisingly high (elongation at break value 2,000%) as compared to other systems.

### 2.3 Chloroprene Rubber

Chloroprene rubber (CR) is well known for its high gum vulcanizate strength arising from strain-induced crystallization. The uncured rubber also shows storage hardening due to slow crystallization. It has excellent physical properties, weather



resistance, thermal resistance, and retain able properties at low temperature. Owing to the presence of halogen in the rubber molecule, chloroprene resists burning inherently better than exclusively hydrocarbon rubbers. The durability of chloroprene rubber components is largely dependent on the tear and tensile strength of the matrix. Incorporation of layered silicate into the CR rubber was reported to show an improvement of tear strength of such composites [21]. CR–clay nanocomposites were also prepared by co-coagulating the rubber latex and an aqueous suspension of clay, and a significant improvement of physical properties like hardness, modulus, tensile and tear strength were noticed [22].

How the physical properties of CRs are influenced by the presence of organo-layered silicate was also studied. In this work, different kinds of nanofillers were incorporated and the resulted properties were compared in order to find the most suitable nanofillers for CR [23]. For this reason, LDH in modified and unmodified form both were selected. In fact, LDH is a typical anionic clay, i.e., a host–guest material consisting of positively charged metal hydroxide sheets with intercalated anions and water molecules. It can be represented by a general formula,  $[M^{2+}_{1-x}M^{3+}_x(OH)_2]^{x+}A_{x/n}^{n-}yH_2O$ , where  $M^{2+}$  and  $M^{3+}$  are divalent and trivalent metal cations such as  $Mg^{2+}$ ,  $Zn^{2+}$ ,  $Ca^{2+}$ , etc. and  $Al^{3+}$ ,  $Co^{3+}$ ,  $Fe^{3+}$ , respectively,  $A^{n-}$  are interlayer anions such as  $CO_3^{2-}$ ,  $Cl^-$  and  $NO_3^-$ . The anions occupy the interlayer region of these layered crystalline materials. The most common naturally occurring LDH clay is hydrotalcite (Mg–Al type) with the chemical formula  $Mg_6Al_2(OH)_{16}CO_3 \cdot 4H_2O$ , with a structure represented in Fig. 9.

In principle, the intercalated anions in the gallery of LDHs can be exchanged with wide varieties of anionic species, both of organic and inorganic origin. This gives LDH a great advantage over layered silicates because, for layered silicates, the interlayer species can only be exchanged with a limited range of positively charged cations, mostly based on alkyl-ammonium. This makes LDH a suitable precursor for polymer nanocomposite preparation [24, 25]. In this section, rubber–LDH nanocomposites are described, including the synthesis and characterization of organomodified LDH, preparation of rubber–LDH nanocomposites and their special properties. Details of work on rubber–LDH nanocomposites is discussed at the end of this review in Sect. 6.

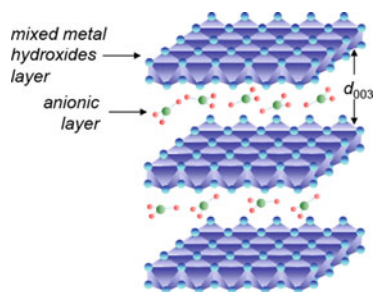


**Fig. 9** Representation of LDH crystal structure

The compounding of CR with fillers and vulcanization ingredients was done by a laboratory size open two-roll mixing mill. All the weights are given in parts per hundred parts of rubber and the recipe for the CR compounds is given in Table 4.

The influence of clay and modified clay on the physical properties of the CR vulcanizates at 5 phr filler concentration is given in Table 5. As is obvious, the modulus values (stresses at 100%, 200% and 300% elongation) increase in all cases after filler loading. Again, the extent of improvement depends on the nature of the nanofillers. In the case of unmodified clay, the increase in 100% and 300% modulus is more with LDH, whereas MMT shows similar enhancement as that observed with

**Table 4** Formulation of chloroprene rubber compounds

Sample code <sup>a</sup>	CR (g)	Filler (5 g)
CR gum	100	–
CR-LDH	100	LDH
CR-MMT	100	MMT
CR-OLDH	100	OLDH
CR-OMMT	100	OMMT
CR-N220	100	Carbon black

*LDH* layered double hydroxide, *MMT* montmorillonite, *OLDH* organomodified LDH, *OMMT* organomodified MMT

<sup>a</sup>Each sample contain 4 g MgO, 5 g ZnO, 0.5 g stearic acid and 1 g ethylene thiourea

**Table 5** Curing characteristics and physical properties of CR vulcanizates reinforced with different types of clay

Compounds	100% modulus (MPa)	300% modulus (MPa)	Tensile strength (MPa)	Elongation at break (%)	Hardness (Shore A)
CR gum	1.08 (1.20)	1.80 (2.12)	15.65 (6.19)	1,406 (846)	52 (54)
	+11	+17	–60	+40	–
CR-LDH	1.45 (1.51)	2.72 (2.97)	14.99 (8.21)	1,053 (736)	54 (56)
	+4	+9	–45	–30	–
CR-MMT	1.37 (1.53)	2.45 (2.80)	16.35 (9.04)	1,085 (731)	54 (57)
	+11	+12	–44	–32	–
CR-OLDH	1.43 (1.48)	2.62 (2.71)	17.16 (5.02)	617 (520)	55 (56)
	+3	+3	–70	–16	–
CR-OMMT	2.23 (2.41)	3.92 (4.23)	21.22 (15.02)	1,088 (842)	62 (63)
	+8	+8	–29	–23	–
CR-N220	1.30 (1.56)	2.49 (3.34)	22.72 (13.04)	1,107 (742)	54 (58)
	+16	+34	–42	–33	–

Data in parenthesis represent the mechanical properties after aging. Data with (+) or (–) signs are the retention values of the mechanical properties

carbon black at the same filler concentration. The organic modification influences the reinforcing efficiency of the clay to a different extent. Whereas organically modified MMT (OMMT) gives significant improvement in modulus values compared to the MMT filled vulcanizates, organically modified LDH (OLDH) gives no significant change. A typical stress–strain plot of these vulcanizates is shown in Fig. 10, where the highly reinforcing nature of OMMT at low strain can be seen. It is apparent that the nature of the surfactants and the net inorganic content of the modified clays play an important role in enhancing the mechanical properties of the CR vulcanizates. It is the inorganic fraction that provides mechanical reinforcement, and the higher its content in the modified clay, the better are the mechanical properties. OMMT contains about 65% of its weight as inorganic layers, whereas OLDH has about 56 wt%. Again, a part of the surfactant in the modified clay might impart plasticizing effects, facilitating polymer chain slippage. As a result, the CR-OMMT vulcanizate shows better mechanical properties than CR-OLDH vulcanizate. Higher surfactant content in OLDH could be a potential cause of lower hardness and elongation at break in CR-OLDH. These values are significantly higher in the case of CR-OMMT among all the CR compounds studied. It can be mentioned here that the considerable decrease of elongation at break of CR-OLDH and the higher elongation at break of CR-MMT cannot be explained solely in terms of the plasticity effect of the surfactant. Other factors like topological constraints, nature of the crosslinks, and crosslinking density also determine the overall physical properties. However, critical discussion of those results is out of the scope of this paper.

Chloroprene rubber also generally offers good compression set properties. A higher percent of the compression set means a permanent deformation of the rubber matrix in a compressed form. The filled vulcanizates show a marked

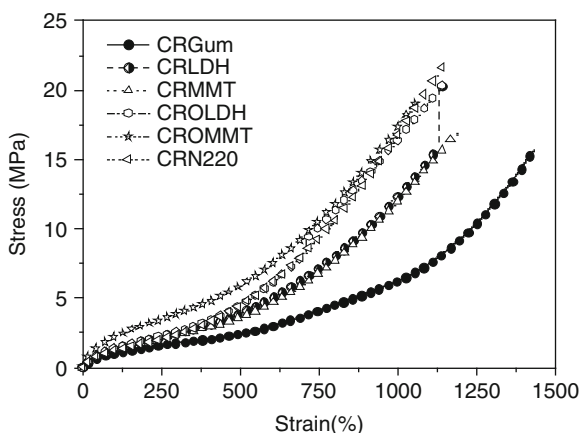


**Fig. 10** Stress–strain behavior of CR gum, CR–clay (*CRLDH* and *CRMMT*), CR–modified clay (*CROLDH* and *CROMMT*), and CR–carbon black (*CRN220*) composites

difference in compression set values in comparison to the gum vulcanizate. The compression set values for all these composites are given in Fig. 11. It is evident that addition of nanofiller in the rubber matrix deteriorates the compression set, as expected. This can be explained by the volume fraction of the filler in the rubber matrix. In the study, 5 phr filler was used in all cases, but their volume fractions were different from each other and depend on the density of the related filler. A higher volume fraction means a higher dilution effect with respect to volume and, hence, lowers the compression properties [26]. Of the unmodified nanofillers, LDH gives a higher compression set, whereas MMT and carbon black (N220) produce comparable set properties. Interestingly, organic modification has no influence on the set properties in the case of LDH, whereas OMMT affects the compression set property of the vulcanizates to a considerable extent. The clays impart mechanical reinforcement of a elastomer thorough different mechanism before and after organic modification. The unmodified clays (both LDH and MMT) have polar –OH groups on the edges of the layered particles, which can form hydrogen bonds with the electronegative chlorine atoms in CR. On the other hand, organically modified clays have a higher interlayer distance, which make them suitable for intercalation of polymer chains in their gallery space. Such polymer–filler interaction always helps in better stress transfer through the interface and, hence, result in improved mechanical properties (Table 5). However, the vulcanizate containing the reinforcing carbon black still shows higher tensile strength than the clay-filled vulcanizates.

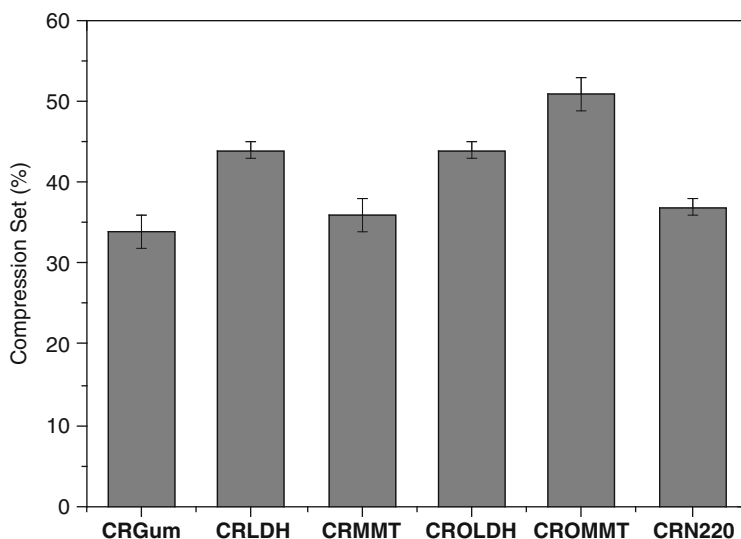


**Fig. 11** Compression set properties of CR gum, CR–clay (*CRLDH* and *CRMMT*), CR–modified clay (*CROLDH* and *CROMMT*), and CR–carbon black(*CRN220*) compounds

## 2.4 Styrene Butadiene Rubber

Increasing attention has been paid to the use of precipitated silica as a reinforcing filler for green tire tread formulations to produce high-performance tires, showing improved rolling resistance and wet grip behavior. Here, the development of advanced coupling silanes provides a better compatibility between rubber and silica, resulting in reduced rolling resistance and improved fuel economy. Solution styrene butadiene rubber (S-SBR) is widely used nowadays as a tire tread, especially in tires of passenger cars where low rolling resistance and high wet grip are the challenging properties. Some literature [27–30] has been found concerning emulsion styrene butadiene rubber (E-SBR) in combination with nanofillers, but the mechanical properties are too poor to consider these systems as potential candidates for practical applications. Ma et al. [27] reported a preparation method using a latex compounding technique, but in this work the ultimate mechanical properties were not described. Mousa et al. [28] describe nanocomposites of SBR and organoclay mixed by a two-roll mill that showed a tensile strength of more than 12 MPa at 10 phr silicate content, but without any direct evidence of formation of a nanocomposite (as shown by XRD or TEM studies). With the help of the latex-compounding technique, layered silicate was dispersed in SBR latex and 3-aminopropyltriethoxysilane was simultaneously intercalated into clay galleries during the co-coagulating procedure [29]. Hexamethoxy methylmelamine (HMMM) has been used as a dispersion agent in the preparation of SBR-layered silicate nanocomposites [30]. According to that study, HMMM swelled the clay gallery, thus facilitating the intercalation of the rubber chain (as revealed by wide-angle X-ray diffraction, WAXD). HMMM in the presence of organoclay enhanced the elastic modulus with minor effects on tensile strength and further modified the ultimate elongation through either a change in the degree of reinforcement or through matrix plasticization. It was also observed that the pristine clay (Na-MMT) is less effective in enhancing the physical properties of the composites because of its narrower gallery height, stronger interplatelet forces, and higher polar surface. In order to improve the interfacial interaction between clay and SBR, unsaturated organic ammonium chloride *N*-allyl-*N,N*-dimethyloctadecylammonium chloride was introduced for in situ modification of MMT before latex compounding. The SBR nanocomposites thus obtained showed a dramatic improvement of tensile strength (from 4 to 18 MPa) [31]. The same group of researcher also successfully utilized hexadecyl trimethyl ammonium bromide and 3-aminopropyl triethoxy silane in SBR–clay nanocomposite preparation. They found that partly rubber-intercalated and partly modifier-intercalated structures were developed during rubber compounding and curing. The tensile strength and the 300M of modified SBR–clay nanocomposites were found to be three times higher than those of gum compounds [32]. SBR–clay was prepared by the surface modification of pristine clay by allylamine, and very interesting properties were found for these nanocomposites [33]. The allylamine molecules served here as a coupling agent between the SBR chain and the surface of the clay

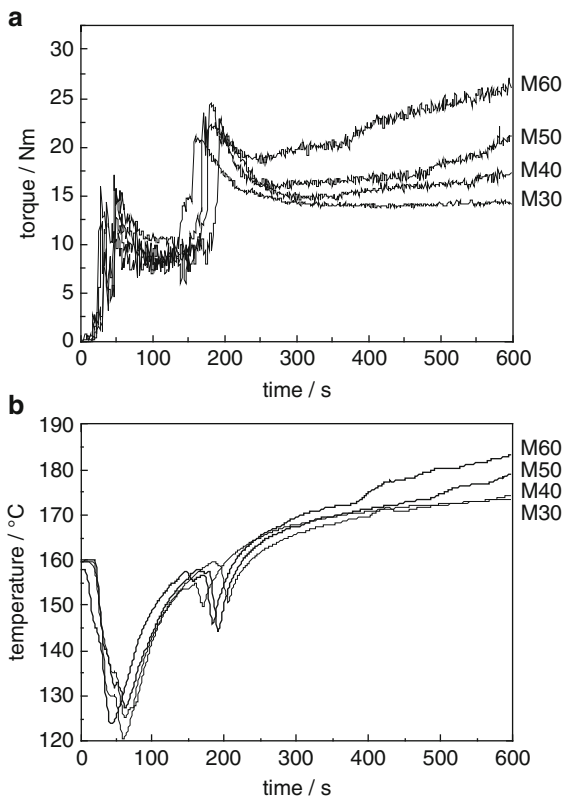
platelets. SBR with different styrene contents were considered for the preparation of rubber–clay nanocomposites. The styrene content of rubber had a pronounced effect on the properties of the nanocomposites and it was found that with increasing styrene content, the physical properties increased [34]. It was also observed that systems cured with peroxide and/or sulfur displayed similar strength, but higher elongation, and that slightly lower modulus values were obtained with the sulfur-cured system. Rubber compounds based on SBR/BR blends containing layered silicate and bis(triethoxysilylpropyl-tetrasulfan) (TESPT) were prepared and characterized by Ganter et al. [35]. The results obtained from those nanocomposites were compared with composites containing commercially available silica. It was found that organoclay vulcanizates exhibited enhanced hysteresis when compared to silica compounds. This observation was related to orientation and sliding of anisotropic silicate layers, as determined by online wide-angle X-ray scattering (WAXS) measurements during cyclic tensile testing. The origin of the higher hysteresis could be explained by reorientation of aggregates in systems with matrix–filler coupling, and by irreversible orientation and sliding of silicate layers for systems with intercalated structure. Preparation and properties of SBR–clay have been discussed by considering different organic amines with different chain lengths as the organic modifier of the clay. With increasing chain length of the amine, there was an increase in tensile strength. A sudden increase in modulus was observed when the chain length of the amine contained ten carbon atoms [36]. Recently, it has been reported that organoclay-based S-SBR polymer nanocomposites could be prepared by using XNBR as a vector to transfer layered silicate into the S-SBR matrix. The rubber matrix obtained in such a way provided a significant improvement of physical properties with only small amounts of filler in the rubber matrix [37, 38]. In that study, the highly polar XNBR was used as a vector to transfer layered silicate into S-SBR. A large amount of organomodified clay was blended into a XNBR matrix at high temperatures (160°C) by an internal mixer and, subsequently, the obtained product was used as a master batch and mixed into the S-SBR. In this way, attempts were made to obtain a good degree of exfoliated clay in the nonpolar S-SBR matrix. This process was described as a new preparation method for S-SBR–clay nanocomposite by a melt compounding route [37, 38].

The contents of the master batch are presented in Table 6. The torque and temperature behavior against time recorded during the mixing process is shown in Fig. 12a, b. The temperature during the mixing process increased up to 180°C. For loadings up to 30 phr organoclay, the torque during mixing of XNBR and organoclay remained constant. In contrast to higher loadings, the torque increased significantly. This effect might be an indication of the intercalation process. The formulations and cure characteristics for the mixing of the master batch with S-SBR are given in Table 7. The curing additives were chosen according to a typical silica-filled green tire formulation. In the samples SB-00 to SB-14 (Table 7), different loadings of master batches were used in various combinations. The samples SB-15 and SB-16 were formulated to obtain the effect of an unfilled XNBR in the composite. Concerning the XNBR content, these mixes are equivalent to SB-12

**Table 6** Preparation of the XNBR master batch

Master batch	XNBR (g)	Organoclay (g)
M-30	100	30
M-40	100	40
M-50	100	50
M-60	100	60

**Fig. 12** Time–torque curves for master batch preparations with XNBR and organoclay in the internal mixture at 160°C and 50 rpm rotor speed (a). Time–temperature curves for master batch preparations with XNBR and organoclay in the internal mixture at 160°C and 50 rpm rotor speed (b)



and SB-14, respectively. It is evident from the table that samples of pure S-SBR and XNBR (SB-00 and XN-00) have higher “maximum rheometric torque” ( $R_{\infty}$ ) than the XNBR-containing SBR samples. However, for every single master batch system, the torque decreases with the increasing amount of master batch. Evidently, the presence of two different kinds of rubber with different polarities provides less torque than expected. The scorch safety seems to be independent of master batch content as well as filler loading. The cure times (listed in Table 7) decrease for the XNBR/S-SBR blend as compared to the pure rubber samples SB-00 and XN-00. For every single master batch system, the cure time increases with the amount of

**Table 7** Recipes for the S-SBR vulcanizates

Mix number	SBR (g)	M-30 (g)	M-40 (g)	M-50 (g)	M-60 (g)	XNBR (g)	Maximum rheometric torque ( $R_{\infty}$ ) (dNm)	Scorch time ( $t_2$ ) (min)	Optimum cure time ( $t_{90}$ ) (min)
SB-00	100	–	–	–	–	–	7.05	1.72	9.59
SB-01	100	5	–	–	–	–	6.40	1.09	8.83
SB-02	100	10	–	–	–	–	6.28	1.24	8.99
SB-03	100	15	–	–	–	–	5.87	1.67	9.00
SB-04	100	–	5	–	–	–	6.45	1.24	8.50
SB-05	100	–	10	–	–	–	6.40	1.27	9.20
SB-06	100	–	15	–	–	–	6.18	1.27	10.17
SB-07	100	–	–	5	–	–	6.66	1.18	7.61
SB-08	100	–	–	10	–	–	6.37	1.26	8.51
SB-09	100	–	–	15	–	–	6.22	1.25	9.29
SB-10	100	–	–	–	5	–	6.91	1.15	9.14
SB-11	100	–	–	–	10	–	6.78	1.30	9.60
SB-12	100	–	–	–	15	–	6.40	1.28	11.44
SB-13	100	–	–	–	20	–	5.48	1.31	11.59
SB-14	100	–	–	–	30	–	5.49	1.34	14.72
SB-15	100	–	–	–	–	9.37	5.87	1.49	8.11
SB-16	100	–	–	–	–	18.75	4.99	1.53	10.21
XN-00	–	–	–	–	–	100	8.53	1.12	16.47

master batch due to the increasing XNBR to S-SBR ratio. For different master batches, the cure time decreases with the amount of organoclay in the master batch, except for the M-60 containing samples; here the cure time is higher than expected. It is also worth mentioning that without organoclay the cure time of an XNBR/S-SBR blend is lower. The results are not quite understood; probably different acceleration effects are taking place due to the well-known interaction of Zn ions with carboxylic groups and the presence of ammoniums salts and organoclay. Results of tensile tests are shown in Fig. 13.

In Fig. 13a, the stress values at 200% elongation are plotted against the amount of clay and compared to the samples without clay, which are plotted against the amount of XNBR. It is evident from this figure that with an increase of filler amount, the modulus increases with a linear tendency. In contrast, in the unfilled samples containing S-SBR and XNBR the corresponding physical values are very low. These observations prove that the obtained higher rigidity of the rubber matrix is not caused by the XNBR part, and support the suggestion of reinforcement caused by the organoclay. Concerning tensile strength, the above-mentioned result is also reflected in Fig. 13b. For the samples with around 5 phr loading, sevenfold higher values in tensile strength are obtained compared to the gum. It is also found from the polynomial fit curve in Fig. 13b that there is a maximum of tensile strength at around 5–8 phr organoclay. At higher loading, the clay particles aggregate and obviously do not contribute to the ultimate strength of the composite. Stress–strain plots are shown in Fig. 13d for some composites. In these stress–strain curves,



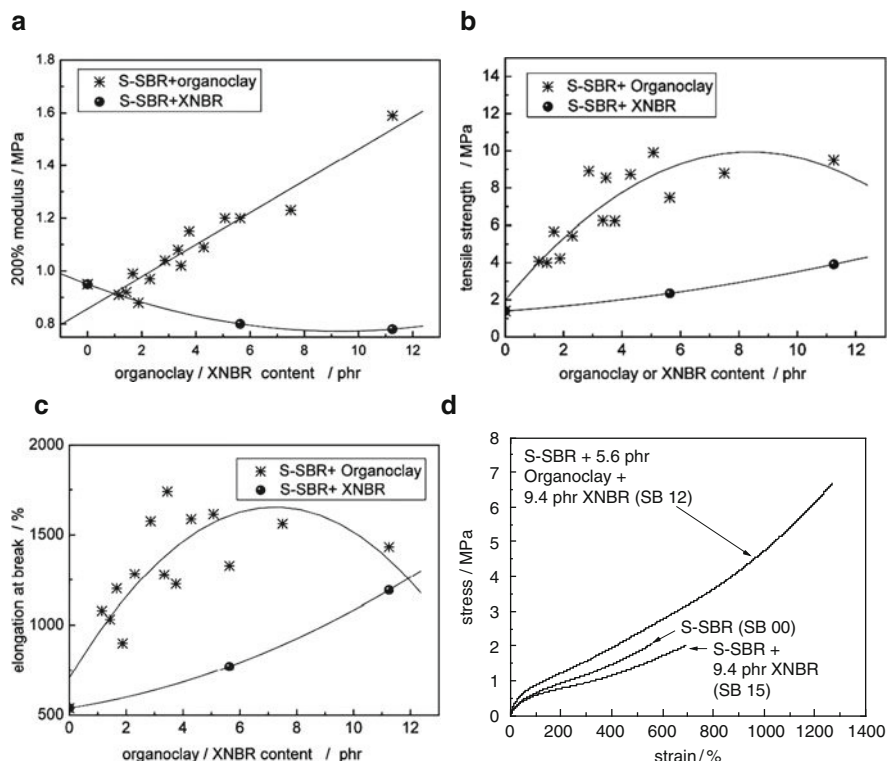


**Fig. 13** Variation of 200% modulus (a), tensile strength (b), and elongation at break (c) with the amount of organoclay and XNBR. Stress–strain diagram of the organoclay–rubber composites (d)

a remarkable effect of the organoclay is observed. The mechanical properties of the nanocomposites become enhanced at higher elongations due to the presence of a small amount of organoclay (4.6 phr) in the rubber matrix. In contrast, an equivalent amount of XNBR without any filler deteriorates the corresponding mechanical properties of the composites. Therefore, it can be stated that the organomodified nanoclay not only provides excellent reinforcement effects to the rubber matrix, but also acts as a compatibilizer between polar and nonpolar rubber, as mentioned before. The investigated types of rubber nanocomposites also showed very high elongation at break values, as presented in Fig. 13c. High elongation at break values are otherwise found in silica-filled rubber compounds [19], with a direct chemical bonding between polymer and silica. In the rubber nanocomposites made of XNBR, S-SBR, and organoclay it can be assumed that the surface silanol groups of the layered silicates react with the carboxyl groups of the XNBR and, thus, direct rubber–filler bonds are formed. In this way, the high elongation properties can be explained.

### 3 Characteristics of the Nanocomposites

#### 3.1 Dynamic Mechanical Properties

##### 3.1.1 Temperature Dependencies

The dynamic mechanical thermal analyzer (DMTA) is an important tool for studying the structure–property relationships in polymer nanocomposites. DMTA essentially probes the relaxations in polymers, thereby providing a method to understand the mechanical behavior and the molecular structure of these materials under various conditions of stress and temperature. The dynamics of polymer chain relaxation or molecular mobility of polymer main chains and side chains is one of the factors that determine the viscoelastic properties of polymeric macromolecules. The temperature dependence of molecular mobility is characterized by different transitions in which a certain mode of chain motion occurs. A reduction of the  $\tan \delta$  peak height, a shift of the peak position to higher temperatures, an extra hump or peak in the  $\tan \delta$  curve above the glass transition temperature ( $T_g$ ), and a relatively high value of the storage modulus often are reported in support of the dispersion process of the layered silicate.

The DMTA measurements were done with organoclay-filled XNBR rubber (Fig. 14). The glass transition process was detectable at  $-10^\circ\text{C}$  and the  $\tan \delta$  maximum decreased slightly with increasing filler content. An additional relaxation process at high temperatures was confirmed, and a shift to a higher temperature of this process with incorporation of organoclay was also noticed [39]. When a temperature sweep was done against the dynamic properties, at constant strain

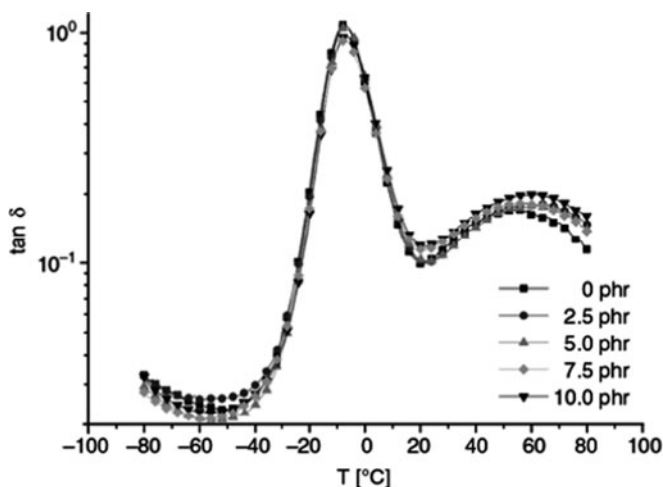


**Fig. 14**  $\tan \delta$  versus temperature of the XNBR vulcanizates containing different amounts of organoclayed silicate

and frequency, the vulcanizates of CR showed two different transitions. At low temperature, the relaxation is correlated to the polymer glass transition, and at high temperature another relaxation occurs due to the melting of the crystalline domains in chloroprene rubber [23].

Figure 15 depicts the  $\tan \delta$  versus temperature plots of the CR vulcanizates containing different types of nanofiller. All the samples show the same  $T_g$  irrespective of their filler type. But the peak height is maximum for OLDH and minimum for OMMT. It is well known that the smaller the  $\tan \delta$  peak, the higher is the reinforcing efficiency of the related filler. Reduced chain mobility owing to physical and chemical adsorption of the CR molecules on the filler surface causes a height reduction of the  $\tan \delta$  peak during dynamic mechanical deformation. So, the presence of only 5 phr OMMT reinforces the CR to a great extent. For better understanding the reinforcement process, the storage tensile modulus ( $E'$ ) is plotted against temperature. Very interesting information can be derived from Fig. 16a.

**Fig. 15** Effect of different kinds of nanofiller on the dynamic loss tangent of CR vulcanizates with temperature

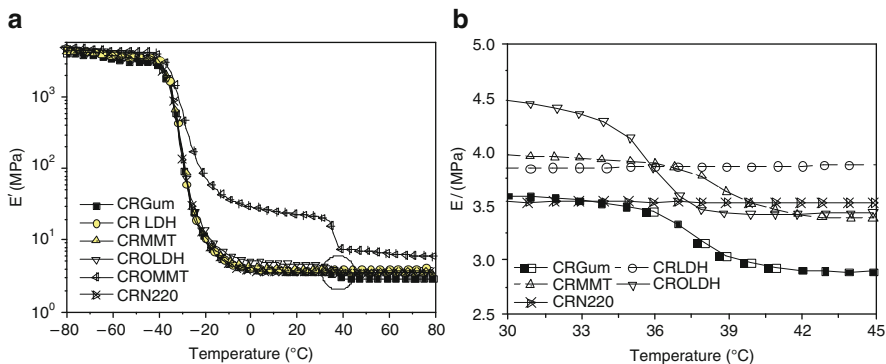
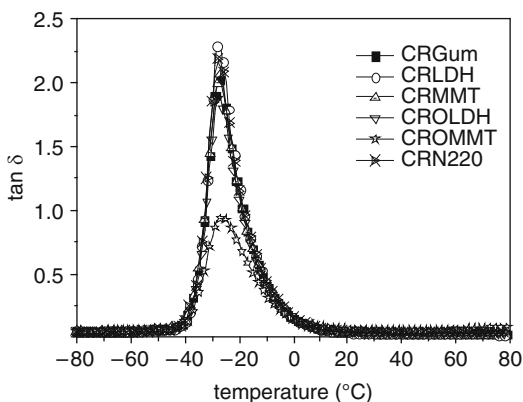


**Fig. 16** Variation of storage modulus with temperature in CR vulcanizates containing different kinds of nanofillers (a). Circled region is shown in more detail in (b)

At room temperature, the storage modulus is increased about fivefold in OMMT-filled vulcanizates. The increment of this value in CR-OLDH is much smaller, whereas unmodified clays give hardly any change at room temperature.

Figure 16a also depicts the influence of nanofillers on the crystallization behavior of the CR vulcanizates. The modified nanofillers facilitate crystal formation, which is reflected in a loss in storage modulus value in the melting region of the crystal domains. This loss is very strong in the case of CR-OMMT, indicating that CR molecules crystallize better in the presence of OMMT. The unmodified MMT also behaves similarly but to a lesser extent (Fig. 16b), which is very similar to the behavior observed in the gum vulcanizates. But, unmodified LDH and N220 completely suppress the crystallization process, resulting in no change in the storage modulus value in this temperature range. This effect is important as it can be utilized to control the storage stability of CR compounds.

A strong influence of the organoclay on the dynamic mechanical properties of S-SBR has also been noticed [38]. Figure 17a, b displays the storage shear modulus  $G'$  and the mechanical loss factor  $\tan \delta$  as a function of temperature for the samples that contain the organoclay–XNBR master batch. The sample with 5 phr master batch (SB-10) and the unfilled S-SBR sample (SB-00) show no significant difference in  $G'$  at room temperature. In contrast, the samples with higher loadings show strong reinforcement effects, resulting in higher  $G'$  values. For example, in the case of SB-11 (10 phr master batch) the increment was 1.65 times compared with S-SBR gum. Additionally, it is interesting to discuss the effect of XNBR on the dynamic mechanical performance of the SBR vulcanizates. The vulcanizate containing 9.37 phr XNBR (SB-15) without filler, equivalent to SB-12 concerning the amount of XNBR, shows a smaller  $G'$  value at room temperature, indicating a lack of compatibility between the two different rubbers. Therefore, it can be stated that organophilic layered silicates not only reinforce the rubber matrix, but also act as a compatibilizer between the different phases. Figure 17b shows the  $\tan \delta$  plot of the nanocomposites. Usually, the  $\tan \delta$  peak indicates the compatibility of two

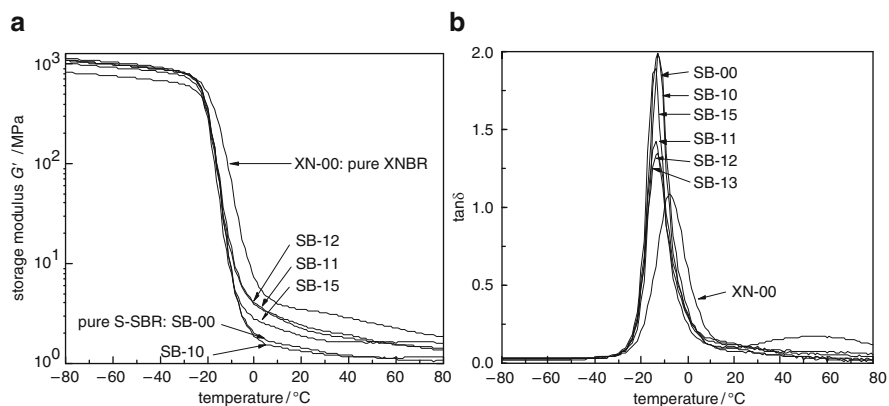


**Fig. 17** Temperature dependence of  $G'$  (a) and  $\tan \delta$  (b) of the organoclay-filled S-SBR rubber composites

polymers in a rubber blend for all nanocomposites. Here, the small amount of XNBR in the samples does not contribute enough thermal relaxation to show a peak broadening due to heterogeneity, hence, a single  $\tan \delta$  peak is obtained. For pure XNBR (XN-00), a second broad  $\tan \delta$  peak appears at higher temperatures (40–80°C). In the cure recipe, zinc oxide was used, which can establish a metallic carboxylate linkage by ionic crosslinking in the rubber matrix. Consequently, these ionic rubber chain segments form ionic clusters, as discussed for the multiple cluster model [40]. The mobility of the rubber chain is restricted in the vicinity of these associated multiples, and this type of ionic force or Columbic attraction force opposes the polymer chain mobility. Therefore, a secondary transition appears at higher temperatures.

It is also interesting to compare the height of the  $\tan \delta$  peak of the composites. It is noteworthy that the smaller the  $\tan \delta$  peak, the higher the reinforcing efficiency of the related filler. Accordingly, for the sample with 5 phr master batch (SB-10) no reinforcement effects can be detected, in contrast to the vulcanizates containing higher loadings of organoclay. Here, a sharp decrease in height of the  $\tan \delta$  peak was observed for SB-11 and SB-12 composites. Especially for SB-11, the peak height was decreased to 32%. The peak height for the sample containing S-SBR and XNBR without organoclay is only slightly decreased, confirming the results for  $G'$ .

### 3.1.2 Strain Dependencies

The interaction between two fillers particles can be investigated by measuring the “Payne effect” of a filled rubber compounds. In this measurement, dynamic properties are measured with strain sweep from a very small deformation to a high deformation. With the increased strain, the filler–filler network breaks and results in a lower storage modulus. This behavior is commonly known as the Payne effect [41]. To study this behavior, strain sweep measurements were done with the filled chloroprene rubber vulcanizates. Figure 18 shows the variation in the storage modulus,  $G'$ , with the double strain amplitude of the cured rubber sample. There is apparently no change in the nature of variation in the storage modulus in the vulcanizates with increasing double strain amplitude. So, it can be said that no Payne effect can be observed in any of the vulcanizates. This indicates that at such a low filler concentration (5 phr) there exists no significant filler–filler network structure. However, the absolute value of  $G'$  is always higher for the filled vulcanizates than for the gum. The OMMT gives maximum increase in  $G'$  value among the vulcanizates, showing again its superior reinforcing nature. Taking the absolute value of  $G'$  as a measure of reinforcement by the nanofiller, the nanofillers can be ranked according to their reinforcing efficiency, i.e., OMMT > OLDH > LDH > MMT > carbon black (N220).

The strain dependence of the elastic storage modulus of clay-filled NBR has been measured and the results compared with those of unfilled vulcanizates. The corresponding data are shown in Fig. 19. From this figure it is revealed that there is no Payne effect, because the  $G'$  values do not decrease with the increase in strain

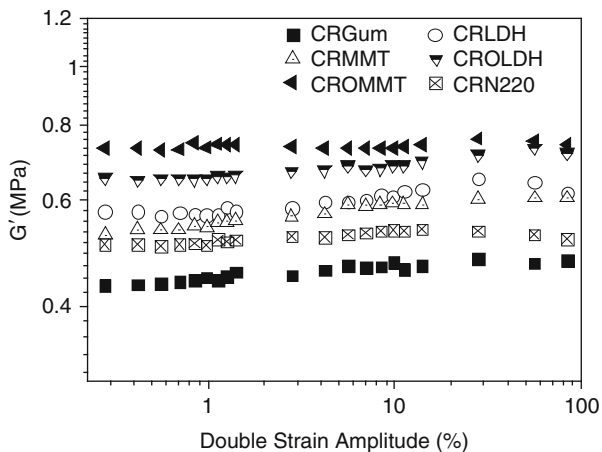


**Fig. 18** Strain dependence of  $G'$  of CR vulcanizates filled with different kinds of nanofillers. The measurements were done by a moving die rheometer (Scarbaeus SIS V50) applying sinusoidal strain at constant frequency of 0.1 Hz at 60°C

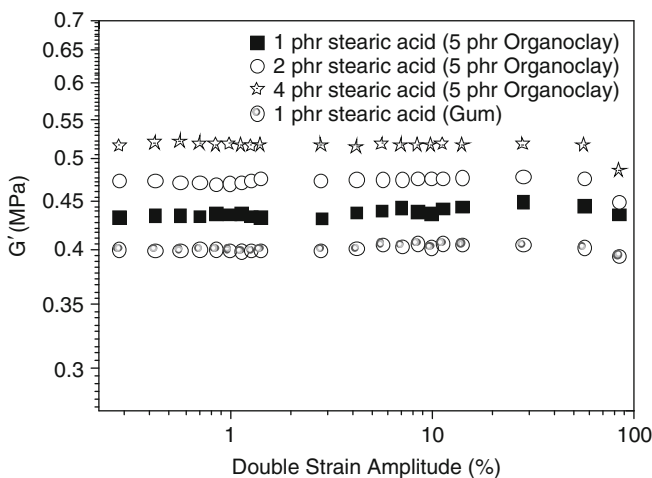
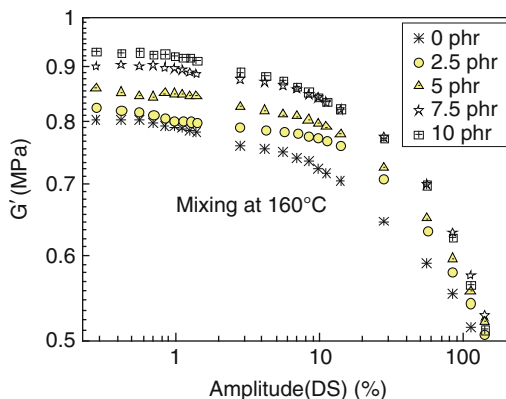


**Fig. 19** Strain dependence of  $G'$  for NBR vulcanizates filled with organoclay

amplitude. Although the absolute value of  $G'$  is not large at this small filler loading, there is some effect on the absolute value of  $G'$  from the stearic acid content in the curing packages. With increasing stearic acid content, the absolute value of  $G'$  also increases. That means that stearic acid supports the exfoliation–intercalation process of the layered silicate, leading to dissociation into very fine nanometer-sized particles. It may be speculated that stearic acid first enters into the gallery gap and

**Fig. 20** Strain dependence of  $G'$  for XNBR vulcanizates filled with organoclay



opens up the layered silicate cluster, thus paving the way for intercalation of other macromolecular chains. The dynamic property measurements at low strain amplitude were also discussed for the filler–filler network as well as for the rubber–filler network at low loading of nanoclay fillers in XNBR matrix. The plots of  $G'$  versus double strain amplitude of the 160°C mixed vulcanizates are shown Fig. 20. It is evident from this figure that up to 10% strain amplitude, the values of  $G'$  are remaining constant in all cases and thereafter a significant decrease in the values is observed. This decrease in  $G'$  is due to slippage of the moving die during the measurements at higher amplitude and not due to the breaking of the filler–filler networks since the same observation is made in the case of the unfilled rubber. The  $G'$  value increases with the increase of filler loading, which is attributed to the hydrodynamic effect of rigid solid particles. At high-temperature mixing (ca. 160°C) the silicate layers are more homogeneously distributed, mainly through the exfoliation process, which enhances the reinforcing capability of the filler significantly. With the increase of filler amount, the formation of bound or trapped rubber (dead rubber) is enhanced. Subsequently, the effective volume of the filler is increased substantially, thereby raising the modulus of the rubber matrix.

### 3.2 Dielectric Analysis

Dielectric relaxation study is a powerful technique for obtaining molecular dipolar relaxation as a function of temperature and frequency. By studying the relaxation spectra, the intermolecular cooperative motion and hindered dipolar rotation can be deduced. Due to the presence of an electric field, the composites undergo ionic, interfacial, and dipole polarization, and this polarization mechanism largely depends on the time scales and length scales. As a result, this technique allowed us to shed light on the dynamics of the macromolecular chains of the rubber matrix. The temperature as well as the frequency window can also be varied over a wide

range. The effect of clay addition on the polymer chain dynamics has been well studied [42]. Rao et al. observed from dielectric spectra that addition of clay in the polymer matrix affected the mobility of polymer chains significantly [43]. Hernandez et al. studied the effects of clay proportion and nanoscale dispersion on the dielectric response of poly(vinyl alcohol)–bentonite nanocomposites [44]. They observed that better clay dispersion promotes chain mobility for the low-temperature secondary relaxations with a plasticization effect. Page and Adachi [45] have reported the dielectric relaxation behavior of nanocomposites based on Na-MMT with a series of polymers. They observed that all the nanocomposites exhibited an additional relaxation process at a temperature below the  $T_g$  of the pure polymer, which was assigned to the segmental motion of the chains intercalated in the MMT interlayers. The dielectric response of layered-silicate-reinforced natural and polyurethane rubber nanocomposites was studied by Psarras et al. [46]. They observed that both the  $\alpha$ -relaxation and  $\beta$ -relaxation were less affected by the presence of the layered silicates in the polyurethane rubber nanocomposites. In addition to these relaxations, they also observed interfacial polarization present in the nanocomposites.

Due to its carboxyl groups and the nitrile content, the high polarity of XNBR provides large values for the dielectric loss  $\epsilon''$ . Examples of the results obtained for the dielectric loss  $\epsilon''$  in dependence of temperature and frequency for the unfilled sample and the sample filled with 10 phr organoclay are given in Fig. 21. In all measurements the glass transition process ( $\alpha$ -process) due to the cooperative segmental motion of the chain is observable, forming a characteristic temperature- and frequency-dependent Vogel–Fulcher behavior. At low temperatures, the Arrhenius-activated  $\beta$ -process can be observed in all samples, which is due to local fluctuations of chain segments or side groups. At high temperatures, the value of  $\epsilon''$  increases extremely with increasing temperatures probably due to conductivity effects or

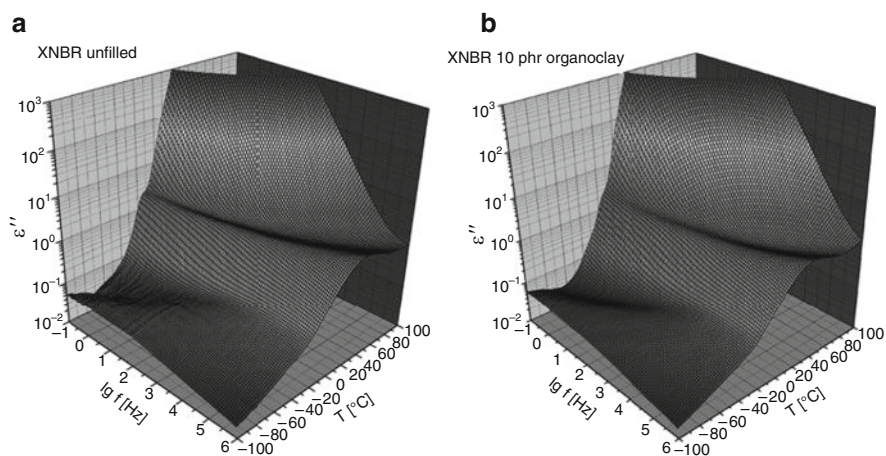


**Fig. 21** Temperature and frequency dependence of dielectric loss  $\epsilon''$  for the unfilled XNBR sample (a) and the sample filled with 10 phr organoclay (b)



electrode polarization. To analyze the high temperature part of the spectra, the analyzing procedure developed by Steeman and van Turnhout [47] was applied to the measured data, which has been reviewed by Wübbenhorst and van Turnhout [48]. This method is based on the Kramers–Kronig relation (1), saying that both  $\epsilon'$  and  $\epsilon''$  carry the same information about relaxation processes and are related by a Hilbert transformation:

$$\epsilon''(\omega_0) = \frac{\sigma_{dc}}{\epsilon_0 \omega_0} + \frac{2}{\pi} \int_0^{\infty} \epsilon'(\omega) \frac{\omega_0}{\omega^2 - \omega_0^2} d\omega, \quad (1)$$

where  $\sigma_{dc}$  is the direct current conductivity,  $\epsilon_0$  the permittivity of space, and  $\omega$  the alternating current frequency.

In this procedure, the derivation of  $\epsilon'$  denoted as  $\epsilon''_{deriv}$  (2) is used in order to obtain narrow and sharp peaks and to eliminate conductivity effects due to the independence of  $\epsilon'$  from ohmic conductivity:

$$\epsilon''_{deriv} = -\frac{\pi}{2} \frac{\partial \epsilon'(\omega)}{\partial \ln \omega} \approx \epsilon''. \quad (2)$$

In the case of broad relaxation peaks like those of the  $\alpha$ -transition, (2) is almost exact and the derivative reproduces the measured frequency-dependent  $\epsilon''$  data. By contrast, for narrow Debye-like processes a peak sharpening is observed and  $\epsilon''_{deriv} \sim \omega^{-2}$  is obtained for large frequencies instead of  $\epsilon'' \sim \omega^{-1}$  [48]. This opens the interesting possibility of obtaining more information about low-frequency relaxation processes of dipolar origin, which are often obscured by strong electrode polarization due to ionic conduction. In the XNBR samples under consideration, ionic conductance probably results from mobile protons due to the presence of carboxylic groups and other ions obtained from the addition of the processing agents zinc oxide and stearic acid. The blocking of ions at the metallic electrodes leads to the pronounced relaxation process at high temperatures and low frequencies (as observed in Fig. 22). This electrode polarization refers typically to sharp Debye-like processes and therefore the application of the derivative considered in (2) is expected to sharpen this undesired peak. As a consequence, other processes of dipolar origin may become visible in the spectrum. The spectrum of the XNBR sample filled with 10 phr is shown in Fig. 23 after applying the derivative method (2). Interestingly, the resulting spectra now show an additional relaxation process at higher temperatures in all investigated samples, which obviously was obscured in the original spectra by the strong electrode polarization. Though this process is still partly covered by electrode polarization, its location and activation behavior can be evaluated. The plot of  $\epsilon''_{deriv}$  against temperature at 0.5 kHz given in Fig. 23 shows an increase of the dielectric loss with increasing content of organoclay. Additionally, a reasonable shift to higher temperatures of this process from the unfilled sample to the filled samples is detectable. This shifting indicates different processes in the unfilled and the filled samples.

**Fig. 22** Temperature and frequency dependence of  $\epsilon''_{\text{deriv}}$  after applying the analyzing procedure (2) for the XNBR filled with 10 phr organoclay

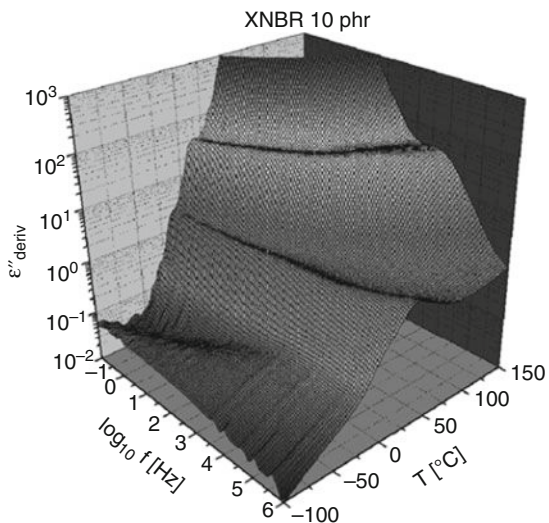
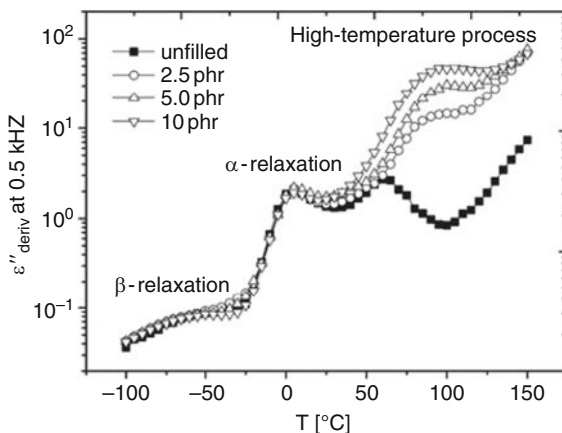


**Fig. 23** Plot of  $\epsilon''_{\text{deriv}}$  against temperature at 0.5 kHz for XNBR samples



### 3.3 XRD Studies

X-ray diffraction is a powerful tool for obtaining a preliminary understanding of the intercalation–exfoliation phenomena of a nanocomposite containing layered silicates. However, though it is a necessary study, it is still not sufficient to establish nanoscale dispersion. Insufficient amount of clay, preferred orientation of clay (especially in the case of rubber processing and molding) and peak broadening always lead to a wrong interpretation of the disappearance of a basal peak like that of the  $\langle 001 \rangle$  plane of a MMT-type clay [49, 50].

Morphological characteristics of LDH, MMT and their modified forms (OLDH and OMMT) have been discussed with respect to their WAXS patterns [23] (Fig. 24). The  $2\theta$ -values along the  $x$ -axis can be converted to layer spacing values ( $d$ ) by the Bragg relationship ( $\lambda = 2d \sin \theta$ , where  $\lambda$  is the wavelength of the radiation). The interlayer distance ( $d$ -value) calculated using Bragg's equation from the first-order basal reflection  $\langle 001 \rangle$  of the unmodified clays is 0.76 nm in LDH and 1.32 nm in MMT. The higher  $d$ -value in the case of MMT is due to the difference in the thickness of the crystal layer, which is about 1.0 nm in MMT and 0.48 nm in LDH. The intercalation of organic molecules in the interlayer space causes shifting of the  $\langle 001 \rangle$  reflection to the lower  $2\theta$  value (Fig. 24). This shifting corresponds to an enlargement of the  $d$ -value to 2.96 nm in OLDH and 2.98 nm in OMMT. The two nanofillers were incorporated into CR and different intercalation behaviors were noticed.

After incorporation of modified and unmodified clay into the CR matrix, very interesting X-ray scattering patterns can be noticed (see Fig. 25). It is evident from this figure that in every case, three very sharp common peaks appear at 1.41, 0.93, and 0.70 nm. Because these peaks are present even in the gum without any filler, it means that rubber additives (like ZnO and MgO along with stearic acid and organic accelerator, or the intermediate products arising from the vulcanization reaction) are responsible for this scattering. However, it is surprising to observe that no peak corresponding to the  $\langle 001 \rangle$  plane of layered silicate in the lower angle region appears for the OMTT-filled CR matrix. Here, we can say that CR, being a polar rubber, finely distributes the layers in the exfoliated form, at least under the area where the measurement was done. It was also noticed that in the presence of OMMT and MMT the peak at 1.41 nm became broader than the gum peak. The broad peak, which merges with the gum rubber peak at 1.41 nm, may come from some crystalline phase of CR itself. In our dynamic mechanical study it is suggested that CR undergoes partial crystallization in the presence of nanofillers, especially in

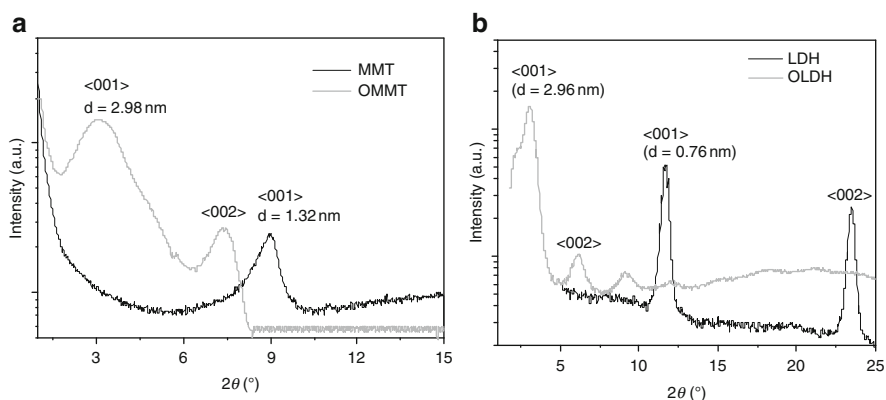


**Fig. 24** WAXD analysis of two types of clays and their organically modified forms: MMT and OMMT (a), LDH and OLDH (b)

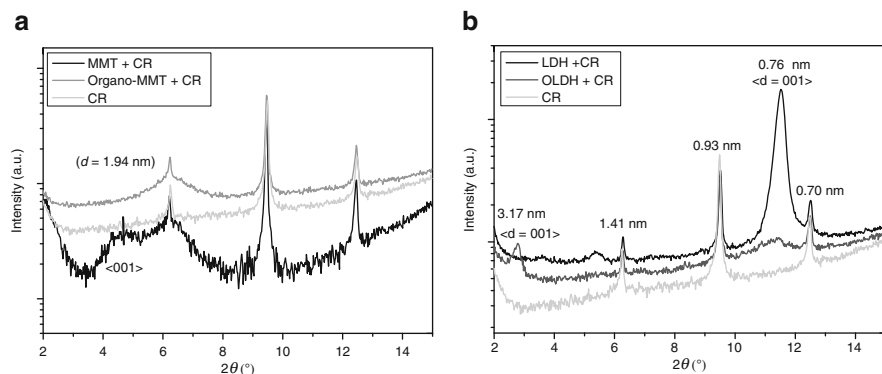


**Fig. 25** WAXD analysis of clay-filled nanocomposites: MMT and OMMT in CR matrix (a), LDH and OLDH in CR matrix (b)

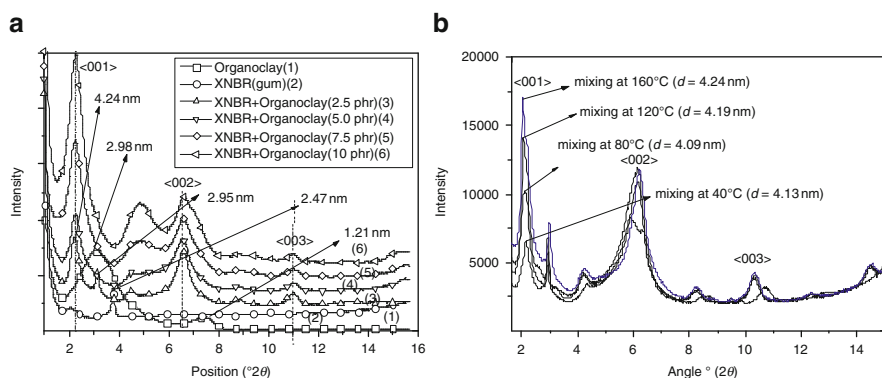


**Fig. 26** WAXD patterns of XNBR reinforced with different amounts of organoclay (a), and 2.5 phr organoclay-filled XNBR vulcanizates processed at different temperatures (b)

the presence of OMMT. So, the presence of these crystalline state responses in the XRD, and the broad peak, coincide with the gum rubber diffraction seen at 1.41 nm.

The WAXS patterns of unmodified clay (MMT) also provide one broad peak in the CR matrix around the  $d$ -spacing of about 1.94 nm. So, the expansion of the gallery gap takes place from 1.32 to 1.94 nm. This small increment of the  $d$ -spacing might arise due to partial distortion of the layered silicate, especially in the edge area of a stack of layered silicate. As far as the XRD traces of LDH and OLDH in CR matrix are concerned, it is observed that the reflection from the  $\langle 001 \rangle$  plane of OLDH comes at 3.17 nm, whereas the pure OLDH has a reflection of the same plane at 2.96 nm. Here, some sort of interaction of the CR chain is also taking place. However, in the case of pure LDH there is no change in the peak position after incorporation of the LDH in the CR matrix.

As far as the XRD patterns of organoclay-filled XNBR are concerned (Fig. 26a), the reflection from the  $\langle 001 \rangle$  plane is shifted towards a lower angle for all vulcanizates,

which were prepared under different mixing conditions. In each case, the interlayer spacing increased to about 4 nm. This observation supports the suggestion that intercalation takes place for all the vulcanizates containing organoclay. The appearance of other peaks can also be seen at higher angles, and the intensities of these entire peaks rise with the increase of organoclay. This observation signifies that a higher amount of organoclay in the rubber matrix results in an ordering of the clay particles and that the particles are rearranged into a more coherent symmetrical form. It is also evident from Fig. 26a that at 2.47 nm, a sharp peak appears in the XNBR gum compound. The presence of this sharp peak can also be observed in the 2.5 phr organoclay-containing XNBR sample, but the position is shifted toward lower angles and the corresponding spacing value is 2.95 nm. Moreover, the same peak has disappeared or merged with the main scattering coming from organoclay at relatively higher loading of organoclay and may be due to the in situ formation of zinc stearate. At higher loading of organoclay, the excess zinc oxide might be adsorbed on the surface of clay whereby the in situ formation is hindered. For organoclay, the main peak appears at 2.98 nm and there is also another reflection at 1.21 nm. So, XRD studies indicates that intercalation is a common process for 2.5–10 phr organoclay mixed at 160°C.

The effect of mixing temperature on the microstructure has also been analyzed by WAXS experiments. The X-ray scattering patterns were taken from 2.5 phr organoclay-filled XNBR matrix at different mixing temperatures. It is observed from Fig. 26b that in all vulcanizates the space gap increases to some extent from low temperature mixing to high temperature mixing. It can also be seen from this figure that the peak intensity becomes more intense in the high temperature mixed compound. Here, higher peak intensity means a higher number of intercalated layered species under the X-ray beam. The maximum number of intercalated layered silicate species appears in the rubber matrix from the aggregated mass of the organoclay. In the case of low temperature mixing, a fewer number of intercalated clay layers makes the reflection of X-rays less intense from the corresponding  $\langle 001 \rangle$  plane.

Figure 27 shows the XRD patterns for the rubber compounds of S-SBR with organomodified layered silicate. A broad peak appears for unmodified clay at about 1.32 nm, and this peak is shifted to 2.98 nm for organoclay. For SB-10, SB-11, and SB-12 the corresponding values are 4.43, 4.01, and 3.82 nm, respectively. The diffraction peak of organoclay is obviously shifted toward the low angle direction, indicating the effective expansion of the interlayer distance of the clay. However, the interlayer spaces decrease with an increase of clay content. Obviously, with increasing filler loading, not enough space is available for the clay layers to occupy their positions without sacrificing the gallery gap.

### 3.4 Transmission Electron Microscopy

TEM pictures give direct visual evidence about the nanoscale dispersion of the layered silicate in the rubber matrix. Figure 28a shows the XNBR matrix filled with

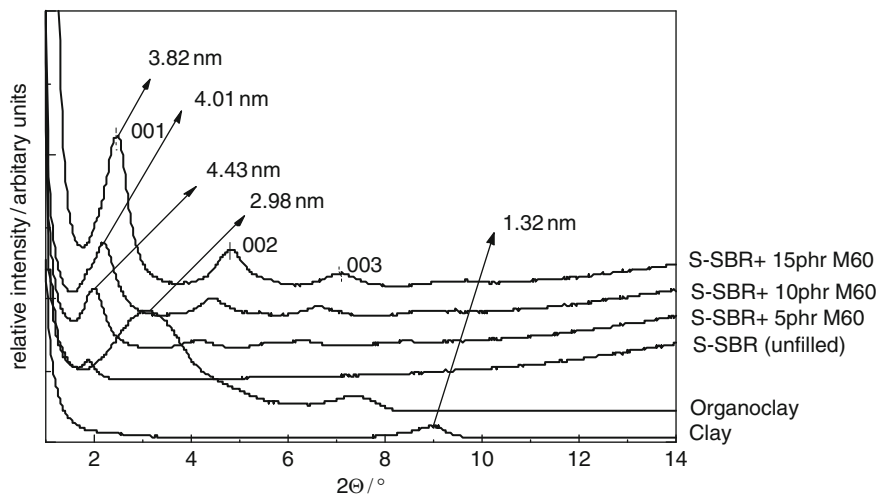


**Fig. 27** XRD spectra of S-SBR reinforced with OMMT. Note that the spectra of the related clays and organoclays are also shown. The position of the (001), (002), and (003) reflexes are indicated

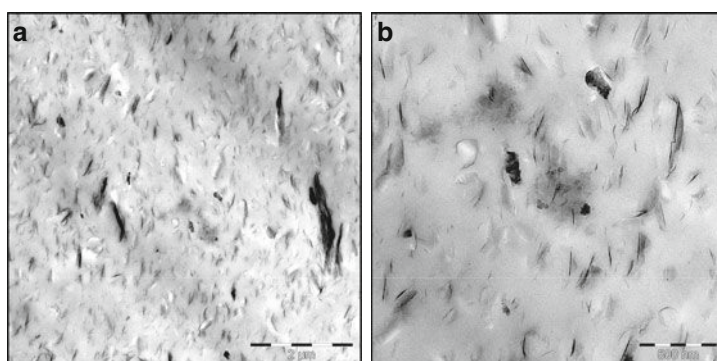


**Fig. 28** TEM image of the XNBR nanocomposite containing 5 phr organoclay (a), and magnification of a selection (b)

5 phr organoclay mixed at 160°C, where most of the clay layers are oriented towards the north–south direction. The silicate layers in the rubber matrix are oriented preferably during the processing, which is quite common for layered silicate–rubber nanocomposites [51]. A closer look shows the simultaneous existence of intercalated and exfoliated structures. Nevertheless, there are still a few agglomerated staged silicate layers, so total exfoliation and intercalation are not achieved through melt processing. Figure 28b is a magnified selection from Fig. 28a. Here, most of the visible silicate layer thickness is around a few nanometers and the length is some multiple of a hundred nanometers. Therefore, it may

be considered that most of the silicate layers are not monolayers but couples of layers attached together.

TEM pictures have been taken from the SBR vulcanizates containing 1.8 phr organoclay. Figure 29a shows the TEM picture of SBR matrix in which the layered silicate was dispersed by using XNBR as a carrier of the organoclay.

It is observed from this figure that there are a lot of small dark lines preferably oriented in a north–south direction. Here, the organoclay is distributed evenly in the whole rubber matrix. Some small dark clusters are shown enlarged in Fig. 29b. These structures are formed due to the separation of the polar XNBR phase from the nonpolar S-SBR matrix. Furthermore, exfoliated layers of organoclay are visible in the interface between the two polymer phases, which obviously promotes a better compatibility between XNBR and S-SBR phases. Figure 29c displays the TEM

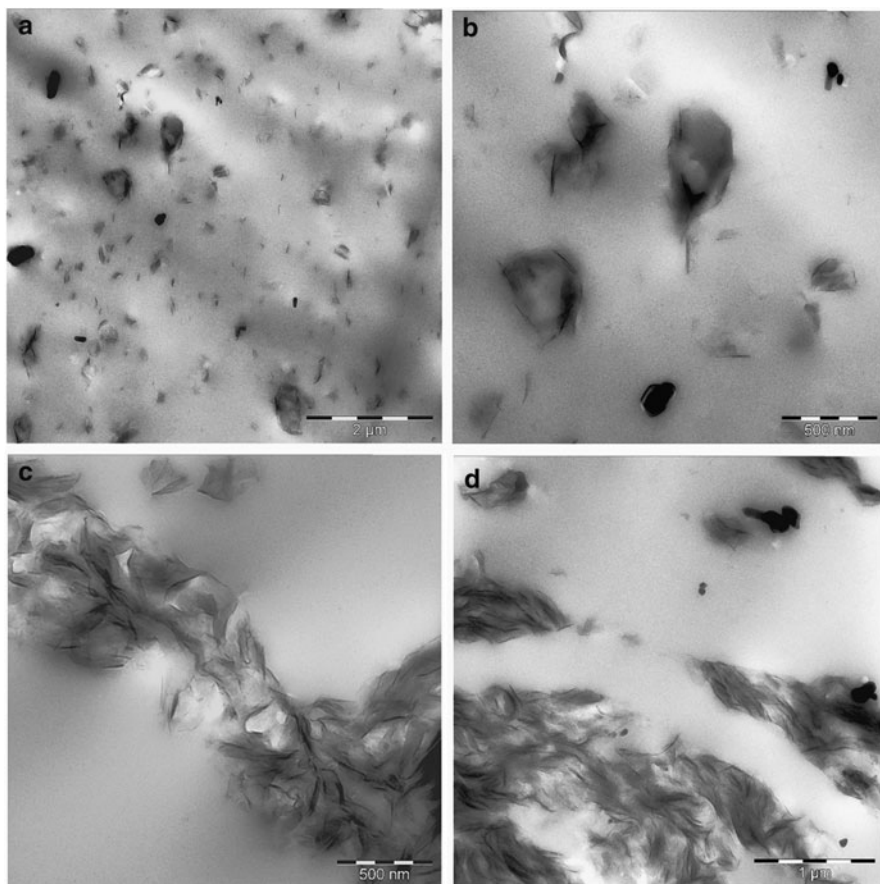


**Fig. 29** TEM images of the SBR nanocomposites containing 1.8 (a), 1.8 (b), 3.7 (c), and 5.6 (d) phr of organoclay

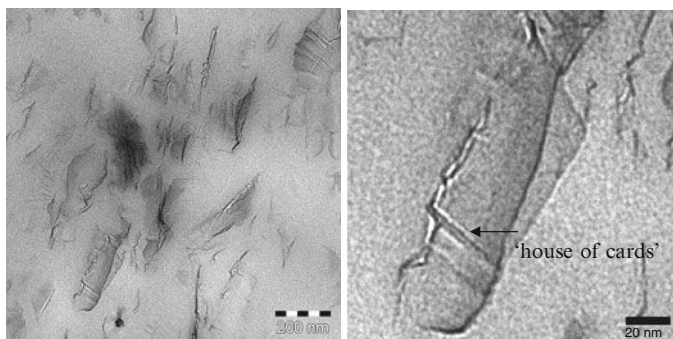


**Fig. 30** TEM images of organoclay-filled CR. Image on the *right* is a magnified selection

image of SBR in which the organoclay concentration was 3.7 phr. Here, layered silicates form local network-like structures remaining in the exfoliated and intercalated state. The rise of such network structures is also seen in the vulcanizate containing a higher amount of organoclay ( $\sim 5.6$  phr, Fig. 29d). No considerable amount of staged (tactoid) layered silicates is observed. Therefore, we conclude that most of the layered silicates are either exfoliated or intercalated and that the rubber matrix is sufficiently reinforced.

A good state of dispersion of the organoclay has been found in the CR matrix. The exfoliated structure can be directly observed from the TEM of the OMMT-filled CR composite (left-hand image in Fig. 30). It is noticed from this micrograph that all silicate layers are exfoliated and distributed very nicely throughout the whole rubber matrix. It is also observed that some of the exfoliated clay platelets form a “house of cards” structure (right-hand image in Fig. 30).

### 3.5 Infrared Spectroscopy

Fourier transform infrared spectroscopy (FTIR) can give useful information on chemical changes occurring in the system. However, the detection of such changes can be challenging because often the new species produced are present in small amounts and they are chemically similar to the initial material, so their absorption peaks are masked.

However, such spectroscopic techniques are sometimes used to more fully understand rubber–clay interaction. For example, XNBR filled with organoclay gave very interesting results with IR studies.

The attenuated total reflection infrared (ATR-IR) spectra taken from organoclay, pure XNBR, and the vulcanizates filled with 5 phr clay and mixed at  $160^{\circ}\text{C}$  temperature, are depicted in Fig. 31. From the spectra, the principal peaks for the pure organoclay are observed at  $2,846\text{ cm}^{-1}$  and  $2,920\text{ cm}^{-1}$  due to the presence of



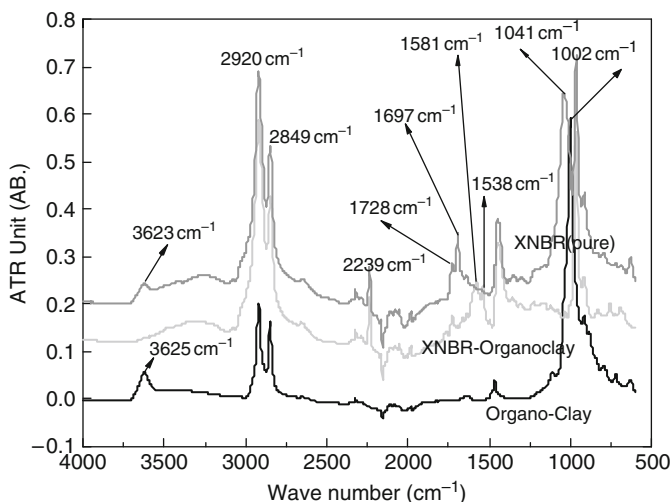


**Fig. 31** ATR-IR spectra of organoclay, pure XNBR (gum), and 5 phr organoclay-filled XNBR vulcanizates mixed at 160°C

aliphatic  $-\text{CH}_2$  groups in the hydrophobic tails of the quaternary amine modifier. The broad peak at around  $3,625\text{ cm}^{-1}$  of this material can be attributed to the presence of  $-\text{OH}$  groups on the surface. The characteristic absorbance for  $-\text{Si}-\text{O}-\text{Si}-$  in the clay is seen at  $1,002\text{ cm}^{-1}$ .

The pure XNBR gives rise to peaks at  $2,920$  and  $2,849\text{ cm}^{-1}$  due to the  $-\text{CH}_2$  groups on the rubber backbone. The characteristic absorbance for  $-\text{C}-\text{N}$  of XNBR can be observed at  $2,239\text{ cm}^{-1}$ . Peaks in the range of  $1,500$ – $1,700\text{ cm}^{-1}$  result from the  $>\text{C}=\text{O}$  group of the carboxylic part in the rubber. The absorption at  $1,040\text{ cm}^{-1}$  arises on account of the asymmetric stretching of the  $-\text{C}-\text{OH}$  in the carboxylic functionality.

A careful study of the spectra for the composites shows that the peaks at  $1,695$  and  $1,728\text{ cm}^{-1}$  disappear in the cured XNBR matrix, being replaced by two new ones at  $1,538$  and  $1,581\text{ cm}^{-1}$ , respectively. These can be assigned to the  $>\text{C}=\text{O}$  stretching in different chemical environments. The former peak corresponds to the stretching in the tetra-coordinated zinc-carboxylate complex, whereas the latter peak corresponds to that in a hexa-coordinated complex. The peak at  $3,625\text{ cm}^{-1}$  on the pure organoclay spectrum disappears in the nanocomposite spectrum, probably owing to an interaction with the  $-\text{COOH}$  groups on the XNBR. Furthermore, a shift in characteristic absorbance of  $-\text{Si}-\text{O}-\text{Si}-$  is observed from  $1,002\text{ cm}^{-1}$  to around  $996\text{ cm}^{-1}$ , i.e.,  $6\text{ cm}^{-1}$  to the lower energy side. A similar transition has been observed by Katti et al. [52] in their studies on polyamide–MMT nanocomposites. The linkage of the  $\text{COOH}$  group on XNBR with the silanol– $\text{OH}$  on the clay surface that, in turn, is already bonded with the silica tetrahedral of MMT, may have caused this shift of the  $\text{Si}-\text{O}$  stretching band in the composite with respect to the organoclay.

## 4 Effect of Vulcanization Ingredients

### 4.1 Effect of Sulfur and Peroxide Curing

It is well known that the presence of an amine compound in the curing recipe provides curing acceleration during the vulcanization process. So, it is easy to speculate that the quaternary ammonium compound (QUAT), which was used for the organic modification of MMT clay, can easily participate in the sulfur curing mechanism. There are some reports about these interactions and, in most cases, they give rise to collapse of the gallery height of the silicate layers [53, 54]. Since in peroxide curing the amine has no role, it is very interesting to compare the clay morphology in the rubber matrix cured by sulfur and with that in matrix cured by peroxide. The XRD peaks at  $2\theta = 3.06^\circ$ ,  $5.47^\circ$ , and  $7.55^\circ$  represent the diffraction of the  $\langle 001 \rangle$ ,  $\langle 002 \rangle$  and  $\langle 003 \rangle$  crystal surface of the silicate particle in the sulfur-cured NBR vulcanizate (Fig. 32a), corresponding to a  $d$ -spacing of 4.35, 1.97, and 1.34 nm, respectively. This indicates that a relatively large gallery expansion in layered silicates has taken place during the melt mixing and curing at  $160^\circ\text{C}$ . In the case of peroxide-cured systems (Fig. 32b), there were three diffraction peaks of the  $\langle 001 \rangle$ ,  $\langle 002 \rangle$ , and  $\langle 003 \rangle$  crystal surface at  $2\theta$  equal to  $3.38^\circ$ ,  $5.68^\circ$  and  $7.80^\circ$ , respectively, corresponding to a  $d$ -spacing of 3.69, 1.88, and 1.26 nm, respectively. Here, the gallery gap between two parallel plates of silicate particles has also been increased to a considerable extent. However, the extent of space increment is higher in the case of the sulfur-cured system as compared with the  $d$ -spacing from the master batch (Fig. 32c). It is also interesting to note that the peak intensity of diffracted X-ray obtained from peroxide-cured compounds is much higher than for sulfur-cured systems (Fig. 32a, b). In this case, the higher peak intensity might come from higher orientations in a particular direction of the layer structure [55]. Higher orientation could be due to the fact that the alignment of layered silicates particles are probably uniformly distributed towards one direction, i.e., highly ordered orientation of clay platelets in peroxide-cured matrix. In contrast, there is no such orientation effect in the sulfur-cured matrix, though both of them are processed through the same procedures. This behavior can be directly justified by TEM. Figure 33a, b displays the TEM pictures of sulfur- and peroxide-cured vulcanizates. It is evident from Fig. 33b that a large number of parallel dark lines are oriented in one direction, and that these dark lines represent the silicate particles in the rubber matrix. On the other hand, Fig. 33a does not show a special orientation of the silicate particles in the rubber matrix. It is also observed that in both cases the particles are distributed very uniformly in the whole visual region. The orientation of the layered silicate in the rubber matrix is expected in the direction of flow during the processing of the rubber compound [51]. This type of spatial distribution should, apparently, be observed irrespective of the curing type because, in both cases (sulfur or peroxide), the rubber compounds were processed by the same procedure. However, sulfur-cured rubber matrix shows an isotropic arrangement of the silicate particles. Therefore, it was assumed

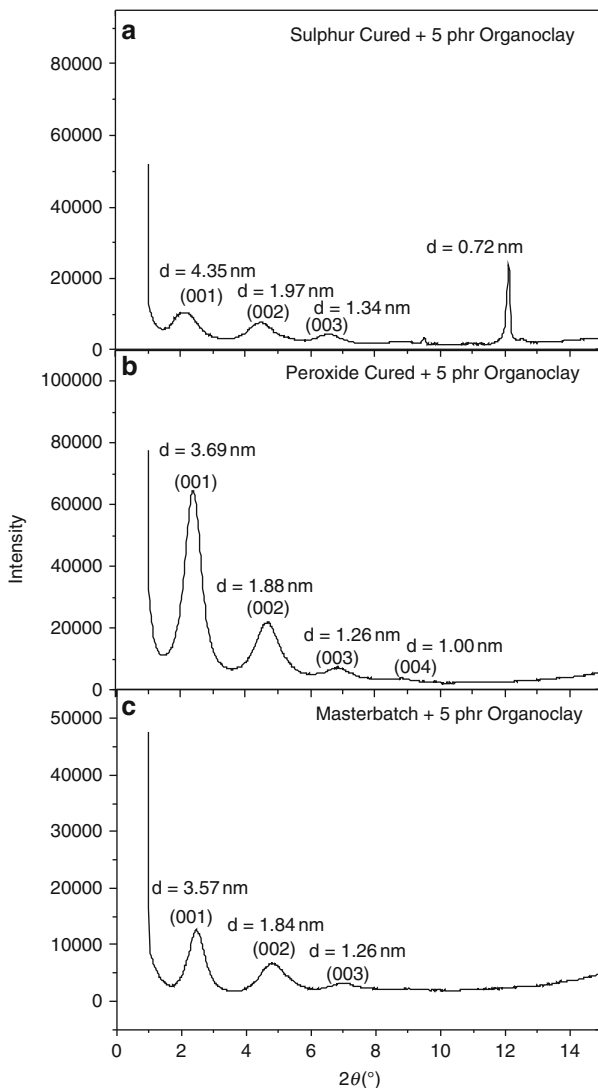


**Fig. 32** WAXD patterns of NBR compounds reinforced with 5 phr organoclay and cured by sulfur (a), peroxide (b), and NBR master batch (c) (without curatives and uncrosslinked)

as a working hypothesis that alignment of the clay layers comes from the mixing direction of the two-roll mill during mixing the rubber with the other rubber additives. This orientation of the clay layers is affected by some of the rubber additives when these curatives are added during the mixing cycle. The clay particles seem to be surrounded by stearic acid and other additives and, hence, the shearing force from the mill is not properly transferred to the clay layers due to slippage

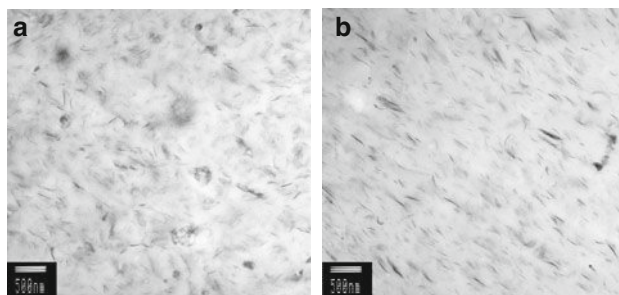


**Fig. 33** TEM images of NBR vulcanizates cured by sulfur (a), and peroxide (b)

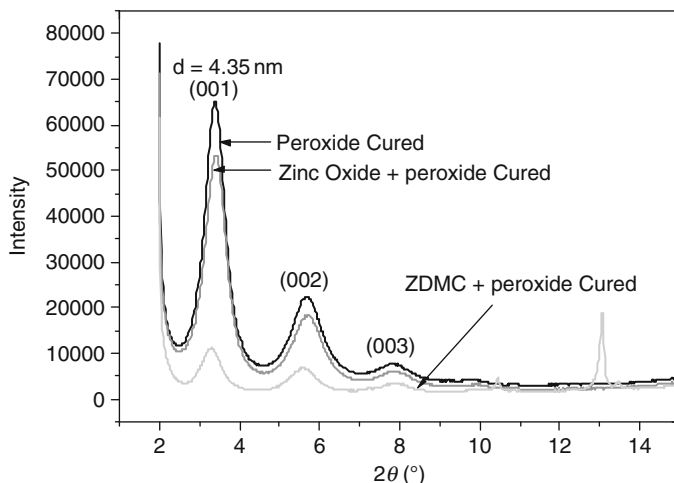


**Fig. 34** WAXD patterns of 5 phr organoclay-filled peroxide-crosslinked NBR in the presence of different vulcanizing ingredients

between the clay layers and rubber chains, whereby the particles no longer remain in the oriented form. On the other hand, in the peroxide-cured system, the shearing force is, more or less, transferred to the particles and the layers are forced to maintain the anisotropy. To explore this in more detail, the individual effect of vulcanization ingredients on this type of anisotropic behavior of the layered silicates was studied, with special on two different peroxide vulcanization systems.

In addition to dicumyl peroxide (DCP), in two different batches zinc oxide (ZnO) or a conventional organic accelerator (ZDMC) were used. Figure 34 depicts the corresponding XRD pattern. In both cases, the peak positions are almost the same as that of the pure peroxide-cured vulcanizates. However, the intensity of the XRD pattern was significantly reduced in the case of ZDMC, and there is only a little effect of ZnO. Obviously, the sulfur-containing zinc salt influences and promotes dispersion and reorientation of the layered

silicates uniformly toward all directions [16]. Detailed studies are required to unravel the mechanism behind this.

## 4.2 Effect of Accelerator Type

Usuki et al. [14] from Toyota, Japan reported that the use of thiuram- and dithiocarbamate-type accelerators in EPDM rubber curing could enhance the exfoliation process of layered silicate. They proposed that when the zinc salt of ZDMC-types of accelerators were used in rubber curing, then the rubber backbone was modified with the grafted and accelerator moiety, and thus the rubber molecules became polar. They also described that this grafting of accelerators took place in a free radical fashion. As a result, this polar rubber molecule intercalated more easily into the gallery gap by virtue of the hydrogen bonds between the polar groups of rubber and the silanol groups of layered silicates.

It has also been reported that the use of silane-coupling agents, e.g., TESPT, can increase the reinforcing ability of clay by virtue of chemical linkage between the silanol group of silicates and the polymers [56, 57]. This type of coupling agent has two types of chemical groups: one that interacts with the hydroxyl groups of silicate and another that is responsible for the attachment with the rubber matrix. ZDP [20, 58] is also a type of multifunctional rubber additive that has the capability to act as a silane-coupling agent like TESPT as well as acting as a rubber-vulcanizing accelerator like ZDMC. The effect of this type of multifunctional rubber additive on the exfoliation–intercalation process of layered silicates was also investigated. A shift of the intensity peak in XRD to lower diffraction angles indicates that intercalation is a common phenomenon for both ZDMC- and ZDP-cured systems, and that ZDP-cured vulcanizates show a higher gallery gap between two successive layers of silicate particles (Fig. 35). There is also a significant reduction of peak intensity of the (002) and (003) crystal faces, with a peak broadening effect that signifies the uneven and irregular fashion of intercalation. Ultimately, it can be assumed that ZDP enhances the intercalation process of the layered silicate. This substance, being a multifunctional rubber additive, plays a special role as compatibilizer between organic polymers and inorganic silicates by providing an extra interaction as proposed in Scheme 1. The scheme shows how ZDP is grafted onto the surface of clay layers, and how this compound acts as a sulfur-crosslinking precursor to the rubber chains, bringing out some sort of compatibility between the clay and rubber. It is also noteworthy to mention that all sulfur-cured gum compounds containing ZDMC show one sharp peak around  $d = 0.72$  nm. It is easily understandable that this scattering comes from sulfur vulcanization ingredients or from the in situ formation of some crystalline product from those sulfur curatives. Pure peroxide-cured rubber and the master batch compound did not show any scattering in this area since it did not contain any other crystalline substances.

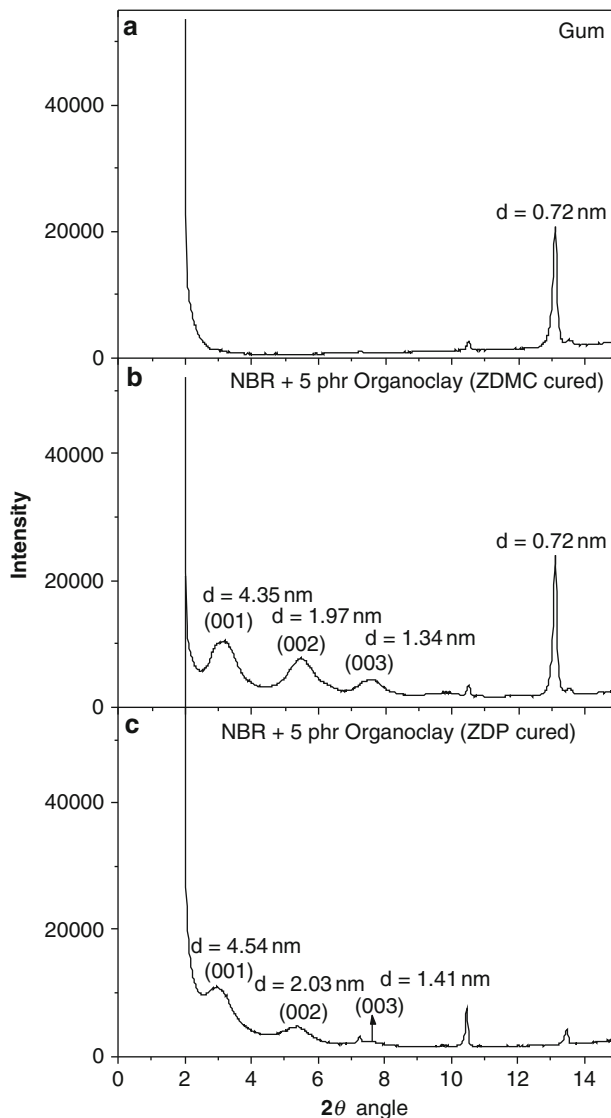


**Fig. 35** WAXD patterns of sulfur- and ZDMC-cured NBR gum (a), sulfur- and ZDMC-cured organoclay-filled NBR (b), sulfur- and ZDP-cured organoclay-filled NBR (c)

### 4.3 Effect of Stearic Acid

Many of the classical processing additives that had been introduced in the early years of rubber technology still remain in common use in various rubber products.

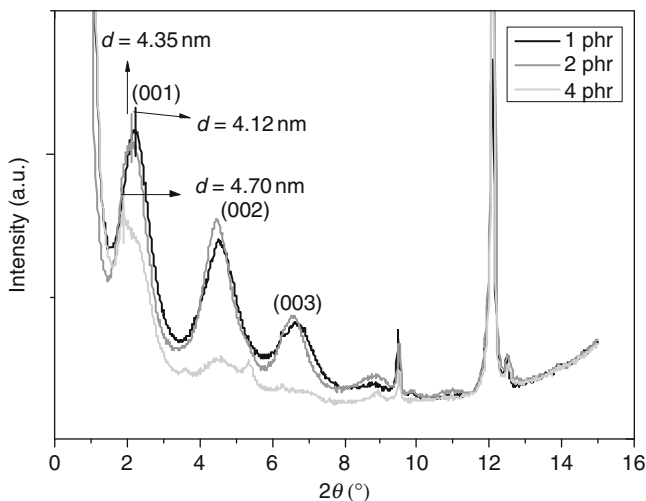


**Fig. 36** WAXD patterns of 5 phr organoclay-filled NBR, cured by sulfur in the presence of 1, 2, and 4 phr stearic acid

Stearic acid is one of these classical additives that are used as activators in the sulfur vulcanization process. Stearic acid [octadecanoic acid,  $\text{CH}_3(\text{CH}_2)_{16}\text{COOH}$ ] is a long chain fatty acid consisting of 18 carbon atoms without double bonds. Recently, it was observed that stearic acid has a beneficial effect on the intercalation–exfoliation process of nanoclay in nitrile rubber [18]. The effect of stearic acid on the exfoliation–intercalation process of the layered silicate has been understood by XRD experiments. For this study, different amounts of stearic acid were taken in sulfur-curing packages. Very interesting XRD patterns have been received from these compounds and the corresponding WAXD patterns are given in Fig. 36. The interlayer distances of the silicate particles in the NBR matrix containing 1, 2, and 4 phr stearic acid are 4.12, 4.35 and 4.70 nm, respectively, whereas in the master batch compound the interlayer distance between two adjacent silicate layers was 3.57 nm. This means that the interlayer distance increased during sulfur mixing and/or curing, and that an excess amount of stearic acid favors the extent of intercalation. With increase of the stearic acid content, the corresponding scattered X-ray peak from the  $\langle 001 \rangle$  crystal face of silicate particles shifts toward lower angles with a higher space gap. Ultimately, at 4 phr stearic acid content the diffraction curves show an almost exfoliated type of scattering pattern at higher order reflections such as  $\langle 002 \rangle$ ,  $\langle 003 \rangle$ , etc. with very few intercalated structures. As a conclusion, a higher amount of stearic acid is recommended for the preparation of rubber-layered silicate nanocomposites. Very recently, Ma et al. [17] also reported that stearic acid increases the gallery gap. However, they did not find any change in the gallery gap after adding the stearic-acid-treated organoclay into the rubber matrix. The space gap between two clay layers was confined to 3.9 nm.

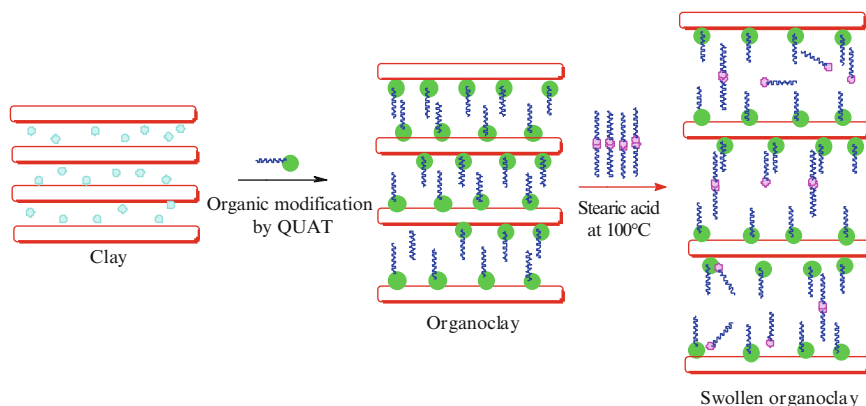


**Fig. 37** Illustration of the gradual modification of MMT clay

It was suggested that stearic acid, which consist of small molecules, enters into the gallery of the layered silicate structure during the mixing and vulcanization processes, thus paving the way for intercalation of the rubber chains.

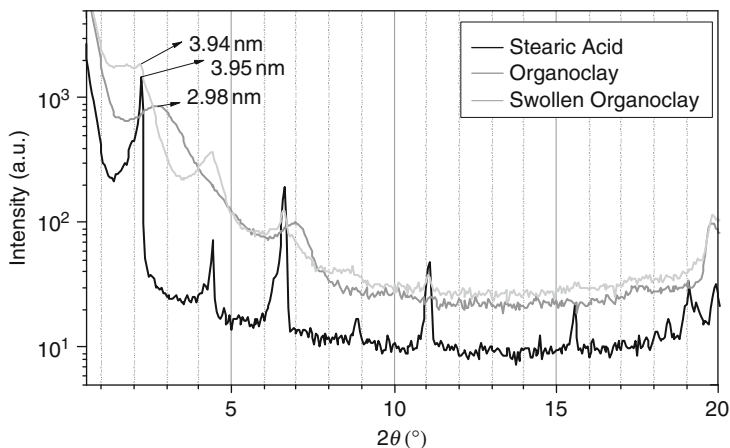
In order to prove the importance of the delaminated layer structure in the direct (melt) intercalation, the intercalation of stearic acid molecules into the clay galleries has been studied by premixing them with organoclay and then successfully incorporating this modified clay into the rubber matrix [59]. A schematic presentation of such modification of clay is given in Fig. 37.

After modification of the organoclay by stearic acid, the interlayer spacing increases from 2.98 to 3.96 nm (Fig. 38). So, the enhancement of the *d*-space has taken place due to the intercalation of stearic acid into the galleries and this pre-intercalation seems to make penetration of the rubber molecules easier and pave the way for nanostructure formation of the final composites.

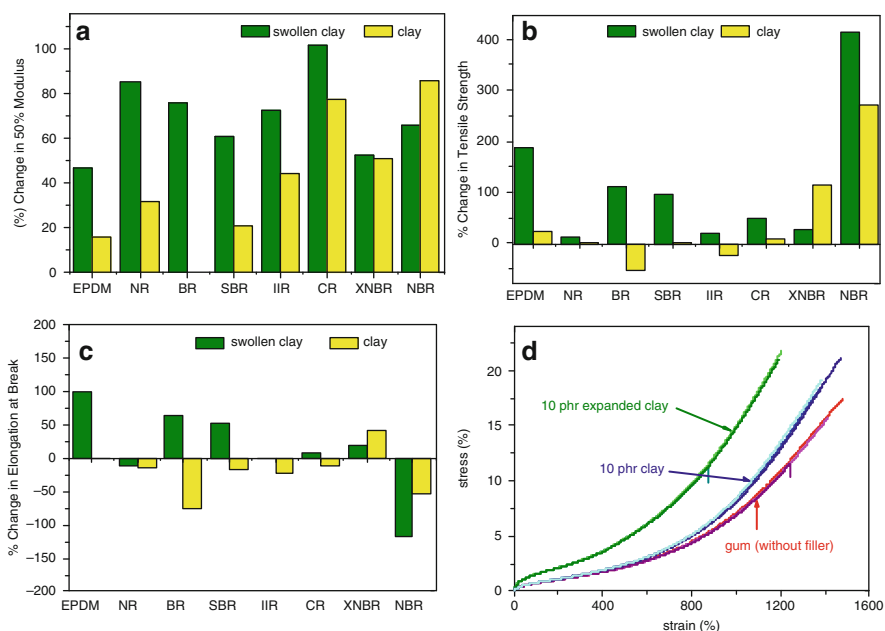
Several kinds of rubber were taken into account to find the intercalation–exfoliation behavior of swollen clay. It is observed from Fig. 39a that the change in modulus at 50% elongation is always higher for all composites (except NBR) containing swollen clay as compared with compounds containing only organoclay. A very remarkable change was shown in polybutadiene rubber (BR): after addition of 10 phr clay the improvement in the 50% modulus was not observed, but as soon as 20 phr swollen clay was incorporated, the modulus increased significantly.

Figure 39b illustrates the improvement of tensile strength with respect to the respective gum compound. It is evident from this figure that improvement of tensile strength is seen for all vulcanizates filled with 10 phr activated clay (except XNBR and NBR), whereas incorporation of only 10 phr organoclay leads to rather small improvements. XNBR and NBR, being polar rubbers, do not undergo further intercalation by activated organoclay since it has already been intercalated by normal mechanical melt mixing and, due to this fact, further improvement of properties could not be achieved. The changes in elongation at





**Fig. 38** WAXD patterns of stearic acid, clay, and swollen clay. The swollen clay was prepared by mixing stearic acid and organically modified clay (Nanofil-15) at the ratio of 1:1



**Fig. 39** Improvement of physical properties of various rubbers through incorporation of clay or swollen clay: 50% modulus (a), tensile strength (b), elongation at break (c), and the stress–strain plots for natural rubber (d). The strain was measured on the basis of clamp distance measurements

break after incorporation of clay and of swollen clay can be seen in Fig. 39c. None of the rubber vulcanizates having swollen clay in their matrix (except XNBR) show higher elongation at break values compared with their respective gum. In the

presence of a small amount of swollen clay, the vulcanizates offer higher modulus values, as shown in Fig. 39a. This finding can be explained by the higher effective volume fraction of the swollen clay, leading to a decrease of the elongation at break.

It will be very interesting to discuss the nature of the stress–strain curve obtained from the vulcanizates. The stress–strain curves obtained from NR compounds are shown in Fig. 39d. It is evident from this figure that the nature of the curves from the compounds containing swollen clay are much steeper and stronger than those from the sample containing only organoclay. It is worth mentioning that a similar type of approach was considered for preparation of rubber–nanoclay composites [17, 59]. However, they did not find any significant reinforcement in mechanical properties. Those composites were prepared by mixing of the compounds at room temperature. Hence, stearic acid possibly did not melt at that mixing condition and the rubber chains could not find space in the gallery by replacing the solid crystal of stearic acid. In our study, the mixing was done above the melting point of stearic acid and at this temperature the rubber chains enter into the layered galleries

The  $d_{(001)}$  values of the clay in different rubber matrices are given in Table 8. It is clear that after incorporation in the rubber matrix the space gap between two successive layers has been increased in all cases. However, the enhancement of the  $d_{(001)}$  values is marginal as compared with the swollen clay. As can be seen in Fig. 40, the peak positions are not changed to a large extent, but the peaks have altered height and broadened width. The intercalation of the rubber chains by pushing the platelets apart and by losing the order of the stacks (changing the crystallinity) are the causes behind these observations. A rough idea about the extent of such a delamination process can be obtained by analysis of the XRD peak area measurements [60]. It can be easily understood that the lower the peak area, the greater the delamination of the clay. Table 8 summarizes the results obtained from such observations over a wide range of rubber systems. Larger areas under the curves have been found from EPDM, XNBR, and BR and smaller areas have been calculated for CR, NR, and butyl rubber (IIR). A very interesting correlation was found between this trend and the improvement of the 50% modulus (stress at 50% elongation) of the swollen-clay-filled vulcanizates. CR, NR, and IIR

**Table 8** Analysis of XRD and DMA data obtained from different rubber vulcanizates containing expanded organoclay

Rubber	XRD	
	$d_{(001)}$ value (nm)	Area under the (001) peak from X-ray pattern (a.u.)
EPDM	4.00	26,899
NR	3.95	5,484
BR	4.19	19,795
S-SBR	4.19	18,676
IIR	4.50	9,422
CR	4.12	1,741
XNBR	4.06	21,102
NBR	4.68	18,346

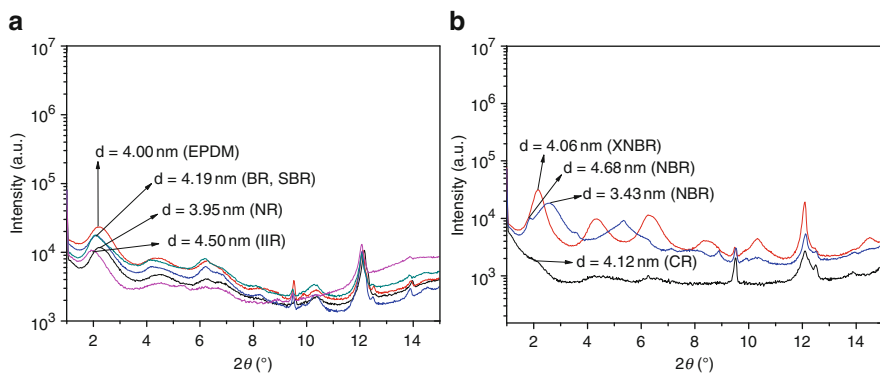


**Fig. 40** WAXD patterns of non-polar rubbers (a) and polar rubbers filled with 20 phr swollen clay (b). All the vulcanized rubbers contain some curing ingredients like organic accelerator, zinc oxide, etc

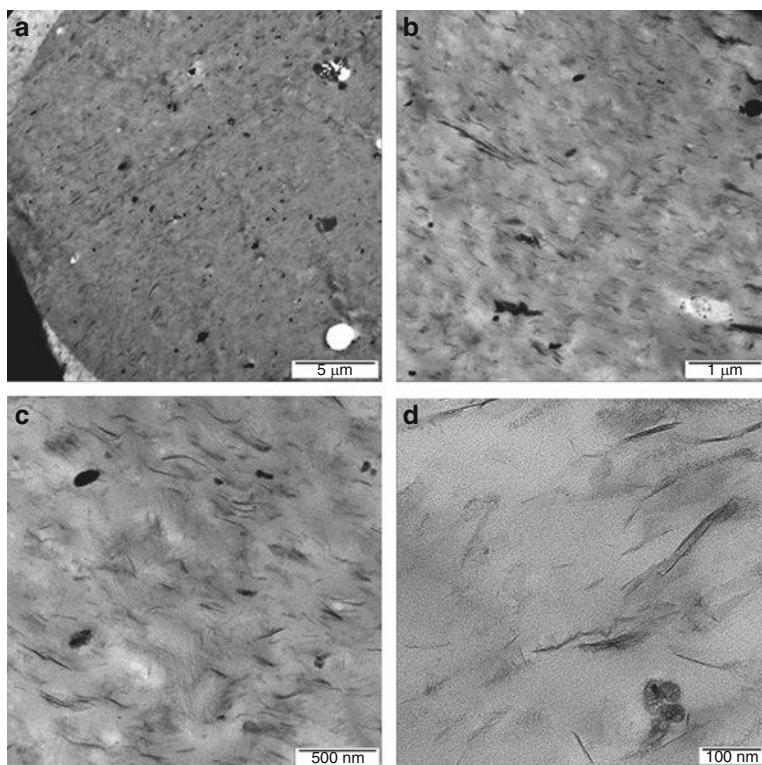


**Fig. 41** TEM images (a–d), at different magnifications, of 10 phr swollen-clay-filled NR

show significant improvement (CR 100%, NR 107%, and IIR 73%) in enhancing the stress at 50% elongation parallel with a higher degree of delamination of the clay layers. In contrast, EPDM shows a poor enhancement (48%, from Fig. 39) of these properties after loading with 20 phr swollen organoclay. This correlation between the calculated areas under the XRD pattern with the enhancement of modulus indicates a nice agreement with each other. However, for XNBR a large area under the XRD was noticed. It was previously reported that XNBR, being a polar rubber, does not offer better physical properties after addition of swollen clay as compared with organoclay because it is already reinforced by organoclay. Most probably the complex crystalline morphology arising from metal-carboxylate (Zn–OOC) [6] clusters contribute to the X-ray reflection and results in the higher peak area. The higher physical properties of the swollen-clay-containing rubber vulcanizates and the expansion of the  $d_{(001)}$  spacing directly lead us to the conclusion that intercalation of rubber chains through the gallery gap is becomes easier with swollen clay than with organoclay.

TEM images also directly corroborate the above conclusion by showing mostly intercalated and some exfoliated silicate clay layers in different rubber matrices. Figure 41 shows TEM images of swollen-clay-filled NR at different magnifications. The overall distribution of clay particles can be observed in Fig. 41a, b. It can be seen from these pictures that there is no big agglomeration of the clay particles. Even at higher magnification (Fig. 41c, d), single clay layers can be detected. Though 20 phr swollen organoclay was employed in this work, the clay particles did not form any big clusters or aggregates throughout the rubber matrix.

## 5 Clay in Rubber Blends

The fundamental justification for blending two or more elastomers is acquisition of the combinatorial and desirable features exhibited by the vulcanizates of the component elastomers in a unique substance. Unfortunately and most commonly, however, it has been found that covulcanization leads to reduction in the mechanical strength of the vulcanizate compared with its expected values. The elastomer blend components that resist gross phase segregation and/or give desirable blend properties are frequently said to have a degree of “compatibility” even though in a thermodynamic sense they are not miscible. Homogeneity of mixing and retention of the compatibility during vulcanization are the most relevant issues pertaining to elastomer blends and microheterogeneity is usually desirable in order to retain the individual properties of the respective elastomer components.

Nevertheless, the compatibility of two rubbers is largely governed by the polarity and the  $T_g$  of the corresponding rubbers. It is very difficult to predict the miscibility of two rubbers only by inspecting the above two factors. Determination of the Hildebrand solubility parameter ( $\delta$ ) by calculation of the Hoy molar

attraction constant [61] could be one way to understand the miscibility of the rubbers in a blend. In unfilled rubber compounds, the domain size of a heterogeneous blend is proportional to the difference of  $\delta$  parameters of the constituent rubbers. With the incorporation of fillers, the  $\delta$  parameter decreases and, hence, the miscibility of the rubbers can be improved. For instance, the rubber domain sizes in blends of BR and isoprene–butadiene rubber (IBR) are highly reduced by adding 30 wt% of silica or carbon black fillers [62]. Here the fillers act like a compatibilizer between two heterogeneous rubbers with two different  $T_g$ . However, for blends of dissimilar elastomers, problems can arise in achieving optimum carbon black distribution between the microphases of the final product. In blends of elastomers that differ significantly in terms of unsaturation or viscosity, carbon black tends to locate preferentially in the higher unsaturation or lower viscosity phase [63]. Polarity is also a factor controlling carbon black migration in elastomer blends. Carbon black has been shown to transfer or migrate between EPDM and CR [64]. However, it was reported that migration of fillers can be restricted if a special technique is followed to process heterogeneous rubber blend compounds [65]. There is plenty of literature on the effect of fillers on the phase separation behavior of several immiscible blends [65–68]. In recent years, various reports have been made that describe the use of organically modified clay as a compatibilizer for several types of immiscible polymer blends by effectively reducing the domain size of the polymer phases. It is described that nanoclays are an attractive alternative to traditional compatibilizers because they can be compounded very easily. These nanoclays are also known to stabilize different crystalline phase of polymers and have also been proved to have the ability to improve the mechanical and thermal properties. For example, Vo and Giannelis [66] reported the compatibility and phase separation behavior of poly(vinylidene fluoride)/nylon-6 blends by the use of organically modified nanoclay. Addition of 5 wt% organoclay and maleic-anhydride-grafted polyethylene was found to be effective in reducing the ethylene–octene copolymer phase size in low density polyethylene/ethylene–octene copolymer blends [67]. Poly( $\epsilon$ -caprolactone)/poly(ethylene oxide) blends were prepared in the presence of nanoclay and it was found that exfoliated silicate platelets were preferentially located at the interface between the two blend phases [68]. The effect of organically modified clay on the morphology and properties of poly(propylene)/poly(butylene succinate)-*co*-adipate blends has been studied and the enhancement of physical properties, thermal stability, and rheological behavior was reported [69]. Several research groups also incorporated nanoclay into different type of rubber blends with the aim of improvement in physical properties [70–72]. It is reported that the preferential accumulation of intercalated clay layers on the phase boundary increased the compatibility of two different polymers when they have strong interactions with organoclay surface. Arroyo et al. [73] observed that organoclays give rise to a finer and more homogeneous dispersion of epoxidized natural rubber in the natural rubber matrix. Preferential accumulation of the exfoliated layered silicates is also observed in the interface of poly( $\epsilon$ -caprolactone)/poly(ethylene oxide) blends [68]. Very recently it was observed that organoclay, remaining in a rubber blend, can provide a dual role:

one role is the enhancement of the rubber–rubber compatibility (A. Das, personal communication) and the other is interfering with the interfacial crosslinking between two different rubber phases [74]. In the following sections, the positive and negative roles of organoclay on the compatibility between two different rubbers are discussed.

## 5.1 CR/EPDM

CR is an extremely versatile synthetic rubber with more than 75 years of proven performance in a broad industry spectrum due to its unique combination of properties: ozone resistance, oil resistance, toughness, dynamic flex life, good adhesion to other materials, and heat resistance up to 100°C [75]. This rubber has been the material of choice for moldings and extrudates of all types, reinforced hoses, roll covers, belting, including conveyor belts, air spring bellows, cable sheathing and insulation for low-voltage cables, sponge rubber, corrosion-resistant linings, sheeting, fabric proofing and footwear, most power belts, boots, hose water suits and water sealant, and numerous other applications. To meet these emerging needs, and for new material development for more demanding applications, improvements in resistance to heat, ozone, and cut growth of CR products are very desirable. The above requirement for CR products could be satisfied by blending with polyolefin elastomers such as ethylene–propylene rubber (EPR) or EPDM, which have better resistance to heat, ozone, and cut growth [76]. However, these CR/EPR or EPDM blends are incompatible [77].

### 5.1.1 Preparation

A typical mixing procedure was followed to obtain the CR/EPDM blend compounds. First, the clay was treated with stearic acid in a mortar and placed in an oven at 100°C for 30 min. After heating, the mass was thoroughly ground with a pestle (keeping it hot) and again the vessel was kept at 100°C. The hot material was cooled to room temperature and again ground. This compound was used as a filler. The EPDM rubber was mixed with ZnO and the stearic-acid-modified clay was incorporated into it in a two-roll mixing mill for 5 min. This mix was added to the premasticated CR and then the curatives (accelerator and sulfur) were incorporated into the rubber compounds. For gum compounds (without any clay), the stearic acid was added after the addition of ZnO to the EPDM. Finally, the rubber compound was compression molded to prepare samples of ~2 mm thickness.

### 5.1.2 Characterization

It was already mentioned that an extra amount of stearic acid has a pronounced effect on the intercalation of layered silicate in nitrile rubber. So, a higher amount of

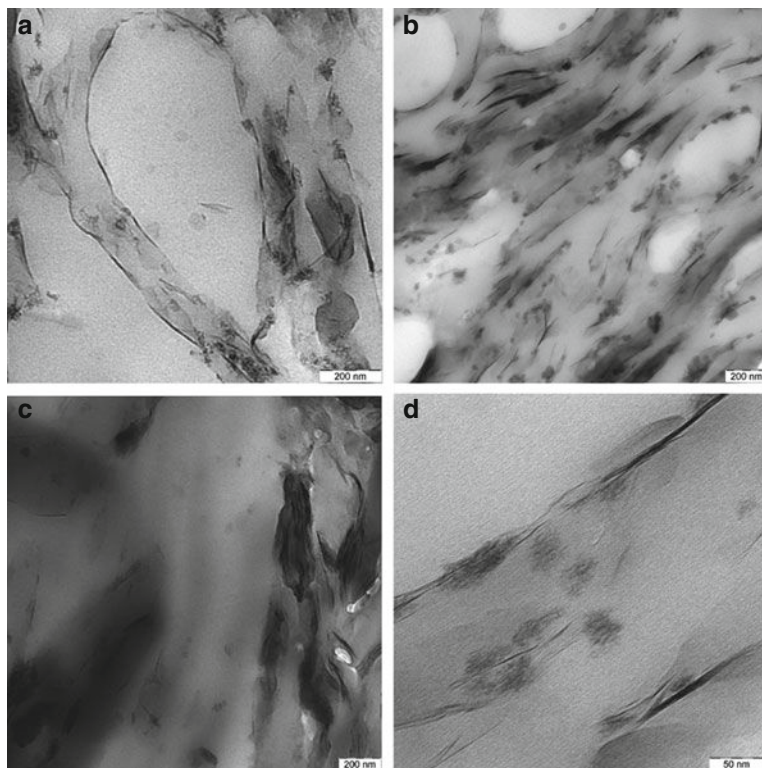


**Fig. 42** TEM images of the blends of 25 EPDM/75 CR (a), 50 EPDM/50 CR (b), 75 EPDM/25 CR (c), and 25 EPDM/75 CR filled with 10 phr nanoclay (d)

stearic acid (10 phr) was added to the organically modified clay to obtain a higher *d*-space for the organoclay in the swollen state. Because the stearic-acid modified organoclay exhibits a higher *d*-space (2.98–3.96 nm), it is expected that a large portion of the clay will form a good degree of intercalated–exfoliated structures in the rubber matrix.

Figure 42 shows TEM images of CR/EPDM blends at the ratios of 75/25, 50/50, and 25/75, all containing 10 phr clay. Each blend was prepared by incorporating all the clay in the EPDM rubber and, subsequently, mixing the resulting composites with CR. It is obvious from Fig. 42a, b that two phases of CR and EPDM coexist with a large number of exfoliated and intercalated clay platelets at the interfaces. The dark phase is most probably CR phase with a higher electron density due to the presence of chlorine atoms in the rubber chains. Remarkably, it was found that there are almost no clay layers in the bright phase rather than in the dark phase. CR, being a polar rubber, forces migration of the clay particles into it, rendering the EPDM phase poor, despite the fact that all the clay was premixed with EPDM. Migration of inorganic clay layers takes place from nonpolar EPDM to polar CR. As far as

viscosity mismatch (Mooney viscosity) is concerned, the migration is also driven by the viscosity difference because the Mooney viscosity of EPDM is higher than the viscosity of CR.

The migration of clay from EPDM to CR phase can also be explained as a wetting/dewetting process between polymers and filler. Hereby, the driving force of filler particle migration is the difference of the interfacial tensions between the rubbers and clay:

$$\Delta\gamma = \gamma_{F-CR} - \gamma_{F-EPDM}, \quad (3)$$

where  $\gamma_{F-EPDM}$ , and  $\gamma_{F-CR}$  are the interfacial tensions between the organoclay filler (subscript F) and EPDM or CR respectively. The interfacial tensions can be calculated using the following equation of Good et al. [78]:

$$\gamma_{sl} = \gamma_s + \gamma_l - 2(\sqrt{\gamma_s^D \gamma_l^D} + \sqrt{\gamma_s^P \gamma_l^P}), \quad (4)$$

where  $\gamma_{sl}$  is the interfacial tension between a solid and a liquid, and  $\gamma_s$  and  $\gamma_l$  are the surface tensions or energies of the liquid or solid, respectively. The superscripts D and P denote their dispersive or polar parts.

Using this equation, the driving force for the filler particle migration, the difference of interfacial tensions  $\Delta\gamma$  can be expressed as:

$$\begin{aligned} \Delta\gamma = & \left[ \gamma_F + \gamma_{CR} - 2(\sqrt{\gamma_F^D \gamma_{CR}^D} + \sqrt{\gamma_F^P \gamma_{CR}^P}) \right] \\ & - \left[ \gamma_F + \gamma_{EPDM} - 2(\sqrt{\gamma_F^D \gamma_{EPDM}^D} + \sqrt{\gamma_F^P \gamma_{EPDM}^P}) \right]. \end{aligned} \quad (5)$$

The dispersive and polar parts of the surface energies were calculated from contact angle measurements with test liquids of different surface tension and polarity, using a modified Wilhelmy technique [79]: Organoclay filler:  $\gamma_F = \gamma_F^D + \gamma_F^P = 24.3 \text{ mJ m}^{-2} + 1.0 \text{ mJ m}^{-2}$  EPDM:  $\gamma_{EPDM} = \gamma_{EPDM}^D + \gamma_{EPDM}^P = 24.2 \text{ mJ m}^{-2} + 7.6 \text{ mJ m}^{-2}$  CR:  $\gamma_{CR} = \gamma_{CR}^D + \gamma_{CR}^P = 22.5 \text{ mJ m}^{-2} + 12.8 \text{ mJ m}^{-2}$ .

After considering the above values of  $\gamma_F$ ,  $\gamma_{EPDM}$  and  $\gamma_{CR}$  from contact angle measurements, the difference interfacial energies  $\Delta\gamma$  according to (3) has a value of  $-3.4 \text{ mJ m}^{-2}$ . This negative value leads to the conclusion that the migration of the clay particles from EPDM phase to CR phase is a thermodynamically favorable process. Exactly similar behavior has also been reported by Gödel et al. [80] while working with multiwalled carbon nanotubes in polycarbonate (PC) and polystyrene–acrylonitrile (SAN) blends. The migration of carbon nanotubes from SAN phase to PC phase was also understood in terms of an interfacial energy driven process.

TEM images (Fig. 42a, b) also supported the overall exfoliation of clay in CR for blends with a ratio of 25/75 and 50/50 of EPDM to CR. A striking difference in the dispersion of the clay can be observed if the TEM image of the 75/25 blend is



compared with the 25/75 and 50/50 blends of EPDM and CR. The existence of various large aggregated structures of the clay indicates a poor dispersion at this particular blend ratio, and the effect was reflected in other properties like a low Young's modulus, etc. (discussed at the end of this section).

It is a common phenomenon that the intercalated–exfoliated clay coexists in the bulk and in the interface of a blend. Previous studies of polymer blend–clay systems usually show that the clay resides either at the interface [81] or in the bulk [82]. The simultaneous existence of clay layers in the interface and bulk allows two functions to be attributed to the nanoclay particles: one as a compatibilizer because the clays are being accumulated at the interface, and the other as a nanofiller that can reinforce the rubber polymer and subsequently improve the mechanical properties of the compound. The firm existence of the exfoliated clay layers and an interconnected chain-like structure at the interface of CR and EPDM (as evident from Fig. 42a, b) surely affects the interfacial energy between CR and EPDM, and these arrangements seem to enhance the compatibility between the two rubbers.

The dependence of the storage modulus ( $E'$ ) on the strain amplitude at very low strain gives an understanding of the impact of the filler network within the rubber matrix. Generally,  $E'$  remains unaltered with increasing strain for an unfilled rubber system. However, for a filled system, the storage modulus decreases with increasing strain. This nonlinear behavior of a filled rubber system is called the Payne effect [41] and yields information about filler–filler networking in the rubber matrix (see Sect. 3.1.2). In our investigations, the plots of  $E'$  versus double strain amplitude of the CR/EPDM blends are shown in Fig. 43a. It is evident from this figure that the gum blend without any filler does not undergo any change in  $E'$  with increasing strain. However, a strong dependency can be observed for all filled samples. Here, all rubber blends are filled with only 10 phr of clay and, obviously, these clay particles, being either exfoliated and/or intercalated, build a strong filler–filler network in the rubber matrix. The preferential localization of the clay at the interface fulfills the demand to remain in contact with hydrogen bonding by the virtue of hydroxyl group of clay (end-to-end coupling). Moreover, it is quite interesting to discuss the very high value of  $E'$  at the low strain region. A very high  $E'$  value ( $\sim 45$  MPa) at low loading of clay ( $< 10$  wt%) has not been reported in the literature so far. For example, the value of  $E'$  was found to be only  $\sim 9$  MPa in a natural rubber filled with 20 wt% of nanoclay [83]. These observations can only be explained if a large amount of delaminated silicate particles come out from the nanoclay stacks through the exfoliation process. In the CR/EPDM blend it can be observed that, with the increase of the EPDM content, the filler–filler networking decreases. This can be attributed to relatively smaller space availability (CR phase) of the clay particles at a fixed volume and, consequently, the clay particles are forced to remain in nonintercalated–exfoliated form (Fig. 42c). This figure also indicates the same explanation for these facts. It is observed from this TEM image of the 75 EPDM/25 CR blend that clay particles remain in the agglomerated form and this finding directly corroborates the above observations. Nevertheless, the single exfoliated particles can be seen in Fig. 42d, where several single clay platelets are embedded in the 25 EPDM/75 CR blend

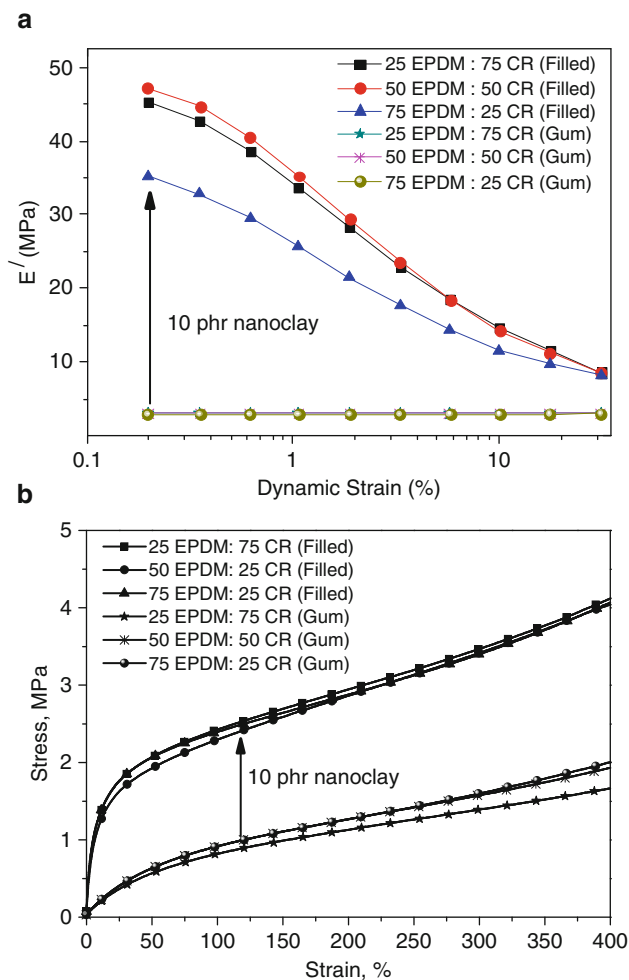


**Fig. 4.3** Effect of dynamic strain amplitude on storage modulus (a). Stress–strain behavior of CR/EPDM blend in the absence and presence of nanoclay (b). For this experiment, tension mode was selected for the variation of the dynamic strain from 0.01 to 40% at 10 Hz frequency

matrix. But, in the stress–strain experiment, at the low strain regime all blends exhibit the same nature (Fig. 4.3b).

Dynamic mechanical analysis (DMA) has been carried out to understand the dynamic response of the blend after the addition of clay. The dependency of the storage modulus obtained from oscillatory tension deformation as a function of temperature is given in Fig. 4.4. All samples show a steep decrease of  $E'$  over the temperature range  $T = -50$  to  $-20^\circ\text{C}$  followed by a rubbery plateau (Fig. 4.4a). The most exciting information, observed in this figure, is the increase of modulus values at room temperature by the addition of clay. The storage modulus increases from 2 MPa to 54 MPa with the addition of only 10 phr clay in the 25 EPDM/75 CR

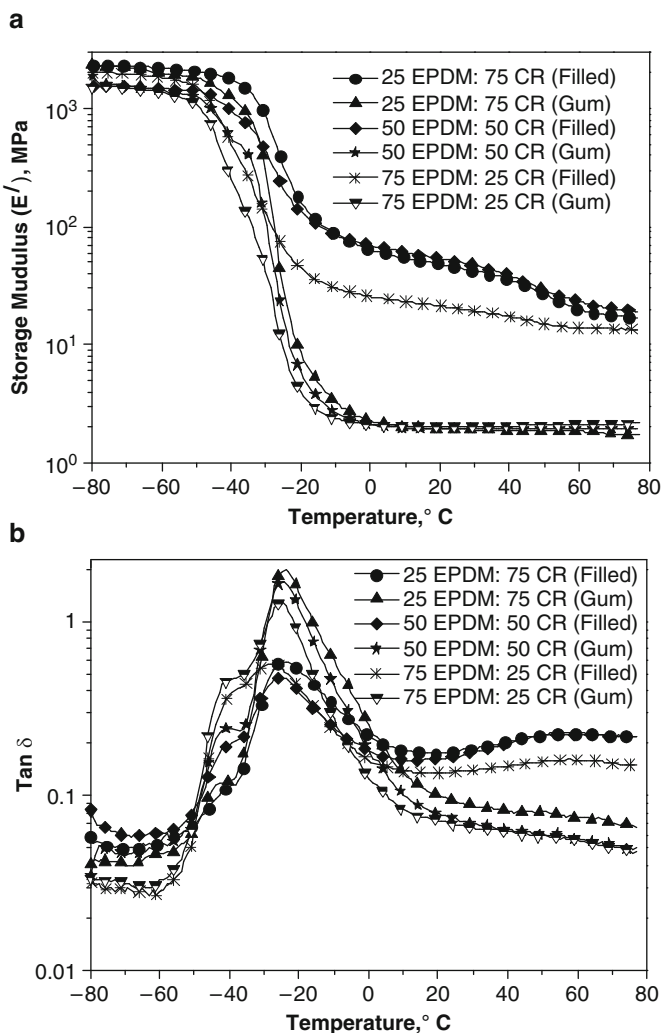


**Fig. 44** Storage modulus ( $E'$ ) versus temperature (a), and  $\tan \delta$  versus temperature (b) plots of CR/EPDM blends in the absence and presence of nanoclay

matrix. A good state of exfoliation of the clay in the CR matrix reinforced the rubber blend very strongly. A sufficiently strong filler–filler interaction as well as the compatibility between CR and EPDM play major roles in giving rise to a very highly reinforced rubber matrix.

The  $T_g$  of a rubber or polymer depends on the structure and cooperative mobility of the chain segments. In the case of partially compatible blends, the  $T_g$  values of the blend components are expected to be shifted toward each other as compared with the pure components. The  $T_g$  values remain largely unaltered for a completely incompatible blend. Fig. 44b shows the  $\tan \delta$  dependencies on the temperature for

**Table 9** Glass transition temperature of EPDM/CR rubber blends

Rubber <sup>a</sup>	Glass transition temperature (°C)					
	Without clay			With clay		
	EPDM peak	CR peak	Separation between two peaks	EPDM peak	CR peak	Separation between two peaks
100:0	−37	<i>a</i>	−	−37	<i>a</i>	−
75:25	−44	−25	19	−42	−26	16
50:50	−42	−25	17	−41	−27	14
25:75	−40	−24	16	−35	−28	7
0:100	<i>a</i>	−24	−	<i>a</i>	−24	−

<sup>a</sup>The curing recipe used in this study was 5 phr zinc oxide, 10 phr stearic acid, 7 phr ZDMC, and 1 phr sulfur.

*a* absent for that particular case

the CR/EPDM blend systems, and the  $T_g$  of the corresponding rubbers are listed in Table 9. The two pure vulcanized rubbers show  $T_g$  at  $-37$  and  $-24^\circ\text{C}$  and, even after incorporation of the clay, the values remain unaltered. However, those rubbers remaining in the blend system showed different  $T_g$  values. It is clear from Table 9 that the  $T_g$  values are closer when the blend matrix is filled with 10 phr clay, which indicates that the clays have a strong capability to increase compatibility between two heterorubbers. A shift of  $9^\circ\text{C}$  was observed for the 75 CR/25 EPDM blend. Exactly the opposite type of behavior was found [74] for an incompatible rubber blend, as revealed by the situation when the clay interferes with the compatibility between chloroprene and XNBR during the self-crosslinking reaction.

It is also important to note that even at higher temperatures ( $40$ – $60^\circ\text{C}$ ), a second flat and broad relaxation process is observed for the blends containing clay. Such a process at the same temperature range has been reported for a CR–clay composite [23]. In that work, we proposed that the rubber (especially CR chain segments) is partially crystallized in the presence of organically modified clay. Very recently [84] such a process has been explained by considering the fact that, during the measurement of the dynamic mechanical properties, the anisotropic fillers are arranged in such a way that they have to reorient by following the applied mechanical field and additional energy dissipation sets, resulting in relaxation at higher temperatures [85]. Finally, from stress–stress experiments it was found that the Young's modulus increases from 1.93 MPa to 27.24 MPa with the addition of 10 phr clay along with 10 phr stearic acid. However, it is evident from Fig. 43b that the improvement of tensile properties is not as high as expected from other studies. Insufficient cross-linking of the rubber matrix could be the reason behind this observation.

## 5.2 CR/XNBR

Various blends of functionally active rubbers are reported to be capable of partial crosslinking at high temperatures in the absence of any curatives. Some of these

self-vulcanizable rubber blends include binary blends of epoxidized natural rubber (ENR)/XNBR, ENR/CR, CR/XNBR, chlorosulfonated polyethylene/XNBR, and ENR/chlorosulfonated polyethylene [86]. For instance, the interfacial crosslinking of CR and XNBR takes place as a result of the reaction of the active tertiary allylic chlorine of CR with the  $-\text{COOH}$  group of XNBR, with the elimination of hydrochloric acid [87]. However, the  $T_g$  of those two rubbers are widely separated and, hence, CR and XNBR are immiscible.

It is also interesting to look into the chemical interactions of organoclay (QUAT-modified MMT) with functionally polar rubbers like XNBR, CR, and their mutual blend. The role of layered silicate on the curing process of CR/XNBR blends was investigated through the study of curing kinetics, mechanical properties, WAXS, and DMA [74].

### 5.2.1 Preparation

The formulations of the rubber compounds are given in Table 10. For the preparation of CR–organoclay and XNBR–organoclay single rubber composites, those two pure rubbers were individually mixed with organoclay at  $180^\circ\text{C}$  by an internal mixer. In order to produce rubber blends, the masticated preblended rubbers were mixed with organoclay at a relatively low temperature of  $100^\circ\text{C}$  using an internal mixer. The mixing time was 10 min for all the samples. After taking out the rubber compounds from the internal mixer, the sulfur curatives were added with an open two-roll mixing mill.

**Table 10** Formulations and physical properties of CR and XNBR and their blends

Mix <sup>a</sup> no.	CR (%)	XNBR (%)	Organoclay loading (phr)	Swelling index	Crosslinking density <sup>c</sup> (mmol/100 g)
1	100	0	0	– <sup>b</sup>	– <sup>b</sup>
2	75	25	0	3.58	1.39
3	50	50	0	3.70	1.21
4	25	75	0	5.11	0.72
5	0	100	0	– <sup>b</sup>	– <sup>b</sup>
6	100	0	10	– <sup>b</sup>	– <sup>b</sup>
7	75	25	10	2.90	1.01
8	50	50	10	3.22	0.82
9	25	75	10	4.14	0.51
10	0	100	10	– <sup>b</sup>	– <sup>b</sup>

<sup>a</sup>The curative packages contained MgO 4 phr, ZnO 5 phr, stearic acid 2 phr, zinc dithiocarbamate 6 phr, sulfur 1 phr, and ethylene thiourea 1 phr

<sup>b</sup>The crosslinking densities of the 100% pure rubbers (uncrosslinked) have not been measured

<sup>c</sup>The crosslinking density of the filled vulcanisate is calculated considering the organoclay as a coarse spherical particle. If we consider the shape factor, the values of the crosslinking density of the filled sample will be much lower than the present values

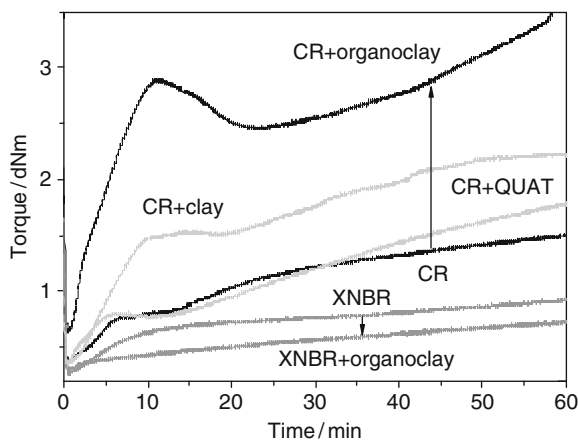
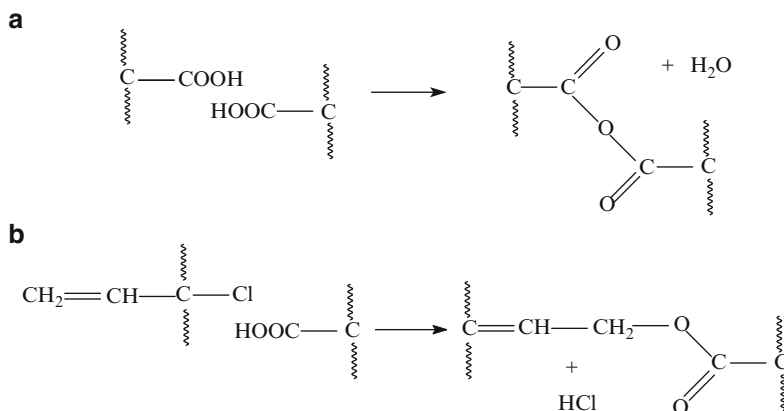


**Fig. 45** Rheographs obtained from CR and XNBR in the presence of some additives at 180°C. Arrows indicate the influence of organoclay on the torque during heating of pure CR and XNBR

### 5.2.2 Characterization

Figure 45 depicts the improvement of torque against time at 180°C for CR and XNBR in the presence of clay, organoclay, and the organic modifier. A QUAT compound (di-steryldimethyl ammonium) was used to modify the clay. To see the effect of this amine modifier, an equivalent amount of that amine was mixed with CR and a rheometric study performed at 180°C. It is evident from Fig. 45 that the torque gradually increases for CR under thermal treatment, but for XNBR the response is little in developing the elastic modulus. The presence of 1.4% of the tertiary allylic chlorine atom on the backbone of CR chain is responsible for this thermal crosslinking [88]. In the presence of MMT clay, the extent of crosslinking is higher than for plain CR. So, the clay acts here as a crosslinking catalyst by actively taking part in thermal dehydrohalogenation reactions. The excess metal cations, present on the surface, might react with the chloride to form metal chloride and thus facilitate the crosslinking reactions [89]. This crosslinking acceleration activity is noticed very well when the CR matrix is filled with amine-modified clay. The QUAT, present in the organoclay as a modifier, is supposed to take part in the initial stage of the thermal reaction, but it should be noted that the presence of this QUAT alone is not able to accelerate the crosslinking. Clay together with QUAT increases the ultimate torque to a considerable extent. This interesting behavior of amine-modified MMT clay with respect to the thermal curing of CR can be called cure synergism by functional fillers. Here, it should be noted that curing or crosslinking of CR cannot be promoted by an organic molecule with only one amine group, but only by the organic molecules with at least two amine groups. These two amine groups anchor the two CR rubber chains by the participation of the tertiary allylic carbon atom of the CR chain in an electrophilic substitution reaction with the nitrogen atom of the amine. This mechanism of CR crosslinking is called

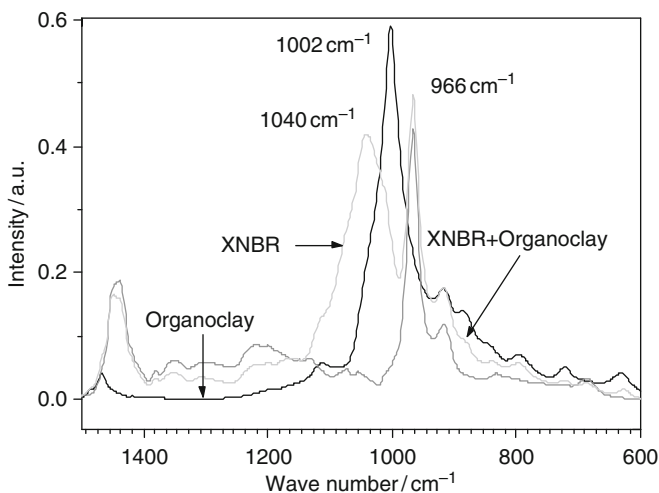


**Scheme 2** Formation of carboxylic anhydride at 180°C temperature as a crosslink in the XNBR matrix (a), and ester linkage between CR and XNBR produced during heating at 180°C (b)

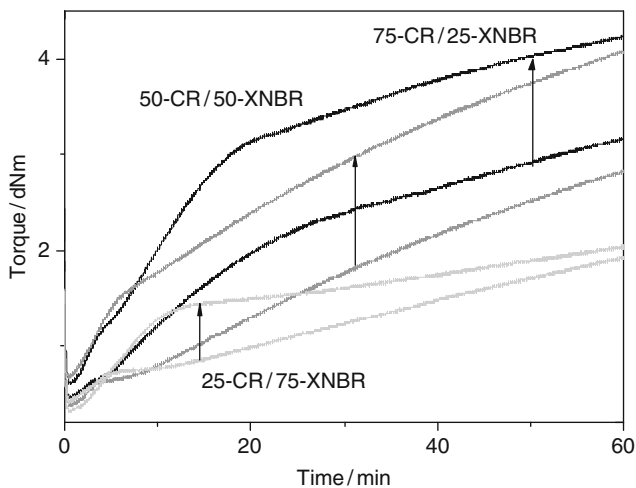
bis-alkylation [90]. In contrast to the above role of organoclay, a negative influence on the thermal crosslinking of XNBR was observed by reducing the ultimate torque. Since the rubbers were heated at 180°C, a dehydration of carboxylic acid may occur, which leads to thermal crosslinking of XNBR. The mechanism is shown in Scheme 2. In the presence of organoclay, the carboxylic group is blocked either by the ammonium compound present on the clay or by the hydrogen bonding between silanol group of clay and carboxylic group of XNBR. Therefore, the carboxylic groups neither undergo a dehydration reaction, nor do they form any acid anhydride crosslinks.

Figure 46 shows the IR spectra of pure XNBR, organomodified layered silicate, and XNBR-layered silicate compound. The XNBR-layered silicate compound was prepared at 180°C in an internal mixer for 10 min. From this figure it can be seen that the out-of-plane vibration of Si–OH ( $1,002\text{ cm}^{-1}$ ) of the organoclay sample has been shifted neatly towards a higher frequency ( $1,040\text{ cm}^{-1}$ ). The silanol groups of silicate particles form a hydrogen bond with the carboxylic group of XNBR, which results in shifting of the Si–OH vibration from lower to higher frequency. However, no significant change in the C=O stretching frequency (not shown in Fig. 46) of the COOH is observed after the incorporation of layered silicate in the XNBR matrix.

It is well established that CR and XNBR undergo a chemical crosslinking reaction without any extra crosslinking agent (Scheme 2b). The influence of organoclay on this self-crosslinking of the rubbers at various compositions is evidenced from the results of a rheometric study at 180°C (Fig. 47). The development of torque of different blends with time is given. This figure shows that all three compositions of the blends, containing 10-phr layered silicate, offer a superior state of cure as compared to their respective gum. The increase of the torque values by the organoclays can be explained by the presence of the hard filler particles and the modification of overall crosslinking density of the rubbers by the organoclay. To understand the self crosslinking between the carboxylic group of XNBR and the



**Fig. 46** ATR-IR spectra of pure XNBR, XNBR–organoclay, and organoclay



**Fig. 47** Rheographs obtained from self-crosslinkable CR/XNBR blends of different composition at 180°C. *Arrows* indicate the development of torque after addition of 10 phr organoclay

tertiary allylic chloride of the CR chain, ATR-IR spectra were obtained. Figure 48 depicts the spectra obtained from two pure virgin rubbers and their blend (75 CR/25 XNBR) in the presence and absence of organoclay. The spectrum obtained from pure CR has some characteristic features, which include a C=C strong band at  $\sim 1,697\text{ cm}^{-1}$  and multiple C-H and C-C bending and stretching vibrations at



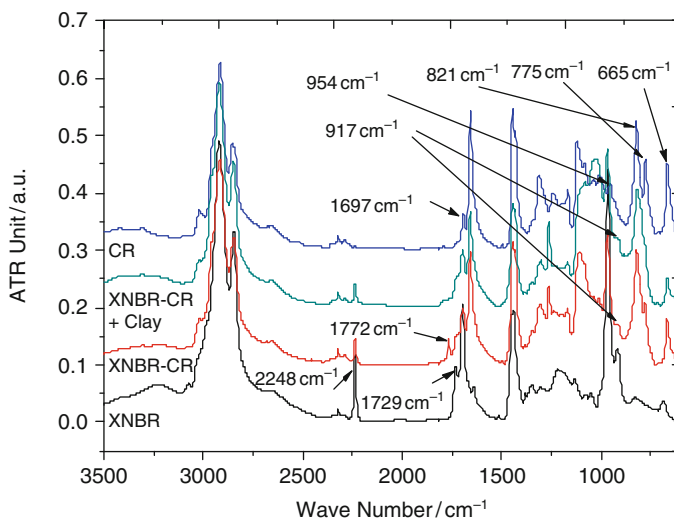


**Fig. 48** ATR-IR spectra of CR and XNBR and their blends in the presence and absence of organoclay

$\sim 1,445$ ,  $1,431$ ,  $1,303$ ,  $1,202$ ,  $1,118$ , and  $1,001$   $\text{cm}^{-1}$ . The C–Cl stretching and bending bands appear at  $821$ ,  $775$ , and  $665$   $\text{cm}^{-1}$ . A small band is also observed for  $=\text{CH}_2$  out-of-plane vibration of the isomerized 1,2-units at  $954$   $\text{cm}^{-1}$ . Obviously, there are some common bands with CR in the pure XNBR spectrum due to the existence of  $\text{C}=\text{C}$ , multiple C–H, and C–C bending and stretching vibrations. The characteristic absorbance of  $-\text{C}\equiv\text{N}$  of XNBR can be observed at  $2,248$   $\text{cm}^{-1}$ . Peaks in the  $1,729$   $\text{cm}^{-1}$  area stem from the  $>\text{C}=\text{O}$  group of the carboxylic part in the rubber. This band is shifted to higher wave number ( $1,772$   $\text{cm}^{-1}$ ) in the spectrum of 75 CR/25 XNBR, which indicates the chemical interaction of carboxylic group of XNBR with the tertiary allylic chlorine of the isomerized 1,2-unit of CR. Interestingly, in the presence of organoclay the characteristic peak for  $>\text{C}=\text{O}$  in ester-type linkage is missing. However, in the area between  $1,772$  and  $1,729$   $\text{cm}^{-1}$ , a broad shoulder-type peak appears on the organoclay-filled CR/XNBR blend. It is assumed that in the presence of organoclay either the surface of XNBR is blocked by the clay platelets or the carboxylic groups form hydrogen bonding with the silanol group of silicate particles without taking part in the crosslinking reactions. It is also observed that the band at  $954$   $\text{cm}^{-1}$ , which is expected to come from the out-of-plane  $=\text{CH}_2$  of CR, disappeared in the blends and a new peak appeared at  $917$   $\text{cm}^{-1}$ . This shifting of peak in both cases indicates that most of the reactive tertiary allylic chloride groups react or that they are consumed by other reactive sites of rubber chains. So, it can be assumed that, in the presence of organoclay, the active groups of CR crosslink with each other rather than react with the XNBR phase, because the active carboxylic groups are

no longer available for this reaction. On the basis of these arguments, we conclude that organoclay promotes a phase-separated morphology of the blends without any chemical crosslinking between CR and XNBR. Discussion about the crosslinking density as well as the swelling index will be insightful in this case. The degree of the swelling (i.e.,  $Q$  values) are given in the Table 10. With the increase of CR content in the blend, the  $Q$  values decrease, which means that CR is more solvent-resistant than XNBR. Another explanation could be given for this if the crosslinking density is correlated with the reciprocal of swelling index. The crosslinking density decreases with a decrease in the CR content in the self-crosslinked blends. This is also true for the blends containing layered silicates. Crosslinking density was determined by solvent swelling method and the values are given in Table 10. It is found from Table 10 that the crosslinking density of the vulcanizates follow the same trend with blend composition as revealed from the swelling study. However, what is more interesting, is that the crosslinking values of the filled sample are always less than the corresponding gum samples. That means that the layered silicates interrupt the self-crosslinking process between tertiary allylic chlorine of CR and the carboxylic group of XNBR. It should be mentioned here that the crosslinking density of the filled sample is estimated by considering the gum state equivalent and using the Einstein–Smallwood equation. If we consider the shape factor [91] of the anisotropic layered silicate particles in this equation, then the crosslinking value of the filled sample would be lowered further below that of the estimated values.

It is also of interest to see in the presence of nanoclay whether the phase-separated morphology of the blend affects the physical properties. As observed from Fig. 49, the 50% moduli of the organoclay-filled self-crosslinked rubber matrix remain more or less same compared to the corresponding unfilled rubber matrix at all blend ratios. Tensile strength is very badly affected by the addition of organoclay, especially in the case of 75 CR/25 XNBR. In order to get the beneficial effect of the layered silicate, the rubber blends were also cured by a sulfur vulcanization package. Remarkable improvements of the 50% modulus, as well as the tensile strength were observed. In addition to the extra self-crosslinks from XNBR and CR, the sulfur vulcanizing package leads to sulfur bridges between two different rubber chains in the blend, depending on the availability of allylic double bonds of the CR. However, in this case, one of the diene rubbers is CR and the fitness of sulfur vulcanization of CR is still a research topic and beyond the scope of the present discussion. However, it is concluded that the physical properties of such types of heterogeneous blends could be improved with layered silicate if sulfur vulcanization becomes one of the choices for crosslinking precursors.

It is evident from Fig. 50 that the self-crosslinked blend of 75 CR/25 XNBR containing 10 phr of organoclay shows no reflection in the  $2\theta$  range of  $1\text{--}9^\circ$ . The absence of any peak in the XRD patterns could be one indication of exfoliation of the organoclay. However, for the other two blends the presence of the characteristic peak of organoclay indicates an intercalated clay morphology in the matrix. The blend containing 50% CR exhibits higher gallery height as compared to the blend with 25% CR.

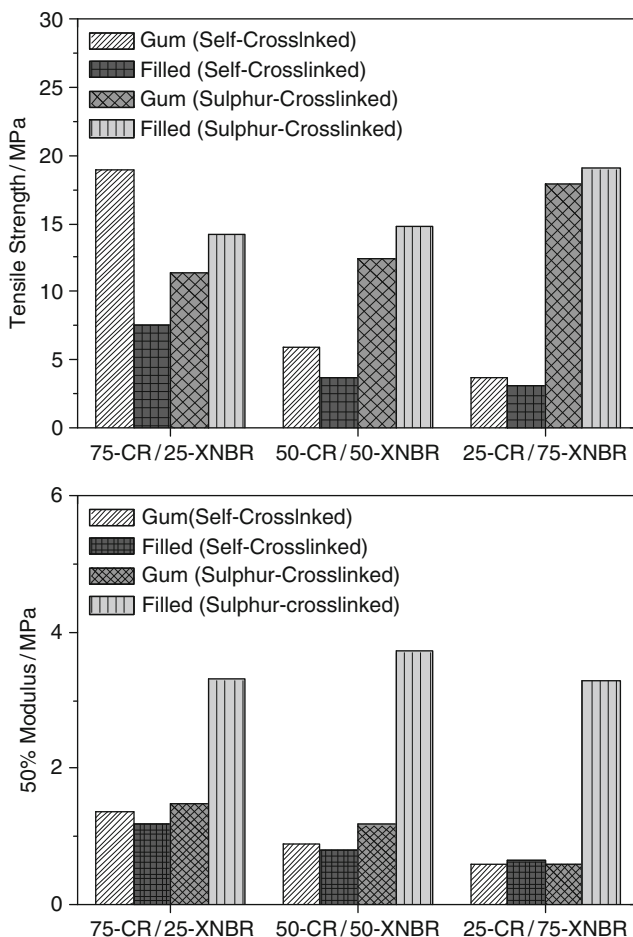


**Fig. 49** Physical properties in terms of tensile strength (*top*) and 50% modulus (*bottom*) for CR-XNBR blends obtained from self-crosslinking and sulfur-crosslinking processes

Though the blends contain the intercalated clay structures, the tensile properties were not improved, as discussed in the previous section. The layers of the organoclay make the blends more immiscible and generate a heterogeneous phase morphology, which ultimately deteriorates the tensile properties of the blend composites. It is interesting to look into the intercalation of the clays in the blends if the rubber blends are efficiently cured by sulfur vulcanization packages. The XNBR–organoclay shows three peaks corresponding to the  $\langle 001 \rangle$ ,  $\langle 002 \rangle$ , and  $\langle 003 \rangle$  planes of the clay, whereas CR–organoclay shows only one peak corresponding to the reflection from the  $\langle 001 \rangle$  plane of the clay (Fig. 50). The gallery height is 3.97 nm for XNBR and 4.85 nm for CR. The higher  $d$ -space of organoclay in pure CR may be due to higher surface energy of the CR, which

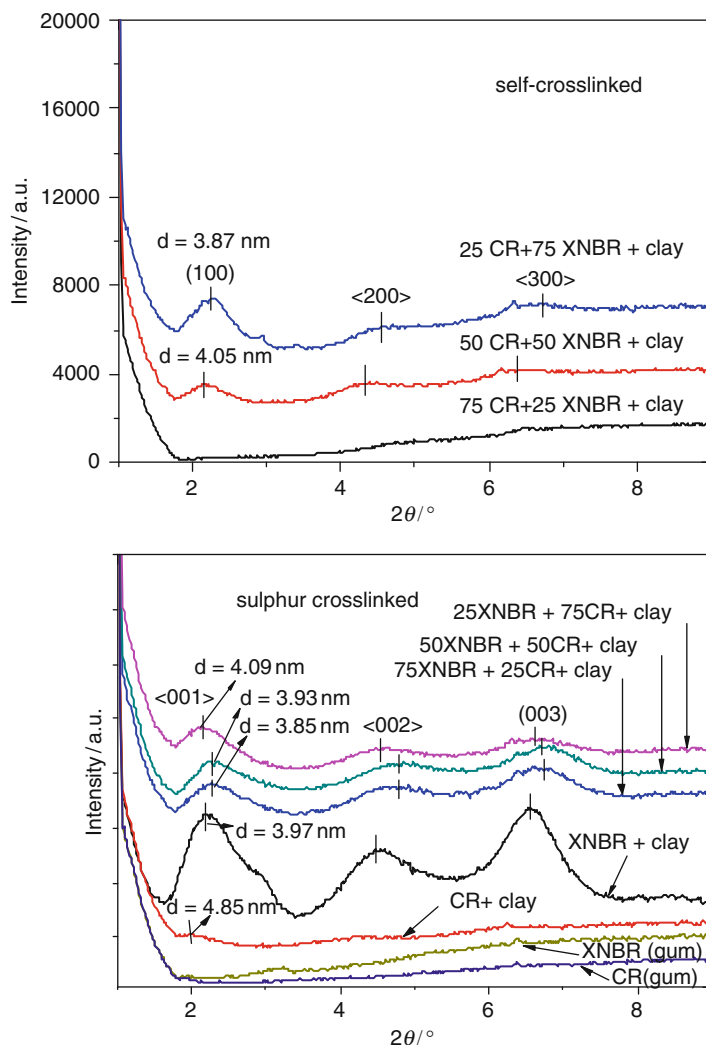


**Fig. 50** WAXD patterns of CR and XNBR and their blends obtained from self-crosslinking (*top*) and sulfur crosslinking (*bottom*) processes

promotes higher intercalation of the CR chains. As far as the diffraction patterns of the blends are concerned, in all cases three distinct harmonic peaks are observed, which are the reflections of  $\langle 001 \rangle$  plane and so on. It is shown that as the content of CR in blends increases from 25% to 75%, the interlayer  $d$ -spacing of the organoclay increases gradually from 3.85 to 4.09 nm, demonstrating that higher CR levels lead to better intercalation of the clay.

The  $T_g$  of a rubber or polymer depends on the structure and cooperative mobility of the chain segments. Only one glass transition is expected if two polymers are

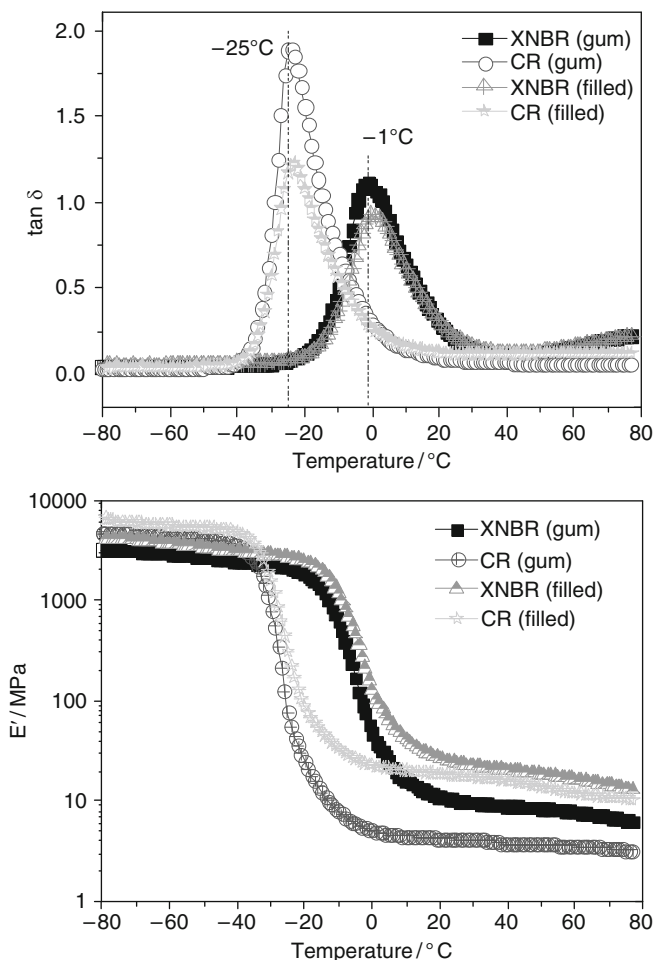


**Fig. 51** DMTA plots of  $\tan \delta$  versus temperature (*top*) and storage modulus versus temperature (*bottom*) for XNBR and CR compounds vulcanized by sulfur

completely miscible. In the case of partially miscible blends, the  $T_g$  values of the blend components are separated but shifted towards each other as compared with the pure components. The  $T_g$  values remain largely unaltered for a completely immiscible blend. Figure 51 shows the  $\tan \delta$  dependencies on temperature for the pure CR and XNBR, crosslinked with sulfur and containing 10 phr organoclay. The results are compared with the corresponding gum rubber matrix without any filler. Gum as well as filled CR rubber matrices show a  $T_g$  at  $-25^{\circ}\text{C}$ , whereas XNBR shows the transition at  $-1^{\circ}\text{C}$ . In both cases, the incorporation of 10 phr organoclay remarkably reduces the peak heights, which indicates strong reinforcement by the organoclay. The presence of intercalated organoclays restricts the mobility of the

rubber chains due to their confinement between the layers. More precisely, it can be stated that the polar nature of CR and XNBR intercalates or exfoliates the silicate layers very efficiently and a strong rubber–filler interaction is established. Section 3.3.2 discusses an additional dielectric relaxation phenomenon, which was mainly governed by the chemical interaction of layered silicate with XNBR at higher temperature than  $T_g$  [39]. The plots of storage modulus ( $E'$ ) with temperature also indicate a strong reinforcement offered by the organoclay, since a considerable increase in  $E'$  of moderate temperatures is observed (Fig. 51). It is clear that two widely separated different  $T_g$  values primarily indicate the immiscibility of the phase if a blend is prepared with those rubbers. The damping behavior ( $\tan \delta$ ) of the blends with increasing temperature delivers some interesting information about the miscibility of the rubber with two different  $T_g$  values. For easy understanding, the  $T_g$  values obtained from temperature sweep experiments are listed in Table 11. It can be seen from this table that with the increase of XNBR content the  $T_g$  values of CR and XNBR shift to a lower temperature in all composites. This decrease in  $T_g$  of the polymers may be explained if one considers the difference in the thermal expansion coefficient of the respective polymers in a blend, resulting in thermal stress across the boundary and development of a negative pressure within the rubber domains. Thus, the free volume of the rubber component increases and, consequently, the motion of the rubber chain becomes easier [92]. After analyzing the data in the table it is observed that the separation factor between the two  $T_g$  peaks is increased in all blends containing layered silicate, and that the difference between those  $T_g$  is maximum for the 50/50 rubber blend. For the clay-containing 50/50 blend, the separation is 26°K, whereas the separation is 20°K for the same blend without organoclay. So, presence of 10 phr organoclay makes the blends more heterogeneous as compared to their virgin composition. This finding also supports the inhibition action of layered silicate to self-crosslinking by blocking the carboxylic group from forming hydrogen bonds with the silanol group of the clay layers, rendering the carboxylic group passive to crosslinking. As far as the storage modulus ( $E'$ ) of the self-crosslinked blends is concerned, a relaxation at 40°C is observed in all the blends (Fig. 52). This relaxation arises due to melting of crystalline domains of the CR chains, and the effect is more prominent in blends of higher CR content without any filler. In the presence of organoclay, the

**Table 11** Glass transition temperature of self-crosslinked CR/XNBR rubber blends

Rubber	Glass transition temperature (°C)					
	Without clay			With clay		
	CR peak	XNBR	Separation between two peaks	CR peak	XNBR peak	Separation between two peaks
100:0	–25	<i>a</i>	–	–25	<i>a</i>	–
75:25	–23	–4	19	–24	–4	20
50:50	–26	–6	20	–28	–2	26
25:75	–29	–8	21	–30	–7	23
0:100	<i>a</i>	–1	–	<i>a</i>	–1	–

*a* absent for that particular case

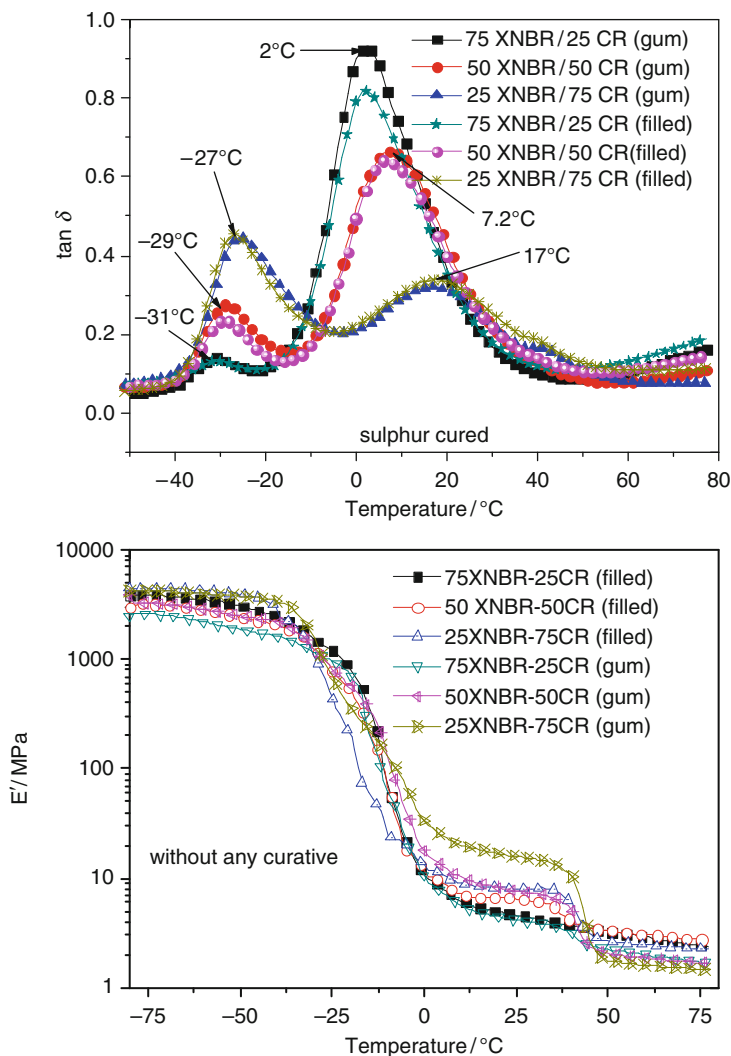


**Fig. 52**  $\tan \delta$  versus temperature plots of CR-XNBR blends vulcanized by sulfur (*top*). Storage modulus versus temperature plots of self-crosslinked CR-XNBR blends (*bottom*)

crystalline nature of the CR phase is reduced. It will be also interesting to discuss the damping behavior of those composites that are crosslinked by sulfur curatives. Figure 52 shows  $\tan \delta$  versus temperature curves obtained from sulfur-crosslinked CR/XNBR blends in the presence and absence of organoclay. All the curves possess two distinct relaxation peaks at different temperatures. It can be observed that with the increase of CR content in the blends, the  $T_g$  values corresponding to XNBR are shifted to a higher temperature to a remarkable extent; the  $T_g$  of XNBR in the

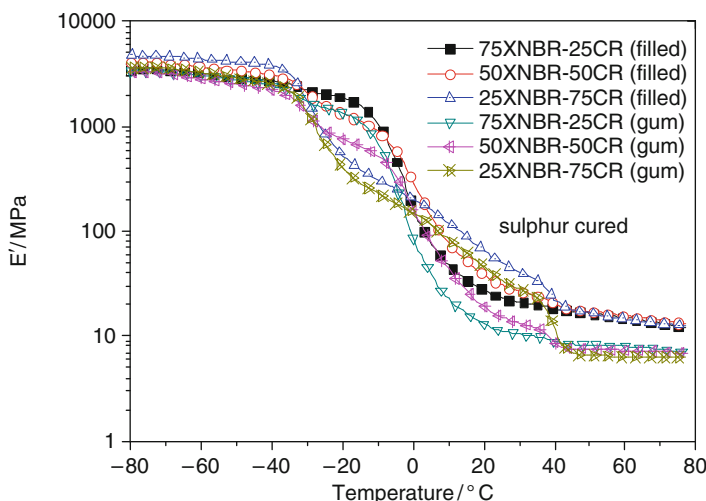


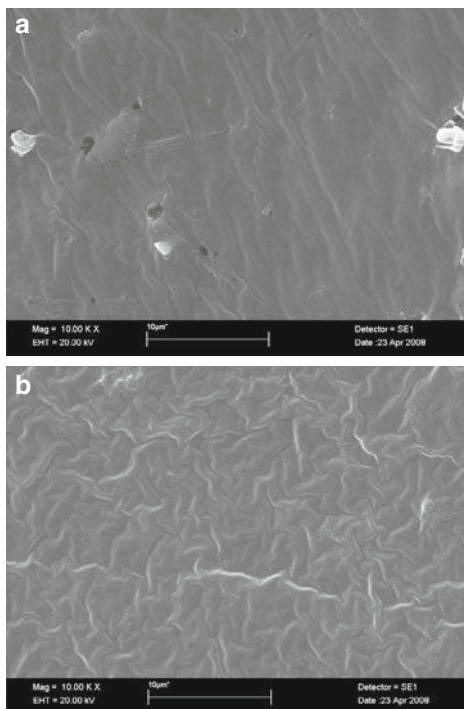
Fig. 53 Storage modulus versus temperature plots of CR-XNBR blends vulcanized by sulfur

25 XNBR/75 CR blend is shifted from  $-1$  to  $17^{\circ}\text{C}$  as compared with pure XNBR. However, the shifting of  $T_g$  of the corresponding CR portion is only a few degrees. This may be explained by considering the polarity difference between XNBR and CR. Migration of curatives can take place from the less polar CR part to the more polar XNBR part and, ultimately, the XNBR phase becomes highly crosslinked. Thus, the mobility of the XNBR chains is greatly reduced and the  $T_g$  increases to a considerable extent. Any significant change in the damping behavior is not noticed after incorporation of the organoclay in the rubber blends. It is also evident from Fig. 52 that  $E'$  decreases with increasing temperature and that all the blends show a three-step relaxation process. The first two steps arise from the glass transition of the CR and XNBR phase and the third relaxation at  $\approx 40^{\circ}\text{C}$  is supposed to come from the microcrystalline phase of CR chain segments. At this temperature, the crystal structures disappear and an extra slippage within the crystal domain of the rubber chain takes place. The same behavior of  $E'$  against temperature can be observed from the sulfur-cured CR/XNBR blends. Figure 53 shows the temperature dependency of the storage modulus of those sulfur-cured samples. From this figure the clear crystalline nature of CR at the blend composition 75 CR/25 XNBR can also be observed. Morphological heterogeneity makes the CR phase more crystalline with the higher content of CR, in spite of a strong sulfur crosslinking network in the blend matrix. However, above  $40^{\circ}\text{C}$  the storage modulus of filled blends show a higher  $E'$  value as compared to the corresponding gum blends, demonstrating the apparent reinforcing ability of organoclay in all blends irrespective of their composition.

The micrographs obtained from scanning electron microscopy are shown in Fig. 54 for the tensile fractured surface of 50 CR/50 XNBR self-crosslinked blend filled with 10 phr layered silicate (Fig. 54a) and for the same blend without any



**Fig. 54** Scanning electron micrographs of the tensile fractured surface of 50 CR/50 XNBR blends with modified layered silicate (a) and without any filler (b)



layered silicate (Fig. 54b). It is evident from Fig. 54a that some agglomerates of organoclay are pulled out from the matrix onto the fractured surface. As compared with Fig. 54b, there is a very clear difference in the texture of the surface. The surface of the gum rubber is more homogeneous and displays a knitting texture, which is a characteristic of a partially compatibilized rubber blend containing XNBR as one of the constituents [93]. In contrast, the surface of filled rubber does not have this texture. The inhomogeneous surface obtained from filled rubber vulcanizates clearly indicates the poor tensile properties. These findings confirm the negative influence of layered silicate on the compatibility of CR and XNBR phases.

## 6 Rubber–Anionic Clay Nanocomposites

During the past decade, rubber-layered silicate nanocomposites have been extensively studied for a variety of applications and in this review the preparation and characterization of such layered silicate–rubber composites is discussed. However, use of another type of clay, called anionic clay or LDH, in the rubber matrix is rather uncommon. In this section, rubber–LDH nanocomposites are described, including the synthesis and characterization of OLDH, preparation of rubber–LDH nanocomposites, and their special properties [94, 95].

## 6.1 Synthesis

It can be easily understood that the homogeneous and stable dispersion of LDH in rubber is a very difficult task because of organic–inorganic incompatibility and strong attractive forces between the two hydroxides layers. However, it is necessary to obtain a homogenous dispersion of nanoparticles in the rubber matrix to get a significant improvement in mechanical properties with a small filler concentration. As mentioned in the discussion in Sect. 2.3, to obtain good dispersion of LDH in the rubber matrix, the organic modification of LDH is necessary before using it as a filler. Generally, there are three main modification methods for preparing OLDH:

1. *Regeneration*: Many LDH materials show a unique phenomenon called “memory effect,” which involves the regeneration of the layered crystalline structure from their calcinated form when the latter is dispersed in an aqueous solution containing suitable anions [96]. This property is often used to synthesize and modify LDH with different types of intercalating anions. The regeneration property shown by LDH is extensively reported in the literature [97, 98].
2. *Anion exchange*: This method takes the advantage of exchangeable interlayer anions present in LDH by other anionic species. Based on this property, the LDH containing one type of intercalating anionic species can be synthesized from the LDH containing another type of intercalating anion. Usually, the original LDH is dispersed in an aqueous solution of the desired anionic species and the dispersion is stirred at room temperature for several hours. However, some anionic species show more affinity for the intergallery region of LDH than others [99].
3. *One step synthesis*: This is an effective and easy method for preparation of OLDH and was developed recently. No additional measures other than controlling the pH of the medium are required to obtain a high degree of intercalation by the surfactant, retaining the high crystallinity independently of the presence of other anions, like  $\text{NO}_3^-$ ,  $\text{CO}_3^{2-}$  and  $\text{Cl}^-$  [100, 101]. During synthesis, the pH value is kept constant by adding suitable amounts of base solution into the system solution containing the modifier agent. After addition of the mixed metal salt solution, the resulting slurry is continuously stirred at the same temperature for some time and then allowed to age in a heater for several hours. This method for modification of LDH is more effective than the other two methods.

## 6.2 Preparation and Characterization of Rubber–LDH Nanocomposites

There are few reports on rubber–LDH nanocomposites in which they have been prepared mostly by solution intercalation methods and not by a conventional technique for processing rubber-based composites [102, 103]. But, the melt

**Table 12** Compound formulations for EPDM–LDH and XNBR–LDH nanocomposites [104]

Ingredient	Ingredient content (phr)	
	EPDM–LDH	XNBR–LDH
Elastomer	100	100
LDH-C10	X <sup>a</sup>	X <sup>a</sup>
ZnO	3.0	1.0
Stearic acid	1.5	1.0
Sulfur	1.5	0.5
MBT	1.5	2.0
TMTD	0.3	–

*MBT* mercaptobenzothiazole, *TMTD* tetramethyl thiuram disulfide

<sup>a</sup>The value of X is 0, 5, 7.5 or 10 phr. Accordingly, the EPDM/LDH system is designated as EL0, EL5, EL7.5 and EL10, and the XNBR/LDH system as XL0, XL5, XL7.5 and XL10

compounding method still remains promising to a large extent for preparing elastomer–LDH nanocomposites. Pradhan et al. [104] investigated how the matrix polarity and the presence of reactive functional groups on the rubber chain influenced the dispersion of LDH particles, the rubber–filler interfacial adhesion and the mechanical properties of the elastomer–LDH nanocomposites prepared by the melt compounding method. Two elastomer matrices widely differing in polarity and chemical nature such as a nonpolar elastomer, i.e., EPDM (surface energy about  $34.0 \text{ mJ m}^{-2}$ ) and a polar functionalized elastomer, i.e., XNBR (surface energy about  $52.0 \text{ mJ m}^{-2}$ ) were chosen as the base matrix. The EPDM–LDH and the XNBR–LDH nanocomposites containing different weight percentages of LDH-C10 (LDH modified by  $\text{C}_{10}\text{H}_{21}\text{SO}_3\text{Na}$ , called C10) were prepared via a melt compounding method. The compound formulations for each set of the nanocomposites are given in Table 12.

The WAXS patterns of two nanocomposites at different LDH concentrations are shown in Fig. 55. The similarity of these patterns between the two systems is that the first three Bragg's reflections of LDH-C10 can be detected in both. This means that the LDH particles are not fully exfoliated in any of the matrices.

However, these reflections were broad and not well defined, indicating that LDH particles in EPDM–LDH nanocomposites had a highly disordered structure. On the other hand, The WAXS patterns of XNBR–LDH nanocomposites (Fig. 55b) revealed distinct evidence of intercalation of the polymer chains in the LDH-C10 particles. The shifting of the first Bragg's reflection to a lower scattering angle corresponded to an increase of the interlayer distance by about 0.80 nm. This meant that a multiple number of XNBR chains were aligned within the interlayer space of LDH-C10. The polar/ionic interaction between the functionalities on XNBR and LDH particles might play a major role in easy intercalation of the XNBR chains within LDH-C10 layers without disturbing the crystalline order of the LDH-C10 particles. On the other hand, in an investigation of CR–LDH nanocomposites [23] it was observed that the first reflection from the nanocomposite showed at 3.17 nm, whereas the pure OLDH had a reflection of the same plane at 2.96 nm. However, in

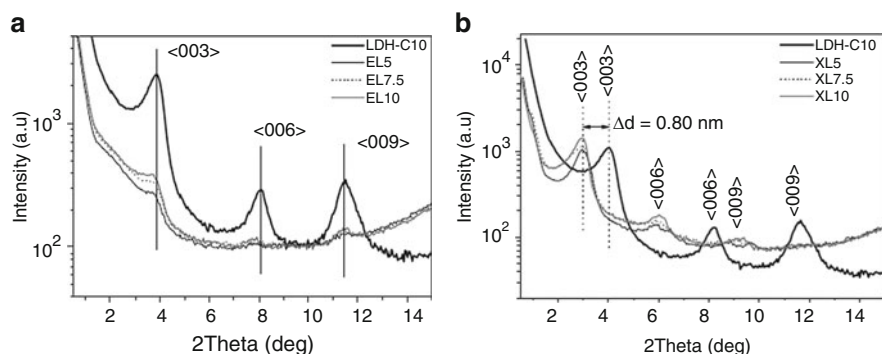


**Fig. 55** WAXS patterns of the EPDM–LDH nanocomposites (a) and XNBR/LDH nanocomposites (b) (the number at the end of sample designation EL and XL indicates the amount of LDH-C10 in phr) [104]

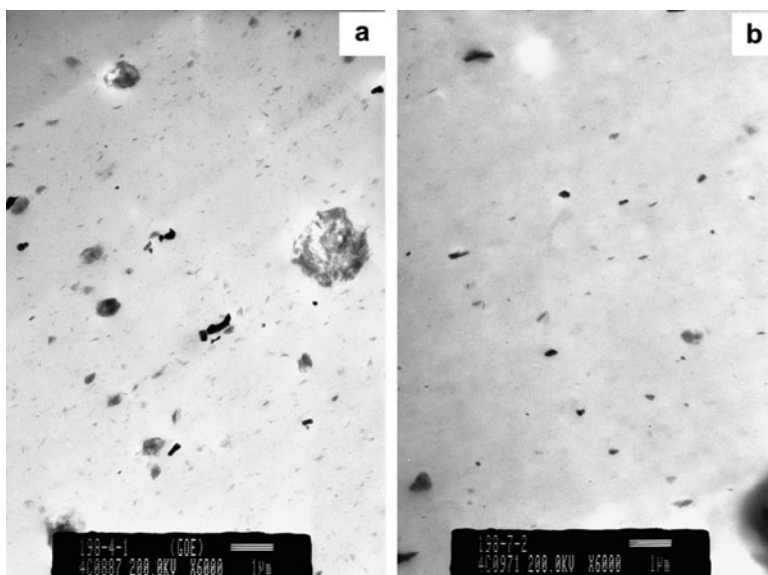


**Fig. 56** TEM micrographs of EPDM–LDH (a) and XNBR–LDH (b) nanocomposites with LDH-C10 content of 5 phr. Scale bars: 1  $\mu\text{m}$  [104]

the case of pure LDH there was no change in the peak position after incorporation of the LDH in the CR matrix.

The conclusions made from the WAXS patterns of the nanocomposites could be further established by analyzing the TEM micrographs of these materials. The micrographs for both the systems containing 7.5 phr of LDH-C10 are shown in Fig. 56. It is clear that in these nanocomposites, LDH-C10 particles were dispersed

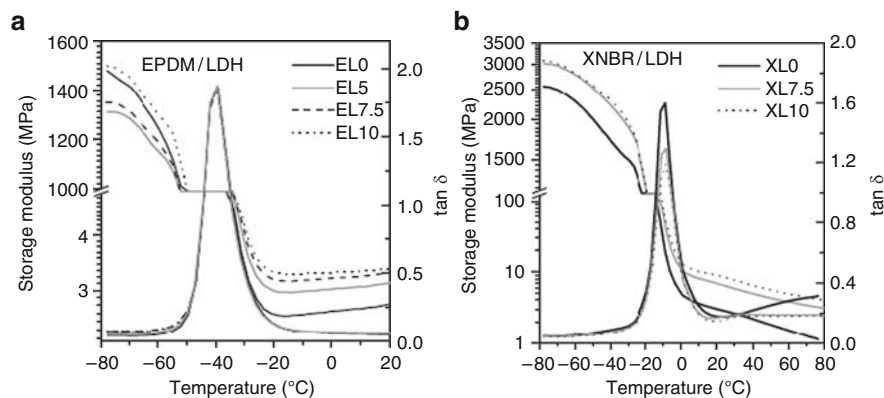


Fig. 57 Dynamic mechanical analyses of EPDM-LDH and XNBR-LDH nanocomposites [104]

in three different forms: as exfoliated fragments with lateral dimension below 100 nm, as primary particles with lateral dimension from a few hundred nanometers to 1–2  $\mu\text{m}$ , and as soft clusters of the primary particles with lateral dimensions of over a few micrometers. In the case of the EPDM-LDH system, the proportions of the last two forms were much higher than the exfoliated fragments, whereas in XNBR-LDH the extent of the exfoliated fragments predominates with less or no cluster formation, showing the homogenous dispersion throughout the matrix, even at this magnification.

The addition of OLDH as nanofiller in rubber must affect significantly the materials properties in comparison to the pristine polymer or conventional composites, including enhanced mechanical properties, increased heat resistance, and decreased flammability.

Pradhan et al. [104] found that the trends in the variation of the storage modulus with increasing LDH-C10 concentration in the low temperature region (below the  $T_g$  of the respective system) were strikingly different between EPDM-LDH and XNBR-LDH systems (as shown in Fig. 57). For XNBR-LDH nanocomposites, the storage modulus increased with increasing LDH-C10 amount, whereas for EPDM-LDH it decreased first and then increased. The authors believed that at low LDH-C10 concentration, the EPDM-LDH nanocomposites showed a softening effect below  $T_g$ . Because LDH-C10 contains a large fraction of its weight as anionic surfactant, a part of this surfactant adhered on the outer surface of the LDH particles might be loosely bound and could eventually increase the mobility of the polymer matrix in the polymer-filler interfacial region. This interfacial plasticizing effect could be more influential when the reinforcing effect of the filler particle is low and when small or no secondary interaction occurs between the polymer and the filler. In the case of EPDM-LDH nanocomposites, there existed a weak interaction at the interface at low LDH-C10 concentration, resulting in a lower storage modulus value at low temperature. However, in the case of XNBR-LDH nanocomposites, due to strong interfacial interaction between LDH-C10 particles and the XNBR

**Table 13** Summary of the mechanical properties of EPDM–LDH and XNBR–LDH nanocomposites [104]

Sample	LDH-C10 content (phr)	Tensile strength (MPa)	SD	200% modulus (MPa)	SD	Elongation at break (%)	SD
EPDM–LDH							
EL0	0.0	1.54	0.08	0.73	0.01	222	16
EL5	5.0	2.38	0.34	0.78	0.01	390	15
EL7.5	7.5	2.68	0.50	0.84	0.01	420	20
EL10	10.0	3.25	0.35	0.85	0.01	505	34
XNBR–LDH							
XL0	0.0	1.94	0.22	0.41	0.01	1,240	59
XL5	5.0	11.96	1.47	1.10	0.01	1,220	40
XL7.5	7.5	16.52	1.32	1.31	0.03	1,205	36
XL10	10.0	17.83	1.59	1.72	0.08	1,047	53

SD standard deviation

matrix, the reinforcing effect dominated over the whole temperature region used in the experiment. At temperatures above  $T_g$ , the segmental movements of the polymer chains become operative and hence the plasticizing effect due to small molecules at the interface becomes less significant. As a result, the storage modulus in both systems increased with increasing LDH-C10 concentration. Figure 57 also shows the variation of  $\tan \delta$  in the two systems with changing LDH-C10 concentration. In EPDMLDH no noticeable change in the maximum  $\tan \delta$  value was observed with increasing LDH-C10 concentration, indicating weak or no interaction between the EPDM matrix and the dispersed LDH-C10 particles. On the other hand, the  $\tan \delta$  maximum steadily decreased with increasing filler concentration in XNBR–LDH, showing once again the strong interaction at the interface. Similar conclusions can also be found in our recent report [105].

For both EPDM–LDH and XNBR–LDH nanocomposites, the various tensile properties are summarized in Table 13 and their typical stress–strain plots are shown in Fig. 58 [104]. In Fig. 58a, the gum vulcanizates of both rubber systems showed typical NR-like stress–strain behavior with a sharp upturn in the stress–strain plot after an apparent plateau region, indicating strain-induced crystallization. With the addition of LDH-C10 in the XNBR matrix, the stress value at all strains increased significantly, indicating that the matrix undergoes further curing (Fig. 58b).

The upturn in the stress–strain plot became more prominent and the plateau region diminished with increasing LDH-C10 concentration. On the other hand, in EPDM–LDH nanocomposites, the overall nature of the stress–strain plot was not changed much except for a significant increase in elongation at break and the tensile strength (Fig. 58c). At higher concentration of LDH-C10, a small upturn in the stress–strain plot could also be observed in EPDM–LDH system. Although in both EPDM and XNBR, LDH-C10 shows a reinforcing effect, the changes in mechanical properties in XNBR are much more significant. The polar/ionic interaction between XNBR and LDH-C10 particles can account for this difference. This means that the

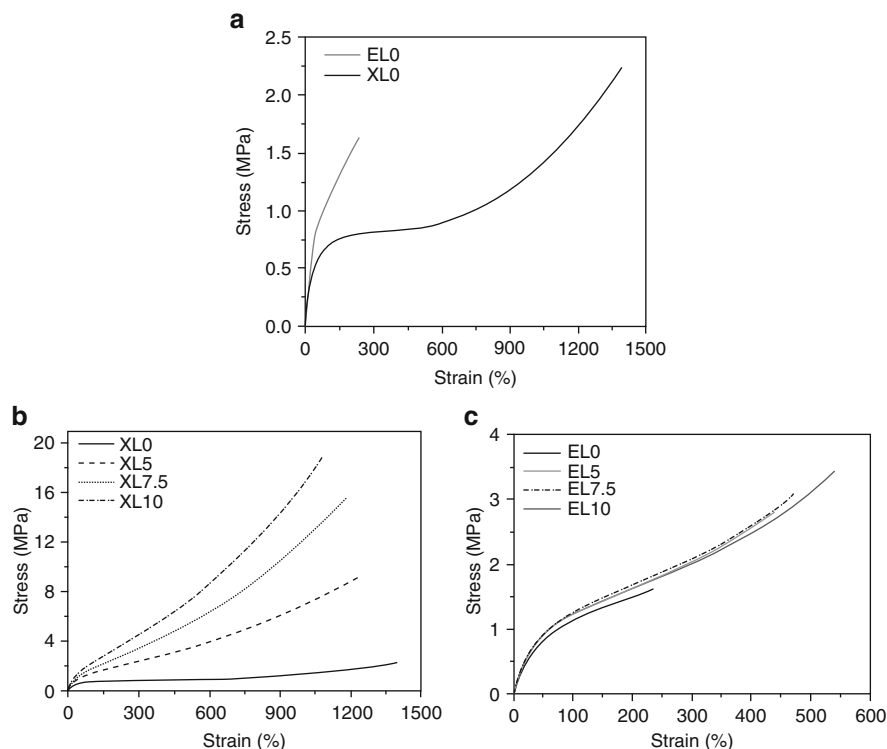


**Fig. 58** Typical stress–strain plots of EPDM and XNBR gum vulcanizates (a), XNBR–LDH nanocomposites (b), and EPDM–LDH nanocomposites (c) [104]

differences in the dispersion of the nanoparticles and the interfacial adhesion directly influence the mechanical properties of the nanocomposites. In the report on rubber nanocomposites containing ethylene vinyl acetate (EVA) having 60 wt% of vinyl acetate content and OLDH as nanofiller, Kuila et al. [106] also found that EVA–LDH nanocomposites showed improved mechanical properties such as tensile strength and elongation at break in comparison with neat EVA.

Unquestionably, rubber materials are used in many applications. However, most rubber materials are flammable and produce large amounts of smoke on burning. In some special application fields, such as in building (flooring), transport, conveying belts, the fire retardancy of rubber materials is necessary. This disadvantage limits their usage in some areas. Usually, halogen-containing flame retardants such as decabromobiphenyl have been most widely used [107]. However, halogen-containing flame retardants produced large amounts of smoke and are corrosive on burning, and thus their use is limited. It was therefore worthwhile to investigate novel methods for improving the flame retardancy of rubber with the halogen-free flame retardants. Although the fire retardant properties of rubber materials are quite important, there are few reports on this aspect. LDH has promise as potential halogen-free flame-retardant for rubber.

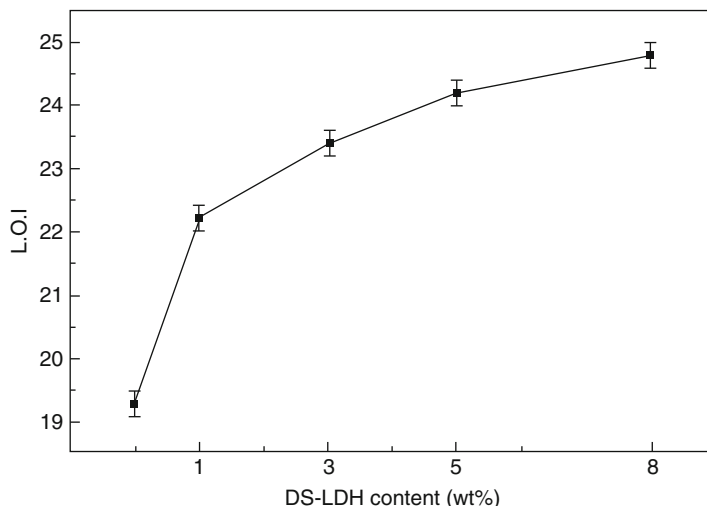


**Fig. 59** Effect of LDH content on the limiting oxygen index values of nanocomposites of EVA-60 and DS-LDH [106]

Kuila et al. [106] studied the flammability of EVA–LDH nanocomposites with different LDH loading. The results shown in Fig. 59 represent the findings on the limiting oxygen index (LOI) of neat EVA and its nanocomposites.

During the burning test, it was observed that burning of pure EVA took place very rapidly in comparison to its corresponding nanocomposites. Calculation showed that the LOI values were relatively higher for the nanocomposites than for neat EVA (19.3). The maximum value of LOI (24.8) was noted for 8 wt% LDH content in EVA. The main reason was attributed to the presence of a char layer in the nanocomposites that impeded burning while acting as a barrier between the burning surface and supplied oxygen. For the nanocomposites with LDH content of 3 wt%, the thickness of the char layer looked thin and weak, whereas beyond 3 wt% of LDH loading, the formation of a thick char layer was likely to suppress the propagating downward flame by disrupting oxygen supply to the burning specimen. On the other hand, the authors also thought that the endothermic decomposition of LDH produced sufficient water vapor to account for the reduction of flammable characteristics in the case of nanocomposites as well as in the case of thermoplastic–LDH nanocomposites [108, 109].

## 7 Conclusion

We have presented several examples of the successful preparation of rubber nanocomposites with layered silicate as the inorganic phase. This review explores the idea that the designing and compounding are key factors in obtaining the



intercalated–exfoliated structure of the clay minerals in the rubber matrix, which ultimately governs the final physical properties of the composites. It has been realized that the melt-intercalation method is more effective if proper processing conditions and compounding techniques are carefully selected. Special attention is required in the selection of vulcanizing ingredients for the rubber formulation in order to achieve a superior degree of intercalation and exfoliation of the organoclay. Compatibility between two chemically dissimilar rubbers was understood by the accomplishment of the exfoliated–intercalated layers at the interface between the rubber phases. It is true that nanoclay does not always provide a positive effect in improving the compatibility between two dissimilar rubbers. In particular, the layered silicates are potentially unable to enhance or improve the compatibility, rather they induce more phase separation at the interface. In the presence of layered silicates, the self-crosslinking reactions between CR and XNBR were studied and the influence of the incorporation of the layered silicates on the physical properties was investigated. It was found that the presence of the intercalated silicate particles in the blend matrix does not improve the physical properties, especially in the case where the blend was vulcanized without the addition of any curatives.

## References

1. Kojima Y, Usuki A, Kawasumi M, Okada A, Fukushima Y, Kurauchi T, Kamigaito O (1993) *J Mater Res* 8:1185
2. de Paiva LB, Morales AR, Diaz FRV (2008) *Appl Clay Sci* 42:8–24
3. Ibarra L, Rodríguez A, Mora I (2007) *Eur Polym J* 43:753
4. Wu YP, Zhang LQ, Wang YQ, Liang Y, Yu DS (2001) *J Appl Polym Sci* 82:2842
5. Goettler LA (2005) 63rd Annual Technical Conference by Society of Plastics Engineers, May 1–5, Boston
6. Das A, Jurk R, Stöckelhuber KW, Majumder PS, Engelhardt T, Fritzsche J, Klüppel M, Heinrich G (2009) *J Macromol Sci Chem* 46:7–15
7. Hwang WG, Wei KH, Wu CM (2004) *Polymer* 45:5729
8. Kim JT, Oh TS, Lee DH (2003) *Polym Int* 52:1203
9. Nah CW, Ryu HJ, Kim WD, Choi SS (2002) *Polym Advn Technol* 13:649
10. Hwang WG, Wei KH, Wu CM (2004) *Polym Eng Sci* 44:2117–2124
11. Liu L, Jia D, Luo Y, Guo B (2006) *J Appl Polym Sci* 100:1905–1913
12. Han M, Kim H, Kim E (2006) *Nanotechnology* 17:403–409
13. Kim JT, Lee DY, Oh TS, Lee DH (2003) *Appl Polym Sci* 89:2633–2640
14. Usuki A, Tugigase A, Kato M (2002) *Polymer* 43:2185
15. Varghese S, Karger-Kocsis J (2004) *J Appl Polym Sci* 91:813
16. Das A, Jurk R, Stöckelhuber KW, Heinrich G (2007) *Express Polym Lett* 1:17
17. Ma Y, Li QF, Zhang LQ, Wu YP (2007) *Polym J* 39:48
18. Das A, Jurk R, Stöckelhuber KW, Heinrich G (2008) *Macromol Mater Eng* 293:479–490
19. Das A, Debnath SC, De D, Naskar N, Basu DK (2004) *Polym Advn Technol* 15:551
20. Das A, De D, Naskar N, Debnath SC (2006) *J Appl Polym Sci* 99:1132
21. Yeh MH, Hwang WS, Cheng LR (2007) *Appl Sur Sci* 253:4777–4781
22. Wang Y, Zhang H, Wu Y, Wang J, Zhang L (2005) *J Appl Polym Sci* 96:318–323
23. Das A, Costa FR, Wagenknecht U, Heinrich G (2008) *Eur Polym J* 44:3456–3465

24. Wang DY, Costa FR, Leuteritz A, Schoenhals A, Anastasia V, Scheler U, Wagenknecht U, Kutlu B, Heinrich G (2010) Polyolefin nanocomposites with layer double hydroxides. In: Mittal V (ed) *Advances in polyolefin nanocomposite*. CRC, Boca Raton
25. Wang DY, Das A, Leuteritz A, Boldt R, Häußler L, Wagenknecht U, Heinrich G (2010) *Polym Degrad Stab* (in press) doi:10.1016/j.polyimdegradstab.2010.03.003
26. Sae-Oui P, Sirisinha C, Thepsuwan U, Hatthapanit K (2007) *Eur Polym J* 43:185–9316
27. Ma J, Xu J, Ren JH, Yu ZZ, Mai YW (2003) *Polymer* 44:4619
28. Mousa A, Karger-Kocsis J (2001) *Macromol Mater Eng* 4:286
29. Jia QX, Wu YP, Wang YQ, Lu M, Zhang LQ (2008) *Comp Sci Technol* 68:1050–1056
30. Al-Yamani F, Goettler LA (2007) *Rub Chem Technol* 80:100–114
31. Jia QX, Wu YP, Xu YL, Mao HH, Zhang LQ (2006) *Macromol Mater Eng* 291:218–226
32. Jia QX, Wu YP, Wang YQ, Lu M, Yang J, Zhang LQ (2007) *J Appl Polym Sci* 103:1826–1833
33. Ma J, Xiang P, Mai YW, Zhang LQ (2004) *Macromol Rapid Commun* 25:1692–1696
34. Sadhu S, Bhowmick AK (2004) *J Appl Polym Sci* 92:698–709
35. Ganter M, Gronski W, Reichert P, Mülhaupt R (2001) *Rubb Chem Technol* 74:221235
36. Sadhu S, Bhowmick AK (2003) *Rubb Chem Technol* 76:860–874
37. Das A, Heinrich G, Jurk R, Stöckelhuber KW, Herrmann W, Recker C, Schmidt C (2007) German Patent File no. 10 2006 014 873.5
38. Das A, Jurk R, Stöckelhuber KW, Engelhardt T, Fritzsche J, Klüppel M, Heinrich G (2008) *J Macromol Sci Chem* 45:144–150
39. Fritzsche J, Das A, Jurk R, Stöckelhuber KW, Heinrich G, Klüppel M (2008) *Express Polym Lett* 2:373
40. Eisenberg A, Hird B, Moor RB (1990) *Macromolecules* 23:4098
41. Heinrich G, Klüppel M (2002) *Adv Polym Sci* 160:1–44
42. Kalgankar RA, Jog JP (2008) *J Polym Sci Phys* 46:2539–2555
43. Rao Y, Pochan JM (2007) *Macromolecules* 40:290
44. Hernandez MC, Suarez N, Martinez LA, Feijoo JL, Mocano SL, Salazar N (2008) *Phys Rev E* 77:051801
45. Page KA, Adachi K (2006) *Polymer* 47:6406
46. Psarras GC, Gatos KG, Karger-Kocsis J (2007) *J Appl Polym Sci* 106:1405
47. Steeman PAM, van Turnhout J (1997) *Colloid Polym Sci* 275:106–115
48. Wübberhorst M, van Turnhout J (2000) *Dielectric Newsletter* 14:1–3
49. Morgan AB, Gilman JF (2003) *J Appl Polym Sci* 87:1327
50. Eckel DF, Balogh MP, Fasulo PD, Rodgers WR (2004) *J Appl Polym Sci* 93:1110
51. Herrmann W, Uhl C, Heinrich G, Jehnichen D (2006) *Polym Bull* 57:395
52. Katti KS, Sikdar D, Katti DR, Ghosh P, Verma D (2006) *Polymer* 47:403
53. Gatos KG, Százdli L, Pukánszky B, Karger-Kocsis J (2005) *Macromol Rapid Commun* 26:915–919
54. Gatos KG, Karger-Kocsis J (2005) *Polymer* 46:3069–3076
55. Vaia RA, Liu W (2002) *J Polym Sci Part B Polym Phys* 40:1590
56. Kim JT, Lee DY, Oh TS, Lee DH (2003) *J Appl Polym Sci* 89:2633
57. Liu L, Jia Y, Luo B, Guo B (2006) *J Appl Polym Sci* 100:1905
58. Das A, Debnath SC, Naskar N, Pal S, Datta RN (2005) *Kautsch Gummi Kunstst* 6:304
59. Ma Y, Wu Y-P, Zhang LQ, Li QF (2008) *J Appl Polym Sci* 109:1925–1934
60. Ishida H, Campbell S, Blackwell J (2000) *Chem Mater* 12:1260
61. Burrell H, (1995) Solubility parameter values. In: Bandrup J, Immergut EH (eds) *Polymer handbook*, 2nd edn. Wiley, New York, pp 337–359
62. Thielen G (2007) *Kautsch Gummi Kunstst* 60:389
63. Ghosh AK, Naskar N, Debnath SC, Basu DK (2001) *J Appl Polym Sci* 81:800
64. Das A, Ghosh AK, Pal S, Basu DK (2004) *Polym Advan Technol* 15:197
65. Das A, Ghosh AK, Basu DK (2005) *Kautsch Gummi Kunstst* 58:230
66. Vo LT, Giannelis EP (2007) *Macromolecules* 40:8271

67. Baghaei B, Jafari SH, Khonakdar HA, Rezaeian I, As'habi L, Ahmadian S (2009) *Polym Bull* 62:255–270
68. Fang Z, Harrats C, Moussaif N, Groeninckx G (2007) *J Appl Polym Sci* 106:3125
69. SinhaRay S, Bandyopadhyay J, Bousmina M (2007) *Macromol Mater Eng* 292:729
70. Kawazoe M, Ishida H (2008) *Macromolecules* 41:2931
71. Zhang P, Huang G, Liu Z (2009) *J Appl Polym Sci* 111:673
72. García-López D, López-Quintana S, Gobernado-Mitre I, Merino JC, Pastor JM (2007) *Polym Eng Sci* 47:1033
73. Arroyo M, Lópej-Manchado MA, Valentin JL, Carretero J (2007) *Comp Sci Technol* 67:1330–1339
74. Das A, Stöckelhuber KW, Heinrich G (2009) *Macromol Chem Phys* 210:189–199
75. Das A, Naskar N, Basu DK (2004) *J Appl Polym Sci* 91:1913
76. Deuri AS, Bhowmick AK (1987) *J Appl Polym Sci* 34:2205–2222
77. Ramesan MT, Mathew G, Kuriakose B, Alex R (2001) *Eur Polym J* 37:719–728
78. Good RJ, Girifalco LA (1960) *J Phys Chem* 64:561
79. Stöckelhuber KW, Das A, Jurk R, Heinrich G (2009) *Proceedings of the 17. NDVak, Dresden*, pp. 112–115. ISBN: 978-3-9812550-1-0
80. Göldel A, Kasaliwal G, Pötschke P (2009) *Macromol Rapid Commun* 30:423–429
81. Voulgaris D, Petridis D (2002) *Polymer* 43:2213
82. Li Y, Shimizu H (2004) *Polymer* 45:7381
83. Ramorino G, Bignotti F, Conzatti L, Riccol T (2007) *Polym Eng Sci* 47:1650
84. Fritzsche J, Klüppel M (2009) *Kautsch Gummi Kunstst* 62:16
85. Ganter M, Gronski W, Reichert P, Mülhaupt R (2001) *Rubber Chem Technol* 74:221
86. Antony P, De SK, Van Duin M (2001) *Rub Chem Technol* 74:376
87. Mukhopadhyay S, De SK (1991) *J Appl Polym Sci* 43:2283
88. Miyata Y, Atsumi M (1988) *J Polym Sci Part A Polym Chem* 26:2561
89. Johnson PR (1976) *Rubber Chem Technol* 49:650
90. Kovacs P (1955) *Rubber Chem Technol* 28:1021
91. Wolf S, Donnet JB (1976) *Rubber Chem Technol* 49:650
92. Tomova D, Kressler J, Radusch HJ (2000) *Polymer* 41:7773
93. Biswas T, Das A, Debnath SC, Naskar N, Das AR, Basu DK (2004) *Eur Polym J* 40:847
94. Sergey V, Ion D, Fan XW, Rigoberto A (2004) *Macromol Rapid Commun* 25:498
95. Wang DY, Wang YZ, Wang JS, Chen DQ, Zhou Q, Yang B, Li WY (2005) *Polym Degrad Stab* 87:171
96. Miyata S (1980) *Clays Clay Miner* 28:50
97. Meyn M, Beneke K, Legaly G (1990) *Inorg Chem* 29:5201
98. Stanimirova TS, Kirov G, Dinolova E (2001) *J Mater Sci Lett* 20:453
99. Khan AI, O'Hare D (2002) *J Mater Chem* 12:3191
100. Wang DY, Costa FR, Anastasia V, Leuteritz A, Scheler U, Jehnichen D, Wagenknecht U, Häußler L, Heinrich G (2009) *Chem Mater* 21:4490
101. Wang DY, Leuteritz A, Wagenknecht U, Heinrich G (2009) *Trans Nonferrous Met Soc China* 6:1470
102. Acharya H, Srivastava SK, Bhowmick AK (2007) *Comp Sci Tech* 67:2807
103. Acharya H, Srivastava SK, Bhowmick AK (2007) *Nanoscale Res Lett* 2:1
104. Pradhan S, Costa FR, Wagenknecht U, Jehnichen D, Bhowmick AK, Heinrich G (2008) *Eur Polym J* 44:3122
105. Thakur V, Das A, Mahaling RN, Roop S, Gohs U, Wagenknecht U, Heinrich G (2009) *Macromol Mater Eng* 94(9):561
106. Kuila T, Srivastava SK, Bhowmick AK (2009) *J Appl Polym Sci* 111:635
107. Khattab MA (2000) *J Appl Polym Sci* 78:2134
108. Costa FR, Wagenknecht U, Heinrich G (2007) *Polym Degrad Stab* 92:1813
109. Costa FR, Saphiannikova M, Wagenknecht U, Heinrich G (2008) *Adv Polym Sci* 210:101

# Surface Modification of Fillers and Curatives by Plasma Polymerization for Enhanced Performance of Single Rubbers and Dissimilar Rubber/Rubber Blends

J.W.M. Noordermeer, R.N. Datta, W.K. Dierkes, R. Guo, T. Mathew, A.G. Talma, M. Tiwari, and W. van Ooij

**Abstract** Plasma polymerization is a technique for modifying the surface characteristics of fillers and curatives for rubber from essentially polar to nonpolar. Acetylene, thiophene, and pyrrole are employed to modify silica and carbon black reinforcing fillers. Silica is easy to modify because its surface contains siloxane and silanol species. On carbon black, only a limited amount of plasma deposition takes place, due to its nonreactive nature. Oxidized gas blacks, with larger oxygen functionality, and particularly carbon black left over from fullerene production, show substantial plasma deposition. Also, carbon/silica dual-phase fillers react well because the silica content is reactive. Elemental sulfur, the well-known vulcanization agent for rubbers, can also be modified reasonably well.

Coated materials are evaluated in S-SBR and in 50:50 blends of S-SBR and EPDM rubbers. In blends, the partitioning of fillers and curatives over the phases depends on differences in surface polarity. In S-SBR, polythiophene-modified silica has a strong positive effect on the mechanical properties because of a synergistic reaction of the sulfur-moieties in the polythiophene coating with the sulfur cure system. In S-SBR/EPDM blends, a coating of polyacetylene is most effective because of the chemical similarity of polyacetylene with EPDM. The effect of

---

J.W.M. Noordermeer (✉), R.N. Datta, W.K. Dierkes, R. Guo, T. Mathew, A.G. Talma, and M. Tiwari

University of Twente, Faculty of Engineering Technology, Department of Elastomer Technology and Engineering (ETE), 7500 AE Enschede, The Netherlands

e-mail: j.w.m.noordermeer@utwente.nl

W. van Ooij

Department of Chemical and Materials Engineering, University of Cincinnati, Cincinnati, OH 45221-0012, USA

polyacetylene coating on fullerene soot in pure S-SBR is practically negligible, but in a S-SBR/EPDM blend, largely improved mechanical properties are obtained (like with silica).

Polyacetylene-modified sulfur is evaluated as a curative in a 50:50 blend of S-SBR/EPDM. In pure S-SBR, the mechanical properties decrease with the polyacetylene coating due to a reduced release rate of the sulfur out of its shell. The cure and mechanical properties of the S-SBR/EPDM blend are nearly doubled because of improved compatibility.

The results demonstrate the versatility of plasma polymerization of various monomers onto rubber fillers and vulcanization ingredients. The largest effects are seen in blends of different rubbers with unequal polarities. Substantial improvements in mechanical properties are seen in comparison with the use of unmodified fillers and curatives.

**Keywords** Blends · Plasma polymerization · Reinforcing fillers · Rubber · Surface polarity · Vulcanization

## Contents

1	Introduction .....	169
2	Plasma Polymerization .....	170
2.1	Hot and Cold Plasma .....	170
2.2	Mechanism of Plasma Polymerization .....	172
2.3	Operational Parameters .....	175
2.4	Plasma Generation .....	177
2.5	Surface Modification of Powder Substrates by Plasma .....	178
2.6	Plasma Modification of Fillers for Rubber Applications .....	179
3	Plasma Polymerization onto Silica and Carbon Black Fillers, and onto Sulfur Vulcanization Agent .....	181
3.1	Plasma Reactors .....	181
3.2	Materials .....	183
3.3	Process Conditions for Plasma Deposition .....	183
3.4	Characterization Techniques for Plasma-Modified Fillers and Sulfur .....	185
3.5	Characterization of Plasma-Coated Powders .....	186
4	Polyacetylene-, Thiophene- and Pyrrole-Coated Silica in Rubber .....	197
4.1	Silica in Pure S-SBR .....	197
4.2	Silica in a S-SBR/EPDM Blend .....	203
5	Polyacetylene-Coated Carbon Black in Rubber .....	207
5.1	Carbon Black in Pure S-SBR .....	207
5.2	Carbon Black in a SBR/EPDM Blend .....	209
6	Polyacetylene-Coated Sulfur in Rubber .....	213
6.1	Sulfur in Pure S-SBR .....	213
6.2	Sulfur in a S-SBR/EPDM Blend .....	214
7	Conclusions .....	216
	References .....	217

## 1 Introduction

Rubber is not a simple material as commonly assumed, but a complicated composite that contains mainly incompatible components. These components (polymers, reinforcing and nonreinforcing fillers, and curing agents) are incompatible due to polarity differences. Furthermore, polymers as such are commonly immiscible in other polymers because they often differ in the degree of carbon–carbon unsaturation and in the heteroatoms contained in the polymer chains and, consequently, possess different polarities. The thermodynamic criterion for miscibility is a negative Gibbs free energy of mixing [1]. The Gibbs free energy of mixing is given by the following equation:

$$\Delta G_m = \Delta H_m - T\Delta S_m. \quad (1)$$

In this equation,  $\Delta H_m$  is the change in enthalpy of mixing, and  $\Delta S_m$  the change in entropy of mixing.  $T$  is the absolute temperature. The change in enthalpy during mixing is the result of the interaction energy between the different components, and is for different polymers mostly positive. This interaction energy arises from hydrogen bonds, dipole interactions, van der Waals interactions, acid–base interactions, and Coulombic interactions. The change in entropy is usually very small due to constraints of the segmental mobility of the polymer chains, and is too small to compensate for the positive enthalpy of mixing. Consequently, immiscibility is more likely for polymer mixtures than miscibility.

Additionally for rubber compounds, the differences in polarity and unsaturation of the various polymers cause different affinities for fillers and curing additives. In blends of different rubber polymers, the reinforcing filler carbon black for instance locates itself preferentially in the phase with the higher unsaturation and/or polarity, leaving the lower unsaturation or nonpolar phase unreinforced. The affinity for carbon black decreases in the following order of polymers [2]:

$$\text{BR} > \text{SBR} > \text{CR} > \text{NBR} > \text{NR} > \text{EPDM} > \text{IIR},$$

where BR = polybutadiene rubber, SBR = styrene-butadiene copolymer rubber, CR = polychloroprene rubber, NBR = acrylonitrile-butadiene copolymer rubber, NR = natural rubber (*cis*-polyisoprene), EPDM = ethylene-propylene-diene copolymer rubber, and IIR = isobutene-isoprene copolymer rubber (butyl rubber).

The consequence is an inhomogeneous distribution of additives in the individual polymer phases and thermodynamic nonequilibrium after mixing. The latter effect may cause demixing and reagglomeration of additives. A well-known example in this regard is the flocculation or reagglomeration of silica in S-SBR compounds [3].

In dissimilar rubber/rubber blends, vulcanization ingredients also preferentially end up in only one of the phases, resulting in overcuring of this phase and undercuring of the other one. An example of this effect is the solubility of “insoluble sulfur,” which is much lower for NBR than for SBR and EPDM.

There are several practical ways to potentially overcome the incompatibility of the main compounding ingredients:

1. Modification of the polymers in order to better match their polarity with the other compound components
2. Surface modification of the fillers and curing agents in order to increase their wettability and interaction with the polymers
3. Adjustment of the mixing process, e.g., Y-mixing [4]

In the following section, a new technique of surface modification of fillers and curing agents will be discussed: plasma polymerization. This technique allows for surface coating of powders, whereby the chemical structure of the coating is determined by the monomer used for the process. The morphology of the substrate is preserved, which is an important precondition for filler treatment. The polarity of the functional groups can be chosen to fit the matrix of the polymer wherein it will be applied.

## 2 Plasma Polymerization

### 2.1 *Hot and Cold Plasma*

Plasma polymerization is a technique for modifying the surfaces of various substrates. It is a thin-film-forming process, whereby these films deposit directly on the surfaces of the substrates. In this process, the growth of low molecular weight monomers into high molecular weight polymer networks occurs with the aid of plasma energy, which involves activated electrons, ions, and radicals. A plasma is a mixture of electrons, negatively and positively charged species, neutral atoms, and molecules. It is considered as being a state of materials, which are more highly activated than in the solid, liquid, or gas phases. Sir William Crooks suggested the concept of the “fourth state of matter” (1879) for electrically discharged matter, and Irving Langmuir [5] first used the term “plasma” to denote the state of gasses in discharge tubes.

The plasma state can be created by a variety of means. In general, when a molecule is subjected to a severe condition, such as intense heat, ionization of the molecule takes place. At temperatures higher than 10,000 K, all molecules and atoms tend to become ionized. The sun and other stars of the universe have temperatures ranging from 5,000 to 70,000 K or more, so they consist entirely of plasma.

In a laboratory environment, plasma is generated by combustion, flames, electric discharge, controlled nuclear reactions, shocks etc. Because a plasma loses energy to its environment mainly by radiation and conduction to walls, the energy must be supplied as fast as it is lost in order to maintain the plasma state. Of the various means of maintaining the plasma state continuously for a relatively long period of

time, the most obvious and most common method is the use of an electrical discharge. For this reason, most experimental work, particularly in the study of plasma polymerization, is carried out using some kind of electrical discharge. Among the many types of electrical discharges, glow discharge is by far the most frequently used in plasma polymerization.

Plasma states can be divided into two main categories: hot plasmas (near-equilibrium plasmas) and cold plasmas (nonequilibrium plasmas). Hot plasmas are characterized by very high temperatures of electrons and heavy particles, both charged and neutral and which are close to their maximal degrees of ionization. Cold plasmas are composed of low temperature particles (charged and neutral molecular and atomic species) and relatively high temperature electrons and they are associated with low degrees of ionization. Hot plasmas include electrical arcs, plasma jets of rocket engines, thermonuclear reaction generated plasmas, etc. Cold plasmas include low-pressure direct current (DC) and radio frequency (RF) discharges, and discharges from fluorescent (neon) light tubes. Corona discharges are also considered to be cold plasmas.

Hot plasmas have an extremely high energy content, which induces fragmentation of all organic molecules to atomic levels and, as a consequence, these plasmas can only be used for generating extremely high caloric energy or to modify thermally stable inorganic materials. Hot plasma applications for processing materials have been created with the use of plasma arc heaters, and three distinct application areas have emerged: synthesis, melting, and deposition. The progress in thermal plasma processing has been limited, however, by an unsatisfactory understanding of the extremely complex reaction kinetics, transport properties, heat transfer, and particle dynamics during gas–solid and gas–gas interactions. As a result, thermal plasma processing has only progressed beyond laboratory and pilot scale stages in a few cases.

Low pressure nonequilibrium discharges, cold plasmas, are initiated and sustained by DC, RF, or microwave (MW) power transferred to a low pressure gas environment, with or without an additional magnetic field. Ultimately, all these discharges are initiated and sustained through electron collision processes under action of specific electric or electromagnetic fields. Accelerated electrons induce ionization, excitation, and molecular fragmentation processes leading to a complex mixture of active species. The work described in this manuscript was carried out using a cold plasma process.

The glow discharge is formed by exposing a gaseous monomer at low pressure (<10 Torr) to an electric field. Energy is transferred by the electric field to release electrons, which collide with molecules, electrodes, and other surfaces. Inelastic electron collisions with molecules generate more electrons, as well as ions, free radicals, and excited molecules. Although the degree of ionization is low, the amount of charged particles plays an important role in the deposition rate and in determining the chemical structure of the plasma film generated. All fragments are very reactive towards surfaces exposed to the plasma and mutually with other fragments. The average electron energy in a low pressure discharge is in the range of 2–5 eV [6]. The electron energy distribution in a low pressure discharge



follows a Maxwellian–Druyvesteyn distribution. There is a high-energy tail, which means that there are some high-energy electrons (8–14 eV), but of lower concentration, which have a significant impact on the overall reaction rates in the plasma.

At low pressures, the electron temperature is much higher than the temperature of the gas. The temperature of an electron with energy of 2 eV will be 23,200 K. Even though the individual electrons are very hot, the system or gas remains at ambient temperature. Because of the very low density and very low heat capacity of the electrons, the amount of heat transferred to the gas and to the walls of the container is very small. Thus the term “cold plasma” derives its meaning from the small amount of heat transferred to the gas or solids in contact with it.

## 2.2 *Mechanism of Plasma Polymerization*

Chemical reactions that occur under plasma conditions are generally very complex [7] and consequently are nonspecific in nature. Such reactions are of merit when special excited states of molecules are required as intermediate states and cannot be achieved, or can only be achieved with great difficulty, by conventional chemical reactions. Thus, plasma polymerization should be recognized as a special means of preparing unique polymers that cannot be made by other methods. The capability of plasma polymerization to form ultrathin films with minimum flaws is unique.

Plasma polymers are deposited on surfaces in contact with a glow discharge of organic or organometallic monomers, in the form of a thin film and/or as a powder. Such films find applications as surface modifiers and in applications where the bulk properties of extremely thin films are desirable.

The following are some important characteristics of plasma polymer films:

1. They can be easily formed with thickness of 50 nm–1  $\mu\text{m}$
2. Such films are often highly coherent and adherent to a variety of substrates, including conventional polymers, glass, and metal surfaces
3. The films are commonly pinhole-free and highly crosslinked
4. Multilayer films or films with grading of chemical or physical characteristics are easily produced by this process

For most practical coating processes, the monomer flows into a plasma reactor with a continuous glow discharge, and is wholly or partially consumed in the conversion to plasma polymer. In such a setup, gaseous by-products and unconverted monomer are continuously pumped out of the reactor.

In a plasma polymerization process, the growth of low molecular weight monomer species to a high molecular weight plasma polymer network takes place. In a chemical sense, plasma polymerization is different from conventional polymerizations, such as radical or ionic. The term *radical polymerization* means that propagating reactions of monomers are initiated by radical species. *Ionic polymerization* means that chemical reactions are propagated by ionic species in the polymerization step. *Plasma polymerization* involves an energy source to

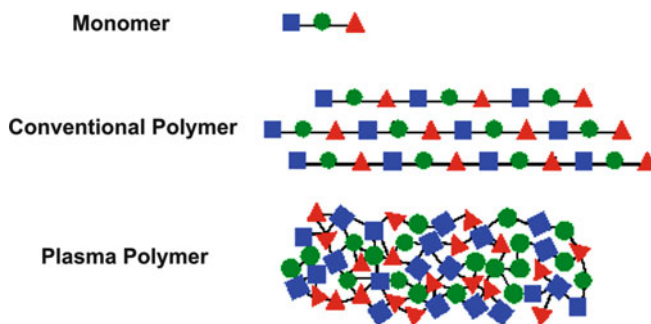
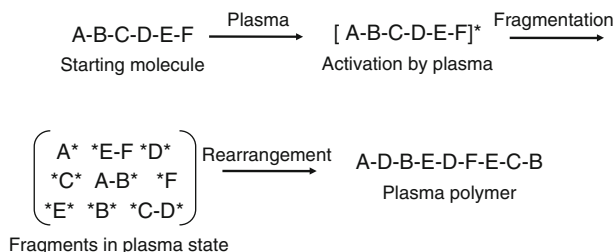


Fig. 1 Schematic representation of a plasma polymer [8]

initiate the polymerization reactions. Polymers formed by plasma are entirely different from those formed by ionic or radical polymerizations. The monomers are transformed into a highly crosslinked three-dimensional network. A schematic representation of a plasma polymer is shown in Fig. 1.

On the basis of various investigations, scientists have proposed different mechanisms for the plasma polymerization process. An ionic mechanism was proposed by Williams and Hayes [9], Haller and White [10], Westwood [11], and Thompson and Mahayan [12], separately. A radical mechanism was proposed by several other investigators [6, 13–17]. The argument for a radical mechanism was based on the observations that (1) the magnitude of energy required to form radicals (3–4 eV) is considerably less than that required to form ions (9–13 eV); (2) the average electron energy in a low pressure discharge is typically 2–5 eV; (3) the radical concentration in discharge ( $10^{-2}$ – $10^{-1}$  of the neutral species) is much higher than the ion concentration ( $10^{-6}$ – $10^{-5}$  of the neutral species); (4) there is no correlation between polymer deposition rate and the ionization potential of the used monomer; and (5) a considerable amount of radicals remain in the deposited polymer.

Yasuda explained the plasma polymerization process by a new concept of atomic polymerization [18]. In the plasma, monomer molecules gain high energy from electrons, ions, and radicals, and are fragmented into activated small fragments and in some cases into atoms. These activated fragments recombine, sometimes accompanied by rearrangement, and the molecules grow to large molecular weight in the gas phase or at the substrate (Fig. 2). The repetition of activation, fragmentation, and recombination leads to polymer formation. This concept is essentially different from the mechanism of conventional polymerization, whereby monomers are linked together through chemical reactions without alteration of the chemical structure of the monomer or, in some cases, with only small alterations by loss of small fragments from two monomers. Therefore, the chemical structure of the formed polymer chains can be predicted from the chemical structure of the monomer. However, the chemical structure of the plasma polymer can never be predicted from the structure of the monomer used, because fragmentation and



**Fig. 2** Schematic representation of plasma polymerization

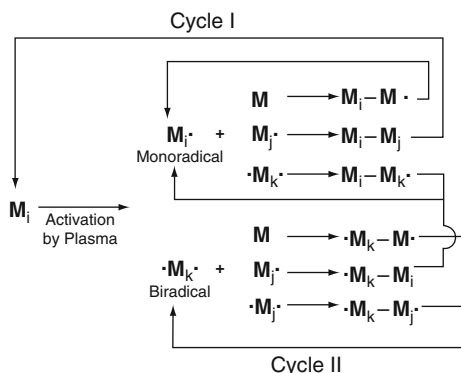
rearrangement of the monomers occur in the plasma. The concept of atomic polymerization is well accepted among various investigators, and it allows the interpretation of features of the plasma polymerization process and of the chemical and physical properties of the formed polymers.

Because both fragmentation and recombination occur in a plasma, starting molecules for plasma polymerization are not restricted to unsaturated compounds, and saturated compounds can also be transformed into polymers. The rate constant of the process will be slightly higher for unsaturated compounds. The propagation reaction in plasma polymerization is not a chain reaction through double bonds, but a stepwise reaction of recombination of biradicals that are formed from fragmentation of the starting compounds by the plasma (Fig. 2).

How the starting molecules are fragmented into activated small fragments depends on the energy level of the plasma and the nature of the monomer molecules. This is a reason why plasma polymers possess different chemical composition when the plasma polymerization is operated at different conditions, such as different monomer flow rate, RF power, and pressure of the reaction chamber, even if the same starting materials are used for the plasma polymerization.

The fragmentation of starting molecules in a plasma is represented by two types of reactions: the elimination of hydrogen atoms and C–C bond scission. Hydrogen elimination is considered to contribute greatly to the polymer-forming process in plasma polymerization. Actually, the gas phase of a closed system after plasma polymerization of hydrocarbons (converted to polymers at yields of 85–90%) is mainly composed of hydrogen, and the amount of hydrogen eliminated by plasma (hydrogen yield per monomer molecule) in the gas phase increases by increasing the number of hydrogen atoms in a hydrocarbon molecule [19]. Therefore, it seems probable that hydrogen atoms are eliminated from monomer molecules by plasma to result in the formation of monoradicals and biradicals and, then, the addition of the radicals to a monomer and the recombination between two radicals proceed to make large molecules with or without a radical. Figure 3 shows an essential polymer-forming process in plasma polymerization, which was proposed by Yasuda [20]. The stepwise reaction may be predominant in the polymer-forming process. Chain reactions of the radicals  $M_i^*$  and  $*M_k^*$ , via double bonds and triple bonds to form polymers, will occur infrequently because of a lower ceiling temperature ( $T_{\text{ceiling}}$ ). The Gibbs free energy ( $\Delta G$ ) of polymerization by chain reactions is:

**Fig. 3** Overall plasma polymerization mechanism



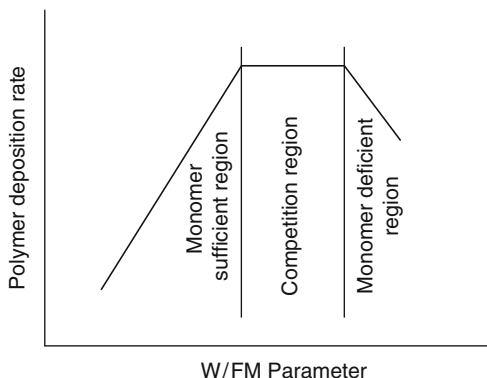
$$\Delta G = \Delta H - T\Delta S. \quad (2)$$

As the reaction temperature is raised, the magnitude of  $-T\Delta S$  increases. When the reaction temperature is raised to  $T_{\text{ceiling}}$ , where the magnitude of  $-T\Delta S$  is equal to  $\Delta H$ , the Gibbs free energy is zero; therefore at  $T_{\text{ceiling}}$  the reaction is at equilibrium between polymerization and depolymerization. This temperature is called the ceiling temperature of polymerization. Above  $T_{\text{ceiling}}$  the polymerization never proceeds spontaneously. The ceiling temperature is a function of pressure, and most monomers at low pressure show lower ceiling temperatures than at 1 atm. Then, the  $T_{\text{ceiling}}$  is too low to expect appreciable polymer formation by the chain reactions. Also, because of the very small number of molecules available in a vacuum, the relatively slow process of step growth polymerization fails to explain the rather rapid formation of polymers that is found in plasma polymerization. Thus, the most acceptable mechanism for plasma polymerization taking place in a vacuum, is the one given by Yasuda.

### 2.3 Operational Parameters

The fragmentation process depends on how much electrical energy (RF power) is supplied to maintain the plasma, how much monomer is introduced into the plasma, and where the monomer molecules interact with activated species of the plasma. Yasuda proposed a controlling parameter or W/FM value, where W, F, and M are RF power [J/s], the monomer flow rate [mol/s], and the molecular weight of the monomer [kg/mol], respectively [21]. The W/FM parameter is an apparent input energy per unit of monomer molecules [J/kg]; therefore, the magnitude of the W/FM parameter is considered to be proportional to the concentration of activated species in the plasma. The polymer formation rate (polymer deposition rate) increases by increasing the W/FM parameter in the operational condition, whereby

**Fig. 4** Domains of polymer deposition. W, F, and M are RF power, the monomer flow rate, and the molecular weight of the monomer, respectively



the activated species have a far lower concentration than monomer molecules in the plasma; this is called the monomer-sufficient region. With a further increase in W/FM, the polymer formation rate levels off (the competition region). The polymer formation rate decreases with further increase of the W/FM parameter because of lack of monomer molecules (the monomer-deficient region). The domains of plasma polymerization are schematically illustrated in Fig. 4.

In the monomer-sufficient region, monomer molecules are subjected to less fragmentation during plasma-polymerization, and plasma polymers with little rearrangement and little loss of groups such as hydrogen, hydroxyl groups, and carbonyl groups are formed. In the monomer-deficient region, monomer molecules are subjected to heavy fragmentation, and plasma polymers with much rearrangement and a large loss of some groups are formed. Usually, plasma polymerization is operated in the monomer-sufficient region. The monomer flow rate is also a factor in controlling plasma polymerization. At a constant level of energy input, an increase of the monomer flow rate results in a decrease of the W/FM parameter and the domain of plasma polymerization may change from the monomer-deficient region to the monomer-sufficient region.

The hydrodynamic factors that influence the plasma polymerization process pose a complicated problem and are of importance in the application of plasma for thin film coatings. When two reaction chambers with different shapes or sizes are used and when plasma polymerization of the same monomer is operated under the same operational conditions of RF power, monomer flow rate, pressure in the reaction chamber etc., the two plasma polymers formed in the two reaction chambers are never identical because of the differences in the hydrodynamic factors. In this sense, plasma polymerization is a reactor-dependent process. Yasuda and Hirotsu [22] systematically investigated the effects of hydrodynamic factors on the plasma polymerization process. They studied the effect of the monomer flow pattern on the polymer deposition rate in a tubular reactor. The polymer deposition rate is a function of the location in the chamber. The distribution of the polymer deposition rate is mainly determined by the distance from the plasma zone and the

direction of pumping flow. The direction of monomer flow has less influence on the distribution of the polymer deposition rate. These results emphasize the importance of (1) the diffusion transport of the energy-carrying species (electrons, ions, radicals) of the plasma; (2) the flow of monomer and product gas, and of fragments generated by the plasma; and (3) the diffusion transport of polymer-forming species and radicals.

A similar investigation of the hydrodynamic effect on the polymer deposition rate using a bell-jar type reactor was done by Kobayashi et al. [23]. The experimental data using two reactors with different shapes indicated that the polymer deposition rate does not become uniform at any spot of the reactor, even if the patterns of the diffusion transport of the energy-carrying species of plasma, of the flow of monomer and product gas, and of the diffusion transport of the polymer-forming species are changed. This means that a certain degree of thickness variation always exists when a plasma polymer is deposited on a stationary substrate in a reactor. The thickness variation can be avoided by moving the substrate when plasma polymer is deposit in the reactor. Inagaki and Yasuda [24] designed a special reactor in which a moving substrate plate was positioned midway between two parallel electrodes and was repeatedly rotated at 60 rpm in and out of the plasma zone. The polymer deposition rate at any place on the moving substrate was very uniform. This aspect is applicable to tubular type reactors.

## 2.4 Plasma Generation

To reach the plasma state of atoms and molecules, energy for the ionization must be absorbed by the atoms and molecules from an external energy source. Furthermore, the plasma state does not continue at atmospheric pressure, but at a low pressure of  $1-10^{-2}$  Torr. The essential items for plasma generation are (1) an energy source for the ionization; (2) a vacuum system for maintaining the plasma state; and (3) a reaction chamber.

Generally, electrical energy is used as the energy source for the ionization of atoms and molecules because of the convenience of handling. Direct current (DC), commercial alternating current (AC) at a frequency of 50 or 60 Hz, and AC with a high frequency of more than 60 Hz, e.g., 10 or 20 KHz (audio frequency), 13.56 MHz (radio frequency), or 2.45 GHz (microwave frequency), are all applicable for energy supply. These electric powers are basically supplied to atoms and molecules in the reaction chamber from a pair of electrodes placed in the reaction chamber in a capacitive coupling manner with the electrical generator. An inductive coupling manner is also possible for electrical generators with a high frequency of more than 1 MHz.

A vacuum system composed of a combination of a rotary pump and an oil diffusion pump is frequently used. Although use of a rotary pump alone can reach low pressures of  $1-10^{-2}$  Torr, use of both rotary and oil diffusion pumps is desirable because less gas remains in the reaction chamber.

The reaction chamber is usually designed according to the substrates to be irradiated with plasma. A bell jar or tubular chamber made of glass or stainless steel is frequently used as a reaction chamber. A bell jar chamber is convenient for massive substrates, and a tubular chamber is better for long substrates like fibers. The reactor contains two electrodes and a substrate stage, which is midway between the electrodes. Using a rotating substrate stage it is possible to obtain a homogenous deposition of plasma polymer.

## ***2.5 Surface Modification of Powder Substrates by Plasma***

Plasma treatment of powder substrates is difficult compared to that of a flat substrate. The main reason for this is the agglomeration of powders and the large surface area per unit mass of the powder. In order to modify the surface, each powder particle must be exposed to plasma. Unexposed regions are seldom modified. Therefore, the surface modification of powder substrates by plasma has to be dealt with differently.

There are four major differences between plasma polymerization on a flat substrate and that on a powder substrate: (1) Powders are characterized by a large surface area per unit mass. The specific surface area for 1 g powder with average particle size 20  $\mu\text{m}$  and density 2,000  $\text{kg/m}^3$  is around 0.15  $\text{m}^2$ , which is two orders of magnitude larger than that of a flat substrate [25]. Therefore, for the same plasma polymerization condition and the same total amount of film deposited per unit time, the thickness of the film deposited on powders will be much smaller than that on a flat substrate. (2) There is a difference in the length of time during which the substrate surface is exposed to the plasma. During a plasma polymerization process, a flat surface is exposed to plasma throughout the process, whereas a powder surface exposes part of its surface periodically to plasma, depending on the shape and mixing efficiency. (3) Since the nature of treatment of powdered materials involves mixing the particles to continuously refresh the surfaces exposed to the plasma, the stability of the plasma in the chamber is affected by interactions between the particles and the plasma. (4) Exhaustion of monomer close to the powder surface is another important factor affecting the film deposition rate. Due to the large surface area, the monomer concentration around the powder substrate is much lower than that around a flat substrate, assuming the deposition conditions are the same. The growth of the plasma polymer on powder surfaces is slowed down because the monomer and radicals around the particle surface are depleted and exhausted. Hence, plasma polymerization on a powder substrate proceeds in a monomer-deficient region. Therefore, plasma polymerizations on powder substrates are to be carried out at an ample supply of monomer.

One of the important aspects is the surface exposure of powder substrates during the plasma modification process. For this, the aggregations of the powders should be destroyed. A fluidized bed is a way to expose all the powder particles to plasma. In this case, the powder is placed on a porous plate in the reactor, which

is positioned vertically, and a gas is injected from the bottom of the reactor. The gas passes through the bed of powder. At more than a critical flow rate of the gas stream, the pressure drops, and the drag on individual powder particles increases. As a result, the powder starts to move and becomes suspended in the gas stream. Using a reactor with a fluidized bed, all surfaces of each powder can be exposed to plasma. Thus, effective surface modification of powders is possible.

Another possible technique for the plasma treatment of powders is based on tumbling of the powder [26]. In this type of reactor, powders are treated remotely from the plasma, i.e., away from the most intense glow. These types of reactors can handle amounts of powder in the range of 300–500 g.

The first attempt to modify powder substrates by plasma polymerization was done by Inagaki et al. [27]. They reported the modification of polyethylene and magnetite powder surfaces by a plasma polymerization process in a fluidized bed reactor. The monomer used for the process was tetrafluoroethylene. Later, Piskin and Atac [28] reported controlled release of the antibiotic ciprofloxacin using RF-glow discharge plasma deposition. The technique of plasma coating of powder substrates has also been utilized in the field of coatings. Corrosion inhibitive paint pigments like tolyltriazole, benzotriazole, and 1,2,4-triazole are soluble in water and therefore cannot be used in paints because they would cause blistering of organic coatings when in contact with moisture. The pigments were encapsulated in a plasma-polymerized thin film to serve as slow-release pigments [25].

Thin organic films were deposited on polymethylmethacrylate (PMMA) powder particles by combining the techniques of plasma polymerization and vacuum fluidization [29]. Monomer hexamethylene disiloxane was used for modifying the surface of these PMMA powders. A thin film of plasma-polymerized pyrrole was deposited on the surfaces of alumina nanoparticles [30]. The diameter of the nanoparticles ranged from 10 to 150 nm in spherical shapes. The particles were treated in a plasma reactor consisting of a Pyrex glass column. The particles were vigorously stirred at the bottom of the tube in order to expose the full powder surface to plasma. The deposited plasma polymer on the surface of alumina nanoparticles was about 2 nm thick. The surfaces of carbon nanotubes were also modified using a plasma polymerization technique [31]. Pyrrole was again used as the monomer for the modification process. Hydroxyapatite (HA) powders were modified by the plasma polymerization technique in order to improve their ease of dispersion in water for biomedical applications. Acrylic acid was used as the monomer for the process [32].

## ***2.6 Plasma Modification of Fillers for Rubber Applications***

In the process of plasma polymerization, a highly crosslinked polymer is deposited on the surface. The deposited plasma polymer changes the surface properties of the substrate dramatically. It modifies the surface of powders in terms of surface energy, functional groups, wettability, interaction with polymers, and dispersion



in polymers. This technique of modifying powder surfaces has received the attention of scientists in the field of rubber technology.

Akovali and Ulkem [33] reported the surface modification of carbon black by plasma polymerization of styrene and butadiene. The effect of such plasma-coated carbon black was studied in a SBR matrix. A slight increase in the tensile strength was observed for the plasma-polymerized styrene-coated carbon black. This was explained by a decrease in the interfacial tension, as the result of the similarities between the treated filler and the matrix at the interface. They also concluded that the plasma coating obtained on carbon black is so thin that no blockage of the pores occurred and that there was no decrease in the original absorptive capacity.

Another attempt by Tricas et al. to modify the surface of carbon black was by the plasma polymerization of acrylic acid [34]. Treatment with acrylic acid made carbon black hydrophilic. Plasma-coated carbon black was mixed with natural rubber and showed increased filler–filler interaction. The bound rubber content was reduced after the surface treatment of the filler. The authors also concluded that the surface of the carbon black was completely covered by the plasma polymer film, preventing the carbon black surface from playing any role in the polymer matrix.

Later, Kang et al. [35] reported surface modification of carbon black using various monomers like acetylene, acrylic acid, butadiene, and oxygen. They concluded that it is possible to manipulate the surface properties of carbon black using plasma polymerization.

Surface modification of silica, another filler used in the rubber industry, has been reported by Nah et al. [36, 37]. The silica surface was modified by plasma polymerization of acetylene. The modified silica was mixed with SBR to study its performance. They observed an increase in reinforcement with the plasma-modified silica and hence better mechanical properties. They also observed an improvement in the dispersion properties for the plasma-coated silica. The authors explained the observed improvement in properties by a mild crosslinking between plasma-polymerized acetylene and the butadiene part of the SBR matrix.

Sulfur, the main crosslinking agent used in the rubber industry, has the problem of poor miscibility with rubbers. During storage of a mixed compound before vulcanization, sulfur tends to bloom to the surface. This migration can create sulfur bloom and spots on the surface that affect the compound's tack properties. Vidal-Escales et al. [38] modified sulfur by the plasma polymerization technique to change its surface polarity. Pyrrole, acetylene, and perfluorohexane were used as the monomers for plasma polymerization. This modification changed the sulfur accessibility and consequently the vulcanization kinetics. Using *N*-cyclohexyl benzothiazole sulfenamide (CBS) accelerator, squalene vulcanization seemed to be affected by the plasma treatment. This is because after the plasma treatment sulfur is encapsulated in a plasma polymer shell, and has to escape out of the shell in order to take its role in the crosslinking reaction.

Vidal et al. [39] reported plasma modification of CBS with different monomers: acrylic acid, acetylene, and perfluorohexane. It was found that by plasma polymerizing appropriate monomers onto the surface of accelerator particles, the onset of its accelerating effect during vulcanization could be controlled. Rheometer testing

clearly showed that scorch times were affected by the plasma-polymerized monomers on the CBS surface, but final crosslink densities of the cured rubbers were almost identical. In the case of CBS with acrylic acid coating, the scorch time was reduced compared to that of unmodified CBS. However, in the case of CBS with plasma-polymerized acetylene and perfluorohexane, the scorch time was observed to be longer.

### 3 Plasma Polymerization onto Silica and Carbon Black Fillers, and onto Sulfur Vulcanization Agent

#### 3.1 Plasma Reactors

For the surface modification of silica and carbon black, a radiofrequency (13.56 MHz) electrode-less tumbler plasma reactor at the University of Cincinnati was used. The schematic reactor design is shown in Fig. 5. It consists of a Pyrex cylinder chamber of 40 cm in length and 20 cm in diameter, with a motor-driven shaft at its center, and two vanes running in opposite directions. The reactor is based on a horizontal mixing principle and is capable of treating 350 g per batch. The powdery materials to be coated are placed at the bottom of the chamber. The plasma

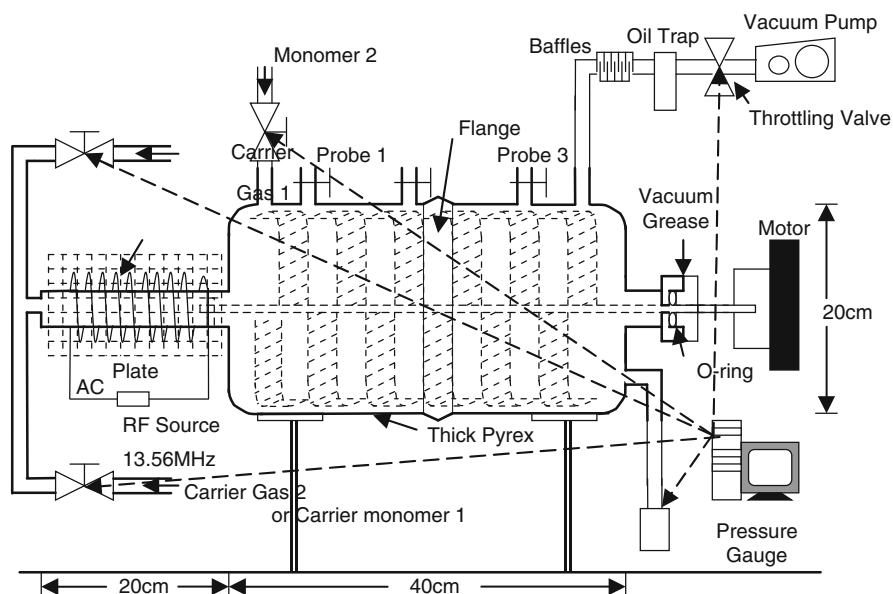
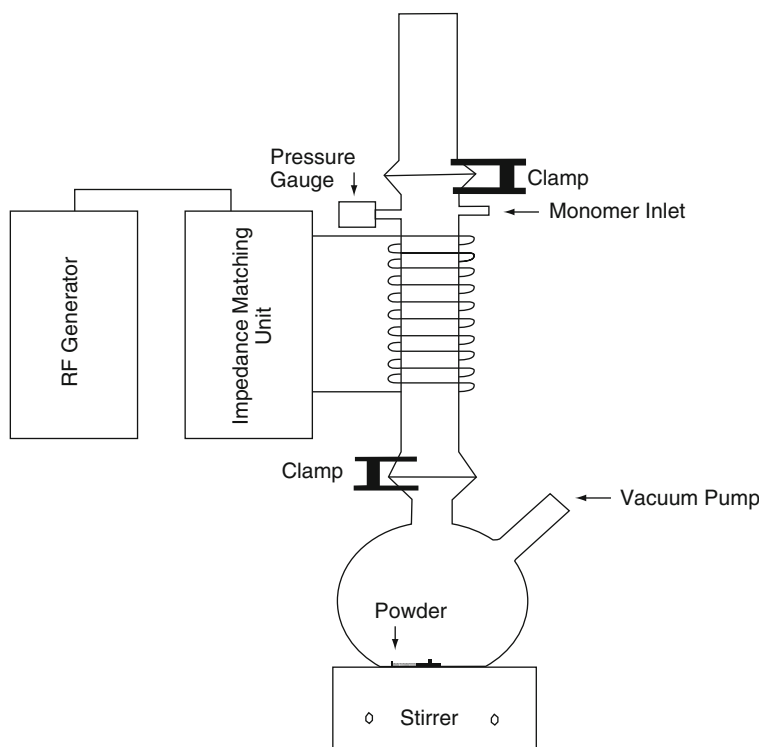


Fig. 5 Schematic representation of the tumbler RF plasma reactor for plasma polymerization onto powders [40]

is generated through the RF copper coil with 5–6 turns wound around one side-zone of the chamber and is maintained by RF radiation generated by a Kenwood Transceiver 530 SP (power range 0–100 W) with matching network. Thus, the powders are treated in a remote zone to avoid direct plasma exposure. The plasma monomer, with or without an extra carrier gas (used optionally), conveys the plasma to the deposition area where the reactions between the excited monomers take place together with the deposition on the powdery substrates. Facilities in this reactor include introduction for both gasses and vapors.

Characterization of this tumbler reactor was carried out via the deposition rate measurement of a plasma polymer film on silicon wafers under different conditions. In the longitudinal direction, the deposition rate decreases significantly when the plasma moves from the central plasma zone to the remote zone. With appropriate shielding, the decay in deposition rate in the longitudinal direction can be effectively reduced. By means of the stirring, a uniform distribution of the plasma deposition is achieved within the chamber.

For the modification of sulfur, a smaller reactor based on the same technique was used, as schematically shown in Fig. 6. The reactor consists of a round bottomed flask attached to a long cylindrical tube. The powder particles are kept at the bottom



**Fig. 6** Schematic representation of the vertical tubular reactor for plasma polymerization onto powders [41]

of the flask and can be stirred with the help of a magnetic stirrer. In order to facilitate good mixing, a brush is attached to the magnet. An outlet of the flask is connected to the vacuum pump. A copper coil of five turns is wound around the tubular region. The coil is further connected to a RF generator via an impedance matching unit. There are two ports at the top of the cylindrical tube. These are slots for connections to the monomer source and for the pressure gauge. The top portion of the reactor is closed using a glass cover with a vent.

The positions of the coil and of the monomer inlet have an influence on the modification process. Optimization experiments of the positions of the coil and monomer inlet were carried out with acetylene, by putting a glass strip inside the reactor covering the whole length of the flask and cylindrical tube, and looking at the deposition obtained at different regions on the glass strip. The most suitable position for the coil was as close to the round bottomed flask as possible. The monomer inlet could be used as such, without any further guiding by additional glass tubes inside the cylindrical tube.

## **3.2 *Materials***

The various substrates, monomer gasses or vapors, rubbers, and vulcanization ingredients are given in Table 1. The materials were used as received, without further purification.

## **3.3 *Process Conditions for Plasma Deposition***

### **3.3.1 *Silica***

The plasma polymerization onto silica was carried out after charging 100 g of dried silica Ultrasil VN3 into the reactor, pumping down to 13 Pa and introducing plasma gasses or monomer vapors for further plasma polymerization. The conditions for the preparation of plasma-polymerized acetylene (PA), pyrrole (PPy) and thiophene (PTh) are presented in Table 2.

### **3.3.2 *Carbon Black***

Different carbon black types, as described in Table 1, were compared concerning their activity in plasma polymerization with acetylene as monomer: Acetylene-plasma deposition was carried out with a monomer pressure of 27 Pa, a RF power of 250 W, and a treatment time of 1 h.

For the in-rubber investigations, the fullerene soot EP-P434 was used. The plasma-treatment conditions were a RF power of 100 W, an acetylene concentration of 40 Pa, and a treatment time of 2.5 h.

**Table 1** Materials used in the investigations

Sample	Category	BET surface area (m <sup>2</sup> /g)	Other characteristics	Supplier
<i>Silica</i>				
Ultrasil VN3	Silica	175	–	Evonik
<i>Carbon blacks</i>				
SP350	Oxidized furnace black	65	pH = 4.4	Evonik
CK3	Gas black	88	pH = 3.5	Evonik
FW 200	Oxidized gas black	550	–	Evonik
CSDPF 2124	Carbon/silica dual phase filler	171	9% silica	Cabot
CSDPF 4210	Carbon/silica dual phase filler	154	55% silica	Cabot
EP-P434	Fullerene soot	70	Fullerene sites	Timcal Graphite and Carbon
E-250G	Conductive carbon black	65	–	Timcal
EMM131	Graphitized E-250G	–	–	Timcal
<i>Gasses and vapors</i>				
Acetylene	C <sub>2</sub> H <sub>2</sub>		99.6% pure	Wright Brothers
Acrylic acid	C <sub>3</sub> H <sub>4</sub> O <sub>2</sub>		99% pure	Sigma-Aldrich
Perfluorohexane	C <sub>6</sub> F <sub>14</sub>		99.6% pure	Sigma-Aldrich
Pyrrole	C <sub>4</sub> H <sub>5</sub> N		99.9% pure	Sigma-Aldrich
Thiophene	C <sub>4</sub> H <sub>5</sub> S		99.9% pure	Sigma-Aldrich
<i>Rubbers</i>				
EPDM	48 wt% ethylene, 9 wt% ethylidene norbornene		Keltan 4703	DSM Elastomers
NBR	35 wt% acrylonitrile, 65 wt% butadiene		Perbunan 3446F	Lanxess
S-SBR	25% styrene, 75% butadiene		Buna VSL 5025-0 HM	Lanxess
<i>Vulcanization ingredients and coupling agent</i>				
CBS	<i>N</i> -cyclohexyl 2-benzothiazol sulfonamide		Santocure CBS	Flexsys NV
DPG	<i>N,N'</i> -Diphenylguanidine		Perkacit DPG	Flexsys
S <sub>8</sub>	Elemental sulfur		<100 mesh (150 μm)	Sigma Aldrich
Stearic acid	–		–	Sigma Aldrich
TESPT	<i>Bis</i> -(triethoxysilyl-propyl)tetrasulfide (coupling agent)		Si 69	Evonik
TMTD	Tetramethyl-thiuram disulfide		Perkacit TMTD	Flexsys
ZBEC	Zinc-dibenzyl-dithiocarbamate		Perkacit ZBEC	Flexsys
ZnO	–		–	Sigma Aldrich

**Table 2** Plasma polymerization conditions for silica using different monomers

Product	RF power (W)	Monomer pressure <sup>a</sup> (Pa)	Reaction time (min)
PA-silica	100	53	90
PPy-silica	100	33	90
PTh-silica	100	20	90

<sup>a</sup>Monomer pressure is an indication of monomer concentration

**Table 3** Plasma treatment conditions for sulphur using various monomers

Sample code	RF power (W)	Monomer pressure <sup>a</sup> (Pa)	Reaction time (min)
PPAS <sub>8</sub> -1	150	26	60
PPAS <sub>8</sub> -2	150	31	60
PPAS <sub>8</sub> -3	150	26	90
PPAS <sub>8</sub> -4	125	26	90
PFHS <sub>8</sub> -1	180	27	60
PFHS <sub>8</sub> -2	180	27	90
PAAS <sub>8</sub> -1	180	27	90
PAAS <sub>8</sub> -2	180	27	120

<sup>a</sup>Monomer pressure is an indication of monomer concentration

PPAS<sub>8</sub> plasma polyacetylene-treated sulfur, PFHS<sub>8</sub> plasma polyperfluorohexane-treated sulfur, PAAS<sub>8</sub> plasma polyacrylic acid-treated sulfur

### 3.3.3 Sulfur

Table 3 shows four sets of conditions for treating sulfur with plasma polyacetylene. The samples designated PPAS<sub>8</sub>-1 to PPAS<sub>8</sub>-4 were used in subsequent studies.

## 3.4 Characterization Techniques for Plasma-Modified Fillers and Sulfur

### 3.4.1 Immersion Test and Water Penetration Measurements: Hydrophobicity

*Solvent test* – A small amount of powder is poured onto the surface of a liquid and its sinking or floating behavior is observed. Liquids of different polarities such as toluene, formamide, ethylene glycol, and water were used.

*Water penetration* – A glass capillary is packed with 5 mg of the filler. One opening is closed with a very fine nylon mesh (pore size 20 μm). The open end of the column is placed in water, and the change in weight over time is measured with a balance [42].

### 3.4.2 Thermogravimetric Analysis: Amount of Deposited Material

A Perkin-Elmer instrument (TGA 7) was used for the thermal analysis. The heating temperature was varied from 50 to 600°C at a rate of 10°C/min, and air was used as purging gas. These measurements provide information about the weight of the plasma-polymer coating per unit weight of the substrate.

### 3.4.3 Time-of-Flight Secondary Ion Mass Spectroscopy: Chemical Structure of the Film

The time-of-flight secondary ion mass spectroscopy (ToF-SIMS) analysis was performed on a CAMECA ION-TOF Model IV spectrometer. This instrument was equipped with a reflection-type ToF mass analyzer and a pulsed 25 kV primary source of monoisotopic  $^{69}\text{Ga}^+$  ions, with a minimum beam size of 500 Å.

### 3.4.4 Scanning Electron Microscopy: Morphology

A Philips Environmental-SEM/EDX (Philips XL30) was used to measure the morphology on untreated and plasma-treated powders. The powders were fixed on the sample holder by double conductive adhesive aluminum tape, and then gold-coated. Secondary electron images were recorded with the scanning electron microscope (SEM) using a 15 keV acceleration voltage.

## 3.5 Characterization of Plasma-Coated Powders

### 3.5.1 Silica

*Hydrophobicity* – Before plasma treatment, silica powder is highly hydrophilic and immediately sinks in water. After plasma film deposition, the material floats on water for several hours. A significant reduction in polarity and in surface energy compared to untreated silica is found, down to the range of 28.4–47.7 mJ/m<sup>2</sup>. The water penetration into powder beds of untreated and plasma-treated silica is shown in Fig. 7. The untreated silica absorbs water very fast, whereas the plasma-treated silicas show a significantly decreased water penetration rate. The lowest rate is found for the polythiophene-coated silica (PTh-silica).

*Amount of deposited material* – The difference in weight loss between coated and untreated silica corresponds to the weight of the plasma-polymerized film deposited on the surface. For the plasma-treated silicas, decomposition of the coating starts at 265°C for polyacetylene, 200°C for polypyrrole, and 225°C for polythiophene, and is complete at 600°C. Between 265 and 600°C, PA-silica shows 6 wt% weight loss, and PPy- and PTh-silicas show 4.5 wt% and 5 wt% loss, respectively.

*Functionalities on the silica surface* – The ToF-SIMS spectra were recorded of the untreated and treated silicas. Figure 8 represents an untreated silica sample, and Fig. 9 an acetylene-treated one. They show a complex structure of a plasma-polymerized acetylene film on the silica surface.

In the spectra of the untreated silica sample, no specific peaks in the low mass region up to 150 amu (atomic mass units) such as from  $\text{C}_2\text{H}_3^+$ ,  $\text{C}_{10}\text{H}_{10}^+$ , and no cluster peaks in the higher mass region are found. The spectra of the acetylene-treated sample do show these specific plasma-polymerized acetylene peaks in the

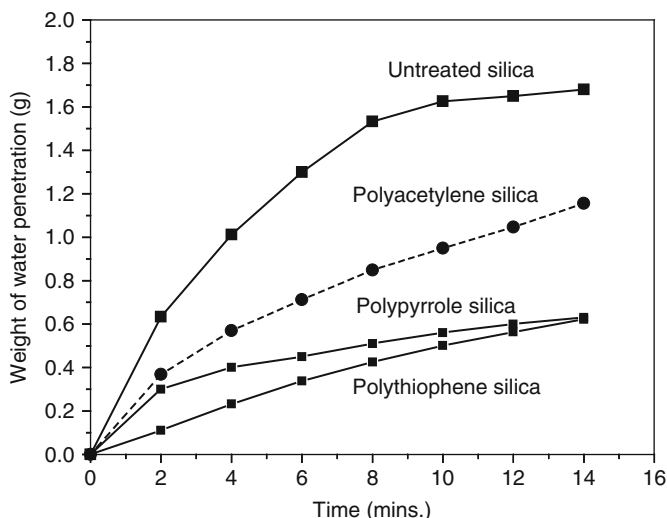


**Fig. 7** Water penetration into powder beds of untreated silica and plasma-polymerized acetylene-, pyrrole-, and thiophene-coated silica

low mass region and strong acetylene-cluster peaks in the higher mass region, indicating a polymeric surface coating on the silica powders.

The spectra of the negative ions of the untreated silica powders (Fig. 8b) have no specific peaks such as from  $C^-$ ,  $CH^-$  in the mass range of 0–40 amu, in contrast to the spectra of the acetylene-treated sample (Fig. 9b), which do show these  $C^-$  and  $CH^-$  peaks again in this mass region. This is another proof of the surface coating on the silica powders.

Similar spectra were recorded for the thiophene- and acetylene-treated samples; in those cases sulfur and nitrogen moieties were detected as well.

*Morphology* – SEM images of untreated and plasma acetylene-treated silica samples are shown in Fig. 10. The PA-silica shows a clear difference in dimensions in comparison to the untreated silica powder: The film deposition occurs onto small-sized aggregates, resulting in larger spherical particles connected into an open structure.

*Discussion* – The morphological properties of active fillers are important aspects of rubber reinforcement. The structure of the reinforcing filler is characterized by aggregates of primary particles, which form cavities for attachment and penetration of polymer molecules. The SEM pictures show that the three-dimensional morphology is basically maintained.

In all the cases of polyacetylene, polythiophene, and polypyrrole coating, the amount of plasma-film deposition was different, caused by the difference in the structure of the three different monomers and their reactivity during the plasma process. PPy- and PTh-silica are more hydrophobic than PA-silica, probably due to the presence of different chemical moieties in the complex film structure deposited onto the silica surface.



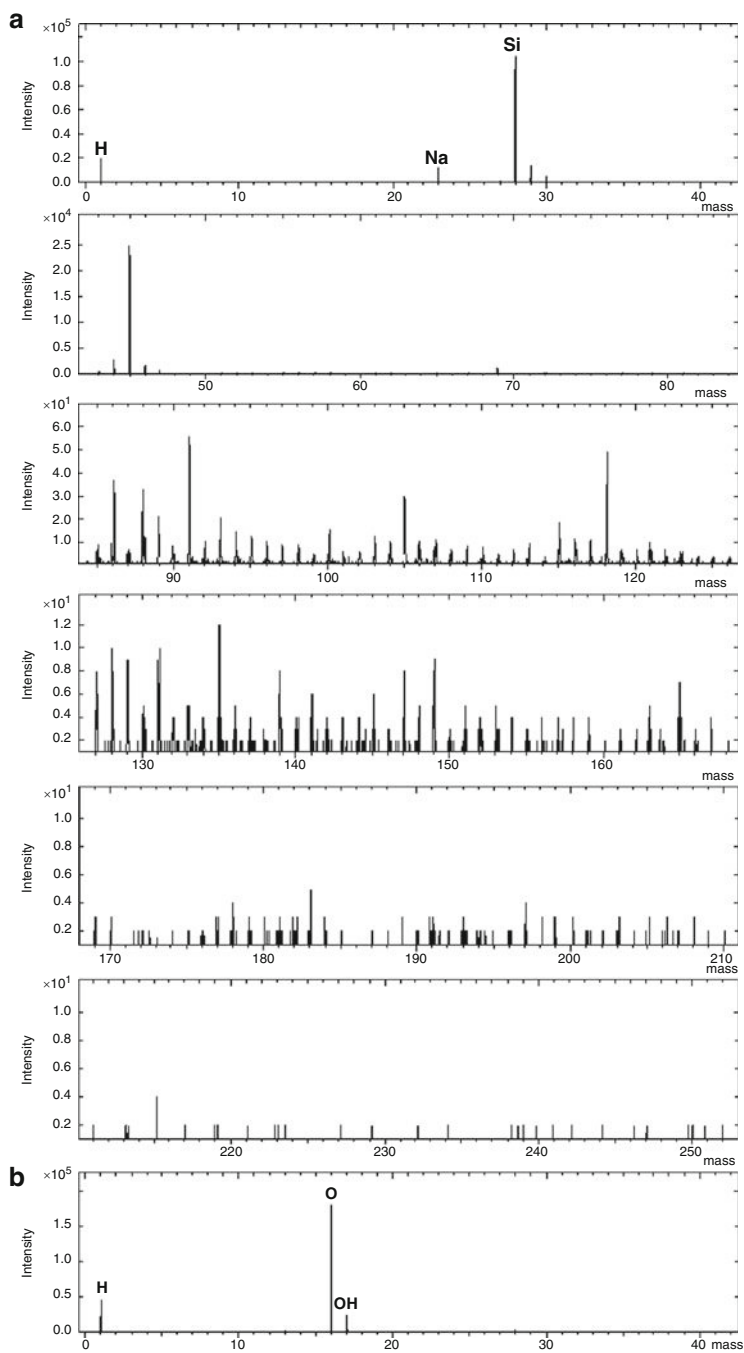


**Fig. 8** ToF-SIMS spectra of untreated silica: (a) positive and (b) negative

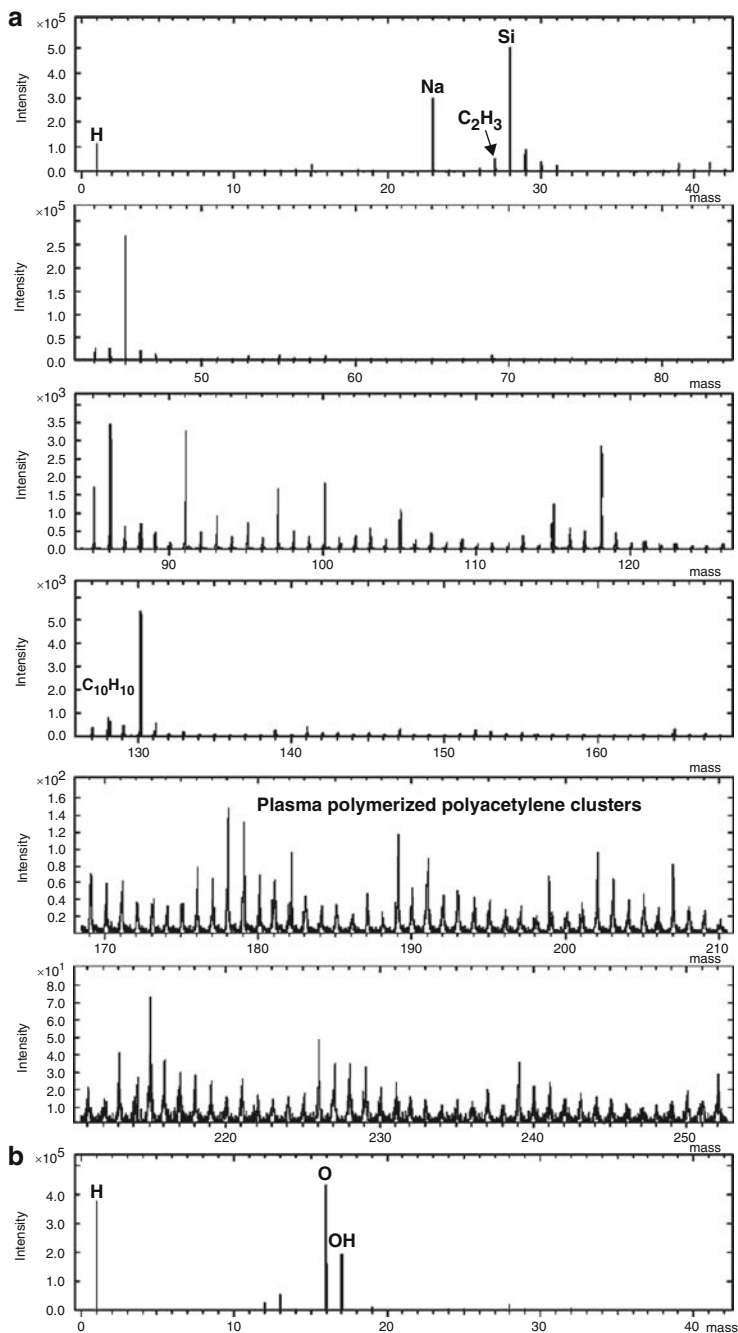


**Fig. 9** ToF-SIMS spectra of plasma-acetylene-coated silica: (a) positive and (b) negative

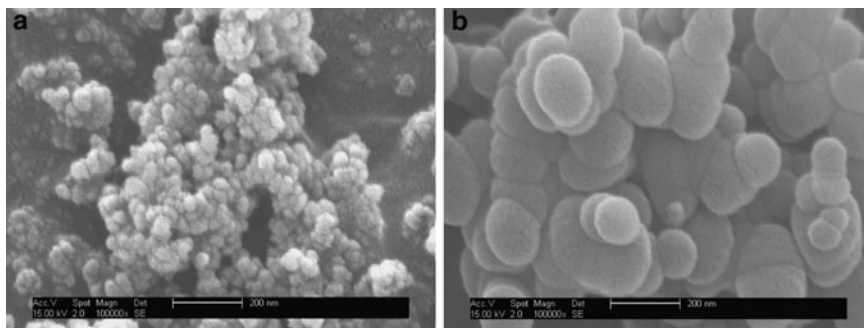


**Fig. 10** SEM images (magnification 100,000 $\times$ ) of untreated silica (a) and PA-silica filler (b)

**Table 4** TGA weight loss for various types of plasma-treated carbon black

Sample	Category	TGA weight loss (%)
SP50	Oxidized furnace black	0.4
CK3	Gas black	0.3
FW 200	Oxidized gas black	3.0
CSDPF 2124	Carbon/silica dual phase filler	1.5
CSDPF 4210	Carbon/silica dual phase filler	2.6
EP-P434	Fullerene soot	14.0
E-250G	Conductive carbon black	2.4
EMM131	Graphitized E-250G	2.3

### 3.5.2 Carbon Black

*Hydrophobicity* – The surface tension of the fullerene soot before treatment was in the range of 70 mJ/m<sup>2</sup>; after deposition of polyacetylene it was reduced to 47.7–57 mJ/m<sup>2</sup>, making it more compatible with polymers.

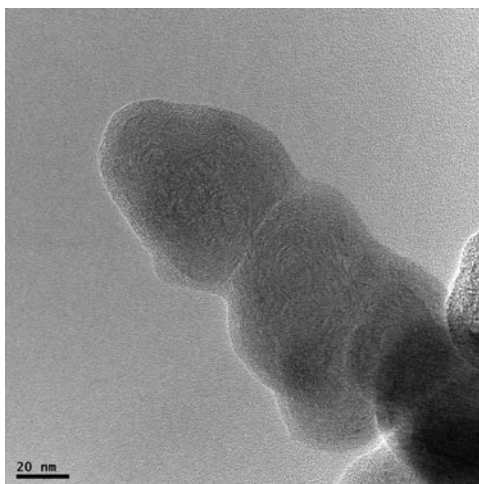
*Amount of deposited material* – Table 4 shows the deposited weight measured with thermogravimetric analysis (TGA) for the different carbon black types after polyacetylene deposition at 27 Pa monomer pressure, 250 W power, and 1 h treatment time. These values show that the most active carbon black is the fullerene soot EP-P434.

This fullerene soot EP-P434 showed a deposition of 5.5% when the RF power was reduced to 100 W, with 40 Pa acetylene and 2.5 h treatment time. This sample will be discussed in detail later for its in-rubber performance: Section 5.

*Morphology* – The TEM picture in Fig. 11 clearly shows the coating on fullerene soot primary particles. The thickness of the coating could be quantified as being 3–5 nm thick.

*Discussion* – Some surface modification does take place on all carbon black samples. On the other hand, in the case of the oxidized gas black, its larger oxygen functionality clearly increases its capability to be modified. The case of carbon/silica dual-phase fillers is similar. The TGA data show that the higher silica content

**Fig. 11** TEM image of plasma-coated fullerene carbon black



on the surface of CSD PF 4210 results in a larger amount of plasma polymer being deposited. This shows that the chemical functionalities and their distribution over the surface play an important role in the surface modification by plasma polymerization. But, the extent of modification of the above-mentioned carbon black samples is in all cases limited in comparison with the ease with which the fullerene carbon black could be modified. The fullerene carbon black after modification shows a substantial amount of plasma polymer deposition and an appreciable reduction in surface energy. The wide difference in behavior arises from the different surface characteristics of the carbon blacks. The surface of oxidized furnace blacks, gas blacks, and oxidized gas blacks contains more oxygen functionalities than a normal rubber grade furnace black (e.g., N330). Similarly, on the surface of the dual phase fillers, silanol groups are present like on silica. In the case of fullerene carbon black, the surface contains fullerenes and fullerene-like structures. In these structures, double bonds are localized and weakly conjugated [43]. This is due to a strong deviation from planarity of the curved surfaces of these molecules (pyramidalization). Fullerenes and higher homologs have an unusually high electron affinity and have been defined as free radical sponges. The presence of these highly active moieties on its surface enhances the reactivity of fullerene carbon black towards plasma coating.

### 3.5.3 Sulfur

*Hydrophobicity* – After surface modification by plasma polyacetylene, sulfur floats on top of ethylene glycol, whereas the untreated sulfur sinks immediately. The surface energy of uncoated sulfur can therefore be scaled in the range of 47.7–50 mJ/m<sup>2</sup> and polyacetylene-encapsulated sulfur in the range of 28.4–47.7 mJ/m<sup>2</sup>.

Polyperfluorohexane-coated sulfur floats on ethylene glycol for hours, whereas sulfur samples coated with the other two polymers sink after minutes, especially acrylic-acid-coated sulfur. As the surface energy of sulfur after encapsulation with a plasma polymer is brought closer to those of the rubbers, better compatibility with these rubbers is to be expected.

*Amount of deposited material* – The thermogravimetric curves of uncoated sulfur and sulfur encapsulated with different plasma polymers are given in Fig. 12. The weight losses in the TGA curves of the different encapsulated sulfur powders are all shifted to a higher temperature compared to uncoated sulfur. The

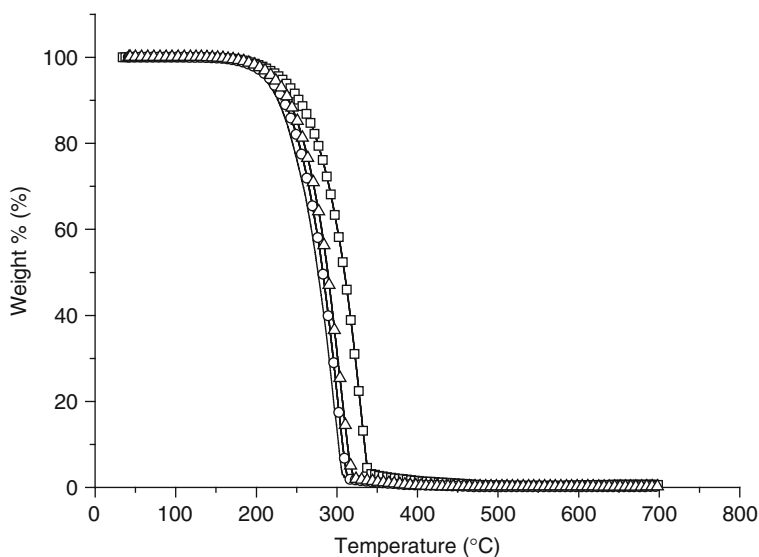


**Fig. 12** TGA thermograms of uncoated sulfur and different plasma-coated sulfurs: *solids line*  $S_8$ ; *squares*  $PPAS_8-2$ ; *circles*  $PFAS_8-2$ ; *triangles*  $PAAS_8-2$

**Table 5** TGA weight loss for various samples of plasma-treated sulfur

Sample code	Amount of coating (%)	Temperature at 5% wt loss (°C)
$S_8$	–	211.0
$PPAS_8-1$	n.a.	231.5
$PPAS_8-2$	1.32	235.0
$PPAS_8-3$	1.51	231.4
$PFHS_8-1$	1.23	211.2
$PFHS_8-2$	4.97	216.8
$PAAS_8-1$	1.4	214.5
$PAAS_8-2$	2.2	222.5

$S_8$  untreated sulfur,  $PPAS_8$  plasma polyacetylene-treated sulfur,  $PFHS_8$  plasma polyperfluorohexane-treated sulfur,  $PAAS_8$  plasma polyacrylic-acid-treated sulfur; *n.a.* not available

amounts of deposition and the temperatures for 5% weight loss are summarized in Table 5. Amongst the three monomers used in the study, acetylene is the most apt to form a plasma polymer, whereby a RF power of only 125 or 150 W is sufficient to create the plasma state. Polyacetylene also provides the largest delay in weight loss and the highest 5% weight loss temperature. The smallest delay is seen for plasma perfluorohexane-treated sulfur, even if it has a larger amount of deposition. The very porous and loose structure of the plasma layer may account for this lowest protection against weight loss.

*Functionalities on the sulfur surface* – ToF-SIMS was applied to both the untreated sulfur and the plasma polymer-encapsulated sulfur to obtain structural information on the outermost layer of the samples. The positive and negative spectra of untreated sulfur are presented in Fig. 13. Compared to Fig. 13b, there are clearly more peaks in the positive spectra in Fig. 13a, which come from hydrocarbon ions in the low molecular weight range. It is interesting to see that sulfur forms almost identical characteristic peaks of  $S_1$ ,  $S_2$  . . . up to  $S_{11}$  in both the positive and the negative spectra.

The positive and negative spectra of plasma polyacetylene-treated sulfur (sample PPAS<sub>8</sub>-2) are given in Fig. 14. In the positive spectra in Fig. 14a, the intensities of the hydrocarbon peaks are increased substantially compared those in Fig. 13a in the low mass range from 0 to 200. The intensities of all sulfur peaks are decreased in all mass ranges, which proves that the sulfur substrate is covered; however not to the full 100%. In the high mass range, specific peak patterns can be observed, which proves the presence of plasma polyacetylene. Not much difference was obtained in the negative spectra in Fig. 14b, where only more noise peaks are seen in the high mass range of 200–400.

In the positive spectra of plasma polyperfluorohexane-treated sulfur (sample PFHS<sub>8</sub>-2), similar changes are obtained compared to untreated sulfur, similar to those in Fig. 14a. As a different monomer was applied, the polymer fraction peaks in the high mass range show a different pattern. The accompanying negative spectra, where the presence of the fluor peak confirms the formation of a fluor-containing polymer, again shows that the surface is not fully covered because the sulfur peaks can still be detected.

The positive and negative spectra of plasma polyacrylic-acid-treated sulfur (sample PAAS<sub>8</sub>-2) show a significantly reduced concentration of sulfur ion peaks, which is a sign of the presence of the coating. This is further evidenced by the characteristic cluster pattern of mass fragments in the positive spectrum, especially in the higher mass fraction region from 200 to 400. No peaks coming from oxygen are detected. The absence of oxygen in the plasma polymer can be attributed to the very high RF power applied for the polymerization process. Such a high power breaks the acrylic acid molecules into atomic species and oxygen gas is formed as a by-product. In former research, a much lower RF power was applied so that the original structure of the monomer was better preserved (W.J. van Ooij, private communication).

*Morphology* – The morphologies of the ground uncoated sulfur and the plasma-polymer-modified sulfur particles are shown in Fig. 15. Compared to the image of

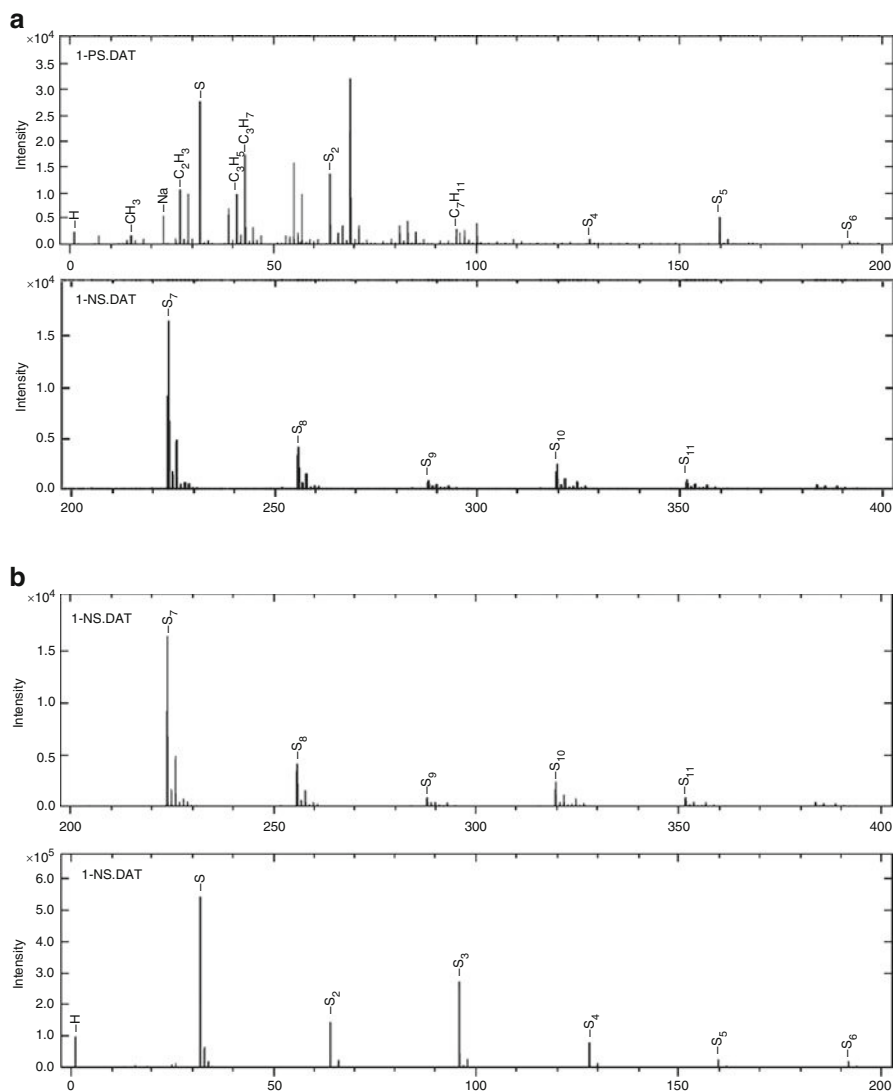


**Fig. 13** (a) Positive ToF-SIMS spectrum of untreated sulfur. (b) Negative ToF-SIMS spectrum of untreated sulfur

uncoated sulfur (Fig. 15a), a different structure is observed in Fig. 15b–d. The sulfur agglomerates after plasma polymerization with acetylene, perfluorohexane, and acrylic acid are rougher because an amorphous layer is deposited on the outside. The size of the encapsulated particles ranges from 10 to 100  $\mu\text{m}$ . In contrast to what has been described in the literature [42, 44, 45], the skin-layer is not free of pin-holes. Instead, there are some flaws present. As sulfur needs to be released from the

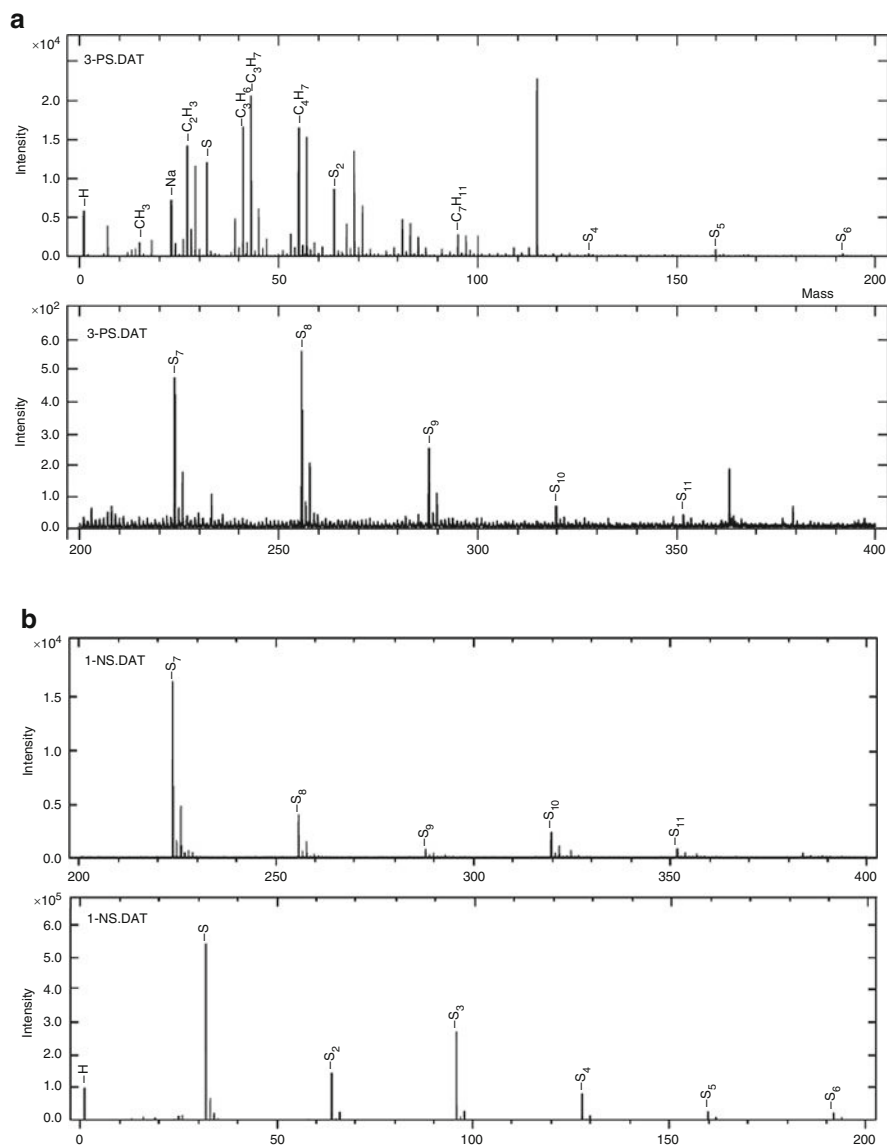


**Fig. 14** (a) Positive ToF-SIMS spectrum of plasma-acetylene-treated sulfur. (b) Negative ToF-SIMS spectrum of plasma-acetylene-treated sulfur

shell before the vulcanization process in a rubber system can proceed, the flawed encapsulation is actually a gateway for future release of the active sulfur.

A core-shell structure can be seen in Fig. 16, which shows a cross-section of about 100 nm of sulfur aggregate encapsulated with polyacetylene. The plasma polymer layer is rather coherent; while in other cases loose structures are also observed.



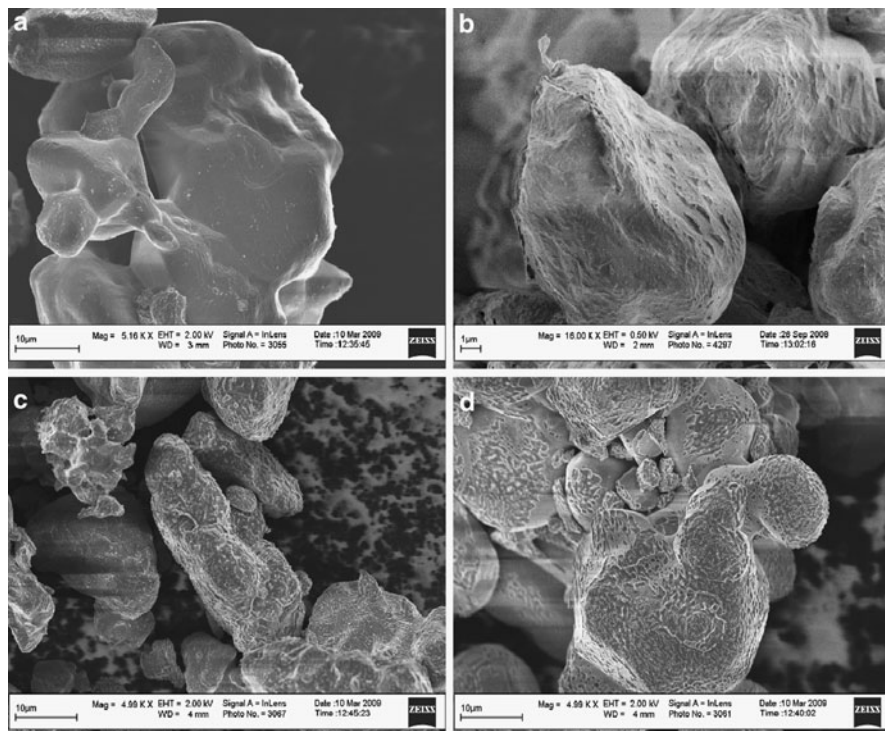


**Fig. 15** SEM images of (a) uncoated sulfur; (b) PPAS<sub>8</sub>; (c) PFHS<sub>8</sub>; (d) PAAS<sub>8</sub>

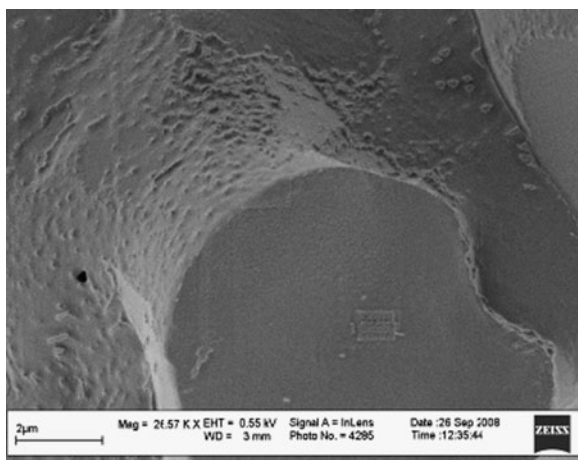


**Fig. 16** SEM image of cross-section of sulfur that has been plasma-coated with polyacetylene

## 4 Polyacetylene-, Thiophene- and Pyrrole-Coated Silica in Rubber

### 4.1 Silica in Pure S-SBR

#### 4.1.1 Compound Preparation

The compositions of the pure S-SBR compounds are given in Table 6. In the recipe containing TESPT, the amount of sulfur was adjusted to compensate for the presence of sulfur contained in TESPT, to represent equimolar quantities in all cases. For the compounding ingredients, see Table 1.

The samples were mixed in two steps, as described in Table 7.

#### 4.1.2 Compound Characterization Methods

*Rheological measurements of nonvulcanized rubber compounds* – Dynamic mechanical measurements were performed using a RPA 2000 dynamic curemeter

**Table 6** Basic formulations for silica-reinforced S-SBR

Component	Content (phr)				
	SU	SPA	SPPy	SPT <sub>h</sub>	ST
S-SBR	100	100	100	100	100
Silica	50	50	50	50	50
ZnO	2.5	2.5	2.5	2.5	2.5
Stearic acid	2.5	2.5	2.5	2.5	2.5
Silane (TESPT)	–	–	–	–	4
Sulfur	1.5	1.5	1.5	1.5	1.05
CBS	1.5	1.5	1.5	1.5	1.5
DPG	1.5	1.5	1.5	1.5	1.5

Sample codes: *SU* S-SBR reinforced with untreated silica; *SPA* S-SBR with PA-silica; *SPPy* S-SBR with PPy-silica; *SPT<sub>h</sub>* S-SBR with PTh-silica; *ST* S-SBR with silanized silica

**Table 7** Mixing procedure for 50 phr silica-reinforced S-SBR

Time (min)	Action
Step 1	
0	Gum rubber, lowering of the plunger
1	ZnO, stearic acid, ½ silica, ½ silane (if applicable)
2	½ silica, ½ silane (if applicable)
4	Sweep
6	Dump
Step 2	
0	Load compound
5	Dump

Sulfur and accelerators were added in a third mixing step on a Schwabenthan 100 mL two-roll mill at a temperature setting of about 40°C

(Alpha Technologies) at a temperature of 100°C, a frequency of 0.5 Hz, and strain amplitude of 0.56–100.04%.

*Filler–filler interaction (Payne effect)* – The introduction of reinforcing fillers into rubbery matrices strongly modifies the viscoelastic behavior of the materials. In dynamic mechanical measurements, with increasing strain amplitude, reinforced samples display a decrease of the storage shear modulus  $G'$ . This phenomenon is commonly known as the Payne effect and is due to progressive destruction of the filler–filler interaction [46, 47]. The  $\Delta G'$  values calculated from the difference in the  $G'$  values measured at 0.56% strain and at 100% strain in the unvulcanized state are used to quantify the Payne effect.

*Bound rubber* – The bound rubber content was measured with toluene as solvent [48, 49]. The nonvulcanized samples (0.2 g) were cut into small pieces and put into a steel-wire basket of very fine mesh, which was immersed in 100 mL of toluene at room temperature for 72 h. The solvent was renewed after 24 h. The extracts were collected and left for 24 h in air and 24 h in vacuo at 105°C to evaporate the solvent. The amount of bound rubber (BdR) is expressed as the percentage of the total polymer content in the compound.

*Cure characteristics and reinforcement parameter ( $\alpha_F$ )* – The cure characteristics were determined using the RPA 2000 dynamic curemeter (Alpha Technologies). The increase in torque at a frequency of 0.833 Hz and 2.79% strain was measured. The optimal vulcanization time ( $t_{90}$ ) of the samples was determined and used for curing of the samples in the press.

The reinforcement parameter ( $\alpha_F$ ) was calculated according to the following equation [50]:

$$\frac{S'_{\max} - S'_{\min}}{S'^0_{\max} - S'^0_{\min}} - 1 = \alpha_F \frac{m_F}{m_P} \quad (3)$$

with  $S'_{\max} - S'_{\min}$  being the curemeter torque difference of silica-filled rubber;  $S'^0_{\max} - S'^0_{\min}$  the torque difference of the gum compound; and  $m_F/m_P$  the filler loading, where  $m_F$  and  $m_P$  correspond to the mass fractions of filler and polymer, respectively.

The reinforcement parameter  $\alpha_F$  is a filler-specific constant that is independent of the cure system and is closely related to the morphology of the filler.

*Relative ranking of crosslink densities* – The apparent crosslink density was determined by swelling the rubber samples in toluene as solvent. The vulcanized samples of 20 × 20 mm<sup>2</sup> size were cut from a 2 mm sheet and immersed in 100 mL of toluene at room temperature for 72 h [51]. The solvent was renewed after 24 h. The sample was removed, blotted quickly with filter paper, and weighed. The samples were collected and left for 24 h in vacuo at 105°C to evaporate the solvent. The swelling value  $Q$ , defined as grams of toluene per gram of rubber hydrocarbon, was calculated as:

$$Q = (\text{swollen weight} - \text{dried weight}) / (\text{original weight} \times 100 / \text{formula weight}).$$

The formula weight is the total weight of the rubber plus compounding ingredients based on 100 parts of rubber. The apparent crosslink density is the reciprocal swelling value,  $1/Q$ .

*Mechanical properties* – Samples were cured in a Wickert laboratory press (WLP 1600/5\*4/3) at a pressure of 100 bar (10 MPa) for the duration of  $t_{90}$  of the samples. The cured sheet dimensions were  $90 \times 90 \text{ mm}^2$  and 2 mm thick. The stress–strain properties of the cured samples were measured on a Zwick Z020 tensile tester according to ISO-37 type 2.

#### 4.1.3 Effect of Plasma-Coated Silica on SBR Compound Properties

The Payne effect of S-SBR compounds filled with untreated silica, PA-, PPy-, and PTh-silicas, and silane-modified silica are shown Fig. 17.

There is a significant difference in the Payne effect between the samples containing untreated and PA-silica (samples designated SU and SPA, respectively). The sample filled with PTh-silica (SPTTh) only shows a slight decrease in the Payne effect compared to sample SU. On the other hand, the PPy-silica-filled sample (SPPy) shows no change in the Payne effect compared to sample SU. The sample filled with silane-modified silica (ST) shows the lowest Payne effect of all, representing the lowest degree of remaining filler–filler interaction.

Figure 18 shows the bound rubber content of samples filled with untreated silica, plasma-treated silicas, and silane-modified silica, as representative of the filler–polymer interactions. Samples SPTTh and SPA show the highest bound rubber contents, and the ST the lowest value. The SPPy sample shows a bound rubber content slightly lower than that of SU.

A high reinforcement parameter  $\alpha_F$  indicates a poor dispersion of a filler in a polymer. In Fig. 19, sample SU shows a high value of the reinforcement parameter,

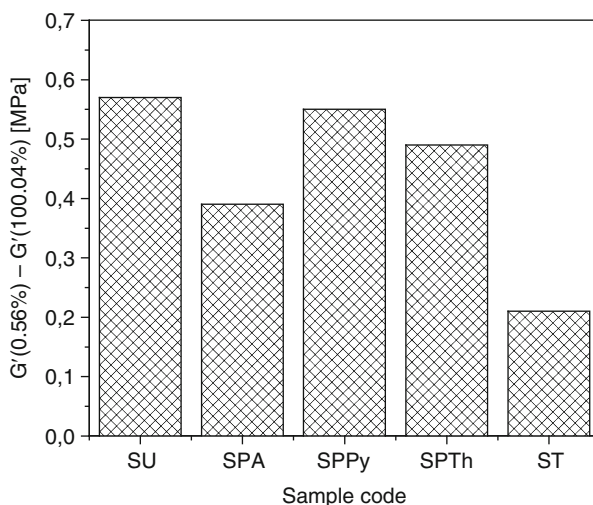


**Fig. 17** Payne effect of untreated silica, PA-, PPy-, and PTh-silicas, and silane-modified silica in S-SBR. Sample codes are detailed in Table 6

**Fig. 18** Bound rubber content of untreated silica, PA-, PPy-, and PTh-silicas, and silane-modified silica in S-SBR

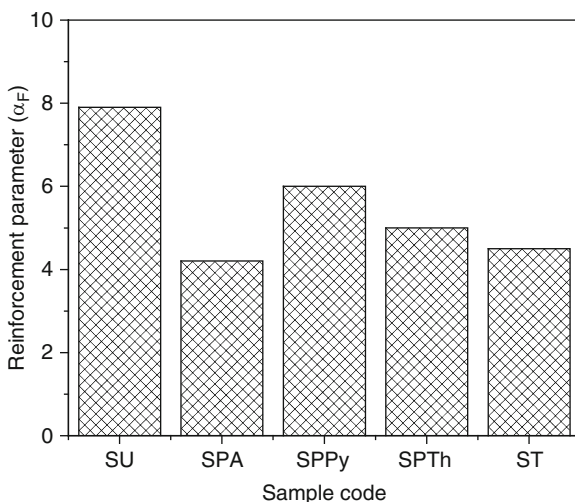
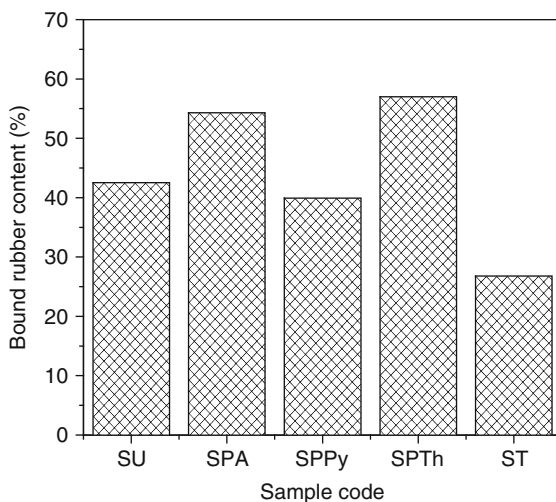


**Fig. 19** Reinforcement parameter of reinforced S-SBR with untreated silica, PA-, PPy-, and PTh-silicas, and silane-modified silica

which indicates a poor degree of dispersion of the filler in the S-SBR matrix, as was expected on basis of the earlier results. Samples SPA and ST show the lowest values, indicating the best dispersion in the polymer matrix in both cases compared to the other fillers.

The stress-strain curves of the silica-filled S-SBR vulcanizates are represented in Fig. 20. In the case of SPTTh, the moduli as well as tensile strength are higher than for all other samples. The samples SPPy and ST still show slightly higher moduli at higher elongations compared to SPA. However, there is only a small variation in tensile strength and elongation at break for all samples, except SPTTh.

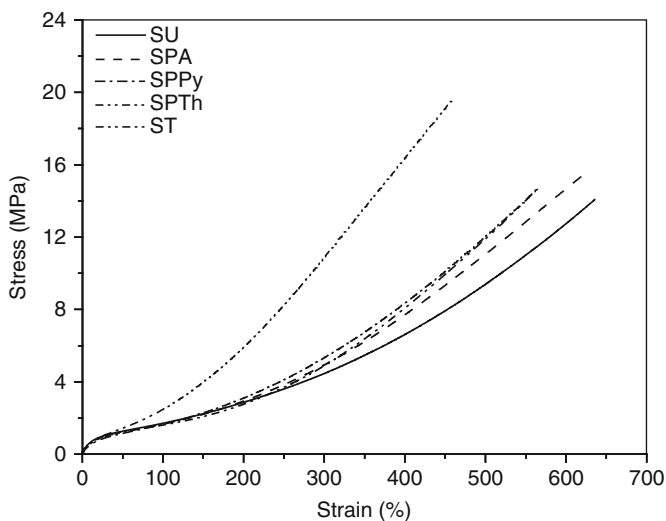


**Fig. 20** Stress–strain curves of reinforced S-SBR with untreated silica, PA-, PPy-, and PTh-silicas, and silane-modified silica

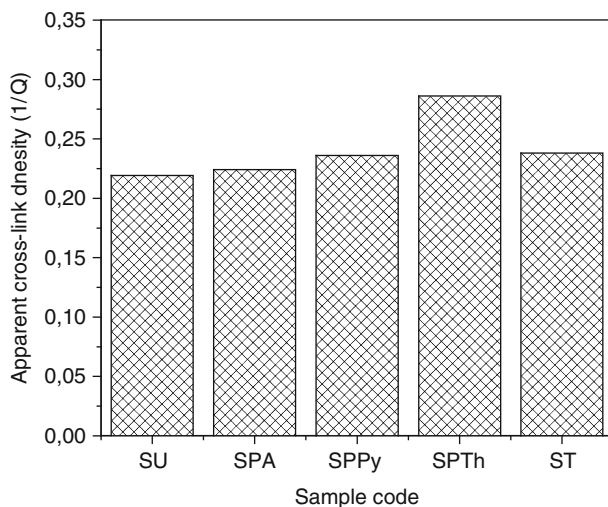


**Fig. 21** Apparent crosslink density of untreated silica, PA-, PPy-, and PTh-silicas, and silane-modified silica in S-SBR

The apparent crosslink densities for the vulcanized samples are shown in Fig. 21. SPTh shows the highest crosslink density; all other crosslink densities are significantly lower and show only minor differences.

#### 4.1.4 Discussion

The physical or chemical interaction of an elastomer with filler surfaces improves dispersion and prevents formation of secondary filler structures due to reagglomeration. The consequence of the reduced filler–filler interaction and enhanced filler–polymer interaction is a decrease in low-strain stiffness and an improvement in the ultimate vulcanizate properties (tensile strength and elongation at break). The plasma coating clearly improves the compatibility and, thus, the dispersion of silica in the S-SBR, as evidenced by the lower Payne effect of the samples containing PA-silica and PTh-silica. The compound with PPy-silica shows a higher Payne effect compared to both other compounds containing plasma-polymerized silica: this surface coating apparently has a lower compatibility with S-SBR. The modification of the polar silica surface by silane leads to the lowest Payne effect due to effective shielding of the silanol groups on the filler surface.

Complete wetting and good filler–polymer interaction of high surface area silicas are essential for a strong reinforcement of hydrocarbon elastomers. The bound rubber results stand out positively for the samples containing acetylene- and thiophene-treated silicas. This indicates a trend of increasing filler–polymer interaction due to a better match of their surface energies, which improves the compatibility of S-SBR with the different plasma-coated silicas. Contrary to what was expected, the silane treatment gives the weakest filler–filler interaction: The filler–polymer interaction in this case is not very strong, probably due to the chemical structure of the silane coating and insufficient coverage of the surface by nonpolar hydrocarbon groups. In this case, the required filler–polymer interaction is only developed during vulcanization.

Compounds containing PA-silica, PTh-silica, or silane-treated silica show the lowest reinforcement parameters in this series. This indicates a good dispersion of the polymer and a low degree of filler–filler interaction, as also shown by the Payne effect values.

Improved dispersion and better surface wetting are expected to influence the stress–strain behavior. However, the question may be raised concerning which tensile properties are most influenced: modulus, tensile strength, or elongation at break. On the basis of rubber elasticity theory, it can be anticipated that strong filler–polymer attachments have a similar effect of increasing the modulus as increased crosslinking. Strong filler–polymer interactions will also result in a contribution to the degree of crosslinking. The relative crosslink density,  $1/Q$ , therefore encompasses elements of real crosslink density, plus polymers attached to the silica surface. Comparing the  $1/Q$  data with the positions of the curves in the stress–strain diagrams, it is clear that there is a direct correlation between moduli (the 100% or 300% values) and the  $1/Q$  values; in this case, the higher the relative crosslink density, the higher the moduli.

Most conspicuous is the steep tensile curve for the S-SBR sample containing PTh-silica. The PTh-silica gives the best improvement in tensile properties in terms of tensile strength, modulus at 100%, and modulus at 300%, but elongation at break is lower. The PA- and PPy-silicas as well as the silane-treated silica result in only a slight

improvement of the tensile properties compared to the untreated silica. The ranking in tensile properties, moduli, and tensile strength parallels the relative order of the crosslink density values, which is higher for PTh-silica-filled S-SBR compared to all other silica types. The sulfur of the polythiophene moieties on the silica surface apparently contributes to the crosslinking network in S-SBR during vulcanization.

## 4.2 Silica in a S-SBR/EPDM Blend

### 4.2.1 Compound Preparations

Table 8 shows the compound compositions employed for this investigation. The mixing procedure was the same as given in Table 7. For the compound characterization methods, see Sect. 4.1.2.

### 4.2.2 Effect of Plasma-Coated Silica on SBR/EPDM Blend Properties

The Payne effects of S-SBR/EPDM blend filled with untreated silica, plasma-modified silicas, and silane-treated silica are shown in Fig. 22.

The blends containing PA-silica and PTh-silica (samples SEPA and SEPT<sub>h</sub>, respectively) show the highest Payne effect values of all samples. The silane-modified silica shows the lowest filler–filler interaction compared to all other silicas.

In Fig. 23, the bound rubber values are shown of S-SBR/EPDM-blend samples filled with untreated silica, plasma-coated silicas, and silane-modified silica. The plasma-treated silicas show in all cases a significantly higher bound rubber content

**Table 8** Compound compositions for silica in the SBR/EPDM blend

Component	Content (phr)				
	SEU	SEPA	SEPT <sub>h</sub>	SEPPy	SET
S-SBR	50	50	50	50	50
EPDM	50	50	50	50	50
Silica	50	50	50	50	50
ZnO	2.5	2.5	2.5	2.5	2.5
Stearic acid	2.5	2.5	2.5	2.5	2.5
Silane (TESPT)	–	–	–	–	4
Sulfur	1.5	1.5	1.5	1.5	1.04
CBS	1.5	1.5	1.5	1.5	1.5
DPG	0.75	0.75	0.75	0.75	0.75
TMTD	0.4	0.4	0.4	0.4	0.4
ZBEC	0.75	0.75	0.75	0.75	0.75

Sample codes: *SEU* SBR/EDPM reinforced with untreated silica; *SEPA* SBR/EDPM with PA-silica; *SEPPy* SBR/EDPM with PPy-silica; *SEPT<sub>h</sub>* SBR/EDPM with PTh-silica; *SET* SBR/EDPM with silanized silica



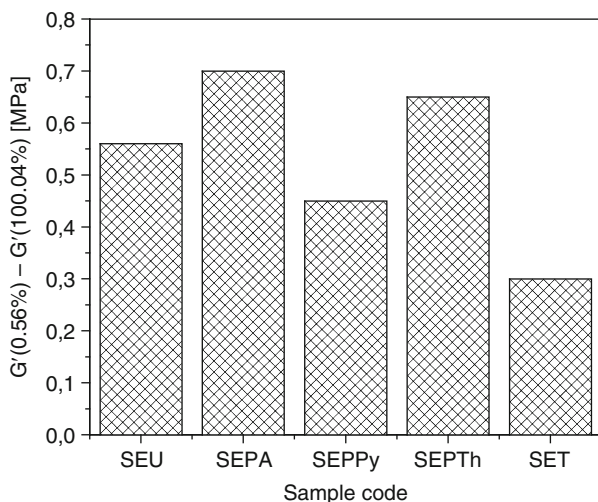


**Fig. 22** Payne effect of untreated silica, PA-, PPy-, and PTh-silicas, and silane-treated silica in a S-SBR/EPDM blend. Sample codes are detailed in Table 8

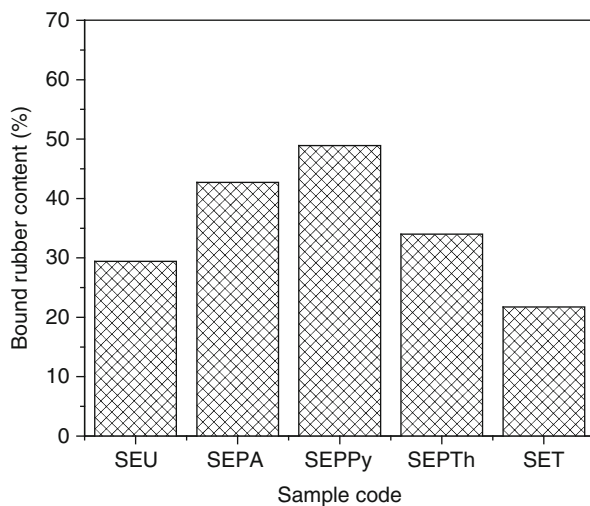


**Fig. 23** Bound rubber content of untreated silica, PA-, PPy-, and PTh-silicas, and silane-modified silica in a S-SBR/EPDM blend

compared to the blends containing untreated (SEU) and silane-treated (SET) silica. The blend filled with PPy-silica shows the highest bound rubber content, while the silane-treated filler results in the lowest value compared to all other combinations.

As mentioned earlier, a lower reinforcement parameter  $\alpha_F$  indicates a better dispersion of a filler in a polymeric matrix. In Fig. 24, SEU shows the highest value for the reinforcement parameter, which indicates the poorest degree of dispersion in

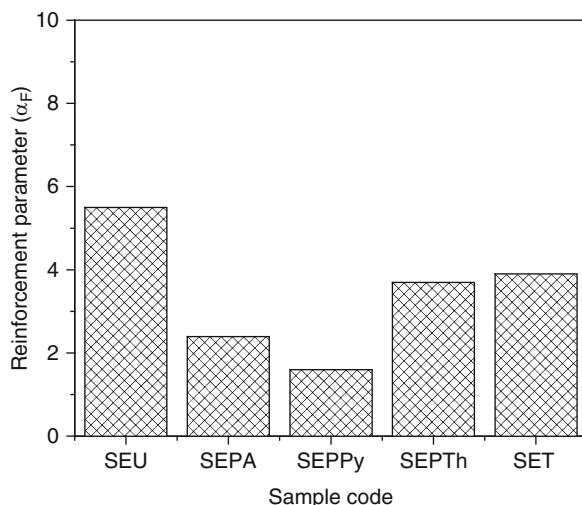


**Fig. 24** Reinforcement parameter of the S-SBR/EPDM blends with untreated silica, PA-, PPy-, and PTh-silicas, and silane-treated silica

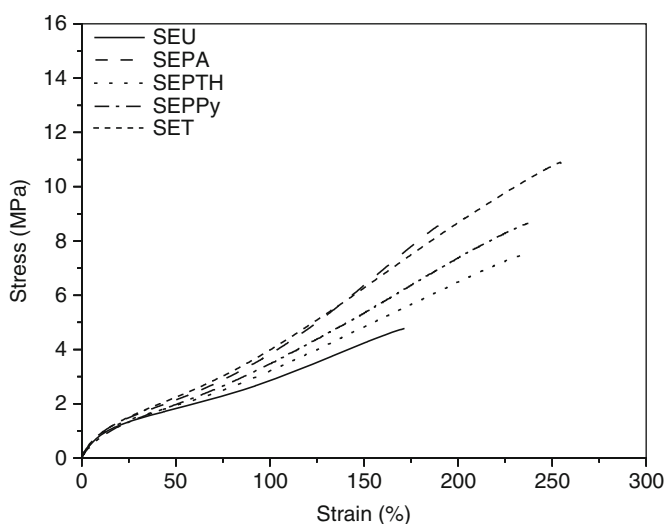


**Fig. 25** Stress–strain curves of reinforced S-SBR/EPDM blends with untreated silica, PA-, PPy-, and PTh-silicas, and silane-treated silica

the matrix. The lowest value and, thus, the best dispersion is found for PPy-silica in the blend.

The stress–strain curves of vulcanizates of S-SBR/EPDM blends filled with untreated silica, plasma-modified silicas, and silane-treated silica are represented in Fig. 25. Incorporation of untreated silica into the blend (sample SEU) leads to

very low values of the moduli, tensile strength, and elongation at break. There is a significant improvement in tensile properties, when plasma-treated silica is used. The sample containing PA-silica (SEPA) shows the highest moduli values, but comparable tensile strength to SEPPy and SEPT<sub>h</sub>. The latter samples show much higher elongations at break. However, SET shows the best tensile strength and elongation at break relative to all other samples.

The relative ranking of crosslink densities of the cured samples is shown in Fig. 26. SEU, SEPPy, and SEPT<sub>h</sub> show mutually similar values of the relative ranking of the crosslink density, lower than the crosslink densities of SEPA and SET.

### 4.2.3 Discussion

For silica, the plasma-pyrrole coating clearly improves the compatibility of the silica in the polymer blend. In contrast to this, the plasma-acetylene and plasma-thiophene treatments cause a high filler–filler interaction. This can be explained by the differences in compatibility between the plasma coatings and the polymers. In the case of PA-silica, the coating results in a higher compatibility towards EPDM in the blend, which could lead to an overconcentration of silica in the EPDM phase, with increased agglomeration of the filler.

The higher amounts of bound rubber for all samples filled with plasma-treated silica demonstrate an improved filler–polymer interaction between the plasma-treated silica and the polymers in the blend compared to untreated and silane-treated silica. The highest filler–polymer interaction for the PPy-silica can be due to the best compatibilization effect of PPy-silica with both polymers in the blend, as

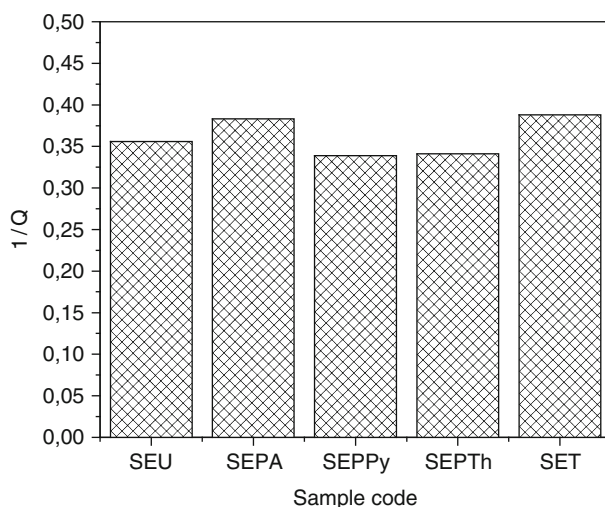


**Fig. 26** Apparent crosslink density ( $1/Q$ ) of S-SBR/EPDM blends with untreated silica, PA-, PPy-, and PTh-silicas, and silane-modified silica

also indicated by the low Payne effect value. The reinforcement parameters for all three plasma-silica-filled samples show a positive effect on dispersion compared to untreated and silane-treated silica. The PA- and PPy-silica-filled S-SBR/EPDM blends (SEPA and SEPPy, respectively) show the best dispersion of all. The higher moduli values of SEPA compared to SEU, SEPPy, and SEPT<sub>h</sub> are most likely due to this better compatibilization and dispersion behavior. The improved compatibility of PA-silica can be explained by a better match of the surface energy with EPDM, which is caused by the presence of ethylene functionalities on the surface of this silica after acetylene plasma polymerization: The chemical structure of the coating strongly resembles the structure of EPDM. SET shows the highest tensile strength value; the most probable reason for this being the chemical filler–polymer coupling reaction that occurs during vulcanization [52]. This is confirmed by the relative ranking of the crosslink density results, which shows a correlation between the crosslink density and moduli at 100%.

Overall, the plasma-treated samples show an improvement in terms of dispersion and tensile properties. Treatment with different plasma monomers show different levels of improvement in terms of dispersion and final vulcanizate properties due to the different levels of compatibilization in the polymer blend and, more specifically, with the different polymers used in this blend. The most important aspect for achieving an optimal balance between the properties of a filled polymer blend for a specific application is the selection of the proper monomer for the plasma modification of the silica surface, in relation to its required compatibility with a particular polymer in the blend.

## 5 Polyacetylene-Coated Carbon Black in Rubber

### 5.1 Carbon Black in Pure S-SBR

#### 5.1.1 Compound Preparations

Because of the limited success in obtaining a sufficient amount of plasma-coating on carbon black (as explained in Sect. 3.5.2) this evaluation was limited to original, unmodified fullerene soot (designated as FS) and its polyacetylene-plasma-coated variant EP-P434 (designated as PCFS). The compound formulations with varying amounts of black, as specified in Table 9 were used in this investigation. Table 10 shows the mixing procedure employed.

#### 5.1.2 Effect of Acetylene-Plasma-Coated Carbon Black on SBR Compound Properties

The Payne effect values of the plasma-coated carbon black at various filler loadings in SBR are shown in Fig. 27. The plasma-coated carbon black shows a lower Payne

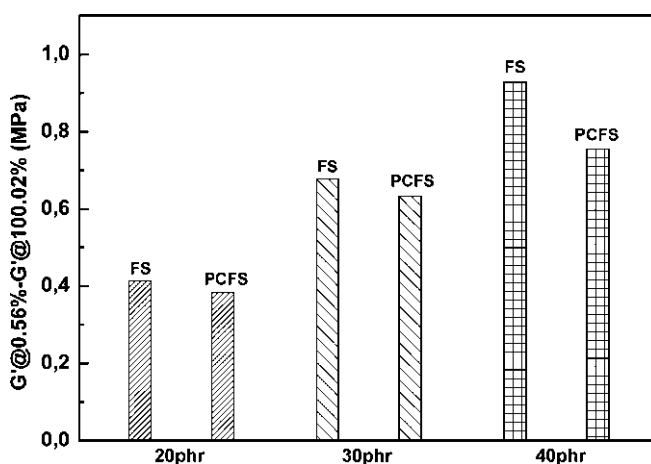
**Table 9** S-SBR compound formulations of samples used for carbon black investigations

Component	Content (phr)		
	20-phr sample	30-phr sample	40-phr sample
SBR	100	100	100
Carbon black	20	30	40
Zinc oxide	4	4	4
Stearic acid	2	2	2
TMQ	1	1	1
CBS	2	2	2
Sulfur	2.5	2.5	2.5

**Table 10** Mixing procedure for the carbon black investigations

Time (min, sec)	Action
0.00	Raise ram, add rubber, lower ram
1.30	ZnO, stearic acid, TMQ, ½ carbon black
2.10	Mixing
3.10	½ carbon black
3.50	Mixing
5.50	Dump

CBS and sulfur were added in a third mixing step on a Schwabenthan 100 mL two-roll mill at a temperature setting of about 40°C

**Fig. 27** Payne effect of fullerene carbon black (*FS*) and plasma-coated fullerene carbon black (*PCFS*) in SBR at increasing loadings

effect at all filler concentrations, whereas the difference in Payne effect values becomes more prominent at higher filler loadings.

The stress-strain curves of the vulcanizates with 40 phr filler loading are shown in Fig. 28. SBR reinforced with plasma-coated carbon black shows a slight improvement in tensile strength relative to SBR with uncoated carbon black. Polyacetylene-coated carbon black can better interact chemically and physically with the elastomer and thus contributes extra to the reinforcement of the elastomer.

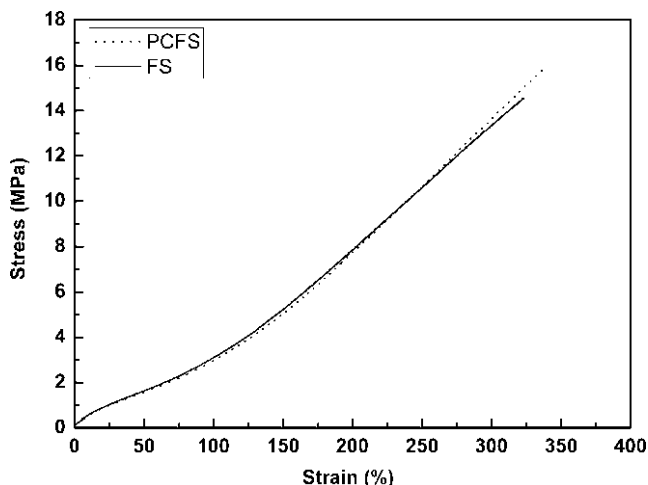


Fig. 28 Stress–strain curve of SBR with 40 phr carbon blacks

### 5.1.3 Discussion

The reduction in filler–filler interaction due to acetylene-plasma treatment is obviously due to the lower surface energy of the coated carbon black. The carbon black shows an appreciable reduction in surface energy after the plasma treatment, towards the range of the polymer S-SBR. This results in a better wetting of the filler particles by the elastomer [53, 54].

The stress–strain behavior of the S-SBR is affected by the presence of the plasma-coated carbon black as well: A slight improvement in tensile strength and elongation at break is observed. The deposition of the plasma-polymer layer makes the original carbon black surface unavailable for direct interaction with rubber. The observed increase in tensile strength and elongation at break can be explained by a better interaction between the plasma-polymerized acetylene and the unsaturated bonds in the polymer through crosslinking intermediates. It has been reported [7], that plasma-polymerized acetylene contains some amount of unsaturation. Admittedly, the observed improvement in the present case is not very substantial.

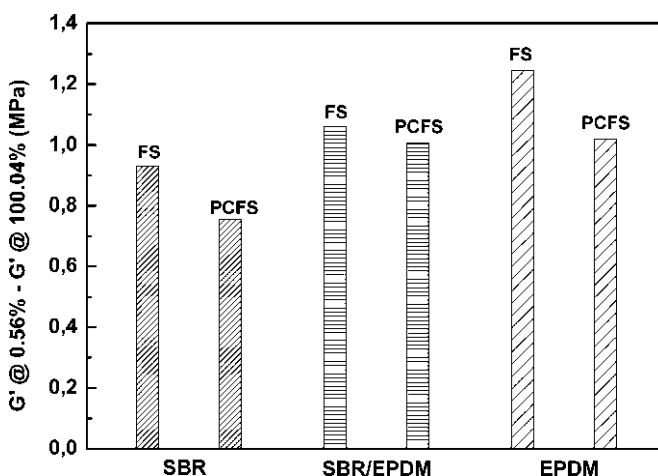
## 5.2 Carbon Black in a SBR/EPDM Blend

### 5.2.1 Compound Preparation

Table 11 shows the composition of the blend. The mixing procedure was again according to the description given in Table 10.

**Table 11** Compound formulation for carbon black in a blend of S-SBR and EPDM

Component	Content (phr)
S-SBR	50
EPDM	50
Carbon black	40
ZnO	4
Stearic acid	2
TMQ	1
CBS	2
Sulfur	2.5

**Fig. 29** Payne effect of carbon blacks in SBR, EPDM, and a 50:50 SBR/EPDM blend

### 5.2.2 Effect of Carbon Blacks on the SBR/EPDM Blend Properties

With the uncoated carbon black, the Payne effect in the SBR/EPDM blend positions itself between those of pure SBR and EPDM. For the plasma-coated carbon black, the blend has a Payne effect value comparable to that of EPDM, at a significantly higher value than the SBR compound (Fig. 29).

Morphological investigation of the blend can give a better idea about the distribution of the filler between the two phases. TEM was used to study the morphology of the filled blend system. For this purpose, thin sections of the SBR/EPDM blend were stained with OsO<sub>4</sub> vapor. Figure 30 shows the TEM images of a 50:50 SBR/EPDM blend with 40 phr carbon black. The image shows that the unmodified fullerene carbon black soot is preferentially located in the SBR phase. The unstained section shows areas occupied and unoccupied by carbon black. Comparing the stained and unstained sections, it is clear that the unoccupied areas in the unstained section are those of EPDM. The TEM image of the blend with the plasma-coated carbon black shows that the filler is better dispersed in the

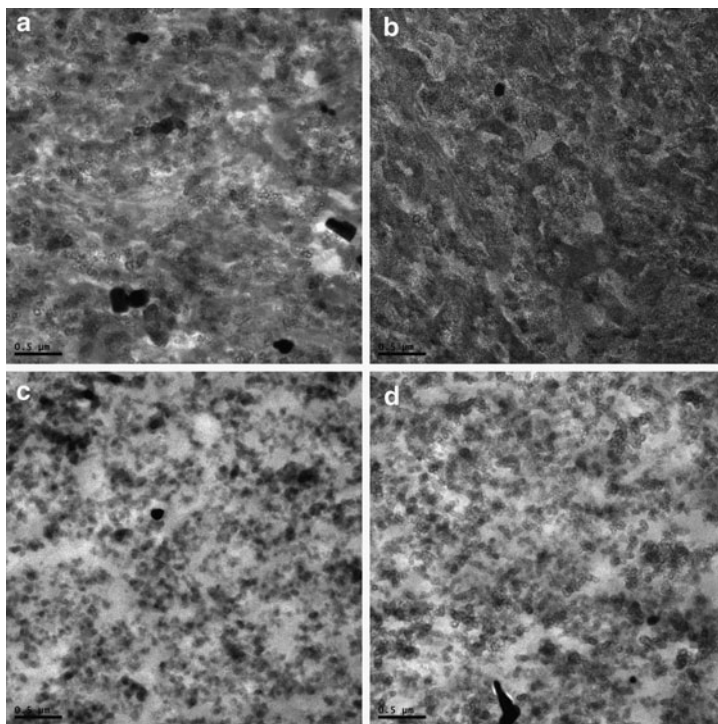


**Fig. 30** TEM images of a 50:50 SBR/EPDM blend with (a) 40 phr fullerene carbon black; (b) plasma-coated fullerene carbon black; (c) unstained section with fullerene carbon black; (d) unstained section with plasma-coated fullerene carbon black

matrix. The unstained section reveals that there are less unoccupied areas, which means that the EPDM phase is now also populated with the plasma-coated carbon black. Admittedly, there are still unoccupied EPDM areas in the blend. However, the addition of plasma-coated carbon black has improved the overall dispersion of the filler in the blend and also between the phases.

The stress–strain curves for the SBR/EPDM blends containing uncoated and plasma-coated carbon black are shown in Fig. 31. The blend with plasma-coated carbon black shows a slightly higher stress development in the stress–strain curve, probably due to the better-filled EPDM phase in the blend.

### 5.2.3 Discussion

In the dissimilar blend under consideration, unmodified carbon black is preferentially located in the more unsaturated phase, the SBR-phase. Compared to the situation in a pure SBR matrix with 40 phr filler, in the 50:50 blend of SBR and EPDM all the filler has approximately only half the volume to occupy. Naturally,



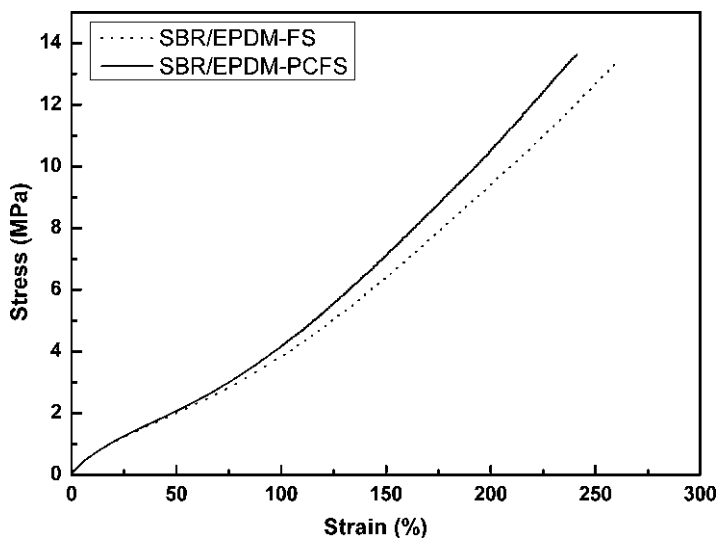


**Fig. 31** Stress–strain curves of the 50:50 SBR/EPDM blend with either uncoated or plasma-coated 40 phr carbon black

the filler–filler interaction is then higher in the preferred blend phase than in the case of pure SBR compound. The SBR/EPDM blend with the plasma-coated carbon black, however, shows a Payne effect similar to that of pure EPDM rubber. This might well be an indication that the EPDM phase is more populated with plasma-coated carbon black and, hence, the blend shows behavior similar to the EPDM rubber. Moreover, the Payne effect value of the SBR/EPDM blend with the plasma-coated carbon black is lower than that with the uncoated version. This can be taken as an indication that the coated filler is better dispersed in the blend than the uncoated version, i.e., the EPDM phase is more populated with the plasma-coated black, and the coated filler in the SBR-phase is better dispersed than the uncoated version.

The TEM image of the SBR/EPDM blend with the plasma-coated carbon black also shows that there is more carbon black in the EPDM phase than in the case of uncoated black. However, the expected improvement in vulcanized properties due to the better dispersion is not very visible from the results obtained. The SBR/EPDM blend with the plasma-coated carbon black only shows a slightly higher stress development in the stress–strain curve. In this case, the total effect of the plasma-coated carbon black will be a combination of the effects of the plasma-coated carbon black in the individual rubber phases in the blend. It might very well be that the less-reinforcing effects of the plasma-coated carbon black are counterbalanced by the positive effects due to the interactions between the unsaturated rubber and the plasma-polymer film, and by the slightly better dispersion and distribution of the plasma-coated carbon black between the phases in the blend. Overall, the effects of plasma coating of carbon black can be ranked as somewhat disappointing.

## 6 Polyacetylene-Coated Sulfur in Rubber

### 6.1 Sulfur in Pure S-SBR

#### 6.1.1 Compound Preparation

Table 12 shows the composition of the S-SBR compound used for these investigations. The sulfur used was either unmodified or one of the four samples of polyacetylene-coated sulfur described in Table 3.

The polymer was masticated in the internal mixer for 5 min; then ZnO and stearic acid were added. Curing agents were added on a two-roll mill and dispersed during 15 min of milling.

#### 6.1.2 Effect of Unmodified and Plasma-Coated Sulfur on the SBR Compound Properties

The cure characteristics for the compounds were measured according to the procedure described in Sect. 4.1.2. From the curemeter data shown in Table 13 it becomes clear that the SBR compounds containing coated sulfur show longer scorch times ( $t_{s2}$ ) and optimal curing times ( $t_{90}$ ) than the compound with uncoated sulfur. The only exception is for sample PPAS<sub>8</sub>-4, which gives a similar optimal curing time to uncoated sulfur (S<sub>8</sub>).

**Table 12** Compound formulation for (modified) sulfur in SBR

Component	Content (phr)
S-SBR	100
EPDM	0
ZnO	5
Stearic acid	2
CBS	1.7
Sulfur	2.5

**Table 13** Cure properties of SBR compounds with different sulfur samples

Sulfur sample code	Scorch time ( $t_{s2}$ ) (min)	Optimal vulcanization time ( $t_{90}$ ) (min)	Min. torque (dN m)	Max. torque (dN m)
S <sub>8</sub>	8.8	19.4	0.1	3.7
PPAS <sub>8</sub> -1	9.0	25.3	0.1	3.5
PPAS <sub>8</sub> -2	9.4	25.1	0.1	3.6
PPAS <sub>8</sub> -3	8.4	24.0	0.1	3.5
PPAS <sub>8</sub> -4	7.6	19.3	0.1	3.7

Preparation details for samples PPAS<sub>8</sub>-1 to PPAS<sub>8</sub>-4 are given in Table 3

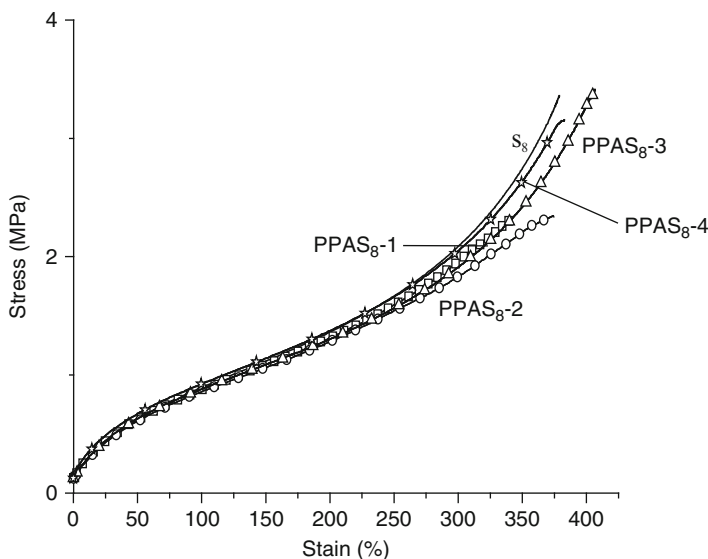


**Fig. 32** Stress–strain properties of carbon-black-reinforced SBR containing different polyacetylene-coated sulfur samples

From Fig. 32, showing the stress–strain properties of pure SBR vulcanized with the different sulfur samples till  $t_{90}$ , it is clear that all microencapsulated sulfur powders give similar or even somewhat reduced ultimate stress–strain properties compared to the uncoated sulfur. The only improvements in tensile properties were obtained for PPAS<sub>8</sub>-3.

### 6.1.3 Discussion

For those cases where an appreciable coating on sulfur was achieved, the scorch and curing times are delayed: the sulfur is released with a certain delay due to the polyacetylene coating. As PPAS<sub>8</sub>-4 was modified with a lower discharge power (see Table 3), the coating may have been too thin to provide an effect on its performance in rubbers. This assumption is supported by the fact that only a very minor change in color was obtained for this sample after the coating. The absence of an effect on reinforcement shows that the sulfur as such has preserved its activity, i.e., crosslinking is not influenced by the acetylene coating.

## 6.2 Sulfur in a S-SBR/EPDM Blend

### 6.2.1 Compound Preparation

Table 14 shows the composition of the blend compound. The mixing procedure was as described in the previous section.

**Table 14** Composition of the SBR/EPDM blend compound

Component	Content (phr)
SBR	50
EPDM	50
ZnO	5
Stearic acid	2
CBS	1.7
Sulfur	2.5

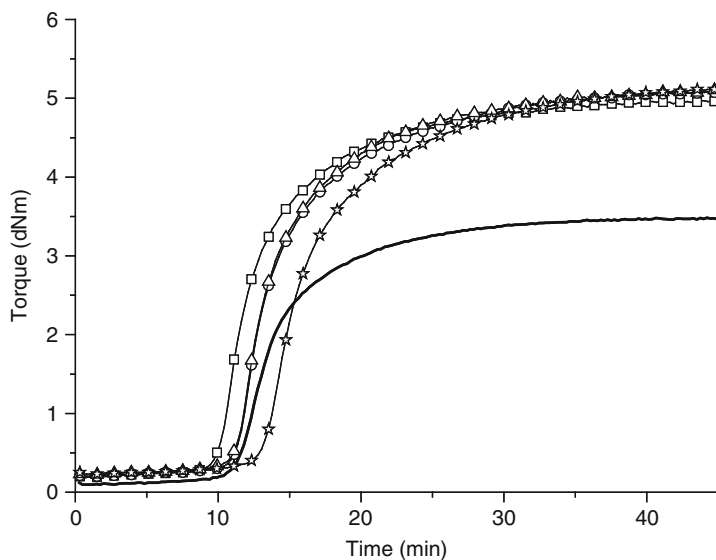


**Fig. 33** Cure-rheograms of the SBR/EPDM blends cured with: *solid line* S<sub>8</sub>; *squares* PPAS<sub>8</sub>-1; *circles* PPAS<sub>8</sub>-2; *triangles* PPAS<sub>8</sub>-3; *stars* PPAS<sub>8</sub>-4

### 6.2.2 Effect of Encapsulated Sulfur on the SBR/EPDM Blend Properties

The vulcanization curves of the SBR-EPDM blends with the various types of coated sulfur are presented in Fig. 33. For all samples, a pronounced increase in the final state of cure (maximum torque) is observed. This demonstrates that S-SBR/EPDM blends cured with plasma-acetylene-encapsulated sulfur provide a better covulcanization behavior.

The tensile properties of the S-SBR/EPDM blends cured with the uncoated and coated sulfur are shown in Fig. 34. It is clear that the compounds with micro-encapsulated sulfur show largely improved tensile strength, elongation at break, and higher moduli.

### 6.2.3 Discussion

Previous work has shown that the solubility of sulfur is somewhat higher in SBR than in EPDM, and that the difference becomes larger with an increase in

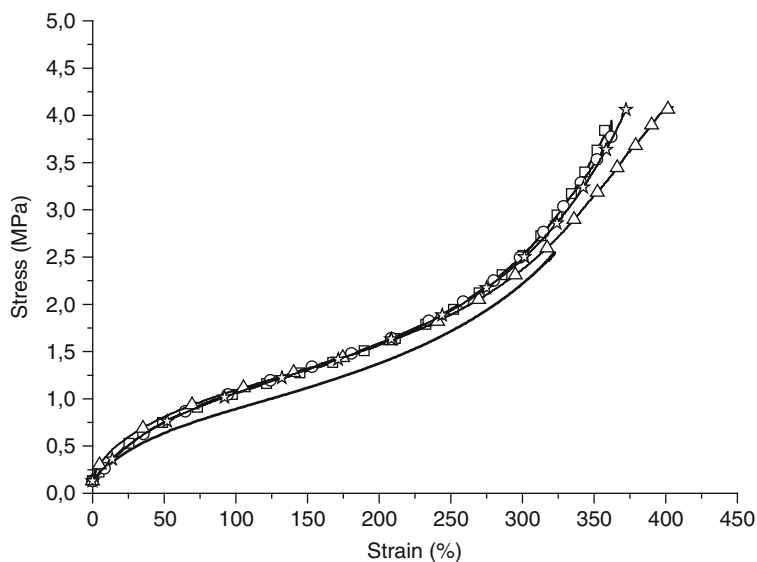


**Fig. 34** Stress–strain properties of the SBR/EPDM blends cured with: *solid line* S<sub>8</sub>; *squares* PPAS<sub>8</sub>-1; *circles* PPAS<sub>8</sub>-2; *triangles* PPAS<sub>8</sub>-3; *stars* PPAS<sub>8</sub>-4

temperature [55]. This solubility difference acts as the driving force for unmodified sulfur to migrate from EPDM to SBR before and during vulcanization. However, the deposition of the polyacetylene layer decreases the surface polarity of the sulfur and, at the same time, the crosslinked polyacetylene shell also decreases the speed of migration by diffusion.

## 7 Conclusions

Comparing the three substrates that were plasma-coated in this study, it has become clear that silica is very easy to encapsulate with a plasma coating, whereas carbon black is difficult to treat because of its inert chemical surface structure. Sulfur is also more difficult to handle, but in this case the incomplete coating is an advantage because the sulfur has to be released from the encapsulation shell in order to be efficient as curing agent. In all cases, the polarity of the substrate is reduced.

For silica in SBR, a polyacetylene coating gives the lowest filler–filler interaction, a good filler–polymer interaction, and the best dispersion compared to untreated and the other plasma-treated samples. However, for the stress–strain properties, the polythiophene-treated sample gives the best results. This shows the importance of sulfur moieties on the surface of the filler, which form a secondary network in the cured materials. In the blend of S-SBR and EPDM rubbers, the situation is less conclusive. The Payne effect, the bound rubber, and

the reinforcement parameter are best for the plasma-pyrrole-treated silica. However, the tensile strength is highest for the silane-modified silica. This demonstrates that filler dispersion in and reinforcing of dissimilar rubber/rubber blends are difficult, and that variable results can be expected dependent on the particular choice of the monomer used for plasma coating. Depending on the particular requirements, a proper selection of the monomer and optimization of the amount of coating have to be made.

Application of a plasma coating onto carbon black is very difficult compared to silica. It was only practically feasible for fullerene soot (left over from the fullerene production), which contains a large amount of reactive groups on its surface. Polyacetylene-plasma-treated fullerene soot provides an improved dispersion in SBR and in a SBR/EPDM blend compared to untreated fullerene black. However, the effect on the stress–strain properties is rather limited and the coating has only a slight effect on the final properties.

A polyacetylene coating applied on sulfur does not negatively influence its activity and speed as curing agent, but it can increase the scorch time. This effect is probably due to a delayed release of the sulfur out of the polymeric shell. In the SBR/EPDM blend, on the other hand, the plasma-treated sulfur results in higher torque values, an indication that the distribution of the plasma-treated sulfur over the different rubber phases is more homogenous, which is the main effect aimed for in the context of this study.

**Acknowledgment** This project was financially supported by the Dutch Technology Foundation STW, the Applied Science Division of NWO, the technology program of the Ministry of Economic Affairs of the Netherlands. It was also supported by Timcal Graphite and Carbon and Hexagon Polymers Compounding.

## References

1. Paul DR, Bucknall CB (eds) (2000) *Polymer Blends*, vol. 2. Wiley, New York
2. Callan JE, Hess WM, Scott CE (1971) *Rubber Chem Technol* 44:814
3. Mihara S (2009) *Reactive processing of silica-reinforced tire rubber*. Enschede, The Netherlands, Ph.D. thesis. ISBN 978-90-365-2839-9
4. van de Ven PM, Noordermeer JWM (2000) *Rubber World*, September 2000
5. Langmuir I (1929) *Phys Rev* 33:954
6. Kobayashi H, Bell AT, Shen M (1974) *Macromolecules* 7:277
7. Yasuda H (1985) *Plasma polymerization*. Academic Press, London
8. Fraunhofer IFAM (2008) Eurobonding. <http://www.eurobonding.org/Englisch/Allgemein/Index.htm>. Last accessed 8 July 2010
9. Williams DT, Hayes MW (1966) *Nature* 209:769
10. Haller I, White D (1963) *J Phys Chem* 67:1748
11. Westwood AR (1971) *Eur Polym J* 7:363
12. Thompson LF, Mahayan KG (1972) *J Appl Polym Sci* 16:2291
13. Denaro AR, Dwens PA, Crawshaw A (1968) *Eur Polym J* 4:93
14. Kobayashi H, Bell AT, Shen M (1973) *J Appl Polym Sci* 17:885
15. Carchano H (1974) *J Chem Phys* 61:3634

16. Tibbitt JM, Jensen R, Bell AT, Shen M (1977) *Macromolecules* 10:647
17. Denaro AR, Dwens PA, Crawshaw A (1969) *Eur Polym J* 5:471
18. Yasuda H (1981) *J Polym Sci Macromol Rev* 16:199
19. Yasuda H, Bumgarner MO, Hillman JJ (1975) *J Appl Polym Sci* 19:531
20. Yasuda H, Wang CR (1985) *J Polym Sci Polym Chem Ed* 23:87
21. Yasuda H, Hirotsu T (1973) *J Polym Sci Polym Chem Ed* 16:743
22. Yasuda H, Hirotsu T (1973) *J Polym Sci Polym Chem Ed* 16:313
23. Kobayashi H, Bell AT, Shen M (1976) *J Macromol Sci A10:491*
24. Inagaki N, Yasuda H (1981) *J Appl Polym Sci* 26:3425
25. Yang H, van Ooij WJ (2003) *Plasma Polym* 8:297
26. van Ooij WJ, Zhang N, Guo S (1999) Surface modification of micron size powders by plasma polymerisation process. In: Blitz JP, Little CB (eds) *Fundamental and applied aspects of chemically modified surfaces*. Royal Society of Chemistry, Cambridge
27. Inagaki N, Tasaka S, Abe H (1993) *J Appl Polym Sci* 48:1433
28. Piskin E, Atac AG (1996) *J Biomed Mater Res* 30:493
29. Chityala A, van Ooij WJ (2000) *Surf Eng* 16:299
30. Shi D, Wang SX, van Ooij WJ, Wang LM, Zhao J, Yu Z (2001) *Appl Phys Lett* 78:1243
31. Shi D, Lian J, He P, Wang LM, van Ooij WJ, Schulz M, Liu Y, Mast DB (2002) *Appl Phys Lett* 81:5216
32. Garreta E, Tricas N, Quintana L, Semino CE, Borros S (2006) *Plasma Process Polym* 3:553
33. Akovali G, Ulkem I (1999) *Polymer* 40:7417
34. Tricas N, Vidal-Escales E, Borros S, Gerspacher M (2003) In: *Proceedings 16th International Symposium on Plasma Chemistry (ISPC-16)*, Taormina, Italy 2003. University of Bari, p 366
35. Kang YC, van Ooij WJ (2006) RF plasma polymerization for surface modification of carbon black rubber filler. ACS Rubber Division Meeting, Cincinnati, 2006. ACS, Akron, Ohio, paper 67
36. Nah C, Huh M-Y, Rhee JM, Yoon T-H (2002) *Polym Int* 51:510
37. Mathew G, Huh Y, Rhee JM, Lee MH, Nah C (2004) *Polym Adv Technol* 15:400
38. Vidal-Escales E, Agullo N, Borros S, van Ooij WJ (2003) *Rubber World*, August 2003
39. Vidal E, Borros S, Agullo N, van Ooij WJ (2001) *Gummi Fasern Kunststoffe* 54:330
40. Zhang N (2000) Masters thesis, University of Cincinnati, USA
41. Mathew T (2008) Surface modification of carbon black by plasma polymerization. Enschede, The Netherlands, Ph.D. thesis. ISBN 978-90-365-2724-8
42. Inagaki N, Tasaka S, Abe H (1992) *J Appl Polym Sci* 46:595
43. Sola M, Mestres J, Duran M (1995) *J Phys Chem* 99:10752
44. Yasuda H (2005) *Plasma Process Polym* 2:293
45. Vidal E, Borros S, Agullo N, van Ooij WJ (2000) ACS Rubber Division Meeting, Cincinnati, Ohio, 2000. ACS, Akron
46. Payne AR (1965) In: Kraus G (ed) *Reinforcement of elastomers*, Chap. 3. Interscience, New York, p 69
47. Gauthier C, Reynaud E, Vassoille R, Ladouce-Stelandre L (2004) *Polymer* 45:2761
48. Wolff S (1981) *Rubber Chem Technol* 55:967
49. Leblanc JL, Hardy P (1991) *Kautsch Gummi Kunstst* 44:1119
50. Wolff S (1970) *Kautsch Gummi Kunstst* 23:7
51. Scott KW, Lorenz O, Parks CR (1964) *J Appl Polym Sci* 8:299
52. Wolff S (1982) *Rubber Chem Technol* 55:967
53. Donnet JB (1986) *Kautsch Gummi Kunstst* 39:1082
54. Donnet JB, Wang MJ, Papirer E, Vidal A (1986) *Kautsch Gummi Kunstst* 39:510
55. Guo R, Talma AG, Datta RN, Dierkes WK, Noordermeer JWM (2008) *Eur Pol J* 44:3890

# Recent Developments on Thermoplastic Elastomers by Dynamic Vulcanization

R. Rajesh Babu and Kinsuk Naskar

**Abstract** A comprehensive overview is given of the recent developments of thermoplastic vulcanizates (TPVs) with special reference to the technological advancements. TPVs combine the high volume molding capability of thermoplastics with the elastomeric properties of thermoset rubber. Therefore, they lend themselves to a broad range of applications in various fields. TPVs represent the second largest group of soft thermoplastic elastomers, after styrenic-based block copolymers. TPVs have undergone evolutionary changes in terms of the selection of polymers, design of crosslinking, compounding techniques, and methods of production, and have achieved better elastic recovery, easy processability and low hardness etc.

**Keywords** Dynamic vulcanization · Polymer blends and alloys · Reactive processing · Thermoplastic elastomers · Thermoplastic vulcanizates

## Contents

1	Introduction: Concept of Dynamic Vulcanization .....	220
1.1	Morphology .....	220
1.2	Rheology .....	222
1.3	Deformation Behavior .....	222
1.4	Production and Processing .....	223
2	Various Types of TPVs: The State of the Art .....	224
2.1	PP/EPDM TPVs .....	224
2.2	TPVs Based on PP/Ethylene- $\alpha$ -Olefin .....	228
2.3	TPVs from Miscible Blends .....	234
2.4	Super TPVs .....	236
2.5	Nanofilled TPVs .....	238
2.6	Oil-Extended TPVs .....	239
2.7	Foamed TPVs .....	240



2.8 Electron Beam Crosslinked TPVs .....	243
3 Concluding Remarks .....	245
References .....	245

## 1 Introduction: Concept of Dynamic Vulcanization

A thermoplastic elastomer (TPE) is a rubbery material with properties and functional performance similar to those of a conventional vulcanized rubber; but it can be processed in a molten state as a thermoplastic polymer. Thermoplastic vulcanizates (TPVs) are a very special class of TPEs prepared by the dynamic vulcanization process, which involves the crosslinking of a rubber phase while it is being mixed with a thermoplastic at elevated temperature. The process needs to be carried out under high shear and above the melting temperature of the thermoplastic component, and at a sufficiently high temperature to activate and pursue the process of vulcanization [1–5]. As a result, products thus obtained consist of crosslinked rubber particles dispersed in a continuous thermoplastic matrix, which explains both their elasticity and melt processability [2]. TPVs were first introduced in 1972 by Gessler [3]. Early work by Fisher [4] on polypropylene (PP)/ethylene propylene diene rubber (EPDM) TPVs with peroxide as the crosslinking agent, resulted in the commercialization of “Uniroyal TPR” thermoplastic rubber. Greater industrial attention was generated only after extensive study of TPVs based on various blend components by Coran and Patel in the 1980s [5–8]. They performed extensive studies on PP and EPDM blends that were dynamically vulcanized with high crosslink density in the rubber phase. These works led to the commercialization of “Santoprene” TPE, which was introduced by Monsanto in 1981. A recent survey indicates that the global annual growth rate of TPVs is about 15%. They are widely used in automotives, wires/cables, biomedical and soft-touch applications etc. In principle, a large number of rubber/thermoplastic-based TPVs are possible and this number is increasing day by day with the introduction of new polymers. The subject has been reviewed by Abdou-Sabet [9], Coran and Patel [10], Karger Kocsis [11], Naskar [12], and others. In this article, recent developments in TPVs are primarily reviewed with the objective not only to update the information but also to appreciate the new advancements in this particular field.

To start with, there is a brief discussion on the morphology, rheology, and processing characteristics of TPVs to aid better understanding of the subject.

### 1.1 Morphology

The evolution of morphology in TPVs is governed by several parameters, including blend composition, viscosity ratio, shear force, and interfacial interaction between

the two polymer phases [13]. Initially, with the addition of a curative, viscosity ratio plays a major role in the morphology evolution (less viscous phase encapsulates the more viscous phase). With a further increase in the curative dosage, the degree of crosslinking increases in the dispersed phase, although there is an abrupt increase in the viscosity ratio resulting in a decrease in particle size. It is expected that applied shear fields will override the viscosity ratio factor. To further clarify, enough crosslinking in the rubber phase causes an immobilization of the particles and therefore they break down under the applied shear field to micrometer-sized smaller particles. The development of a dispersed phase morphology from a cocontinuous one is depicted in Fig. 1.

It is generally accepted that one of the major advantages of the dynamically cured blends over unvulcanized blends is that the morphology is fixed on crosslinking and is not altered by subsequent melt processing. Radusch et al. [14] studied the morphology generation during the process of dynamic vulcanization for phenolic-resin-cured PP/EPDM TPVs. Sengupta and Noordermeer [15] report the first use of electron tomography in reconstructing the 3D morphology in TPE blends. Schematic representation of 2D transmission electron microscopy (TEM) and 3D tomography images for oil-extended PP/EPDM TPVs are depicted in Fig. 2. An easy identification of blend morphology can be carried out on the blend compositions using 3D tomography, where conventional TEM imaging gives misleading information. 3D tomography technique gives a higher resolution than any other

**Fig. 1** Development of morphology in a thermoplastic vulcanizate from cocontinuous (*left*) to dispersed phase (*right*) [14]

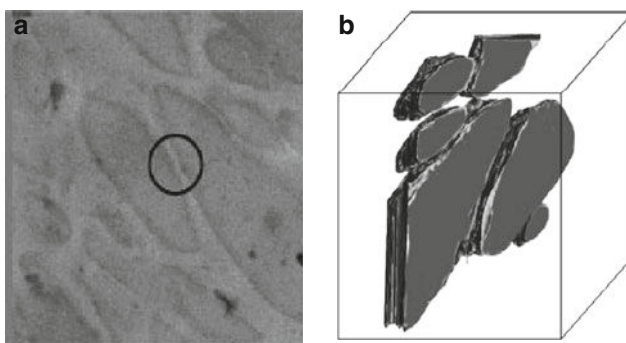
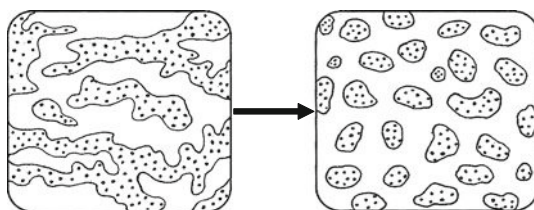


**Fig. 2** (a) 2D TEM image of oil-extended PP/EPDM TPVs. Crosslinked EPDM particles are separated by circle. (b) 3D model of blend showing EPDM dispersed particles

microscopic technique, and is applicable to blends with dispersed as well as cocontinuous morphologies.

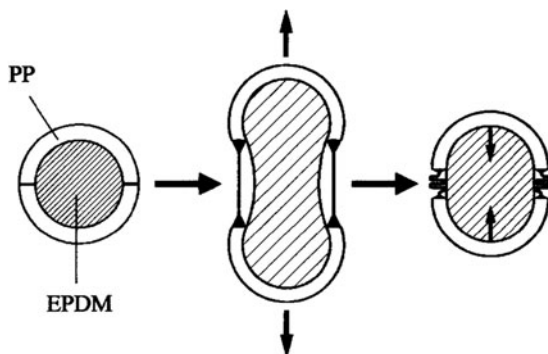
## 1.2 Rheology

Goettler et al. [16] were the first to study the technical importance of the TPVs in terms of rheological characteristics using a capillary rheometer. Han et al. [17] described the comparative rheological study of PP and PP/EPDM uncrosslinked and dynamically crosslinked blends, using various rheological instruments to measure steady shear flow, uniaxial extension, and oscillation flow properties of the compounds. Steeman et al. [18] reported that TPVs have a yield stress for flow and that the value increases with the increase in elastomer component in the TPV. An extensive study of rheological response of PP/EPDM blends and the TPVs with phenolic resin as crosslinking agent was explored by Jain et al. [19]. Katbab et al. [20, 21] discussed the formation of morphology and correlated it with the mechanical and rheological properties for the nonreinforced and reinforced (carbon black and silica fillers) TPVs. Chatterjee et al. [22] analyzed the rheological response of nanosilica-filled PP-based TPVs. Rheological behavior of dynamically and statically vulcanized blends of PP and styrene-butene-styrene triblock copolymer (SBS), with reference to the effect of various crosslinking agents, was studied by Ichazo et al. [23]. The linear viscoelastic properties of PP/styrene ethylene butadiene styrene block copolymer (SEBS) blends and PP/EPDM TPVs are described in terms of composition ratio and in terms of the oil diffusion and distribution in the blend components by Sengers et al. [24]. Recently, Leblanc [25] studied the nonlinear viscoelastic properties of the various commercially available TPVs with varying hardness using a Fourier transform rheometer (FT-rheo) to gain insight into the morphology developed and into the subtle role played by the extractable content such as oil and plasticizers.

## 1.3 Deformation Behavior

The crosslinking of the elastomer phase in PP/EPDM blends results in better rubber-like properties. The elastic modulus increases and the permanent deformation after unloading (tension or compression set) decreases. Analyses during tensile testing of the TPV and finite element modeling (FEM) [26] showed that, during deformation in the solid state, the PP phase only yields partially. The thin PP layers yield in the equatorial region (perpendicular to the load applied) of the elastomer particles and the rest of the PP phase remains unaffected. Soliman et al. [27] studied the deformation mechanism of phenolic-resin-cured PP/EPDM TPV. According to the authors, during the stretching process of PP/EPDM TPV most of the PP acts as glue between the EPDM particles, which are deformed. Only a

**Fig. 3** Sketch illustrating the deformation and recovery of dynamically vulcanized blends [27]



small fraction of the PP is irreversibly deformed (i.e., yields). During the recovery process, this PP fraction is partially pulled back by the recovery of the EPDM. Schematic representation of the deformation and recovery of the dynamically vulcanized blends is shown in Fig. 3. Oderkerk et al. [28] studied the micromechanical deformation and strain recovery process of nylon6/EPDM TPVs by using atomic force microscopy (AFM) and TEM. During straining, the plastic deformation is initiated in those zones where the nylon matrix between the rubber particles is the thinnest. Even at high strains, the thick ligaments of the nylon matrix remain almost undeformed and act as adhesion points holding the rubber particles together.

#### **1.4 Production and Processing**

TPVs based on PP/EPDM are produced using either batch or continuous mixing techniques. The most common batch mixers are internal mixers, such as the Banbury mixer, Barbendar plasticoder, etc. On an industrial scale, TPVs are typically produced in corotating twin-screw extruders, allowing a large degree of process flexibility [29]. To date, the dynamic vulcanization processes have not been entirely satisfactory for making soft compositions because, as the rubber level rises, the resulting composition becomes less processable. For example, the compositions give poor extrudates and sometimes cannot be extruded at all. The fabrication method and equipment for TPVs are essentially the same as those for the thermoplastic in the material. Thermoplastic injection molding does not involve vulcanization, so it leads to short cycle time and easy control over processing defects. Extrusion from TPVs is widely used to fabricate intricate profiles, tubing, hose and electrical insulation, and jacketing. Blow molding, thermoforming, and heat welding can also be done with TPV-based materials. Unlike thermoset rubber, the generation of hollow articles via blow molding is possible. However, it is generally advisable to dry a TPV prior to processing to avoid process defects.

## 2 Various Types of TPVs: The State of the Art

### 2.1 PP/EPDM TPVs

Most commercially important TPVs are based on the blends of EPDM (with saturated main chain, giving excellent stability against heat, oxygen, and ozone to the corresponding TPVs) and PP. Several crosslinking agents have been employed to crosslink the EPDM phase in PP/EPDM blends: activated phenol–formaldehyde resins, (commonly known as resol-resins), coagent-assisted peroxides, platinum-catalyzed hydrosiloxane, vinyltrialkoxysilane/moisture, catalyzed quinonedioxime, and bisthiols etc. [30]. PP/EPDM-based TPVs are traditionally crosslinked with acid-activated resol. The reaction mechanism of resol crosslinking of 2-ethylidene norbornene (ENB)-containing EPDM was extensively investigated by van Duin and coworkers [31] using a low molecular weight model compound and  $^{13}\text{C}$  NMR spectroscopy. Abdou-Sabet [32] demonstrated that the rubber-like properties of PP/EPDM or PP/nitrile rubber (NBR) TPV could be improved by using a dimethylol-octyl phenol curing resin. Improvements in compression set, oil resistance, and processing characteristics of the material were achieved. These improvements went beyond those expected from the state of cure, and are probably due to in situ formation of a block copolymer between the rubber particles and the PP matrix. The graft copolymer was assumed to be generated through the functionalization of PP with dimethylol-octyl phenol, which then reacts with the rubber-like EPDM or NBR. Phenolic resin curatives having a majority of dibenzyl-ether linkages were unexpectedly found to be effective in crosslinking the rubber in a blend of a crystalline polyolefin and EPDM [33]. Their effectiveness exceeds that of conventional phenolic resins for many TPV compositions. TPVs cured with conventional phenolic resins often stain painted surfaces when in contact. This has resulted in the exclusion of TPVs cured with phenolic resins from many applications where the elastomer will have extended contact with a painted surface, such as the body of cars, structural moldings, and glass to metal laminates. When the phenolic resin curatives are esterified (e.g., acetylated, tosylated, silylated, or phosphorylated) before use as a curative, the amount of staining is reduced or even eliminated. Furthermore, because of the consequent off-white color and the formation of black specks in phenolic-resin-cured TPVs other crosslinking systems have also been developed, such as platinum-catalyzed hydrosilane and peroxide/coagent. Lopez Manchado and Kenny [34] employed a special crosslinking agent such as benzene-1,3-bis(sulfonyl)azide for the preparation of TPV. They concluded that the sulfonyl-azide group can act as an effective crosslinking agent for the elastomeric phase and as a coupling agent between the elastomeric and thermoplastic phases. The cure rate, the final crosslink density, the thermal stability of the crosslinks formed, the safety, health and environmental characteristics of the chemicals used, and the cost price are all relevant parameters for the final choice of a crosslinking system.

Naskar and Noordermeer [35–38] studied the influence of various peroxides having different chemical structures on the PP/EPDM TPVs at fixed as well as

varied blend ratios. Table 1 summarizes the physical properties of different peroxide-cured PP/EPDM TPVs at varied blend ratios. Three main parameters have been identified that primarily govern the final mechanical properties of the TPV: the solubility parameter of a peroxide relative to the polymers, PP and EPDM; the decomposition mechanism of the peroxide; and the kinetic aspects of the peroxide fragmentation. Variation of the tensile strength and compression set of the TPV with the various peroxides can be related to the solubility parameter of the peroxide and the rubber. The closer the solubility parameter of the peroxide to that of the EPDM, the higher the tensile strength and the better the compression set property. Amongst various peroxides taken for the investigation, dicumyl peroxide (DCP) in the presence of triallyl cyanurate (TAC) as a coagent was found to give the overall best balance of physico-mechanical and elastic recovery properties in PP/EPDM TPVs.

It is worth noting that commonly used peroxides generally produce volatile decomposition products, which provide an unpleasant smell or can show a blooming effect. For example, the typical sickly sweet smell of acetophenone, one of the decomposition products of DCP, is well known. On the other hand, blooming phenomena can take place due to the formation of dihydroxy isopropyl benzene from the decomposition of di(*tert*-butylperoxyisopropyl) benzene (DTBPIB), because of its limited solubility in the rubber matrix. Hence, multifunctional peroxides were developed to overcome the above-mentioned drawbacks of the commonly employed peroxides [37]. They contain functional unsaturated groups (having coagent functionality) in addition to a peroxide group. In this manner, part of the

**Table 1** TPV compositions at varied PP/EPDM blend ratios (with peroxide concentration of 9 meq) and the corresponding properties

Composition and properties	TPV sample							
	1	2	3	4	5	6	7	8
EPDM content (phr)	200	200	200	200	200	200	200	200
PP content (phr)	50	100	50	100	50	100	50	100
DTBPH content (phr)	3.3	3.3	–	–	–	–	–	–
DTBPHY content (phr)	–	–	2.9	2.9	–	–	–	–
DTBPIB content (phr)	–	–	–	–	3.8	3.8	–	–
DCP content (phr)	–	–	–	–	–	–	6.1	6.1
TAC content (phr)	4.0	4.0	4.0	4.0	4.0	4.0	4.0	4.0
1076 content (phr)	0.4	0.4	0.4	0.4	0.4	0.4	0.4	0.4
168 content (phr)	0.4	0.4	0.4	0.4	0.4	0.4	0.4	0.4
Tensile strength (MPa)	4.2	6.7	3.9	6.2	4.5	6.6	4.7	7.4
Elongation at break (%)	455	419	401	387	440	416	472	375
Modulus at 300% (MPa)	3.3	5.9	3.5	5.7	3.5	5.6	3.4	5.5
Hardness (Shore A)	61	85	61	86	63	87	61	88
Overall crosslink density ( $v + PP$ ) $\times 10^5$ (mol/ml)	9.9	18.6	12.0	16.3	8.9	17.5	13.5	19.3

*EPDM* Ethylene propylene diene rubber with 50 wt% paraffinic oil, *PP* polypropylene, *DTBPH* 2,5-dimethyl-2,5-di(*tert*-butylperoxy)hexane (40% pure), *DTBPHY* 2,5-dimethyl-2,5-di(*tert*-butylperoxy)hexyne-3 (45% pure), *DTBPIB* di(*tert*-butylperoxyisopropyl)benzene (40% pure), *DCP* dicumyl peroxide (40% pure), *TAC* triallyl cyanurate (50% pure), 1076-Irganox 1076, 168-Irgafos 168

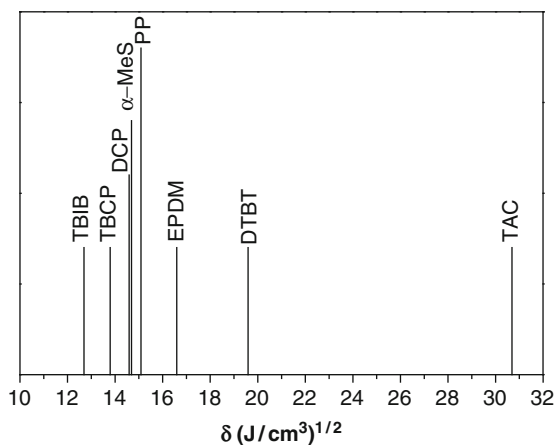
decomposition products are no longer volatile, nor give rise to smell or blooming phenomena. The multifunctional peroxides provide performance properties for TPV that are comparable with commonly used coagent-assisted peroxides. Chemical names and structures of the multifunctional peroxides studied are shown in Table 2. Particularly 2,4-diallyloxy-6-*tert*-butylperoxy-1,3,5-triazine (DTBT) which turns out to be a good alternative for the DCP/TAC combination. DTBT has a solubility parameter in the high side of the spectrum, which directs this peroxide and coagent combination preferentially to the EPDM phase during mixing. The ranking of these solubility parameter values is graphically depicted in Fig. 4.

The coagent functionality of this compound helps to improve the crosslinking effect, and is comparable with DCP. Moreover, the multifunctional peroxides investigated provide by-products after their decomposition, but without an unpleasant smell, unlike DCP. Comparative physical properties of the PP/EPDM TPVs

**Table 2** Chemical names and structures of the multifunctional peroxides studied

Chemical name	Chemical structure
1-(2- <i>tert</i> -Butylperoxyisopropyl)-3-isopropenyl benzene (TBIB) (71% purity)	
2,4-Diallyloxy-6- <i>tert</i> -butylperoxy-1,3,5-triazine (DTBT) (95% purity)	

**Fig. 4** Relative ranking of solubility parameters ( $\delta$ ) of the various compounds investigated at 180°C



prepared by conventional peroxide/coagent combination and multifunctional peroxide are shown in Table 3.

From the decomposition mechanism and the products formed it can be deduced that DCP primarily generates cumyloxy radicals, which further decompose into highly reactive methyl radicals and acetophenone, having a typical sweet smell. Similarly, *tert*-butyl cumyl peroxide (TBCP) forms large quantities of acetophenone, as this compound still half-resembles DCP. From the decomposition products of 1-(2-*tert*-butylperoxyisopropyl)-3-isopropenyl benzene (TBIB), it can be deduced that the amount of aromatic alcohol and aromatic ketone are below the detection limit ( $<0.01$  mol/mol decomposed peroxide); furthermore no traces of other decomposition products could be identified. This implies that most likely the initially formed aromatic decomposition products reacted with the substrate by the formation of adducts. In addition, unlike DCP, there is no possibility of TBIB (because of its chemical structure) forming acetophenone. As DTBT contains the same basic *tert*-butyl peroxide unit as TBIB, it may be anticipated that their primary decomposition products will be similar. This also explains why the decomposition products obtained from the multifunctional peroxides do not provide an unpleasant smell, unlike DCP [37, 38].

Influences of the different methacrylates and 1,2-polybutadiene as coagents on the mechanical and rheological properties of the peroxide-cured PP/EPDM TPVs were reported by Rishi and Noordermeer [39, 40]. They interpreted the results in terms of solubility parameter and cure kinetics. The effects of coagents on both processing and properties of the compound depend on the nature of the polymer, type of peroxide, and other compounding ingredients. Among the methacrylate

**Table 3** Compositions and comparative physical properties of various PP/EPDM TPVs prepared by conventional DCP/TAC combination and multifunctional peroxide

Composition and properties	TPV sample					
	1	2	3	4	5	6
EPDM content (phr)	200	200	200	200	200	200
PP content (phr)	50	100	50	100	50	100
DTBT content (phr)	1.5 (5)	3.0 (10)	4.5 (15)	–	–	–
DCP content (phr)	–	–	–	3.4 (5)	6.8 (10)	10.1 (15)
TAC content (phr)	–	–	–	1.7 (10)	3.4 (20)	5.1 (30)
1076 content (phr)	0.4	0.4	0.4	0.4	0.4	0.4
168 content (phr)	0.4	0.4	0.4	0.4	0.4	0.4
Tensile strength (MPa)	3.0	4.3	5.2	4.7	5.5	5.1
Elongation at break (%)	412	593	504	548	419	368
Modulus at 300% (MPa)	2.7	2.9	3.6	3.2	4.4	4.4
Hardness (Shore A)	66	67	68	63	66	68
Overall crosslink density ( $v + PP$ ) $\times 10^5$ (mol/ml)	2.1	4.5	8.4	7.5	16.0	17.5

EPDM ethylene propylene diene rubber with 50 wt% paraffinic oil extended, PP polypropylene, DTBT 2,4-diallyloxy-6-*tert*-butylperoxy-1,3,5-triazine (95% pure), DCP dicumyl peroxide (40% pure), TAC triallyl cyanurate (50% pure), 1076-Irganox 1076, 168-Irgafos 168

Values in the parentheses correspond to the milliequivalent concentration of corresponding peroxide and coagent per 100 parts of pure EPDM rubber



coagents studied, trimethylol propane trimethacrylate (TMPTMA) shows the best overall balance of properties. In another approach, PP/EPDM blends were cross-linked by silane grafting in the presence of a small amount of peroxide. Fritz and coworkers [41] studied the tension set and repeated tensile stress to characterize the elastic properties of organosilane-crosslinked PP/EPDM TPV. Grafting, hydrolysis, and condensation crosslinking reactions were carried out in a single-stage process.

Recently, Han et al. [42] developed a new method of developing PP/EPDM TPV using supercritical propane. In this method, PP and EPDM are first dissolved in a supercritical fluid in certain concentrations to form a homogeneous solution, followed by the addition of peroxide curatives. The vulcanization of the EPDM phase was carried out by stirring the solution at 175°C and 650 bar pressure for 1 h. The polymer was then precipitated by reducing the pressure to below the cloud-point and subsequently reducing the temperature at constant pressure to the ambient temperature. The advantage of this method is that it provides much smaller size of the dispersed EPDM domains as compared to the melt blending technique.

Maiti et al. [43] explored the use of gas phase EPDM (GEPDM)/PP TPVs. GEPDM is generally produced by using carbon black during the polymerization step to prevent the EPDM particles from agglomerating. The granular nature of GEPDM, having a high surface area, is unique and leads to significant cost saving and processing feasibility. Attempts have been made to study the effect of the addition of carbon black and silica as fillers in dynamically cured PP/EPDM blends. A conventional EPDM/PP system was compared with a GEPDM/PP system in terms of heat aging, processability, crosslink density, morphology, and physical properties. The GEPDM/PP system was found to exhibit better behavior in all respects.

## **2.2 TPVs Based on PP/Ethylene- $\alpha$ -Olefin**

Ethylene- $\alpha$ -olefins or polyolefin elastomers or plastomers (POEs) are a relatively new class of polymers that emerged from recent advances in metallocene polymerization catalysis. Representing one of the fastest growing synthetic polymers, POEs can be substituted for a number of generic polymers including ethylene propylene rubbers (EPM or EPDM), ethylene vinyl acetate (EVA), styrene block copolymers (SBCs), and poly(vinyl chloride) (PVC). POEs are compatible with most olefinic materials and offer unique performance capabilities for compounded products. In less than a decade, POEs have emerged as a leading material for automotive exterior and interior applications [primarily in thermoplastic olefins (TEOs) via impact modification of PP], wires and cables, extruded and molded goods, film applications, medical goods, adhesives, footwear, and foams. The key features are uniform intermolecular and intramolecular comonomer distribution, low extractability, comonomer-dependent melting point, and low ash content. The uniform

comonomer insertion resulted in a low density product and the physical properties span the range between plastic and elastomeric behavior [44].

Very recently, attempts have been made to develop PP/EOC TPVs. In order to make TPVs based on PP/EOC blend systems, phenolic resin is ineffective because the latter needs the presence of a double bond to form a crosslinked network structure. Peroxides can crosslink both saturated and unsaturated polymers without any reversion characteristics. The formation of strong C–C bonds provides substantial heat resistance and good compression set properties without any discoloration. However, the activity of peroxide depends on the type of polymer and the presence of other ingredients in the system. It has been well established that PP exhibits a  $\beta$ -chain scission reaction (degradation) with the addition of peroxide. Hence, the use of peroxide only is limited to the preparation of PP-based TPVs. Lai et al. [45] and Li et al. [46] studied the fracture and failure mechanism of a PP-metallocene based EOC based TPV prepared by a peroxide crosslinking system. Rajesh et al. [47] made a detailed investigation of the peroxide-cured PP/EOC TPVs. The investigation started by studying the influence of structurally different peroxides with varying concentrations at a fixed blend ratio of 50/100 PP/EOC blends. The study was broadened to understand the effect of molecular characteristics (particularly molecular mass) on the property enhancement of the samples by dynamic vulcanization. Two types of EOCs having the same octene content but differing in their molecular masses were studied. The observed mechanical properties were determined to be a function of the ratio between the degree of degradation in the PP phase and the extent of crosslinking in the EOC phase. TBCP gives the best overall balance of properties for the PP/high molecular weight EOC (PP/EH)-based TPVs, whereas DCP shows the best for the PP/low molecular weight EOC (PP/EL)-based TPVs. The PP/EL blend system requires a relatively higher concentration of curatives, as compared with the PP/EH system, to achieve an optimum level of physical properties. The study clearly illustrates the complexity associated with the peroxide activity for a given polymer system. Furthermore, they concluded that the choice of the best peroxide to fulfill specific requirements could not be made entirely on the basis of the peroxide efficiency and reactivity at a particular temperature.

The scope of the peroxide-cured PP/EOC TPVs is broadened by studying the influence of different coagents [48]. Generally, coagents are multifunctional vinyl monomers that are highly reactive towards free radicals either by addition reaction and/or by hydrogen abstraction. Chain scission could be retarded by stabilizing the PP macroradicals by the addition reaction across the double bond in the vinyl monomer (coagent) [49]. Hence, the addition of a coagent in the PP/EOC blend increases the crosslinking efficiency in the EOC phase and decreases the degradation in the PP phase. It not only improves the end-use properties but also decreases the peroxide concentration and aids the flow characteristics during processing. Among the various coagents studied, the most interesting properties were observed for TPVs containing *N,N'*-*m*-phenylene dimaleimide (MPDM). A clear divergence is inferred when comparing the performance of different coagents on the delta torque values obtained from the cure study in EOC gum vulcanizate and the final

mechanical properties of PP/EOC TPVs. In the cure study, TAC shows the higher state of cure on pure EOC vulcanizate but, when examining the properties of PP/EOC TPVs, MPDM shows the best balance of mechanical properties. They concluded that the coagent, which increases the state of cure in EOC phase, is not necessary to improve the PP/EOC TPVs. MPDM is shown to effectively behave as a compatibilizer for the PP/EOC blend system and thereby improvement is significant. The observed mechanical properties are in line with the phase morphology and tensile fractographic analysis. Nonetheless, a good dispersion is crucial in order to obtain a high quality product. Therefore, it is necessary to explore the processing conditions or parameters that can minimize the extent of degradation in the PP phase and thus improve the ultimate mechanical properties in PP/EOC TPVs. Three different mixing methods were studied, and the corresponding flow diagram is shown in Fig. 5 [50]. TPVs prepared by adding EOC curative master batch to the molten PP (phase mixing method) exhibit better mechanical properties and finer phase morphology than those prepared by preblending and the split addition method. The best overall balance of properties was obtained at 2 phr concentrations in the phase mixing method [50].

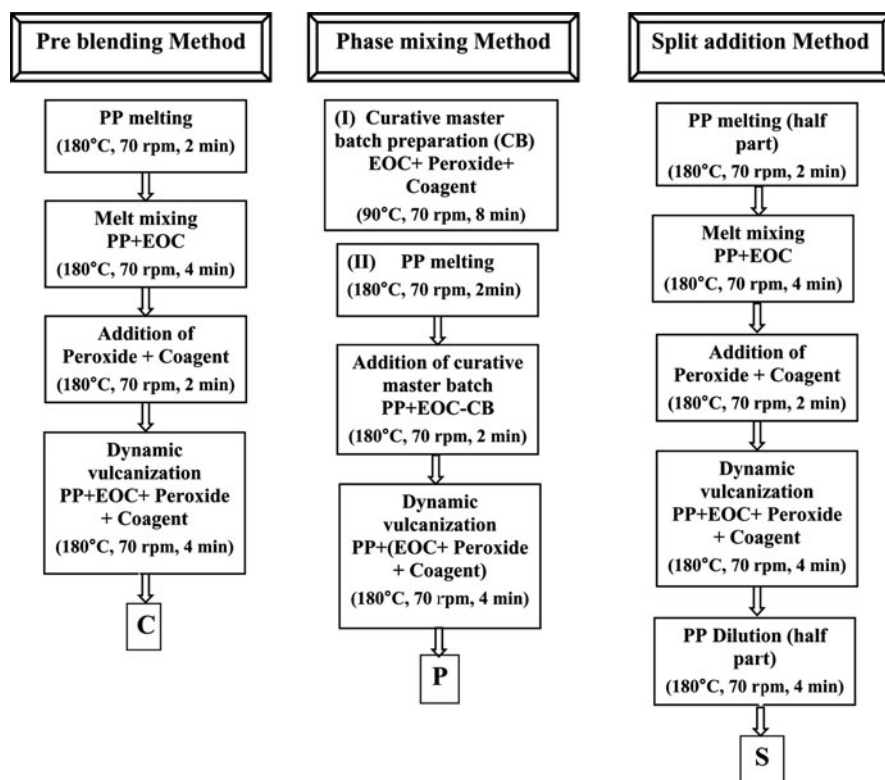
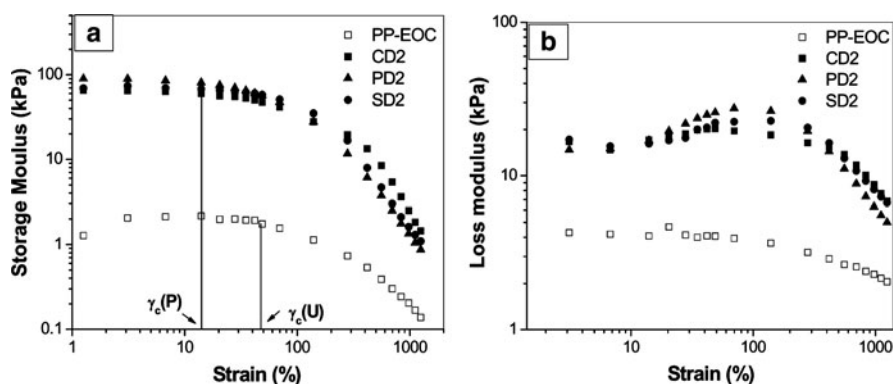


Fig. 5 Preparation of thermoplastic vulcanizates by various methods

A variety of rheological observations such as the Payne effect, modulus recovery, and shear rate sensitivity were studied by carrying out frequency and strain amplitude sweeps in a rubber process analyzer (RPA 2000) [51]. Principally, the rheology of TPV can be analogically compared with that of the rubber filled with active fillers. The strain dependence viscoelastic characteristics of PP/EOC TPVs prepared by three different mixing sequences are depicted in Fig. 6. According to Payne, nonlinearity is due to disintegration of the filler network structure of the secondary agglomerates. However, in the case of TPVs, the secondary structure corresponds to the crosslinked EOC domains dispersed in the PP matrix in the form of aggregates and/or agglomerates. Indeed, nonlinearity of TPVs can then be imagined to be associated both with the mechanism of disintegration of agglomerated EOC domains and with the debonding of crosslinked EOC domains from the PP matrix phase. In uncrosslinked blends, the nonlinearity at higher strain level is due to the disintegration or breakdown of trapped molecular entanglement network and/or debonding of macromolecular chains of PP anchored to the continuous EOC phase. Dependence of the loss modulus on strain amplitude depends on the rates of network breakdown and reformation as well as sliding of macrochains at the domain surface. The magnitudes of the loss maxima are substantially emphasized for the phase-mixed TPVs. This could be related to the energy dissipation produced by the breakdown of crosslinked EOC aggregates.

Experiments on recovery of dynamic functions after the application of large strain amplitude perturbation were performed to understand the modulus recovery kinetics. To determine the recovery kinetics, samples underwent the following test sequences: (a) frequency sweep, (b) strain sweep, (c) relaxation time of 2 min, (d) frequency sweep, (e) strain sweep, (f) relaxation time of 2 min, (g) frequency sweep, and (h) strain sweep [50]. Figure 7 shows the comparative subsequent strain sweep results performed immediately after a relaxation time of



**Fig. 6** Variation of viscoelastic properties as a function of strain amplitude of uncrosslinked and dynamically vulcanized blends at 180°C: (a) storage modulus, (b) loss modulus. *CD2* TPV prepared by preblending, *PD2* TPV prepared by phase mixing, *SD2* TPV prepared by split addition

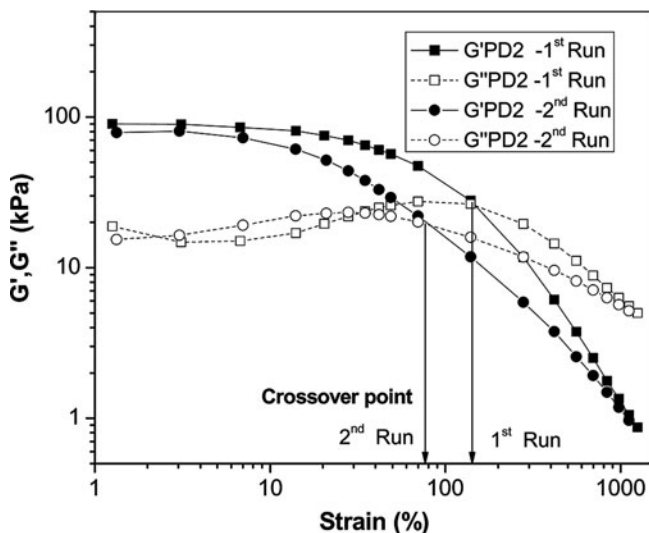


**Fig. 7** Storage ( $G'$ ) and loss modulus ( $G''$ ) of phase-mixed TPVs plotted as a function of strain amplitude. *Closed symbols* represent the first run and *open symbols* the second measurement after relaxation and frequency sweep. PD2 TPV prepared by phase mixing

2 min and a frequency sweep (for clarity only phase-mixed TPV is shown in Fig. 7). The typical qualitative feature of the Payne effect, i.e., the decrease of  $G'$  and the appearance of  $G''$  max in the subsequent strain sweep test, is observed. However, the linear range decreased ( $\gamma_c$  at lower strain amplitude) and both the moduli ( $G'$  and  $G''$ ) decrease with the formation of  $G''$  max at lower strain amplitude in the subsequent strain sweep test. These evolutions are associated with the nonreversal deformation of the network (by the disintegration of cross-linked EOC aggregates and/or agglomerates), with dewetting of the EOC domains from the PP matrix, and with rupture of the chain entanglements and chains that connect aggregates.

This corresponds to the so called Mullins effect or stress softening effect. It was observed that all the dynamic stress softening is achieved in the second sweep (second run) and only minor effects take place in a subsequent sweep (third run). Furthermore, it is observed from Figs. 6 and 7, that the linear complex modulus (modulus at 2% strain) of TPVs is reformed to a large extent (more than 90% of the initial or linear modulus is recovered) in the subsequent strain sweep. In the literature it has been reported that, when the calcium-carbonate-filled polyethylene (PE) (highly loaded particulate-filled PE) is subjected to a subsequent strain sweep [27], the onset of nonlinearity shifted to the higher deformation (strain %) and a drastic decrease was observed in the initial storage modulus. However, in the case of TPVs the reverse is observed, i.e., the initial storage modulus is regained to a large extent and the onset of linearity is shifted to the lower deformation.

### 2.2.1 Reinforcement Mechanism

Two important factors, namely particle size and chain bridging effects, primarily determine the reinforcing characteristics of the TPVs. In TPVs, the difference between the surface energy of the PP matrix and the crosslinked EOC particles leads to adsorption of the PP molecule onto the surface of the crosslinked EOC particles through a segmental interdiffusion mechanism or joint shell mechanism. Smaller crosslinked EOC particles have a higher tendency to adsorb the PP chains on the surface and, hence, form more trapped PP chains by connecting the particles. The adsorbed chains on the surface of the domains via physical and/or chemical adsorption generally broaden the relaxation spectrum towards longer times, which is reflected in the higher dynamic modulus and viscosity in the frequency and strain sweep experiments.

Another important factor for the reinforcement mechanism is the chain bridging effect, i.e., the influence of matrix molecular weight on the property improvement. When the matrix chain length is sufficiently long, PP chains are immobilized by chain adsorption at one or several points along their chain lengths, which affects their stress response on the dynamic experiments. In other words, the generated labile bonds alter the mobility and dynamic stiffness. High molecular weight species or long chain molecules efficiently transfer the stress from the crosslinked domains to the matrix. This contributes to the reduction in the interlayer slip between matrix and dispersed domains, which gives rise to an increase in dynamic function in the frequency sweep and to retraction of dynamic functions after subsequent strain perturbation [38]. Figure 8 illustrates the difference in binding

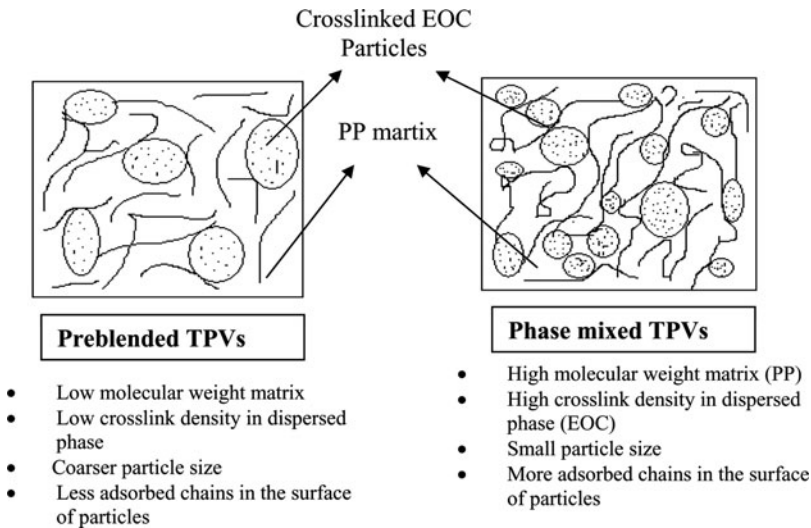


**Fig. 8** Possible structure developed by TPVs prepared with preblended TPVs (conventional method) and phase-mixed TPVs at 2 phr concentration of DCP

of the particles and the particle size of the TPVs prepared by preblending (conventional method) and by phase mixing, both using an equal concentration of curative (2 phr is the optimized concentration). The phase-mixed TPV shows a higher modulus value at low strain and more nonlinear behavior. Morphological analysis shows that the phase-mixed TPV exhibits very small particle size whereas the preblended TPV shows the largest. Smaller crosslinked EOC particles have a higher tendency to adsorb the PP chains on the surface and, hence, form more trapped PP chains by connecting the particles. The adsorbed chains on the surface of the domains via physical and/or chemical adsorption generally broaden the relaxation spectrum towards longer times, which is reflected in the higher dynamic modulus and viscosity in the frequency and strain sweep experiments.

A new TPV, based on a PP matrix in which a metallocene-type ethylene octene (EO) copolymer is crosslinked by a silane crosslinking system to form a dispersed phase, was characterized by Fritz et al. [52]. The EO copolymers are grafted with vinyl organosilanes, then blended with PP, hydrolyzed, and water-crosslinked in a corotating, intermeshing twin-screw extruder. The resulting TPVs are easy to process into articles showing an attractive range of properties. They can easily be colored to any desired shade. The reduced cost of ingredients is another advantage of the newly developed TPVs.

### 2.3 TPVs from Miscible Blends

Recently, a new concept in the preparation of TPVs has been introduced, based on the reaction-induced phase separation (RIPS) of miscible blends of a semicrystalline thermoplastic in combination with an elastomer, with the potential for obtaining submicrometer rubber dispersions. This RIPS can be applied to a variety of miscible blends, in which the elastomer precursor phase was selectively crosslinked to induce phase separation. Plausible schematic representation of the morphological evolution of dynamic vulcanization of immiscible and miscible blends is shown in Fig. 9. For immiscible blends, dynamic vulcanization leads to a decrease in the size

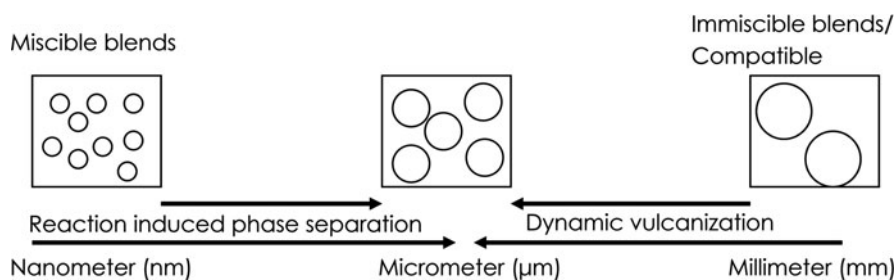


**Fig. 9** Plausible representation of morphology evolution of reactive blending of immiscible and miscible blends

of crosslinked rubber particle. However, particle size increases from the nanometer range to submicrometer range in the case of miscible blends.

Inoue et al. [53] showed that TPVs can be prepared by dynamic vulcanization of miscible blends based on poly(vinylidene fluoride) (PVDF) and acrylic rubber (ACM). They found the existence of a complex morphology in which a small number of nanosized ACM particles are dispersed in a PVDF matrix. Since miscible thermoplastic–elastomer blends are limited due to their low gain in entropy upon mixing, the use of a low molar mass elastomer precursor in combination with a semicrystalline thermoplastic might be advantageous. RIPS of homogeneous poly( $\epsilon$ -caprolactone) (PCL) and epoxy resin, based on poly(propylene oxide) (PPO) mixtures, were studied by Abee et al. [54] using triethyl tetra amine (TETA) as a curative. They observed that up to 80 wt% of microsized crosslinked rubber particles could be dispersed in the thermoplastic PCL matrix, without the use of large shear forces (as normally applied during dynamic vulcanization of TPVs) or the need for additional compatibilization. The tensile properties of PCL/PPO blends containing 40 wt% PCL were cured as a function of temperature. The rubber particle size decreases from 3.0 to 0.9  $\mu\text{m}$  when the curing temperature ( $T_{\text{cure}}$ ) was increased from 80 to 140°C as visualized in Fig. 10. Interestingly, decreases in tensile modulus, elongation at break, and tensile strength are observed with decreasing rubber particle size, which is in contrast to the studies of Coran and Patel [7, 8] on PP/EPDM TPVs. The authors suggested that connection of the rubber particles causes the morphology to shift from a dispersed droplet-like structure towards a cocontinuous structure. Since the tensile modulus of the crosslinked PPO is much lower ( $\sim 2$  MPa) than the tensile modulus of PCL ( $\sim 280$  MPa), interconnection of the PPO particles will decrease the modulus of the TPV.

Similarly, the elongation at break and the tensile strength of the crosslinked PPO are lower than those of PCL, which explains the decrease in elongation at break and decrease in tensile strength of the TPVs as shown in Fig. 11. By increasing  $T_{\text{cure}}$ , not only the rubber particle size decreases, but also the connectivity increases.

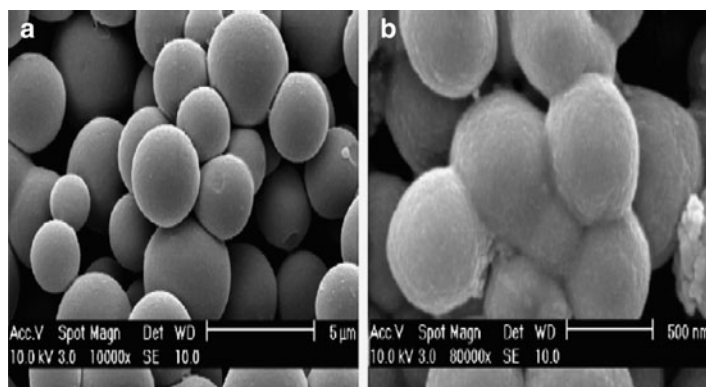


**Fig. 10** SEM images of PCL/PPO blends containing 60% PCL after full curing at (a) 80°C and (b) 140°C (PCL was preferentially extracted)



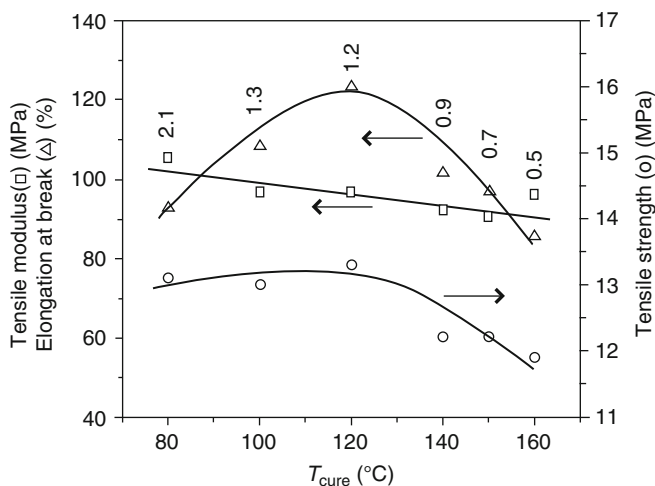


**Fig. 11** Effect of  $T_{\text{cure}}$  on tensile properties for PCL/PPO blends containing 60% of PCL (numbers indicate rubber particle size; arrows indicate the respective properties)

As a result, the positive effect of the particle size reduction on the tensile properties seems to be counteracted by the negative effect of the rubber connectivity.

In another system, miscible blends of PE and lauryl methacrylates (LMA) were in situ polymerized/crosslinked to yield submicrometer rubber particle sizes ranging from 70 to 400 nm [55]. Divinyl benzene (DVB) was used as a crosslinking system for LMA (rubber precursor). Typical TPV morphologies consisting of a crosslinked PLMA rubber dispersion (gel content >90%) in a PE matrix and, consequently, typical TPV solid-state properties are obtained.

The materials are melt-processable and a critical stress for flow is observed, similar to conventional PP/EPDM-based TPVs. Application of static crosslinking leads to (partial) connectivity of the rubber particles via chemical bridging of grafted PE chains. Dynamic preparation conditions caused the connected structure to break-up, which led to a significant enhancement of the mechanical properties and the melt processability. The addition of 25–80 wt% extender oil resulted in a reduced complex viscosity and yield stress in the melt, without deteriorating the mechanical properties. The relatively good elastic recovery and excellent final properties of these high hardness TPVs can be explained in terms of the submicrometer rubber dispersions.

## 2.4 Super TPVs

As the name implies, these classes of TPVs are used for special purpose applications, such as high temperature utilization, oil resistant condition, fatigue resistance etc. Only limited research has been pursued so far in the field of super TPVs, and

there is hardly any openly published literature available in this field because of commercial sensitivity. A few research works in a related field have been patented by Dow Corning Corporation [56, 57] related to silicone-based TPVs. Potential areas for the application of silicone-based TPVs could be the wire and cable industries and for soft-touch appliances. A detailed comparative study on peroxide-cured TPVs based on ethylene- $\alpha$ -olefin/silicone rubber at fixed and varied blend ratios was studied by Basuli et al. [58, 59]. Solid and melt state properties were found to increase with an increase in the concentration of ethylene- $\alpha$ -olefin content. Rheological studies were performed to confirm the pseudoplastic nature of these TPVs. Soares et al. [60] developed TPEs based on PP and acrylic rubber with special emphasis on the effect of the reactive compatibilization and dynamic vulcanization. The compatibilization with the maleic-anhydride-functionalized PP/TETA system resulted in a significant improvement in the mechanical properties, better oil resistance, lower tension set, and a lower rate of stress relaxation. The dynamic vulcanization process was only effective for compatibilized blends. For the PP/TETA blend, the vulcanized rubber particles presented lower particle size, which were effectively surrounded by the PP matrix, characterizing an actual TPV. However, superior mechanical performance and finer morphology with smaller rubber particle size was achieved for nonvulcanized/compatibilized blends. Table 4 shows some of the commercially available super TPVs.

Yun et al. [61] developed styrenic thermoplastic vulcanizates (STPVs) for long-term high-temperature applications. These STPVs consist of PP as the continuous phase and a crosslinked modified hydrogenated styrenic block copolymer (mHSBC) as the dispersed phase. Detailed structural information was not disclosed by the supplier and the authors believe that HSBC may have reactive groups in the main chain. They compared STPVs with conventional TPVs (CTPVs) containing EPDM/PP. The STPVs showed a 20% improvement in solvent resistance after 500 h of immersion in IRM 903 oil at 125°C, and the swelling in oil did not increase with time. The elastic recovery was 50% better than with CTPVs. Tensile property retention was approximately 10% higher after aging for 1,440 h at 125°C when compared to CTPVs. These observed property improvements for STPVs relative to CTPVs can possibly be explained by the unique morphology of the resulting STPV

**Table 4** Commercially available super TPVs<sup>a</sup>

Grade name	Elastomer type	Matrix phase	Supplier
TPSiV	Silicone	Polyamide (PA), thermoplastic polyurethane (TPU)	Dow Corning
Zeotherm	Polyacrylate (ACM)	Polypropylene (PP), PA, polyester	Zeon
E-TPV	Ethylene acrylate	Thermoplastic copolyester (COPE)	Dupont
Uniprene-XL	Hydrogenated-styrene block copolymer (H-SBC)	PP	Teknor-Apex
Serel	Styrene butadiene (SSBR)	PP	Goodyear
Septon V	H-SBC, reactive hard block	SBC triblock	Kuraray

<sup>a</sup>Robert Eller Associates Inc. (2004) <http://www.robertellerassoc.com/>

compounds. It was shown that STPVs have dual-network morphology consisting of micrometer-sized rubber domains with a nanometer-sized substructure. It is believed that these nanosized substructures are clusters of polystyrene hard segments. This seems to be the only difference in morphology between the STPVs and CTPVs, which may explain the excellent long-term elastic recovery, good solvent resistance, better aging properties, and heat stability of the STPVs. This new TPV technology is expected to bridge the gap between PP/EPDM TPVs and the more costly engineering TPVs.

Novel styrenic-based TPEs based on blends of a thermoplastic (polystyrene or styrene acrylonitrile) with a rubber (styrene butadiene or ethylene vinylacetate), with special reference to compatibilization and dynamic vulcanization, were reported by Patel et al. The performance properties were correlated with the interaction parameter and the phase morphology of the blend components [62].

## 2.5 *Nanofilled TPVs*

TPVs are often blended with fillers such as clay, calcium carbonate, glass fiber, carbon black, talc etc., to improve the stiffness, heat distortion temperature, and dimensional stability and also to reduce the cost. However these fillers also increase the weight of the TPVs, rendering them less attractive for aerospace, automotive, and marine applications. On the other hand, similar benefits can be afforded without the weight penalty by using a small amount of nanofiller. In general, the extent of property enhancement depends on many factors, including the aspect ratio of fillers, their degree of dispersion, orientation in the matrix, and the adhesion of the fillers to the matrix interface. Nanofillers are a new generation of filler, which have at least one characteristic length scale in the order of nanometers, with varying shapes ranging from isotropic to highly anisotropic (needle like, sheet like) elements. Owing to the nanoscale dimension they have ultralarge interfacial areas between the polymers and the fillers. Nanofillers range through nanoclay, nanosilica, nanographite, carbon nanotubes, and carbon nanofibers, etc.

Few reports are available on the reinforcement of commercially available PP/EPDM TPVs (Santoprene grades). Mishra et al. [63] have studied and compared the reinforcing tendency of nanobased and microbased fillers. Cloisite 20A and talc fillers are melt-blended with Santoprene grade TPVs. It was found that the tensile modulus of 5 wt% Cloisite-filled TPV nanocomposite was higher than that of the 20 wt% talc-filled microcomposite. In another similar study, a graphite-based TPV nanocomposite was prepared and evaluated in terms of electrical conductivity [64]. Electrically conductive PP/EPDM TPV/expanded graphite (EG) has been successfully prepared via melt compounding of maleic-anhydride-grafted PP (PP-g-MA)/EG master batch and a commercially available TPV material. Three different grades of natural graphite flake (NGF), graphite intercalated compound (GIC), and exfoliated graphite (EG) have been employed and compared. Correlation between graphite microstructure, and electrical conductivity as well as melt

**Table 5** Properties of maleated EPM-based TPV<sup>a</sup> at various nanosilica concentrations

TPV properties	Nanosilica <sup>b</sup> content (phr)				
	0	5	10	15	20
Tensile strength (MPa)	6.1	6.5	6.6	7.6	7.7
Elongation at break (%)	184	180	189	190	150
Modulus at 100% (MPa)	5.2	5.4	4.6	6.2	6.9
Hardness (Shore A)	70	79	80	83	86
Tear strength (N/mm)	12.1	12.2	13.1	14.2	15.1

<sup>a</sup>TPV is composed of 100 phr m-EPM, 60 phr PP, 10 phr m-PP, 25 phr paraffinic oil, 1 phr Si-69 [bis(triethoxysilylpropyl)polysulfide], 2 phr DCP (98% pure), and 4 phr TAC (50% pure)

<sup>b</sup>Nanosilica particle size is 15 nm and purity 99.5%

rheological behavior has been studied. Maleated PP (m-PP) was found to be much more effective in separating EG nanolayers, which is attributed to the higher interfacial interaction between PP-*g*-MA and EG, synergized with its multiporous structure. Lee et al. [65] studied the addition of nanoscale platelets derived from layered silicates treated with an organic modifier in uncrosslinked and dynamically crosslinked PP/EPDM blends. In the case of dynamically crosslinked blends, with an increase in organoclay loading, the tensile modulus increased by 170% at 8 wt% clay loading, whereas tensile strength continuously decreased. In another study, PP/EPDM TPVs were reinforced with nanoclay and evaluated with special reference to the antivibration performance [66].

Reinforcement of maleated EPM (m-EPM)-based TPVs have been studied using various concentrations of nanosilica by Chatterjee and Naskar [22]. Because of the nonpolar nature of PP and the large surface area of polar nanosilica particles, it was challenging to achieve good dispersion of nanosilica in the polymer matrices. To improve the dispersion of nanosilica in PP, m-PP was used as a compatibilizer. Table 5 shows the TPV compositions and corresponding physical properties. With the increase of nanosilica concentrations, significant improvements in the tensile strength, tensile modulus, impact strength, swelling resistance, and thermal properties of TPVs were achieved.

## 2.6 Oil-Extended TPVs

Processing oil is a well-known additive for rubbers and is commonly employed in PP/EPDM TPVs [10–12]. It lowers the hardness and improves the processability. The oil, in most cases paraffinic oil, can be considered as a low molecular weight olefin. The difference in polarity between the three components is small, and the oil is present in both the PP and in the elastomer phases [67]. In order to understand the mechanical and the rheological properties of olefinic thermoplastic elastomers (OTPEs), the concentration of oil in each phase must be known.

Several methods have been proposed to estimate the oil distribution, such as the integration of surface area of TEM images [68] and quantitative NMR analysis

[69]. In the latter method, however, about 30 wt% of the oil could not be traced in either the PP or the elastomer phase. The integration of the surface area in TEM images can be misleading in some cases. At high elastomer content, the overlapping elastomer particles can give an impression that the content of the elastomer phase is higher than it is. The determination of the actual oil concentration by measuring the reduction in the glass transition temperatures ( $T_g$ ) is inaccurate using DSC or DMA, because the glass transition dynamics of the two phases overlap. Therefore, it is expected that the blends can be made useable for dielectric spectroscopy by the addition of a probe molecule. Sengers et al. [70, 71] investigated the distribution of oil in PP/SEBS blends and PP/EPDM TPVs in detail using dielectric spectrometry. The oil distribution coefficient,  $K$ , is the ratio of the oil concentration in the PP phase over the oil concentration in the elastomer phase. In general,  $K$  is lower than 1, indicating that the oil prefers to be in the elastomer phase. The effect of the composition or the temperature on the value of  $K$  is unknown. It has been stated that the oil migrates to the PP phase upon melting of this phase and acts there as a processing agent. At crystallization of the PP phase, the oil is pushed out of the PP phase and absorbed by the elastomer phase. This mechanism, however, has never been proven. The oil distribution was determined by modeling of the dielectric loss factor ( $\epsilon''$ ) values of the blends in the  $T_g$  regime from the ones of the binary mixtures. The mean value for the oil distribution coefficient was found to be 0.6 for PP/SEBS blends and 0.63 for TPVs.

## 2.7 Foamed TPVs

The primary applications for foamed TPEs are found in the automotive, appliances, sports equipment, and construction industries. The main target for foamed TPVs is the automotive seal for door and window enclosures, replacing conventional sealing profiles made from sponge EPDM. Foamed TPV can be coextruded or combined with dense TPVs and PP materials to replace the more complex EPDM seal systems [72]. Foamed TPVs offer several advantages over conventional foamed EPDM, which include flexibility in profile design, weight reduction, recyclability, and better compression set at low densities. Dutta and Cakmak [73, 74] studied foaming of TPV and suggested that with the proper choice of blowing agent and by optimum balance of curative loading, foam density as low as  $0.55 \text{ g/cm}^3$  could be obtained. Employing a high temperature chemical blowing agent (CBA), namely *p*-toluene sulfonyl semicarbazide (cellogen-RA), prevents appreciable decomposition during blending and subsequent compounding. A CBA activator, namely surface-treated urea (BIK-OT), in the blend lowers the foaming temperature and considerably reduces the density. The authors used sulfur-cured blends (100/35 EPDM/PP) with 1 phr, and the above-mentioned CBA/activator combination to achieve a density as low as  $0.55 \text{ g/cm}^3$ . The degree of cure in the rubber phase was found to play a major role in determining the degree of foamability. The result suggested that the foamability of the blend is reduced linearly with an increase in the state of

cure. TPVs with a lower crosslink level can be extrusion foamed to yield extrudates with acceptable surface quality. The preparation of low density TPV foams is very difficult, partly due to the need to foam the PP component, which is the only ingredient in a TPV composition that can be foamed. Furthermore, in a low hardness grade, the PP content is very low. Therefore, in order to make TPV foam with a specific gravity of  $0.3 \text{ g/cm}^3$ , it may be necessary to foam the PP phase to a specific gravity of  $0.05 \text{ g/cm}^3$ . Additional complications are related to the rheological properties of TPVs. Higher loading and fully crosslinked rubber particles in the polymer melt may affect melt integrity and the stability of the foaming process.

Both physical and chemical methods can be employed to foam a TPV. Two major suppliers are involved in the development of foamed TPVs. DSM Elastomers utilizes a recompounded water-releasing chemical compound (WCC) that can produce water upon heating above the activation temperature in the melt [75]. The foaming process can be done on the standard extruders with standard screws. The resulting foam has a uniform, fine, closed-cell structure with a smooth surface. In addition, due to unexpected reactions during decomposition of the CBA and foaming, CBA-blown TPV foam usually has an open-celled structure that leads to more water absorption, which is not favorable for sealing purposes. DSM claims that their foaming technology can be used to produce TPV foams with a density of  $0.15\text{--}0.90 \text{ g/cm}^3$ .

Other approaches have been reported using a physical blowing agent (PBA) developed by Advanced Elastomer Systems (AES) [76]. Water as a PBA was used from the standpoint of cost and environmental requirements. AES claims that the state of water blown technology can give specific gravity as low as 0.2. The process requires a special type of extruder equipped with a highly effective heating/cooling system, a special screw designed for mixing water with the polymer melt, and a water metering pump capable of continuously dosing a small amount of water with high accuracy. The water should be injected into the polymer melt under a high-enough pressure to maintain the water in a liquid state. It should be mentioned here that the mixing of a polymer melt and water is not easy because the viscosities differ by the order of 5. The key steps to obtain foamed TPVs are a uniform dosage of water, effective mixing, and optimum amount and rate of injection of water. Several advantages are offered by water-foamed TPVs in automotive seals, including lower component production cost (apart from the initial investment of a special type of extruder), elimination of hazardous blowing agents, and recyclability of scraps. However, it cannot completely replace the foamed EPDM component in certain special application areas.

Spatiael et al. [77] studied the foaming behaviors of several TPV formulations containing various amounts of branched PP resin with water as the blowing agent, while the extensional viscosity of the materials with different formulations was measured and considered. The authors indicated that the replacement of a small amount of linear PP with branched PP improved the foam density and cellular structure. However, as the added content of branched PP was increased, a worse foamability was observed. They concluded that there exists an optimal amount of

branched content. Kim et al. [78] studied the foaming behavior of commercially available TPV (Santoprene 121-68 W228) with respect to the type and concentration of various blowing agent such as nitrogen (BOC Gas, 99.9% purity), carbon dioxide (CO<sub>2</sub>) (BOC Gas, 99.5% purity), *n*-butane (Matheson, 99.0% purity), and water in high-pressure experiments. Comparison of results was evaluated in terms of the expansion behavior, the cell-number density, and the foam structure under the different processing conditions. Typical cell structures of TPV foams at equal concentration (1 wt%) of various blowing agents are shown in Fig. 12. TPV foam with N<sub>2</sub> and CO<sub>2</sub> showed a finer and more uniform cell structure than with *n*-butane and water. However, the TPV foam with N<sub>2</sub> produced a uniform and fine cell structure with a smooth surface. This indicates that N<sub>2</sub> could be a very good PBA for TPV material. However, it depends on the application. If the product requires a lower density, then CO<sub>2</sub> or *n*-butane are better. If the product requires a finer cell structure, N<sub>2</sub> is better. Kropp et al. [79] carried out a comparative study by foaming three types of TPEs with CO<sub>2</sub> and using hydrocerol as a nucleating agent. These materials were thermoplastic polyurethane (TPU), a styrene-based TPE (SEBS) and a PP/EPDM TPV. They found that foaming was most difficult with the PP/EPDM TPV. The foam density they could reach was 0.76 g/cm<sup>3</sup> and the foam structure was not uniform. They found that a specific TPU-type showed the best foamability; a SEBS-type was also successfully foamed; and that a PP/EPDM TPV especially developed for water foaming was the most difficult to foam with CO<sub>2</sub> as PBA.

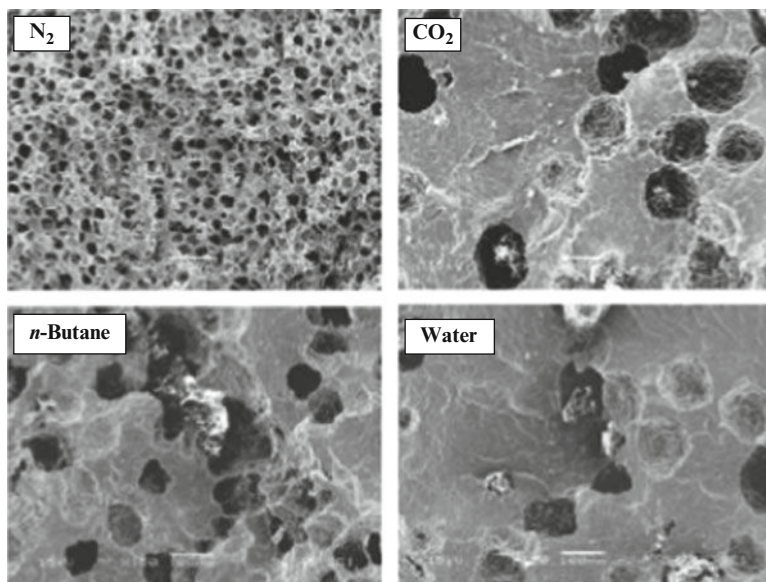


**Fig. 12** Cell structure of foamed TPVs formed by various blowing agents at 1 wt% concentration at 160°C

Expandable microspheres are a rather different blowing agent for the formation of TPEs and were recently studied by Lean et al. [80]. The microsphere is an elastic thermoplastic pellet that contains a gaseous expanding agent (blowing agent). When the pellets are heated, the pressure of the gas contained in them increases and this leads to an irreversible increase in volume of the microspheres, which become up to 50 times greater than their original size.

## 2.8 *Electron Beam Crosslinked TPVs*

Besides some advantages, chemical crosslinking agents have some limitations, which means exploring another path to find a suitable alternative. The electron beam (EB)-processing of polymers has gained a special importance because it requires a shorter time, provides an improved state and rate of cure, involves no external crosslinking agent, and is versatile in application. Recently, Naskar et al. [81] were involved in the development of a novel TPV based on PP and EPDM prepared by EB-induced reactive processing. Electron-induced reactive processing is a novel technique whereby chemical reactions are induced through spatial and temporal precise energy input via high energy electrons under dynamic conditions of melt mixing. A 1.5 MeV electron accelerator was directly coupled to an internal mixer in order to induce chemical reactions by energy input via high energy electrons under dynamic conditions of melt mixing of PP and EPDM. Figure 13 shows a schematic representation of the unique EB curing setup. In this novel process, the penetration depth of electrons is limited to a part of the mixing volume. The total mixing volume is modified due to the change of polymer mass within the penetration depth of electrons during the mixing process. Furthermore, the electron treatment time and electron energy control the dose rate and penetration depth, respectively.

In this novel process, electron treatment time also influences the ratio of radical generation rate to mixing rate (dose per rotation), and electron energy controls the ratio of modified volume to total mixing chamber volume ( $r_{vol}$ ). The performance properties of dynamically electron crosslinked 50/50 PP/EPDM blends were pursued with special reference to various conditions such as absorbed dose, electron treatment time, and electron energy of the electron-induced reactive processing. Table 6 summarizes the mechanical properties of the TPVs prepared by EB reactive processing. It can be concluded that electron-induced reactive processing with 1.5 MeV electrons for 15 s at an absorbed dose of 100 kGy should give the best balance of mechanical properties for our experimental setup. The experimental results clearly indicated that two processes are simultaneously occurring, contributing to enhancement in the mechanical properties: (a) in situ compatibilization of PP and EPDM, and (b) crosslinking in the EPDM phase. Both processes depend on absorbed dose as in the traditional electron treatment under static conditions. Moreover, they depend on electron treatment time as well as electron energy. Electron treatment time correlates with dose rate and radical



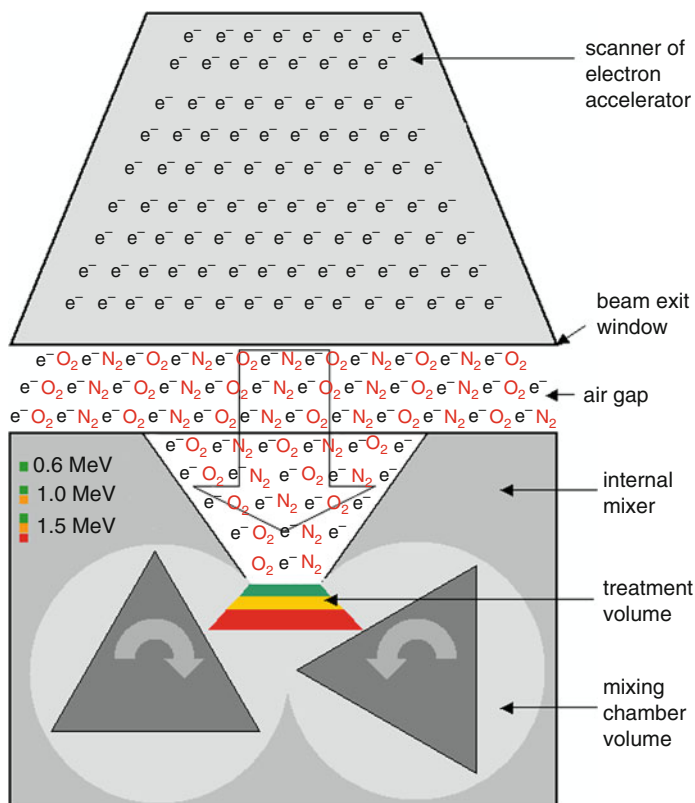


**Fig. 13** EB curing setup: coupling of an electron accelerator with an internal mixer

**Table 6** Physical properties of electron-induced dynamic vulcanization of 50/50 PP/EPDM blend ratio at various conditions

Electron energy (MeV)	Dose (kGy)	Treatment time (s)	Elastic modulus (MPa)	Tensile strength (MPa)	Elongation at break (%)
0	0	0	112	4.7	46
1.5	25	60	159	7.0	135
1.5	50	60	156	9.2	298
1.5	100	60	173	9.8	282
1.5	100	30	191	9.5	215
1.5	100	15	176	14.7	624
0.6	50	60	150	8.2	168

generation rate. Thus, it has been concluded that the radical generation rate of electron-induced reactive processing controls the structure, morphology, and properties of PP/EPDM vulcanizate at a fixed mixing rate and a fixed mixing temperature range.

### 3 Concluding Remarks

Currently TPVs are the fastest growing segment of the elastomer market and occupy a vital position in the family of TPEs because of their huge potential. However, there are still some unsolved technological problems, which are associated with a lack of proper understanding of the TPVs. Both the process of TPV production and the structure–properties relationship of the TPVs are still a mystery. For this reason, the development of TPV-based products is generally pursued by a somewhat trial and error method. More scientific investigation is required to gain better insight into the process of dynamic vulcanization. For instance, the development of morphology during dynamic vulcanization in a batch process, as well as in a twin-screw extruder for a continuous process, is still not clear. The TEM photomicrographs of the final TPV morphology differ from a conventional 2D image to a 3D image. Sometimes, it is very difficult to distinguish between a true dispersed phase morphology and a true cocontinuous morphology. Distribution of oil over the two phases during mixing and its redistribution upon cooling of a TPV melt is still a topic of controversy. As mentioned, the deformation mechanism and elasticity of TPVs are still not well understood. Hence, even better models are required to explain why TPVs behave in a fully elastic manner. More fundamental studies are needed on TPV-melt rheology to explain the excellent processability of TPVs even at a very high EPDM/PP blend ratio. Furthermore, development of novel crosslinking agents with simple crosslinking chemistry could well be explored to enrich the field of applications of TPVs in the future.

### References

1. Legge NR, Holden G (1987) Thermoplastic elastomers – a comprehensive review. Hanser, Munich
2. De SK, Bhowmick AK (1990) Thermoplastic elastomers from rubber plastic blends. Horwood, London
3. Gessler AM, Haslett WH (1962) US Patent 3,037,954. (to Esso Research and Engineering Company)
4. Fisher WK (1973) US Patent 3,758,643. (to Uniroyal Inc.)
5. Coran AY, Patel R (1982) US Patent 4 355 139
6. Coran AY, Patel RP (1980) Rubber Chem Technol 53:141
7. Coran AY, Patel RP (1981) Rubber Chem Technol 54:91
8. Coran AY, Patel RP, William D (1982) Rubber Chem Technol 55:116
9. Abdou-Sabet S, Patel RP (1991) Rubber Chem Technol 64:769
10. Coran AY, Patel RP (1997) In: Al-Malaika S (ed) Reactive modifier for polymers. Chapman and Hall, London
11. Kocsis K (1999) In: Shonaike GO, Simon GP (eds) Polymer blends and alloys – thermoplastic rubbers via dynamic vulcanization. Marcel Dekker, New York
12. Naskar K (2007) Rubber Chem Technol 80:504
13. Harrats S, Thomas S, Groeninckx G (2006) Micro and nano structured multiphase polymer blend systems – phase morphology and interface. CRC, Boca Raton

14. Radusch HJ, Pham T (1996) *Kautsch Gummi Kunstst* 49:249
15. Sengupta P, Noordermeer JWM (2005) *Macromol Rapid Commun* 26:542
16. Goettler LA, Richwine JR, Wille FJ (1982) *Rubber Chem Technol* 55:1448
17. Han PK, White JL (1995) *Rubber Chem Technol* 68:728
18. Steeman P, Zoetelief W (2000) In: *Conference proceedings SPE/ANTEC 2000, Orlando, FL*. CRC, Boca Raton, p 3297
19. Jain AK, Gupta NK, Nagpal AK (2000) *J Appl Polym Sci* 77:1488
20. Katbab AA, Nazockdast H, Bazgir S (2000) *J Appl Polym Sci* 75:1127
21. Katbab AA, Bazgir S, Nazockdast H (2004) *J Appl Polym Sci* 92:2000
22. Chatterjee K, Naskar K (2008) *Polym Eng Sci* 48:1077
23. Ichazo M, Hernandez M, Gonzalez J, Albano C, Dominguez N (2004) *Polym Bulletin* 51:419
24. Sengers WGF, Sengupta P, Noordermeer JWM, Picken SJ, Gotsis AD (2004) *Polymer* 45:858
25. Leblanc JL (2006) *J Appl Polym Sci* 101:4193
26. Boyce MC, Socrate S, Kear K, Yeh O, Shaw K (2001) *J Mech Phys Solids* 49:1323
27. Soliman M, van Dijk M, van Es M, Shulmeister V (1999) In: *Conference proceedings SPE/ANTEC 1999, New York*. CRC, Boca Raton, p 1947
28. Oderkerk J, de Schaetzen G, Goderis B, Hellemans L, Groeninckx G (2002) *Macromolecules* 35:6623
29. Van Duin M, Machado AV (2005) *Polym Degrad Stab* 90:340
30. Naskar K (2009) In: White J, De SK, Naskar K (eds) *Rubber technologists handbook, vol 2*. Smithers Rapra Technology, Shawbury, UK
31. Van Duin M (2006) *Macromol Symp* 233:11
32. Abdou-Sabet S, Puydak RC, Radar CP (1996) *Rubber Chem Technol* 69:476
33. Medsker RE, Gilbertson GW, Patel R (1997) Patent EP 850991 A1 (to Advanced Elastomer Systems)
34. Lopez Manchado MP, Kenny JM (2001) *Rubber Chem Technol* 74:198
35. Naskar K, Noordermeer JWM (2003) *Rubber Chem Technol* 76:1001
36. Naskar K (2004) *Dynamically vulcanized PP/EPDM thermoplastic elastomers*. Ph.D. thesis, University of Twente, The Netherlands
37. Naskar K, Noordermeer JWM (2004) *Rubber Chem Technol* 77:955
38. Naskar K, Noordermeer JWM (2004) *Kautschuk Gummi Kunststoffe* 57:235
39. De Risi FR, Noordermeer JWM (2007) *Rubber Chem Technol* 80:83
40. De Risi FR (2007) *The role of coagents in peroxide cured PP/EPDM TPVs*. Ph.D. thesis, University of Twente, The Netherlands
41. Fritz HG, Anderlik R (1993) *Kautschuk Gummi Kunststoffe* 46:374
42. Han SJ, Lohse DJ, Radosz M, Sperling LH (1998) *Macromolecules* 31:1998
43. Maiti M, Patel J, Naskar K, Bhowmick AK (2006) *J Appl Polym Sci* 102:5463
44. McNally T, McShane P, Nally GM, Murphy WR, Cook M, Miller A (2002) *Polymer* 43:3785
45. Lai SM, Chin FC, Chiu TY (2005) *Eur Polym J* 41:3031
46. Li Z, Kontopoulou M (2006) *J Polym Eng* 26:633
47. Babu RR, Singha NK, Naskar K (2009) *J Appl Polym Sci* 113:1836
48. Babu RR, Singha NK, Naskar K (2009) *J Appl Polym Sci* 113:3207
49. Dluzeski PR (2001) *Rubber Chem Technol* 74:451
50. Babu RR, Singha NK, Naskar K (2009) *Polym Eng Sci* 50:455–467. doi: 10.1002/pen.21553
51. Babu RR, Singha NK, Naskar K (2009) *J Polym Res* (in press). doi: 10.1007/s10965-009-9354-z
52. Fritz HG, Boel U, Cai Q (1999) *Polym Eng Sci* 39:1087
53. Li Y, Oono Y, Kadowaki Y, Inoue T, Nakayama K, Shimizu H (2006) *Macromolecules* 39:4195
54. Abee R, Goossens H, van Duin M (2008) *Polymer* 49:2288
55. Abee R, Goossens H, van Duin M, Spoelstra A (2009) *Eur Polym J* 45:503
56. Gornowicz GA (2000) *Thermoplastic silicone elastomers based on fluorocarbon resin*. US Patent 6015858, USA

57. Gornowicz GA, Zhang H (2000) Thermoplastic silicone vulcanizates prepared by condensation cure. US Patent 6153691, USA
58. Basuli U, Chaki TK, Naskar K (2008) *J Appl Polym Sci* 108:1079
59. Basuli U, Chaki TK, Naskar K (2008) *eXPRESS Polym Lett* 2:846
60. Soares BG, Santos DM, Sirqueira AS (2008) *eXPRESS Polym Lett* 2:602
61. Yun J, Patel R, Worley Darnell C II (2007) *J Appl Polym Sci* 105:2996
62. Patel JD, Maiti M, Naskar K, Bhowmick AK (2005) *Rubber Chem Technol* 78:893
63. Mishra JK, Kim GH, Kim I, Chung IJ, Ha CS (2004) *J Polym Sci B Polym Phys* 42:2900
64. Katbab AA, Hrymak AN, Kasmadjian K (2008) *J Appl Polym Sci* 107:3425
65. Lee KY, Goettler LA (2004) *Polym Eng Sci* 44:1103
66. Wu JH, Li CH, Chiu HT, Shong ZJ, Tsai PA (2009) *J Thermoplastic Compos Mater* 22:503
67. Ellul MD (1998) *Rubber Chem Technol* 71:244
68. Jayaraman K, Kolli VG, Kang SY, Kumar S, Ellul MD (2004) *J Appl Polym Sci* 93:113
69. Winters R, Lugtenburg J, Litvinov VM, van Duin M, de Groot HJM (2001) *Polymer* 42:9745
70. Sengers WGF, Wübbenhorst M, Picken SJ, Gotsis AD (2005) *Polymer* 46:6391
71. Sengers WGF, van den Berg O, Wübbenhorst M, Gotsis AD, Picken SJ (2005) *Polymer* 46:6064
72. Dufton P (2001) Thermoplastic elastomers – a Rapra industry analysis report. Rapra Technology, Shawbury, UK
73. Dutta A, Cakmak M (1992) *Rubber Chem Technol* 65:778
74. Dutta A, Cakmak M (1992) *Rubber Chem Technol* 65:932
75. Brzoskowski R, Wang Y, La Tulippe C, Dion B, Cai H, Sadeghi H (1998) In: Conference proceedings SPE/ANTAC 1998, Atlanta, GA. CRC, Boca Raton, p. 3204
76. Beaver LH III (2004) Extrusion foaming of TPVs using water-filled polymers. In: Conference proceedings SPE/ANTEC 2004, Chicago, IL. SPE, Newtown, CT, pp.4234–4238
77. Spitael P, Macosko CW, Sahnoune A (2002) In: Conference proceedings SPE/ANTEC 2002, San Francisco, CA. SPE, Newtown, CE
78. Kim SG, Park CB, Sain M (2008) *J Cell Plastics* 44:53
79. Kropp D, Michaeli W, Herrmann T, Schroder O (1998) *J Cell Plastics* 34:304
80. Lena J, Rüdiger RK (2003) *Kunststoffe* 93:40
81. Naskar K, Gohs U, Wagenknecht U, Heinrich G (2009) *eXPRESS Polym Lett* 3:677



# PTFE-Based Rubber Composites for Tribological Applications

M.S. Khan and G. Heinrich

**Abstract** The unique properties of rubber, along with its diverse applications, have prompted a great deal of interest among researchers to explore advanced multi-functional materials for special purpose applications by incorporating various filler materials into the rubber matrix. This article deals with the application of a relatively new class of materials based on the addition of polytetrafluoroethylene (PTFE) powder to rubber matrixes for preparing PTFE-based elastomeric composites. Besides other properties, the remarkably low friction coefficient of PTFE enables its utilization for tribological applications. However, PTFE in rubbers has not been fully explored, mainly due to its inherent chemical inertness and incompatibility. The present work describes the electron modification of PTFE powder to improve its compatibility with rubber matrixes, the state of the art regarding its application in rubbers, and the preparation of PTFE-based elastomeric composites for tribological applications. It has been demonstrated that, in addition to the improvement in engineering properties, the chemical coupling of modified PTFE powder with rubber matrixes can significantly improve the friction and wear properties of the host elastomer. In addition, a new class of chloroprene composites, with exceptional mechanical and dispersion properties due to chemical coupling of electron-modified PTFE particles and chloroprene rubbers, has been produced. An explanation of the proposed chemical reaction mechanism between the irradiated PTFE and chloroprene rubber, along with a detailed characterization of the compatibility, dispersion, and chemical coupling is presented.

---

M.S. Khan (✉)

Leibniz-Institut für Polymerforschung Dresden e.V., Hohe Straße 6, 01069 Dresden, Germany  
e-mail: Khan@ipfdd.de

G. Heinrich

Leibniz-Institut für Polymerforschung Dresden e.V., Hohe Straße 6, 01069 Dresden, Germany  
Technische Universität Dresden, Institut für Werkstoffwissen-schaft, Dresden, Germany

**Keywords** Chemical coupling · Elastomer · Electron-beam modification · Friction and wear properties · Mechanical properties

## Contents

1	Introduction .....	251
2	Polytetrafluoroethylene .....	253
2.1	Polymerization, Manufacturing, and Properties .....	253
2.2	Radiation-Induced Modification of PTFE .....	255
2.3	Chemically Coupled PTFE-Based Compounds .....	257
2.4	State of the Art: PTFE for Tribological Applications .....	258
3	PTFE-Based EPDM Rubber Composites .....	262
3.1	Electron Modification of PTFE Powder and Sample Preparation .....	262
3.2	Characterization of PTFE Powder .....	264
3.3	Peroxide-Crosslinked Rubber Composites .....	268
3.4	Electron-Beam-Crosslinked Rubber Composites .....	288
4	Newly Developed PTFE-Coupled Chloroprene Composites .....	295
4.1	Rheometric Characterization .....	297
4.2	Compatibility and Dispersion .....	298
4.3	Mechanical Properties .....	299
4.4	Chemical Coupling Investigations .....	304
4.5	Possible Chemical Coupling Mechanism .....	306
5	Summary .....	306
	References .....	309

## Abbreviations

$\mu$	Friction coefficient
$\sigma_{\text{red}}$	Reduced stress
-COF	Carbonyl fluoride group
-COOH	Carboxylic acid group
$\Delta M$	Apparent crosslinking density
CR	Chloroprene rubber
E-beam	Electron beam
EPDM	Ethylene-propylene-diene rubber
$f(\lambda)$	Deformation function
$k$	Specific wear rate
kGy	KiloGray
phr	Parts per hundred of rubber
PTFE	Polytetrafluoroethylene
$t_{90}$	Optimum cure time
Tan delta	Mechanical energy dissipation

## 1 Introduction

Elastomers derived from “elastic polymers” are a special class of polymeric materials composed of long, chain-like crosslinked molecules with exceptional elastic mechanical properties. The high elastic memory, high ultimate elongation, and low elastic modulus in comparison to engineering thermoplastics recommend elastomers for a wide range of special purpose applications. More than half of all rubber produced worldwide is consumed in the production of automobile tires alone while the rest is utilized in mechanical goods such as mountings, seals, gaskets, belts, and hoses, and in consumer products.

Although natural rubber has the longest history of use as elastomer and is still one of the most important industrial polymers, it now competes with synthetic elastomers such as ethylene-propylene-diene rubber (EPDM), chloroprene rubber (CR), styrene-butadiene rubber (SBR), and acrylonitrile-butadiene rubber (NBR) because of the diversity of the properties offered by these man-made compounds over a wide range of applications. Versatility in polymer design and performance requirements have also resulted in the development of new synthesis routes, processing procedures, and rubber formulations to meet specific demands. Although the desired properties can be acquired to a great extent by variation of physical characteristics such as resiliency, flexibility, extensibility, and durability, it has not been possible to resolve a few inherent disadvantages associated with elastomers. One such drawback is the significantly poor tribological properties of rubber compounds. Enhanced tribological properties of rubber compounds are not only required for tire performance but also for non-tire rubber goods in which the elastomeric structure is in direct contact with a relatively hard counter-surface.

For this reason, there has been a renewed interest in rubber tribology because of the properties required for rubber in engineering applications such as dynamic and static sealing, gaskets, automotive weather stripping etc. [1]. Figure 1 shows a variety of sealing and gasket components that are required for different applications in a typical automotive engine unit. This necessitates exploring how the requested friction and wear performance can be fulfilled by the formulation of rubber compounds for a specific requirement. For this reason, use of polytetrafluoroethylene (PTFE) powder as a potential friction-modifier additive has gained a huge interest due to its significantly low friction coefficient. However, these efforts have not been wholly successful, especially in rubbers, due the difficulty of obtaining homogeneous mixtures and high PTFE loading. This problem is the result of PTFE's unique properties, most probably its highly hydrophobic and inert surface, which resists wetting and compatibility. As such, uniform mixing and chemical coupling of PTFE in rubbers has not been achieved with any commercially significant success. There is indeed a strong motivation to probe into new techniques and procedures for the use of PTFE powder as solid lubricant in a vast range of rubber compounds for tribological applications. In addition



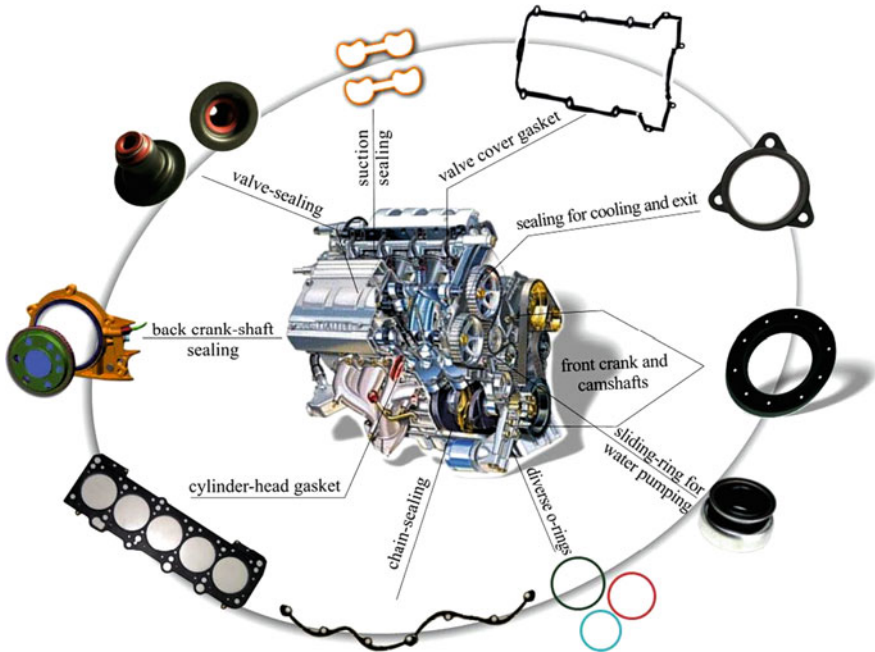


**Fig. 1** Dynamic and static sealing in a motor engine [1]

to the property requirements, this motivation is also encouraged by the demand for adapting sustainable technologies by replacing polymeric components in tribological applications where fluid and grease lubricants fail or possess potential risk to the surrounding environment.

In the present work, the friction and wear properties of PTFE-filled EPDM rubber are investigated. With the help of electron irradiation, the inherent poor wetting and dispersion of PTFE powder is enhanced. Electron irradiation provides a wide range of advantages for the modification of the inert PTFE surface. Chain scission of PTFE powder generates radicals that are either trapped as persistent radicals in the crystalline structure of PTFE or, in atmospheric conditions, react partially with oxygen to form carbonyl fluoride groups ( $-\text{COF}$ ) and later with water vapor to form carboxylic acid groups ( $-\text{COOH}$ ). The presence of such reactive radicals and functional groups promote PTFE as an attractive choice for effective use of PTFE powder in a wide range of polymers. Taking advantage of these specific radiation-induced modifications, chemical coupling of PTFE powder with speciality rubber matrixes such as EPDM and CR is achieved by a simple reactive-mixing process. In addition to improved tribological properties, the corresponding chemical coupling of modified PTFE powder with rubber matrixes can significantly improve the engineering properties of the rubber compounds.

## 2 Polytetrafluoroethylene

### 2.1 Polymerization, Manufacturing, and Properties

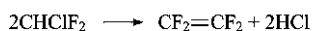
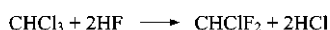
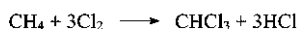
PTFE, a homopolymer of tetrafluoroethylene (TFE) monomer, is a highly crystalline white-to-translucent solid polymer with extremely high molecular weight (range  $10^6$ – $10^7$  g/mol) and viscosity ( $10^{10}$ – $10^{12}$  Poise at  $380^\circ\text{C}$ ). Polymerization of TFE monomer gives the perfluorinated straight-chain high polymer PTFE with the chemical formula  $(\text{CF}_2\text{--CF}_2)_n$ . TFE (molecular weight 100 g/mol) is a colorless, tasteless, odorless nontoxic gas. It is stored as a liquid and polymerized usually above its critical temperature of  $33.3^\circ\text{C}$  and below its critical pressure of 3.94 MPa. Besides being used for polymerization of PTFE homopolymer, it can also be used in the copolymerization with hexafluoropropylene, ethylene, perfluorinated ether, and as a comonomer in a variety of terpolymers. Figure 2 shows the main steps involved in the manufacture of TFE monomer.

Hydrogen fluoride is manufactured by the first step while chloroform and other chloromethanes are produced in succeeding steps. Chloroform is then fluorinated with hydrogen fluoride to chlorodifluoromethane, which upon pyrolysis produces TFE. Although the polymerization mechanism is not a typical emulsion type, some of the principles of emulsion polymerization are applied. The two products are distinctly different, even though both are chemically high molecular weight PTFE polymers. Table 1 shows the processing, properties, and uses of various grades of PTFE in different electrical, mechanical, and chemical applications [2].

Commercial PTFE is manufactured by two different polymerization techniques:

1. Suspension polymerization: either little or no dispersion agent is used and vigorous agitation is maintained. A precipitated resin, commonly referred to as *granular resin*, is produced.
2. Emulsion polymerization: a sufficient amount of dispersing agent and mild agitation is employed. This produces small colloidal particles dispersed in the aqueous reaction medium. In this procedure, called aqueous dispersion polymerization, precipitation of the resin particles is avoided. The coagulated dispersion produced by emulsion polymerization is often called a *fine-powder* or *PTFE dispersion*.

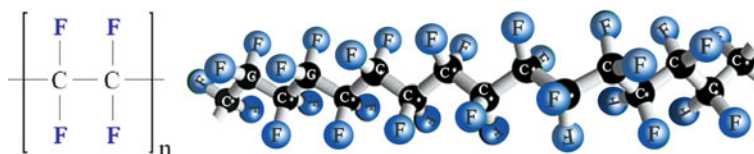
The exceptional thermal and chemical stability of PTFE originate in the strength of its primary chemical bonds. The carbon–fluorine bond energy is the highest currently known among organic compounds [3, 4]. In addition, the fluorine atoms



**Fig. 2** Basic manufacturing steps involved in TFE monomer production

**Table 1** Applications of PTFE resins

Resin grade	Processing	Description	Main uses
Granular			
Agglomerates	Molding, preforming, sintering Ram extrusion	Free-flowing powder	Gaskets, packing, seals, electronic components, bearings, sheet, rod, heavy-wall tubing; tape and molded shapes for nonadhesive applications
Coarse	Molding, preforming, sintering	Granulated powder	Tape, molded shapes, nonadhesive applications
Finely divided	Molding, preforming, sintering	Powder for highest quality, void-free moldings	Molded sheets, tape, wire wrapping, tubing, gaskets
Presintered	Ram extrusion	Free-flowing powder granular	Rods and tubes
Fine powder			
High reduction ratio	Paste extrusion	Agglomerated powder	Wire coating, thin-walled tubing
Medium reduction ratio	Paste extrusion	Agglomerated powder	Tubing pipe, overbraided hose, spaghetti tubing
Low reduction ratio	Paste extrusion	Agglomerated powder	Thread-sealant tape, pipe liners, tubing, porous structures
Dispersion			
General purpose	Dip coating	Aqueous dispersion	Impregnation, coating, packing
Coating	Dip coating	Aqueous dispersion	Film, coating
Stabilized	Coagulation	Aqueous dispersion	Bearings

**Fig. 3** Chemical (*left*) and molecular (*right*) structure of PTFE

also strengthen the main chain carbon–carbon bond. Another factor that contributes to the unique character of PTFE is the crowding of the fluorine atoms around the main chain, which forces a helical conformation of the polymer backbone in the crystal lattice (Fig. 3) [5, 6]. The dense packing of the relatively large fluorine atoms yields an impenetrable shield that protects the carbon backbone from chemical attack, and increases the stiffness of the molecular chain. Due to the relatively smooth molecular profile of the helical chains, the PTFE crystal structure essentially consists of a hexagonal packing of cylinders [7].

The limited contact area between the chains in the crystal lattice results in weak intermolecular interactions and a high chain mobility. The latter, in turn, is responsible for the outstanding low friction characteristics of PTFE, and, somewhat

unexpected, for the high melting point of PTFE (327°C), as the high chain mobility in the solid state results in a low entropy of fusion. That high chain mobility is also the origin of a wide range of mechanical properties, such as a relatively low yield stress, high fracture toughness down to cryogenic temperatures, and susceptibility to plastic creep (so-called cold flow) [8].

### 2.1.1 PTFE Micropowders

The PTFE micropowders, also called waxes, are TFE homopolymers with molecular weights significantly lower than that of normal PTFE. The molecular weight for micropowders varies from  $2.5 \times 10^4$  to  $2.5 \times 10^5$  g/mol, whereas that of normal PTFE is of the order of  $10 \times 10^6$  g/mol. Micropowders are usually white in color and are friable. The average agglomerate particle size is between 5 and 10  $\mu\text{m}$  whereas the primary particles are approximately 0.2  $\mu\text{m}$  in diameter. These micropowders are commonly used as additives in a wide variety of applications, for example where chemical resistance, weathering resistance, and a wide temperature application range are required. Most importantly, the low friction properties of these micropowders are obviously of significant advantage in many applications.

Micropowders are added to variety of materials used in industry, where they provide nonstick and sliding properties. They are incorporated into the product by blending and grinding. PTFE micropowders are commonly used in plastics, elastomers, inks, lubricants, and lacquer finishes. Lubricants containing micropowders are used for bearings, valve components, and other moving parts where sliding friction must be minimized or eliminated. Nonstick finishes that required good release properties (e.g., in the food and packaging industry) commonly use PTFE micropowders.

In some applications, the high heat stability of micropowders can be utilized over a reasonably wide temperature range. The maximum service temperature is normally 260°C, provided the crystalline melting point is between 320°C and 335°C. Exposure above 300°C leads to degradation and possible evolution of toxic decomposition products. The particulate morphology of PTFE micropowder in printing inks provides desirable gloss to the printed product. Its inherent lubricity results in good wear and slip properties and in surface smoothness. The chemical resistance of micropowder is as high as that of high molecular weight PTFE. It is therefore used in applications requiring service in a strong or corrosive chemical environment such as concentrated mineral acids and alkalis. PTFE micropowder is not attacked by organic solvents, which also contributes to good weatherability [2].

## 2.2 *Radiation-Induced Modification of PTFE*

For the last 50 years, radiation processing by gamma rays, electron beams (E-beams) or X-rays has been an effective technique for improving the end-use properties of various kinds of polymers. The main applications for modification of

polymer materials through radiation are crosslinking, degradation, and grafting. For irradiation technologies, gamma rays from radioactive isotopes such as cobalt 60, high-energy electrons from electron accelerators, and X-rays converted from high-energy electrons are used. When gamma rays, electrons, or X-rays interact with a polymer material, their energy is absorbed by the polymer material and reactive species such as excited atoms, molecules, ions, and free radicals are generated. In the presence of these reactive species, various specific transfers of energy and complex chemical reactions take place.

The three fundamental processes that result from electron modification of polymers are degradation, crosslinking, and grafting. Crosslinking and degradation occur simultaneously. The ratio of their kinetics depends on the chemical structure of the polymer to be modified as well as on the treatment conditions. In general, polymers are divided into those that predominantly crosslink and those that predominantly degrade.

In degradation, the molecular weight of the polymer is reduced through chain scission. Some of the polymers that undergo degradation at room temperature include PTFE, polypropylene (PP), and cellulose. Although degradation usually brings about deterioration of the mechanical properties of polymers and needs to be avoided in many cases (e.g., radiation sterilization), some good applications have been found for chain scission of polymers by radiation. Examples of applications for degradation are the production of fine PTFE powders by simple and easy degradation (i.e., particle size reduction for fine powders); melt flow rate adjustments (high molecular weight to low molecular weight compounds); and compatibility improvement for coupling with other polymers [9]. When a polymer such as PTFE is irradiated in air, the oxygen and moisture in the air cause oxidation in addition to degradation. The generation of polar functional groups such as the carboxylic acid groups on PTFE can help to improve the compatibility of PTFE with other polymers. A schematic of the radiation-induced degradation of PTFE in presence of oxygen is shown in the Fig. 4. As well as special purpose surface modification techniques [10], E-beam irradiation provides a wide range of advantages for the modification of inert PTFE surfaces [11]. E-beam irradiation generates free radical and functional groups in PTFE due to chain scission. In the presence of air, these radiation-induced radicals react partially with oxygen to form carbonyl fluoride groups ( $-\text{COF}$ ), which further react with water vapor to form carboxylic acid groups ( $-\text{COOH}$ ) on the surface of PTFE [12–17].

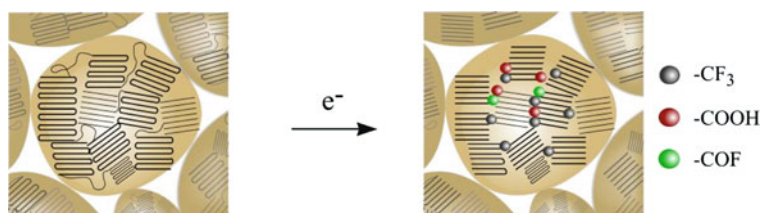


Fig. 4 Radiation-induced degradation of PTFE

### 2.3 Chemically Coupled PTFE-Based Compounds

Chemically coupled PTFE-based compounds were initially produced from irradiated PTFE micropowders and polyamide (PA) in a reactive extrusion process. High shear rate under melt processing conditions was necessary to obtain a good distribution and reagglomeration of the PTFE micropowder. To achieve a coupling reaction, an enhanced interaction between the carboxylic acid groups on the surface of the PTFE microcrystals and the amide groups of the molten PA matrix is necessary. The mechanism of block copolymer formation by transamination reactions is shown in Fig. 5. It was further demonstrated that for the chemical coupling of PTFE with other matrix polymers, in particular rubber compositions, a further modification of the carboxylic-acid-functionalized PTFE with other functional groups is necessary. This can be done by transforming the  $-\text{COOH}$  groups into amide groups by the reaction of the irradiated PTFE micropowders with  $\epsilon$ -caprolactam.

For chemical coupling of electron-irradiated PTFE powder with rubber compounds, the presence of olefinic double bonds is necessary. Taking advantage of the persistent free radicals, formed by electron irradiation of PTFE, direct coupling of olefinic unsaturated matrix polymers like styrene-butadiene-styrene block copolymers (SBS), acrylonitrile-butadiene-styrene block copolymers (ABS), NBR, EPDM etc. during a reactive extrusion process is possible. These radically coupled PTFE-rubber compounds have been previously investigated by Lehmann et al. for tribological applications [19, 20]. The radically coupled PTFE elastomeric compounds were produced by a low-temperature reactive processing technique. The olefinically unsaturated polymers such as SBS, NBR, and EPDM are radically coupled during reactive blending. During mixing, the reactive perfluoroalkyl-(peroxy) radicals react with these olefinically unsaturated polymers. Figure 6 shows the schematics of the radical coupling of the unsaturated diene-containing elastomers [21, 22].

First investigations showed that coupling activity depends on the morphology of the PTFE powder, irradiation dose, and processing conditions such as temperature etc. The coupling activity of the PTFE powder with rubbers was determined by Fourier transform infrared (FTIR) spectroscopy. The PTFE powder was separated from the soluble rubber matrix in a good solvent during successive centrifugation processes. The insoluble or extracted PTFE powder shows strong adsorption bands of the coupled rubber matrix. On the basis of these results, Haberstroh et al. later demonstrated the use of simple and competitive irradiation and shear mixing processes for development of novel materials based on carbon-black-filled

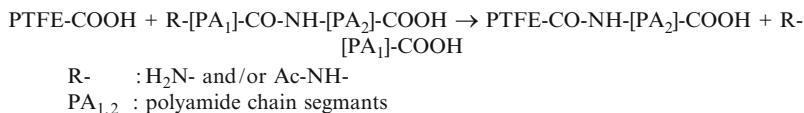
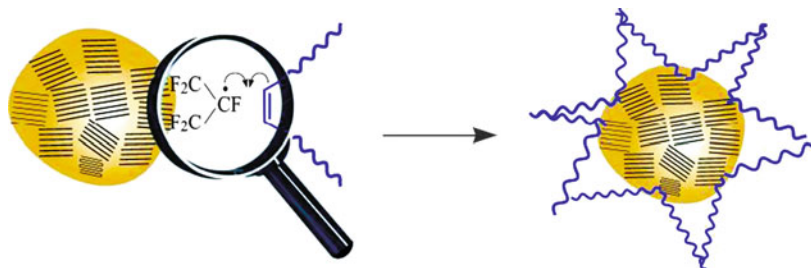


Fig. 5 Mechanism of the formation of PTFE-PA block copolymers [18]



**Fig. 6** Radical coupling mechanism of modified PTFE radicals and the unsaturated diene EPDM

NBR containing irradiated PTFE micropowder for high performance tribological applications [23].

#### **2.4 State of the Art: PTFE for Tribological Applications**

It has long been a desire to combine the properties of an elastomer with those of PTFE. Past efforts to produce compositions with beneficial combined properties have not been wholly successful. In addition, past attempts to incorporate PTFE into rubber have been generally limited to attempts and compositions containing no more than 20 wt% of PTFE loading. Such compositions have failed to provide a sufficient combined benefit from the properties of PTFE and elastomers to have great commercial importance. Higher PTFE loadings could not be obtained because of the difficulty in achieving homogeneous dispersion in the elastomer composition. This was mainly the result of PTFE's unique properties, most probably due its highly hydrophobic surface, which resists wetting and adhesion. Because of these properties, homogeneous dispersion and chemical coupling of PTFE powder both in natural and synthetic rubbers have not been achieved in compositions with any commercially significant incorporation of PTFE, due to the associated poor wetting and dispersion of PTFE powder.

The extremely low friction properties of PTFE are well known, but there is little work disclosed in the literature on compounding this material with different types of elastomers. Initially, PTFE was used in specialty polymers such as silicone and fluorosilicone rubber for sealing and dynamic applications owing to their superior temperature and chemical resistance. However, their relatively low tear strength and abrasion resistance restrict their useful application. For this reason, Crandell used PTFE as a reinforcing additive to improve the tear resistance of silicone rubbers [24], while by the late 1960s it was being used in fluoroelastomers [25, 26]. Although the fibrillation of the high molecular weight PTFE during shearing action inside the roll mills effectively reinforces elastomers, it also leads to deterioration of some other mechanical properties. For this reason, the practical level of application of the addition of high molecular weight PTFE powder is

limited. Although the compounding of elastomers with PTFE powder may produce vulcanizates with reduced frictional properties, the PTFE loading required to affect even a marginal improvement so diminishes the physical properties of the vulcanizate that the practical applications of these compounds are severely limited. Simply, if a material could be found that would reduce the surface frictional properties and not appreciably deteriorate, or even improve, the physical properties of the vulcanizate, such an approach would be attractive. Consequently, this approach to production of low-surface-friction elastomers based on neoprene and silicone compounds resulted both in low physical and friction properties due to the poor compatibility of PTFE powder [27]. Alternatively, efforts were also dedicated to provide low-friction surface coatings to elastomers and thermoset substrates by depositing a thin PTFE film coating while maintaining intact the bulk properties of the compounds. The attempt was successful for coating metals but a failure for elastomers due to inability of elastomeric substrates to sustain high-temperature PTFE film coating [27, 28].

PTFE powder was also used in SBR, NBR, and butyl rubber (IIR). The principal cause of the great improvement in tensile and tear strength was believed to be due to the formation of oriented PTFE fibers in the elastomer matrix [29]. Fluoroelastomers and PTFE powder were also compounded and kneaded until PTFE was fibrillated and the blend could be used as an adhesive agent, a sealing agent, a packing material, or as reinforcing material in instruments employed in corrosive environments [30]. New elastomer–PTFE compositions and compounding procedures were developed for improving the mechanical properties (tensile strength, elastic modulus) of low-strength ethylene propylene (EP) and silicone elastomers by effective fibrillation of PTFE powder. Similarly, in the case of high-strength rubbers such as nitrile and NBR, as little as 2–6 wt% of PTFE powder was incorporated to improve the vulcanizate strength and modulus. These compositions could be useful, e.g., for O-rings, seal lips (for hydraulic and pneumatic cylinders), seals for pumps, valves etc. The improvement in the desired properties of the composition with such a low PTFE loading was attributed to the formation of a network of entangled fibers due to high shearing of the PTFE powder during compounding. The fibrillated PTFE provides a high ratio between fiber length and fiber diameter (aspect ratio). On the other hand, finely ground particulate PTFE (lacking fibrillation) was also modified by special-purpose etching procedures to enhance interaction with the rubber matrix. This helped to improve the tensile strength and modulus of elasticity of rubber compounds [31, 32]. With growing demands for high performance compounds for sealing applications (gaskets etc.), different processing techniques and procedures were also employed in which the crosslinked domains of silicone, fluorosilicone, etc. as minor components were introduced in the bulk of stretched PTFE films and sheets [33, 34].

Polymers were never intended to be bearing- or wear-resistant materials and in fact are usually unsuitable for tribological purposes. Hence, the number of polymers with valuable tribological properties is limited. Table 2 shows the most important polymers used for tribological applications along with their tribological characteristics [35].



**Table 2** Tribological characteristics of typical polymers

Polymer	Tribological characteristics
Polytetrafluoroethylene (PTFE)	Low friction but high wear rate; usually blended with other polymers or reinforced as a composite material. High operating temperature limit (excess of 150°C)
Polyamide	Moderate coefficient of friction and low wear rate. Medium performance bearing material. Wear accelerated by water. Relatively low temperature limit
Polyacetals	Performance similar to nylon. Durable in rolling contacts
Polyetheretherketone (PEEK)	High operating temperature limit. Resistant to most chemical reagents. Suitable for high contact stress. High coefficient of friction in pure form
Ultra high molecular weight polyethylene (UHMWPE)	Very high wear resistance even when water is present. Moderate coefficient of friction. Good abrasive wear resistance. Relatively low temperature limit
Polyurethanes	Good resistance abrasive wear and to wear under rolling conditions. Relatively high coefficient of friction in sliding
Polyimide	High performance polymers, suitable for high contact stresses and high operating temperatures
Epoxides and phenolics	Used as binders in composite materials

Most polymer surfaces are worn by a harder counter-face during contact. A basic feature of almost all polymers is that a transfer film is formed when sliding against a harder counter-face, which has a strong influence on the tribology of polymers. The polymer that provides a classic example of transfer films formation is PTFE. Although there is probably a strong adhesion between a metallic surface and any other polymers, the special molecular structure of PTFE causes a mechanism of film transfer that is particular to PTFE. A block of PTFE in contact with a harder counter-face loses material as a series of laminas, resulting in low friction but a high wear rate due to its characteristic molecular structure [36]. In tribology, PTFE is a well-known and commonly used polymer for solid lubrication. PTFE can also be used as an additive to improve the lubricant and tribological properties of thermoplastics, coatings, greases, and inks. Concentrations ranging from 1 up to 20 wt% give better wear resistance and release properties. Figure 7 shows the wear rate and friction coefficients of unfilled polymers, polymer blends, and polymer composites used in tribological studies [37].

As can be seen, PTFE has a significantly low friction coefficient but high wear rate. High performance engineering polymers like PEEK and polyimide (PI) have good wear resistance but a high friction coefficient. In general, neat polymers lack the tribological performance required for most applications. For this reason, and especially in the case of high wear rate and low friction coefficient, materials like PTFE are extensively used as antifriction additives, bulk matrixes, or in conjunction with various kinds of nanoparticles to obtain high performance solid lubricating polymeric composites. Fundamental studies addressed the tribology of rubbers some decades ago [38–44]. Although these pioneering works contributed to our state of knowledge on this field, many questions related to the friction and wear of

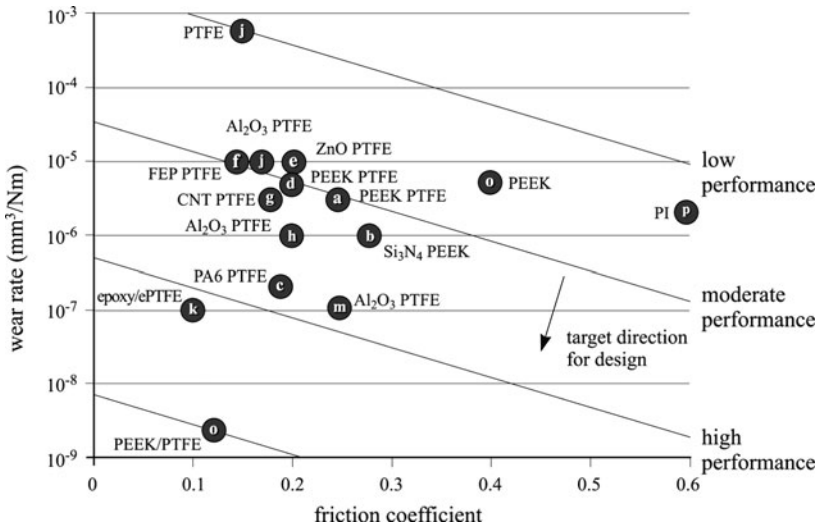


**Fig. 7** Multivariate plot of wear rate versus friction coefficient for various unfilled polymers, polymer blends, and polymer composites

rubbers remained open. Numerous investigators in recent years have studied the frictional behavior of elastomers. The bulk of their endeavors have been directed towards understanding the influence of this behavior on the skidding characteristics of tires and towards deriving suitable mechanisms for the frictional behavior under these conditions [45–51].

Nowadays, there is a renewed interest in rubber tribology because of the property requirements for rubbers in engineering applications. This has necessitated exploration into how the requested performance can be met by the formulation of the rubber. Different formulations have been investigated, e.g., fluoroelastomer matrix into which silica-based glass fibers are incorporated. The glass fibers serve to reinforce the elastomer and also serve as friction modifiers to provide the desired coefficients of friction [52]. Fluoroelastomers were also filled with carbon fibers for improved tribological performance at elevated temperatures [53]. The fluoroelastomer is compounded with particles of a relatively hard material, such as beads or fibers of glass, ceramics, and carbon black [54]. Various kinds of friction modifiers including fibrous (glass, carbon, asbestos etc.) and powdered (molybdenum disulfide, silica, graphite etc.) fillers have also been incorporated in various combinations to produce epoxy-rubber-based compounds [55]. Besides this, tribological works on rubbers containing novel reinforcing fillers, such as organophilic clay [56] and carbon nanofibers and carbon nanotubes have also been studied [57, 58]. EPDM rubbers filled with carbon black were also studied in different test configurations. It was found that with increasing carbon black content, the specific wear rate was reduced irrespective of the testing configuration.

However, the coefficient of friction depended on the rubber composition, test duration, and the type of testing rig [59, 60]. Depending on the test conditions and the concentration of carbon black, the abrasion resistance could be significantly reduced for isoprene rubber. The enhanced wear resistance is attributed to the increase in the strength and hardness of the matrix by adding carbon black [61]. More recently, friction tests were performed on synthetic wiper rubber samples (EPDM and CR) with varying modulus and tangent modulus [62]. A good rubber formulation and an adapted surface treatment and coating can improve these phenomena. The rubber formulation should take into account the modulus and the tangent modulus, which have an influence on dry friction. Improved wiping is only possible by a good understanding of the tribological, mechanical, and vibroacoustic parameters that control the contact.

### 3 PTFE-Based EPDM Rubber Composites

#### 3.1 *Electron Modification of PTFE Powder and Sample Preparation*

PTFE powder was modified with irradiation doses of 20, 100, 200, 300, 400, and 500 kGy using the electron accelerator ELV-2 from Budker Institute of Nuclear Physics, Novosibirsk, Russia, installed at the Leibniz Institute of Polymer Research Dresden. Figure 8 shows the schematics of the ELV-2.

Figure 9 shows the processing parameters and steps involved in the modification of PTFE powder with 100 kGy dose. The electron treatment was carried out

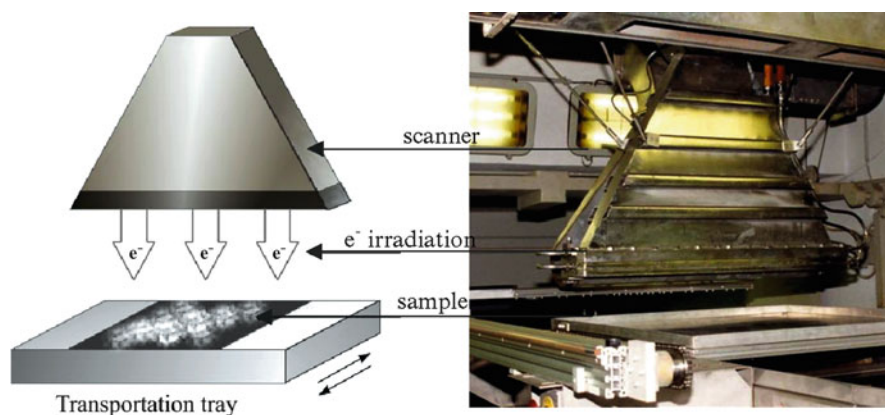


**Fig. 8** Schematics of the radiation zone, showing the high energy electrons scanned through the electron accelerator (ELV-2)

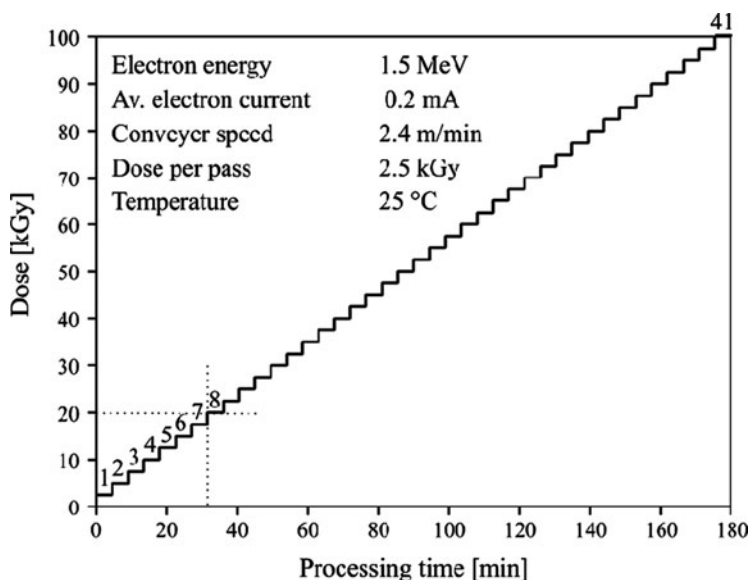


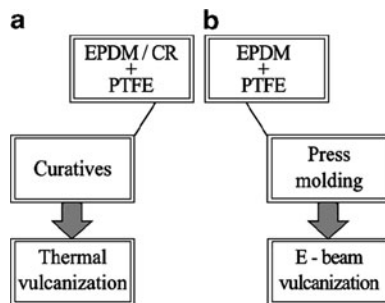
**Fig. 9** Processing parameters and number of steps involved in the electron modification of PTFE powder with a 100 kGy dose

in air and at room temperature with an absorbed dose of 2.5 kGy per pass and at an average dose rate of 10 kGy/h. The tray passes under electron accelerator. Each pass delivers 2.5 kGy, e.g., for 20 kGy, eight passes are required ( $8 \times 2.5 = 20$  kGy). Similarly, to achieve 100 kGy, a further 80 kGy (33 passes) is added to the previous 20 kGy (eight passes). Therefore, for 100 kGy, a total of  $33 + 8 = 41$  passes are required, as shown in Fig. 9.

An optimum processing time of 180 min is required for a complete cycle of 100 kGy dose. A shutdown time of at least 8 h was necessary after every 100 kGy addition to allow sufficient diffusion of oxygen in the PTFE powder. The total time for the whole process from 20 to 500 kGy was approximately 50 h, including the 8 h shutdown intervals after every 100 kGy addition. To achieve 500 kGy, the doses were added to the PTFE powder in 100 kGy steps. These treatment parameters were chosen in order to avoid excess temperature rise, which might favor deactivation of the radical formation, as well as to control agglomerate size and chemical structure via absorbed dose. Further information on the electron accelerator (ELV-2) facility can be found in [11].

Rubbers and PTFE powder were first premixed in an internal mixer for 5 min at a temperature of  $100^{\circ}\text{C}$  and at a rotor speed of 50 rpm. Figure 10 shows two different crosslinking routes, i.e., thermally or using electron irradiation. In the case of EPDM, crosslinking was performed thermally and also with electron irradiation.

**Fig. 10** Schematics of thermal (a) and electron irradiation (b) crosslinking



### 3.1.1 Thermal Crosslinking of EPDM and CR

In the case of thermal crosslinking, the corresponding curatives were added to each of the EPDM and CR rubbers on a two-roll laboratory mill at room temperature. A constant friction ratio of 1.2 was maintained between the milling rolls. Approximately 2 mm sheets were drawn out from the mill and cured in a hot press at a pressure of 10 MPa and a temperature of 170°C and 160°C for EPDM and CR, respectively, for their corresponding optimum cure time ( $t_{90}$ ).

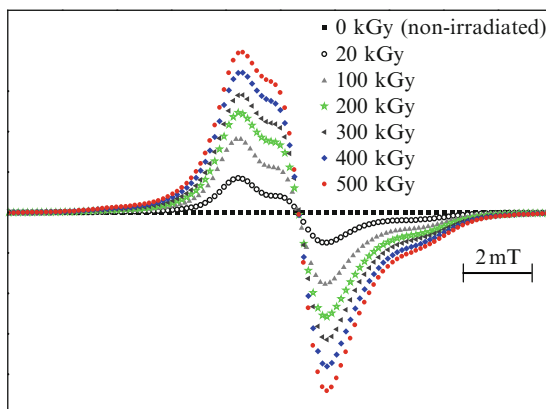
### 3.1.2 Electron Irradiation Crosslinking of EPDM

In the case of crosslinking with electron irradiation, material from an internal mixer was placed between thin nonsticking polyesters films for press molding at a temperature of 150°C and a pressure of 5 MPa in an electrically heated press for 3 min to obtain rubber blocks of dimension 110 × 110 × 2 mm. The molded samples of PTFE-filled EPDM were then irradiated for crosslinking with 200 kGy under atmospheric conditions and at room temperature of 25°C. Crosslinking with 200 kGy was accomplished in five passes with an absorbed dose of 40 kGy per pass and at an average dose rate of 25 kGy/min. The processing time was 8 min with an electron energy and current of 1.5 MeV and 4 mA, respectively.

## 3.2 Characterization of PTFE Powder

Figure 11 shows the electron spin resonance (ESR) spectra of the E-beam-irradiated and nonirradiated PTFE powder (L100X). The ESR spectra show a systematic increase in the signal with increasing irradiation dose. Nonirradiated PTFE powder produced no signal due to the absence of reactive free radicals. The increase in signal indicates that the radical concentration increases with increasing irradiation dose or modification. The 500 kGy-irradiated PTFE powder, having the highest spin numbers, shows the highest radical concentration. E-beam treatment generates

**Fig. 11** Electron spin resonance (ESR) spectra of PTFE powder after irradiation



persistent reactive free radicals and functional groups on the surface due to degradation of PTFE powder by chain scission.

It has been reported that PTFE in the presence of air undergoes C–F and C–C scission during energy-rich electron-modification processes [63, 64]. C–F scission results in secondary radicals, whereas C–C scissions produce primary free radicals. These free radicals react with atmospheric oxygen to yield stable perfluoroalkylperoxy radicals. Besides these peroxy radicals, carbonyl fluoride (–COF) groups are also formed, which hydrolyze in the presence of atmospheric moisture to form –COOH groups. The complete reaction mechanism can be found in [65]. Chemical changes introduced in PTFE after exposure to electron treatment were monitored by FTIR spectroscopy. Figure 12 shows several new bands in the infrared spectrum of modified PTFE. The peak at  $1,884\text{ cm}^{-1}$  was identified with –COF groups and the peaks at  $1,810\text{ cm}^{-1}$  and  $1,777\text{ cm}^{-1}$  with free and associated –COOH groups, respectively. Figure 13 shows the influence of absorbed dose on the mean agglomerate size of PTFE powder.

It can be seen that the mean agglomerate size of PTFE powder decreased systematically with irradiation dose. This suggests that the mean agglomerate size of PTFE powder can be controlled via irradiation dose. The decrease in agglomerate size is due to chain scission of PTFE powder. High molecular weight PTFE is reduced to low molecular weight PTFE. The highest absorbed dose of 500 kGy shows the smallest mean agglomerate size. The mean agglomerate size delivered by the supplier of virgin nonmodified PTFE powder was  $17.7\text{ }\mu\text{m}$  compared to our determined agglomerate size of  $5.0\text{ }\mu\text{m}$ . This might be due to the ability of PTFE powder to reagglomerate, as can be seen in the particle size distribution in Fig. 14.

The particle size distribution suggests that nonirradiated PTFE powder has a broad particle size distribution compared to 500 kGy-irradiated PTFE powder. The nonirradiated PTFE powder shows a characteristic bimodal distribution compared to the unimodal distribution of 500 kGy-irradiated PTFE powder (Fig. 14). This specific bimodal distribution clearly signifies that nonirradiated PTFE powder is mainly composed of bigger agglomerates that tend to reagglomerate. By contrast,

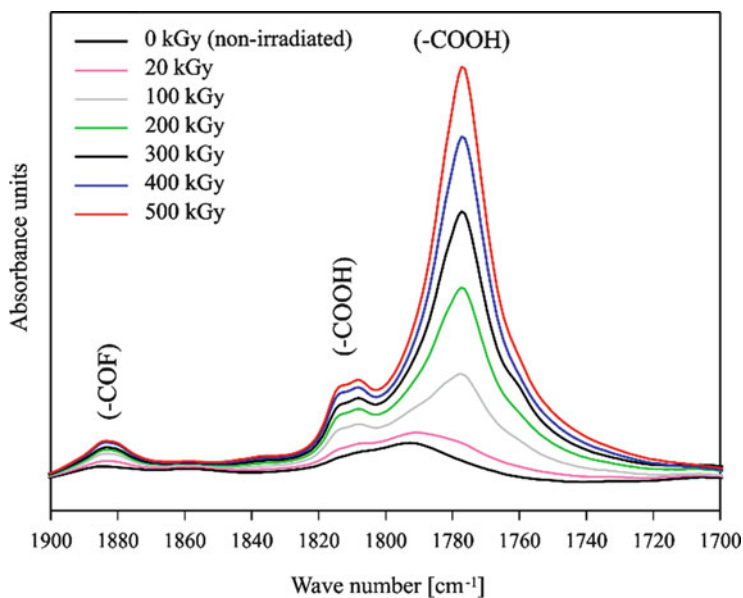


Fig. 12 Infrared spectra ( $1,900\text{--}1,700\text{ cm}^{-1}$ ) of PTFE powder after modification

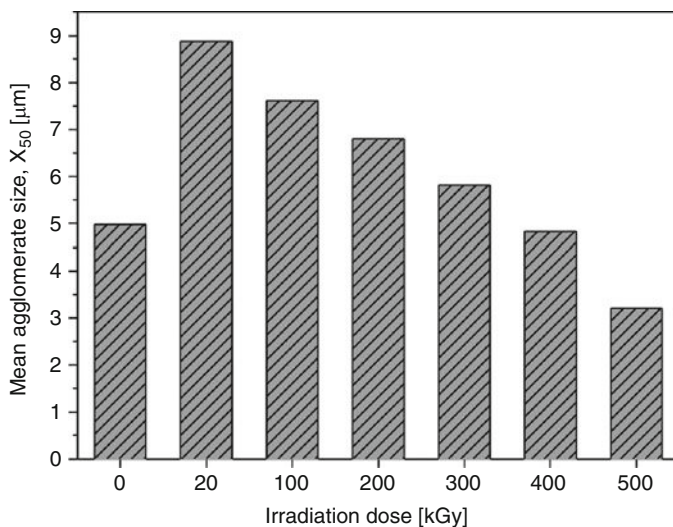
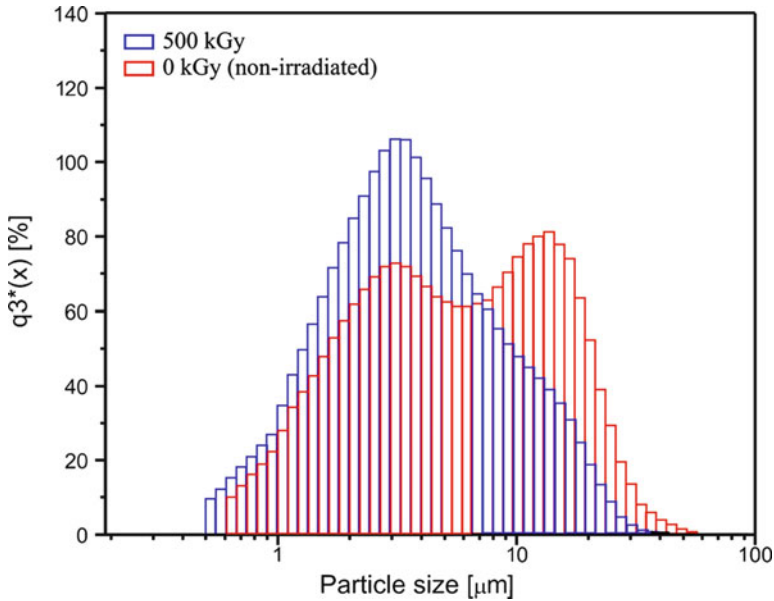
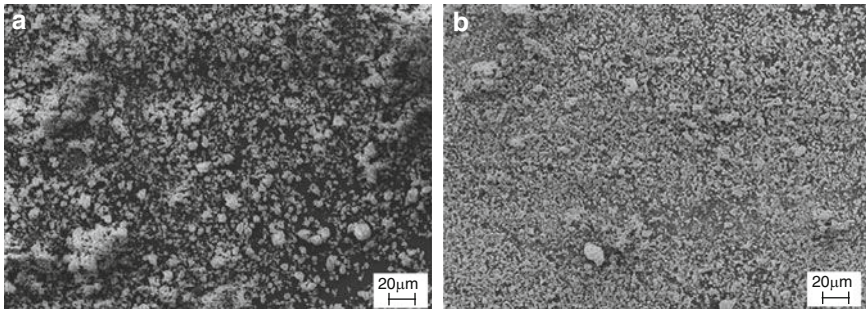


Fig. 13 Mean agglomerate size of PTFE powder as a function of irradiation dose

the distribution of 500 kGy-irradiated PTFE powder indicates finely dispersed smaller agglomerate particles. This can also be seen in the SEM micrographs of 500 kGy-irradiated PTFE powder (Fig. 15). The effect of irradiation dose on the



**Fig. 14** Percentage density distribution ( $q_3^*$ ) as a function of particle size



**Fig. 15** SEM micrographs of (a) non- and (b) 500 kGy-irradiated PTFE powder

agglomerate morphology of nonirradiated and 500 kGy-irradiated PTFE powder is shown in Fig. 15. It is evident that the agglomerate size and morphology of these powders are apparently distinguishable from each other. Nonirradiated PTFE powders are huge solid-structured agglomerates formed by the random reagglomeration of PTFE agglomerates. In comparison, 500 kGy-irradiated PTFE powder shows fine homogeneous coarse particles dispersed individually over the area, without the formation of huge agglomerates.

Figure 16 shows result of contact angle measurements on PTFE powders having different irradiation doses in comparison to nonmodified (0 kGy-irradiated) PTFE powder. The horizontal line indicates the contact angle of a typical commercial



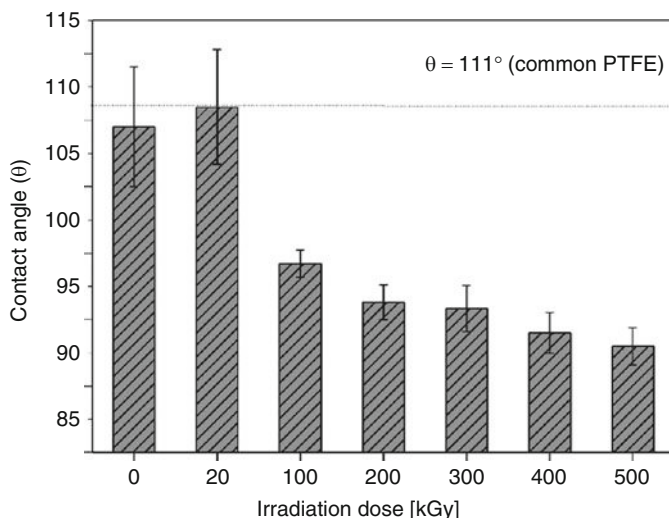


**Fig. 16** Effect of the absorbed dose on the contact angle of PTFE disks. The *horizontal line* indicates the contact angle value of a commercial PTFE

PTFE. It can be seen that the water contact angles of irradiated PTFE disks are lower than that of the nonmodified PTFE disk and systematically decrease with increasing irradiation dose.

The water contact angle of  $111^\circ$  of nonirradiated PTFE powder indicates its inherently hydrophobic behavior. Modification by different irradiation doses results in a decrease in contact angle from  $111^\circ$  to  $92^\circ$  for 500 kGy-irradiated PTFE powder. That is, compared with nonmodified PTFE, the wettability of 500 kGy-irradiated PTFE is significantly increased. The increase in wettability is due to the strong interaction between water and the hydrophilic groups ( $-\text{COF}$  or  $-\text{COOH}$ ) generated on the surface of PTFE powder after electron treatment in the presence of air. As can be seen, increasing absorbed dose results in lower contact angles due to the generation of oxygen-containing groups on the PTFE surface. Lower contact angles correspond to higher surface energy and thus higher adhesion and higher interfacial compatibility. As shown in Fig. 12, an increasing absorbed dose results in a higher concentration of  $\text{C}=\text{O}$  groups ( $1,777\text{ cm}^{-1}$ ). This shows that the chemical structure of PTFE powder was changed due to electron treatment.

### 3.3 Peroxide-Crosslinked Rubber Composites

The effects of electron irradiation on the properties of EPDM along with the optimization of PTFE loading for desired properties have been investigated. For preliminary investigations, PTFE powder L100X was modified with irradiation doses of 20, 100, and 500 kGy and then incorporated into EPDM at loadings of

10– 60 phr (parts per hundred of rubber). PTFE-based EPDM composites have been characterized with respect to the effect of electron irradiation, irradiation dose, and PTFE loading on mechanical, friction, and wear properties. Further, the chemical compatibility and dispersion of PTFE powder in EPDM has been characterized by transmission electron microscopy (TEM), scanning electron microscopy (SEM), and differential scanning calorimetry (DSC). As known, the inherent poor wetting and dispersion of PTFE restricts its effective application, especially in rubber compositions. This section shows that with the help of electron irradiation the inherent hydrophobic and incompatible PTFE surface can be successfully functionalized to enhance its dispersion and, simultaneously, its compatibility with EPDM by a radical coupling mechanism.

### 3.3.1 Influence of PTFE Loading

#### Cure Analysis

An oscillating disk rheometer is a useful tool for monitoring the cure characteristics of a rubber compound. The apparent crosslink density or delta torque ( $\Delta M = \text{maximum} - \text{minimum torque}$ ) is one of the most important parameters that is provided by the curing curve. These curves are used to measure the effects of PTFE powder on the cure efficiency of EPDM filled with varying PTFE loadings and with PTFE subjected to varying irradiation doses. Figure 17 shows  $\Delta M$  values expressed in decinewton meters (dN m) as a function of PTFE loading for various composites in comparison with EPDM gum. As can be seen,  $\Delta M$  decreases with irradiation dose

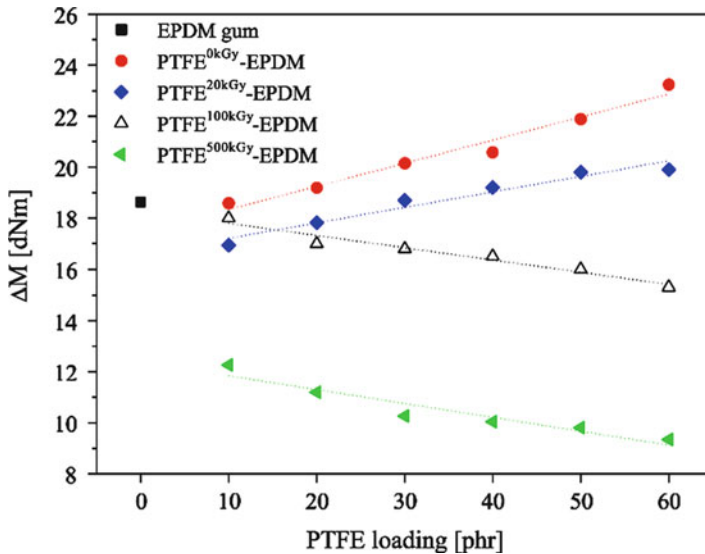


Fig. 17 Delta torque ( $\Delta M$ ) values as a function of PTFE loading

at constant PTFE loading. However, at constant irradiation dose and increasing PTFE loading, comparatively distinct  $\Delta M$  behavior is observed. For composites containing unmodified PTFE (PTFE<sup>0kGy</sup>-EPDM) and 20kGy-irradiated PTFE (PTFE<sup>20kGy</sup>-EPDM), an increase in  $\Delta M$  is observed with increased loading, whereas for PTFE<sup>100kGy</sup>-EPDM and PTFE<sup>500kGy</sup>-EPDM  $\Delta M$  decreases with PTFE loading. PTFE<sup>500kGy</sup>-EPDM shows a  $\Delta M$  value even less than that for EPDM gum (zero loading). However, in some cases EPDM gum has  $\Delta M$  even higher than or equal to that for PTFE<sup>20kGy</sup>-EPDM.

It should be noted that  $\Delta M$  is only a measure of an apparent crosslink density of compounds. It is beyond the scope of the present work to investigate in detail the effective crosslinking (physical and chemical). However, for a qualitative assessment it can be concluded that the apparent crosslink density decreases or is influenced by the E-beam irradiation of PTFE powder. PTFE<sup>500kGy</sup>-EPDM composites show much lower  $\Delta M$  and hence lower apparent crosslink densities. It can be inferred that the state of cure and crosslinking efficiency are strongly dependent on irradiation dose. Table 3 shows the optimum curing time ( $t_{90}$ , time required to reach 90% of the  $\Delta M$ ) as a function of PTFE loading and irradiation dose for different PTFE-filled EPDM composites.

As presented in Table 3, a significantly shorter curing time is observed for PTFE<sup>500kGy</sup>-EPDM, whereas PTFE<sup>0,20,100kGy</sup>-EPDM show extended curing periods. Lower  $t_{90}$  values correlate to more rapid cure rates. This indicates that the use of increasing radiation dose for modification of the PTFE powder allows faster or incomplete curing of the composites. PTFE<sup>500kGy</sup>-EPDM shows much lower  $\Delta M$  and  $t_{90}$ . The influence of irradiation of PTFE powder on some other desired properties will be discussed in detail in the following sections.

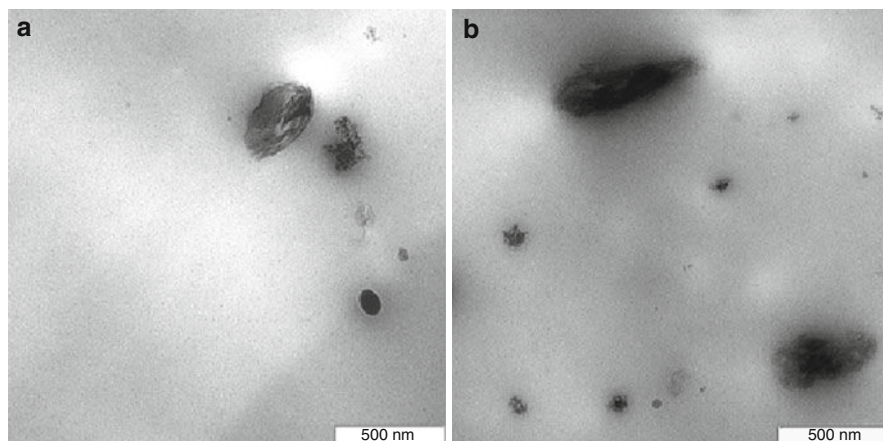
### Compatibility and Dispersion Behavior

Figure 18 shows TEM micrographs of PTFE<sup>0kGy</sup>-EPDM and PTFE<sup>500kGy</sup>-EPDM. The enhanced interfacial compatibility in the case of PTFE<sup>500kGy</sup>-EPDM can be seen in Fig. 18b, which shows that the irradiated PTFE agglomerates are embedded and partially enwrapped by EPDM.

No clear and visible interphase can be seen between the two incompatible polymers. Slightly light and dark regions around irradiated PTFE powder are an

**Table 3** Optimum curing time of PTFE-filled EPDM composites

Filler loading (phr)	Optimum cure time, $t_{90}$ (min)			
	PTFE <sup>0kGy</sup> - EPDM	PTFE <sup>20kGy</sup> - EPDM	PTFE <sup>100kGy</sup> - EPDM	PTFE <sup>500kGy</sup> - EPDM
0 (EPDM gum)	14.8	–	–	–
10	15.2	13.6	15.3	11.1
20	14.8	14.0	15.6	10.5
30	15.6	12.4	14.5	8.5
40	15.8	13.4	14.2	8.3
50	15.0	12.7	15.2	8.1
60	14.9	12.9	15.5	8.4



**Fig. 18** TEM micrographs of (a) PTFE<sup>0kGy</sup>-EPDM and (b) PTFE<sup>500kGy</sup>-EPDM

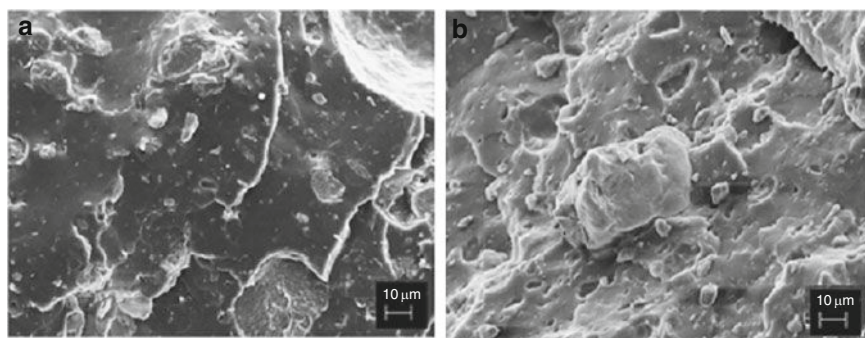


**Fig. 19** SEM micrographs of (a) PTFE<sup>0kGy</sup>-EPDM and (b) PTFE<sup>500kGy</sup>-EPDM

indication of a reinforced compatible interphase due to radical coupling with EPDM. It is also observed that irradiated PTFE agglomerate acts as a PTFE core surrounded by an EPDM shell. On the other hand, PTFE<sup>0kGy</sup>-EPDM shows nonirradiated PTFE powder as solid embedded bodies lacking interfacial compatibility with EPDM (Fig. 18a). The interfaces are distinctively separated from each other. No mutual compatible interphase exists as compared to PTFE<sup>500kGy</sup>-EPDM. The irradiated PTFE particles, due to enhanced compatibility and dispersion, are slightly oriented under high shearing during reactive blending. However, nonirradiated PTFE powder, being inert, remains as huge rounded agglomerates even under high shearing. This behavior can also be seen in microdispersion in EPDM. Figure 19 shows SEM micrographs of the tensile fractured surfaces of PTFE<sup>0kGy</sup>-EPDM and PTFE<sup>500kGy</sup>-EPDM.

It is evident that the surface features are apparently distinguishable from each other. The PTFE<sup>500kGy</sup>-EPDM surface is smooth, with agglomerates embedded

and homogeneously dispersed in EPDM matrix whereas PTFE<sup>0kGy</sup>-EPDM shows an uneven, inhomogeneous surface with large vacuoles on the fractured surface. This indicates that PTFE particles are being pulled out of the matrix on application of stress due to the absence of interfacial interaction or coupling with matrix. It can be observed that nonirradiated PTFE particles are bigger in size and tend to form huge irregular agglomerates in the EPDM matrix, even under high shearing during blending operations. Nonirradiated PTFE particles lack both the compatibility and the dispersion efficiency. Being incompatible they are not covered by EPDM molecules and, hence, tend to segregate in the EPDM matrix.

Figure 20 shows the thermal traces of (a) nonirradiated and 500 kGy-irradiated PTFE powder and (b) the corresponding PTFE<sup>0kGy</sup>-EPDM and PTFE<sup>500kGy</sup>-EPDM composites. The crystallization peak of 500 kGy-irradiated PTFE powder shifts to a lower temperature of about 303.5°C. Also, the crystallization onset occurred at lower temperature and continued down to approximately 290°C. These distinct variations in 500 kGy-irradiated in comparison to nonirradiated PTFE powder is due to the E-beam treatment process, which caused degradation of 500 kGy-irradiated PTFE powder. The molecular weight decreases due to chain scission and leads to PTFE macromolecules of different chain lengths. As a result, the crystallization peak occurs at lower temperatures and the crystallization process continues until much lower temperatures in comparison to nonirradiated PTFE powder.

In the case of blends, PTFE<sup>500kGy</sup>-EPDM shows two crystallization peaks located at distinct temperatures. The second crystallization step at a lower temperature (also called fractionated crystallization) occurred at 278.4°C along with the bulk crystallization peak at 298.6°C [66, 67]. The area of the first bulk crystallization peak is smaller than the area of the second peak. However, the crystallization temperature (298.6°C) of the first peak is close to that of the 500 kGy-irradiated PTFE powder (303.5°C). The first crystallization peak is attributed to the content of PTFE powder in EPDM having comparatively bigger and incompatible agglomerates. The PTFE agglomerates could be compatibilized only on the surface, and the core consists of pure agglomerated PTFE powder. These agglomerates show crystallization

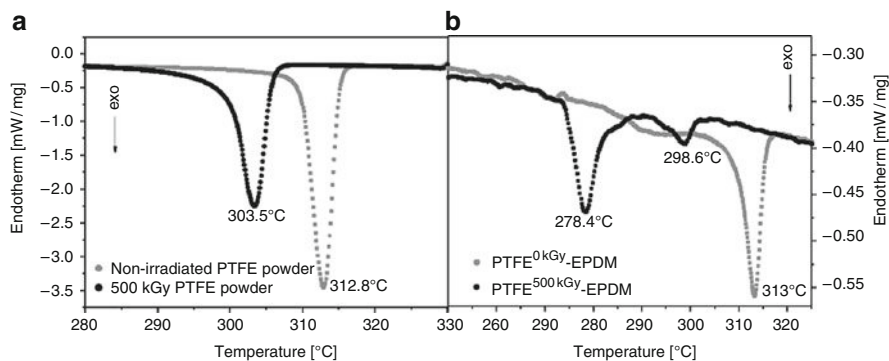


**Fig. 20** DSC cooling scans of the (a) nonirradiated and 500 kGy-irradiated PTFE powders and (b) their corresponding PTFE-EPDM vulcanizates

temperatures similar to pure PTFE bulk crystallization. However, for PTFE<sup>0kGy</sup>-EPDM, no fractionated crystallization is observed, only bulk crystallization similar to nonirradiated PTFE powder at 313°C. This stems from the fact that nonirradiated PTFE powder is difficult to deagglomerate and disperse homogeneously. The variation in the position of the transition-melting peaks observed in PTFE<sup>500kGy</sup>-EPDM is due to the specific chemical compatibility of the E-beam-modified PTFE with EPDM. This unique fractionated crystallization behavior is mainly due to the fine dispersion of 500 kGy-irradiated PTFE powder in EPDM. The outstanding dispersion of 500 kGy-irradiated PTFE powder is also attributed to its comparatively smaller particle size and enhanced compatibility. PTFE<sup>0kGy</sup>-EPDM on the other hand has significantly poor dispersion and compatibility with EPDM.

Physical Properties

Figure 21 shows the tensile strength at break as a function of PTFE loading for different PTFE–EPDM composites containing E-beam-irradiated or nonirradiated PTFE powder, in comparison with the EPDM gum.

In the case of irradiated PTFE powder, the tensile strength of the corresponding EPDM composites increases with increased loading and reaches a maximum value at 30 phr, followed by a decrease in the tensile strength above 30 phr. For a given formulation, 30 phr is the threshold filler loading above which the poor compatibility and dispersibility of PTFE powder in EPDM results in deterioration of the stress–strain properties. On the other hand, tensile strength at break of PTFE<sup>0kGy</sup>-EPDM gradually decreases with increasing PTFE loading. This clearly

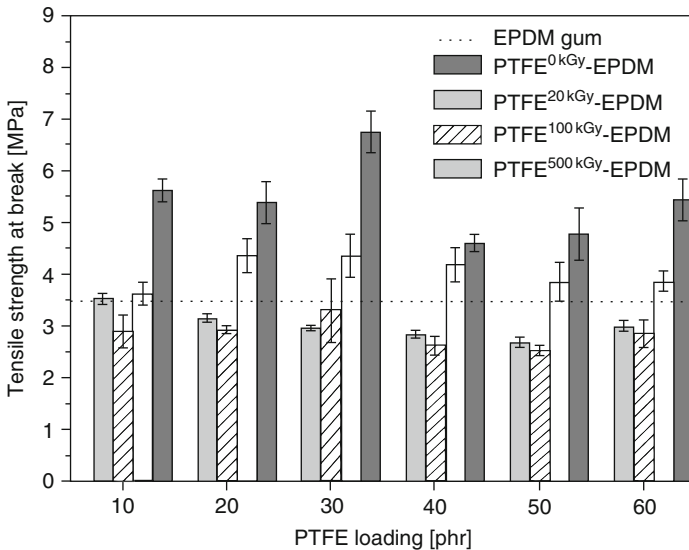


Fig. 21 Tensile strength at break as a function of PTFE loading

indicates the poor dispersion and compatibility of nonirradiated PTFE powder with EPDM. For this reason, the tensile strength of PTFE<sup>0kGy</sup>-EPDM is even lower than that of EPDM gum. Figure 22 shows the elongation at break as a function of PTFE loading. The elongation at break increases with PTFE loading. Similarly, as in the case of tensile strength, a 30 phr PTFE loading provides the maximum elongation followed by a decrease with increasing PTFE loading above 30 phr. Nonirradiated PTFE powder has elongation at break similar to that of EPDM gum.

Figure 23 displays the stress at 100% elongation (the so-called modulus 100% or M100) as a function of PTFE loading. The M100 decreases significantly for PTFE<sup>100kGy</sup>-EPDM and PTFE<sup>500kGy</sup>-EPDM, whereas PTFE<sup>0kGy</sup>-EPDM and EPDM-PTFE<sup>20kGy</sup>-EPDM show the highest M100 with increasing PTFE loading up to 30 phr. However, the corresponding values of PTFE<sup>100kGy</sup>-EPDM and PTFE<sup>500kGy</sup>-EPDM are lower even than that of EPDM gum. Above 30 phr PTFE loading, M100 decreases by a significant amount for all irradiation doses.

### Friction and Wear Properties

Beside mechanical characterization, one important aim of this work is the evaluation of the effects of E-beam modification of PTFE powder on the friction and wear properties of PTFE-filled EPDM composites crosslinked by a radical-initiated peroxide system. Friction and wear properties of EPDM composites were

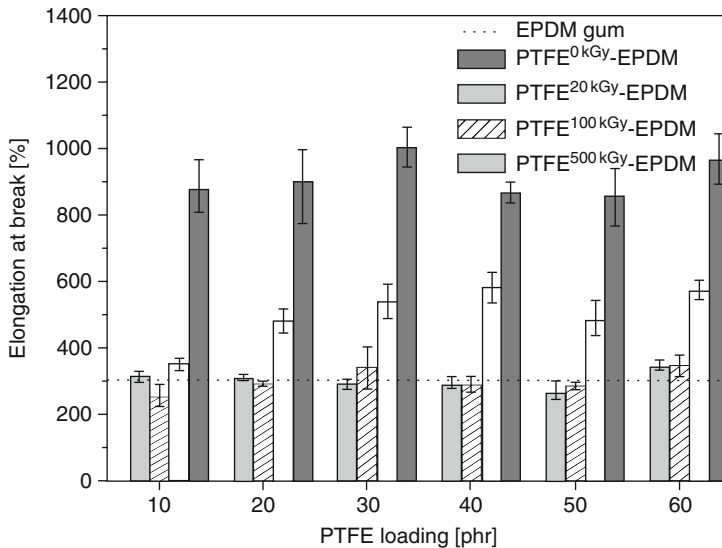


**Fig. 22** Elongation at break as a function of PTFE loading

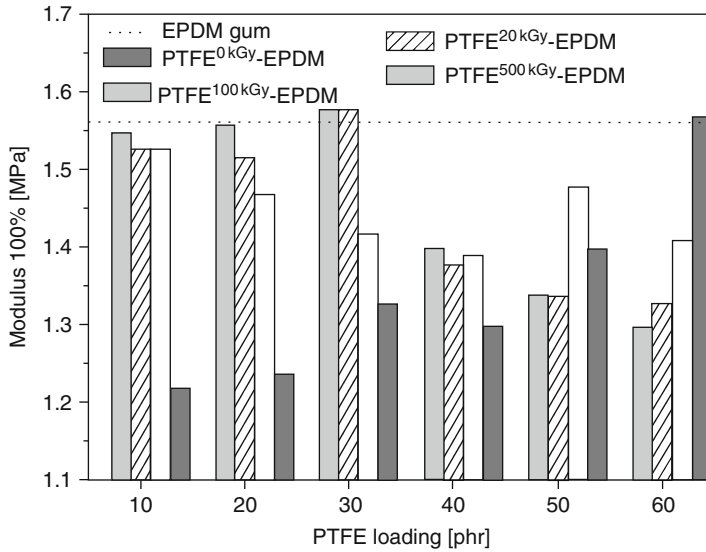
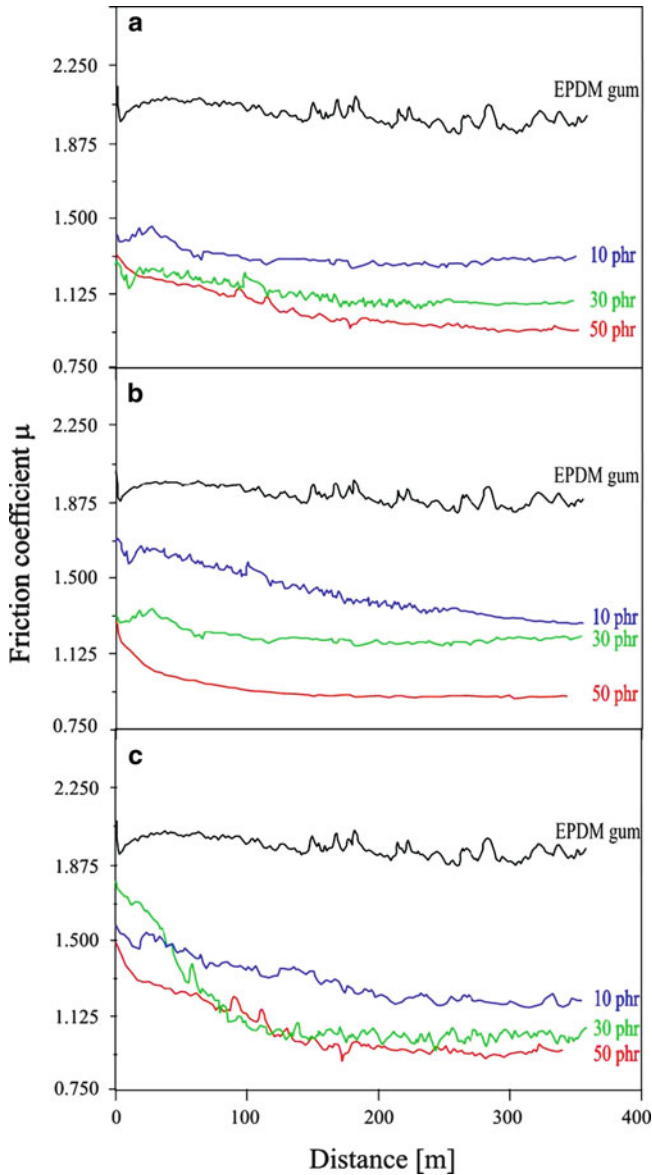


Fig. 23 Modulus 100% as a function of PTFE loading

determined with the help of a pin-on-disk tribometer in sliding contact with a steel ball at room temperature without lubrication. In this section, the corresponding friction and wear properties for low-dose (20 kGy) and high-dose (500 kGy) irradiated PTFE powder in comparison with nonirradiated (0 kGy) PTFE powder is investigated. As a preliminary study, the effects of PTFE loading, irradiation dose, and radiation-induced chemical changes on the friction and wear properties of PTFE–EPDM composites were measured. The average friction coefficient ( $\mu$ ) of EPDM gum and PTFE–EPDM composites as a function of PTFE loading is shown in Fig. 24. It can be seen that the friction coefficients of all PTFE-filled EPDM vulcanizates decrease in contrast to EPDM gum. A gradual decrease in friction coefficient can be observed with increasing PTFE loading. The friction coefficient decreased from 2.1 for EPDM gum to just less than 1.0 for the highest PTFE loading. However, at constant PTFE loading, the friction coefficient is weakly dependent on irradiation dose as no significant reduction was achieved with the use of irradiated PTFE. It can be observed that the starting friction coefficient ( $\mu_{\text{initial}}$ ) varies for different PTFE–EPDM composites. PTFE<sup>0kGy</sup>–EPDM and PTFE<sup>20kGy</sup>–EPDM have almost similar (1.32) and comparatively lower  $\mu_{\text{initial}}$  values for all PTFE loadings. In contrast, PTFE<sup>500kGy</sup>–EPDM shows the highest  $\mu_{\text{initial}}$  values (1.5 or higher).

This variation in friction behavior could be due to the specific apparent crosslink densities or  $\Delta M$  values, as shown in Fig. 17. Both PTFE<sup>0kGy</sup>–EPDM and PTFE<sup>20kGy</sup>–EPDM have higher  $\Delta M$  values and therefore have lower  $\mu_{\text{initial}}$  values. Even a slight variation in  $\Delta M$  results in different  $\mu_{\text{initial}}$  values. As soon as  $\Delta M$  decreases, as in the case of PTFE<sup>500kGy</sup>–EPDM, a significant increase in  $\mu_{\text{initial}}$  is





**Fig. 24** Friction coefficient behavior of (a) PTFE<sup>0kGy</sup>-EPDM, (b) PTFE<sup>20kGy</sup>-EPDM, and (c) PTFE<sup>500kGy</sup>-EPDM

observed. With decreasing  $\Delta M$ , both the modulus and stiffness decrease and the mechanical energy dissipation increases. Both of these bulk properties result in significantly higher  $\mu_{\text{initial}}$ . Lower modulus of the compounds result in larger contact area with the counter-body and therefore a high friction coefficient is

expected. The decrease in  $\Delta M$  is primarily caused by the adverse influence of irradiated PTFE powder on the peroxide crosslinking of PTFE–EPDM composites. The factors that influence the peroxide curing of EPDM are reported in [68, 69]. However, the main disadvantage of peroxide-induced curing is the undesired interference of free radicals with additives, which leads to a reduction of the crosslinking efficiency. E-beam-irradiated PTFE powder reduces the crosslinking efficiency of the corresponding PTFE–EPDM composites due to the presence of peroxide free radicals. Since the driving force of peroxide curing is the free radicals, they energetically react with other reactive species to pair with each other. The result is that a large number of peroxide free radicals are consumed wastefully rather than participating in the curing process.

Figure 25 shows the specific wear rate ( $k$ ) of EPDM gum and PTFE–EPDM composites as a function of PTFE loading. Both PTFE<sup>0kGy</sup>–EPDM and PTFE<sup>20kGy</sup>–EPDM show significantly lower  $k$  values compared to EPDM gum and PTFE<sup>500kGy</sup>–EPDM. PTFE<sup>500kGy</sup>–EPDM shows increasing  $k$  with PTFE loading.

For 30 and 50 phr loading,  $k$  was even higher than for EPDM gum. For PTFE<sup>20kGy</sup>–EPDM,  $k$  remained constant, whereas PTFE<sup>0kGy</sup>–EPDM showed the lowest  $k$ . The magnitude of friction coefficient values at the beginning of the loading has a significant influence on the wear mechanism during further testing. The specific wear rate ( $k$ ) clearly indicates a strong correlation with  $\Delta M$  of the compounds. With increasing  $\Delta M$  (as in the case of PTFE<sup>0kGy</sup>–EPDM and PTFE<sup>20kGy</sup>–EPDM)  $k$  is significantly lower. As  $\Delta M$  decreases,  $k$  increases significantly, as in the case of PTFE<sup>500kGy</sup>–EPDM. The variation in the magnitude of  $\Delta M$

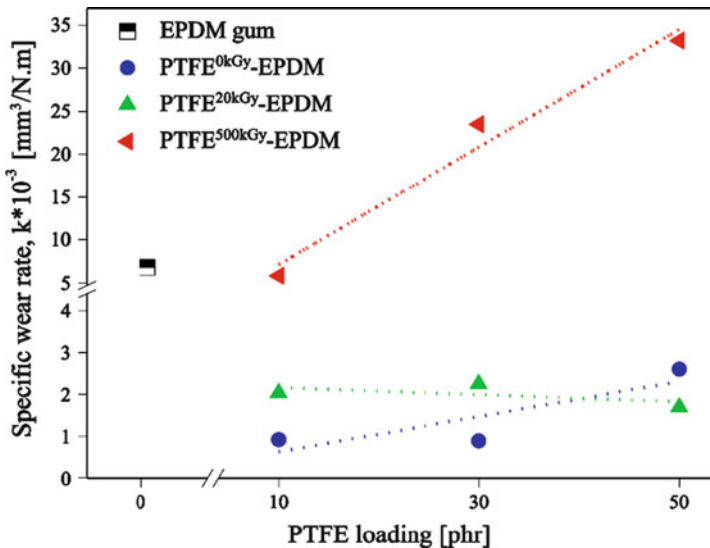


Fig. 25 Specific wear rate ( $k$ ) of EPDM gum and PTFE-filled EPDM vulcanizates as a function of PTFE loading

is strongly correlated to its wear properties. As can be seen in Figs. 17 and 25,  $k$  varies according to the  $\Delta M$  value. It is also interesting that EPDM gum has significantly higher  $\Delta M$  than PTFE<sup>500kGy</sup>-EPDM but shows a similar  $k$  value to that of 10 phr PTFE<sup>500kGy</sup>-EPDM. This suggests that vulcanizates suffer from different modes of wear, depending on their unique composition and bulk properties.

### Analysis of the Wear Mechanism

In general, particle size, shape, and distribution all play important roles in the wear of different filled systems [70–72]. The average friction coefficient values are almost similar for PTFE-EPDM composites having comparatively different mean agglomerate size and distribution (Figs. 13 and 14). SEM micrographs of the wear scars of EPDM gum, PTFE<sup>500kGy</sup>-EPDM, and PTFE<sup>20kGy</sup>-EPDM are shown in Fig. 26.

The scars suggest that wear in these three different compounds occurred by different mechanisms. EPDM gum shows a characteristic failure mode due to the absence of PTFE powder. In the case of EPDM gum, the solid materials detached from the surface due to adhesion with the counter-body. However, in the presence of PTFE powder the sliding contact area of the PTFE-EPDM composites with the counter-surface seems to change. In the case of the PTFE<sup>20kGy</sup>-EPDM composite, having higher  $\Delta M$  (Fig. 17), the contact area shows smoother surfaces with small detachments around the PTFE powder. In this case, the wear mechanism is mainly characterized by the detachment of PTFE agglomerates. In contrast, for the PTFE<sup>500kGy</sup>-EPDM composite, having significantly lower  $\Delta M$  (Fig. 17), the wear scar is characterized by disruption in deep regions of the EPDM matrix. A wavy pattern exists with fronts transversely oriented to the sliding direction. Figure 27 shows the high magnification topography of PTFE<sup>20kGy</sup>-EPDM and

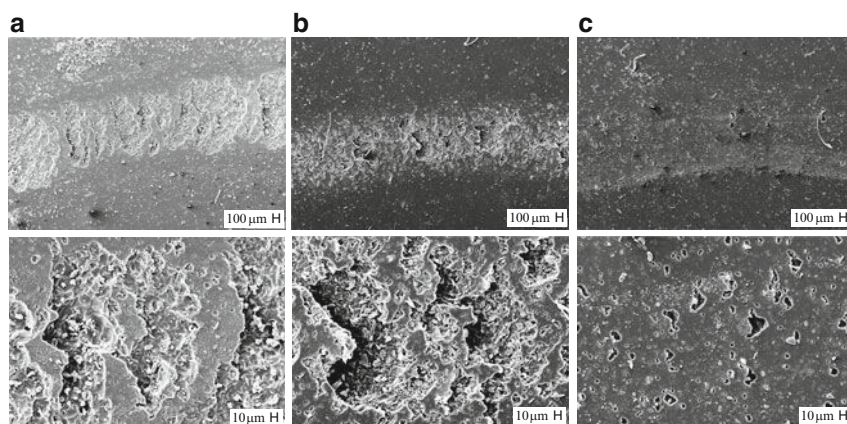


**Fig. 26** SEM micrographs showing the worn surfaces of (a) EPDM gum, (b) PTFE<sup>500kGy</sup>-EPDM, and (c) PTFE<sup>20kGy</sup>-EPDM. Lower images are magnifications of upper images

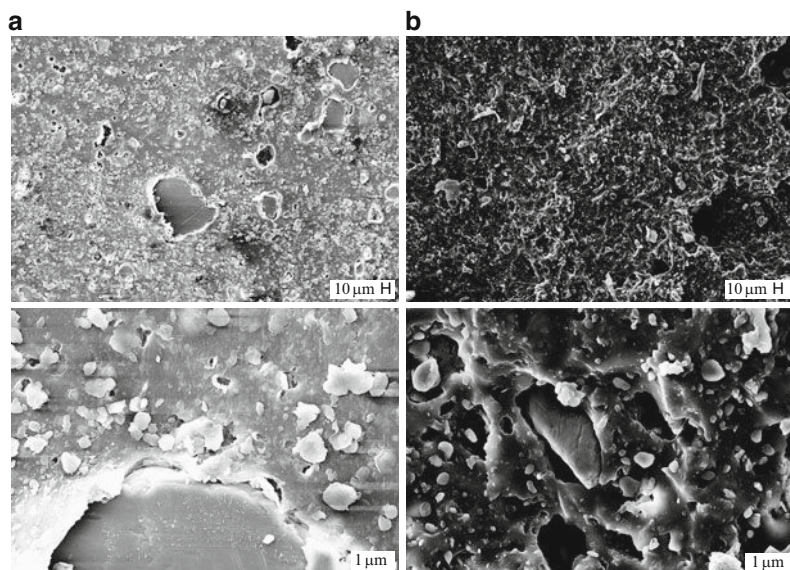


**Fig. 27** SEM micrographs showing the worn surfaces of (a) PTFE<sup>20kGy</sup>-EPDM and (b) PTFE<sup>500kGy</sup>-EPDM. Lower images are magnifications of upper images

PTFE<sup>500kGy</sup>-EPDM. The surface of the PTFE<sup>20kGy</sup>-EPDM indicates the presence of large PTFE agglomerates. The large agglomerates appear to have been firmly embedded and excessively abraded by the counter-surface. Many unperturbed smaller agglomerates surrounding the huge agglomerate with, surprisingly, no signs of wear by the counter-surface can be seen. In the case of PTFE<sup>500kGy</sup>-EPDM vulcanizates, the worn topography resembles that of the EPDM gum (except the presence of PTFE powder). The mode of deformation in these materials has occurred in the deep regions or at the interfaces between the matrix and small particles.

### Relationship Between Mechanical Properties and Wear Properties

The mechanical properties of EPDM gum and PTFE-EPDM composites as a function of PTFE loading are summarized in Table 4. PTFE<sup>500kGy</sup>-EPDM has significantly greater tensile strength at break, elongation at break, and tear resistance than both PTFE<sup>0kGy</sup>-EPDM and PTFE<sup>20kGy</sup>-EPDM but significantly lower hardness. With increasing PTFE loading, hardness increases and specific wear rate ( $k$ ) is expected to decrease, as shown in Fig. 25 for PTFE<sup>0kGy</sup>-EPDM and PTFE<sup>20kGy</sup>-EPDM. However, it is interesting to note that in the case of PTFE<sup>500kGy</sup>-EPDM with increasing PTFE loading,  $k$  increases with increasing hardness. This suggests that another parameter is influencing  $k$ . This wear-rate-controlling parameter could be the apparent crosslink density ( $\Delta M$ ). The result also suggests that a threshold value of  $\Delta M$  exists below which  $k$  is independent of

**Table 4** Mechanical properties as a function of PTFE loading and irradiation dose for different PTFE–EPDM composites

PTFE loading (phr)	Irradiation dose (kGy)	Tensile strength at break ( $\sigma_B$ ) (MPa)	Elongation at break ( $\epsilon_B$ ) (%)	Tear resistance (N/mm)	Hardness (Shore A°)
0 (EPDM gum)	–	3.48	304	2.97	54.7
10	0	3.53	315	3.04	60.0
	20	2.90	254	3.10	59.1
	500	5.63	875	6.01	53.2
30	0	2.97	289	2.97	62.3
	20	3.30	342	3.16	61.4
	500	6.75	1005	8.16	55.3
50	0	2.67	267	2.80	63.4
	20	2.52	286	3.50	62.4
	500	4.78	858	9.31	56.9

hardness. The hardness may influence  $k$  above this threshold value of  $\Delta M$ , as in the case of PTFE<sup>0kGy</sup>–EPDM and PTFE<sup>20kGy</sup>–EPDM. In addition, numerous other successful correlations of  $k$  with various mechanical properties such as tensile strength, elongation, and hardness for various kinds of polymer composites have been made in the past [73–76].

These investigations have explicitly concluded that the key to developing any such correlation is strictly dependent on unambiguously identifying the dominating properties of the material that control and inhibit wear. Similar is the case of PTFE<sup>500kGy</sup>–EPDM, where a  $\Delta M$  of less than critical value results in significantly higher  $k$ . In such a case, the chemical composition of the rubber itself, whether filled or unfilled, appears to have no effect in reducing wear. However, it is appropriate to mention that, in general, the frictional properties of rubber-like materials depend not only on sliding speed, temperature, and normal load but also depend on the typical surface characteristics of the load counter-face [48]. The results presented in the present work are valid only for the load and sliding speed of 1.0 N and 0.05 m/s, respectively.

### 3.3.2 Influence of Irradiation Dose

The preliminary investigations suggested that electron irradiation of PTFE powder undoubtedly influences the friction and wear properties of EPDM through peroxide crosslinking. For this reason, this section investigates the friction and wear properties of 30 phr (L100X PTFE powder) PTFE–EPDM composites for a complete range of irradiation doses i.e., 20, 100, 200, 300, 400, and 500 kGy. These investigations are necessary in order to analyze the tendency in friction and wear behavior of EPDM containing PTFE powders modified with increasing doses of irradiation. The influence of radiation-induced chemical changes in irradiated PTFE powder on the bulk properties (hardness, mechanical energy dissipation etc.) of EPDM and its dependency on friction and wear properties is systematically discussed. We are

systematically characterizing the influence of the PTFE modification (20, 100, 200 ... 500 kGy) on various properties of the EPDM composite and how does these properties effect the friction and wear behavior.

### Curing Characteristics

Figure 28 shows the effect of E-beam modification of PTFE on the curing characteristics such as  $\Delta M$  and curing time ( $t_{90}$ ). In general,  $\Delta M$  allows a qualitative assessment of the state of cure for the determination of crosslinking density of composites. The magnitude of  $\Delta M$  corresponds to the degree of crosslink density. As can be seen, both  $t_{90}$  and  $\Delta M$  gradually decrease with the use of more highly irradiated PTFE powder in EPDM. PTFE<sup>0kGy</sup>-EPDM shows the highest  $t_{90}$  and  $\Delta M$  followed by EPDM gum, whereas PTFE<sup>500kGy</sup>-EPDM shows the lowest values. In other words, an inverse relationship can be suggested between  $\Delta M$  and absorbed dose.

### Mechanical Properties

Figure 29 shows the tensile strength and elongation at break of PTFE-EPDM composites as a function of irradiation dose. The horizontal lines represent EPDM gum. In the case of PTFE<sup>0kGy</sup>-EPDM, tensile strength and elongation at break are lower than that of composites containing modified PTFE. With increasing absorbed dose, the tensile strength and elongation at break of modified-PTFE-coupled EPDM composites increase systematically. Tensile strength and elongation at break of EPDM gum and PTFE<sup>0kGy</sup>-EPDM are almost the same because of poor

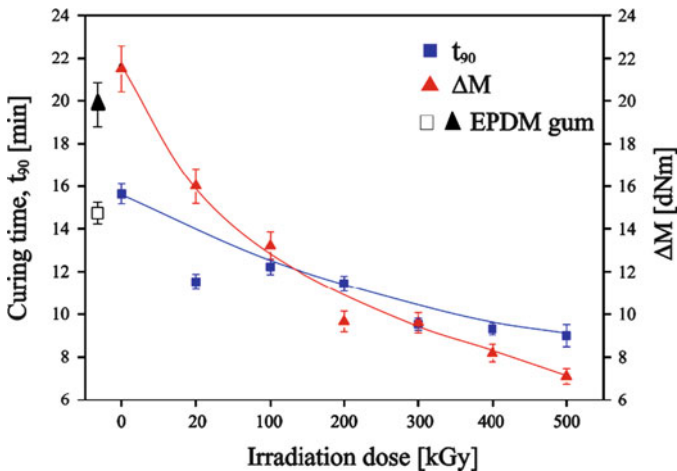


**Fig. 28** Optimum cure time ( $t_{90}$ ) and delta torque ( $\Delta M$ ) of EPDM gum and PTFE-EPDM composites

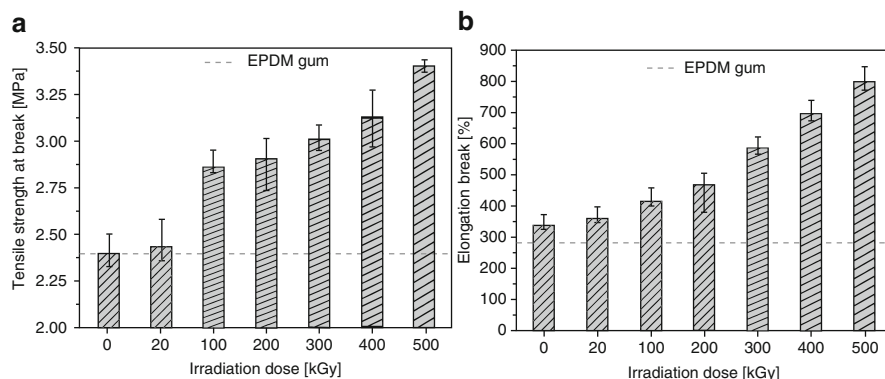


**Fig. 29** Tensile strength at break (a) and elongation at break (b) as a function of irradiation dose

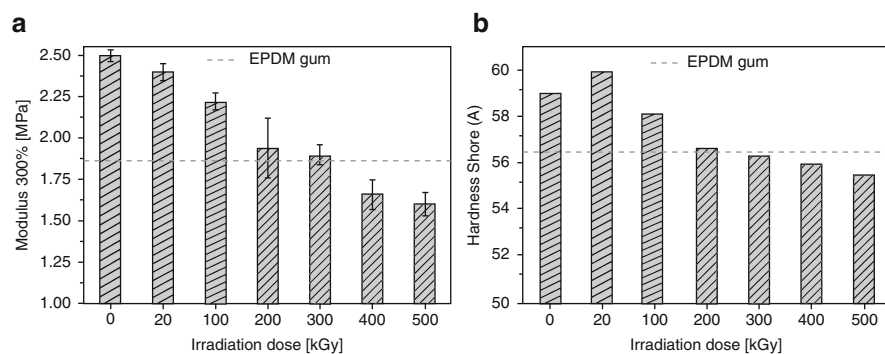


**Fig. 30** Modulus 300% (a) and hardness (b) as a function of irradiation dose

compatibility and dispersion. On the other hand, PTFE<sup>500kGy</sup>-EPDM shows the highest tensile strength and elongation at break. Modified PTFE particles having smaller agglomerate sizes and compatible surfaces enhance its degree of dispersion and compatibility. The improvement in the mechanical properties of EPDM filled with electron-treated PTFE is essentially due to the synergistic effect of their homogeneous dispersion and desirable compatibility.

Figure 30a displays the stress at 300% elongation (the so-called modulus 300% or M300) as a function of absorbed dose. The M300 decreases for PTFE-EPDM composites containing PTFE modified with increasing irradiation dose. PTFE<sup>0kGy</sup>-EPDM shows the highest M300. However, the corresponding values of PTFE<sup>400kGy</sup>-EPDM and PTFE<sup>500kGy</sup>-EPDM are lower even than that of EPDM gum. Figure 30b shows the corresponding Shore (A) hardness values of PTFE-EPDM composites. The effect of the dose of irradiation absorbed by the PTFE powder on composite hardness can be seen in the decreasing values of hardness. EPDM filled with PTFE subjected to irradiation doses higher than 20 kGy results in decreasing hardness values of PTFE-EPDM composites. PTFE<sup>20kGy</sup>-EPDM has

the highest hardness while PTFE<sup>500kGy</sup>-EPDM showed the lowest. It is interesting to note that the hardness of the composites above PTFE<sup>200kGy</sup>-EPDM is even lower than that of EPDM gum.

### Friction and Wear Properties

Friction in general is a complex process that characterizes the interaction between surfaces of solid bodies in contact with each other. The molecular mechanical theory unifies the well-known deformation and adhesion theories to explain the complicated interaction between solid bodies in contact. However, friction of viscoelastic elastomers sliding against a hard counter-surface results in more complex behavior. In addition to parameters such as temperature, velocity, and normal load, their high viscoelastic behavior results in a spatial distribution of real contact area that varies both locally and temporally during cyclic loading. Generally, the real contact area is only a fraction of the nominal contact regions. The four mechanisms shown in Fig. 31 strongly influence both the friction and wear behavior of soft viscoelastic materials sliding against a solid rough counter-surface [77]:

- (a) Breaking of the adhesive bonds or the boundary layers
- (b) Plastic deformation of the contacting area zones
- (c) Plowing due to roughness peaks and wear debris
- (d) Elastic hysteresis due to damping

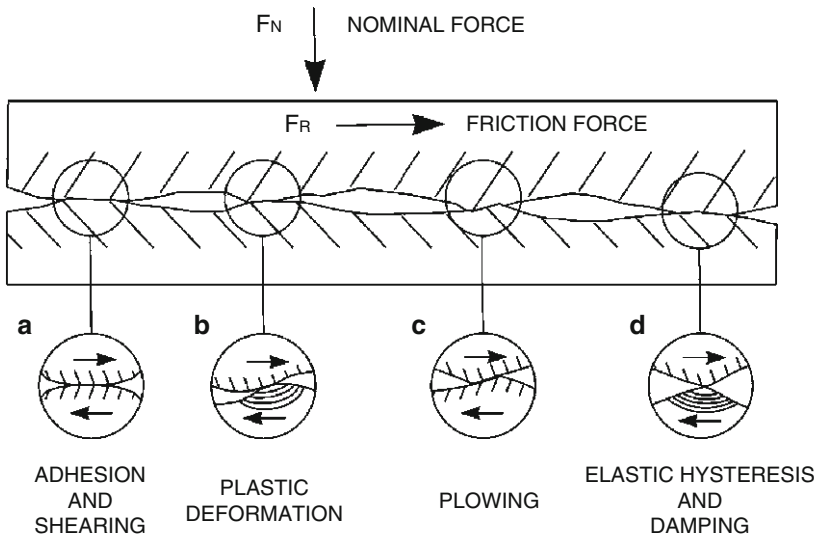


**Fig. 31** Friction and wear mechanisms involved in viscoelastic solid bodies sliding against a rough counter-surface



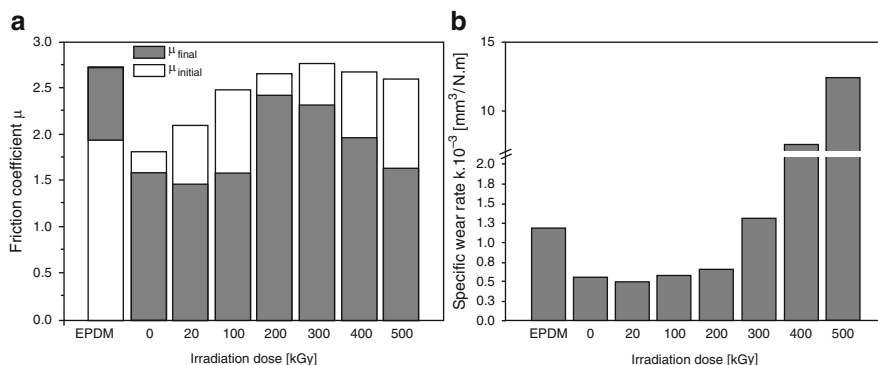


**Fig. 32** Friction coefficient (a) and specific wear rate (b) of EPDM gum and PTFE–EPDM composites as a function of irradiation dose

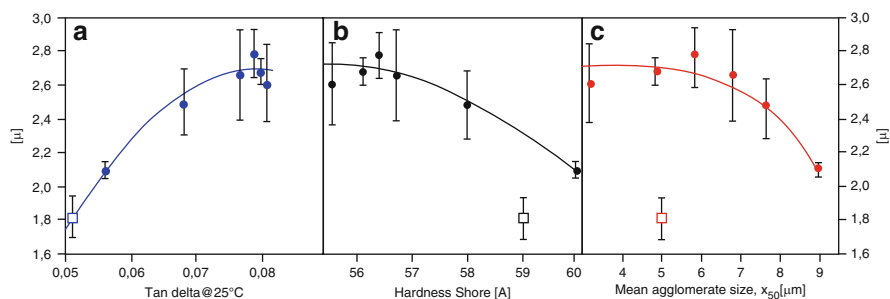
The friction and wear properties of the PTFE-filled EPDM are discussed in the context of the above mentioned mechanisms.

Figure 32 shows the friction coefficient and specific wear rate of PTFE–EPDM composites in comparison to EPDM gum. Figure 32a indicates that the friction coefficient of EPDM gum in comparison to PTFE–EPDM composites increased during the course of measurement. All samples display a characteristic run-in process. The friction coefficient values decreased in a range from 9 to 37% till the end of the measurements. As shown in Fig. 32b,  $k$  increased with absorbed dose or decreasing  $\Delta M$ . The lowest  $k$  value of  $0.5 \times 10^{-3} \text{ mm}^3 \text{ N m}^{-1}$  is observed for PTFE<sup>0kGy</sup>–EPDM, having the highest  $\Delta M$  (Fig. 28). Moreover, a minor increase in wear rate is observed up to an irradiation dose of 200 kGy (PTFE<sup>200kGy</sup>–EPDM), which corresponds to a  $\Delta M$  value of approximately 10 dN m. Above this threshold, a maximum  $k$  value of  $12.56 \times 10^{-3} \text{ mm}^3 \text{ N m}^{-1}$  is achieved for PTFE<sup>500kGy</sup>–EPDM, having the lowest  $\Delta M$  of approximately 7 dN m. X-ray photoelectron scattering (XPS) analysis of PTFE<sup>0kGy</sup>–EPDM and PTFE<sup>500kGy</sup>–EPDM surfaces prior to friction and wear testing suggests that the ratio of fluorine to carbon is similar, within the experimental uncertainty. This result indicates that the surfaces are chemically similar whether filled with modified or unmodified PTFE powder. On the other hand, evaluation of surface roughness before wear testing supports the fact that the vulcanizate surfaces have almost similar microroughness. Both results suggest that the vulcanizate surfaces are chemically and topographically similar before wear testing. This indicates that friction processes are comparable at the beginning of the loading.

For all materials, the adhesive mechanism and the plastic deformation should be the main processes. During testing, the variation in friction coefficient values could be influenced by the specific  $\Delta M$  behavior. Since  $\Delta M$  corresponds to the crosslink density of a composite, for a qualitative assessment it can be concluded that the crosslink density decreases with increasing absorbed dose. PTFE<sup>500kGy</sup>–EPDM showed much lower  $\Delta M$  and  $t_{90}$  values. It can be inferred that the state of cure is strongly dependent on the irradiation dose absorbed by the PTFE powder.

The magnitude of friction coefficient values at the beginning of the loading have a significant influence on the wear mechanism during further testing. Therefore, the friction coefficient at the beginning is correlated to  $\tan \delta$  at  $25^\circ\text{C}$ , hardness, and mean agglomerate size. As shown in Fig. 33a, the friction coefficient increased with increasing  $\tan \delta$  for PTFE–EPDM composites containing modified PTFE. Also, the value for the PTFE<sup>0kGy</sup>–EPDM composite fits well according to this dependency. It suggests that the  $\tan \delta$  value of a composite influences the friction coefficient and could be a friction-controlling parameter. The  $\tan \delta$  value characterizes the energy dissipation due to internal friction in these compounds. It was observed that the loss factor increases with the irradiation dose absorbed by the PTFE powder. Assuming that the stiffness and storage modulus of PTFE–EPDM composites remain constant, the friction energy produced by the counterbody should be better dissipated and, therefore, the friction coefficient should decrease; however, an increase in friction coefficient was observed. Another reason for increasing  $\tan \delta$  values is the decrease in storage modulus at constant loss modulus. Felhös and Karger-Kocsis report the same tendency that, with decreasing stiffness, the friction coefficient increases for carbon-black-filled EPDM [59].

Figure 33b shows friction coefficient as a function of composite hardness. For PTFE–EPDM composites containing modified PTFE, the friction coefficient decreases with increasing hardness. On the other hand, PTFE<sup>0kGy</sup>–EPDM, with hardness less than PTFE<sup>20kGy</sup>–EPDM, shows the lowest friction coefficient as well as the highest  $\Delta M$  (Fig. 28). This indicates that hardness alone does not influence the friction behavior. The gradual decrease in hardness values with increasing irradiation of the PTFE powder in EPDM is due to the influence of the modified PTFE powder on the peroxide-induced crosslinking of PTFE–EPDM composites. The main factors that influence the peroxide cure efficiency of EPDM are reported in [68, 69]. One disadvantage of the use of peroxide for crosslinking is the undesired interference with additives, which can act as radical scavengers and thus cause a reduction in the crosslinking efficiency. In general, the efficiency of the crosslinking mode depends not only on the chemical composition of the polymer, but also on the presence of additives, such as antioxidants. E-beam-modified PTFE



**Fig. 33** Friction coefficient ( $\mu$ ) as a function of (a)  $\tan \delta$  at  $25^\circ\text{C}$ , (b) hardness, and (c) mean agglomerate size. Squares indicate PTFE–EPDM composites containing nonmodified PTFE and circles modified PTFE

powder seems to have an adverse effect on the crosslinking efficiency of the corresponding PTFE–EPDM composites due to the presence of radical and functional groups on the modified PTFE powder.

Figure 33c shows that for PTFE–EPDM composites containing modified PTFE, the friction coefficient decreased steadily with increasing mean agglomerate size. However, PTFE<sup>0kGy</sup>–EPDM has a lower friction coefficient than modified-PTFE–EPDM composites having the same mean agglomerate size but significantly higher  $\Delta M$  value. This suggests that the mean agglomerate size of PTFE powder is not a friction-controlling property and that a further additional parameter is influencing the friction behavior.

In contrast to the frictional behavior, the specific wear rate depends both on tan delta and hardness. Figure 34a shows  $k$  as a function of tan delta. As can be seen, a threshold exists for tan delta values up to which a minor increase in specific wear rate is observed. However, above this limit  $k$  increases significantly, as observed for PTFE<sup>300kGy</sup>–EPDM, which corresponds to a  $\Delta M$  value of less than 10 dN m (Fig. 28). Figure 34b shows wear rate as a function of hardness. Similarly, at first, the wear rate increases slightly with decreasing hardness. However, for PTFE<sup>300kGy</sup>–EPDM and higher it rises significantly.

Again this behavior is due to the significantly lower  $\Delta M$  value (less than 10 dN m). Figure 34c shows  $k$  as a function of mean agglomerate size. For PTFE–EPDM composites containing modified PTFE,  $k$  decreased with increasing mean agglomerate size. In contrast, PTFE<sup>0kGy</sup>–EPDM shows a lower  $k$  value than modified-PTFE–EPDM composites having the same mean agglomerate size but higher  $\Delta M$  values. This suggests that the  $\Delta M$  value and crosslinking density of these compounds are important wear-controlling parameters.

## Wear Mechanism

SEM micrographs of the wear scars of EPDM gum and PTFE–EPDM composites are shown in Fig. 35. EPDM gum shows a characteristic failure mode caused by

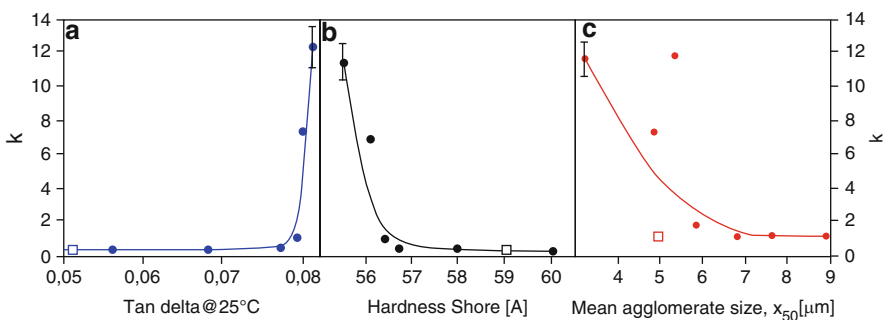


**Fig. 34** Specific wear rate ( $k$ ) as a function of (a) tan delta at 25°C, (b) hardness, and (c) mean agglomerate size. Squares indicate PTFE–EPDM composites containing nonmodified PTFE and circles modified PTFE

the absence of PTFE powder. EPDM gum failed by detachment of the solid material from the surface by an adhesive mechanism with the counter-body. However, in the presence of PTFE powder in EPDM, the sliding contact area of the PTFE–EPDM composites with the counter-surface seems to change. In the case of PTFE<sup>0,20,100kGy</sup>–EPDM, having  $\Delta M$  higher than 13 dN m (Fig. 28), the contact areas show smoother surfaces with small detachments around the PTFE powder and mostly abraded PTFE agglomerates in the matrix (Fig. 35b–d). In this case, the wear mechanism is mainly characterized by the detachment of PTFE

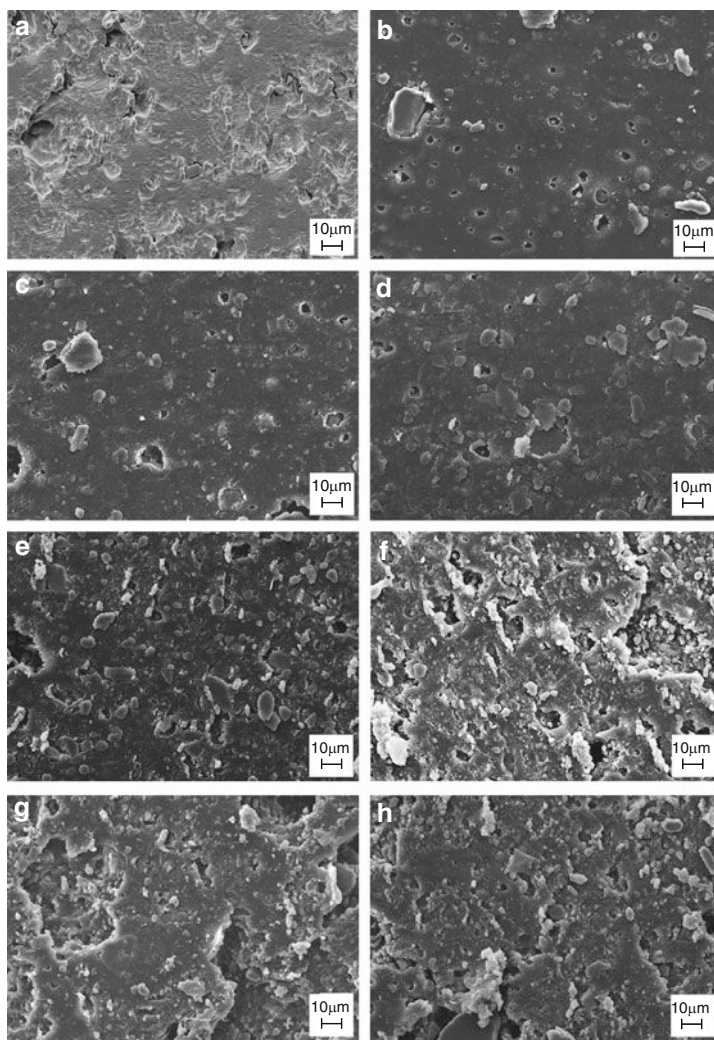


**Fig. 35** SEM showing the worn surfaces of (a) EPDM gum, and of PTFE–EPDM composites containing (b) nonmodified PTFE, or (c–h) 20,100, 200, 300, 400, and 500 kGy-irradiated PTFE

agglomerates. In contrast, PTFE<sup>200...500kGy</sup>-EPDM, having  $\Delta M$  less than 10 dN m, show contact areas characterized by a disruption in deep regions of the matrix. A wavy pattern exists, with fronts transversely oriented to the sliding direction. The depth of the waves increases with the dose absorbed by the PTFE powder, i.e., with decreasing  $\Delta M$ . Due to the presence of many unperturbed smaller PTFE agglomerates with surprisingly no signs of wear by the hard counter-surface (as can be seen in Fig. 35e-h), a different failure mechanism is involved.

### ***3.4 Electron-Beam-Crosslinked Rubber Composites***

The present study focuses on using electron irradiation instead of peroxide for crosslinking of EPDM filled with 30 phr L100X (0 kGy-irradiated), L100X (500 kGy-irradiated), and commercially available MP1100 and MP1200 PTFE powders. Since  $\Delta M$  and hardness both influence the friction and wear properties, PTFE-EPDM composites should be produced with a hardness higher than the critical value of 58 Shore (A). With the help of electron irradiation for crosslinking, the effect of radiation-induced changes in PTFE powder on peroxide crosslinking of EPDM is significantly reduced. Therefore, any substantial changes in hardness values at a specific crosslinking irradiation dose should arise solely from the PTFE powder itself. The composites were produced in a specific and controlled manner so that the influence of morphology, dispersion, and surface activity of different PTFE powders on physical and especially on friction and wear properties could be realized. These investigations are of significant importance regarding the application of PTFE powder in rubber compounds.

#### **3.4.1 Characterization with Respect to Chemical Coupling**

##### **Optimization of Crosslinking Dose**

In order to investigate the effect of morphology, dispersion, and chemical coupling, the composites should have hardness higher than the critical value of 58 Shore (A). Peroxide crosslinking of PTFE-EPDM composites containing electron-modified PTFE powder is strongly influenced by the irradiation-induced changes in PTFE powder. The hardness of PTFE-EPDM composites varies according to the irradiation dose used for modifying the PTFE powder. For this reason, EPDM was crosslinked using electron irradiation in order to suppress this undesired effect on the composite hardness. The dose for irradiation crosslinking was determined relative to the required hardness values of the PTFE-EPDM composites. This was achieved by monitoring the influence of crosslinking dose on the hardness. Figure 36 shows the influence of irradiation dose on hardness of

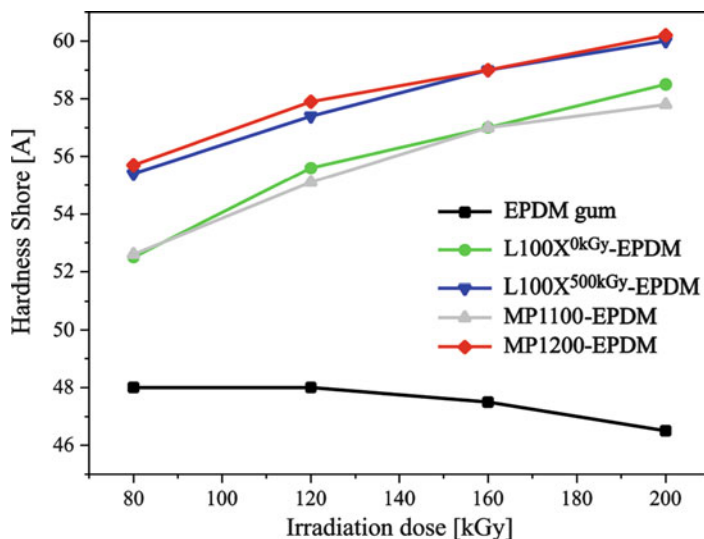


**Fig. 36** Comparison of hardness values of EPDM gum and rubber composites as a function of crosslinking irradiation dose

EPDM rubber and PTFE–EPDM composites. It can be seen that the optimum dose for crosslinking of EPDM rubber is about 80–120 kGy. Above 120 kGy, hardness decreases due to chain scission of EPDM. However, in the presence of PTFE powder, the hardness of PTFE–EPDM composites increases as expected. L100X<sup>500kGy</sup>–EPDM and MP1200–EPDM show the highest hardness whereas L100X<sup>0kGy</sup>–EPDM and MP1100–EPDM show the lowest. This behavior is in contradiction to that observed in peroxide-induced crosslinking of L100X<sup>500kGy</sup>–EPDM. It suggests that the variation in hardness of different composites at any specific absorbed dose results from differences in the chemical coupling between PTFE powders and EPDM. This can be clearly seen in the different hardness values of L100X<sup>0kGy</sup>–EPDM and L100X<sup>500kGy</sup>–EPDM. However, at an optimum crosslinking dose of 200 kGy, all of the PTFE–EPDM composites attained the required minimum hardness value of 58 Shore (A).

### Physical and Dynamic Mechanical Properties

The effects of PTFE powders on the mechanical properties of PTFE–EPDM composites are shown in Fig. 37. As expected, PTFE–EPDM composites containing modified PTFE show enhanced properties compared to those with nonmodified PTFE (L100X<sup>0kGy</sup>–EPDM). There is no significant variation in tensile strength and elongation at break values of the modified-PTFE–EPDM composites. However, L100X<sup>500kGy</sup>–EPDM shows the highest M100 and M200, followed by MP1200–EPDM and MP1100–EPDM. The L100X<sup>0kGy</sup>–EPDM composite

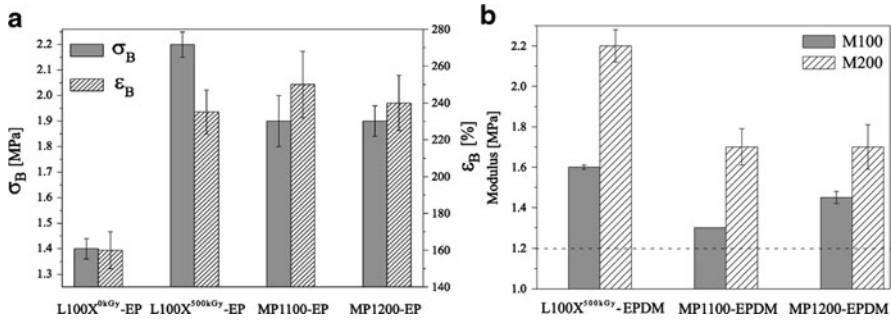


**Fig. 37** Comparison of mechanical properties of PTFE–EPDM composites: (a) tensile strength at break ( $\sigma_B$ ) and elongation at break ( $\epsilon_B$ ); (b) moduli M100 and M200. The horizontal line indicates the M100 of the composite containing nonmodified PTFE (L100X<sup>0kGy</sup>-EPDM)

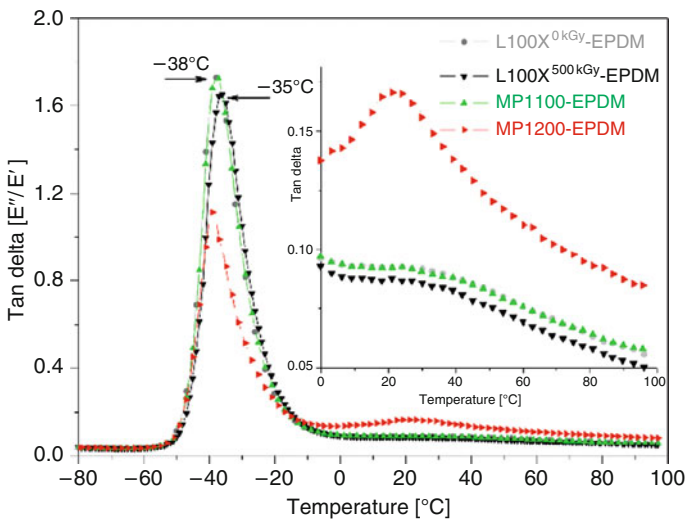


**Fig. 38** Tan delta behavior of the vulcanizates as a function of temperature

(horizontal broken lines) shows the lowest. M200 was not achieved by L100X<sup>0kGy</sup>-EPDM. This reinforcement effect in the case of L100X<sup>500kGy</sup>-EPDM is due chemical coupling of PTFE powder with EPDM. The effect of reinforcement can also be seen in the dynamic mechanical properties.

Figure 38 shows tan delta curves of the corresponding PTFE–EPDM composites as a function of temperature. As can be seen, the glass transition temperature ( $T_g$ ) is only slightly influenced by addition of different PTFE powders to EPDM. The peak-height increases from MP1200–EPDM to L100X<sup>500kGy</sup>-EPDM and reaches the maximum value for L100X<sup>0kGy</sup>-EPDM and MP1100–EPDM. The L100X<sup>0kGy</sup>-EPDM, MP1100–EPDM, and MP1200–EPDM composites show

similar  $T_g$  of about  $-38^\circ\text{C}$ , whereas L100X<sup>500kGy</sup>-EPDM has a higher  $T_g$  value of about  $-35^\circ\text{C}$ .

This shift in  $T_g$  to higher temperature is due to the restricted mobility of the polymer chains. Figure 38 also shows the magnified tan delta curves of the compounds in the temperature range of friction and wear testing. L100X<sup>500kGy</sup>-EPDM shows the lowest tan delta, while L100X<sup>0kGy</sup>-EPDM and MP1100-EPDM show similar behavior at a slightly higher level. The upturn in tan delta behavior of MP1200-EPDM could be due to the relaxation processes associated with the radiation-induced effects on the crystallite structure of PTFE powder.

### Compatibility and Dispersion

Table 5 shows the relative concentration of C=O groups determined in the region  $1,840\text{--}1,740\text{ cm}^{-1}$ . It can be observed that C=O concentration varies in different PTFE powders. L100X<sup>0kGy</sup> PTFE powder shows no C=O groups, while L100X<sup>500kGy</sup> PTFE powder shows the highest concentration. Both MP1100 and MP1200 have almost similar C=O concentrations, which is three times less than that of L100X<sup>500kGy</sup> PTFE powder. The higher C=O concentration in the case of L100X<sup>500kGy</sup> PTFE powder suggests a significantly lower contact angle or higher wettability. Lower contact angle corresponds to higher surface energy and enhanced interaction with polar compounds such as water. However, the enhanced compatibility of irradiated PTFE and EPDM cannot be explained by the presence of these functional groups since EPDM, being a nonpolar compound, does not interact via polar or H-bonding forces. The other influencing factor is the relative concentration of persistent free radicals trapped in the crystalline structure at the surface of irradiated PTFE powders.

The free radicals affect the properties through radical coupling with the unsaturated olefinic double bonds in the rubber compound. The overall (bulk and surface) radical concentration of PTFE powders normalized to L100X<sup>500kGy</sup> PTFE powder (100%) suggests that MP1100 has the highest radical concentration (125.6%), while MP1200 (56.3%) has the lowest. However, the degree of chemical coupling might

**Table 5** Relative concentration of C=O groups of PTFE powders, as determined by integrating the area under the curve

PTFE powder properties	L100X <sup>a</sup>	MP1100 <sup>b</sup>	MP1200 <sup>b</sup>
Polymerization process	Emulsion	Emulsion	Suspension
Irradiation dose (kGy)	500	500	500
Primary particle size (nm)	70–80	200	Unknown
Mean agglomerate size ( $\mu\text{m}$ )	3.65	4	3
Carboxylic groups (C=O) (%)	44.13	15.13	15.48
Radical concentration (%) <sup>c</sup>	100	125.6	56.3
Specific surface area ( $\text{g}/\text{m}^2$ )	26	7–10	1.5–3

<sup>a</sup>Irradiated in the Leibniz-Institute

<sup>b</sup>Commercially irradiated powders

<sup>c</sup>Radical concentration normalized to L100X PTFE powder



also depend on the amount of radicals available on the surface of PTFE agglomerates for chemical coupling with EPDM. In such cases, the surface-available radical concentration is of significant importance.

Figure 39 shows the scanning micrographs of PTFE–EPDM composites. It can be seen that L100X<sup>0kGy</sup>–EPDM demonstrates poor compatibility and dispersion. It shows bigger agglomerates with poor dispersion behavior in EPDM. This is due to the highly inert and hydrophobic surface of PTFE powder, which lacks interaction and chemical compatibility. For this reason, PTFE powder is modified with electron irradiation in order to simultaneously enhance its poor wetting and dispersion characteristics. This can be seen in the enhanced dispersion behavior of L100X<sup>500kGy</sup> PTFE powder in the EPDM matrix. The enhanced compatibility due to the chemical coupling by radical mechanism helps in deagglomeration and dispersion of PTFE agglomerates during the reactive processing. Grafted EPDM chains on the surface of PTFE particles interact with the EPDM matrix and, as such, extensive shearing and deagglomeration provides new active sites for chemical coupling with the olefinic unsaturated diene of EPDM. This helps in reinforcement and, simultaneously, in improvement in properties of L100X<sup>500kGy</sup>–EPDM. MP1100 shows the best dispersion of the PTFE powders investigated. This is mainly due to the ability of this special grade of PTFE powder to deagglomerate to its primary particle size of 0.2  $\mu\text{m}$ . Both MP1100 and L100X<sup>500kGy</sup> PTFE powders are embedded firmly in the EPDM matrix.

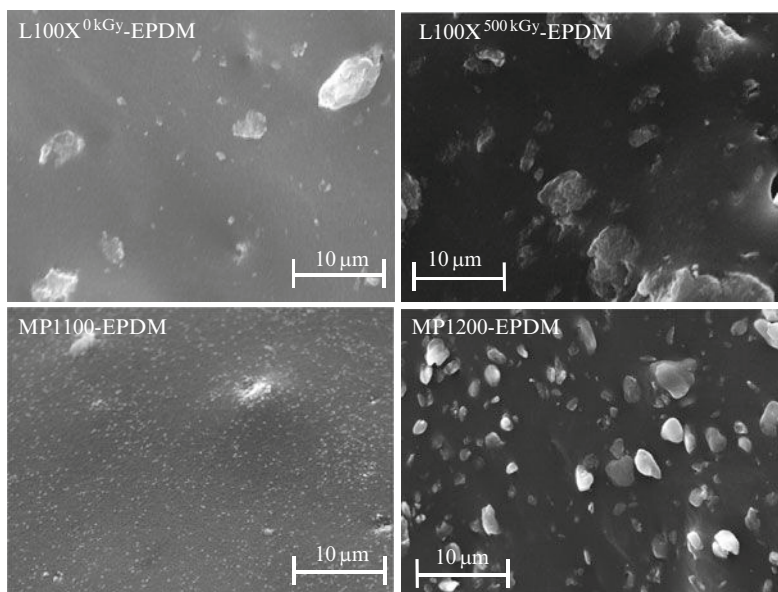


**Fig. 39** SEM micrographs of the cryogenically fractured surfaces of different PTFE–EPDM composites, showing PTFE morphology and dispersion in EPDM

However, L100X grade is difficult to disperse uniformly compared to MP1100, even though both are produced by emulsion polymerization. On the other hand, MP1200 PTFE powder, having a solid morphology, is difficult to deagglomerate even under high shearing. One can observe that MP1200 agglomerates are pulled out of EPDM on application of stress. This clearly indicates the lower degree of compatibility of the bigger MP1200 agglomerates. The surface of EPDM indicates the presence of many PTFE particles. This clearly shows the difficulty in obtaining uniform dispersion of MP1200 in EPDM matrix.

### 3.4.2 Characterization of Friction and Wear Behavior

#### Friction Behavior

Figure 40 shows the friction behavior of PTFE–EPDM composites sliding against a hard spherical ball. The friction curves demonstrate that the friction coefficients of all composites decrease during the course of testing. The friction coefficient values decrease from initial to final values within a range of 4–100%. As can be seen, the composites show different behaviors both at the beginning and during the course of testing. MP1100–EPDM shows the highest friction values compared to all other compounds. Moreover, a sudden decrease in the initial friction coefficient is observed for all compounds except MP1100–EPDM. After a steady state is achieved, the friction coefficient of MP1200–EPDM and L100X<sup>0kGy</sup>–EPDM remains almost constant up to the end of measurements. By contrast, MP1100–EPDM shows a

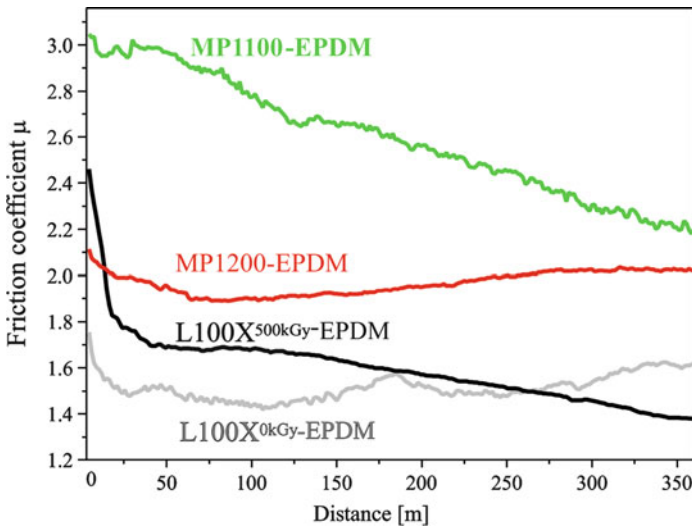


**Fig. 40** Comparison of the friction behavior of PTFE–EPDM composites as a function of sliding distance

gradual decrease in friction coefficient. This behavior can be approximated by a linear function with a negative slope.

Similarly, L100X<sup>500kGy</sup>-EPDM shows the same behavior after steady state condition has been achieved. However, the slope is less than that for MP1100-EPDM. This clearly shows the influence of PTFE powders on the friction behavior of EPDM matrix. The higher friction values of MP1100-EPDM could be due to the direct interaction of the counter-body with EPDM. As shown in Fig. 39, the surface of MP1100-EPDM is the smoothest of all the investigated compounds due to its enhanced compatibility and excellent dispersion. There is almost no indication of PTFE particles on the surface. Only a few agglomerates are visible. Thus, there is a rare possibility for MP1100 PTFE powders to form a transfer film during sliding contact with counter-body. This results in a significantly higher friction coefficient throughout the testing time. On the other hand, all other composites show significantly lower friction values. This is due to the presence of PTFE agglomerates on the surface, which allows a direct interaction with the counter-surface once the EPDM layer is removed. This can be clearly seen in the sudden decrease in friction coefficients shown in Fig. 40. Moreover, a further decrease in the case of L100X<sup>500kGy</sup>-EPDM compared to L100X<sup>0kGy</sup>-EPDM and MP1200-EPDM is observed. This could be due to the interaction of the embedded PTFE agglomerates in wear track of L100X<sup>500kGy</sup>-EPDM with counter-body. This facilitates in easy sliding of the counter-body against a wear track covered with PTFE particles.

## Wear Behavior

Figure 41 shows the specific wear rate ( $k$ ) of PTFE-EPDM composites. As can be seen, specific wear rate responded in accordance with friction behavior. MP1100-EPDM with its significantly high friction coefficient suffered from higher wear rate. Similarly, L100X<sup>0kGy</sup>-EPDM and MP1200-EPDM, having low friction coefficients, show comparatively lower wear rates.

Figure 42 shows SEM micrographs of the wear scars of composites after repeated sliding of the counter-body. It can be seen that different wear mechanisms occur in different composites. In the case of L100X<sup>0kGy</sup>-EPDM, wear behavior is characterized by the detachment of PTFE agglomerates from EPDM due to its significantly poor compatibility with EPDM. At higher magnification, the SEM also shows the presence of flattened agglomerates. This indicates that PTFE powder may have been transferred to the counter-surface. However, in the case of L100X<sup>500kGy</sup>-EPDM, the wear track is smooth. It shows the presence of a significant amount of embedded PTFE agglomerates that have been flattened or abraded by repeated sliding of the counter-body. This is in accordance with the friction mechanism described before. The interaction of counter-body with PTFE agglomerates results in both the lowest wear rate and friction coefficient. In contrast, MP1100-EPDM shows a rough wear track due to the detachment of significantly large lumps from the top of the surface. The wear mechanism is

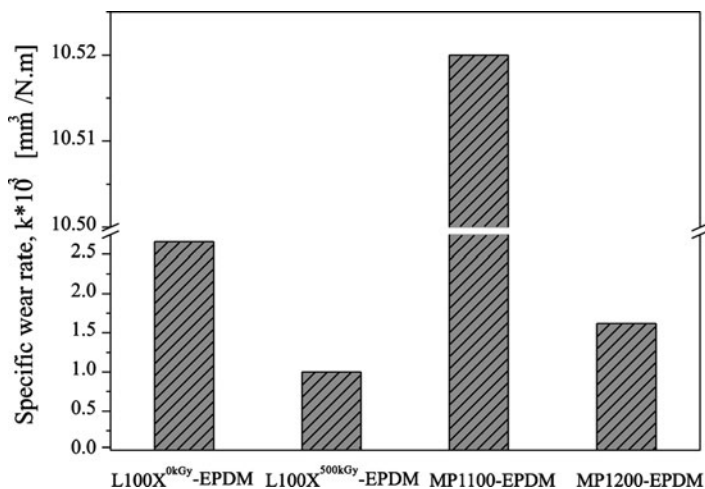
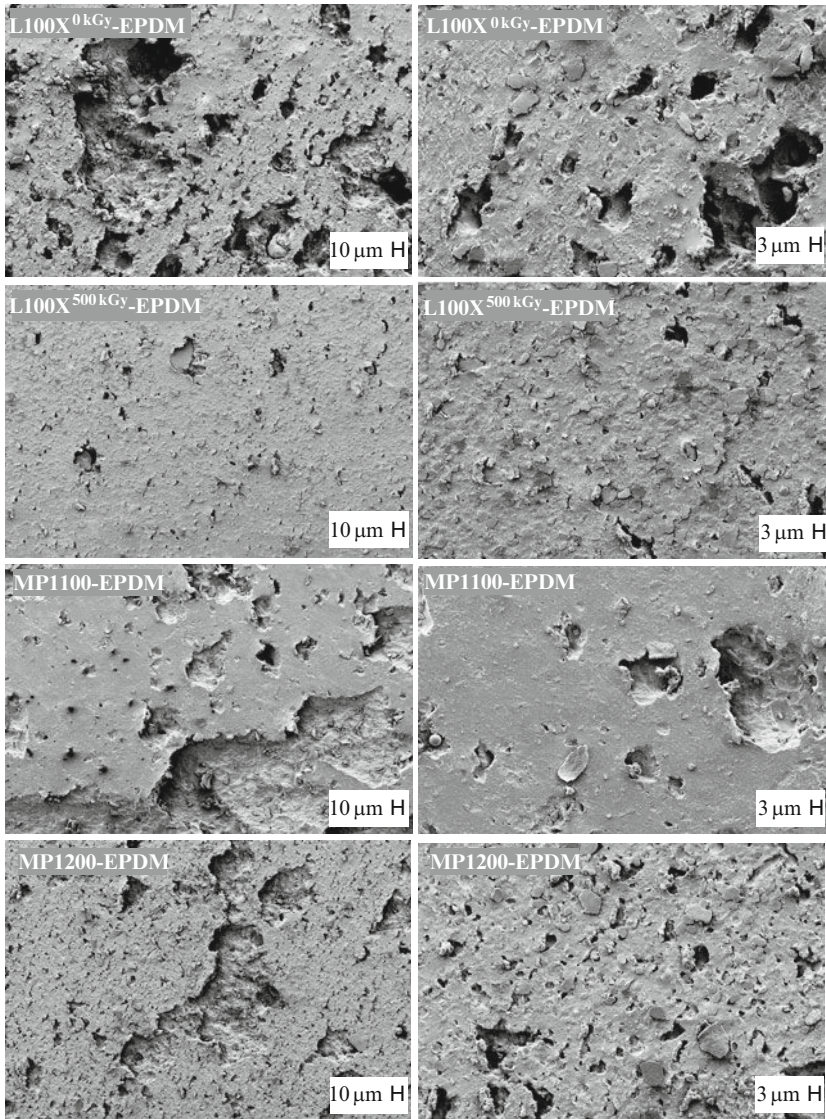


Fig. 41 Comparison of the specific wear rate ( $k$ ) of PTFE-EPDM composites

similar to the delamination type of wear that has occurred in the deep regions of EPDM. At higher magnification, one can observe that no PTFE agglomerates are visible for contact with counter-body. Thus, almost no PTFE has been transferred to the counter-surface. MP1200-EPDM suffered from a wear mechanism similar to that of MP1100-EPDM and L100X<sup>0kGy</sup>-EPDM. Comparatively smaller lumps than for MP1100-EPDM have been removed from the top of the surface. On the other hand, because MP1200 is bigger and less compatible, agglomerates are removed from EPDM, similar to the case for L100X<sup>0kGy</sup>-EPDM. One can observe the presence of these detached PTFE agglomerates on the wear track surface.

#### 4 Newly Developed PTFE-Coupled Chloroprene Composites

It has been discussed previously in detail that chemical coupling of the PTFE powder is a prerequisite for effective use of PTFE powder in rubber matrixes. Chemical coupling enhances the compatibility of PTFE powder and consequently results in better dispersion and, ultimately, in improvement of the final properties of the rubber compound. This section discusses a new class of chemically coupled PTFE-filled CR compounds. CR, with its inherently outstanding properties, is categorized as suitable for sealing and gaskets applications. CR rubber, being highly polar, is sufficiently deactivated by electronegative chlorine atoms so that the direct chemical coupling with PTFE powder by a radical coupling mechanism is not possible. A new approach to the coupling reaction mechanism is proposed that is based on the Lewis acid concept, which is also applicable to crosslinking of CR in



**Fig. 42** SEM micrographs of wear track (contact area) showing the wear mechanisms involved in different PTFE–EPDM composites. Images on the *right* are magnifications of those on the *left*

the presence of MgO and ZnO. Chemical coupling between CR and modified PTFE is based on the availability of special structures in CR (olefinic unsaturated 3,4-chloroprene structures) and the functional groups in PTFE (carboxylic acid groups). Some new findings and results that have not been previously investigated for CR rubber are reported.

### 4.1 Rheometric Characterization

Figure 43 show the curing rheographs of pure chloroprene (CR gum) and PTFE-reinforced CR composites. The two most important parameters obtained from curing curves are  $\Delta M$  and optimum curing time ( $t_{90}$ ). The maximum torque is closely related to the modulus of the rubber composites. The difference between maximum and minimum torque ( $\Delta M$ ) can be used as an indirect indication of the measure of an apparent crosslink density, while  $t_{90}$  is a useful estimate of the cure rate of a rubber composite. As can be seen,  $\Delta M$  and, thus, the crosslink density increase continuously with the increase in the irradiation dose used to modify the PTFE powder (Fig. 43). The results confirm that electron-modified PTFE powder also takes part in the crosslinking reaction and gives rise to the additional crosslink density. Both curing parameters ( $\Delta M$  and  $t_{90}$ ) increase with the increase in the irradiation dose. This is an important observation because both parameters are related to the effect of radiation-induced changes on the state of cure and the crosslinking density of CR composites. It can be observed that  $\Delta M$  values for all CR composites containing PTFE powder are higher than those for the CR gum. In addition,  $\Delta M$  increases with the use of increased irradiation dose for modifying the PTFE powder. PTFE<sup>500kGy</sup>-CR shows the highest  $\Delta M$  value, while PTFE<sup>0kGy</sup>-CR shows the lowest. For a qualitative assessment, it can be concluded that the apparent crosslink density increases due to irradiation of PTFE powder. PTFE<sup>500kGy</sup>-CR composite has the highest  $\Delta M$  and hence the highest apparent crosslink density. On the other hand, PTFE<sup>0kGy</sup>-CR has a value of  $\Delta M$  lower than that of CR composites containing irradiated PTFE powder.

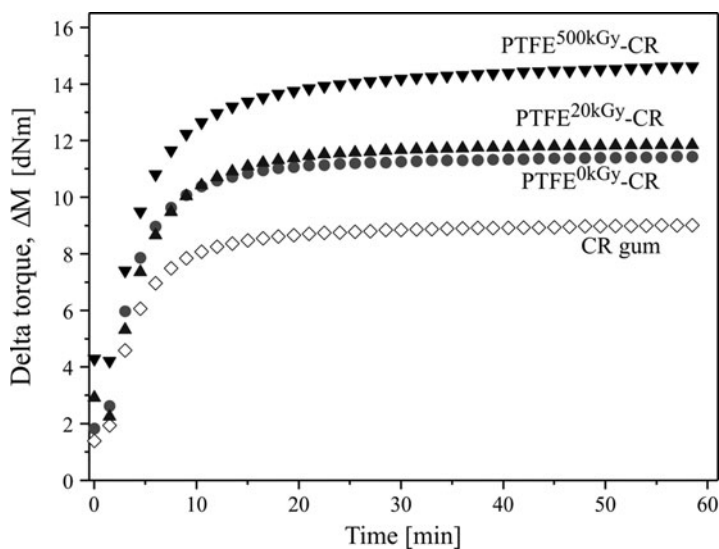
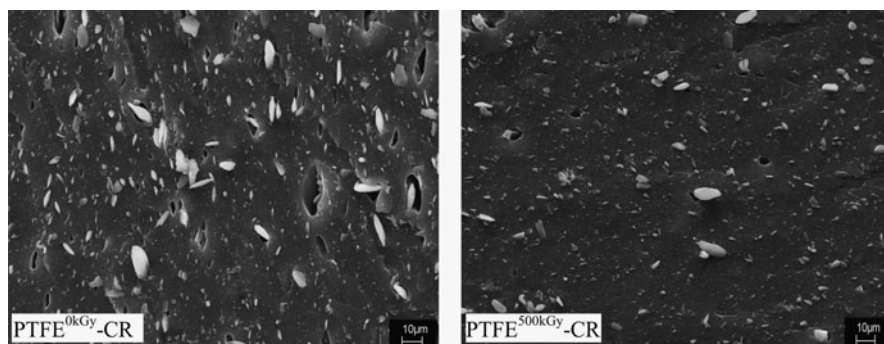


Fig. 43 Rheographs of PTFE-reinforced chloroprene composites in comparison with the pure chloroprene (CR gum)

## 4.2 Compatibility and Dispersion

SEM micrographs of the tensile fractured surfaces of PTFE<sup>0kGy</sup>-CR and PTFE<sup>500kGy</sup>-CR are shown in Fig. 44. The PTFE agglomerates are dispersed in the CR matrix without much agglomeration. The particle size, as shown in the images, varies considerably. The average size of large agglomerates is in the order of 10–15  $\mu\text{m}$ . The PTFE<sup>500kGy</sup>-CR composite surface is smooth and the agglomerates are embedded and homogeneously dispersed in the CR matrix (Fig. 44, right), whereas PTFE<sup>0kGy</sup>-CR shows the presence of large vacuoles on the fractured surface (Fig. 44, left).

This indicates that the PTFE particles are being pulled out of the matrix on application of stress. The microstructures of the corresponding CR composites measured by TEM are shown in Fig. 45. The enhanced interfacial compatibility of modified PTFE particles in PTFE<sup>500kGy</sup>-CR is clearly visible in the corresponding TEM micrographs. The modified agglomerate particles are embedded and partially enwrapped by the CR matrix. No clear and sharp interphase is



**Fig. 44** SEM micrographs of fractured surfaces of chloroprene reinforced with nonmodified (*left*) and modified (*right*) PTFE

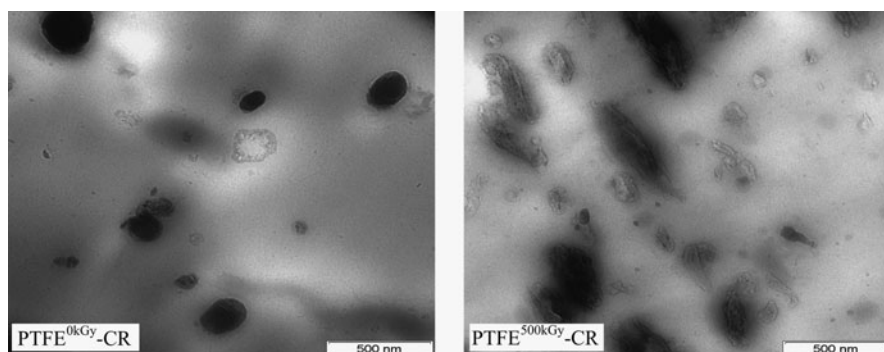


**Fig. 45** TEM micrographs of chloroprene reinforced with nonmodified (*left*) and modified (*right*) PTFE

visible between the two polymeric phases. Slightly light and dark regions around modified PTFE powder are an indication of a reinforced compatible interphase.

On the other hand, PTFE<sup>0kGy</sup>-CR (containing nonmodified PTFE powder) acts as a solid rigid body lacking interfacial compatibility with the CR matrix. The sharp interface distinctively separates the two incompatible polymers from each other. It is important to note that the filler particles in PTFE<sup>500kGy</sup>-CR, as compared to those in PTFE<sup>0kGy</sup>-CR, are slightly elongated and stretched in a specific direction. In addition to indicating strong adhesion or compatibility with the CR matrix, this also proves that the PTFE particles are soft and deformable. The modified PTFE particles, due to enhanced chemical coupling with CR, have been oriented under the application of strong shearing during reactive blending. However, the inert nonirradiated PTFE particles maintain the spherical shape even under high shearing.

### 4.3 Mechanical Properties

Typical stress–strain curves for the pure CR gum and the composites containing irradiated and nonirradiated PTFE powder are shown in Fig. 46. The addition of PTFE particles increases the elastic modulus of the CR matrix. In the presence of irradiated PTFE particles, the modulus of the CR matrix increases relative to that of a matrix containing nonirradiated PTFE particles.

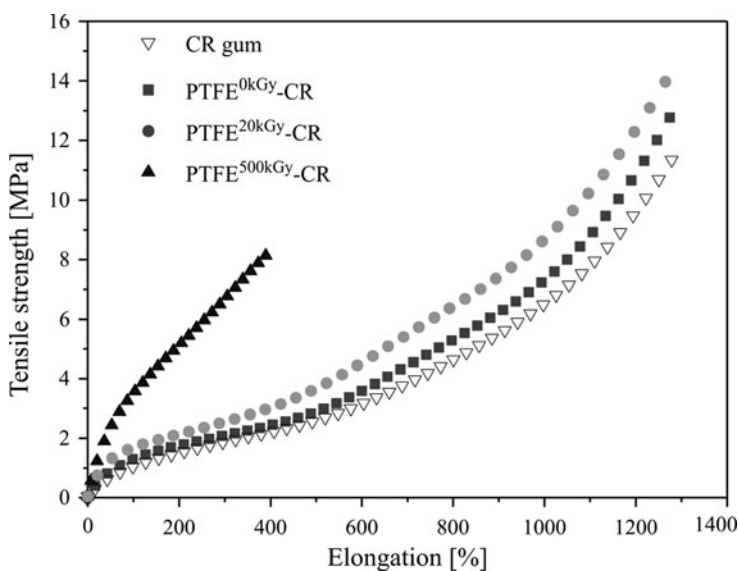


**Fig. 46** Stress–strain curves for the pure chloroprene rubber (CR gum) and PTFE-based chloroprene composites



Other interesting features of elastomeric networks can be revealed using the plots of the reduced stress,  $\sigma_{\text{red}} = \sigma/(\lambda - \lambda^{-2})$  against inverse extension ratio  $\lambda^{-1}$ . This can be analyzed from the stress–strain behavior described by a phenomenological expression suggested by Mooney [78] and Rivlin and Saunders [79]:

$$\frac{\sigma}{\lambda - \lambda^{-2}} = C_1 + C_2\lambda^{-1}, \quad (1)$$

where  $\sigma$  is the applied stress,  $\lambda$  is the extension ratio, and  $C_1, C_2$  are the Mooney–Rivlin (MR) constants related to the network structure and the flexibility of the network chains.  $C_1$  is directly proportional to the number of elastically active network chains per unit volume of the rubber. The elastically active crosslinking density is given by  $\nu = 2C_1/RT$ , where  $R$  is the gas constant and  $T$  is absolute temperature. The value of  $C_2$  can be related to the number of the elastically effective trapped entanglements, to the number of steric obstructions, and to other network defects.

In the case of filled systems, the two latter effects provide a substantial contribution to  $C_2$  compared with the influence of trapped entanglements [80]. For filled systems, the estimated or apparent crosslinking density can be analyzed with the help of the Mooney–Rivlin equation using the assumption that the hard filler particles do not undergo deformation. This means that the macroscopic strain is lower than the intrinsic strain (local elongation of the polymer matrix). Thus, in the presence of hard particles, the macroscopic strain is usually replaced by a true intrinsic strain:

$$\lambda = 1 + \varepsilon X, \quad (2)$$

where  $\varepsilon$  is the macroscopic elongation and  $X$  is an amplification factor. The latter can be defined as:

$$X = 1 + 2.5\phi_f + 14.1\phi_f^2, \quad (3)$$

where  $\phi_f$  is the volume fraction of the spherical filler particles. This definition is based on the Guth–Gold equation [81]:

$$G = G_0(1 + 2.5\phi_f + 14.1\phi_f^2), \quad (4)$$

where  $G_0$  is the modulus of the unfilled matrix. This equation is based on the Einstein's equation for the viscosity of a suspension of spherical rigid particles. Hence, the Guth–Gold equation takes into account the effect of hydrodynamic reinforcement arising from the inclusion of rigid particles into the polymer matrix. According to the Mooney–Rivlin equation, the plot of reduced stress,  $\sigma_{\text{red}} = \sigma/(\lambda - \lambda^{-2})$ , as a function of inverse extension ratio,  $\lambda^{-1}$ , should yield a linear curve, from which the values of  $C_1$  (y-intercept) and  $C_2$  (slope) can be readily obtained from the stress–strain curves [82].

### 4.3.1 Experimental Setup

A series of six stress–strain cycles with a crosshead rate of 600 mm/min was applied to specimens having a parallel length of 25 mm and a cross-section of  $1 \times 4 \text{ mm}^2$  on a tensile testing machine. The samples were continuously stretched in six hysteresis cycles up to 60% of their elongation at break values, as shown in Fig. 47. This procedure is an established one and widely practiced for elastomeric composites reinforced with fillers such as carbon black and silica, which tend to build a strong filler–filler network [83].

In the case of PTFE powder, a pronounced networking is not expected because of the microscopically large and chemically inert PTFE agglomerates. Therefore, it is expected that any contribution to the overall crosslink density should arise solely from the effective chemical coupling between the PTFE powder and the CR matrix. After the sixth cycle, a tensile test (results shown by the dotted line in Fig. 47) was performed with a cross-head rate of 25 mm/min in order to estimate the true deformation,  $\lambda$ , of the specimen. For this purpose, an optical 2D deformation analysis system based on a grating technique (ARAMIS from GOM, Germany) and coupled with a 1.3 megapixel camera was used. For optical analysis it is necessary to imprint a random pattern on the sample surface. ARAMIS software compares the optical images of different load steps to calculate the displacement and the deformation of the sample. A detailed description of the use of ARAMIS for deformation analysis is given in [84]. Figure 48 shows the schematics of the procedure adapted for estimating deformation in the specimen.

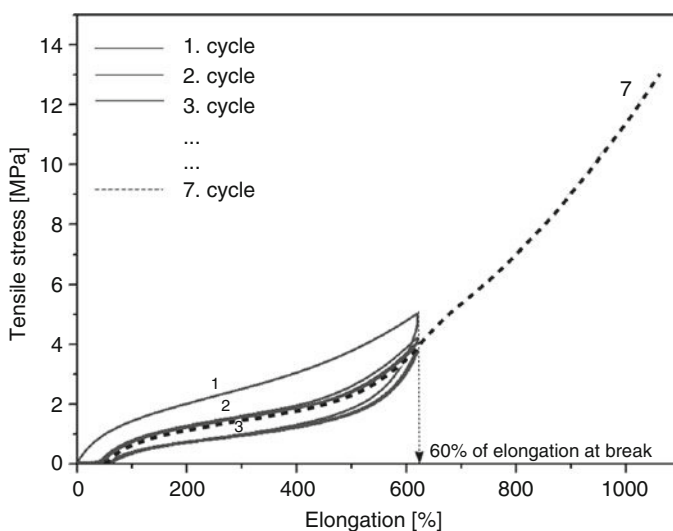


**Fig. 47** Typical stress–strain curves of PTFE-based chloroprene composites. The first six hysteresis cycles are shown with *solid lines*. The seventh curve (*dotted line*) was investigated using an optical method

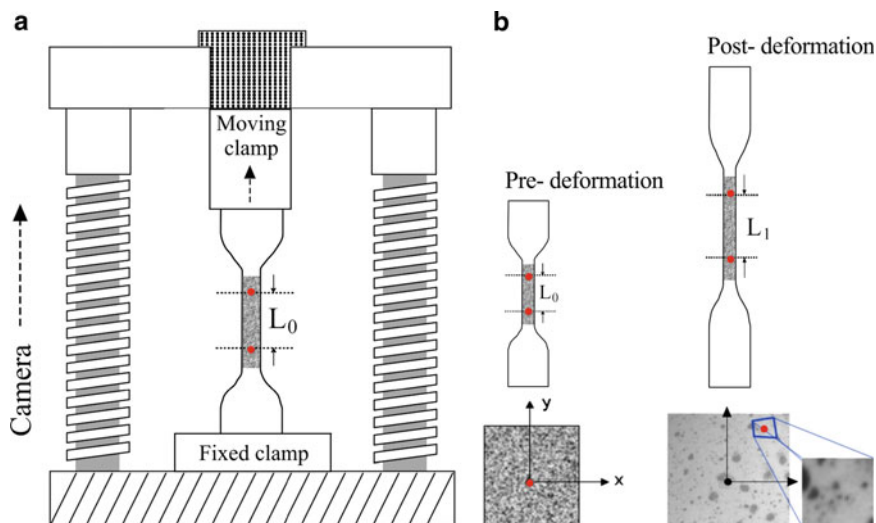


**Fig. 48** Schematics showing (a) the tensile testing rig holding the sample between clamps for uniaxial deformation and (b) deformation stages in the sample, recorded with an optical imaging system.  $L_0$  is the original length of the sample, and  $L_1$  the length after deformation

It should be considered that in the case of plotting  $\sigma_{\text{red}} = \sigma / (\lambda - \lambda^{-2})$  against inverse extension ratio ( $\lambda^{-1}$ ), the nominal stress  $\sigma$  is defined as the force divided by the undeformed cross-sectional area of the sample and  $\lambda$  is the extension ratio, defined as the ratio of deformed to the undeformed length of the sample stretched in the uniaxial direction (as shown in Fig. 3). For PTFE powder, the intrinsic strain is deduced from (2) by defining  $X = 1$ :

$$\lambda = 1 + \varepsilon. \quad (5)$$

This assumption is based on the fact that PTFE agglomerates are soft and deformable particles in comparison to conventional (hard) fillers such as carbon black and silica for which (2) was originally derived. Morphological analysis (shown in Fig. 5) reveals that PTFE agglomerates can be considered as soft deformable particles.

Therefore, it is assumed that the particles are deformed with the same extension ratio as applied to the bulk sample. On plotting the reduced stress ( $\sigma_{\text{red}}$ ) against inverse extension ratio ( $\lambda^{-1}$ ) (as shown in Fig. 49), the curves obtained are found to be linear in the intermediate region. The extrapolated intercept with the y-axis ( $C_1$ ) is identified as the contribution arising from the chemical crosslinks. For the studied composites the value of  $C_1$  varies according to the degree of chemical coupling between PTFE powder and CR matrix. Figure 49a shows the comparison of the unfilled CR (CR gum) and CR filled with 10, 20, and 30 phr of nonirradiated PTFE powder. It can be seen that all curves show a similar value of  $C_1 \cong 0.22$  MPa at the y-axis intercept. This signifies that nonirradiated PTFE powder is not chemically

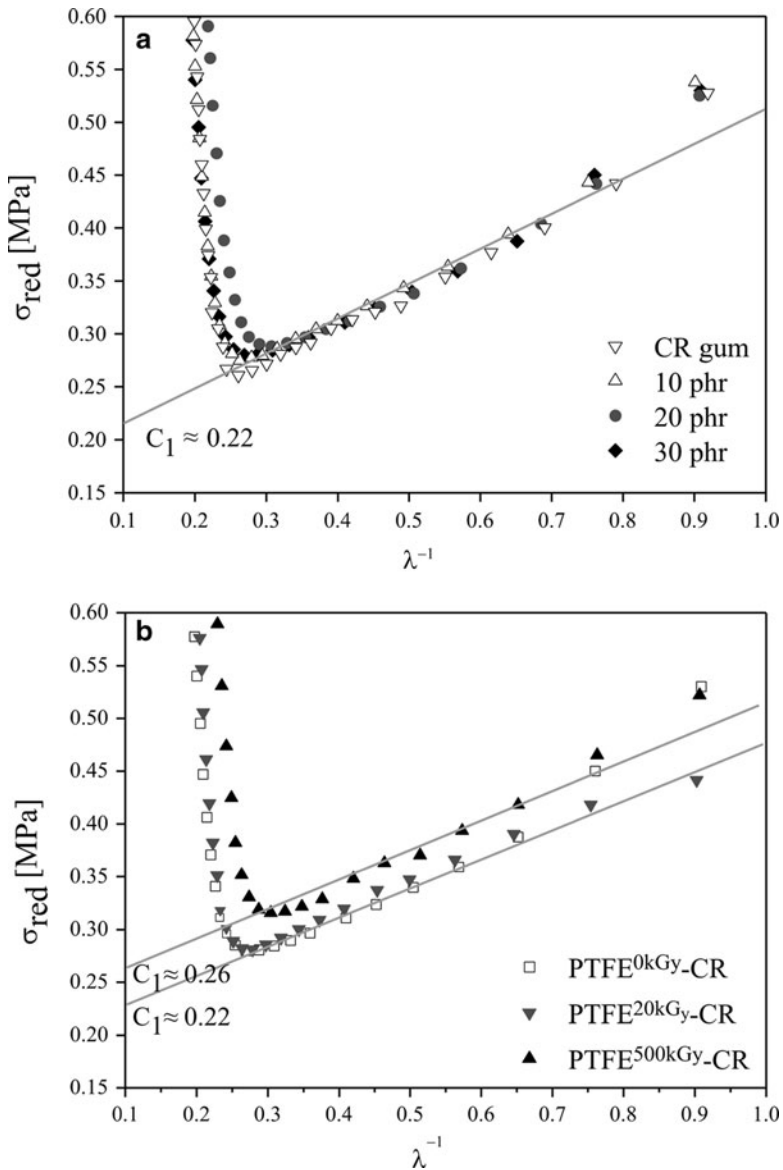


**Fig. 49** Mooney–Rivlin plots of reduced stress ( $\sigma_{red}$ ) against deformation ( $\lambda$ ) for (a) CR gum and PTFE<sup>0kGy</sup>-CR at 10, 20, and 30 phr loading; and (b) comparison of PTFE<sup>500kGy</sup>-CR with PTFE<sup>0kGy</sup>-CR and PTFE<sup>20kGy</sup>-CR.  $C_1$  is the contribution to  $\sigma_{red}$  arising from chemical crosslinking

coupled to the CR matrix, as expected for these two incompatible polymers. Additionally, as the network chains are stretched, a considerable decrease in reduced stress is observed for all CR composites. This effect is due to reduction in the effectiveness of entanglements due to slippage. At higher elongations, large

and rather abrupt upturns in the reduced stress can be seen. This increase in reduced stress is attributed to the finite extensibility of the network chains [85] and to the induced crystallization of elastomer under stretching by molecular orientation at high strains [86]. Figure 49b shows the comparison of the  $C_1$  values of PTFE<sup>0kGy</sup>-CR, PTFE<sup>20kGy</sup>-CR, and PTFE<sup>500kGy</sup>-CR for 30 phr PTFE loading. It is worth noting that PTFE<sup>500kGy</sup>-CR shows a higher  $C_1$  value than PTFE<sup>0kGy</sup>-CR, while there is no influence on the chemical crosslink density of PTFE<sup>20kGy</sup>-CR due to a significantly lower irradiation dose. However, the  $C_1$  contribution in the case of PTFE<sup>500kGy</sup>-CR increases due to the formation of a higher number of chemical crosslinks between PTFE powder and the CR matrix. The significant improvement in the mechanical and dispersion properties in the case of PTFE<sup>500kGy</sup>-CR is due to the higher degree of chemical coupling.

#### 4.4 Chemical Coupling Investigations

Samples (without adding curatives) at high shear blending of PTFE powder and CR in the internal mixer were produced as described in Sect. 3.1. PTFE powder was separated from soluble CR and analyzed for FTIR investigation. FTIR analysis requires the solution to be completely free of CR gels. About 5 g of CR-PTFE blend was dissolved in chloroform at 50°C and afterwards centrifuged. The solution above the solid sediment was later decanted. Chloroform was again added to the solid residue and the mixture stirred overnight. The solution was centrifuged and decanted from the solid residue. This process was repeated five times. Following the cleaning procedure, methanol was added to the solid residue and stirred vigorously overnight. The methanol solution was again decanted and the solid residue dried under vacuum at 80°C. PTFE powder was separated from CR without the formation of insoluble gels. The solid PTFE powder was pressed into 10 μm thin films and investigated using FTIR spectroscopy. Figure 50 shows the FTIR spectra of CR gum, 500 kGy-irradiated PTFE powder, PTFE<sup>500kGy</sup>-CR blend, and PTFE<sup>0kGy</sup>-CR blend. As can be seen in Fig. 50a for the CR gum, the characteristic CH-stretching vibrations occur at 3,023, 2,917, and 2,843 cm<sup>-1</sup>, whereas the bending vibration can be seen at 1,443 and 1,430 cm<sup>-1</sup>.

Peaks at 1,693 and 1,660 cm<sup>-1</sup> indicate stretching of the C=C double bonds in the CR matrix. Comparing 500 kGy-irradiated PTFE powder and its PTFE<sup>500kGy</sup>-CR blend (as shown in Fig. 50b), a significantly stronger CR absorption band in the 1,660 cm<sup>-1</sup> region due to the stretching of the C=C bond in CR is observed. In the case of 500 kGy-irradiated PTFE powder no such absorption bands are visible.

Therefore, this absorption in the FTIR spectra is considered to be an indirect indication of the chemical coupling of CR to irradiated PTFE powder. The presence of CH absorption bands in PTFE<sup>500kGy</sup>-CR in the region of 3,100–2,800 cm<sup>-1</sup> is not indicative of the coupling of CR to PTFE powder. These bands might have originated from the materials and solvents utilized in the centrifugation and

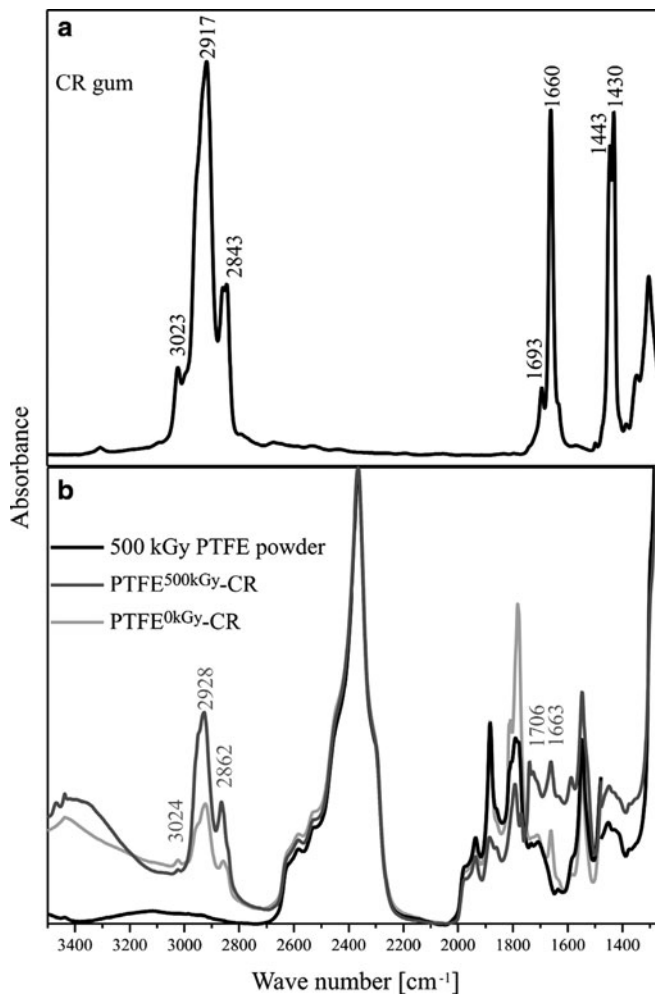


**Fig. 50** FTIR spectra of (a) CR gum and (b) 500 kGy-irradiated PTFE powder, PTFE<sup>500kGy</sup>-CR, and PTFE<sup>0kGy</sup>-CR

extraction processes. The presence of stronger CR absorptions in the PTFE<sup>500kGy</sup>-CR blend spectrum as opposed to the PTFE<sup>0kGy</sup>-CR spectrum provides an indication of a stronger chemical coupling between the irradiated PTFE powder and the CR matrix. The absorption bands in PTFE<sup>0kGy</sup>-CR at 1,661 cm<sup>-1</sup> are significantly weaker than in the PTFE<sup>500kGy</sup>-CR blend. The FTIR investigations provide only indirect evidence that irradiated PTFE powder is chemically coupled to the CR matrix. Further conclusive investigations are required to obtain direct evidence of the existence and nature of the chemical coupling between irradiated PTFE powder and the CR matrix.

## 4.5 Possible Chemical Coupling Mechanism

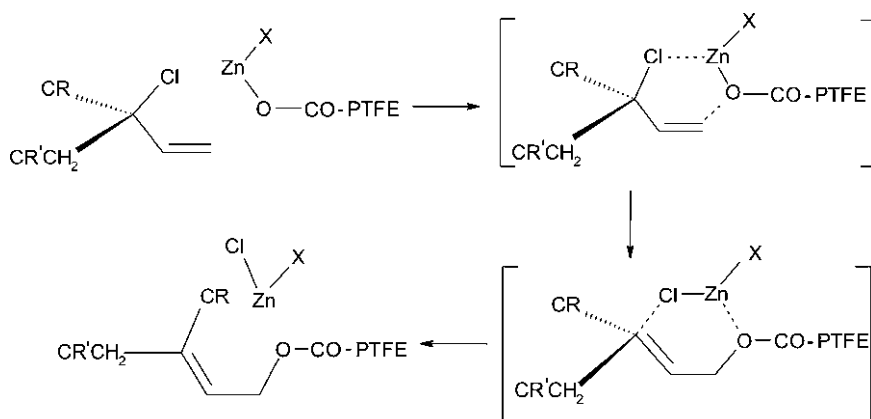
Although the vulcanization mechanisms are well established for other elastomers, vulcanization of CR is a complicated process and has not been, until now, well understood. To our knowledge, there are only a few studies that discuss the vulcanization chemistry of CR [87]. The vulcanization mechanism for CR proposed in these pioneering studies was considered to be a planar three-component reaction mechanism in which the structural and special peculiarities were fully taken into consideration. Here, we propose an explanation of the chemical coupling mechanism between the CR matrix and electron-modified PTFE powder based on the similar vulcanization mechanism of CR. Such a mechanism can also be applied to vulcanization of CR in the presence of a ethylenethiourea compound.

The chemical coupling between the CR matrix and PTFE powder is based on the presence of special structures in CR (olefinic unsaturated 3,4-chloroprene) and the functional groups (carboxylic acid) in PTFE. As mentioned previously,  $-\text{COOH}$  groups at the surface of PTFE particles are generated during irradiation of PTFE if carried out in the presence of atmospheric conditions. However, these  $-\text{COOH}$  groups are highly inert and unlikely to initiate a coupling reaction with CR if unaided. As a prerequisite, similar to the initiation of vulcanization of CR, these  $-\text{COOH}$  groups require activation by reaction with Zn or Mg salts to initiate the chemical coupling with CR. During the vulcanization process, the  $\text{ZnCl}_2$  acts as a strong Lewis acid and serves to accelerate the reaction. Similarly, activation of PTFE powder bearing  $-\text{COOH}$  groups ( $\text{PTFE}^{\text{COOH}}$ ) at the surface can be achieved with  $\text{ZnO}$  either prior to or during the reactive mixing with CR. However, it should be realized that the latter procedure might result in either the premature vulcanization of the CR matrix or in the formation of successful functionalization of PTFE powder, i.e.,  $\text{PTFE}^{\text{COOZn-X}}$ , where X can be  $-\text{OH}$ ,  $-\text{Cl}$ , or another  $\text{PTFE}^{\text{COO-}}$ . The degree of reaction depends on the processing conditions and kinetics of these reaction processes.

The proposed mechanism is based on a two-component chemical coupling reaction following the chemical bonding (electron redistribution). Figure 51 explains the suggested reaction mechanism, where the interaction of functionalized PTFE powder ( $\text{PTFE}^{\text{COOZn-X}}$ ) with the CR matrix during shear blending results in the formation of a six-member ring (Fig. 51, top right). Further, the corresponding chemical interaction between the different atoms results in the formation of an in situ conjugated transfer state. After the redistribution of electrons, the formation of a chemically coupled CR-PTFE molecule is then realized with the elimination of the  $\text{ZnClX}$  compound (Fig. 51, below right). The molecular system is then stabilized by the transformation of the carbon atom into CR position 2 from a tetrahedron to a planar configuration.

## 5 Summary

PTFE powder can be incorporated as a reinforcing additive in different rubber matrixes if enhanced mechanical, friction, and wear properties are desired. However, the different friction, wear, and chemical coupling mechanisms in



where X is -OH, -Cl or PTFE<sup>COO-</sup>)

**Fig. 51** Possible reaction mechanism of modified PTFE powder and chloroprene rubber

PTFE-based rubber compounds are responsible for their unique behavior. The morphology, dispersion, and chemical coupling of the PTFE powder are critically dominant in controlling friction and wear as well as the mechanical properties. In order to study this aspect, the vulcanizates were produced with hardness values higher than the critical 58 Shore (A) by crosslinking PTFE-filled EPDM compounds using electron irradiation instead of peroxide. This was achieved by monitoring the influence of increasing crosslinking irradiation dose on the hardness of the vulcanizate. The friction and wear properties of L100X, MP1100, and MP1200 EPDM vulcanizates with comparable hardness but different morphology, dispersion and chemical coupling were investigated. MP1100-EPDM vulcanizate maintains excellent dispersion but shows significantly poor friction and wear properties. However, MP1200-EPDM and L100X<sup>0kGy</sup>-EPDM show comparatively improved friction and wear properties but are characterized by poor dispersion and chemical compatibility of the PTFE powder with EPDM. On the other hand, L100X<sup>500kGy</sup>-EPDM shows significantly improved physical, dynamic mechanical, and tribological properties. This is attributed to the specific chemical coupling between L100X<sup>500kGy</sup> PTFE powder and EPDM. The enhanced friction and wear properties results from the embedment of L100X<sup>500kGy</sup> PTFE agglomerates in the EPDM matrix along with its ability to transfer PTFE to the wear track. As such, a constant source of lubrication due to the PTFE transfer phenomenon is formed at the counter-surface, which helps in easy sliding of the counter-body against a wear track.

It has been shown that, with the help of irradiation, the incompatible PTFE surface can be functionalized to enhance its compatibility with rubber matrixes. A loading of 30 phr PTFE has been found sufficient to improve the mechanical and friction properties. Furthermore, the influence of radiation-induced free radicals and structural alterations on the properties of rubber compounds has been investigated. The radicals generated during irradiation are available for chemical coupling



with the unsaturated olefinic double bonds in EPDM. Low-temperature shear mixing of electron-modified PTFE powder with rubber produces PTFE-coupled rubber compounds with the desired mechanical properties.

The use of irradiated PTFE powder in EPDM gives enhanced mechanical properties as compared to composites containing nonirradiated PTFE. The existence of compatibility between modified PTFE powder and EPDM is indirectly revealed by TEM, DSC, and SEM. TEM shows that modified PTFE powder (500 kGy-irradiated) is obviously but partially enwrapped by EPDM as compared to nonirradiated PTFE powder. This leads to a characteristic compatible interphase around the modified PTFE. The resultant chemically coupled PTFE-filled EPDM demonstrates exceptionally enhanced mechanical properties. Crystallization studies by DSC also reveal the existence of a compatible interphase in the modified-PTFE-coupled EPDM. The synergistic effect of enhanced compatibility by chemical coupling and microdispersion of PTFE agglomerates results in improvement of mechanical properties of PTFE-coupled EPDM compounds. In summary, an effective procedure both for the modification of PTFE powder as well as for the crosslinking of PTFE-filled EPDM by electron treatment has been developed for the preparation of PTFE-coupled EPDM compounds with desired properties.

PTFE powder was also incorporated into CR rubber. The use of modified PTFE powder as a reinforcing additive in CR results in chemical coupling with CR. Significant improvement in properties by using a higher irradiation dose to modify the PTFE powder was observed. A new approach to the chemical coupling reaction mechanism is proposed. The coupling between CR and PTFE is based on the availability of special structures (olefinic unsaturated 3,4-chloroprene) in CR and the functional groups ( $-\text{COOH}$  groups) in PTFE. These  $-\text{COOH}$  groups were chemically activated by Zn or Mg salts for chemical coupling with CR. This can be done either by activating  $\text{PTFE}^{\text{COOH}}$  with Zn salts prior to reactive mixing with CR or during mixing of  $\text{PTFE}^{\text{COOH}}$  and CR in the presence of ZnO in the mixing chamber. The latter procedure for activating  $\text{PTFE}^{\text{COOH}}$  might result either in premature vulcanization of CR with ZnO or in formation of  $\text{PTFE}^{(\text{COOZn})-X}$ . The degree of the reactions depends on processing parameters and the kinetics of these reaction processes. In conclusion, PTFE-coupled rubber compounds prepared by the described approach offer the potential use of PTFE powder in a wide range of rubber compounds for special purpose applications. Accordingly, they are promising in various fields.

The state of the art in friction and wear of PTFE-filled rubbers include the effects of many important system parameters, such as the composition of the rubber formulation, particle dispersion, bulk mechanical properties, ability of transfer film formation, and the chemistry between PTFE powder and the rubber matrix. Although the present study has explicitly highlighted the potential of PTFE powder in rubber matrixes with significant property improvements in the friction, wear, and physical properties, it has simultaneously opened a new field regarding the use of PTFE powder in rubber compounds, with some challenging tasks for chemists, engineers, and material scientists.

## References

1. Bock E (2004) GAK Gummi Fasern Kunststoffe 3:180
2. Gangal SV (1989) Tetrafluoroethylene polymers. In: Mark HF, Bikales NM, Overberger CG, Menges G (eds) Encyclopedia of polymer science and engineering, vol 16. Wiley, New York, p 577
3. Cottrell TL (1958) The strength of chemical bonds. Butterworth, London
4. Sheppard WA, Sharts CM (1969) Organic fluorine chemistry. W. A. Benjamin, New York
5. Bunn CW, Cobbold AJ, Palmer RP (1958) J Polym Sci 28:365
6. Pierce RHH, Clark ES, Whitney JF, Bryant WMD (1956) Crystal structure of polytetrafluoroethylene. Abstract of papers, 130th meeting of the American Chemical Society, Atlantic City, 9S
7. Doban RC, Sperati CA, Sandt BW (1955) Soc Plastic Eng 11:30
8. Scheirs J (1997) Modern fluoropolymers. Wiley, New York
9. Cheng S, Kerluke DR (2003) Radiation processing for modification of polymers. IBA Advanced Materials Division, San Diego
10. Khan AA, Stewart CW (1984) US patent 4469864
11. Dorschner H, Lappan U, Lunkwitz K (1998) Nucl Instrum Methods Phys Res 139:495
12. Lappan U, Geißler U, Lunkwitz K (2000) Radiat Phys Chem 59:322
13. Lunkwitz K, Brink HJ, Handte D, Ferse A (1989) Radiat Phys Chem 33:523
14. Lunkwitz K, Lappan U, Scheler U (2004) J Fluorine Chem 125:863
15. Lappan U, Geißler U, Lunkwitz K (1999) J Appl Polym Sci 74:1571
16. Lappan U, Lunkwitz K (1995) Zeitschrift für Physikalische Chemie 191:209
17. Bürger W, Lunkwitz K, Pompe G, Petr A, Jehnichen D (1993) J Appl Polym Sci 48:1973
18. Lehmann D, Hupfer B, Lappan U, Pompe G, Häußler L, Jehnichen D, Janke A, Reinhardt R, Lunkwitz K, Franke R, Kunze K (2002) Designed Monom Polym 5:317
19. Lehmann D, Klüpfel B (2005) DE Patent 10 2004 016 873 A1
20. Lehmann D, Klüpfel B (2005) WO Patent 2005/042599 A1
21. Lehmann D, Hupfer B, Lappan U, Geißler U, Reinhardt R, Lunkwitz K (2000) Materialwissenschaft Werkstofftechnik 31:666
22. Klüpfel B, Lehmann D, Heinrich G, Linhart C, Haberstroh E, Kunze K, Hufenbach W, Dallner C, Künkel R, Ehrenstein GW (2005) Kautschuk Gummi Kunststoffe 58:226
23. Haberstroh E, Linhart C, Epping K, Schmitz T (2006) Kautschuk Gummi Kunststoffe 59:447
24. Crandell WH (1955) Rubber World 133:236
25. Kaufman MH, Gonzales J (1968) Rubber Chem Technol 41:527
26. Magner LM, Punderson JO (1969) US patent 3484503
27. Nash HC, Kohn EJ (1963) Studies on reducing the surface friction of elastomers. Naval Research Laboratories, Washington, DC
28. Paulus GF, Huron P (1966) US Patent 3293203
29. Kaufman MH (1976) US Patent 3940455
30. Morita S (1983) US Patent 4387168
31. Peters WE (1986) US Patent 4596839
32. Peters WE (1987) WO Patent 87/03515
33. Dillon JA (1988) WO Patent 88/04982
34. Rubin EA (1997) WO Patent 97/03812
35. Gwidon W, Stachowiak W, Batchelor WA (2001) Engineering tribology, 2nd edn. Butterworth-Heinemann, Oxford
36. Bunn CW, Howells ER (1954) Nature 4429:549
37. Burriss DL, Boesl B, Bourne GR, Sawyer WG (2007) Macromol Mater Eng 292:387
38. Schallmach A (1958) Wear 1:384
39. Schallmach A (1963) Wear 6:375
40. Moore DF, Geyer W (1972) Wear 22:113

41. Moore DF, Geyer W (1974) *Wear* 30:1
42. Barquins M, Roberts AD (1986) *J Phys D* 19:547
43. Briggs GAD, Briscoe BJ (1975) *Wear* 35:357
44. Persson BNJ (2001) *J Chem Phys* 115:3840
45. Heinrich G (1997) *Rubber Chem Technol* 70:1
46. Heinrich G, Dumler HB (1998) *Rubber Chem Technol* 71:53
47. Heinrich G, Klüppel M, Vilgis TA (2000) *Comput Theoret Polym Sci* 10:53
48. Klüppel M, Heinrich G (2000) *Rubber Chem Technol* 73:578
49. Berger HR, Heinrich G (2000) *Kautsch Gummi Kunst* 53:200
50. Persson BNJ, Tartaglino U, Albohr O, Tosatti E (2005) *Phys Rev B* 71:035428
51. Persson BNJ, Tartaglino U, Tosatti E (2004) *Kautsch Gummi Kunst* 57:532
52. Bjerk R, Brandon W, Engelkin F, Jero J (1975) US patent 3898361
53. Scher H, Ungar SI (1983) US patent 4400423
54. Bjerk R, Brandon W, Engelkin F, Jero J (1977) US patent 4045402
55. Defrank MP (1978) US patent 4131590
56. Gatos KG, Kameo K, Karger-Kocsis J (2007) *Express Polym Lett* 1:27
57. Karger-Kocsis J, Felhös D, Thomann R (2008) *J Appl Polym Sci* 108:724
58. Felhös D, Karger-Kocsis J, Xu D (2008) *J Appl Polym Sci* 108:2840
59. Karger-Kocsis J, Mousab A, Major Z, Békési N (2008) *Wear* 264:359
60. Felhös D, Karger-Kocsis J (2008) *Tribol Int* 41:404
61. El-Tayeb NSM, Nasir RMD (2007) *Wear* 262:350
62. Koenen A, Sanon A (2007) *Tribol Int* 40:1484
63. Golden JH (1960) *J Polym Sci* 45:534
64. Hagiwara M, Tagawa T, Amemiya H, Araki K, Shinohara L, Kagiya T (1976) *J Polym Sci* 14:2167
65. Fisher WK, Corelli JC (1981) *J Polym Sci* 19:2465
66. Häussler L, Pompe G, Lehmann D, Lappan U (2001) *Macromol Symp* 164:411
67. Pompe G, Häussler L, Pötschke P, Voigt D, Janke A, Geißler U, Hupfer B, Reinhardt G, Lehmann D (2005) *J Appl Polym Sci* 98:1308
68. Dluzneski PR (2001) *Rubber Chem Technol* 74:451
69. Endstra WC, Wreemann CTJ (1993) Peroxide crosslinking of EPDM rubbers. In: Cheremisinoff NP (ed) *Elastomer technology handbook*. CRC, Boca Raton
70. Tanaka K, Kawakami S (1982) *Wear* 79:221
71. Lancaster JK (1968) *J Phys D* 1:549
72. Yang ACM, Ayala JE, Bell A, Scott JC (1991) *Wear* 146:349
73. Vaziri M, Spurr RT, Scott FH (1988) *Wear* 122:329
74. Tewari US, Bijwe J (1991) *Tribol Int* 24:247
75. Rajesh JJ, Bijwe J, Tewari US (2001) *J Mater Sci* 36:351
76. Bijwe J, Awtade S, Satapathy BK, Ghosh AK (2004) *Tribol Lett* 17:187
77. Pigors O (1999) *Werkstoffe in der Tribotechnik: Reibung, Schmierung und Verschleißbeständigkeit von Werkstoffen und Bauteilen*. Dt.Verl.f.Grundst.ind, Leipzig
78. Mooney M (1940) *J Appl Phys* 11:582
79. Rivlin RS, Saunders DW (1951) *Philos Trans R Soc Lond Ser A* 243:251–258
80. Heinrich G, Vilgis TA (1993) *Macromolecules* 26:1109
81. Guth E, Gold O (1938) *Phys Rev* 53:322
82. Eisele U, Müller HK (1990) *Kautschuk Gummi Kunststoffe* 43:9
83. Heinrich G, Klüppel M, Vilgis TA (2002) *Curr Opin Solid State Mater Sci* 6:195
84. Lomov SV, Boisse P, Deluycker E (2008) *Compos Appl Sci Manuf* 39:1232
85. Treloar LRG (2005) *The physics of rubber elasticity*, 3rd edn. Oxford University Press, New York
86. Mark JE, Erman B (1988) *Rubber elasticity. A molecular primer*. Wiley, New York
87. Johnson PR (1976) *Rubber Chem Technol* 49:650

# Index

## A

- Accelerators, 27, 96, 128
- Acetylene-plasma-coated carbon black, 207
- Acrylic rubber (ACM), 7, 24, 35, 42, 235
  - adhesion, 57
- Acrylonitrile butadiene rubber (NBR), 15, 94, 251
- Adhesion, 57
- AFM, 10, 48, 73, 223
- Alloys, 219
- Autohesive tack, 60

## B

- Barrier properties, 53
- BIMS, 43, 60
- Bis-alkylation, 146
- Bis(triethoxysilylpropyl-tetrasulfan) (TESPT), 105, 128
- Blends, 167
- tert-Butyl cumyl peroxide (TBCP), 227
- 1-(2-tert-Butylperoxyisopropyl)–3-isopropenyl benzene (TBIB), 227

## C

- Calcium carbonate, 1, 37, 232, 238
- Carbon black, 5, 26, 86, 97, 103, 136, 167, 183, 190
  - rubber, polyacetylene-coated, 207
- Carbon nanofibers (CNFs), 36
- Carbon nanotubes (CNTs), 6, 37, 61, 85, 87, 139, 179, 238
- Carboxylated nitrile rubber (XNBR), 89, 164
- Chemical coupling, 249
- Chlorinated polyethylene (CPE), 34
- Chlorodifluoromethane, 253
- Chloroform, 253
- Chloroprene rubber (CR), 99, 251, 295
  - EPDM, 137
  - XNBR, 143

- Cloisites, 13, 34, 72
- Crosslinking, 7, 35, 54, 84, 137, 226, 236, 288
  - density, 64, 102, 144
  - electron irradiation, 288
  - ionic, 89, 112
  - peroxide, 127
  - sulfur, 128
  - thermal, 145
- N*-Cyclohexyl benzothiazole sulfenamide (CBS), 180

## D

- Debonding, 59, 231
- Deformation behavior, 222
- Degradation, 36, 49, 94, 229, 256, 272
- Delamination, 8, 54, 73, 131, 133, 295
- Density functional theory (DFT), 75
- 2,4-Diallyloxy–6-tert-butylperoxy–1,3,5-triazine (DTBT), 226
- Di(tert-butylperoxyisopropyl) benzene (DTBPIB), 225
- Dicumyl peroxide (DCP), 225
- Dielectric relaxation, 114
- Dimethyloctyl phenol, 224
- Divinyl benzene (DVB), 236
- Dynamic mechanical analysis (DMA), 38
- Dynamic mechanical thermal analyzer (DMTA), 109
- Dynamic vulcanization, 219

## E

- Elastomers, 1, 249
  - thermoplastic, 219
- Electrical conductivity, 51
- Electromagnetic interference (EMI), 51
- Electron beam (EB) modification, 244, 249
- Electron irradiation, 252
- EMI shielding, 51

- Epoxidized natural rubber (ENR)/silica, 7, 24  
 Epoxy resin, 235  
 Ethyl acrylate–butyl acrylate–acrylic acid, 57  
 Ethylene– $\alpha$ -olefins, 228  
 Ethylene octene, metallocene-type, 234  
 Ethylene propylene (EP), 259  
 Ethylene propylene diene methylene rubber (EPDM) rubber, 5, 96, 167, 169, 251  
 – PTFE-filled, 252  
 Ethylene propylene rubber (EPR), 6, 137, 228  
 Ethylene vinyl acetate (EVA), 34, 76, 228  
 2-Ethylidene norbornene (ENB), 224  
 Exfoliation, 8  
 – quantification, 62
- F**  
 Filler–filler interaction (Payne effect), 43, 112, 140, 198, 202, 207, 231  
 Finite element modeling (FEM), 76, 222  
 Flame retardancy, 1, 14  
 Flory–Rehner network theory, 64  
 Fluorocarbon elastomer (FKM), 15, 24, 45  
 Fluoroelastomer, clay, 56  
 – nanocomposites, mechanical properties, 31  
 Fluoro-hectorite, 87  
 Friction, 249  
 Fullerene carbon black (FS), 208  
 Fullerene soot EP-P434 183, 190
- G**  
 Gas barrier properties, 54  
 Gas permeation, 56  
 Gas phase EPDM (GEPDM), 228  
 Gas-impermeable nanoclay, 54
- H**  
 Hectorite, 87  
 Hexamethoxy methylmelamine (HMMM), 104  
 High resolution transmission electron microscopy (HRTEM), 4  
 HNBR/SP, 32  
 Hyberbranched polyols (HBPs), 62  
 Hydrogen fluoride, 253  
 Hydrogenated nitrile butadiene rubber (HNBR)–nanoclay, 8  
 Hydrogenated styrenic block copolymer, modified (mHSBC), 237
- I**  
 Ionic polymerization, 172  
 Isoprene–butadiene rubber (IBR), 136
- J**  
 Johnson–Kendall–Roberts (JKR), 11
- L**  
 Latex-in-melt mixing, 18  
 Lauryl methacrylates (LMA), 236  
 Layered double hydroxides (LDHs), 85  
 Limiting oxygen index (LOI), 163  
 Liquid rubber adhesion, 58
- M**  
 Mechanical properties, 249  
 Melt mixing, 15, 18, 125, 131, 243  
 Metal oxides, 1, 37  
 Modulus reduction factor (MRF), 7  
 Molecular dynamic (MD) models, 75  
 Montmorillonite, 18, 85, 87  
 Mullins effect, 232  
 Multiscale methods, 76  
 MWCNT, 41
- N**  
 Nanoassembly exfoliation, quantification, 62  
 Nanocomposites, 1, 85  
 Nanofibers, 1, 37  
 Nanofillers, 1, 44, 50, 87  
 Nanosilica, 24, 31, 34, 42, 85, 222, 238  
 Nanotubes, 1, 51, 77, 84, 139, 179, 238  
 Natural rubber (NR), 15, 69, 96, 140, 169, 180, 251  
 – epoxidized, 7, 136, 144  
 Neutron scattering, 4  
 Nitrile rubber (NBR), 89, 94, 130, 137, 224  
 Nylon–6 44  
 – clay, 17, 26  
 – EPDM, 223  
 – PVF, 136
- O**  
 Olefinic thermoplastic elastomers (OTPEs), 239  
 Organic modification, 85  
 Organoamines, 5  
 Organo-modified sodium montmorillonite clays (o-MMTs), 18
- P**  
 Particle–polymer interaction, 6  
 Payne effect, 43, 112, 140, 198, 202, 207, 231  
 – S-SBR, 199  
 Peroxides, crosslinking, 125, 168, 288  
 – multifunctional, 226  
 Phenolic resins, curatives, 224

- m-Phenylene dimaleimide (MPDM), 229
  - Phyllosilicate, 87
  - Physical blowing agent (PBA), 241
  - Plasma polymerization, 167, 170
  - Plasma-coated fullerene carbon black (PCFS) 208
  - Plasma-coated powders, 186
  - PNCSL2 17
  - Poly( $\epsilon$ -caprolactone) (PCL), 235
    - poly(ethylene oxide), 136
    - poly(propylene oxide), 235
  - Poly(isobutylene-co-para-methylstyrene) BIMS/clay, 5
  - Poly(propylene oxide) (PPO), 235
  - Poly(styrene-ethylene-co-butylene-styrene), 11
  - Poly(vinyl chloride) (PVC), 228
  - Poly(vinylidene fluoride) (PVDF), 235
  - Polyacetylene, 167, 187, 193, 197, 207
  - Polyamide, 124, 237, 257, 260
    - silica, 203
  - Polyester polyurethane (PPU), 61
  - Polyethylene (PE), highly loaded particulate-filled, 232
  - Polyethylene butylene (PEB), 12
  - Polymer blends/alloys, 219
  - Polymer nanocomposites (PNCs), 4
    - lamellar, 8
  - Polyolefin elastomers, 228
  - Polyoligo sesquioxane (POSS), 87
  - Polypropylene (PP), 6, 57
    - EPDM, 6, 220
    - isotactic (iPP), 6
  - Polysulfide elastomer, 58
  - Polytetrafluoroethylene (PTFE), 249
  - Polyurethane (PU), 5
    - elastomer adhesion, 61
    - thermoplastic, 237
  - Polyvinyl alcohol (PVA)/silica hybrid, 7
  - Processing behavior, 20
  - PTh-silica, 186, 203
- Q**
- Quaternary ammonium compound (QUAT), 125
- R**
- Raman spectra, 4
  - Reaction-induced phase separation (RIPS), 234
  - Reactive processing, 219
  - Reinforcement, 85, 233
    - factor, 25
    - fillers, 167
  - Rheological behavior, 20
  - Rubber, 1, 167
    - blends, clay, 135
    - clay, 85, 156
    - curatives, 85
    - LDH, 156
    - nanocomposites, transitions, 38
- S**
- Scanning probe microscopy (SPM), 4
  - Sealings, 252
  - Self-consistent field theory (SCF), 75
  - Sepiolite, 87
  - Silica, nanoparticles, 1, 77
    - plasma-coated, 199
  - Silicates, layered, 15, 27, 41, 51, 87, 94, 128, 149, 164, 239
  - Small angle X-ray scattering (SAXS), 4, 13
  - Sodium montmorillonite clays, 18
  - Squalene vulcanization, 180
  - S-SBR, 167
    - EPDM, 203
  - Stearic acid, 129
  - Strain, 42
  - Stress softening effect, 232
  - Stress-strain, 97, 299
  - Styrene block copolymers (SBCs), 228
  - Styrene butadiene rubber (SBR), 10, 96, 104, 167, 251
    - EPDM, carbon black, 209
  - Styrene ethylene butadiene styrene block copolymer (SEBS), 11, 15, 28, 222, 242
    - clay, 12
  - Styrene-based block copolymer/silicate nanocomposites, 6
  - Styrenic thermoplastic vulcanizates (STPVs) 237
  - Sulfur curing, 18, 27, 95, 125, 137, 167, 180
    - PFHS, 193
    - polyacetylene, 185, 191, 217
    - polyacrylic acid, 193
    - polyperfluorohexane-coated, 192
    - prevulcanization, 37
    - rubber, polyacetylene-coated, 213
    - S-SBR, 213
    - vulcanization, plasma polymerization, 181
  - Super TPVs, 236
  - Surface area factor (SAF), 62
  - Surface modification, 167
  - Surface polarity, 167
  - Swelling, 64
- T**
- Tensile testing, 302
  - Tetraethoxysilane (TEOS), 24
  - Tetrafluoroethylene (TFE), 253
  - Thermoplastic elastomers, 219

Thermoplastic olefins (TEOs), 228  
Thermoplastic polyurethane (TPU), 237  
Thermoplastic vulcanizates (TPVs), 219

- electron beam crosslinked, 243
- foamed, 240
- nanofilled, 238
- oil-extended, 239

*p*-Toluene sulfonyl semicarbazide  
(cellogen-RA), 240  
Tortusity factors, 55  
Triallyl cyanurate (TAC), 225  
Triethyl tetra amine (TETA), 235  
Trimethylol propane trimethacrylate  
(TMPTMA), 228

**V**

Vulcanizates, thermoplastic, 219, 230  
Vulcanization, 18, 167

- electron-induced dynamic, 244
- ingredients, 125

**W**

Water penetration, 185  
Water-releasing chemical compound  
(WCC) 241  
Wear properties, PTFE, 249, 252

**X**

XRD, 11, 117

**Y**

Young's modulus, 64

**Z**

ZDP, 128  
Zinc dimethyl dithiocarbamate  
(ZDMC), 97, 127  
Zinc dithiophosphate, 97  
Zinc oxide (ZnO), 127